Untersuchungen von Metall-organischen Gerüstverbindungen in den Bereichen der Wirt-Gast-Verbindungen und der Katalyse

Inaugural-Dissertation

zur Erlangung des Doktorgrades
der Mathematisch-Naturwissenschaftlichen Fakultät
der Heinrich-Heine-Universität Düsseldorf

vorgelegt von

Marcus Nikolaus Augustinus Fetzer
aus Bonn

Düsseldorf, November 2025

aus dem Institut für Anorganische Chemie und Strukturchemie I – Nanoporöse und nanoskalierte Materialien

der Heinrich-Heine-Universität Düsseldorf

Gedruckt mit der Genehmigung der
Mathematisch-Naturwissenschaftlichen Fakultät der
Heinrich-Heine-Universität Düsseldorf

Berichterstatter:

1. Univ.-Prof. Dr. Christoph Janiak

2. Univ.-Prof. Dr. Christian Ganter

Tag der mündlichen Prüfung: 17.12.2025

Eidesstattliche Erklärung

Ich, Marcus Nikolaus Augustinus Fetzer, versichere an Eides statt, dass die vorliegende Dissertation von mir selbstständig und ohne unzulässige fremde Hilfe unter Beachtung der „Grundsätze zur Sicherung guter wissenschaftlicher Praxis“ an der Heinrich-Heine-Universität Düsseldorf erstellt worden ist. Die aus fremden Quellen direkt oder indirekt übernommenen Inhalte wurden als solche kenntlich gemacht. Die Arbeit wurde bisher weder im Inland noch im Ausland in gleicher oder ähnlicher Form einer anderen Prüfungsbehörde vorgelegt. Es wurden keine früheren erfolglosen Promotionsversuche unternommen.

Düsseldorf, 26.11.2025

Ort, Datum

Unterschrift

Danksagung

Zuallererst bedanke ich mich sehr herzlich bei Herrn Prof. Dr. Christoph Janiak, der mich zu Beginn der Corona-Pandemie in seinen Arbeitskreis aufgenommen und mir dadurch meine Promotion ermöglicht hat. Auch möchte ich mich für die tatkräftige Unterstützung bedanken, die ich besonders gegen Ende meiner Promotion von ihm erhalten habe.

Bei Herrn Prof. Dr. Christian Ganter bedanke ich mich für die Übernahme des Koreferats.

Besonders möchte ich mich bei Herrn Jun.-Prof. Dr. Markus Suta für die überaus hilfreiche Unterstützung bedanken. Sowohl die Zeit, die du dir für meine Probleme genommen hast, als auch die vielen anregenden Gespräche im Bereich der Chemie, aber auch abseits davon, waren sehr wertvoll für mich.

Ein großer Dank gilt auch den Festangestellten Jutta Bourgeois, die mir bei allen organisatorischen Fragen hilfreich zur Seite stand, Marcell Demandt und Annette Ricken, die mich bei allen technischen Fragen so gut es ging unterstützt haben, und besonders bei Birgit Tommes, sowohl für die vielen Hilfestellungen als auch für die vielen unterhaltsamen Stunden. Darüber hinaus danke ich dem gesamten CeMSA@HHU-Team für die zahlreichen Messungen, die es für mich durchgeführt hat.

Des Weiteren möchte ich mich ganz herzlich bei Herrn Dr. István Boldog für die vielen anregenden Unterhaltungen sowohl im Bereich der synthetischen Chemie als auch abseits der Chemie bedanken. Es war mir immer eine Freude, mich mit dir zu treffen und über die unterschiedlichsten Themen zu diskutieren.

Besonders möchte ich mich an dieser Stelle noch bei Herrn Robert Oestreich für die gute Zusammenarbeit und die Unterstützung bei den unterschiedlichen Sorptionsmessungen bedanken. Bei den Herren Takin Haj Hassani Sohi, Daniel Komisarek und Philipp Seiffert bedanke ich mich sehr herzlich für die Hilfe bei Problemen mit den PXRDs und die vielen Einkristalle, die für mich vermessen wurden. Das Gefluche aus eurem Büro wird mir fehlen. Dennis Woschko, Marilyn Kaul und Dustin Jordan danke ich für die schöne Zeit an warmen Tagen außerhalb des Labors ebenso wie Tim Müller, Hanibal Othman, Till Strothmann, Aysenur Limon, Soheil Abdpour, Nabil Assahub und Lukas Eisenhuth für die vielen Hilfestellungen und die schöne Zeit in der Uni. Meinen übrigen und ehemaligen Mitdoktoranden im Arbeitskreis danke ich ganz herzlich für die freundliche Aufnahme in den Arbeitskreis, die sehr hilfreiche Unterstützung bei allen Fragen und das sehr angenehme Miteinander.

Ein besonders großer Dank geht an die Erstbesetzung unseres Büros, das Bärchenbüro, welches aus Christian Jansen, Alex Spieß, Vasily Gvilava und zeitweise Stefanie Bügel besteht. Vielen Dank, dass ihr mich so freundlich und offen aufgenommen habt, mir bei allen fachlichen Fragen mit Rat und Tat zur Seite standet und mir immer wieder meine offensichtlich großen geografischen Lücken bei Geotastic aufgezeigt habt. Es war für mich ein großes Glück, in euer Büro zu kommen. Die Flaggen kann ich bis heute nicht.

Ein weiterer besonderer Dank geht an die zweite Besetzung des Büros, die aus Dietrich Püschel, Annette Vollrath (die beste Masterandin, die ich hatte), Thi Hai Yen Beglau (auch liebevoll Ping Pong genannt) und später Max Vieten bestand. Danke, dass ihr (besonders Ping Pong) oftmals abends noch so lange mit mir in der Uni wart. Danke auch für die vielen schönen Stunden abseits des Labors und die sehr angenehme Zeit, die ich mit euch verbringen durfte.

In beiden Fällen war es mir immer eine Freude, morgens zu euch in die Uni zu kommen und zu sehen, was der Tag so bringt. Ohne euch wäre die Zeit deutlich schwieriger gewesen.

Ein besonders großer Dank geht an Daniel Wunsch, der mir Zeit meines Studiums unterstützend zur Seite stand und ohne den ich es nicht so weit geschafft hätte.

Bei der Familie Josel möchte ich mich sehr für das Interesse an meiner Promotion bedanken. Es ist mir immer eine Freude, abseits der Uni mit jemandem über die Chemie zu reden.

Bei meiner Familie, besonders bei meinen Eltern Albert und Gisela, möchte ich mich sehr für die Unterstützung, das Korrekturlesen diverser Arbeiten und die unendliche Geduld mit mir während meines Studiums bedanken. Ein weiterer Dank geht an meine Geschwister Christopher und Friederike, die mir die Freude an der Chemie vermittelt haben und mir alles über Chemie beigebracht haben, was ich heute weiß.

Abschließend möchte ich mich bei meiner Frau Katharina für die große Geduld mit mir bedanken, wenn ich mal wieder die Zeit im Labor überzogen habe, die Hilfe sowohl beim Anfertigen von Publikationen als auch dieser Arbeit und das Verständnis und ihre Unterstützung in schwierigen Momenten, besonders wenn es mal nicht so lief, wie ich es mir vorgestellt hatte.

Vielen Dank

Wahre Wissenschaft erfindet nichts neu.

Sie beobachtet und versteht,

erklärt und beschreibt,

verbessert und kopiert,

strebt vorwärts und treibt an.

Wissenschaft ist keine Magie, viel mehr noch:

Sie zeigt uns den Zauber der Welt

-von Karl Huberdt Kreis

Inhaltsverzeichnis

Kurzzusammenfassung

Die vorliegende Arbeit umfasst drei Themenschwerpunkte. Ein Teil der Arbeit befasst sich mit der Synthese von MOFs, die Anwendung in unterschiedlichen Katalysen finden. So wurde in der ersten Publikation der Fokus auf die Synthese neuer Präkatalysatoren für die elektrochemische Sauerstoffentwicklungsreaktion (OER) gelegt. Hierfür wurden die zwei halbleitenden Metall-Phosphonat-Gerüste Co_2[1,4-NDPA] und Zn_2[1,4-NDPA] (1,4-NDPAH_4 = 1,4-Naphthalindiphosphonsäure) hergestellt. Besonders das Co_2[1,4-NDPA] erzielte mit einer Tafelsteigung von 43 mV/dec im alkalischen Elektrolyten (1 mol/l KOH) und einer niedrigen Überspannung von 374 mV bei einer Stromdichte von 10 mA/cm^2 sein besonders hohes Potential als Präkatalysator in der OER. In Kombination mit einer Nickelschaum-Elektrode (NF) konnte über einen Zeitraum von 30 Stunden bei einer Stromdichte von 50 mA/cm^2 eine vergleichbare OER-Aktivität zu den heutigen Standardmaterialien Pt/C/RuO_2@NF gemessen werden. Des Weiteren wurde auch die Umwandlung des Co_2[1,4-NDPA]-Präkatalysators in seine aktive Spezies untersucht.

Eine zweite Publikation aus dem Bereich der Katalyse beschäftigt sich mit der Synthese und Anwendung eines Rhodium-basierten Koordinationspolymers in der heterogenen Carben-Transferreaktion. Hierfür wurde im ersten Schritt das Koordinationspolymer synthetisiert und durch unterschiedliche analytische Verfahren wie Zersetzungs-NMR, FT-IR, TGA, DR-UV-Vis-Spektroskopie oder REM gepaart mit EDX charakterisiert. Durch eine Modellreaktion mit Methylphenyldiazoacetat und Styrol wurde die katalytische Aktivität untersucht. Dabei konnte festgestellt werden, dass der Katalysator über sechs Zyklen abgebaut wird und nur noch 30 % der Anfangsmenge zurückgewonnen werden konnte. Zur breiten Anwendung wurden über 25 unterschiedliche Katalysen durchgeführt, wobei hier besonders die Ergebnisse mit Medikamenten oder Naturstoffen interessant sind.

Der zweite Teil dieser Arbeit beschäftigt sich mit dem Bereich der Wirt-Gast-Verbindungen. Hierfür wurde in einer Publikation das Metall-Phosphonat-Gerüst TUB41 ([Cu(4,4´-bpy)$_{0.5}$(1,4-NDPAH_2)]) phasenrein synthetisiert und durch unterschiedliche Verfahren auf seine Stabilität hin untersucht. Durch die Verwendung zweier Linker ergibt sich eine Struktur mit Kanälen von 4 × 2 Å mit hydrophilen und hydrophoben Bereichen in der Kanalstruktur. Dies ermöglicht es TUB41 sowohl CO_2 als auch H_2O aufzunehmen, da sich beide Moleküle an unterschiedlichen Orten in den

Kanälen befinden. Diese räumliche Trennung der beiden Gast-Moleküle in der Struktur wurde auch durch molekulardynamische Berechnungen gestützt. Berechnungen der mittleren quadratischen Verschiebung deuten darauf hin, dass beide Moleküle durch die Porenstruktur stark eingeschränkt sind.

Eine andere Publikation in diesem Bereich beschäftigt sich mit den photophysikalischen Eigenschaften eines säurestabilen Bodipy-Farbstoffs als Gast in unterschiedlichen Zirkonium-MOFs. Hierfür wurde der Farbstoff sowohl post-synthetisch als auch *in situ* in die unterschiedlichen MOFs eingebracht. Alle hergestellten Komposite zeigen dabei eine Lumineszenz im grünen Wellenlängenbereich. Durch die Bestimmung der genauen Beladung konnte für die *in situ* hergestellten Komposite das Verhältnis zwischen nicht beladenen, einfach beladenen und mehrfach beladenen Poren berechnet werden. Eine mehrfache Beladung zeigt dabei eine Änderung in der Emissionsbande. Des Weiteren konnte durch Änderung der MOFs und der damit einhergehenden Porengröße eine längere Lebenszeit festgestellt werden. In Abhängigkeit zum jeweiligen MOF wurden unterschiedliche Quantenausbeuten von bis zu 77 % gemessen.

Der letzte Themenschwerpunkt befasst sich mit der Verwendung von Modulatoren. Hier wurde in einem Review-Artikel anhand unterschiedlicher Literaturquellen der Einfluss von Modulatoren auf MOFs und ihre Anwendung diskutiert. Grundsätzlich lässt sich sagen, dass durch die Verwendung unterschiedlicher Modulatoren die gebildeten MOFs in ihrer Größe, Form, Porosität und Stabilität stark beeinflusst werden. Auch ihre jeweiligen Anwendungen können durch die Verwendung unterschiedlicher Modulatoren gezielt optimiert werden, wodurch mithilfe von Modulatoren ein gezieltes MOF-Design erreicht wird. Dadurch eröffnet sich ein großes Potential für unterschiedliche Anwendungen.

Abstract

This work covers three main topics. One part of the work deals with the synthesis of MOFs that are used in various catalytic applications. The first publication focused on the synthesis of new pre-catalysts for the electrochemical oxygen evolution reaction (OER). For this purpose, the two semiconducting metal phosphonate frameworks Co_2[1,4-NDPA] and Zn_2[1,4-NDPA] (1,4-NDPAH_4 = 1,4-naphthalenediphosphonic acid) were produced. Co_2[1,4-NDPA] achieved its particularly high potential as a pre-catalyst in OER with a slope of 43 mV/dec in alkaline electrolyte (1 mol/l KOH) and a low overpotential of 374 mV at a current density of 10 mA/cm^2. In combination with a nickel foam electrode (NF), OER activity comparable to that of the current standard materials Pt/C/RuO_2@NF was measured over a period of 30 hours at a current density of 50 mA/cm^2. Furthermore, the conversion of the Co_2[1,4-NDPA] pre-catalyst into its active species was also investigated.

A second publication in the field of catalysis deals with the synthesis and application of a rhodium-based coordination polymer in the heterogeneous carbene transfer reaction. For this purpose, the coordination polymer was first synthesized and characterized using various analytical methods such as digestion NMR, FT-IR, TGA, DR-UV-Vis spectroscopy, and SEM paired with EDX. The catalytic activity was investigated using a model reaction with methyl phenyldiazoacetate and styrene. It was found that the catalyst was degraded over six cycles and only 30% of the initial amount could be recovered. For broad application, more than 25 different catalyzes were carried out, with the results with drugs or natural substances being particularly interesting.

The second part of this work deals with the field of host-guest compounds. For this purpose, the metal phosphonate framework TUB41 ([Cu(4,4'-bpy)$_{0.5}$(1,4-NDPAH_2)]) was synthesized in a single phase and its stability was investigated using various methods. The use of two linkers results in a structure with channels of 4 × 2 Å with hydrophilic and hydrophobic areas in the channel structure. This enables TUB41 to absorb both CO_2 and H_2O, as both molecules are located at different places in the channels. This spatial separation of the two guest molecules in the structure was also supported by molecular dynamics calculations. Calculations of the mean-squared displacements indicate that both molecules are strongly restricted by the pore structure.

Another publication in this field deals with the photophysical properties of an acid-stable Bodipy dye as a guest in different zirconium MOFs. For this purpose, the dye was introduced into different MOFs both post-synthetically and in situ. All composites produced exhibit luminescence in the green wavelength range. By determining the exact loading, the ratio between unoccupied, single-occupied, and multiple-occupied pores could be calculated for the composites produced in situ. Multiple occupancy shows a change in the emission band. Furthermore, a longer lifetime was observed by changing the MOFs and the associated pore size. Depending on the respective MOF, different quantum yields of up to 77% were measured.

The last topic focuses on the use of modulators. Here, a review article discussed the influence of modulators on MOFs and their application based on various literature sources. Basically, it can be said that the use of different modulators strongly influences the size, shape, porosity, and stability of the MOFs formed. Their respective applications can also be specifically optimized by using different modulators, which allows for targeted MOF design with the help of modulators. This opens up great potential for different applications.

Publikationsliste

Die vorliegende kumulative Dissertation wurde im Zeitraum von November 2020 bis November 2025 am Institut für Anorganische Chemie und Strukturchemie I – Nanoporöse und nanosaklierte Materialien der Heinrich-Heine-Universität Düsseldorf unter der Aufsicht von Prof. Dr. Christoph Janiak angefertig.

Erstautorschaften:

Thi Hai Yen Beglau[+], Marcus N. A. Fetzer[+], Istvan Boldog, Tobias Heinen, Markus Suta, Christoph Janiak, Gündoğ Yücesan: "Exceptionally Stable And Super-Efficient Electrocatalysts Derived From Semiconducting Metal Phosphonate Frameworks"

Chemistry-a European Journal **2024**, *30*, e202302765.
DOI: 10.1002/chem.202302765

[+]Die Autoren haben zu gleichen Anteilen zu dieser Publikation beigetragen.

Fahime Bigdeli[+], Marcus N. A. Fetzer[+], Berna Nis, Ali Morsali, Christoph Janiak. "Coordination modulation: a way to improve the properties of metal–organic frameworks"

Journal of Materials Chemistry A **2023**, *11*, 22105-22131. DOI: 10.1039/d3ta03077f

[+]Die Autoren haben zu gleichen Anteilen zu dieser Publikation beigetragen.

Claire Empel[+], Marcus N. A. Fetzer[+], Suman Sasmal, Till Strothmann, Christoph Janiak, Rene M. Koenigs: "Unlocking catalytic potential: a rhodium(II)-based coordination polymer for efficient carbene transfer reactions with donor/acceptor diazoalkanes"

Chemical Communications **2024**, *60*, 7327-7330. DOI: 10.1039/d4cc01386g

[+]Die Autoren haben zu gleichen Anteilen zu dieser Publikation beigetragen.

Robert Oestreich[+], Marcus N. A. Fetzer[+], Yifei Zhang, Andreas Schreiber, Alexander Knebel, Markus Suta, Christoph Janiak, Gabriel Hanna, Gündoğ Yücesan: "Stable Ultramicroporous Metal–Organic Framework with Hydrophilic and Hydrophobic Domains for Selective Gas Adsorption"

Angewandte Chemie-International Edition **2025**, *64*, e202513788.
DOI: 10.1002/anie.202513788

[+]Die Autoren haben zu gleichen Anteilen zu dieser Publikation beigetragen.

Marcus N. A. Fetzer, Maximilian Vieten, Aysenur Limon, Christoph Janiak: "Encapsulation of a Highly Acid-Stable Dicyano-Bodipy in Zr-Based Metal–Organic Frameworks with Increased Fluorescence Lifetime and Quantum Yield Within the Solid Solution Concept"

Molecules **2025**, *30*, 4151. DOI. 10.3390/molecules30214151

Co-Autorschaften

Eguekeng Idriss, Sylvain Tome, Tchouateu Kamwa Rolande Aurelie, Achile Nana, Juvenal G. Deutou Nemaleu, Chongouang Judicaël, Alex Spieß, Markus N. A. Fetzer, Christoph Janiak, Marie-Annie Etoh: "Engineering and structural properties of compressed earth blocks (CEB) stabilized with a calcined clay-based alkali-activated binder"
Innovative Infrastructure Solutions **2022**, *7*, 157.

Rolande Aurelie Tchouateu Kamwa, Sylvain Tome, Judicael Chongouang, Idriss Eguekeng, Alex Spieß, Markus N.A. Fetzer, Kamseu Elie, Christoph Janiak, Marie-Annie Etoh: "Stabilization of compressed earth blocks (CEB) by pozzolana based phosphate geopolymer binder: Physico-mechanical and microstructural investigations"
Cleaner Materials **2022**, *4*, 100062.

Dominik Moritz Steinert, Alexa Schmitz, Marcus Fetzer, Philipp Seiffert, Christoph Janiak: "A caveat on the effect of modulators in the synthesis of the aluminum furandicarboxylate metal-organic framework MIL-160"
Zeitschrift für anorganische und allgemeine Chemie **2022**, *648*, e202100380.

Soheil Abdpour, Lars Rademacher, Marcus N. A. Fetzer, Thi Hai Yen Beglau, Christoph Janiak: "Iron-Containing Nickel Cobalt Sulfides, Selenides, and Sulfoselenides as Active and Stable Electrocatalysts for the Oxygen Evolution Reaction in an Alkaline Solution"

Solids **2023**, *4*, 181–200.

René Blaise Ngouateu Lekene, Tobie Matemb Ma Ntep, Marcus N. A. Fetzer, Till Strothmann, Julius Ndi Nsami, Christoph Janiak: "The efficient removal of ibuprofen, caffeine, and bisphenol A using engineered egusi seed shells biochar: adsorption kinetics, equilibrium, thermodynamics, and mechanism"
Environmental Science and Pollution Research **2023**, *30*, 100095–100113.

Jean Yves Sikapi Fouda, Agnes Antoinette Ntoumba, Philippe Belle Ebanda Kedi, Thi Hai Yen Beglau, Marcus Fetzer, Till Strothmann, Tchangou Armel Florian, Sone Enone Bertin, Vandi Deli, Emmanuel Jean Teinkela Mbosso, Gustave Leopold Lehman, Emmanuel Albert Mpondo Mpondo, Gisele Etame Loe, Francois Eya'ane Meva, Christoph Janiak: "Impregnation of textile cotton material with Cymbopogon citratus-mediated silver nanoparticles and investigations by light, electron and hyperspectral microscopies"
Journal of Pharmacognosy and Phytochemistry **2023**,*12(5)*:135-146.

Sherman Lesly Zambou Jiokeng, Tobie J. Matemb Ma Ntep, Marcus N. A. Fetzer, Till Strothmann, Cyrille G. Fotsop, Ignas Kenfack Tonle, Christoph Janiak: "Efficient Electrochemical Lead Detection by a Histidine-Grafted Metal–Organic Framework MOF-808 Electrode Material"
ACS Applied Materials & Interfaces **2024**, *16*, 2, 2509–2521.

Soheil Abdpour, Marcus N. A. Fetzer, Robert Oestreich, Thi Hai Yen Beglau, István Boldog, Christoph Janiak: "Bimetallic CPM-37(Ni,Fe) metal-organic framework: enhanced porosity, stability and tunable composition"
Dalton Transactions. **2024**, *53*, 4937.

Jean Baptiste Hzounda Fokou, Annick Christianne Nsegbe, Beglau Thi Hai Yen, Marcus N. A. Fetzer, Elise Nadia Mbogbe, Maeva Jenna Chameni Nkouankam, Pamela Ngadie Mponge, Marie Tryphene Magaly Ngo Yomkil Baleng, Sylvie Pascale Songue, Chris Rosaire Ninpa Kuissi, Juliette Koube, Bertin Sone Enone, Agnes Antoinette Ntoumba, Francois Eya'ane Meva, Christoph Janiak: "Anti-inflammation Study of Cellulose-Chitosan Biocomposite-Based *Tetrapleura tetraptera* (Taub) Dried Fruits Aqueous Extract"

BioNanoScience **2024**, *14*, 699–709.

Patrice Kenfack Tsobnang, Christelle Ivane Azambou, Roussin Lontio Fomekong, Tobie Junior Matemb Ma Ntep, Marcus N. A. Fetzer, Arnaud Kamdem Tamo, Christoph Janiak: "Structural properties and thermal decomposition of three heteroleptic coordination polymers with oxalate, 2-aminomethylpyridine and metal = Zn^{2+}, Ni^{2+} and Cu^{2+}"

Journal of Solid State Chemistry **2025**, *346*, 125282.

Hanibal Othman, Robert Oestreich, Vivian Küll, Marcus N. A. Fetzer, Christoph Janiak: "Synthesis and Characterization of Covalent Triazine Frameworks Based on 4,4′-(Phenazine-5,10-diyl)dibenzonitrile and Its Application in CO_2/CH_4 Separation"

Molecules **2025**, *30*(15), 3110.

Francois Eya'ane Meva, A. Rita Pereira, Sandrine Elodie Ngnihamye, Armel Florian Tchangou Njiemou, Agnes Antoinette Ntoumba, Jean Baptiste Hzounda Fokou, Thi Hai Yen Beglau, Marcus N. A. Fetzer, Marilyn Kaul, Bianca Schlierf, Ulrich Armel Mintang Fongang, Phillipe Belle Ebanda Kedi, Simone Veronique Fannang, Marietta Herrmann, Christoph Janiak: "Magnesium Hydroxide Nanoneedles Derived from *Anthocleista schweinfurthii* Gilg (Loganiaceae) Support Mesenchymal Stromal Cell Proliferation and Wound Healing"

Journal of Inorganic and Organometallic Polymers and Materials 2025. DOI: 10.1007/s10904-025-03833-1.

Sheta M. Sheta, Said M. El-Sheikh, Mahmoud T. Abo-Elfadl, Ahmed Younis, Mohkles M. Abd-Elzaher, Hanibal Othman, Till Strothmann, Marcus N. A. Fetzer, Istvan Boldog, Christoph Janiak: "Apoptosis-Inducing Fe^{2+}/*β*-Cyclodextrin Supramolecular Nano–Particulate Complex as an Anticancer Drug Platform and Cancer-Diagnostic Tool Prototype"

ChemMedChem **2025**, *0*, e202500665.

Abkürzungsverzeichnis

4,4‘-bpy	4,4‘-Bipyridin
BET	Brunauer-Emmett-Teller
Bspw.	Beispielsweise
Bzw.	Beziehungsweise
CAS	*Chemical Abstracts Service*
CCDC	*Cambridge Crystallographic Data Centre*
COF	*Covalent Organic Frameworks*
DABCO	1,4-Diazabicyclo[2.2.2]octan
DCM	Dichlormethan
DiKTa	Chinolino-[3,2,1-de]acridin-5,9-dion
dt.	deutsch
DUT	*Dresden University of Technology*
EDX	*Energy dispersive X-ray spectroscopy* (dt. Energiedispersive Röntgenspektroskopie)
ee	*enantiomeric excess* (dt. Enantiomerenüberschuss)
engl.	Englisch
et al.	*et alii* (dt. und andere)
FWHM	*Full Width at Half Maximum* (dt. Halbwertsbreite)
Gew. %	Gewichtsprozent
H_2adc	Acetylendicarbonsäure
H_2bdc	Terephthalsäure
H_2bpdc	Biphenyldicarbonsäure
H_2O_2	Wasserstoffperoxid
H_3bbc	1,3,5-Tris(4′-carboxy[1,1′-biphenyl]-4-yl)benzol
H_3btc	Trimesinsäure
H_3tsb	1,3,5-Tris(sulfomethy)benzol

H_4bdp	1,4-Benzildiphosphonsäure
H_4btec	Pyromellitsäure
H_4tbapy	1,3,6,8-Tetrakis(p-benzoesäure)pyren
HbIM	Benzimidazol
HER	*hydrogen evolution reaction* (dt. Wasserstoffentwicklungsreaktion)
HKUST	*Hong Kong University of Science and Technology*
HMIm	2-Methylimidazol
HSAB	*Hard and Soft Acids and Bases* (dt. Harte und weiche Säuren und Basen)
IR	Infrarotspektroskopie
IRMOF	*Isoreticular MOF*
IUPAC	*International Union of Pure and Applied Chemistry*
LAG	*liquid-assisted grindig* (dt. Flüssigkeitsunterstütztes Vermahlen)
MIL	*Matériaux de l'Institut Lavoisier*
MOF	*metal-organic frameworks* (dt. Metall-organische Gerüstverbindungen)
MR-TADF	*multi-resonance thermally activated delayed fluorescence*
NF	*Nickel foam* (dt. Nickelschaum)
NMR	*Nuclear magnetic resonance spectroscopy* (dt. Kernspinresonanz-spektroskopie)
NU	*Northwestern University*
OER	*oxygen evolution reaction* (dt. Sauerstoffentwicklungsreaktion)
OLED	*organic light emitting diode* (dt. organische Leuchtdiode)
PdDt	*Palladium bis(dithiolene)*
PXRD	*Powder X-Ray Diffraction* (dt. Pulverröntgendiffraktometrie)
Ref.	Referenz
REM	Rasterelektronenmikroskopie
RhB	Rhodamin B
rISC	*reverse intersystem crossing*

RT	Raumtemperatur
SBU	*secondary building unit* (dt. sekundäre Baueinheit)
TGA	Thermogravimetrische Analyse
TUB	Technische Universität Berlin
UiO	*Universitetet i Oslo*
UV	Ultraviolett
ZIF	*zeolitic-imidazolate frameworks* (dt. Zeolithische Imidazolat Gerüstverbindungen)

1. Einleitung

1.1 Metall-organische Gerüstverbindungen

Metall-organische Gerüstverbindungen (engl. *metal-organic frameworks*, kurz MOFs) stellen eine Unterkategorie der Koordinationspolymere dar. Nach IUPAC (engl. *International Union of Pure and Applied Chemistry,* deutsch Internationale Union für reine und angewandte Chemie) werden MOFs als „Koordinationsnetzwerke mit organischen Liganden, die potenzielle Hohlräume aufweisen“ definiert.[1] Ihr Grundgerüst besteht dabei aus sich wiederholenden anorganischen und organischen Bausteinen, wodurch sich ihre makroskopische zwei- bzw. dreidimensionale Struktur ausbildet (Abbildung 1).

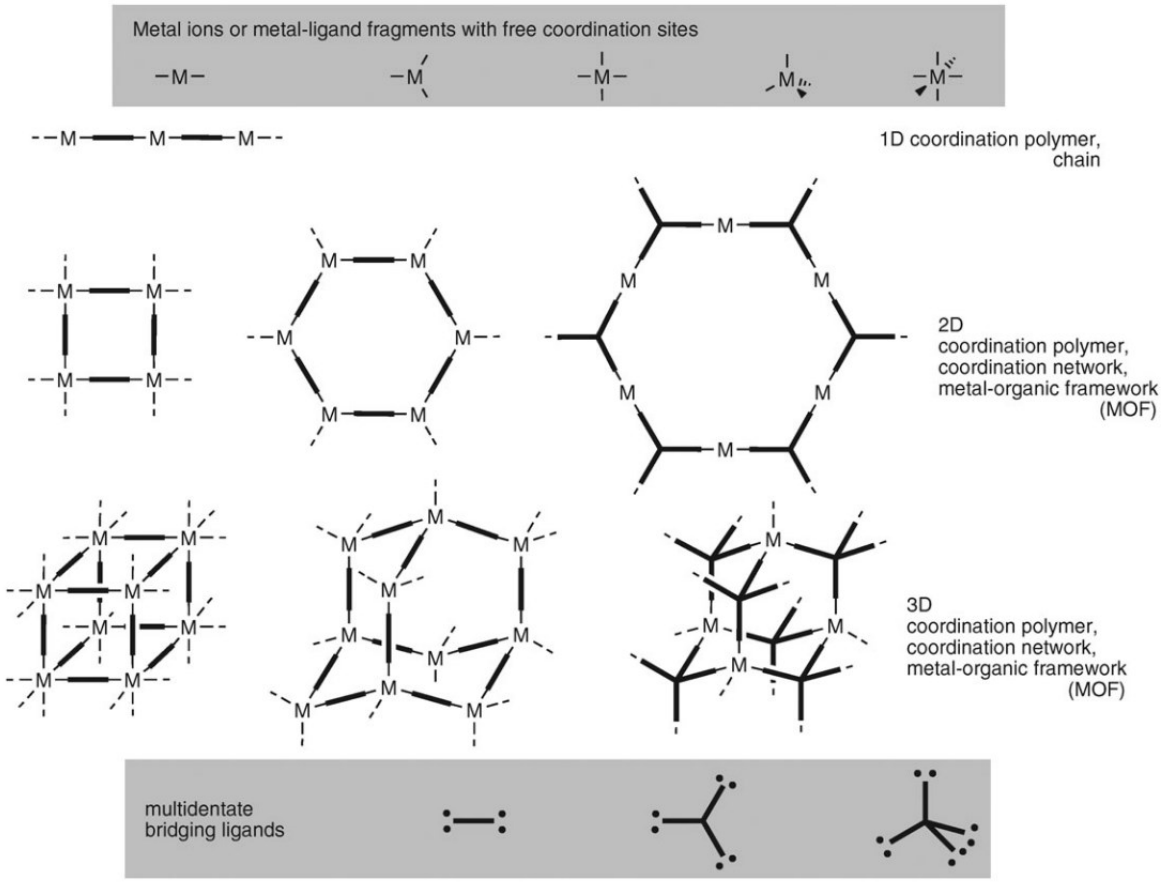

Abbildung 1: *Schematische Darstellung der Strukturbildung von ein- und mehrdimensionalen Verbindungen durch die Verwendung von Metallionen und organisch verbrückenden Liganden. Nachdruck mit Genehmigung von Ref.[2] Copyright 2010, The Royal Society of Chemistry.*

Eine der ältesten und bekanntesten dreidimensionalen Koordinationsverbindungen stellt hier das Pigment Berliner Blau (auch Preußisch Blau) dar, welches aus Fe^{2+}- und Fe^{3+}-Ionen besteht, die durch Cyanidanionen verbrückt sind und somit unendliche dreidimensionale Netzwerke ausbilden. Während die Verbindung erstmalig Anfang des 18. Jahrhunderts gezielt synthetisiert wurde, wurde die Struktur im Laufe des 20. Jahrhunderts durch moderne Untersuchungsmethoden vollständig aufgeklärt.[3] Ein weiterer Meilenstein in der Synthese anorganisch/organischer Hybridverbindungen war die Entdeckung des ersten metallorganischen Komplexes ($K[PtCl_3(C_2H_4)]H_2O$), der von Zeise Anfang des 19. Jahrhunderts synthetisiert und später auch als Zeise-Salz benannt wurde.[4] Diese beiden Verbindungen zeigen den Beginn der modernen Koordinations- und Komplexchemie auf, die bis zur heutigen Zeit reges Interesse weckt und Anwendung in den unterschiedlichsten Bereichen wie der Katalyse oder der OLED-Technik findet.[5]

1989 leisteten Robson und Hoskins mit ihren Arbeiten einen großen Beitrag im Bereich der Koordinationspolymere. Sie synthetisierten erstmals auf Basis rationaler topologischer Designprinzipien dreidimensionale unendliche Netzwerke durch die Verknüpfung von tetraedrischen oder oktaedrischen Zentren über stäbchenförmige organische Verbindungseinheiten. Diese Arbeiten stellen damit die Grundlage der retikulären Chemie dar, welche auf dem Prinzip der Verknüpfung von molekularen Bausteinen durch gerichtete Bindungen basiert.[6] Auf der Grundlage dieses Konzeptes entstanden verschiedene Materialklassen, wozu neben den zeolithischen-imidazolat Gerüstverbindungen (engl. *zeolitic-imidazolate frameworks*, ZIFs) oder den kovalent-organischen Gerüstverbindungen (engl. *covalent organic frameworks*, COFs) auch die Klasse der MOFs zählt.[7] Der Begriff MOF wurde hierbei erstmals 1995 von Yaghi *et al*. sowohl für die Struktur der Verbindung $Cu(4,4'\text{-bpy})_{1.5}\cdot NO_3(H_2O)_{1.25}$ (4,4'-bpy = 4,4'-Bipyridin) als auch für die Struktur der Verbindung $CoC_6H_3(COOH_{1/3})_3(NC_5H_5)_2\cdot 2/3NC_5H_5$ verwendet.[8] Für seine Mühen auf dem Gebiet der metall-organischen Gerüste wurde Omar M. Yaghi zusammen mit Susumu Kitagawa und Richard Robson mit dem Nobelpreis für Chemie 2025 ausgezeichnet.[9]

Eines der bekanntesten und bestuntersuchten MOFs ist das von Yaghi *et al*. 1999 synthetisierte MOF-5.[10] Die Arbeit an MOF-5 und weitere Pionierarbeiten, wie die Synthese von HKUST-1 (*Hong Kong University of Science and Technology*) 1999 von Williams *et al*., MIL-101 (*Matériaux de l'Institut Lavoisier*) 2005 von Férey *et al*. oder

UiO-66 (*Universitetet i Oslo*) 2008 durch die Gruppe von Lillerud *et al*. weckten das wissenschaftliche Interesse im Bereich der MOFs.[11] Dies führte dazu, dass der Bereich der MOFs in den folgenden Jahren ein kontinuierlich wachsendes Forschungsgebiet der Chemie wurde. Dies wird anhand von Abbildung 2, welche die stetig steigende Anzahl an Publikationen pro Jahr zeigt, verdeutlicht.

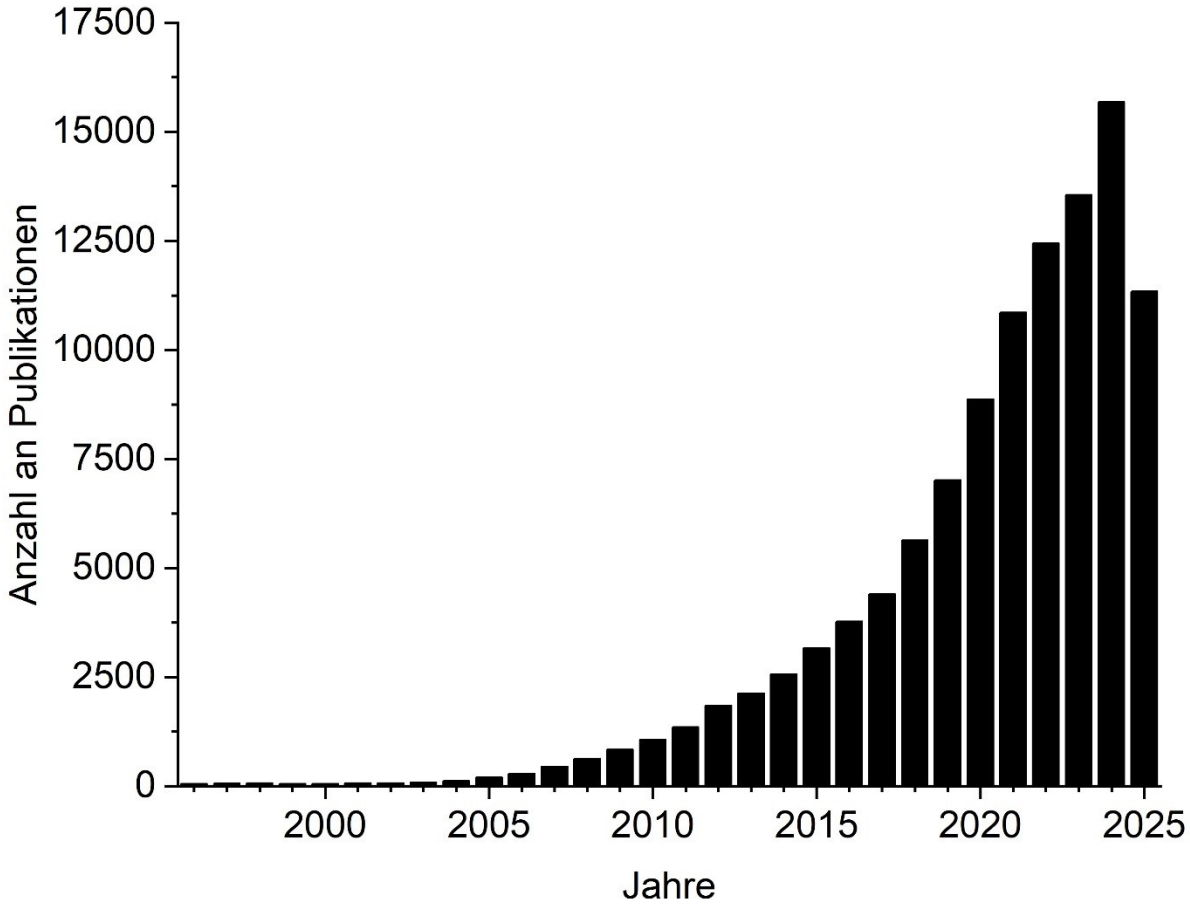

Abbildung 2: *Suchergebnisse zu Veröffentlichungen auf dem Gebiet metall-organischer Gerüstverbindungen im CAS SciFinder® im Zeitraum von 1995 bis 2025. Der Suchbegriff „metal-organic framework“ wurde verwendet und auf Veröffentlichungen in Journalen und Review-Artikeln begrenzt. Durchführung der Suche im August 2025.*[12]

1.2 Aufbau von MOFs

Metall-organische Gerüstverbindungen zeichnen sich als Hybridmaterialien von anorganischen und organischen Bausteinen aus. Die hier verwendeten anorganischen Metallzentren oder -cluster werden als *secondary building unit* (SBU) bezeichnet und bilden Knotenpunkte, die über organische Linker miteinander verbunden sind. Durch diese Verknüpfung bildet sich die für MOFs typische mehrdimensionale Netzstruktur und ihre damit einhergehende Porosität aus.[13] Aufgrund ihrer hohen Vielfalt an SBUs und Linkern sowie ihre vielfältige Art, diese zu kombinieren oder zu modifizieren, setzen sich MOFs dank ihres gezielten Aufbaus von anderen porösen Materialien wie Aktivkohlen, Zeolithen oder Aluminiumsilikaten deutlich ab.[2, 14] SBUs bestehen klassischerweise aus Metall-Oxo-Clustern, die aufgrund ihrer Koordination die Struktur und räumliche Anordnung des Netzwerks wesentlich beeinflussen.[15] Die Struktur der SBU ist dabei stark von den verwendeten Metallkationen abhängig. So bilden beispielsweise Kupferionen, welche als Cu^{2+} vorliegen, mit organischen Säuren wie Terephthalsäure (H_2bdc), welche in der Reaktion deprotoniert als Linkermoleküle fungieren, bevorzugt eine Schaufelrad-Struktur (engl. *paddlewheel*) aus. Dabei ordnen sich vier Linkermoleküle in äquatorialer Position an. Zwei weitere Liganden- oder Linkermoleküle, die sich von den verwendeten organischen Säuren unterscheiden, befinden sich in axialer Position. Dadurch bildet sich im Falle von H_2bdc eine zweidimensionale Schichtstruktur, das CuBDC, aus.[16] Diese Paddlewheelstruktur ist auch in HKUST-1 aufzufinden. Durch die Verwendung von zusätzlichen stickstoffbasierten Linkern wie bspw. 1,4-Diazabicyclo[2.2.2]octan (DABCO) können so im Fall von CuBDC auch dreidimensionale MOF-Strukturen gebildet werden, die als DMOFs bekannt sind.[17] Im Vergleich dazu kann Zink unter Verwendung des Linkers H_2bdc auch eine Schaufelrad-Struktur, die als MOF-2 bekannt ist, ausbilden. Des Weiteren kann durch Anpassung der Syntheseparameter mit dem gleichen Metall-Linker-Paar aus Zink und H_2bdc die bereits zuvor erwähnte MOF-5-Struktur synthetisiert werden, deren SBU aus einem tetrametallischen $Zn_4O(O_2CR)_6$-Cluster besteht, welcher ein μ_4-oxo Zentrum besitzt (siehe Abbildung 3).[10, 18]

Neben der Schaufelrad-Struktur, die bevorzugt von Kupfer, aber auch anderen M^{2+}-Metallen ausgebildet wird, zeigen auch andere Metalle charakteristische SBU-Strukturen. So bilden dreiwertige Metallkationen, insbesondere Cr^{3+} oder Fe^{3+}, bevorzugt trinukleare $M_3O(O_2CR)_6L_3$-Cluster wie in MIL-101(Cr) oder MIL-100(Fe)

aus.[19] Vierwertige Metallkationen wie Ti^{4+}, Zr^{4+} oder Hf^{4+} zeigen in der Regel komplexere, multinukleare und unterschiedlich verbrückte Cluster-Strukturen.[15b, 20] Bekannte Vertreter vierwertiger Metallkationen sind die MOFs UiO-66, MOF-808, NU-1000 oder MIL-125.[11c, 21] Sie alle zeichnen sich durch eine erhöhte Stabilität aus. Eine Übersicht über verschiedene SBUs zeigt Abbildung 3. Die hier gezeigten SBUs geben allerdings nur einen kleinen Ausschnitt aller möglichen SBUs und deren Strukturen wieder.

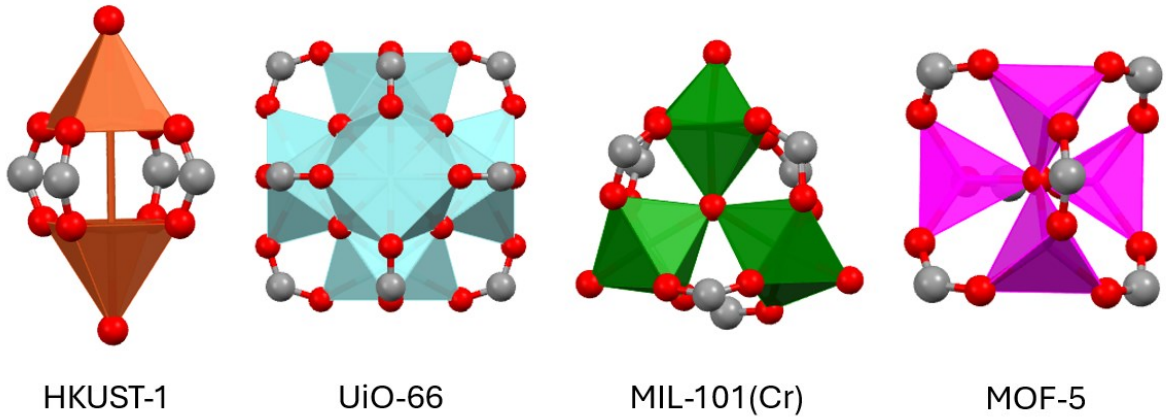

Abbildung 3: *Beispielhafte SBU-Polyeder der MOFs HKUST-1, UiO-66, MIL-101(Cr) und MOF-5. Die Strukturen wurden aus den CCDC hinterlegten cif-Dateien 112954 (HKUST-1),[11a] 752051 (UiO-66),[22] 605510 (MIL-101 (Cr))[23] und 256965 (MOF-5)[10] erstellt.*

Als alternative Bausteine zu den voneinander separierten SBU-Clustern, welche in der Regel aus Metall-Oxo-Verbindungen bestehen, sind auch kettenförmige lineare bzw. quasi-lineare Anordnungen für verschiedene Metalle bekannt. Häufig wird diese Art von MOFs durch dreiwertige Metallionen gebildet, wobei sie sich über unendliche *cis*- und *trans*-μ-OH verbrückte Sauerstoff-Metall-Bindungen aufbauen.[15c, 24] Das wahrscheinlich bekannteste Beispiel für diese Gruppe von MOFs ist MIL-53, das aus *trans*-μ-OH verbrückten AlO_6-Oktaedern besteht und in Abbildung 4 dargestellt ist.[25] MIL-53 ist bekannt für seine unterschiedlichen kleinporigen (np) und großporigen (lp) Strukturen. Im Falle von Zink ist in der Literatur eine bemerkenswerte strukturelle Vielfalt an MOFs dokumentiert.[10, 18, 26] Neben den bereits oben erwähnten „klassischen“ Strukturen, die durch Carbonsäuren gebildet werden können, existieren auch Verbindungen, die auf Stickstoff als koordinierendem Element basieren. Die so genannten zeolithischen Imidazolat-Gerüstverbindungen (ZIF) unterscheiden sich in

ihrer SBU grundlegend von den Carboxylat-basierenden MOFs. Sie bestehen aus mononuklearen, tetraedrischen Einheiten des Bindungstyps $Zn(NR)_4$. Eines der bekanntesten Beispiele dieser Verbindungklasse ist ZIF-8. In dessen Struktur werden die einzelnen tetraedrischen Zentren durch die beiden Stickstoffatome des Imidazols verbrückt. Die dadurch entstandene poröse Struktur, die in Abbildung 4 dargestellt ist, weist im Verhältnis zum Porendurchmesser (11,6 Å) sehr kleine Porenöffnungen (3,4 Å) auf.[27]

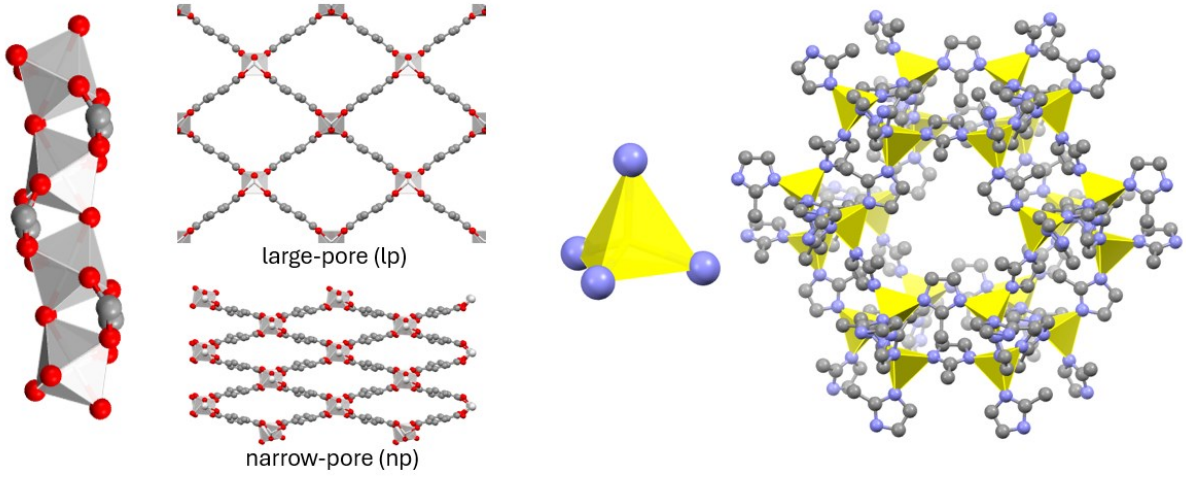

Abbildung 4: *MIL-53 SBU und ZIF-8 SBU jeweils mit Abbildungen der Poren. Die Strukturen wurden aus den CCDC hinterlegten cif-Dateien 220475-220477 (MIL-53)[25] und 1429243 (ZIF-8)[28] erstellt.*

Neben der großen Anzahl an unterschiedlichen SBUs wird die Morphologie eines MOFs in gleichem Maße durch die vielseitigen Strukturen der eingesetzten Linker bestimmt. Die entscheidendste Grundvoraussetzung an ein Linkermolekül ist dessen Mehrzähnigkeit, da ohne diese Eigenschaft eine Verbrückung der einzelnen SBUs nicht möglich wäre. Die hierbei benötigten funktionellen Gruppen, die an die SBUs binden, können sowohl Carboxylat- als auch Stickstoff-, Sulfonat-[29] oder Phosphonatbasiert[30] sein, wobei der überwiegende Teil aller MOFs durch Carboxylat-Linker synthetisiert wird. Neben den verschiedenen funktionellen Gruppen, die als Linker in der MOF-Synthese Anwendung finden, spielt aber auch deren Symmetrie, Größe und Zähnigkeit eine entscheidende Rolle. Die einfachste Struktur eines MOF-Linkers ist ein bidentater linearer Aufbau, wie bei der Acetylendicarbonsäure (H_2adc) oder der bereits erwähnten Terephthalsäure (H_2bdc).[19a, 31] Weitere mehrzähnige

Linker sind beispielsweise Trimesinsäure (H_3btc), die einen tridentaten Linker darstellt und in der Synthese von HKUST-1 oder MOF-808 verwendet wird.[11a, 32] Als tetradentate Linker sind hier Pyromellitsäure (H_4btec) oder 1,3,6,8-Tetrakis(*p*-benzoesäure)pyren (H_4tbapy) als Beispiele nennenswert. Sie werden in den Synthesen von MIL-120 und NU-1000 verwendet.[21b, 33] Einige literaturbekannte Vertreter unterschiedlicher Linkermoleküle sind in Abbildung 5 gezeigt.

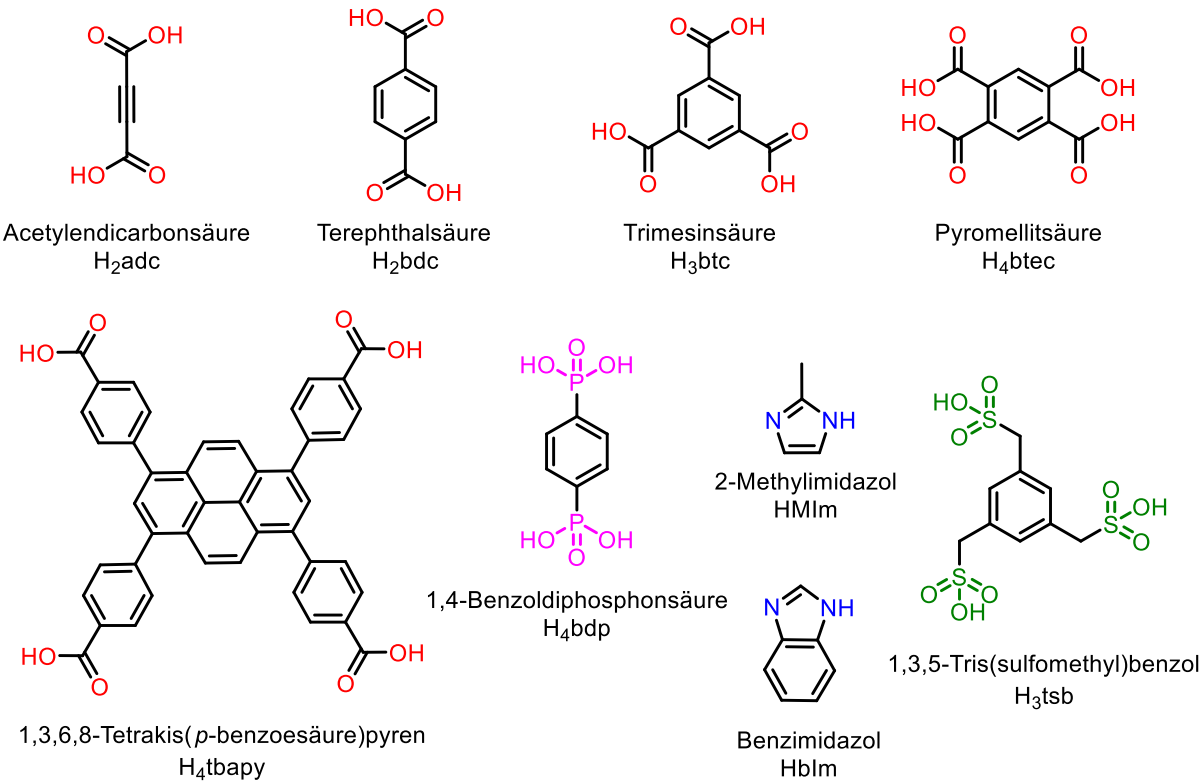

Abbildung 5: *Eine Auswahl literaturbekannter Linker, die in den Synthesen unterschiedlichster MOFs Anwendung finden. Die verbrückenden Einheiten wurden des Verständnisses halber in unterschiedlichen Farben dargestellt. Rot: Carbonsäuren, rosa: Phosphonsäuren, blau: Stickstoffeinheiten, grün: Sulfonsäuren.*

Durch eine Vergrößerung der verwendeten Linker können isoretikuläre MOF-Strukturen synthetisiert werden. Die Strategie der isoretikulären Strukturen konnte 2002 von Yaghi für die Synthese der IRMOF-Serie gezeigt werden. Ausgehend von der bereits bekannten Struktur des MOF-5 (IRMOF-1) konnten so zahlreiche neue MOFs durch Variation an linearen Linkern hergestellt werden. Dabei bleibt die SBU und damit die grundlegende Topologie erhalten. Abbildung 6 zeigt einige Beispiele der von Yaghi beschriebenen IRMOF-Serie. So konnten durch die Variation der Linker gezielt sowohl das freie Volumen als auch die Kristalldichte der synthetisierten MOFs

angepasst werden.[34] Es wurde allerdings auch beobachtet, dass mit zunehmender Linkergröße von isoretikulären MOFs eine erhöhte strukturelle Instabilität der resultierenden Netzwerke auftritt. Diese Instabilität manifestiert sich insbesondere in einer gesteigerten Tendenz zum Kollabieren des hergestellten Gerüstes.[35] Parallel dazu nimmt die Wahrscheinlichkeit der Ausbildung interpenetrierter Strukturen zu, da das durch längere Linker generierte größere Porenvolumen die gegenseitige Durchdringung mehrerer Gerüststrukturen energetisch begünstigt.[36]

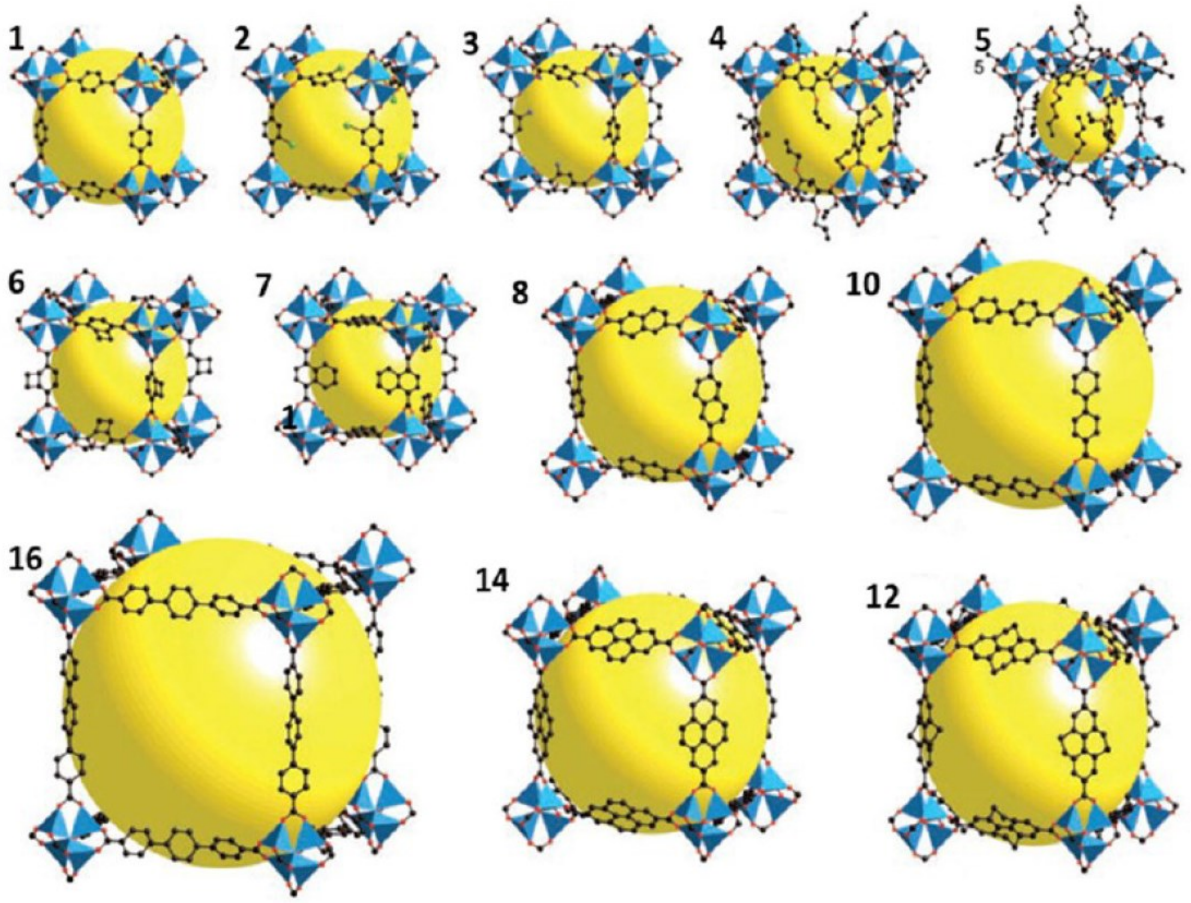

Abbildung 6: *Darstellung unterschiedlicher nicht interpenetrierter IRMOFs. Nachdruck mit Genehmigung von Ref.[37] Copyright 2019 American Chemical Society.*

Abseits der auf Zink basierten IRMOFs sind weitere gut untersuchte Beispiele für isoretikuläre Strukturen sowohl für UiO-66 (H_2bdc) als auch für HKUST-1 (H_3btc) bekannt. Mit zunehmender Linkergröße, die durch das Einfügen von weiteren Benzol-Einheiten in die Linkerstruktur erfolgt, können so die MOFs UiO-67 (H_2bpdc = Biphenyl-4,4′-dicarbonsäure) bezogen auf UiO-66 und MOF-399 (H_3bbc = 1,3,5-Tris(4′-carboxy[1,1′-biphenyl]-4-yl)benzol) bezogen auf HKUST-1 hergestellt werden. Dabei behalten beide MOF-Strukturen dieselbe Topologie, nehmen aber sowohl im

Porendurchmesser als auch in ihren BET-Oberflächen (*Brunauer-Emmett-Teller*) stark zu.[38] Abbildung 7 zeigt beide isoretikulären Strukturen mit den entsprechenden Linkern.

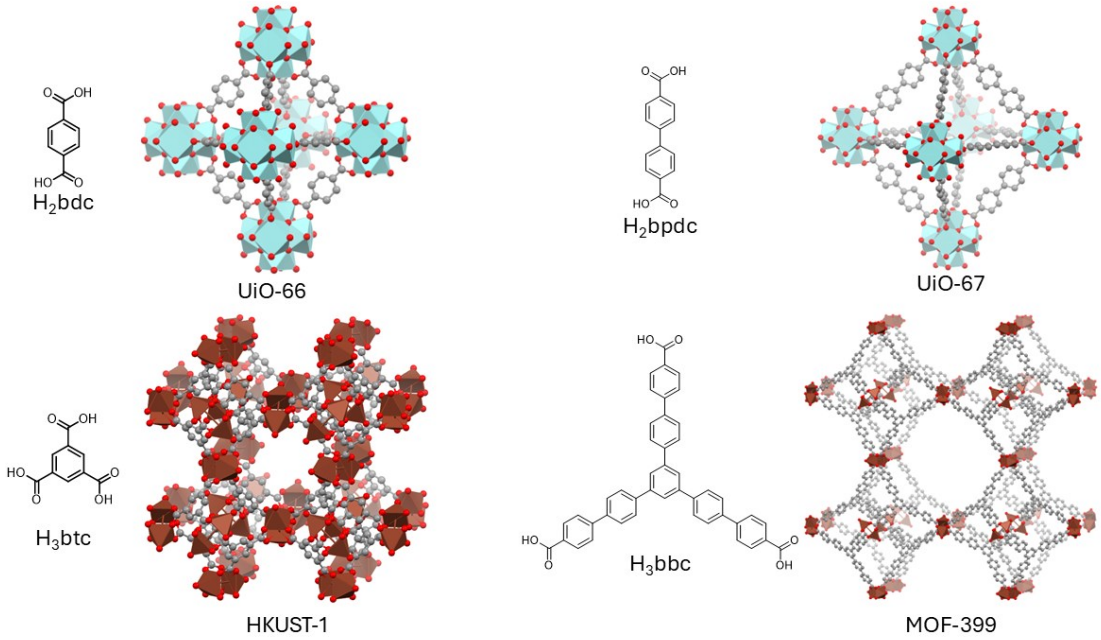

Abbildung 7: *Darstellung der verwendeten organischen Linker und der sich ergebenden isoretikulären Einkristallstrukturen. Die Strukturen wurden aus den CCDC hinterlegten cif-files 752051 (UiO-66),[22] 960486 (UiO-67),[39] 112954 (HKUST-1)[11a] und 780452 (MOF-399)[38b] erstellt.*

Neben der Linkergröße wird die Stabilität der sich bildenden MOFs besonders unter Zuhilfenahme des HSAB-Konzepts (*hard and soft acids and bases,* dt. harte und weiche Säuren und Basen) erklärt. Die Härte wird dabei sowohl von der Ladung als auch von der Größe der Ionen beeinflusst. So zeigt sich, dass weiche Lewis-Basen wie beispielsweise Imidazolate als Linker mit weichen, wenig hochgeladenen Metallen als Lewis-Säuren wie beispielsweise Zn^{2+} oder Co^{2+} stabile Strukturen ausbilden. Die Kombination von harten Linkern und weichen Metallen dagegen zeigt eine weitaus weniger hohe Beständigkeit gegenüber äußeren Einflüssen. Dies wird anhand der Beispiele HKUST-1 und MOF-5 deutlich. Sie kombinieren Carboxylat-Linker als harte Lewis-Base mit den im Vergleich dazu eher weichen Lewis-Säuren Cu^{2+} (HKUST-1) bzw. Zn^{2+} (MOF-5). Die daraus resultierenden MOFs weisen eine geringe Stabilität auf und können daher schon durch Luftfeuchtigkeit zersetzt werden.[40] Im Vergleich dazu zeigen harte Metalle wie Zr^{4+} bzw. Cr^{3+} in Kombination mit Carboxylaten eine

besonders hohe Stabilität. Als Beispiel sollen hier die MOFs UiO-66 und MIL-101 (Cr) genannt werden, die eine äußerst hohe Beständigkeit sowohl über einen breiten pH-Bereich als auch gegenüber verschiedenen Lösungsmitteln zeigen.[41] Abbildung 8 stellt beispielhaft einige Metallkationen und organische Linker unter Berücksichtigung des HSAB-Konzeptes dar. Die Grenzen zwischen harten und weichen Säuren und Basen sind allerdings fließend, was eine eindeutige Zuordnung von Metallen und Linkern erschwert.

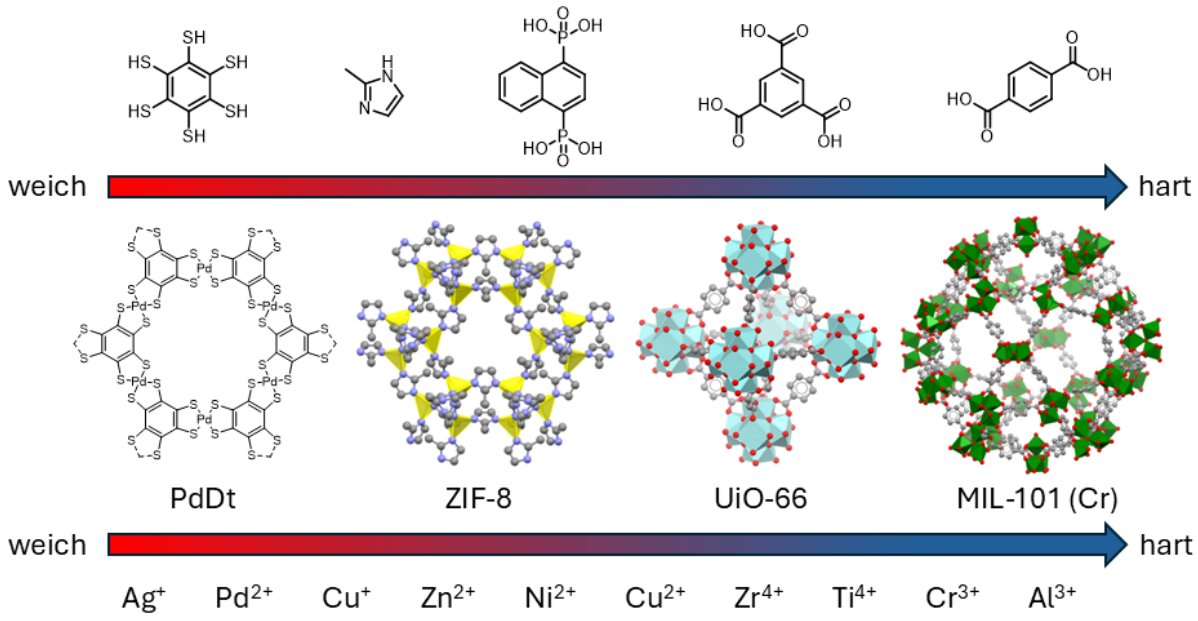

Abbildung 8: *Zuordnung einiger Metallionen und Linker unter Berücksichtigung des HASB-Konzeptes und sich daraus ergebende MOF-Strukturen. Die Strukturen wurden aus den CCDC hinterlegten cif-Dateien 1429243 (ZIF-8),[28] 752051 (UiO-66)[22] und 605510 (MIL-101 (Cr))[23] erstellt. Im Falle von PdDt[42] hingegen wurde die Struktur gezeichnet.*

Um die gewünschten Strukturen und Eigenschaften der gewünschten MOFs gezielt zu erhalten, spielen neben den verwendeten Metallclustern bzw. Metallzentren und organischen Linkern sowohl die jeweiligen Synthesebedingungen als auch die Zugabe von Hilfsmitteln wie Modulatoren eine entscheidende Rolle. Die hierbei am häufigsten verwendete Synthesemethode ist die Solvo- bzw. Hydrothermalsynthese. Die eingesetzten Edukte werden dabei unter erhöhtem Druck und erhöhter Temperatur zur Reaktion gebracht. Die dadurch verbesserte Löslichkeit der verwendeten Edukte begünstigt die Bildung der gewünschten MOFs. Neben dem klassischen Ansatz, der

Solvothermalsynthese, sind heutzutage eine Vielzahl unterschiedlicher Synthesemethoden bekannt. Einen Überblick über die unterschiedlichen Methoden soll Abbildung 9 geben.

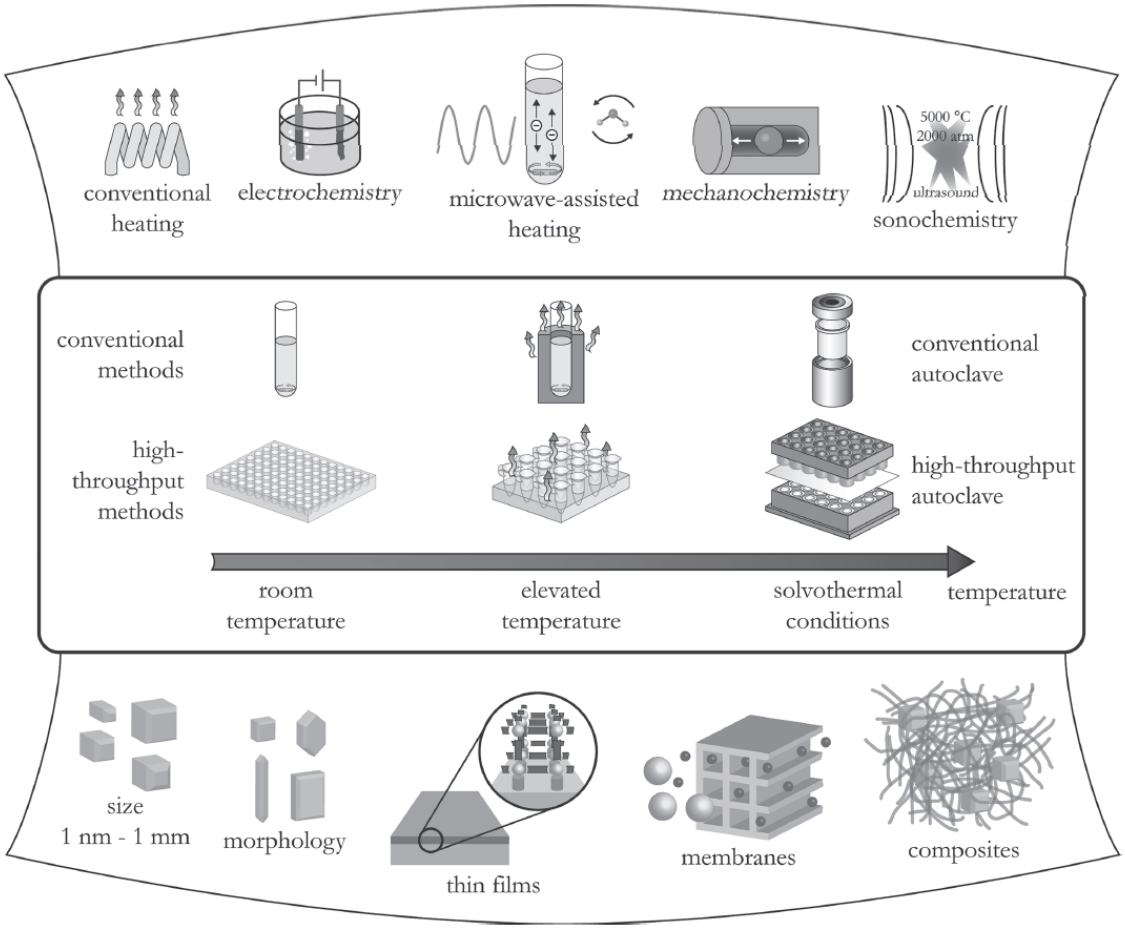

Abbildung 9: *Auszug möglicher bekannter Synthesemethoden, -bedingungen und Reaktionsprodukten. Nachdruck mit Genehmigung von Ref.[43] Copyright 2012 American Chemical Society.*

Eines der Hauptziele dieser neuen Synthesemethoden liegt in der Minimierung von Energieverbrauch, Kosten und der Reduzierung bzw. Vermeidung gefährlicher Substanzen. Hierbei zeigen alle Methoden ihre jeweiligen Vor- und Nachteile. So führen beispielsweise mikrowellenunterstützte oder mechanochemische Synthesen zu einer geringeren Reaktionszeit, guter Skalierbarkeit und einem geringeren Bedarf an Lösungsmittel, benötigen allerdings auch spezielles Equipment und zeigen deutliche Probleme bei der Kontrolle von Morphologie und Partikelgröße.[44]

Neben der Synthesemethode nehmen die bereits erwähnten Modulatoren einen besonders großen Einfluss auf die MOF-Synthesen. In der Regel handelt es sich dabei

um Monocarbonsäuren oder Salz- bzw. Flusssäure. Während Monocarbonsäuren in direkter Konkurrenz zu den verwendeten Linkern stehen und dadurch eine Kristallisation verlangsamen, zeigt Salzsäure besonders in der Synthese der UiO-MOFs eine deutliche Beschleunigung der MOF-Bildung.[38a, 45] Durch die Verwendung solcher Modulatoren kann es zum Einbau von Defektstellen kommen. Hierbei unterscheidet man zwischen Linker- und Clusterdefekten, also dem Verlust einzelner Linkermoleküle im Gitter oder der Abwesenheit ganzer Metallcluster in der Gitterstruktur (siehe Abbildung 10).

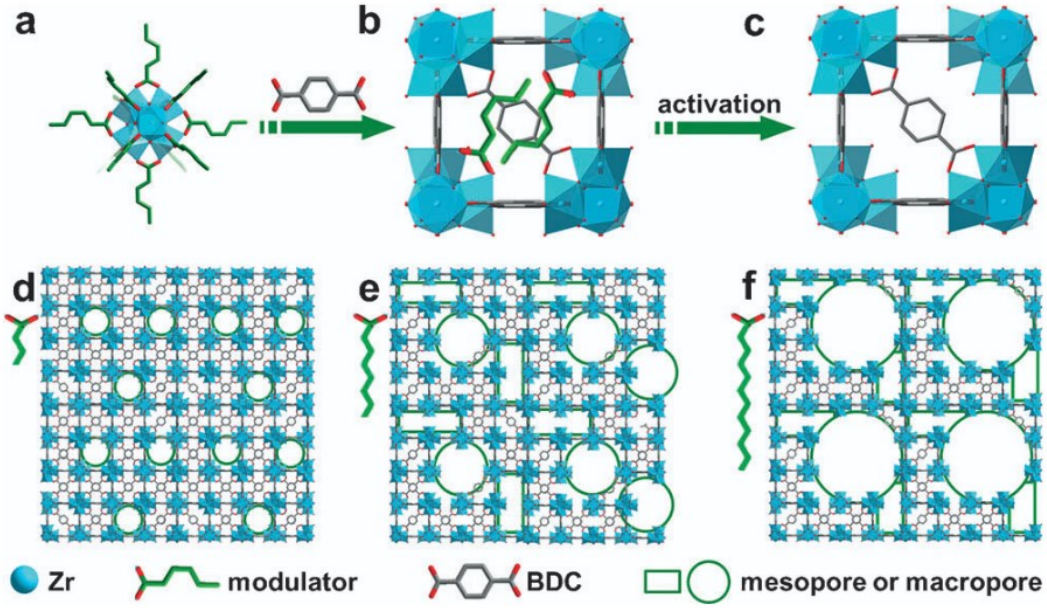

Abbildung 10: *Darstellung von Linker- und Clusterdefekten in Abhängigkeit zu den verwendeten Modulatoren. a-c beschreibt die Synthese eines defekten MOFs. d-f zeigt unterschiedliche Porengrößen, die durch Defekte erzeugt werden. Nachdruck mit Genehmigung von Ref.[46] Copyright 2017, Wiley-VCH Verlag GmbH & Co. KGaA, Weinheim.*

Dies kann sowohl die Oberfläche als auch das Porenvolumen der hergestellten MOFs maßgeblich beeinflussen.[47]

Abgesehen von der Porosität beeinflussen Modulatoren auch in weiteren Bereichen der MOF-Synthese maßgeblich die Eigenschaften des Materials. Durch die Verwendung unterschiedlicher Modulatoren lässt sich beispielsweise auch die Partikelgröße oder Morphologie beeinflussen. Eines der beeindruckendsten Beispiele für eine veränderte Morphologie wurde von Liu *et al.* publiziert.[48] Sie zeigten, dass

durch die Zugabe von *p*-Toluylsäure als Modulator mit zunehmender Menge die Morphologie des MOFs NENU-3a erfolgreich von oktaedrisch zu kubisch bei konstanter Temperatur geändert werden konnte (siehe Abbildung 11).

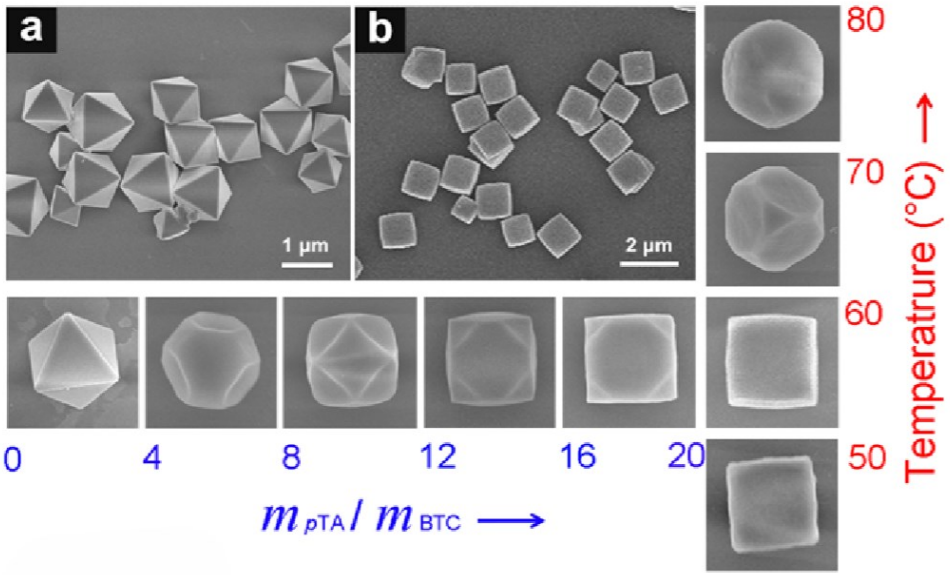

Abbildung 11: *a) und b) zeigen die Morphologieänderung in Abhängigkeit von der verwendeten Menge an Modulator bei gleichbleibender Temperatur. Nachdruck mit Genehmigung von Ref.[48] Copyright 2015 American Chemical Society.*

Diese Beobachtung konnte dadurch erklärt werden, dass der verwendete Modulator bevorzugt mit einer der im MOF vorhandenen Facetten in Wechselwirkung tritt. Dadurch ändert sich die Wachstumsrate der jeweiligen Facetten und mit ihr die Morphologie der entstehenden MOF-Partikel. Oberhalb von 50 °C wird eine weitere Änderung der Morphologie deutlich, nämlich die hin zu kugelförmigen Partikeln.

Diese Beispiele zeigen, welchen bedeutenden Einfluss Modulatoren und Synthesemethoden auf die erhaltenen MOF-Strukturen und deren Eigenschaften besitzen.

1.3 Phosphonat-MOFs

Wie bereits erwähnt stellen Phosphonat-MOFs eine besondere Form der MOFs dar. Die hierbei verwendeten organischen Linker besitzen Phosphonsäuregruppen, die auf unterschiedliche Weise an die vorhandenen Metallzentren binden können. Hierbei hat auch der pH-Wert einen deutlichen Einfluss auf die sich bildenden Strukturen. In Abhängigkeit vom Deprotonierungsgrad der verwendeten Phosphonsäuren können sie als ein- oder zweiwertige Linkermoleküle auftreten, wodurch es zu unterschiedlichen Bindungssituationen kommt. Dadurch ergibt sich eine Vielzahl von möglichen Strukturen, die durch die jeweiligen Bindungssituationen an den Metallzentren bestimmt werden.[49] Diese Eigenschaft erschwert eine Vorhersage ihrer Koordinationschemie. In Abbildung 12 sind die unterschiedlichen Bindungssituationen schematisch dargestellt.

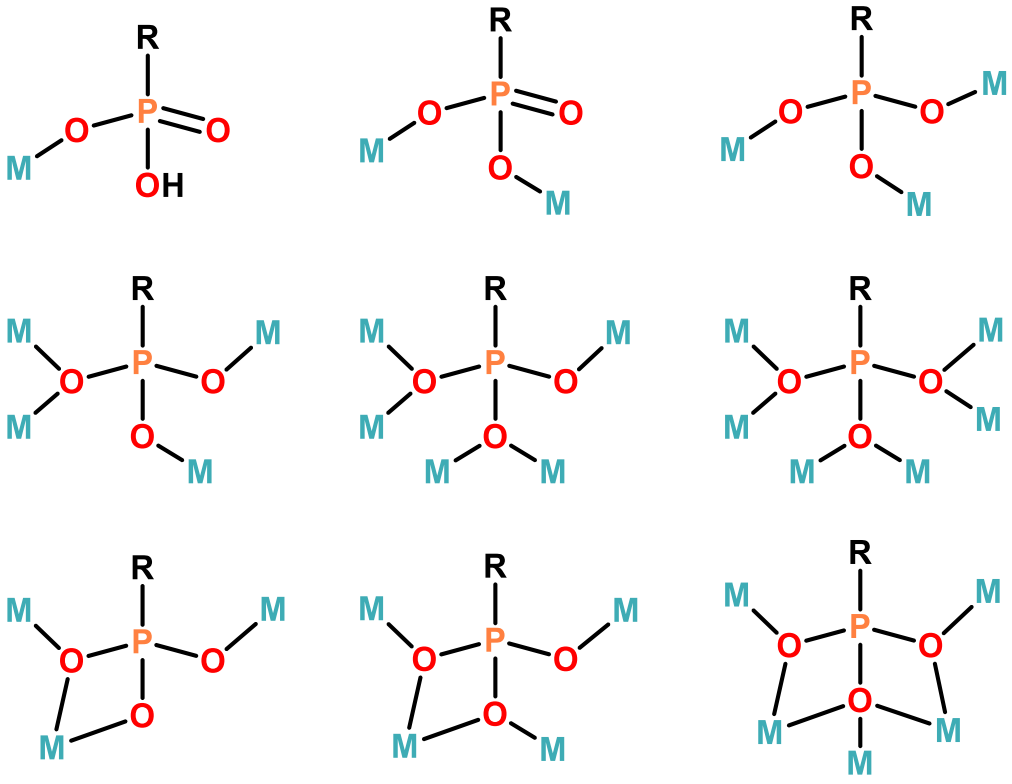

Abbildung 12: *Verschiede Bindungssituationen zwischen Phosphonatlinkern und Metallzentren. Die Verbindungen wurden in Anlehnung an D. Sahoo et al. gezeichnet.*[49]

Die Synthese poröser Gerüststrukturen auf Phosphonatbasis wird allgemein, im Vergleich zu Carboxylat-MOFs, als große Herausforderung gesehen. Hierbei spielt nicht nur die zunehmend schlechtere Löslichkeit der verwendeten Linker mit

steigender Anzahl an Phosphonsäuregruppen eine entscheidende Rolle, sondern auch die starken Phosphonat-Metallbindungen, die eine Reversibilität der Bindungen unterdrücken. Diese Irreversibilität führt zur schnellen Bildung von amorphen und wenig- bis nichtporösen Materialien, welche häufig nur sehr schwierig strukturell charakterisiert werden können.[50]

Trotz dieser Schwierigkeiten sind diverse Phosphonat-MOFs heutzutage bekannt. Die große Vielfalt setzt sich dabei sowohl durch eine hohe Anzahl verschiedener Linker als auch durch eine große Vielfalt der verwendeten Metalle zusammen. So sind sowohl Phosphonat-MOFs mit Übergangsmetallen wie beispielsweise Kupfer,[51] Nickel[52] oder Zirkonium[53] bekannt als auch Lanthanoide wie Lanthan,[54] Gadolinium oder Terbium[55] und Hauptgruppen-Elementen wie Strontium,[56] Aluminium[57] oder Indium[50a].

Abseits ihrer im Vergleich zu Carboxylat-MOFs schwierigen Synthesen besitzen Phosphonat-MOFs auch viele Vorteile, die sie zu einem interessanten Forschungsfeld machen. Dank ihrer starken Metall-Phosphonat-Bindung besitzen sie eine besonders große Stabilität gegenüber äußeren Einflüssen wie Hitze, Feuchtigkeit oder in pH-Bereichen, in welchen die meisten Carboxylat-MOFs an ihre Grenzen kommen. Diese Eigenschaften machen sie zu vielversprechenden Kandidaten für Anwendungen in anspruchsvollen Umgebungen. Durch ihre hohe Vielzahl an möglichen Phosphonatlinkern und ihre Kombinationsfähigkeit mit verschiedenen Metallen können auch Phosphonat-MOFs, ähnlich wie Carboxylat-MOFs, auf ihre jeweilige Anwendung hin optimiert werden. Ihre unterschiedlichen Anwendungs- bzw. Forschungsbereiche sind vielfältig und umfassen dabei unter anderem die Bereiche der Adsorption,[58] Katalyse,[59] Ionen- und Protonenleitfähigkeit, Magnetismus[60] oder der Photolumineszenz.[61]

Ein Beispiel für die Forschung und mögliche Anwendung im Bereich der Ionenleiter lieferten Zhang *et al.* durch die Synthese neuer Festkörper-Ionenleiter auf Basis von Phosphonat-MOFs. Sie verwendeten dafür als Linker 2,5-Dihydroxy-1,4-benzoldiphosphonsäure in Gegenwart eine Zink-Salzes. Das so erhaltene MOF konnte mittels Lithium- oder Natriumalkoholat deprotoniert und für die Ionenleitfähigkeit aktiviert werden.[62] Diese Ergebnisse könnten zu neuen interessanten Ansätzen in der Batterieentwicklung führen. Auch im Bereich der Photolumineszenz konnten durch Phosphonat-MOFs interessante Ergebnisse erzielt werden. So konnten Huang *et al.*

nicht nur ein lumineszierendes Phosphonat-MOF synthetisieren, sondern auch zeigen, dass durch Erhitzung oder Bestrahlung mit UV-Licht sowohl eine strukturelle Änderung als auch eine Änderung in der Lumineszenz induziert werden kann.[63] Dieser reversible Effekt zeigt großes Potenzial im Bereich der Datenspeicherung.

Zusammenfassend lässt sich sagen, dass Phosphonat-MOFs ein interessantes Forschungsgebiet darstellen. Ihre außergewöhnliche chemische und thermische Stabilität ermöglicht neuartige, für Anwendungen optimierte Materialien. Besonders in Bereichen mit hohen Temperaturen, hoher Feuchtigkeit oder stark variierenden pH-Werten zeigen Phosphonat-MOFs ihr volles Potenzial. Gleichzeitig gilt es zwischen den jeweiligen Anwendungsbereichen und den Herausforderungen bei der Entwicklung von Phosphonat-MOFs abzuwägen. Hohe Herstellungskosten, geringe Skalierbarkeit und ein hoher Material- und Syntheseaufwand stellen limitierende Faktoren für eine großtechnische Anwendung von Phosphonat-MOFs dar.

1.4 Anwendung von MOFs

Aufgrund ihrer hohen Porosität, ihrer Stabilität und ihrer strukturellen Flexibilität sind MOFs vielversprechende Materialien in unterschiedlichen potenziellen Anwendungsbereichen. Die dabei am häufigsten untersuchten Gebiete befassen sich aufgrund der besonders hohen Porosität mit der Gassorption, der Gasspeicherung und der Gastrennung.[64] Weitere interessante Anwendungsgebiete sind in Abbildung 13 exemplarisch dargestellt.

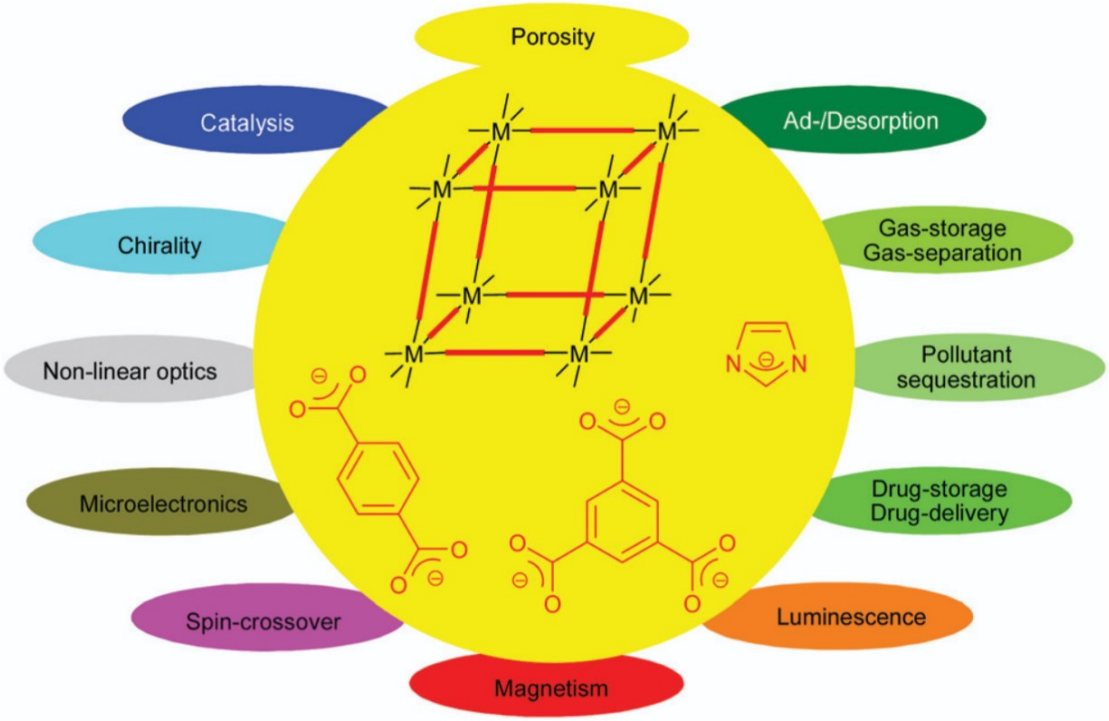

Abbildung 13: *Schematische Darstellung eines MOFs und unterschiedlicher Linker sowie interessante Eigenschaften und beispielhafte Anwendungsgebiete von MOFs. Nachdruck mit Genehmigung von Ref.[65] Copyright 2012 The Royal Society of Chemistry.*

Im Bereich der Wirkstoff- bzw. Medikamentenbeladung und des Medikamententransports liegt der Hauptfokus auf der Entwicklung neuer Medikament-Komposite, welche die verwendeten Wirkstoffe in Ihrem Wirkungsgrad erheblich steigern sollen. So zeigten Soltani *et al.*, dass durch die Einlagerung von Chloramphenicol in ZIF-8 ein Komposit hergestellt werden konnte, welches in simulierten infizierten Umgebungen einen schnelleren und besseren Wirkungsgrad als

reines Chloramphenicol erzielen konnte.[66] Im Bereich der Krebstherapie haben beispielsweise Zhang *et al.* den Wirkstoff Doxorubicin in eine auf Gadolinium und Ytterbium basierende MOF-Matrix eingebettet.[67] Diese konnten Sie mittels Verwendung von Glucose erfolgreich verschließen, wodurch eine ungewünschte Freisetzung auf dem Weg zur Tumorzelle verhindert werden konnte. Des Weiteren konnte die Biokompatibilität durch die Beschichtung mit Glucose gesteigert werden. Neben den Erfolgen in der Krebstherapie konnten durch die Verwendung der hergestellten Komposite auch die bildgebenden Verfahren wie MRT und CT herangezogen werden. Diese zwei Beispiele sollen hier nur einen sehr kleinen Ausblick auf das Forschungsgebiet der Medikamentenanwendung geben. Eine umfassende Beschreibung dieses Forschungsbereiches ist in diesem Rahmen allerding nicht möglich. Tiefer soll hier auf die Bereiche Katalyse und Lumineszenz eingegangen werden.

1.4.1 Katalyse

MOFs zeigen großes Potenzial im Bereich der heterogenen Katalyse. Je nach verwendetem Metall, Synthesemethode und der Zuhilfenahme von Modulatoren oder anderen Hilfsmitteln können Sie gezielt für unterschiedliche Katalysen optimiert werden. So können durch die Verwendung von Modulatoren Linkerdefekte entstehen, die zu offenen Koordinationsstellen an den Metallclustern führen. Diese freien Koordinationsstellen bilden die katalytisch aktiven Zentren in diesen MOF-Strukturen. Dadurch können unterschiedlichste Reaktionen wie beispielsweise die Knoevenagel-Kondensation im Fall von Chen *et al*. durchgeführt werden.[68] Für diese Kondensation benutzten sie das MOF BIT-58. Hierbei wirkten die durch Modulation freien Ce^{3+}-Zentren als Lewis-Säure-Katalysator. Auch ZIF-8 ist für seine katalytische Wirkung bezüglich der Knoevenagel-Kondensation bekannt. So gelang es Spieß *et al*., ein auf Holz basierendes ZIF-8-Komposit herzustellen, das einen Umsatz von 89 % bei Raumtemperatur (RT) erreichte.[69] Durch die Synthese verschiedener MOF-basierter Komposite können viele weitere Arten an Reaktionen katalysiert werden. Hier sollen als Beispiele die Arbeiten von Cai *et al*. und Li *et al*. dienen. Cai *et al*. waren in der Lage, auf Wolfram basierende Polyoxometallate in eine hochporöse UiO-66 Struktur einzulagern. Das dadurch erhaltene Komposit konnte in unterschiedlichen [3+3]-Cycloadditionen erfolgreich verwendet werden.[46] Li *et al*.

konnten ein auf MOF-808 basierendes Komposit herstellen, welches Palladium-Nanopartikel eingebettet in einem Kunststoffpolymer trägt. Dieses Komposit ermöglichte ihnen, sowohl Suzuki-Kupplungen als auch asymmetrische Aldolreaktionen und deren Kombinationen mit hohen Ausbeuten und hohen Enantiomerenüberschüssen (engl. *enantiomeric excess*, *ee*) durchzuführen.[70] Neben der Synthese solcher Komposite können durch die Verwendung entsprechender Linker in der MOF-Synthese auch katalytisch aktive Komplexe im MOF gebildet werden. Dies sollen die Arbeiten von Dang *et al*. oder Rahman *et al*. beispielhaft zeigen.[71] Beide verwendeten Linker, die in der gebildeten MOF-Struktur in der Lage waren durch die Zugabe weiterer Metallsalze wie Palladiumacetat oder Kobaltnitrat, aktive Metallkomplexe im MOF zu bilden. Dadurch konnten sowohl Heck-Kupplungen als auch verschiedene oxidative Kupplungen realisiert werden.
Ein weiterer Anwendungsbereich der heterogenen MOF-Katalyse ist die katalytische Zersetzung schädlicher Verbindungen. Hier konnten Jin *et al*. durch die Verwendung von Rhodamin B (RhB) als formgebendes Hilfsmittel das MOF MIL-125-NH_2 synthetisieren. Die dadurch erhaltene hochporöse Struktur ermöglicht es, Toluol an Luft photokatalytisch zu zersetzen.[72] Den Ansatz der photokatalytischen Zersetzung verwendeten auch Alamgir und Talha *et al.* in ihrer Arbeit. Sie synthetisierten dafür das MOF BUT-206, welches unter UV-Licht in der Lage war, den Farbstoff Kristallviolett in wässriger Lösung zu zersetzen.[73] In Gegenwart von Wasserstoffperoxid (H_2O_2) konnten Sarkar *et al*. mit einer Zn-BTC Struktur zeigen, dass sowohl RhB als auch Methylenblau unter sichtbarem Licht erfolgreich zersetzt werden kann.[74]

Als letzter Punkt im Bereich der Katalyse soll hier noch auf die Spaltung von Wasser eingegangen werden. Grundsätzlich wird zwischen der Wasserstoff freisetzenden Reaktion (engl. *hydrogen evolution reaction*, HER) und der Sauerstoff freisetzenden Reaktion (engl. *oxygen evolution reaction*, OER) unterschieden, welche an den unterschiedlichen Elektroden ablaufen. In diesem Abschnitt soll allerdings nur die OER besprochen werden. Das Hauptaugenmerk in diesem Bereich liegt darauf, Metalle wie Palladium, Platin, Ruthenium oder Iridium, die meistens als Standardmaterialien verwendet werden, durch preiswertere und besser verfügbare Metalle zu ersetzen. Dabei werden MOFs und kohlenstoffbasierte MOF-Komposite als Präkatalysatoren verwendet (siehe Abbildung 14).

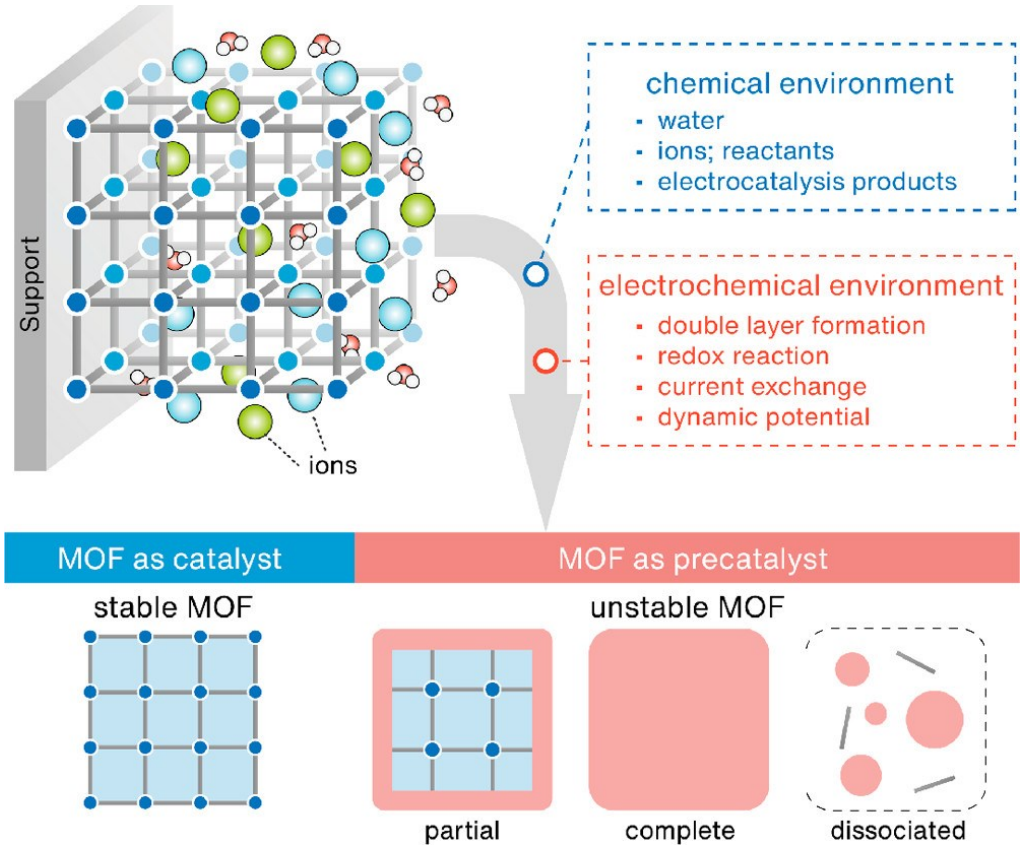

Abbildung 14: *Schematische Darstellung der chemischen und elektrochemischen Umgebung des MOFs während der Elektrolyse mit dem Verweis auf die Stabilität bzw. Zersetzung. Nachdruck mit Genehmigung von Ref.[75] Copyright 2021 American Chemical Society.*

Es gilt dabei, einige Hürden wie eine verbesserte Leitfähigkeit im MOF oder eine hohe Porosität mit vielen offenen Metallzentren zu überwinden.[76] Durch die Verwendung von stark sauren oder basischen Bedingungen kommt es zur Auflösung der MOF-Struktur. Dies hat zur Folge, dass beispielsweise Carboxylat-Linker durch OH^--Ionen ersetzt werden und sich so Schichten aus Metallhydroxiden bilden.[77] Diese Hydroxide bilden während der elektrochemischen Behandlung die katalytisch aktiven Spezies.[78] Durch die Verwendung von Kompositen wie Ketjenblack, Kohlenstoffnanoröhren oder Graphenoxid soll die Leitfähigkeit während der elektrochemischen Behandlung erhöht werden.[79]

1.4.2 Lumineszenz

Die Lumineszenz von MOFs ist heutzutage ein weit verbreitetes Forschungsgebiet. Neben der Anwendung in der Sensorik[80] werden lumineszente MOFs auch in den Bereichen der Thermometrie[81] oder der Optoelektronik[82] verwendet. Hierbei kann die Lumineszenz grundsätzlich auf zwei unterschiedliche Arten erzeugt werden. Zum einen durch die Verwendung lumineszenter Linker oder SBUs, durch die ein lumineszentes MOF synthetisiert werden kann. Zum anderen durch Wirt-Gast-Verbindungen, bei denen durch das Einbringen eines lumineszenten Gastes in die MOF-Wirtsverbindung ein lumineszentes Komposit erreicht werden kann. Hierbei unterscheidet man zwischen den post-synthetisch hergestellten Kompositen und den *in situ* synthetisierten Kompositen. Beide Methoden zeigen dabei sowohl Vor- als auch Nachteile. Die unterschiedlichen Synthesemethoden können durch die Abbildung 15, welche von Ryu *et al*. publiziert wurde, verdeutlicht werden.[83]

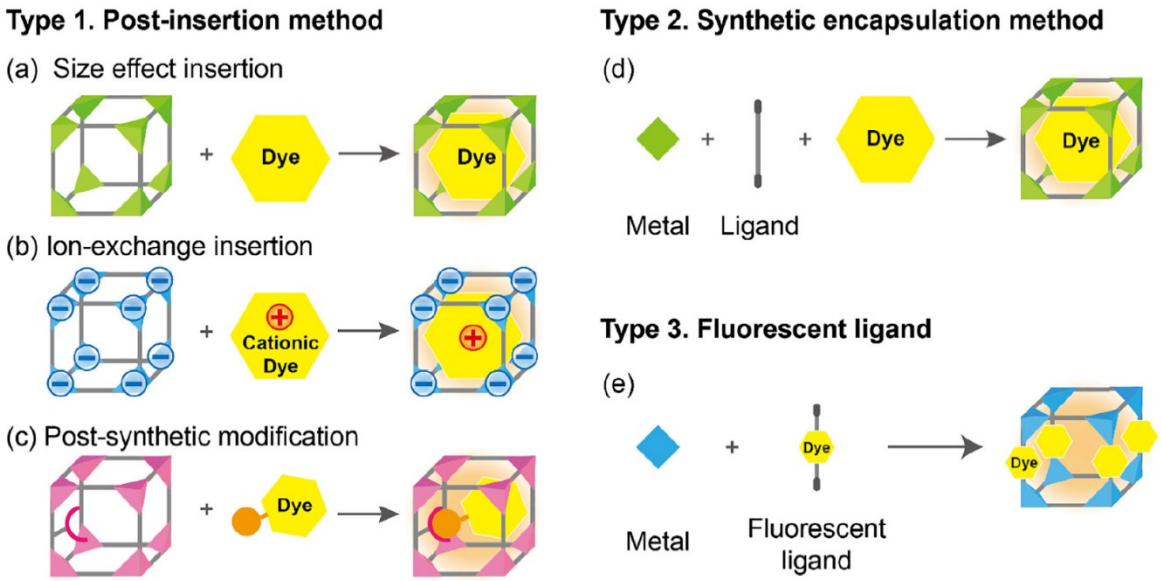

Abbildung 15: *Schematische Darstellung unterschiedlicher Synthesemethoden zur Herstellung lumineszenter MOFs. Nachdruck mit Genehmigung von Ref.[83] Copyright 2018 Elsevier.*

Während eine SBU-basierte Lumineszenz meistens von den Lanthanoiden Europium und/oder Terbium ausgeht, wird eine linkerbasierte Lumineszenz im MOF von einer Vielzahl organischer Verbindungen erreicht.[84]

In den Wirt-Gast-Kompositen werden die lumineszenten Eigenschaften organischer Emitter ausgenutzt. So können durch die Verwendung einzelner Emitter Komposite

synthetisiert werden, die der jeweiligen Wellenlänge des Emitters in Lösung entspricht. Hierbei kann eine Konzentrationsabhängigkeit sowohl in Bezug auf die Intensität als auch auf die emittierende Wellenlänge beobachtet werden.[85]

Die so hergestellten Komposite können bezüglich ihrer Emission durch die Einlagerung weiterer Farbstoffmoleküle mit unterschiedlichen Emissionswellenlängen auf die jeweiligen Anwendungen abgestimmt werden. Ziel dabei ist es häufig, Weißlichtemitter herzustellen. So zeigten Liu *et al.* in ihrer Arbeit, dass sie durch mehrfache Beladung mit unterschiedlichen Farbstoffmolekülen in der Lage waren, ein Weißlicht emittierendes ZIF-8 Komposit herzustellen.[82] Einen ähnlichen Ansatz verwendeten Chen *et al.* bei der Einlagerung von Fluorescein, RhB und 7-Hydroxycoumarin in Cyclodextrin basierte MOFs (siehe Abbildung 16).[86]

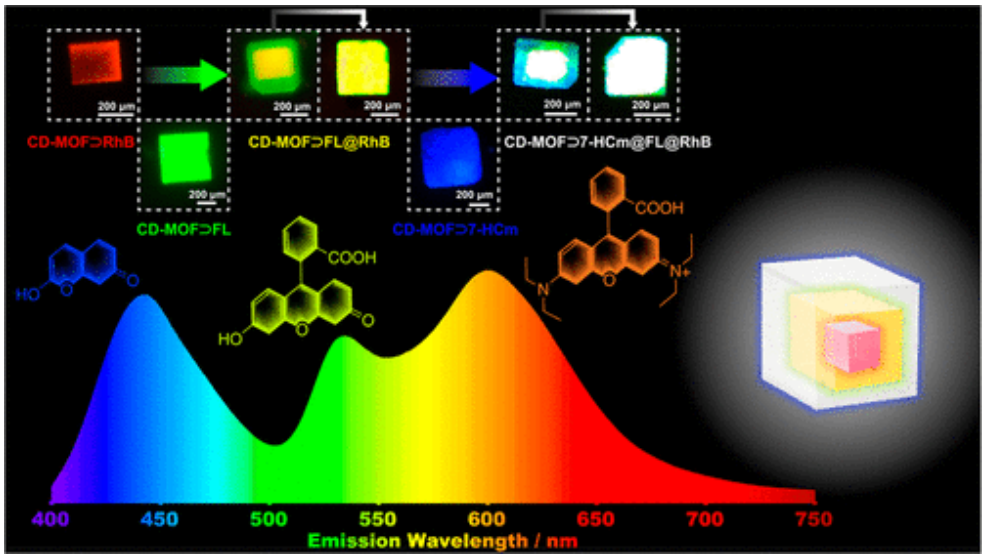

Abbildung 16: *Schematische Darstellung des von Chen et al. hergestellten Komposites. Nachdruck mit Genehmigung von Ref.[86] Copyright 2019 American Chemical Society.*

Des Weiteren können durch die Einlagerung eines Farbstoffs in eine MOF-Matrix auch die photophysikalischen Eigenschaften wie Lebenszeit und Quantenausbeute deutlich beeinflusst werden. So zeigten bspw. Xiong *et al.*, dass durch die Einlagerung eines Farbstoffes in ein MOF lumineszente Spezies gebildet werden können, die eine deutlich verlängerte Lebenszeit besitzen.[87] Ein ähnliches Verhalten im Vergleich zum Farbstoff als Feststoff konnte auch in der Arbeit von Püschel *et al.* gezeigt werden.[88]

Neben der Anwendung und Optimierung im Bereich der Leuchtstoffe und photophysikalischen Eigenschaften werden solche Komposite anhand ihrer

Lumineszenz auch als Sensoren für bspw. Metallionen oder Sprengstoffe untersucht.[89] So konnten Zhang *et al.* zeigen, dass durch die Einlagerung des Farbstoffs Fluorescein in die MOF-Matrix bio-MOF-1 ein effektiver lumineszenter Sensor für die Detektion von Fe^{3+}-Ionen hergestellt werden konnte.[90] Unter allen vermessenen Metallionen zeigte nur Eisen ein nahezu vollständiges Quenching der zuvor vermessenen Lumineszenz. Xiong *et al.* gelang es, durch die post-synthetische Einlagerung von Acriflavin in ein auf Europium basierendes MOF einen Hypochlorid-Anionen (ClO^--Ionen) Sensor zu entwickeln, der in Anwesenheit von ClO^--Ionen seine Emissionsbande von grün (511 nm) zu rot (621 nm) wechselt.[91] Im Bereich der Sprengstoffsensorik konnten Wang *et al.* durch einen Ionenaustausch einen kationischen Farbstoff in die Poren von bio-MOF-1 einlagern. Dieses Komposit zeigt in Abhängigkeit zu dem zu detektierenden Sprengstoff eine Ab- bzw. Zunahme der Lumineszenz.[92]

Häufig kommt es aber auch zu Kompositen, die auf unterschiedliche Verbindungen reagieren. So konnten Li *et al.* durch Ihre Synthese eines mit Eosin Y beladenen Zirkonium-MOFs des Typen UiO einen Sensor sowohl für Fe^{3+}-Ionen als auch für $Cr_2O_7^{2-}$-Ionen und Nitroaromaten herstellen.[93] Dies hat den Vorteil, dass für unterschiedliche Verbindungen nur ein Sensor benötigt wird. Da es sich allerdings bei allen Detektionen um eine Unterdrückung der Lumineszenz handelt, kann dies schnell zu falsch positiven Ergebnissen führen.

Abschließend soll hier gesagt werden, dass alle Anwendungsbereiche interessante Ansätze für die Erforschung zukünftiger Materialien bieten. Eine genauere Betrachtung kann im Rahmen dieser Arbeit aufgrund des Umfangs aller Gebiete nicht geleistet werden.

2. Zielsetzung und Motivation

Ziel dieser Arbeit ist sowohl die Synthese und Charakterisierung von neuen metall-organischen Gerüstverbindungen (MOFs) als auch die Anwendung unterschiedlicher Verbindungen in den Bereichen der Einlagerung verschiedener Farbstoffe, der MOF-basierten Katalyse und der Sorption. Für die Einlagerung haben sich hierbei zwei verschiedene Verbindungen als besonders interessant herausgestellt. Zum einen die Klasse der Bodipy-Farbstoffe. Diese haben in den letzten Jahren aufgrund ihrer guten Eigenschaften als Leuchtstoffe in vielen Bereichen der heutigen Forschung Anwendung gefunden. Dabei werden sie hauptsächlich in Lösungen verwendet, die keine stark sauren pH-Werte aufweisen. Ziel dieses Projektes soll die Synthese eines säurestabilen Bodipy-Farbstoffes sein, der sich gut in unterschiedliche MOFs einlagern lässt. Diese Komposite sollen anschließend hinsichtlich ihrer Lumineszenz-Eigenschaften untersucht werden. Die zweite Klasse der Farbstoffe besteht aus multiresonanten thermisch verzögerten aktivierten Fluoreszenz-Emittern (engl. *multi-resonance thermally activated delayed fluorescence*, MR-TADF). Diese Art der Emitter sind ein bedeutender Gegenstand aktueller Forschung im Bereich der OLED-Technik und optoelektronischer Geräte. Hierbei soll durch die Synthese und Einlagerung solcher Emitter deren photophysikalische Eigenschaften im MOF als Festkörperlösung (engl. *solid solution*) untersucht werden.

Für den Bereich der Katalyse sollen sowohl die auf MOFs basierende Wasserspaltung als auch die Carbentransfer-Reaktion betrachtet werden. Ersteres unter der Zurhilfenahme eines neu hergestellten Phosphonat MOFs, welcher als Präkatalysator in Verbindung mit einer Nickelschaumelektrode Anwendung in der Wasserspaltung findet. Die Carbentransfer-Reaktion soll hierbei durch ein auf Rhodium basierendes Koordinationspolymer stattfinden. Diese Art der Reaktion ist bereits gut in der Literatur beschrieben. In den meisten Fällen werden dafür homogene Katalysatoren verwendet. Ziel dieses Projektes ist es, durch das zuvor hergestellte Koordinationspolymer eine gute Reaktivität eines heterogenen Katalysators mit einer hohen Recyclingrate zu erreichen. Im letzten Projekt soll die Synthese des benötigten Linkers und des bereits aus der Literatur bekannten MOFs TUB41 optimiert werden. Das dadurch gewonnene TUB41 soll anschließend genauer im Hinblick auf seine Stabilität und Selektivität im Bereich der CO_2- und Feuchtigkeitssorption untersucht werden.

3. Kumulativer Teil

In den nachfolgenden Unterkapiteln werden die bereits publizierten Ergebnisse als Erstautor für diese Dissertation dargestellt. Alle Publikationen werden mit einer kurzen Zusammenfassung beschrieben und die jeweiligen eigenen Anteile an der jeweiligen Publikation aufgeführt. Jede Publikation steht mit einer eigenen Aufzählung für sich. Alle gezeigten Abbildungen, Tabellen und Schemata folgen nicht dem Haupttext dieser Dissertation. Ebenso wird die verwendete Literatur in jeweils separaten Verzeichnissen am Ende jeder Veröffentlichung aufgelistet, wodurch es zu einer mehrfachen Zitation einiger Quellen kommen kann. Die Publikationen sind in chronologischer Reihenfolge aufgeführt.

Veröffentlichungen als Co-Autor werden in einem separaten Kapitel jeweils mit einer kurzen Zusammenfassung und den eigenen Anteilen an den jeweiligen Publikationen aufgelistet.

Weitere Ergebnisse, welche bislang nicht publiziert sind, werden in den Kapiteln 5 und 6 beschrieben. Kapitel 5 beinhaltet bereits Entwürfe für Publikationen. Kapitel 6 beinhaltet noch zu bearbeitende Ergebnisse.

3.1 Exceptionally Stable And Super-Efficient Electrocatalysts Derived From Semiconducting Metal Phosphonate Frameworks

Diese Arbeit wurde veröffentlicht in

Thi Hai Yen Beglau[+], Marcus N. A. Fetzer[+], Istvan Boldog, Tobias Heinen, Markus Suta, Christoph Janiak and Gündoğ Yücesan, *Chemistry-a European Journal* **2024**, *30*, e202302765.

DOI: 10.1002/chem.202302765; Ref.[94]

[+]Die Autoren haben zu gleichen Anteilen zu dieser Publikation beigetragen.

Kurzzusammenfassung

In dieser Studie stellen wir zwei neue halbleitende Metallphosphonat-Gerüste vor, Co_2[1,4-NDPA] und Zn_2[1,4-NDPA] (wobei 1,4-NDPA^{4-} für 1,4-Naphthalindiphosphonat steht). Diese Gerüste weisen optische Bandlücken von

1,7 eV bzw. 2,5 eV auf, die im halbleitenden Bereich liegen. Der aus Co_2[1,4-NDPA] als Vorläufer gewonnene Elektrokatalysator zeigte eine geringere Überspannung von 374 mV bei der OER mit einer Tafel-Steigung von 43 mV dec^{-1} bei einer Stromdichte von 10 mA cm^{-2} in einem alkalischen Elektrolyten (1 mol L^{-1} KOH), was auf eine deutlich überlegene Reaktionskinetik hindeutet. Die OER-Leistung von Co_2[1,4-NDPA]-Materialien als Präkatalysatoren in Verbindung mit Nickelschaum (NF) zeigte im Vergleich zum Stand der Technik Pt/C/RuO_2@NF nach 30 Stunden in 1 mol L^{-1} KOH eine außergewöhnliche Langzeitstabilität bei einer Stromdichte von 50 mA cm^{-2} für die Wasserspaltung. Um Einblicke in den OER-Mechanismus zu gewinnen, wurde außerdem die Umwandlung von Co_2[1,4-NDPA] in seine elektrokatalytisch aktiven Spezies untersucht.

Anteile an der Publikation:

- Planung des Forschungsprojekts und Durchführung der Literaturrecherche mit Unterstützung von Dr. Gündoğ Yücesan.
- Synthese und Charakterisierung von 1,4-Naphthalindiphosphonat sowie von den Metallphosphonat-Gerüsten Co_2[1,4-NDPA] und Zn_2[1,4-NDPA].
- Untersuchung und Bewertung zur Charakterisierung von PXRD- und IR-Messungen.
- Bewertung der elektrochemischen Leistung der OER und der gesamten Wasserspaltung von β-$Co(OH)_2$, physikalische Vermischung von β-$Co(OH)_2$ und Ligand [1,4-NDPAH4] und kommerziellem RuO_2 als Referenzmaterialien durch Frau Dr. Thi Hai Yen Beglau.
- Untersuchungen und Bewertung der gesamten elektrochemischen Leistung der OER und der gesamten Wasserspaltung in einem alkalischen Medium (1 mol L^{-1} KOH) von Co_2[1,4-NDPA] und Zn_2[1,4-NDPA] durch Frau Dr. Thi Hai Yen Beglau.
- Untersuchungen und Bewertung der Kristallstruktur durch Herrn Tobias Heinen und Dr. Istvan Boldog.
- Untersuchungen und Bewertung der optischen Messungen durch Herrn Jun. Prof. Dr. Markus Suta.

Chemistry–A European Journal
Research Article
doi.org/10.1002/chem.202302765
Chemistry Europe
European Chemical Societies Publishing
www.chemeurj.org

Exceptionally Stable And Super-Efficient Electrocatalysts Derived From Semiconducting Metal Phosphonate Frameworks

Thi Hai Yen Beglau[+],[a] Marcus N. A. Fetzer[+],[a] Istvan Boldog,[a] Tobias Heinen,[a] Markus Suta,[b] Christoph Janiak,*[a] and Gündoğ Yücesan*[a]

Two new isostructural semiconducting metal-phosphonate frameworks are reported. Co_2[1,4-NDPA] and Zn_2[1,4-NDPA] (1,4-NDPA^{4-} is 1,4-naphthalenediphosphonate) have optical bandgaps of 1.7 eV and 2.5 eV, respectively. The electrocatalyst derived from Co_2[1,4-NPDA] as a precatalyst generated a low overpotential of 374 mV in the oxygen evolution reaction (OER) with a Tafel slope of 43 mV dec^{-1} at a current density of 10 mA cm^{-2} in alkaline electrolyte (1 mol L^{-1} KOH), which is indicative of remarkably superior reaction kinetics. Benchmarking of the OER of Co_2[1,4-NPDA] material as a precatalyst coupled with nickel foam (NF) showed exceptional long-term stability at a current density of 50 mA cm^{-2} for water splitting compared to the state-of-the-art Pt/C/RuO_2@NF after 30 h in 1 mol L^{-1} KOH. In order to further understand the OER mechanism, the transformation of Co_2[1,4-NPDA] into its electrocatalytically active species was investigated.

Introduction

During the last two decades, metal organic frameworks (MOFs) have been one of the most active research areas.[1,2] MOFs provide rich structural diversity and reticular chemistry to optimize pore sizes and surface areas in porous materials.[3–6] Furthermore, MOF surface areas can be decorated with a large variety of organic functional groups via linker design as well as post-synthetic modifications.[7–11] The rich structural diversity of MOFs has been well reflected in their potential application areas such as small molecule capture,[12–14] small molecule storage,[15] electrode materials,[16,17] electrochemical energy storage,[18] magnetism,[19,20] drug delivery,[21–23] heterogeneous catalysis,[24–27] electrocatalysis,[28] etc. Among these applications, electrocatalysis of the oxygen evolution reaction (OER) is one of the fundamental steps in electrochemical systems such as water splitting or zinc-air batteries.[29–31] Design and synthesis of novel OER electrocatalysts with fast kinetics, excellent catalytic activity and stability has been extensively studied during the last years. Metal-based oxides such as IrO_2 and RuO_2 are the current bench-mark materials for OER due to their low overpotential and large current density.[32] However, high cost, poor durability, and low earth reserves of IrO_2 and RuO_2 hinder the feasibility of these compounds for industrial applications.[33] As an alternative to IrO_2 and RuO_2, MOFs are recently emerging as precatalysts for electrocatalysis of the hydrogen evolution (HER), oxygen evolution (OER), and oxygen reduction reactions (ORR).[34–37] Such compounds could potentially provide more feasible and environmentally friendlier options towards industrialization of OERs.[38] In the current state of the art, MOFs generally function as precatalysts, undergoing a sequence of structural reconfigurations, such as hydrolysis, metal ion leaching, and oxidation of the metal ions in the alkaline medium to generate an active catalyst such as [$M(OH)_2$-$M(O)_x(OH)_y$].[39]

One of the unexplored material types in electrocatalysis is the use of recently emerging semiconducting metal-phosphonate frameworks. Hypothetically, the use of narrow band gap or semiconducting MOFs might help improve OER kinetics, and currently there is a limited number of narrow band gap MOFs in the literature.[40] Our research group has recently reported on the electrical conductivity of microporous phosphonate MOFs and layered metal phosphonates.[17,20,41–44] The reported semiconducting phosphonate MOFs by our group have narrow band gaps between 1.4 and 2.5 eV. We have previously shown that changing the identity and coordination environment of the metal ions in isostructural MOFs and hydrogen-bonded organic framework (HOFs) are important tools for fine band-gap tuning of the framework.[43,45] The band gap of a compound might be an indicator for the ease of an electron transfer step in electrocatalytic reactions.[46,47] For example, the Co^{3+}/Co^{2+} couple is currently intensely investigated for photocatalytic water splitting because the respective reduction potential at

[a] T. H. Y. Beglau,[+] M. N. A. Fetzer,[+] I. Boldog, T. Heinen, C. Janiak, G. Yücesan
Institute of Inorganic and Structural Chemistry
Heinrich Heine Universität Düsseldorf
Universitätstr. 1, 40225, Düsseldorf (Germany)
E-mail: janiak@uni-duesseldorf.de
guendog.yuecesan@hhu.de
[b] M. Suta
Inorganic Photoactive Materials, Institute for Inorganic Chemistry and Structural Chemistry
Heinrich Heine University Düsseldorf
Universitätsstr. 1, 40225 Düsseldorf (Germany)

[+] These authors contributed equally to this work.

Supporting information for this article is available on the WWW under https://doi.org/10.1002/chem.202302765

pH = 7 is $E^0 \sim +1.41$ V > +1.23 V for the OER of pure water.[48] Furthermore, phosphonate-MOFs could exhibit exceptional thermal stabilities above 400 °C and chemical stabilities between pH = 0 and 12.[49–54]

In this work, we successfully synthesized two new dense isostructural semiconducting metal phosphonate frameworks namely Co_2[1,4-NDPA] and Zn_2[1,4-NDPA] (where 1,4-NDPA^4 is 1,4-naphthalenediphosphonate) by hydrothermal methods in pure water. The structures were characterized by single crystal X-ray diffraction (XRD), powder-XRD, infrared (IR) and scanning electron microscopy (SEM) with energy dispersive X-ray analysis (EDX). Optical measurements were carried out to determine the absorption onset of the materials. The Co_2[1,4-NDPA] and Zn_2[1,4-NDPA] materials were used for OER on a glassy carbon electrode. Furthermore, the materials were used as cathode and anode on nickel foam (NF) and compared with commercial platinum on carbon (Pt/C) (cathode catalyst) and RuO_2 (anode catalyst) couple for water splitting. The formation of the active species derived from Co_2[1,4-NPDA] was investigated to understand the OER mechanism.

Results and Discussion

Synthesis

Chemicals were purchased from Aldrich, Alfa Aesar and TCI chemicals, and used without further purification. 1,4-naphthalenediphosphonic acid, 1,4-NDPAH_4 was synthesized according to the literature.[17,55] A detailed description of the linker synthesis can be found in the Supporting Information. Co_2[1,4-NDPA] and Zn_2[1,4-NDPA] were synthesized under the same hydrothermal reaction conditions. $Co(NO_3)_2 \cdot 6H_2O$ (273 mg, 0.93 mmol) or $Zn(NO_3)_2 \cdot 6H_2O$ (276 mg, 0.93 mmol), 1,4-naphthalenediphosphonic acid (100 mg, 0.34 mmol) and 4,4′-bipyridine as a modulator (40 mg, 0.25 mmol) and 10 mL of ultrapure water were placed in a Parr Teflon-lined autoclave. After brief mixing of the reaction mixture, the autoclave was closed and heated to 200 °C for 72 hours. Afterwards, the product was washed three times with 10 mL of ultrapure water and one time with 10 mL acetone prior to drying. The product was dried in air at room temperature, yielding dark blue crystal plates of Co_2[1,4-NDPA] and white crystal plates of Zn_2[1,4-NDPA].

Crystal structure description

The structures of Co_2[1,4-NDPA] and Zn_2[1,4-NDPA] were determined and refined using single crystal X-ray diffraction methods. As depicted in Figure 1a, the two isostructural compounds Co_2[1,4-NDPA] and Zn_2[1,4-NDPA] exhibit a pillared layered metal phosphonate network. The layered secondary building unit (SBU) is constructed from tetrahedrally coordinated Co^{2+} or Zn^{2+} atoms and phosphonate groups ($-PO_3^{2-}$) from the fully deprotonated 1,4-NDPA^4 linkers, forming isolated four-membered M–O–M–O rings (M = Co or Zn), surrounded by six eight-membered M–O–P–O-M–O-P–O rings to give a layered network of Co_2[1,4-NDPA] and Zn_2[1,4-NDPA] (Figure 1a and 1b). The actual topology of the layered SBU of Co_2[1,4-NDPA] and Zn_2[1,4-NDPA] is unprecedented among other layered metal phosphonate frameworks with a 3,3,4 L25 net type (see Supporting Information for topological characterization). The layered SBUs are connected by aromatic naphthalene units of 1,4-NDPA^4 to form the three-dimensional framework (see Figure 1a and Supporting Information). The analysis for purity of the single-crystalline phase was done by PXRD. As shown in the PXRD (Figure 2), both Co_2[1,4-NDPA] and Zn_2[1,4-NDPA] show good agreement with simulation and were synthesized as single crystalline phases. As depicted in Figures S1 to S3, the intercentroid distances between the naphthalene moieties for Co_2[1,4-NDPA] and Zn_2[1,4-NDPA] are, respectively, 3.91 Å and 3.97 Å and shortest C···C distances

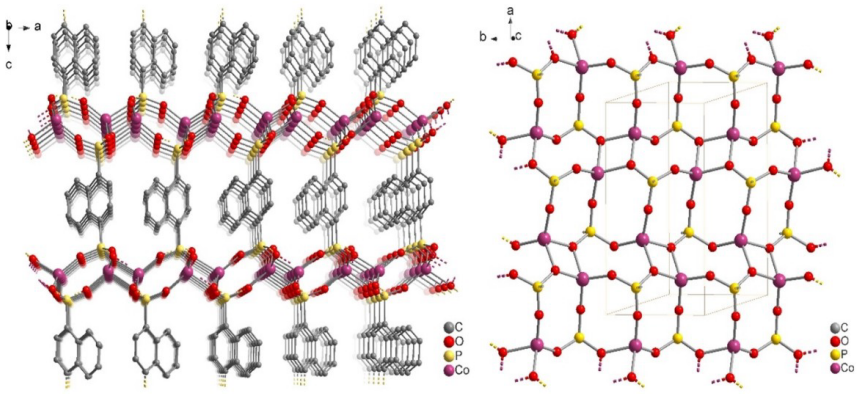

Figure 1. (a) Section of the packing diagram of the three-dimensional structure of Co_2[1,4-NDPA]. (b) Structure of the layered inorganic building unit of Co_2[1,4-NDPA] (isostructural to Zn_2[1,4-NDPA]).

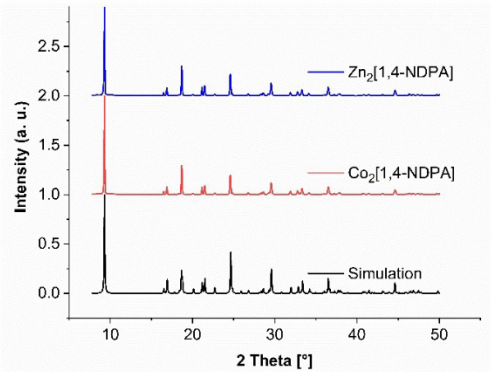

Figure 2. PXRD of the single-crystalline phase in agreement with the simulation from the structure of Zn_2[1,4-NDPA].

3.40–3.48 Å and 3.35–3.44 Å, which are similar to interlayer distances of graphite (for a more detailed description of the crystal structure see Supporting Information).

Optical measurements

Based on the marked color difference of Co_2[1,4-NDPA] and Zn_2[1,4-NDPA], diffuse reflectance spectra were measured on powdered samples of these two compounds in an integrating sphere setup (Ulbricht sphere). If the thickness of the powder slab is sufficiently high such that transmittance along the layer is negligible, the absorbance A of the powder scales with the Kubelka-Munk function K/S given by Equation (1):

$$\frac{K}{S} = f(R_\infty) = \frac{(1-R_\infty)^2}{2R_\infty} \propto A \quad (1)$$

with R_∞ as the diffuse reflectance of the powder layer. The Kubelka-Munk spectra of Co_2[1,4-NDPA] and Zn_2[1,4-NDPA] are depicted in Figure 3. Both spectra show a strong increase around 500 nm (~2.5 eV) and are very similar in that wavelength range. This absorption is assigned to an interband transition, which is expectedly strongly localized at the naphthalene moieties. The low onset energy (< 3 eV) for strong absorption indicates a semiconducting behavior of the two compounds. The strong increase in absorption below 400 nm in the ultraviolet (UV) range of Zn_2[1,4-NDPA] explains why the related powdered compound appears colorless under daylight. The Kubelka-Munk spectrum of Co_2[1,4-NDPA] reveals additional low-energetic broad absorption bands in the range between 500 nm and 700 nm (onset of ~1.7 eV in the energy domain), which are absent in the Zn analogue and thus have to be identified as localized transitions due to the presence of tetrahedrally coordinated Co(II) in Co_2[1,4-NDPA]. The electronic transitions of the tetrahedrally coordinated $3d^7$ ion Co^{2+} can be in principle interpreted by means of the Tanabe-Sugano diagram of an octahedrally coordinated $d^{10-7}=d^3$ ion. Comparison to other literature-reported examples of Co^{2+}-doped purely inorganic oxides such as spinel-type $MAl_2O_4{:}Co^{2+}$ (M = Zn, Mg),[56,57] willemite-type[58] $Zn_2SiO_4{:}Co^{2+}$ or wurtzite-type[59] binary compounds $MX{:}Co^{2+}$ (M = Zn, X = O, S) offering tetrahedrally coordinated sites for Co^{2+} allows the assignment to a $^4A_2(^4F) \rightarrow {}^4T_1(^4P)$ ligand field transition of the observed absorption bands in that wavelength range (see Figure 3). The dark blue color of Co_2[1,4-NDPA] can be related to both the absorption in the deep red to near infrared range ($\lambda > 650$ nm) on the one hand and the strong reflection of light in the blue range of the

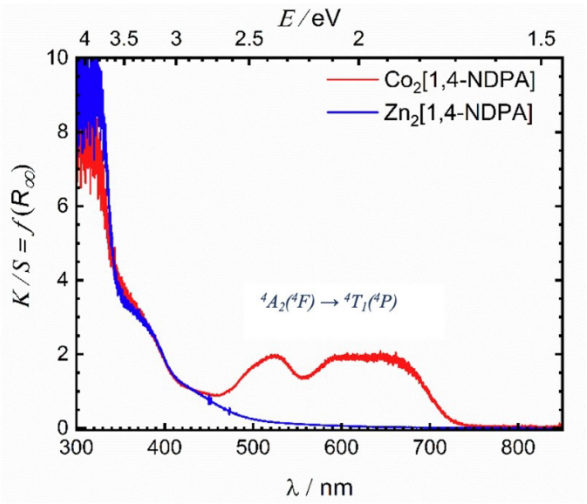

Figure 3. Optical Kubelka-Munk spectra of powdered Co_2[1,4-NDPA] (red) and Zn_2[1,4-NDPA] (dark blue) obtained from diffuse reflectance spectra at room temperature. The localized Co(II)-based ligand field transition is denoted

visible spectrum. Similar colors are known from the pigment Thénard blue ($CoAl_2O_4$) with high concentrations of Co^{2+}, which crystallizes in a spinel-type structure and in which the Co^{2+} ions also occupy tetrahedrally coordinated sites.

Electrocatalytic performance of the OER

The electrochemical OER is an anodic half-cell reaction and produces O_2 at a theoretical input of 1.23 V (vs. reversible hydrogen electrode (RHE)). We investigated the OER using Co_2[1,4-NDPA] and Zn_2[1,4-NDPA] as precatalysts in a 1 mol L^{-1} KOH electrolyte (pH = 14) and the obtained results were compared with commercial RuO_2. We used a glassy carbon rotating disk electrode (GC-RDE) with a geometric area of 0.196 cm^{-2} at a rotating velocity of 1600 rpm in a standard three-electrode system. The mass loading of electrocatalysts on the GC-RDE was quantified at 0.23 mg cm^{-2} (see Supporting Information for details). The polarization curves were generated by the linear sweep voltammogram (LSV) of Co_2[1,4-NDPA] and Zn_2[1,4-NDPA] and are compared to β-$Co(OH)_2$, a physical mixture of β-$Co(OH)_2$ and the ligand 1,4-$NDPAH_4$ and commercial RuO_2 in the same Nafion ink (see Supporting Information about how the ink for the electrode was prepared). The synthesized β-$Co(OH)_2$ and physical mixture of β-$Co(OH)_2$ and the ligand 1,4-$NDPAH_4$ were used as reference catalysts. Figure 4a presents the polarization curves of the samples after 20 cyclic voltammetry (CV) cycles of activation at a scan rate 50 mV s^{-1}, in order to get a stable state of the catalysts on the GC-RDE surface. The overpotentials of the various working electrodes are determined to be 374 mV for Co_2[1,4-NDPA], 380 mV for β-$Co(OH)_2$, 392 mV for the physical mixture of β-$Co(OH)_2$ and the ligand 1,4-$NDPAH_4$, 408 mV for Zn_2[1,4-NDPA] and 318 mV for RuO_2 at the current density of 10 mA cm^{-2} (see Figure 4a).

The Tafel plots are usually obtained in a potential range where the current is predominantly controlled by catalysis kinetics (non-mass-transfer restriction).[60] Therefore, we evaluated electrocatalytic kinetics for the OER of the precatalysts Co_2[1,4-NDPA] and Zn_2[1,4-NDPA] by generating their corresponding Tafel slopes. As seen in Figure 4b, the linear portion of the Tafel plot was fitted using the equation $\eta = a + b \times \log j$, where η and j represent the overpotential and the current density, respectively; b is the Tafel slope and a represents the cathodic intercept that is related to the exchange current density.[60] The smaller Tafel slope often refers to more favorable OER kinetics and a better electrocatalytic activity. The OER is a four-electron transfer reaction with a sequence of steps and intermediates, such as MO, MOOH or physisorbed peroxide species.[60] One of the most accepted OER mechanisms is the Krasil'shchikov's pathway, given in Reactions (1)–(4) with their corresponding Tafel slopes (b).[61–63]

$$M + OH^- \leftrightarrows MOH + e^-,\ b = 120\ mV\,dec^{-1} \quad (1)$$

$$MOH + OH^- \leftrightarrows MO^- + H_2O,\ b = 60\ mV\,dec^{-1} \quad (2)$$

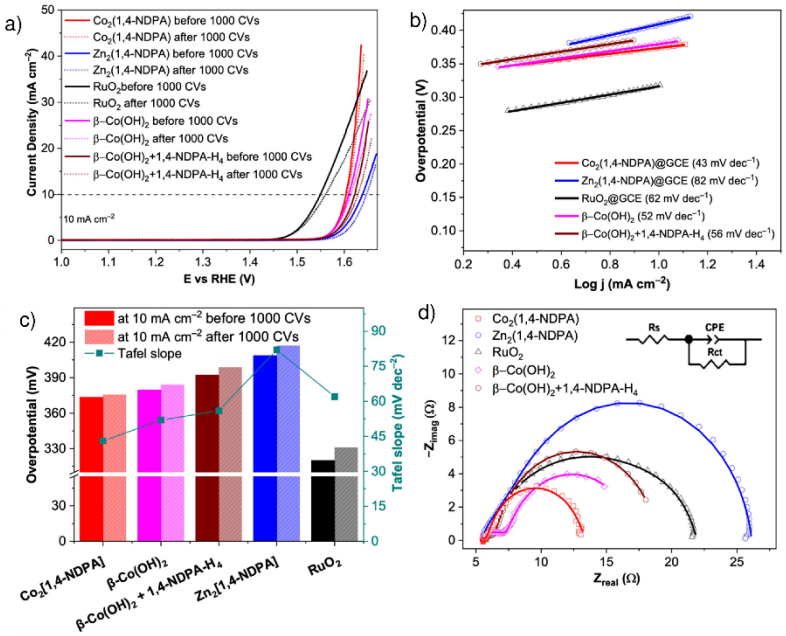

Figure 4. a) OER polarization curves before and after 1000 CVs in 1.0 mol L^{-1} KOH (pH = 14) b) OER Tafel plots obtained from the OER polarization curves c) corresponding overpotentials (columns) before and after 1000 CVs at 10 mA cm^{-2} and Tafel slopes (dark cyan dots). (d) raw data Nyquist plots at 1.6 V vs. RHE (symbol) and fitting to an equivalent model (solid line) from EIS test of Co_2[1,4-NDPA], Zn_2[1,4-NDPA], β -$Co(OH)_2$, physical mixture of β -$Co(OH)_2$ and ligand 1,4-$NDPAH_4$ and RuO_2 and benchmark material RuO_2 on GC-RDE.

$$MO \rightarrow MO + e^{-}, b = 45\ mV\,dec^{-1} \quad (3)$$

$$2MO \rightarrow 2M + O_2, b = 19\ mV\,dec^{-1} \quad (4)$$

Based on the Krasil'shchikov's pathway, a Tafel slope of $b = 43\ mV\,dec^{-1}$ to the OER involving Co_2[1,4-NDPA] corresponds to reaction (3) as a rate determining step. The Tafel slope of Zn_2[1,4-NDPA] ($b = 82\ mV\,dec^{-1}$) falls in between the values of the reaction (1) and (2). This can be attributed to stronger OH^- binding to Zn^{2-} ions that accelerates the rate of electron transfer in Reaction (1) (Figure 4b). As presented in Table S6, the Tafel slope of the electrocatalysts derived from Co_2[1,4-NDPA] and Zn_2[1,4-NDPA] is much lower than RuO_2 (62 mV dec^{-1}), β-$Co(OH)_2$ (52 mV dec^{-1}, the physical mixture of β-$Co(OH)_2$ and the ligand 1,4-$NDPAH_4$ (56 $mV\,dec^{-1}$) and other Co-based catalysts in the literature,[38] which suggest its superior reaction kinetics. In addition, the stability of the electrocatalysts derived from Co_2[1,4-NDPA] and Zn_2[1,4-NDPA] was investigated and compared with the commercial benchmark RuO_2 after 1000 continuous CVs. The electrocatalysts derived from Co_2[1,4-NDPA] and Zn_2[1,4-NDPA] showed stronger durability compared to β-$Co(OH)_2$, the physical mixture of β-$Co(OH)_2$ and the ligand 1,4-$NDPAH_4$, and RuO_2, as they exhibited only minor positive shifts of 2 and 8 mV, respectively. RuO_2, β-$Co(OH)_2$, and the physical mixture of β-$Co(OH)_2$ and the ligand 1,4-$NDPAH_4$ showed an increase of the overpotential by 14, 4 and 6 mV, respectively, at the current density of 10 $mA\,cm^{-2}$ after 1000 CVs (see Figure 4c).

To better understand the OER kinetics, an electrochemical impedance spectroscopy (EIS) measurements were carried out at 1.6 V in a frequency range of 0.1 Hz to 100 kHz in 1 $mol\,L^{-1}$ KOH. The semicircles in the high-frequency range of the Nyquist plots are attributed to charge-transfer resistance, which is equivalent for all catalysts. The Nyquist plots of catalysts Co_2[1,4-NDPA], Zn_2[1,4-NDPA], β-$Co(OH)_2$ and the physical mixture of β-$Co(OH)_2$ and ligand 1,4-$NDPAH_4$ and RuO_2 were curve-fitted to the model to evaluate the charge transfer resistance (R_{ct}) (see Figure 4d). The small R_{ct} value indicates the efficient electron transfer between the active sites of catalysts derived from Co_2[1,4-NDPA] and Zn_2[1,4-NDPA] and the electrolyte ion during OER. Co_2[1,4-NDPA] has the smallest R_{ct} value of 8 Ω, which is obviously smaller than that of β-$Co(OH)_2$ (10 Ω), the physical mixture of β-$Co(OH)_2$ and the ligand 1,4-$NDPAH_4$ (13 Ω), RuO_2 (16 Ω) and Zn_2[1,4-NDPA] (21 Ω).

Overall electrochemical water splitting

The overall water splitting contains two half reactions, which are the hydrogen evolution reaction (HER) and the oxygen evolution reaction (OER). The Co_2[1,4-NDPA] and Zn_2[1,4-NDPA] materials were coated on the surface of NF with a uniform thin layer (see SI for experimental details). Both the anode and cathode was constructed by employing the Co_2[1,4-NDPA] or Zn_2[1,4-NDPA] materials in the alkaline electrolyzer with 1 $mol\,L^{-1}$ KOH. The integrated commercial platinum on carbon (Pt/C) (cathode catalyst) and RuO_2 (anode catalyst) couple (Pt/C@NF/RuO_2@NF) was also tested for comparison. As expected, the LSV curves in Figure 5a show that the Pt/C@NF/RuO_2@NF couple catalysed the water electrolysis with an overpotential of 278 and 340 mV at a current density of 10 and 50 $mA\,cm^{-1}$, respectively. Therefore, the catalysts derived from Co_2[1,4-NDPA]@NF (312 mV) and Zn_2[1,4-NDPA]@NF (371 mV) show a lower overpotential compared to the performance of the glassy carbon electrode. Additionally, the activity of Co_2[1,4-NDPA]@NF is higher than the benchmark RuO_2@NF, reaching a practical current density of 200 $mA\,cm^{-2}$ at 1.63 V. The long-term stability plays an important role to evaluate electrocatalysts for practical water electrolysis.

The long-term stabilities of the catalysts derived from Co_2[1,4-NDPA] and Zn_2[1,4-NDPA] and the commercial Pt/C/RuO_2 couple in 1 $mol\,L^{-1}$ KOH was further checked by a chronopotentiometric test applying a constant current density at 50 mA cm^{-2} continuously for 30 h. The potential of the catalysts derived from Co_2[1,4-NDPA]@NF and Zn_2[1,4-NDPA]-

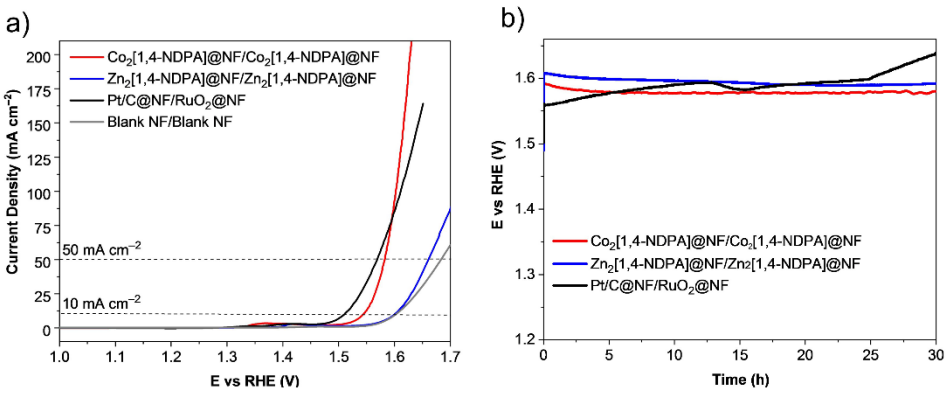

Figure 5. (a) Polarization curves and (b) the long-term stabilities in the electrolysis at a current density of $\eta = 50\ mA\,cm^{-2}$ by chronopotentiometric measurements of Co_2[1,4-NDPA], Zn_2[1,4-NDPA], Pt/C/RuO_2 on NF for overall water splitting in 1 $mol\,L^{-1}$ KOH.

@NF remained nearly unchanged during the whole measurement. In contrast, the commercial benchmark Pt/C/RuO_2@NF couple showed an increasing working potential at the current density of 50 mA cm^{-2} over 30 h. Consequently, the electrocatalysts derived from Co_2[1,4-NDPA] and Zn_2[1,4-NDPA] adhered well on the surface of NF after the stability test, as proven by SEM and element mapping (Figure S10 and Figure S11).

Zheng *et al.* point out that the metal-organic-framework based catalysts are precatalysts, and change to active phases during the electrochemical treatment under alkaline condition (1 mol L^{-1} KOH).[37] Therefore, we tested the chemical stability of Co_2[1,4-NDPA] by soaking the material in the alkaline electrolyte (1 mol L^{-1} KOH) for 30 min and 24 h, in order to gain a better understanding of the activation mechanism. The PXRD pattern of Co_2[1,4-NDPA] after 24 h in 1 mol L^{-1} KOH revealed the presence of cobalt hydroxide species (Figure 6). in the form of α-$Co(OH)_2$ (ICDD: 74-1057) and β-$Co(OH)_2$ (ICDD: 30-0443). It was indicated that the active sites in α/β-$Co(OH)_2$ are responsible for the excellent electrocatalyst performance.[64–66]

Thermal stability

The thermal stability of the Co_2[1,4-NDPA] and Zn_2[1,4-NDPA] was investigated by thermogravimetric analysis (TGA) measurements under a nitrogen atmosphere. Co_2[1,4-NDPA] and Zn_2[1,4-NDPA] show exceptional thermal stability where the organic components start to decompose at ca. 650 °C with 29.1 % experimental weight loss (theoretical 30.9 %) for Zn_2[1,4-NDPA]. The TGA curve of Co_2[1,4-NDPA] indicates a more gradual weight loss with a sharp mass decrease above 650 °C (see Figure S7).

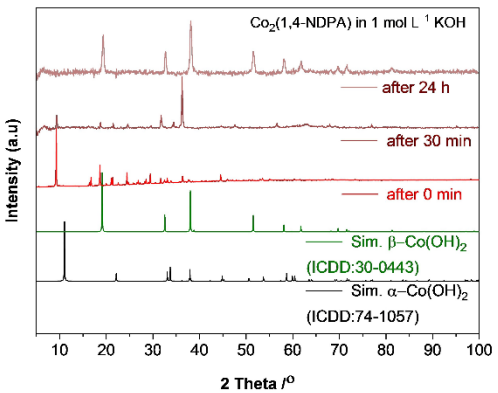

Figure 6. PXRD patterns of Co_2[1,4-NDPA], after 30 min and 24 h in 1 mol L^{-1} KOH; reflections from β-$Co(OH)_2$ (ICDD:30-0443) and α-$Co(OH)_2$ (ICDD: 74-1057).

Conclusions

Herein, we report the hydrothermal synthesis of the two new semiconducting metal-phosphonate frameworks Co_2[1,4-NDPA] and Zn_2[1,4-NDPA], and we have shown that changing the metal ions in isostructural semiconducting metal-phosphonate frameworks can be used to tune band gap and semiconducting properties. Both powdered compounds have absorption onsets at around 500 nm (2.5 eV), derived from photoluminescence optical Kubelka-Munk spectra data, which are strongly localized at the naphthalene moieties. Furthermore, Co_2[1,4-NDPA] shows a second onset at 700 nm (1.7 eV) which has to be identified as ligand-field transitions localized at the Co center with its low energetic $^4A_2(^4F)\rightarrow{}^4T_1(^4P)$ ligand field transition of tetrahedrally coordinated d^7-Co(II). We have furthermore used the new semiconducting metal-phosphonate frameworks as precatalysts for the OER reaction. We have shown that both Co_2[1,4-NDPA] and Zn_2[1,4-NDPA] are remarkable precatalysts for the OER reaction in water splitting with overpotentials of 374 mV for Co_2[1,4-NDPA] and 408 mV for Zn_2[1,4-NDPA] for a glassy carbon rotating electrode system and 312 mV and 371 mV on NF at a current density 10 mA cm^{-2}. The Tafel slope of 43 mV dec^{-1} in 1 mol L^{-1} KOH at a current density of 10 mA cm^{-2} of the Co_2[1,4-NDPA] precatalyst indicates its superior reaction kinetics compared to the commercial benchmark material RuO_2 or other compound families like metal phosphides and some reported MOFs in the literature. Besides, its good reaction kinetics, electrocatalyst derived from Co_2[1,4-NDPA] also shows remarkably improved activity, compared to RuO_2 on NF for water splitting reaching a current density of 200 mA cm^{-2} at 1.63 V. This work also demonstrated the exceptionally high stability of the derived active species of β-$Co(OH)_2$ and β-CoOOH catalysts by using Co_2[1,4-NDPA] as a precatalyst in 1 mol L^{-1} KOH for 30 h at a constant current density of 50 mA cm^{-2}. Several features may contribute to the excellent OER performance of the catalyst derived from Co_2[1,4-NDPA] when compared to the concurrently studied RuO_2, β-$Co(OH)_2$ and physically mixed β-$Co(OH)_2$ with the ligand 1,4-NDPAH_4. For example, the Co_2[1,4-NDPA] precatalyst might hypothetically generate a more uniform distribution of α/β-$Co(OH)_2$ and 1,4-NDPA-H_4 ligand on the surface of the glassy carbon electrode creating superior OER activities compared to the concurrently studied systems. All these results demonstrate that both materials, but especially the Co_2[1,4-NDPA] are potential candidates for industrial applications as precatalysts for OER in water electrolysis.

Supporting Information

Additional detailed experimental and characterization methods; synthesis progress; crystallography information; FTIR measurement; thermogravimetric analysis; electrochemical measurement; SEM and SEM-EDX before and after electrolysis; OER performance comparison; and topological analysis.

Deposition Numbers 2235305 (for Co_2[1,4-NDPA]), 2212088 (for Zn_2[1,4-NDPA]) contain the supplementary crystallographic

data for this paper. These data are provided free of charge by the joint Cambridge Crystallographic Data Centre and Fachinformationszentrum Karlsruhe Access Structures service.

Acknowledgements

G.Y. acknowledges financial support from DFG through grant YU-267/2-1. M.S. gratefully acknowledges funding from a materials cost allowance of the Fonds der Chemischen Industrie e.V. and a scholarship from the "Young College" of the North-Rhine Westphalian Academy of Sciences and Arts. C.J. thanks the DFG for funding within the Priority Program SPP 1928/2 COORNETs (grant Ja466/43-1). Open Access funding enabled and organized by Projekt DEAL.

Conflict of Interests

The authors declare no competing financial interest.

Data Availability Statement

The data that support the findings of this study are available in the supplementary material of this article.

Keywords: electrocatalysis · phosphonates · semiconducting materials

[1] J. D. Evans, B. Garai, H. Reinsch, W. Li, S. Dissegna, V. Bon, I. Senkovska, R. A. Fischer, S. Kaskel, C. Janiak, et al., *Coord. Chem. Rev.* **2019**, *380*, 378–418.
[2] H. Furukawa, K. E. Cordova, M. O'Keeffe, O. M. Yaghi, *Science* **2013**, *341*, 1230444.
[3] Z. Chen, H. Jiang, M. Li, M. O'Keeffe, M. Eddaoudi, *Chem. Rev.* **2020**, *120*, 8039.
[4] O. M. Yaghi, M. O'Keeffe, N. W. Ockwig, H. K. Chae, M. Eddaoudi, J. Kim, *Nature* **2003**, *423*, 705.
[5] S. Canossa, Z. Ji, C. Gropp, Z. Rong, E. Ploetz, S. Wuttke, O. M. Yaghi, *Nat. Rev. Mater.* **2023**, *8*, 331.
[6] P. Tholen, Y. Zorlu, J. Beckmann, G. Yücesan, *Eur. J. Inorg. Chem.* **2020**, 1542.
[7] M. Kalaj, M. S. Denny, K. C. Bentz, J. M. Palomba, S. M. Cohen, *Angew. Chem. Int. Ed.* **2019**, *58*, 2336.
[8] Z. Wang, S. M. Cohen, *J. Am. Chem. Soc.* **2007**, *129*, 12368.
[9] S. M. Cohen, *Chem. Rev.* **2012**, *112*, 970.
[10] S. M. Cohen, *J. Am. Chem. Soc.* **2017**, *139*, 2855.
[11] X. Kong, H. Deng, F. Yan, J. Kim, J. A. Swisher, B. Smit, O. M. Yaghi, J. A. Reimer, *Science* **2013**, *341*, 882.
[12] J.-B. Lin, T. T. Nguyen Tai, R. Vaidhyanathan, J. Burner, M. Taylor Jared, H. Durekova, F. Akhtar, K. Mah Roger, O. Ghaffari-Nik, S. Marx, et al., *Science* **2021**, *374* (6574), 1464.
[13] H. A. Evans, D. Mullangi, Z. Deng, Y. Wang, S. B. Peh, F. Wei, J. Wang, C. M. Brown, D. Zhao, P. Canepa, et al., *Sci. Adv.* **2022**, *8*, eade1473.
[14] B. E. R. Snyder, A. B. Turkiewicz, H. Furukawa, M. V. Paley, E. O. Velasquez, M. N. Dods, J. R. Long, *Nature* **2023**, *613* (7943), 287.
[15] M. P. Suh, H. J. Park, T. K. Prasad, D. W. Lim, *Chem. Rev.* **2012**, *112*, 782.
[16] D. Sheberla, *Nat. Mater.* **2017**, *16*, 220.
[17] K. Siemensmeyer, C. A. Peeples, P. Tholen, F. J. Schmitt, B. Çoşut, G. Hanna, G. Yücesan, *Adv. Mater.* **2020**, *32*, e2000474.
[18] J. Liu, X. Song, T. Zhang, S. Liu, H. Wen, L. Chen, *Angew. Chem. Int. Ed.* **2021**, *60*, 5612.
[19] E. Coronado, G. Mínguez Espallargas, *Chem. Soc. Rev.* **2013**, *42*, 1525.
[20] C. A. Peeples, D. Kober, F.-J. Schmitt, P. Tholen, K. Siemensmeyer, Q. Halldorson, B. Çoşut, A. Gurlo, A. O. Yazaydin, G. Hanna, et al., *Adv. Funct. Mater.* **2021**, *31*, 2007294.
[21] S. Rojas, A. Arenas-Vivo, P. Horcajada, *Coord. Chem. Rev.* **2019**, *388*, 202.
[22] P. Horcajada, R. Gref, T. Baati, P. K. Allan, G. Maurin, P. Couvreur, G. Férey, R. E. Morris, C. Serre, *Chem. Rev.* **2012**, *112*, 1232.
[23] P. Horcajada, T. Chalati, C. Serre, B. Gillet, C. Sebrie, T. Baati, J. F. Eubank, D. Heurtaux, P. Clayette, C. Kreuz, et al., *Nat. Mater.* **2010**, *9*, 172.
[24] A. Corma, H. García, F. X. Llabrés i Xamena, *Chem. Rev.* **2010**, *110*, 4606.
[25] X. Wang, X. Han, J. Zhang, X. Wu, Y. Liu, Y. Cui, *J. Am. Chem. Soc.* **2016**, *138*, 12332.
[26] D. Dang, P. Wu, C. He, Z. Xie, C. Duan, *J. Am. Chem. Soc.* **2010**, *132*, 14321.
[27] L. Zhu, X. Q. Liu, H. L. Jiang, L. B. Sun, *Chem. Rev.* **2017**, *117*, 8129.
[28] S. Jin, *ACS Energy Lett.* **2019**, *4* (6), 1443.
[29] H.-F. Wang, L. Chen, H. Pang, S. Kaskel, Q. Xu, *Chem. Soc. Rev.* **2020**, *49*, 1414.
[30] J. Suntivich, K. J. May, H. A. Gasteiger, J. B. Goodenough, Y. Shao-Horn, *Science* **2011**, *334* (6061), 1383.
[31] A. Mahmood, W. Guo, H. Tabassum, R. Zou, *Adv. Energy Mater.* **2016**, *6*, 1600423.
[32] C. C. L. McCrory, S. Jung, J. C. Peters, T. F. Jaramillo, *J. Am. Chem. Soc.* **2013**, *135*, 16977.
[33] S. Dou, C.-L. Dong, Z. Hu, Y.-C. Huang, J.-l. Chen, L. Tao, D. Yan, D. Chen, S. Shen, S. Chou, et al., *Adv. Funct. Mater.* **2017**, *27*, 1702546.
[34] Y. Yang, Y. Yang, Y. Liu, S. Zhao, Z. Tang, *Small Science* **2021**, *1*, 2100015.
[35] F. Sun, Q. Li, H. Xue, H. Pang, *ChemElectroChem* **2019**, *6*, 1273.
[36] B. R. Wygant, K. Kawashima, C. B. Mullins, *ACS Energy Lett.* **2018**, *3*, 2956.
[37] W. Zheng, L. Y. S. Lee, *ACS Energy Lett.* **2021**, *6*, 2838–2843.
[38] C. Zhang, Q. Qi, Y. Mei, J. Hu, M. Sun, Y. Zhang, B. Huang, L. Zhang, S. Yang, *Adv. Mater.* **2023**, *35*, 2208904.
[39] B. Singh, A. Yadav, A. Indra, *J. Mater. Chem. A* **2022**, *10*, 3843.
[40] L. S. Xie, G. Skorupskii, M. Dincă, *Chem. Rev.* **2020**, *120*, 8536.
[41] Y. Zorlu, L. Wagner, P. Tholen, M. M. Ayhan, C. Bayraktar, G. Hanna, A. O. Yazaydin, Ö. Yavuzçetin, G. Yücesan, *Adv. Opt. Mater.* **2022**, *10*, 2200213.
[42] M. M. Ayhan, C. Bayraktar, K. B. Yu, G. Hanna, A. O. Yazaydin, Y. Zorlu, G. Yücesan, *Chem. Eur. J.* **2020**, *26*, 14813.
[43] C. A. Peeples, A. Çetinkaya, P. Tholen, F.-J. Schmitt, Y. Zorlu, K. Bin Yu, O. Yazaydin, J. Beckmann, G. Hanna, G. Yücesan, *Chem. Eur. J.* **2022**, *28*, e202104041.
[44] P. Tholen, L. Wagner, J. G. A. Ruthes, K. Siemensmeyer, T. H. Y. Beglau, D. Muth, Y. Zorlu, M. Okutan, J. C. Goldschmidt, C. Janiak, et al., *Small* **2023**, 2304057.
[45] P. Tholen, C. A. Peeples, M. M. Ayhan, L. Wagner, H. Thomas, P. Imbrasas, Y. Zorlu, C. Baretzky, S. Reineke, G. Hanna, et al., *Small* **2022**, *18*, 2204578.
[46] H.-J. Liu, C.-Y. Chiang, Y.-S. Wu, L.-R. Lin, Y.-C. Ye, Y.-H. Huang, J.-L. Tsai, Y.-C. Lai, R. Munprom, *ACS Catal.* **2022**, *12*, 6132.
[47] L.-C. Wang, B.-H. Liu, C.-Y. Su, W.-S. Liu, C.-C. Kei, K.-W. Wang, T.-P. Perng, *ACS Appl. Nano Mater.* **2018**, *1*, 3673.
[48] S. Chen, T. Takata, K. Domen, *Nat. Rev. Mater.* **2017**, *2*, 17050.
[49] P. Salcedo-Abraira, S. M. F. Vilela, A. A. Babaryk, M. Cabrero-Antonino, P. Gregorio, F. Salles, S. Navalón, H. García, P. Horcajada, *Nano Res.* **2021**, *14*, 450.
[50] M.-F. Qin, Q.-Q. Mu, S.-S. Bao, X. Liang, Y. Peng, L.-M. Zheng, *ACS Appl. Energ. Mater.* **2021**, *4*, 4319.
[51] C. Healy, K. M. Patil, B. H. Wilson, L. Hermanspahn, N. C. Harvey-Reid, B. I. Howard, C. Kleinjan, J. Kolien, F. Payet, S. G. Telfer, et al., *Coord. Chem. Rev.* **2020**, *419*, 213388.
[52] K. J. Gagnon, H. P. Perry, A. Clearfield, *Chem. Rev.* **2012**, *112*, 1034.
[53] G. Yücesan, Y. Zorlu, M. Stricker, J. Beckmann, *Coord. Chem. Rev.* **2018**, *369*, 105.
[54] A. Bulut, M. Wörle, Y. Zorlu, E. Kirpi, H. Kurt, J. Zubieta, S. Grabowsky, J. Beckmann, G. Yücesan, *Acta Crystallogr. Sect. B* **2017**, *73*, 296.
[55] T. Rhauderwiek, K. Wolkersdorfer, S. Oien-Odegaard, K. P. Lillerud, M. Wark, N. Stock, *Chem. Commun.* **2018**, *54*, 389.
[56] J. Ferguson, D. L. Wood, L. G. Van Uitert, *J. Chem. Phys.* **1969**, *51*, 2904.
[57] P. J. Dereń, W. Strék, U. Oetliker, H. U. Güdel, *Phys. Status Solidi B* **1994**, *182*, 241.
[58] T. C. Brunold, H. U. Güdel, E. Cavalli, *Chem. Phys. Lett.* **1996**, *252*, 112.
[59] H. A. Weakliem, *J. Chem. Phys.* **1962**, *36*, 2117.
[60] T. Shinagawa, A. T. Garcia-Esparza, K. Takanabe, *Sci. Rep.* **2015**, *5*, 13801.
[61] G. Li, L. Anderson, Y. Chen, M. Pan, P.-Y. Abel Chuang, *Sustain. Energy Fuels* **2018**, *2*, 237.

[62] L. Sondermann, W. Jiang, M. Shviro, A. Spieß, D. Woschko, L. Rademacher, C. Janiak, *Molecules* **2022**, *27*, 1241.
[63] Y. Matsumoto, E. Sato, *Mater. Chem. Phys.* **1986**, *14*, 397.
[64] A. Bergmann, T. E. Jones, E. Martinez Moreno, D. Teschner, P. Chernev, M. Gliech, T. Reier, H. Dau, P. Strasser, *Nat. Catal.* **2018**, *1*, 711.
[65] X. Bu, C. Chiang, R. Wei, Z. Li, Y. Meng, C. Peng, Y. Lin, Y. Li, Y. Lin, K. S. Chan, et al., *ACS Appl. Mater. Interfaces* **2019**, *11*, 38633.
[66] P. W. Menezes, C. Panda, C. Walter, M. Schwarze, M. Driess, *Adv. Funct. Mater.* **2019**, *29*, 1808632.

Manuscript received: August 25, 2023
Accepted manuscript online: September 15, 2023
Version of record online: November 8, 2023

Chemistry–A European Journal

Supporting Information

Exceptionally Stable And Super-Efficient Electrocatalysts Derived From Semiconducting Metal Phosphonate Frameworks

Thi Hai Yen Beglau, Marcus N. A. Fetzer, Istvan Boldog, Tobias Heinen, Markus Suta, Christoph Janiak,* and Gündoğ Yücesan*

Table of Contents

1. Synthesis

1.1. Synthesis of tetraethyl naphthalene-1,4-diylbis(phosphonate)

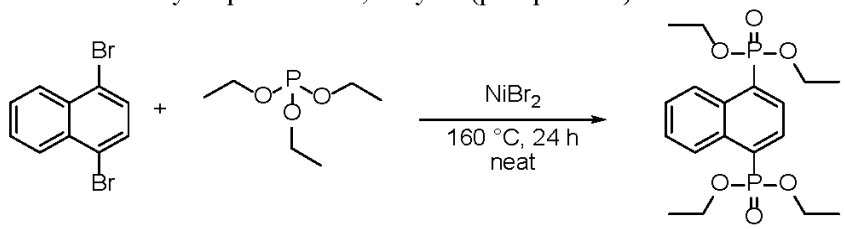

Under a nitrogen flow, 1,4-dibromonaphthalene (5,1 g, 17.8 mmol) was placed in a three-neck round-bottom flask equipped with a stirring bar. The flask was heated to 160 °C to melt the 1,4-dibromonaphthalene. To the melted 1,4-dibromonaphthalene $NiBr_2$ (0.5 g, 2.2 mmol) was added. Finally, triethyl phosphite (7.8 g, 46.9 mmol) was added dropwise over a period of 7 h. The reaction was stirred at the same temperature for 24 h. The crude product, a dark brown to orange oil, was purified by column chromatography using a mixture of EtOAc and EtOH (9:1 v:v). The product was isolated as a colorless oil with a yield of 3.8 g (9.5 mmol, 53.3 %).

^{1}H NMR (300 MHz, $CDCl_3$) δ 8.63-8.59 (m, 2H), 8.29-8.22 (m, 2H), 7.68-7.64 (m, 2H), 4.27-4.07 (m, 8H), 1.32 (t, J = 7.1 Hz, 12H); $^{31}P\{^{1}H\}$ NMR (121 MHz, $CDCl_3$) δ 17.4 (s); $^{13}C\{^{1}H\}$ NMR (75 MHz, $CDCl_3$) δ 132.9-132.4, 131.6 (d, J = 3.6 Hz), 129.2 (d, J = 3.5 Hz), 127.6, 127.3, 62.5 (d, J = 3.0 Hz), 16.3.

1.2. Synthesis of naphthalene-1,4-diphosphonic acid (1,4-NDPA-H_4)

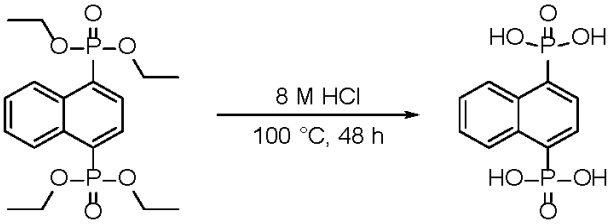

Tetraethyl naphthalene-1,4-diylbis(phosphonate) (3.8 g, 9.5 mmol) was mixed with 100 mL of 8 M hydrochloric acid and refluxed for 24 h. The white precipitate was filtered off and dried at 60 °C under reduced pressure to obtain 2.5 g (yield: 95 %) of pure acid.

^{1}H NMR (300 MHz, DMSO-d_6) δ 8.69-8.65 (m, 2H), 8.08-8.01 (m, 2H), 7.64 (dd, J=6.5, 3.4 Hz, 2H); $^{31}P\{^{1}H\}$ NMR (121 MHz, DMSO-d_6) δ 11.0 (s);

$^{13}C\{^{1}H\}$ NMR (75 MHz, DMSO-d_6)δ 135.6 (d), 132.4 (d), 130.3-129.9 (m), 127.8 (s), 126.4 (s).

2. Crystallography

A suitable dark blue crystal of Co_2[1,4-NDPA], or white in the case of Zn_2[1,4-NDPA] was mounted on a microloop in a drop of immersion oil. The measurement was performed using a XtaLAB Synergy (Rigaku) single crystal diffractometer equipped with a PhotonJet microfocus sealed tube X-ray source (Cu-Kα, λ = 1.54184 Å) at 100 K under a nitrogen gas stream (Oxford Cryostream liquid nitrogen cooling system). The data collection calculation, data reduction and adsorption correction were performed using CrysAlis PRO.[1] The structure was solved by SHELX-2018,[2] and refined using Olex.[3]

The structures were refined as inversion twins. The hydrogen atoms were placed geometrically and refined with Uiso(H) = 1.2 Ueq(C) thermal displacement parameters. The relevant crystal and structure refinement data is collected in Table S1.

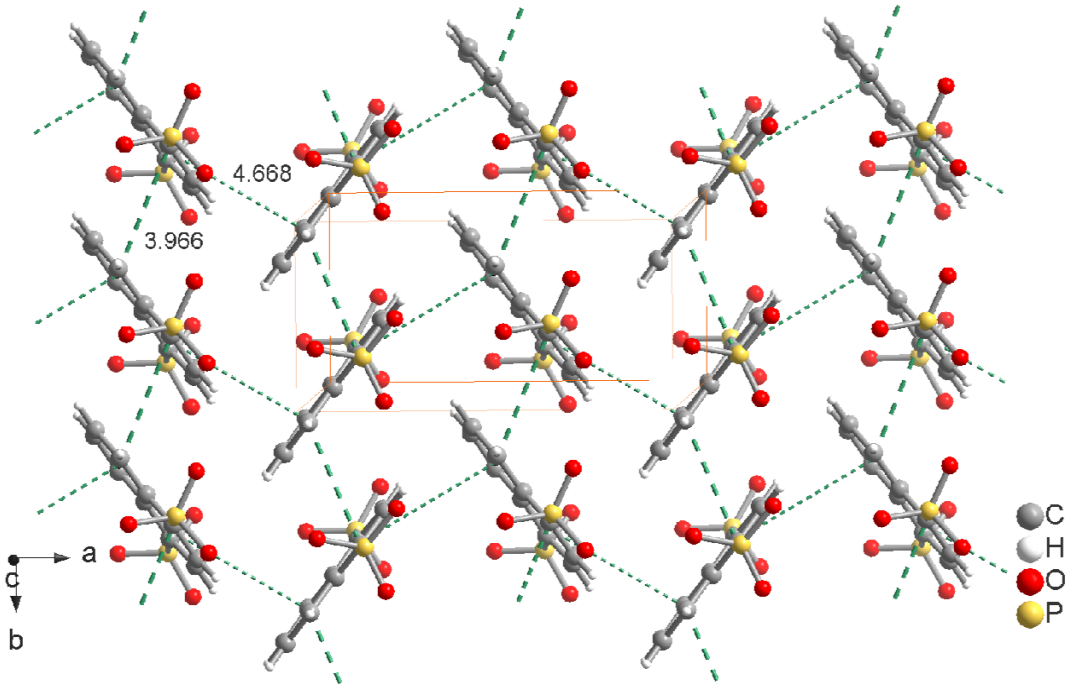

Figure S1. Presentation of π··· π interactions between the naphthalene moieties in Co_2[1,4-NDPA], **1**. The longer-dash lines show the intercentroid distances between the face-to-face interacting naphthalene moieties (3.97 Å), while the shorter-dash lines the edge-to-face ones (4.67 Å, note the presence of contiguous chains sustained by either type of the interactions.).

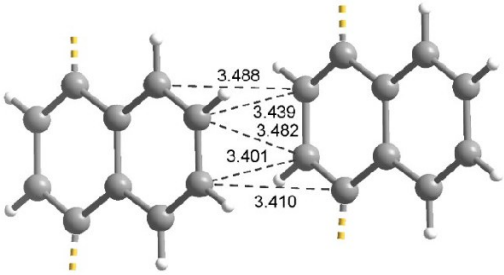

Figure S2. The shortest C···C contacts between the naphthalene moieties in Co_2[1,4-NDPA]

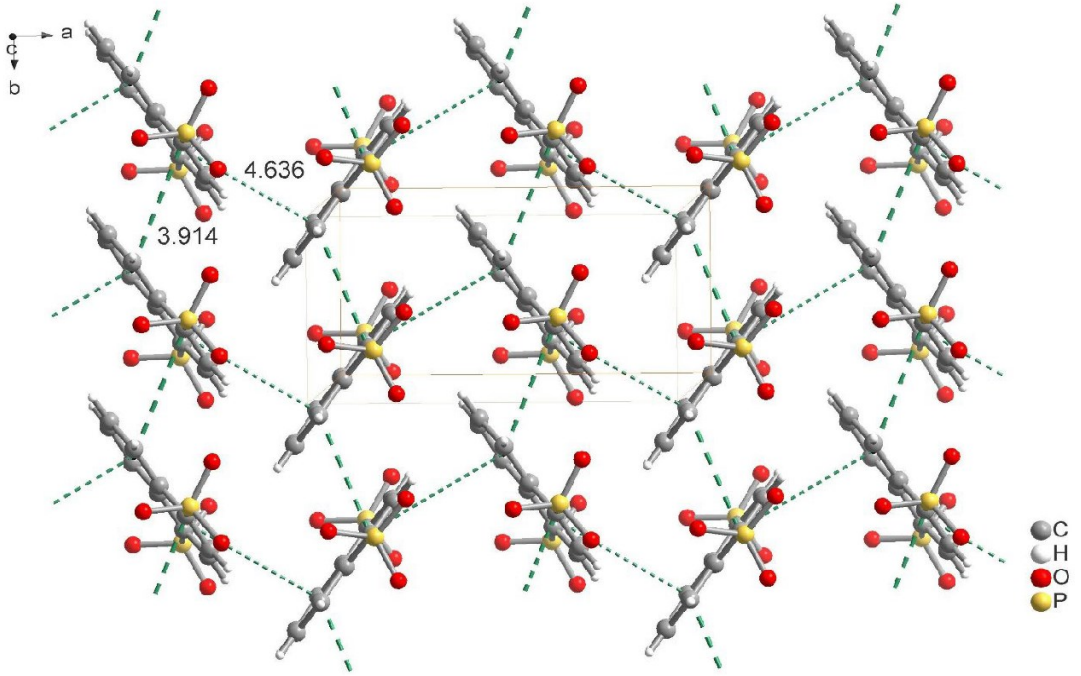

Figure S3. Presentation of π··· π interactions between the naphthalene moieties in Zn_2[1,4-NDPA]. The longer-dash lines shows the intercentroid distances between the face-to-face interacting naphthalene moieties (3.91 Å), while the shorter-dash lines the edge-to-face ones (4.64 Å, note the presence of contiguous chains sustained by either type of the interactions.).

Table S1 Crystal data and structure refinement for Co_2[1,4-NDPA] and Zn_2[1,4-NDPA]

	Co_2[1,4-NDPA]	**Zn_2[1,4-NDPA]**
Empirical formula	$C_{10}H_6O_6P_2Co_2$	$C_{10}H_6O_6P_2Zn_2$
M_r /g mol^{-1}	401.95	414.83
T /K	100(1)	100(1)
Wavelength / Å	1.54184	1.54184
Crystal system	Orthorhombic	Orthorhombic
Space group	*Pna*2$_1$ (no. 33)	*Pna*2$_1$ (no. 33)
a /Å	10.99806(17)	10.8927(4)
b /Å	5.63586(9)	5.5934(2)
c /Å	19.0334(3)	19.0195(6)
V /Å^3	1179.76(3)	1158.81(7)
Z	4	4
Calc. density / g cm^{-3}	2.263	2.378
μ / mm-1	24.848	7.962
F(000)	792	816
Crystal size /mm^3	0.1 × 0.07 × 0.02	0.06×0.03×0.02
θ range /°	4.646 to 78.575	4.65 to 79.00
Index ranges (*hkl*)	[-13, 11]; [-6, 6]; [-23, 22]	[-13, 13], [-7, 6], [-24, 22]
Reflections collected	7548	11741
Independent refl. (R_{int})	2150 (0.0302)	2227 (0.068)
Completeness / % to θ /°	67.684	99.9
Data / restraints / parameters	2150 / 1 / 182	2227 / 115 / 182
Goodness-of-fit (GooF)	1.060	1.069
$R[F^2 > 2\sigma(F^2)]$, $wR2$ [a)]	0.0264, 0.0718	0.0522, 0.1401
$R1$, $wR2$ (all data)	0.0274, 0.0722	0.0545, 0.1432

Inversion twin component sizes	0.336(6)	0.56(8)/0.44(8)
Largest diff. peak and hole	0.538, -0.428	2.283, -1.073
CCDC deposition number	**2235305**	**2212088**

[a)]Full-matrix least-square refinement on F^2 as implemented in SHELX. $R1 = \Sigma||F_o| - |F_c||/\Sigma|F_o|$; $wR2 = \{\Sigma[w(F_o^2-F_c^2)]^2/\Sigma[w(F_o^2)^2]\}^{1/2}$ where $w^{-1} = [\sigma^2(F_o^2) + (aP)^2 + bP]$, $P = [2F_c^2 + \mathrm{Max}(F_o^2, 0)] / 3$, a and b are refined parameters; $\mathrm{GooF} = \{\Sigma[w(F_o^2-F_c^2)^2] / (n-p)\}^{1/2}$.

PXRD pattern comparison and LeBail fitting for Co_2[1,4-NDPA].

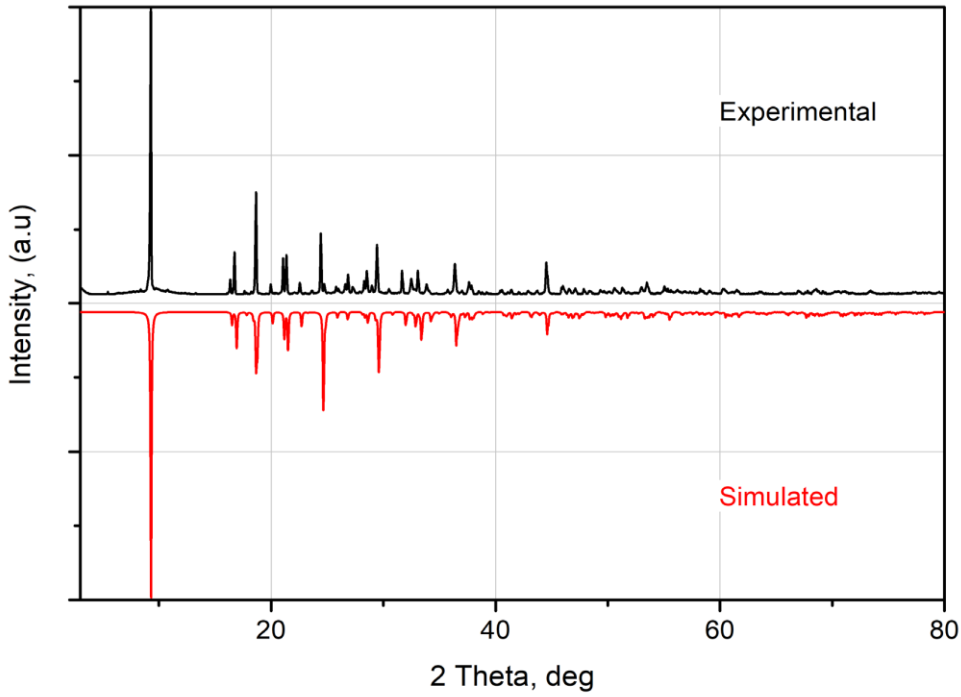

Figure S4. Comparison of the background-subtracted experimental and simulated PXRD patterns shown in a mirror-image like arrangement for Co_2[1,4-NDPA].

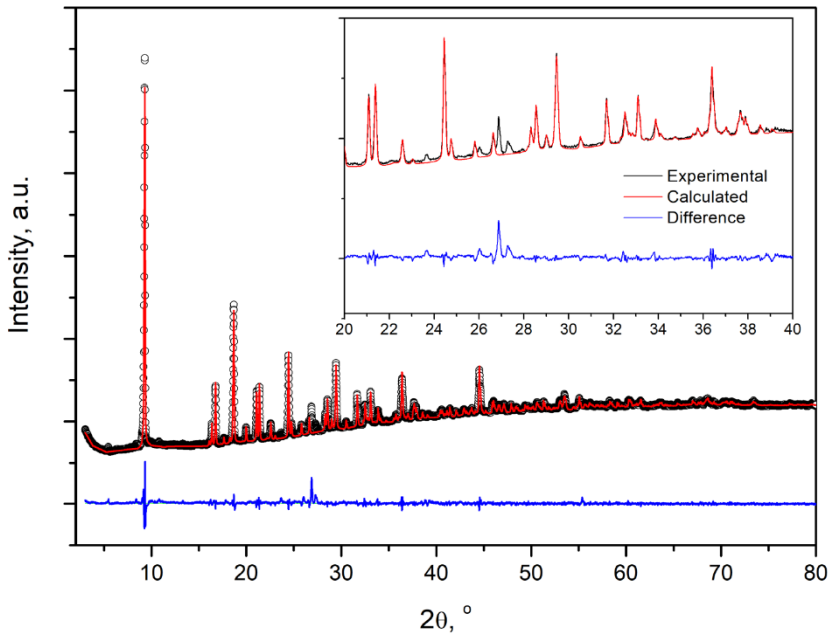

Figure S5. LeBail fitting of the experimental pattern of Co_2[1,4-NDPA], performed by the software Jana-2006; the experimental pattern was collected at 295 K (LeBail fit refines the cell parameter and tests the correctness of the chosen symmetry).[4] The results of the fitting: *P*na2_1; a = 11.00904 Å, b = 5.643041 Å, c = 18.98074. R_p = 1.21, GoF = 3.03. Only a minor amount of impurities present.

3. FT-IR spectroscopy

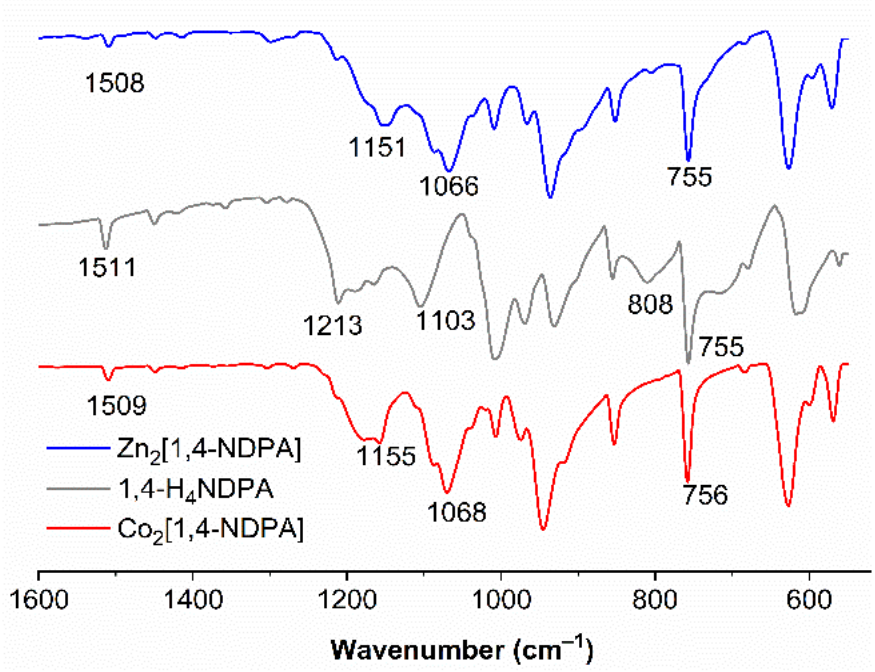

Figure S6.

The ATR-IR spectra of Co_2(1,4-NDPA) and Zn_2(1,4-NDPA) together with the pure linker. Spectrum of the linker 1,4-NDPA-H_4 corresponds to M. J. Bialek, J. Janczak, J. Zon, CrystEngComm, 2013, 15, 390.

4. Thermogravimetric analysis

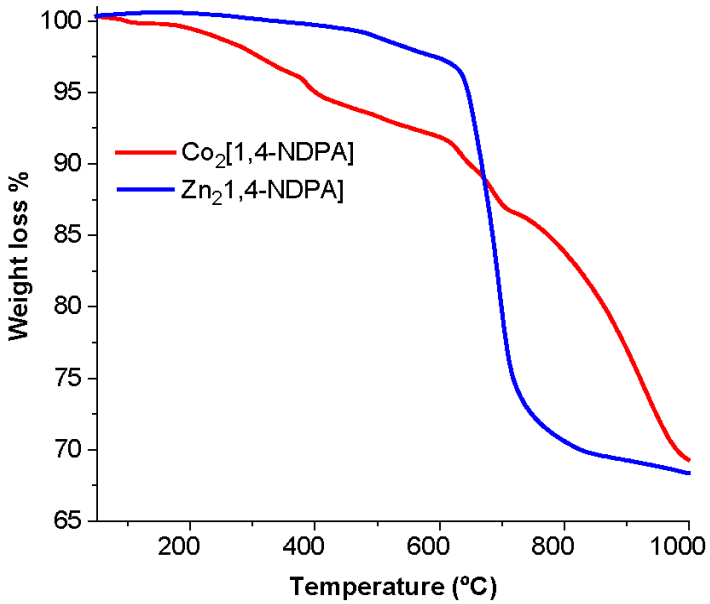

Figure S7. TGA curves of Co_2[1,4-NDPA] and Zn_2[1,4-NDPA] under N_2 atmosphere with a heating rate of 5 K/min.

The thermal stability of the Co_2[1,4-NDPA] and Zn_2[1,4-NDPA] were investigated by thermogravimetric analysis (TGA) measurements under a nitrogen atmosphere. Co_2[1,4-NDPA] and Zn_2[1,4-NDPA] show exceptional thermal stability where the organic components start to decompose at ca. 650 °C with 29% experimental weight loss (theoretical 30.9 %) for Zn_2[1,4-NDPA]. TGA curve of Co_2[1,4-NDPA] indicates a more gradual and broad weight loss until 1000 °C (See Figure S7).

5. Electrochemical measurement

All electrochemical experiments were performed by a Gamry Interace 1000 instrument in a three-electrode cell system at room temperature using a rotating disk glassy-carbo electrode (RD-GCE, 5 mm in diameter) at a rotation of 1600 rpm. 1.0 mol L^{-1} KOH (pH=14) solution was used as electrolyte and nitrogen was purged through the cell to remove oxygen for 30 min before the measurements. Samples were tested with the RD-GCE as working electrode, a reversible hydrogen electrode (RHE) as a reference electrode and a Pt plate as a counter electrode. 2.5 mg of pre-catalysts were dispersed in 250 μL ethanol + 250 μL DI water + 50 μL 5 wt.% Nafion solution by sonication for 30 min. Then, 10 μL of the well–dispersed pre-catalysts (0.23 mg cm^{-2}) were covered on the RD-GCE with drying at room temperature before testing. All linear sweep voltammetry (LSV) curves were recorded by sweeping the potential from 0.9 – 1.7 V vs RHE with scan rate 5 mV s^{-1}. Cyclic voltammetry (CV) measurements were carried out in the potential range between 1.0 – 1.7 V (vs RHE) with a scan rate of 10 mV s^{-1}. Each measurement was repeated 5 times in order to avoid any incidental error. The accelerated stability tests of the Co_2[1,4-NDPA] and Zn_2[1,4-NDPA] precatalysts for OER were performaned at room temperature by potential cycling for 1000 cycles at 100 mV s^{-1}. At the end of the cycling, the final catalyst formed on the working electrode was again subjected to polarization measurements at the scan rate 5 mV s^{-1}. In all measurements, the iR drop was compensated by the ohmic resistance arising from the electrolyte/contact resistance of the setup, and measured by electrochemical impedance spectroscopy (EIS).

For overall water splitting (both HER and OER) tests, the pre-catalysts were coated on commercial nickel foam (NF) which was used as both anode and cathode. The catalyst@NF electrode was fabricated by drop–casting the catalyst ink on the surface of pre–treated Ni foam which was dried at 60 °C under vacuum atmosphere. The loading was around 1 mg cm^{-2} by weighing the electrode before and after the catalyst deposition. The potential scan range was from 0.8 –1.8 V. The stability tests were carried out using a controlled current electrolysis where the potential was recorded at a constant current density of 50 mA cm^{-2} over a period of 30 h in 1.0 mol L^{-1} KOH electrolyte.

6. SEM and SEM-EDX before and after electrolysis

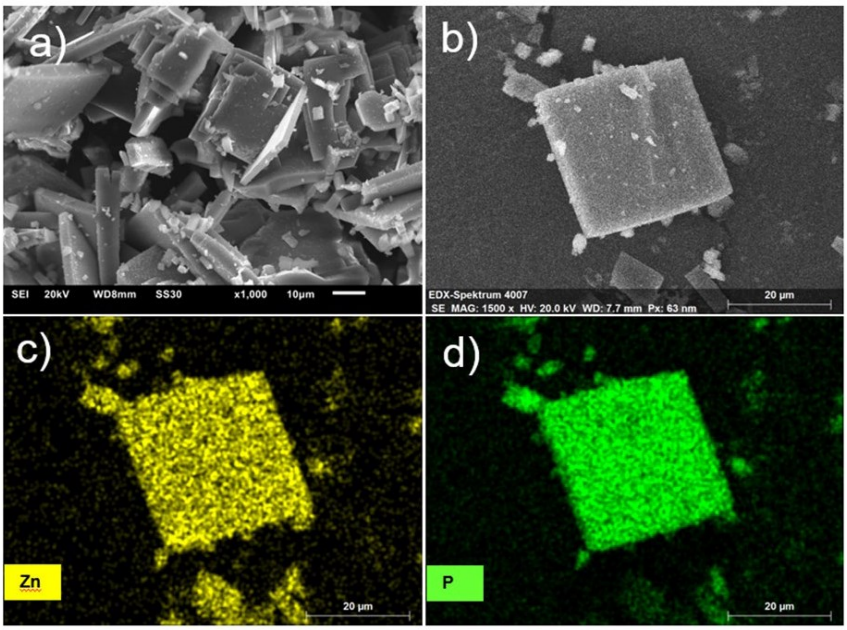

Figure S8. a) and b) SEM images of Zn_2[1,4-NDPA] and the corresponding elemental mapping of c) Co and d) P.

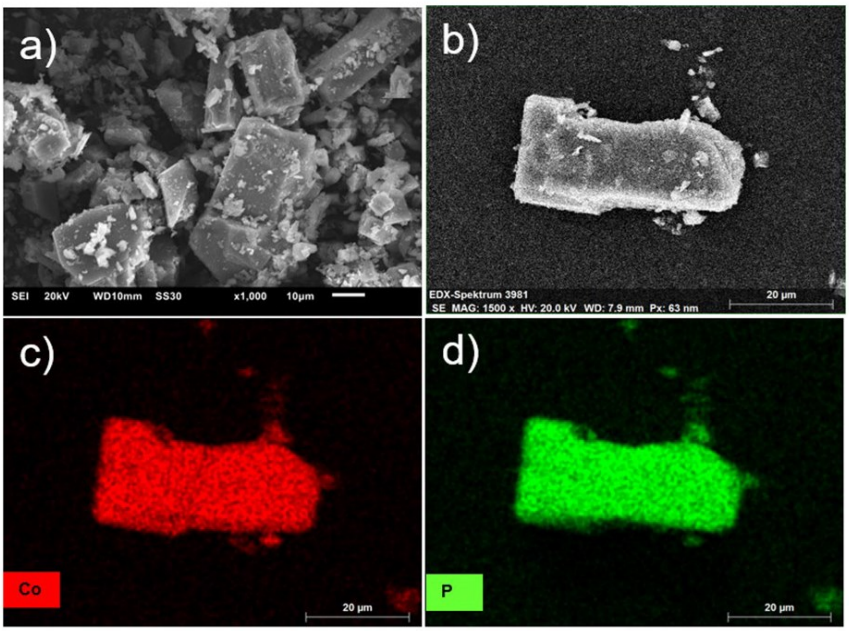

Figure S9. a) and b) SEM images of Co_2[1,4-NDPA] and the corresponding elemental mapping of c) Zn and d) P.

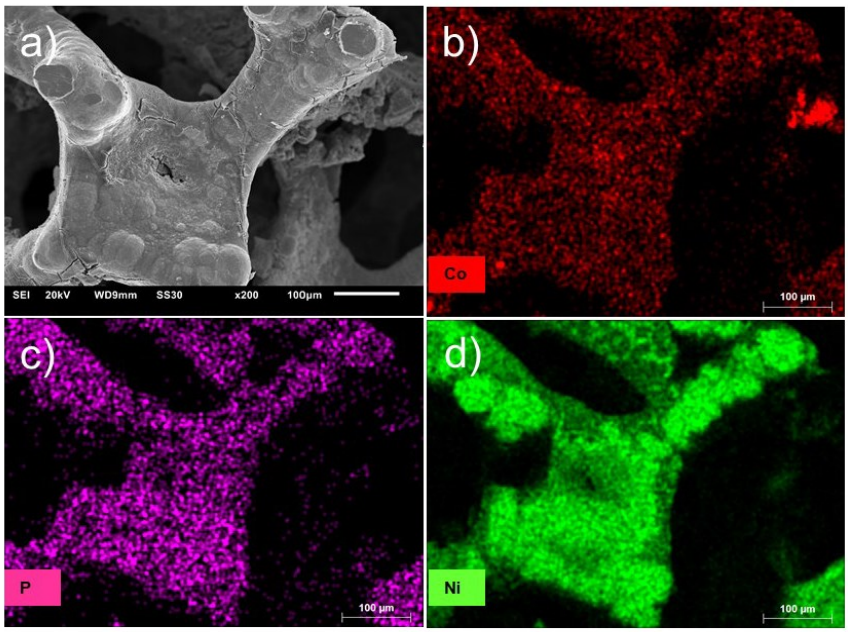

Figure S10. a) SEM images of the Co_2[1,4-NDPA]@NF electrode after 30 h of OER and corresponding elemental mapping of b) Co, c) P and d) Ni.

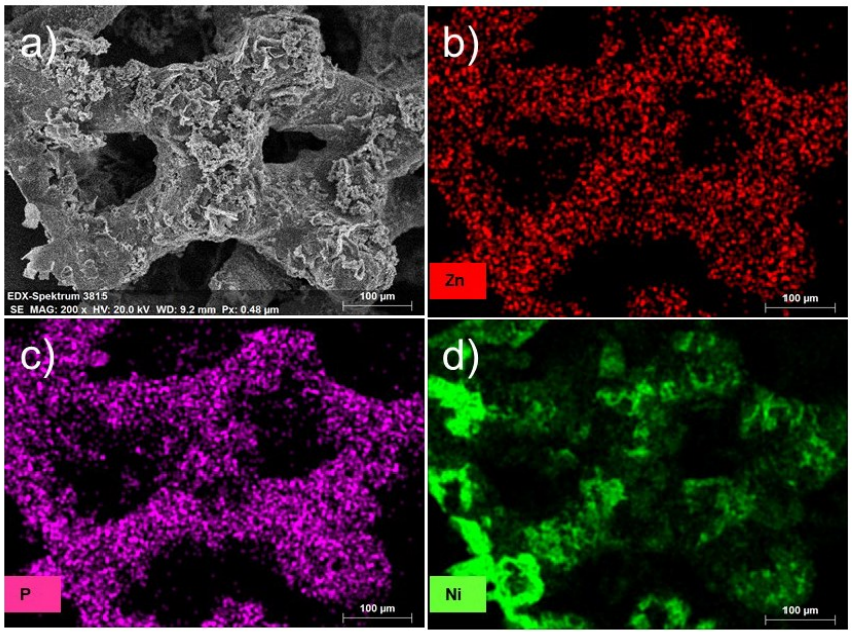

Figure S11. a) SEM image of Zn_2[1,4-NDPA]@NF electrode after 30 h of OER and corresponding elemental mapping of b) Zn, c) P and d) Ni

Table S5. SEM-EDX analysis of the ratio between metal and phosphorus of Co_2[1,4-NDPA] and Zn_2[1,4-NDPA] (theor. 1:1) before and after 30 h of electrolysis in 1 mol L^{-1} KOH electrolyte.

Sample	Molar ratio		Before OER		After OER	
	Metal	P	Metal	P	Metal	P
Co_2[1,4-NDPA]	1.3	1	1.1	1	99	1
Zn_2[1,4-NDPA]	1.3	1	1.1	1	5	1

Moreover, to further evaluate the OER activity of the Co_2[1,4-NDPA] and Zn_2[1,4-NDPA] precatalyst Table S6 compares the overpotentials and Tafel slopes at s current density of 10 mA cm^{-2} with previously reported Co- and Zn- catalysts. The Co_2[1,4-NDPA] and Zn_2[1,4-NDPA] precatalysts exhibit smaller or similar overpotentials and Tafel slopes at a current density of 10 mA cm^{-2}, in line with their good OER catalytic activity.

7. PXRD of synthesised β–$Co(OH)_2$ and physical mixing of β–$Co(OH)_2$ and the ligand 1,4-NDPA–H_4.

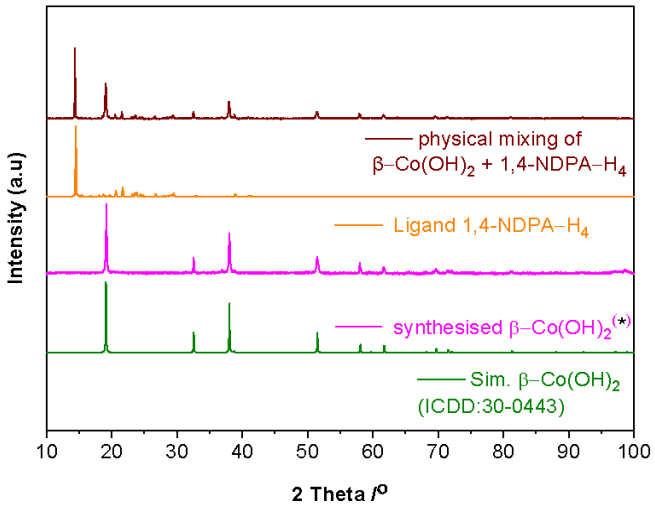

Figure S12. PXRD of the β–$Co(OH)_2$, ligand 1,4-NDPA–H_4 and physical mixing of β–$Co(OH)_2$ and ligand 1,4-NDPA–H_4 and simulation of β–$Co(OH)_2$ (ICDD: 30-0443)

(*) The β–$Co(OH)_2$ was used as a reference material for Co_2[1,4-NDPA]. 653 mg $Co(NO_3)_2 \cdot 6H_2O$ and 200 mg NaOH were added in 20 mL H_2O and ultrasonicated to homogenize. The solution was transferred into 50 mL Teflon line stainless-steel autoclave and put in oven at temperature of 180 °C in 12 h, followed by cooling to room temperature. The final products were obtained after washed

several time with DI water and ethanol via centrifugation (10,000 rpm, 10 min), followed by drying at 60 °C. The as-obtained powder was confirmed the structure by PXRD and denoted as β–$Co(OH)_2$.

8. OER performance comparison.

Table S6. Comparison of OER performance for several Co/Zn-based electrocatalysts.

Catalyst	Electrolyte (mol L^{-1} KOH)	Substrate	Overpotential η (mV) at 10 mA cm^{-2}	Tafel slope (mV dec^{-2}) at 10 mA cm^{-2}	Reference
Co_2[1,4-NDPA]	1	GCE	374	43	This work
Zn_2[1,4-NDPA]	1	GCE	408	82	This work
Co_2[1,4-NDPA]	1	NF	312	-	This work
Zn_2[1,4-NDPA]	1	NF	371	-	This work
RuO_2	1	GCE	318	62	This work
Co-MOF-74	1	GCE	377	193	5
Co-ZIF 67	0.1 mol L^{-1} NaOH	GCE	420	78	6
Co-BTC	1	NF	540	86	7
CoP	1	NF	390	65	8
Co_3O_4	1	GCE	530	47	9
CoP	1	GCE	390	50	10

NF: Nickel Foam, GCE: Glassy Carbon Electrode

9. Topological Analysis

The nearly planar 2D inorganic SBU, {$M(RPO_3)$}, (M = Co or Zn) is represented by a 3,3,4L25 topology (short symbol: {4.5.6}{4.5^2.6.7.8}{5^2.6}), which is essentially a relatively simple tiling of 4-, 5-,6- gons in a ratio of 1:2:1. As the tiling could not be achieved using regular n-gons, it is not particularly important. Yet, the Topos database lists more app. 50 occurrences of different compounds with this topology. There are no strictly similar metal phosphonate layers.

References

1. Rigaku, OD, *CrysAlis PRO*. Rigaku Oxford Diffraction Ltd, 2020, Yarnton, England
2. G. M. Sheldrick, *Acta Cryst. Sect. C*, 2015, 71, 3–8.
3. O. V Dolomanov, L. J. Bourhis, R. J. Gildea, J. A. K. Howard, and H. Puschmann, J. Appl. Crystallogr., 2009, 42, 339–341.
4. V. Petříček, M. Dušek, and L. Palatinus, Crystallographic Computing System JANA2006: General features. *Zeitschrift Für Kristallographie - Crystalline Materials*, 2014, 229(5), 345–352.
5. Z. Gao *et al.*, Synthesis, Characterization, and Electrocatalytic Activity Exploration of MOF-74: A Research-Style Laboratory Experiment. *Journal of Chemical Education*, 2021, 98, 3341-3347
6. S. Ghoshal *et al.*, ZIF-67 Based Highly Active Electrocatalysts as Oxygen Electrodes in Water Electrolyzer. 2018, *ACS Appl. Energy Mater.* 2, 5568
7. D. H. Taffa, D. Balkenhohl, M. Amiri, M. Wark, Minireview: Ni–Fe and Ni–Co Metal–Organic Frameworks for Electrocatalytic Water-Splitting Reactions. *Small Structures* 2022, 2200263
8. Z. Li *et al.*, Fe–Co–Ni trimetallic organic framework chrysanthemum-like nanoflowers: efficient and durable oxygen evolution electrocatalysts. *Journal of Materials Chemistry A,* 2022, 10, 4230-4241
9. A. J. Esswein, D. G. Nocera, Hydrogen production by molecular photocatalysis. *Chem. Rev.* 2007, 107, 4022
10. A. Dutta, A. K. Samantara, S. K. Dutta, B. K. Jena, N. Pradhan, Surface-Oxidized Dicobalt Phosphide Nanoneedles as a Nonprecious, Durable, and Efficient OER Catalyst. *ACS Energy Letters* 2016, 1, 169-174

3.2 Coordination modulation: a way to improve the properties of metal–organic frameworks

Diese Arbeit wurde veröffentlicht in

Fahime Bigdeli[+], Marcus N. A. Fetzer[+], Berna Nis, Ali Morsali and Christoph Janiak, *Journal of Materials Chemistry A* **2023**, *11*, 22105-22131.

DOI: 10.1039/d3ta03077f; Ref.[95]

[+]Die Autoren haben zu gleichen Anteilen zu dieser Publikation beigetragen.

Kurzzusammenfassung

Metallorganische Gerüste (MOFs) sind äußerst wertvolle Hybridmaterialien, die in der Forschung große Aufmerksamkeit auf sich gezogen haben. Ein Grund für diese Attraktivität ist die Gestaltbarkeit ihrer wichtigen Porositätseigenschaften wie Oberfläche, Oberflächenchemie, Porenform, Größe und Größenverteilung. Die Koordinationsmodulationsmethode bietet eine nützliche Möglichkeit, die Porosität sowie Größe und Form von MOFs weiter zu modifizieren, wobei Modulatoren während der MOF-Synthese als Leitmittel fungieren. In dieser Übersicht diskutieren wir die Koordinationsmodulation mit verschiedenen Arten von Modulatoren, Synthesetechniken, die Wirkung von Modulatoren sowie den Einfluss von Modulatoren auf die Eigenschaften der modulierten MOFs und ihre Anwendung.

Anteile an der Publikation:

- Die Projektidee erfolgte durch Herrn Prof. Dr. Ali Morsali.
- Der erste Entwurf wurde von Fahime Bigdeli und Berna Nis vorgenommen.
- Die Überarbeitung, Korrektur, umfassende Literaturrecherche und das Verschriftlichen neuer Abschnitte erfolgte in Zusammenarbeit mit Herrn Prof. Dr. Christoph Janiak.

Journal of Materials Chemistry A

ROYAL SOCIETY OF CHEMISTRY

REVIEW

View Article Online
View Journal | View Issue

Cite this: J. Mater. Chem. A, 2023, 11, 22105

Coordination modulation: a way to improve the properties of metal–organic frameworks

Fahime Bigdeli, †[a] Marcus N. A. Fetzer,†[b] Berna Nis,[bc] Ali Morsali *[a] and Christoph Janiak *[b]

Received 24th May 2023
Accepted 27th September 2023

DOI: 10.1039/d3ta03077f

rsc.li/materials-a

Metal–organic frameworks (MOFs) are highly valuable hybrid materials that have drawn significant research attention. One reason for such attractiveness is the designability of their important porosity features such as surface area, surface chemistry, pore shape, size, and size distribution. The coordination modulation method provides a useful way to further modify the porosity, size and shape of MOFs, whereby modulators act as guiding agents during the MOF synthesis. In this review, we discuss coordination modulation with various types of modulators, synthesis techniques, the action of modulators, as well as the effect of modulators on the properties of the modulated MOFs and their application.

1. Introduction

Metal–organic frameworks (MOFs) are potentially porous coordination networks with metal nodes and bridging organic ligands, called linkers. It is essential to control the morphology and porosity of MOFs in order to advance their potential applications without altering the basic chemical framework structure. Various methods, such as microwave (MW) heating, ultrasonic (US) and surface active agent (surfactant)-assisted syntheses, and coordination modulation have been used to control MOF formation.[1,2] The rate and direction of crystal growth can also be affected by modulators that may in turn change the crystallinity and phases of the MOFs.[3–7]

Modulation is a popular and easy method for tuning MOFs by applying an auxiliary ligand named modulator. In 2009, Tsuruoka *et al.* were apparently the first to report a modulator effect in MOF synthesis.[5] Traditionally, both inorganic and organic acids or bases have been used as modulators in MOF synthesis. This classical approach provides a solid foundation for MOF modulation. In addition, amino acids, which are characterized by both acidic and basic functionality, are proving to be versatile modulators,[8,9] as are surfactants, polyoxometallates, and various guest molecules. These various species enable finely tuned MOF structures.

The crucial factor in modulating MOF formation is the interaction between the chosen modulators and the organic linkers or the inorganic metal centers. This interplay between the different modulators, organic components and metal ions is the cornerstone for precise control of MOF synthesis if the modulator has a coordinating group, similar to the linker of MOF, it can compete with the linker for coordination to the metal ion during the framework assembly. The presence of a coordinating modulator can affect the nucleation process and its kinetics. Further, the growth of the framework is influenced by this competition, leading to specific morphologies, crystal sizes, and porosity features. If the modulator is (in addition) an acid or base then it will also influence the pH of the reaction medium and, thus, the acid–base equilibrium of the linker if this is derived by deprotonation from its (carboxylic or azole) acid precursor.[10]

Several monodentate carboxylic acids have been reported in the literature as modulators such as formic acid (FA), acetic acid (AA), benzoic acid (BA), dodecanoic acid, or lauric acid.[11] The use of carboxylate or carboxylic acid modulators is frequent since multitopic carboxylate linkers are one of the main linker types in MOFs.[5,12–14] Basic modulators include pyridine,[15–17] sodium hydroxide,[18] or ammonium hydroxide.[19] The most commonly used surfactants are cetyltrimethylammonium bromide (CTAB), sodium dodecylbenzenesulfonate (SDBS) or sodium dodecyl sulfate SDS.[20–22]

Thus, modulating conditions may also be beneficial for the formation of specifically MOF nanoparticles.[5,7,23–25] At the nano-dimension, the diffusion path length is shorter, allowing guest molecules to enter the pores more quickly. Additionally, the larger outer surface area relative to the volume makes more active functional groups on the outside of the MOF particles accessible for interactions.[7,23,26] Furthermore, modulation can lead to the formation of highly crystalline products due to the slowed growth rate of the crystal.[1,27] In addition, modulators can facilitate the formation of clusters[28] and some topologies of the MOFs.[29]

[a]Department of Chemistry, Faculty of Sciences, Tarbiat Modares University, Tehran 14115175, Iran. E-mail: morsali_a@modares.ac.ir

[b]Institut für Anorganische Chemie und Strukturchemie, Heinrich-Heine-Universität Düsseldorf, Universitätsstr. 1, D-40225 Düsseldorf, Germany. E-mail: janiak@uni-duesseldorf.de

[c]Department of Chemistry, Bursa Technical University, Bursa 16310, Turkey

† These authors contributed equally to this work.

Table 1 Examples for the effect of modulators

Effect	Modulator[a]	Examples	Ref.
Crystal phase	BA	Zr-SXU-1, Zr-SXU-2, Zr-SXU-3	33
	BA	MIL-101 (Cr), MIL-88B (Cr)	34
	TFA	NU-1000, NU-901	35
Size	AA	MIL-101 (Cr)	36
	MNA	CuNDC	37
	NH_4OH	$Co_2(bim)_4$	38
Morphology	CTAB	NMOF-1	25
	AA, FA	MIL-88A (Fe)	39
Defects	Carboxylic acid	UiO-66	40
	1-HMIM	BIT-58	41
Porosity	Citric acid	HKUST-1	42
	FA, AA, DFA, TFA	UiO-66	43
Surface area	AA	UiO-67	27
	MeOH	MIL-88B (Fe)	44
Stability	TFA, AA	UiO-66	45
Low temperature	AA	UiO-66	46
	HCl	UiO-66	47
	FA	DUT-67, UiO-66-NH_2, MOF-801	48

[a] List of abbreviations (alphabetical order): AA = acetic acid, BA = benzoic acid, CTAB = cetyltrimethylammonium bromide, DFA = difluoroacetic acid, FA = formic acid, 1-HMIM = 1-methylimidazole, MNA = 6-methoxy-2-naphtholate, TFA = trifluoroacetic acid.

Despite lack of sufficient in-depth knowledge at the molecular level to understand the modulation mechanism, modulation allows the MOF properties to be changed and adapted or improved to potential applications.[6,30–32] For example, MOF films with applications in catalysis and gas separation can be formed through the growth of crystal faces in certain directions.[23] In addition, by applying these modulation control techniques, we can gain a better understanding about the fundamentals of the framework assembly mechanism.[24]

In this review, we aim to address the synthesis methods of modulated MOFs and the effect of modulation on their properties. Table 1 shows an introductory overview on the general effect of modulation on the properties of MOFs and this synthesis processes using various examples.

2. Types of modulators

2.1 Inorganic acids

Inorganic acids, such as aqueous HF or HCl, can directly shift the acid–base equilibrium of the organic linker acid to the protonated state. The deprotonation of the linker precursor acid to form the conjugated base anion is a requirement for the actual anionic linker coordination to the metal ions. Hence, an added acid will acid–base equilibrium of the linker to its acid form which consequently slows down the formation of the coordination network.[24,49] Thereby, the crystallinity of the MOF can be improved. Further, the anions of inorganic acids, such as F^-, Cl^-, SO_4^{2-}, NO_3^- are also coordinating ligands to metal ions. Thereby, this anionic ligand can compete with the linker for coordination to the metal ion during the framework assembly.

Using concentrated HCl as a protonation modulator is a well-studied approach in the literature. It can increase the number of defective sites in UiO MOFs by replacing a linker with coordinating chloride ligands and by increasing the acidity of the reaction medium and the hydrolysis rate of the solution.[19]

In 2013, Katz *et al.* analyzed the effects of HCl as a modulator on the formation of UiO-66, UiO-67, and their functionalized derivatives such as UiO-66-NH_2. The results of this study showed that the use of HCl as a modulator resulted in obtaining phase-pure and reproducible results.[47]

Fluoric acid, HF, has also been used for the synthesis of MOFs, including MIL-101(Cr),[50,51] UiO-66,[52] MIL-53 (ref. 53) and Al-MOFs.[54] These MOFs have sizes ranging from nano- to micrometers and regular morphologies. During the MOF synthesis, the fluorine anions can form strong metal-fluoride bonds with the metal centers, which then directly compete with the linkers used. The presence of HF modulator has been demonstrated to be effective in controlling morphology, size and volume of pores, and acidity of the reaction medium during the synthesis of MOFs.[50,55,56]

In addition to the direct competition with the linkers, the anion of the inorganic acid modulator also contributes to charge balancing. This significantly influences the process of self-assembly of the MOF.[54]

2.2 Inorganic bases

Inorganic basic modulators, with their alkaline properties, increase the solubility of the organic carboxylic acid precursors of the linkers by deprotonating the acid to the carboxylate anion. The increased solubility then leads to faster nucleation and the formation of smaller MOF crystallites. Additionally, basic modulators can form hydroxides or oxides with the metals involved, further accelerating the nucleation process. Ammonium hydroxide is a frequently employed base in MOF synthesis due to its effectiveness in enhancing linker solubility and facilitating nucleation, influencing the size and structure of the resulting MOF crystals.[57–59] Abid *et al.* synthesized a series of UiO-66 MOFs with different concentrations of ammonium hydroxide as modulator. They were able to show that with increasing modulator concentration, the particle size decreased while the pore size increased.[57]

2.3 Carboxylate modulators

The use of monocarboxylate modulators like formic acid, acetic acid, and benzoic acid is typical in the synthesis control of carboxylate MOFs.[4,12–14] The metal–ligand coordination equilibrium between the monocarboxylate modulator and the oligocarboxylate linker affects the nucleation process, which is in turn connected to reaction kinetics.[60] Shearer *et al.* examined the impact of acetic acid (AA), formic acid (FA), difluoroacetic acid (DFA), and trifluoroacetic acid (TFA) at different concentrations on the synthesis of UiO-66 MOFs in terms of crystallinity, surface area and defects. Their work revealed that all these modulators, also at different concentrations, exerted a beneficial influence on the formation of UiO-66.[43]

The use of monocarboxylate modulators in their anionic form, *e.g.* sodium acetate, can also influence the deprotonation equilibrium of the oligocarboxylic acid linker precursor.[1,49]

2.4 Amino acid modulators

Amino acids are appealing modulating agents due to their abundance and the wide variety of side chains in their structure, which can result in unique modulating properties. Diverse amino acids, such as proline, phenylalanine, and glycine, can be effective modulators for the synthesis of MOFs, especially Zr and Hf MOFs, ZIFs and the UiO-66 series. This can result in high-quality crystals with proper pore size and morphology, thereby increasing their application potential.[9,61,62] Amino acids are divided into five categories based on side-chain polarity: aromatic, aliphatic non-polar, polar uncharged, positively charged, and negatively charged. Unlike inorganic acid modulators, amino acids have been employed to a lesser extent for the purpose of synthesizing MOFs in a controlled manner.

Liang *et al.* investigated the effect of 20 natural amino acids as modulators on the synthesis of ZIF-8 in an aqueous solution. It was observed that the size and morphology of the ZIF-8 particles depended on the chemical nature of the amino acids, especially in terms of their polarity. By increasing the hydrophobic property of non-polar amino acids, the morphology of ZIF-8 changed from spheroid and dodecahedron to rhombic and truncated cube, respectively. This change was accompanied by a decrease in particle size and an increase in the number of particles. The polar neutral amino acids exhibited a similar orientation. Small spheres of ZIF-8 were formed by the negatively charged amino acids. When a mixture of two different amino acids was used, two types of particle distributions were produced, relating to the MOFs synthesized by two different amino acids as modulators separately.[63]

2.5 Amine modulators

Amine modulators can deprotonate the carboxyl acid linker precursor and also assume the role of competitive ligands in bonding with metal centers. Thus, through these two functions, they may modify the nucleation and crystal growth process. Cravillon *et al.* indicated that the presence of *n*-butylamine modulator during the synthesis of ZIF-8 led to the production of ZIF-8 nanocrystals. However, increasing the amount of *n*-butylamine eventually did not result in smaller particles, as the amine then acted as a competing ligand with the imidazolate linker.[24]

Lu *et al.* successfully synthesized NH_2-MIL-53(Al) nanoplates using a urea modulator *via* a one-step hydrothermal method. This nanoplate was then employed as a fluorescent probe for the highly selective analysis of free chlorine in water.[64]

Taddei *et al.*, studied the effect of substituting amine functional groups in benzoic acids on defect sites and electronic properties of MOF. The framework structure of the selected ABAs include 2-aminobenzoic acid (2-ABA), 3-aminobenzoic acid (3-ABA), 4-aminobenzoic acid (4-ABA), and 3,5-diaminobenzoic acid (3,5-DABA). Benzoic acid (BA) without amine substitution was also used to better evaluate the impact of amine groups on MOF performance. They confirmed that MOF band gaps can be influenced by defect engineering with the help of different aminobenzoic acids as modulators. These results demonstrate that the band gap can be modified by altering the position or number of amine groups in the aromatic ring. By using ABA modulators as species for defect engineering, a narrowing of the HOMO–LUMO gap will ensue.[65]

2.6 Surfactant modulators

The main characteristic of surfactants is their amphiphilic behaviour based on the fact that they have both a polar head group and a long non-polar tail. The effect of surfactant modulators such as sodium dodecyl sulfate (SDS) or cetyltrimethylammonium bromide (CTAB) on MOF structures depends upon the molecular interactions between the functional polar head groups of the surfactant and the surface of the growing MOF.[66] They can either undergo adsorption onto crystal facets on the surface of MOF structure to favor one direction of growth, or function as capping agents to take control over particle size and morphology during the MOF formation process.[67] The charge density of the surfactant head is critical for controlling the size and shape of MOFs. By using polyvinylpyrrolidone (PVP), Cai *et al.* showed that the structure of Fe-MIL-88B changes from hexagonal bipyramids to bipyramidal hexagonal prism as a function of the concentration of PVP, with a concomitant increase in particle size in one direction, from 1.8 to 5.4 nm. This type of morphology change occurred due to the preferential interaction of the pyrrolidone with the iron ions.[68] Surfactants can be used to introduce mesopores in otherwise microporous MOFs during the synthesis.[69] The formation of micelles in solution by surfactants provides a template where the MOF can grow around. The mesopores are then surrounded by the walls of the micropore MOF. After the surfactant is removed through washing processes, mesopores remain in the MOF structure.[23]

Surfactant or surfactant/co-surfactant liquids form emulsions from hydrophilic and hydrophobic phases. The dispersed phases can be considered a large number of sites that facilitate chemical reactions, particularly towards nanomaterials.[70,71] Using these microemulsions, it is possible to modulate the features of MOFs through parameters such as ratio of solvents and surfactants,[72] additives,[70] and temperature.[73]

2.7 Polyoxometallate modulators

Polyoxometalates (POMs) are inorganic anionic clusters and can act as structure-directing agents through hydrogen bonding, coordination interactions, and electrostatic interaction.[74] POMs may affect the coordination bonding between metal centers and organic ligands during the MOF synthesis. Therefore, they can control the nucleation and growth processes, which in turn affects the morphology and size of MOFs.[75] Wang *et al.* achieved the regular and uniform morphologies of octahedrons and hollow hierarchical spheres by using Keggin-type POMs (sodium phosphotungstate, abbreviated as NaPW) as a modulator in the synthesis of nano$[Cu_3(BTC)_2]_n$ (BTC = benzene-1,3,5-tricarboxylate) (Fig. 1).[76]

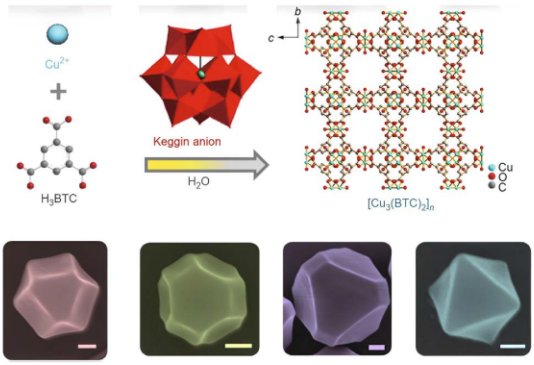

Fig. 1 Schematic representation of the synthesis of $[Cu_3(BTC)_2]_n$ nanoparticles modulated by POM and water. At the bottom, TEM/SEM images of the uniform $[Cu_3(BTC)_2]_n$ nanocrystals can be seen (scale bar is 200 nm).

In the report of Xu *et al.*, uniform hierarchical Fe/Co-BTC nanotubes were prepared using NaPW modulator, which exhibited appealing properties, such as increased specific area, large pores, and low density, leading to an increase in the number of active sites for desirable catalytic applications for the detoxification of sulfur compounds by O_2.[77]

2.8 Gas modulators

The field of gas modulation in MOFs remains relatively uncharted within the domain of MOF synthesis. In this methodology, distinct gases are intentionally introduced into the reaction autoclave under elevated pressures. A crucial prerequisite in this context is the specific interaction between the chosen gas and the metal species employed in the synthesis. This compatibility favors the interactions between the gas molecules and the metal atoms, facilitating and promoting the controlled formation of MOFs. In the example of Monteagudo-Olivan *et al.* the reaction time of MIL-88A(Fe) and MIL-53(Fe/Al)-Fa could be shortened with the aid of CO and O_2 gas at a pressure of 6 bar.[78]

2.9 Large organic molecule modulators

Large organic molecule modulators comprise a category of molecules that exert a discernible influence on MOF formation due to their size and structural properties. These modulators span a broad spectrum, ranging from relatively small molecules such as caffeine to larger molecules such as rhodamine B or polyethylene glycol. In the case of caffeine, the effect of these modulators is shown by interactions with the organic linkers *via* hydrogen bonds.[79,80] Among the largest representatives of this class are the porous polystyrenes. In this context, MOF formation is induced within the porous structure of the polystyrene framework itself. Following MOF formation, the polystyrene modulators are removed, leading to the formation of MOFs with different and tailored properties.[81]

In principle, when considering the influence of modulator molecules on MOF synthesis, it becomes important to account for the template effect. The template effect arises due to the size and structure of the modulator molecules, which can shape the resulting MOF structure. A notable example of this complex relationship is exemplified in the work of Liédana *et al.*, who investigated the role of caffeine in the synthesis of NH_2-MIL-88B(Fe). On one hand, it can be viewed as a template, on the other hand, the interaction of caffeine with the MOF and the resulting structure is also considered.[82]

Such examples highlight the challenges in drawing a clear demarcation between the roles of modulators and templates in MOF synthesis. The transition between these roles can indeed be seamless, and it may vary depending on the specific modulator, the MOF system, and the concentration at which the modulator is employed.

3. Synthesis modification of MOFs by modulators

In hydrothermal MOF synthesis, multiphase products can be obtained which are difficult to separate, as MOFs cannot be recrystallized. Finding the optimal conditions to synthesize MOFs with high-quality crystallinity and desired properties is of interest in research.[83] Utilizing modulators, in addition to the structural metal and linker units, is another parameter that can be effective in the synthetic approaches.[1,84] As mentioned previously, the nature of the modulators, their functional group, pK_a, and relative concentrations are factors to control the assembly of the MOF,[85–87] either through intermediate modulator-metal coordination or modulator-linker interactions, such as hydrogen bonds.[88]

Vakili *et al.* showed that the synthesis methods are effective in using the necessary amount of HCl modulator for the synthesis of UiO-67 crystals, and 135 and 65 equiv. of HCl are required in the microwave and solvothermal methods, respectively. By increasing the amount of modulator HCl for the synthesis of UiO-67, the amount of produced MOF also increased. This could be attributed to the presence of water in the HCl solution, which facilitates the hydrolysis of Zr salts and provides the required oxygen molecules for the formation of secondary building units (SBUs). This, in turn, accelerates the formation of UiO-67 (eqn (1)). In addition, increasing the concentration HCl as a modulator leads to an increase in the specific surface area of the MOF, albeit up to an optimal amount of the modulator.[89,90]

$$6ZrCl_4 + 6H_2bpdc + 8H_2O \rightarrow Zr_6(O)_4(OH)_4(bpdc)_6 + 24HCl \quad (1)$$

The use of modulators can lead to the formation of a single-phase product, as well as improved crystallinity and reproducibility.[91,92] For example, Shaikh *et al.* prepared several pure phases of Zr-MOFs (PCN-222, PCN-223, MOF-525) by adjusting the synthetic conditions, including the type and concentration of modulator and the acidity of the reaction medium. The modulators employed in the study were carboxylic acid species,

including trifluoroacetic acid, trichloroacetic acid, difluoroacetic acid, chloroacetic acid, formic acid, acetic acid, propionic acid, trimethylacetic acid, hexanoic acid (C6), decanoic acid (C10), myristic acid (C14), stearic acid (C18), pentafluorobenzoic acid, 2,6-difluorobenzoic acid, 4-nitrobenzoic acid, benzoic acid, and 4-methoxybenzoic acid.[93]

If the modulator is incorporated into an initially formed MOF, *e.g.* as a labile terminal ligand at the metal ions, it could be removed to form open metal sites (coordinatively unsaturated sites).[94] Additionally, the modulator ligand can be post-synthetically replaced with another ligand to introduce a desired functional group.

The morphology, size, crystallinity, and uniformity of MOF particles can be altered by the use of modulators.[95] Uniformity and separated MOF particles are significant factors for numerous applications. Albuquerque and Herman used benzoic acid (BA) as a modulator during a microwave-assisted continuous flow synthesis at high temperature with a brief reaction time. Without the use of BA, this led to smaller agglomerated particles in the reagent. Using the optimum amount of modulator, particles with a uniform shape and increased crystallinity could be obtained.[96] In addition, the orientation of the crystal growth by modulators plays an influential role in the formation of high crystalline MOF films.[97]

The synthesis of MOFs can be highly sensitive to reaction conditions such as temperature, concentration, and solvent. Interestingly, Zahn *et al.* reported that the MOF Zr-FMA could be synthesized in both water and *N*,*N*-dimethylformamide (DMF) solvent in the presence of FA modulator. As expected, the nucleation rate declined with increasing modulator concentration in water, while the reaction rate increased with increasing modulator concentration in DMF. This result is justified by the presence of a minuscule amount of water in commercial FA, which expedited the MOF-forming process in the organic solvent.[98]

Liu *et al.* applied BA and trifluoroacetic acid (TFA) as modulators and a small amount of water to form the Fe-based porphyrinic MOF M-PMOF-3(Fe), which had not been previously obtained by other methods. Concurrent with modulator coordination, the water molecules increase the nucleation rate by hydrolysis of the metal salt.[99]

The use of HNO_3 as a modulator instead of HF in the synthesis of MIL-101(Cr) resulted in a yield of over 80%, with an average $S_{BET} > 3200\ m^2\ g^{-1}$ in repeated experiments in a small-scale laboratory synthesis. This is a significant improvement compared to the average yield of 50% observed in most published syntheses with and without HF. The large-scale synthesis of MIL-101(Cr) could use the finding of HNO_3 addition, producing more than 100 g of the product with near 70% yield and a BET-surface area around $4000\ m^2\ g^{-1}$. The modulator AA together with seeding could decrease the reaction temperature to as low as 160 °C, which is significantly lower than 220 °C typically used in published procedures with and without HF, while still maintaining a relatively good yield and BET surface area of the product.[50] Thus, it is possible to replace HF with other modulators in MOF synthesis, allowing for the synthesis to be conducted under more benign conditions and reducing the health risks associated with HF.[100]

With respect to surfactants and emulsions, often reverse microemulsions have been utilized for the synthesis of MOFs.[101] Reverse emulsions are created when water droplets are dispersed in a hydrophobic organic solvent or oil. Microemulsions, in particular, are composed of dispersed droplets with radii ranging from 5–50 nm. In reverse microemulsions for MOF synthesis, two-micellar systems, containing either the metal salt or the organic linker, were mixed and the reaction was initiated through coalescence.[102] The reaction temperature in the reverse microemulsion synthesis of MOFs was between 0 °C and 120 °C.[103] To date, no reverse emulsion syntheses of MOFs have been carried out at temperatures higher than 180 °C.

On the other hand, an alternative approach has been explored in the literature, wherein surfactants assume the role of capping agents in MOF synthesis. In this context, the critical emphasis is not centered on the formation of micelles but rather on the direct interaction that transpires between the MOF surface and the surfactant molecules themselves.[104]

A less conventional synthesis method for MOFs is dry gel conversion (DGC).[90] This method involves placing a small amount of the solvent at the bottom of the Teflon reactor and the starting materials on a porous support to physically separate the solvent and reactant mixture (Fig. 2). The ability to recover and reuse the solvent after the reaction and to use only one-sixth or less of the solvent volume compared to the solution synthesis on the same scale makes this process an economically and ecologically attractive option for industrial DGC application.[90]

The importance of using modulators in the DGC method is highlighted. When BA is employed as a modulator in the synthesis of nano- to micro-sized Zr-based UiO-MOFs, the resulting product is more stable and of thick consistency. Without a modulator in the reaction system, much of the MOF is washed away through the pores with the solvent which loses its reusability. With BA or HCl as modulator in the DGC synthesis, the BET surface areas for UiO-66, UiO-66-NH_2, and UiO-67 were in good agreement with literature values, with yields up to 93%.[90]

3.1 Post-synthetic modulator exchange

Post-synthetic procedures refer to follow-up reactions or treatments of the already formed MOF. In principle, the solvent

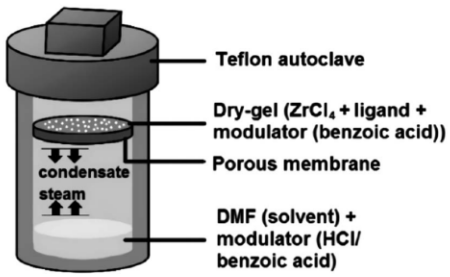

Fig. 2 Schematic representation of the reactor setup for DGC. Reproduced from ref. 90 with permission from The Royal Society of Chemistry, copyright 2017.

removal from the MOF pores upon activation is already a post-synthetic procedure.[105] Additionally, when MOFs have large enough pores to provide the access of reagents, generally metal clusters with labile coordination ligands and functional groups at the linker can be sites for a post-synthetic process.[106] Removing or exchanging a labile coordinating modulator ligand is a simple and inexpensive post-synthetic reaction.[107]

Hu *et al.* used a post-synthetic exchange of modulator ligand to prepare chiral MOF-808 by replacing metal-coordinated formate with chiral ligands. It should be noted that the large size of the MOF-808 pores was essential for the successful exchange (Fig. 3).[108] However, the necessary porosity can also be provided by creating a defective MOF structure through coordination modulation.[65]

Drache *et al.* enhanced the stability of the DUT-67 (a Zr-based MOF with 2,5-thiophenedicarboxylate linker) against water removal by increasing the hydrophobicity of the pore surfaces through the exchange of post-synthetic modulator ligands such as formate, acetate or propionate with fluorinated carboxylate ligands.[106]

In another report by Drache *et al.*, the modulated DUT-67 was prepared by using formate modulator and modified post-synthetically by diluted acids including HCl or H_2SO_4 to enhance catalytic activity. The small size of DUT-67 crystals allowed anion exchange to be performed easily with a short treatment time and low concentration of the acidic solution. The exchange of the modulator with inorganic acids (for charge balance), resulted in the formation of DUT-67 with high crystallinity and porosity, hydrophilicity as well as increased acid strength, leading to high activity in the catalytic reactions.[109]

Ardila-Suárez *et al.* synthesized a defective MOF-808 with the AA modulator, which had additional meso-pores in the structure.

The following post-synthesis treatment with sulfuric acid not only exchanged acetate with (hydrogen) sulfate on the Zr clusters, but also the benzene-1,3,5-tricarboxylate linkers were sulfonated, increasing the thermal stability and number of acidic sites of the Zr-MOF.[95]

It is possible that interpenetration could lead to a reduction in the size of the pores and the available space; however, this is not always the case. The interpenetrated Zn-MOFs $[Zn_4OL_3]\cdot$guest (NJU-Bai1) and $[Zn_4OL_3DMF_2]\cdot$guest (NJU-Bai2), H_2L = 4,4′-(carbonylimino)dibenzoic acid, were synthesized by Duan *et al.* using the amino acid modulator L-tyrosine. The resulting compounds are interpenetrated MOFs with larger pores, demonstrating a high capacity to adsorb hydrogen gas. In addition, it has been shown that structural features can be controlled by altering the concentration of the modulator and the reaction temperature (Fig. 4).[110]

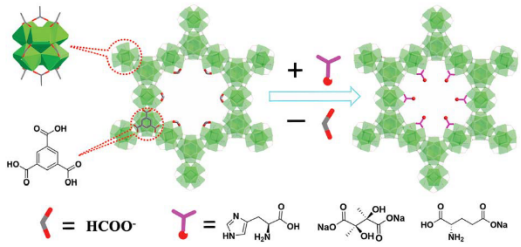

Fig. 3 The structure of MOF-808 and the schematic representation of post-synthesis exchange of the formate modulator with chiral ligands towards MOF-808-His, MOF-808-Tar and MOF-808-Glu. Reproduced from ref. 108 with permission from The Royal Society of Chemistry, copyright 2020.

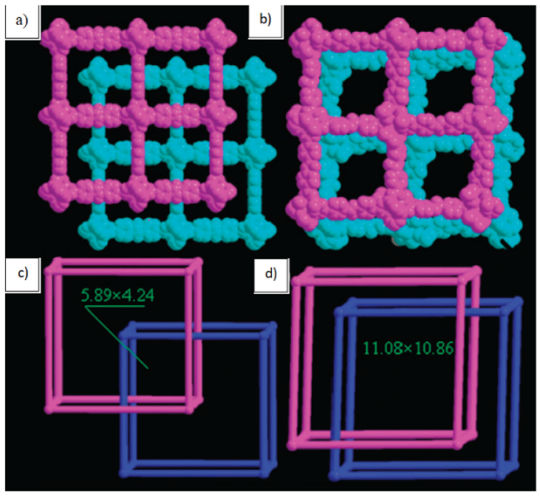

Fig. 4 (a) Section of interpenetrated NJU-Bai1 and (b) NJU-Bai2, (c) schematic representation of the small uniform pore size in NJU-Bai1 (d) and the large pore in NJU-Bai2 as the shifted framework in the presence of modulator L-tyrosine. Reproduced from ref. 110 with permission from The Royal Society of Chemistry, copyright 2011.

4. Action of modulators

4.1 Morphology and size of MOF crystallites

Altering the concentration, molar ratio, and acidic strength of modulators can affect the morphology and size of the MOF crystallites.[28] Frequently, a modification in morphology is also accompanied by an alteration in size; therefore, these two features are treated together here. Size-only changes are given in Section 4.2.

The mechanism of modulator function, which is in competition with the linker, was demonstrated by Tsuruoka *et al.* on the crystal growth direction of $[Cu_2(NDC)_2(DABCO)]$ (1,4-NDC = 1,4-naphthalenedicarboxylate; DABCO = 1,4-diazabicyclo[2.2.2] octane) when acetic acid (AA) was added as a modulator into the reaction medium. Crystal growth for DABCO–copper coordination occurs along the [001] direction, while 1,4-NDC–copper coordination happens along the [100] direction. Acetate and 1,4-NDC possess the same carboxylate functionality, which leads to their competition for coordination with copper. This competition results in the crystal growth more in the [001] direction.[5]

For Cu-MOF $[Cu_2(NDC)_2(DABCO)]$ (NDC = 1,4-naphthalene dicarboxylate), different morphologies have even been obtained by monocarboxylic acid or amine modulation for controlling

the selective growth of different crystalline facets of the MOF which gave rise to new morphologies (Fig. 5). These MOF nanocrystals exhibited enhanced crystallinity and gas absorption compared to the original MOF materials.[111]

Brasil *et al.* reported a change of Tb^{3+}-doped La-MOFs (with the linker 1,3-BDC) from micro-rods to flower-like small particle agglomerates by an increase in the concentration of the AA modulator.[11]

Umemura *et al.* showed that in the synthesis of $[Cu_3(BTC)_2]_n$ (Cu–BTC, HKUST-1) crystals, where BTC = benzene-1,3,5-tricarboxylatean, an increase in the concentrations of *n*-dodecanoic acid or lauric acid modulators led to morphology transformations from octahedron to cuboctahedron as well as a truncated cube and a cube. At a lauric acid/ligand ratio (w) of 50, the octahedral morphology still did not change. Further increasing this ratio then caused a morphology transition because of the thermodynamic stabilization of the growth face, giving rise to a cuboctahedron ($w = 75$), a truncated cube ($w = 100$), and a cube ($w = 125$).[6]

By changing the modulators in the synthesis of HKUST-1 to sodium formate or sodium acetate or triethylamine, additional morphologies can be obtained. This behavior was investigated by Wang *et al.* When sodium formate was introduced in various ratios, ranging from 1 to 5 equivalents relative to the linker, the HKUST-1 structure remained detectable by powder X-ray diffraction (PXRD) analysis. Already with the addition of one equivalent of sodium formate, a strong change in morphology from octahedral to platelet-like could be observed. This change in morphology can be attributed to the modulator's capping effect, which inhibits further growth. In comparison, triethylamine does not lead to capping, but favors faster nucleation by increasing the pH. Consequently, this led to a dramatic reduction in crystal size, shrinking from the range of 2.5–3 μm to 200–250 nm as the concentration of triethylamine increased.[112]

Li *et al.* were able to synthesize an yttrium-based MOF by using yttrium nitrate and BTC. By using sodium acetate as a modulator, the size of the crystals could be greatly influenced from 5 μm brick-like crystals to 0.5 μm wide and 2 μm long rods. This can be explained by the capping of the surface. These rods show a particularly good uptake of arsenate (Section 5.7).[113]

In the work of Han *et al.*, UiO-66 crystals were synthesized using hydrofluoric acid as the modulator (Fig. 6). The fluoride ion has two distinct functions: it balances the charge by coordination to Zr in oxygen defective sites, and it influences the direction of crystal growth through coordinative competition with the organic linkers. The resulting UiO morphologies then also differ in their gas uptake.[52]

Chin *et al.*[1] found that the use of the modulator sodium acetate resulted in the formation of NH_2-MIL-53(Al) as nanorods, while the use of NaOH as modulator led to more isotropic growth and the production of smaller-sized particles, but no nanorods were formed anymore (Fig. 7). The stronger base (NaOH) increases the concentration of the deprotonated NH_2-BDC^{2-} linker, BDC = 1,4-benzenedicarboxylate. Increasing the molar ratio of AA to Al-salt from 0 to 30 during the synthesis of NH_2-MIL-53(Al) led to an increase in the length-to-width aspect ratio of the needles (Fig. 8); further increases in the ratio then caused the formation of large aggregates.[1]

Li *et al.* conducted an investigation into the influence of 4-*n*-butylbenzoic acid on the formation of 2D Cu(BDC) structures. Their findings revealed a correlation between the concentration of the modulator and the resulting structure. Increasing the modulator concentration from 1 : 1 (linker to modulator) to 1 : 10 resulted in the transformation of the initial nanosheet configuration into nanoflower. Further increasing the amount of modulator from a ratio of 1 : 20 eventually resulted in sheet structures.[114]

To exert control over the formation of MIL-125 morphology, Yang *et al.* introduced butyric acid as a modulator into the synthesis process. In the absence of a modulator, the typical circular platelets of MIL-125, featuring two {001} facets, were obtained. However, the introduction of butyric acid as a modulator induced the development of truncated octahedral structures, showcasing two {001} facets along with eight {101} facets (Fig. 9).[115]

This growth behavior highlights that butyric acid, as a modulator, exhibits a stronger interaction with the {101} facet compared to the {001} facet. Consequently, the growth of the

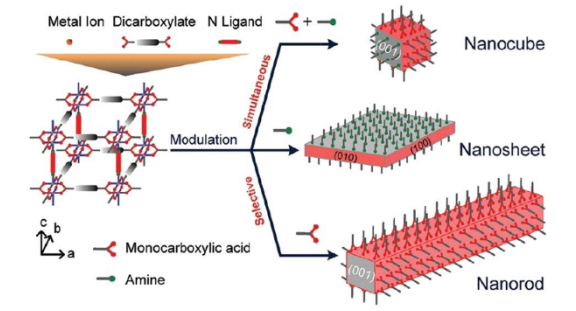

Fig. 5 Control of morphologies of $[Cu_2(NDC)_2(DABCO)]$ by modulators. Reproduced from ref. 111 with permission from the American Chemical Society, copyright 2012.

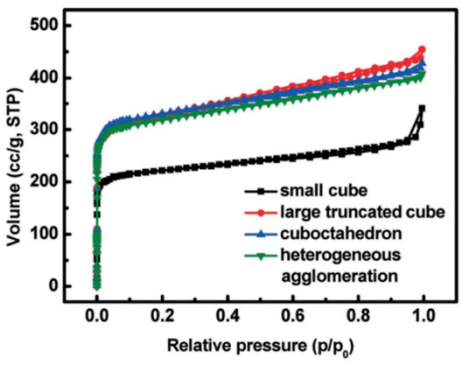

Fig. 6 Ar sorption isotherms of UiO-66 with different crystal sizes and morphologies. Reproduced from ref. 52 with permission from The Royal Society of Chemistry, copyright 2015.

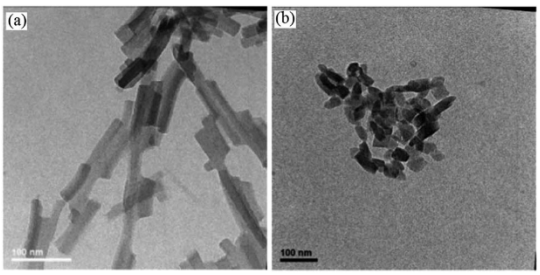

Fig. 7 Transmission electron microscopy (TEM) images of (a) NH_2-MIL-53(Al) nanorods (sodium acetate as modulator); (b) NH_2-MIL-53(Al) nanoparticles (NaOH as modulator). Reproduced from ref. 1 with permission from The Royal Society of Chemistry, copyright 2012.

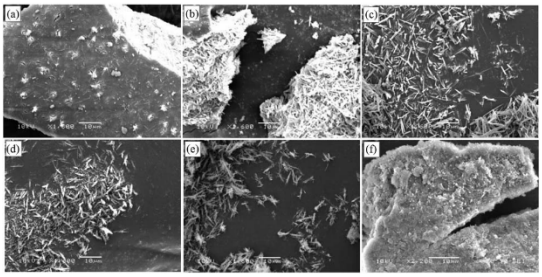

Fig. 8 Scanning electron microscopy (SEM) images of NH_2-MIL-53(Al) prepared by changing the molar ratio of AA to $Al(NO_3)_3 \cdot 9H_2O$: (a) 10 (b) 20 (c) 30 (d) 40 (e) 50 (f) 60. All reactions were performed at 120 °C for 3 days in DMF. Reproduced from ref. 1 with permission from The Royal Society of Chemistry, copyright 2012.

{101} facets is decelerated, resulting in structural formation following the Bravais, Friedel, Donnay, and Harker (BFGH) law. This reduced growth rate also gives rise to smaller crystals in the modulated MIL-125. Interestingly, the different morphologies show different behavior with respect to their catalytic activity (see Section 5.1).[115]

Part of us illustrated the size- and morphology-controlled syntheses of $[Zn_2(OBA)_2(4\text{-BPDB})]_n \cdot 2(DMF)$ (TMU-4), $[Zn(OBA)(4\text{-BPDH})_{0.5}]_n \cdot 1.5(DMF)$ (TMU-5), and $[Zn(OBA)(4\text{-BPMB})_{0.5}]_n \cdot 1.5(DMF)$ (TMU-6), OBA = 4,4-oxybis(benzoate), 4-BPDB = 1,4-bis(4-pyridyl)-2,3-diaza-1,3-butadiene, by adjusting the concentration of the AA modulator together with temperature and reaction time. The formed rod and plate morphologies vary with these parameters, and by decreasing the concentration of the modulator at the same temperature and time, MOFs with uniform morphologies and smaller sizes can be produced (Fig. 10).[60]

A nanorod morphology of $\{[Cu_2(BDC)_2(DABCO)] \cdot 2DMF \cdot 2H_2O\}$ was formed by using the modulator AA. Replacing BDC with BDC-NH_2 led to the formation of a nanotube morphology by the same modulator. This morphology change may be associated with the hydrogen bonding of acetate ions to the amino groups, thereby scavenging acetate and allowing the particles to grow in one-dimension. The results also indicate that at high concentrations of reactants, the modulator gradually loses its function to change the morphology.[100]

Modulation is effective in forming kinetic or thermodynamic products. In the work of Bara *et al.*, the presence of a modulator (like acetic acid (AA), benzoic acid (BA), dichloroacetic acid (DCA), formic acid (FA), HCl, L-Proline (L-Pro), and trifluoroacetic acid (TFA)) facilitates the formation of the thermodynamic product of interpenetrated MIL-126(Fe) over non-interpenetrated MIL-88D(Fe) by slowing down the nucleation process such that the hydrogen bonds created between adjacent networks lead to the formation of the interpenetrated phase. In addition, they developed an effective synthetic approach for the

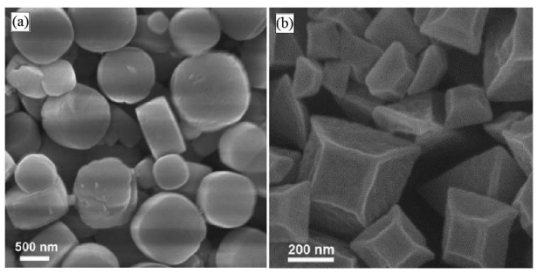

Fig. 9 SEM images of (a) MIL-125 and (b) MIL-125-TRO. Reproduced from ref. 115 with permission from The Royal Society of Chemistry, copyright 2020.

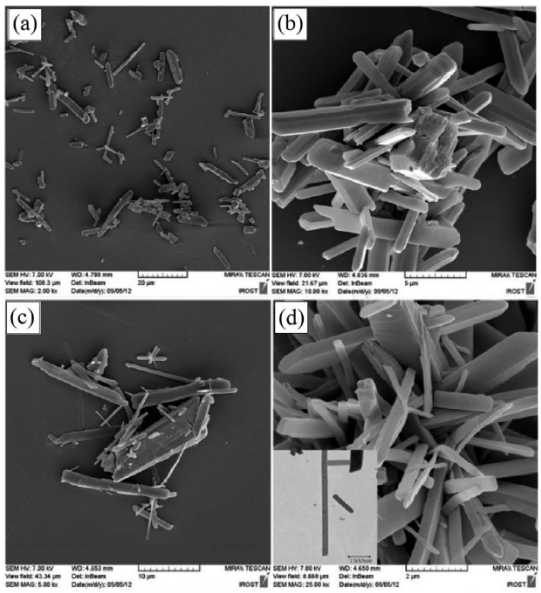

Fig. 10 Field-emission SEM (FE-SEM) images of TMU-5 samples prepared with different ratio (r) between AA and OBA: (a) $r = 15$, (b) $r = 10$, (c) $r = 5$, (d) $r = 2$, (inset is TEM image, scale 1500 nm) at $T = 100$ °C, 24 h. The concentration of OBA ($c = 0.025$ mol L^{-1}) is the same in all syntheses. Reproduced from ref. 60 with permission from the American Chemical Society, copyright 2015.

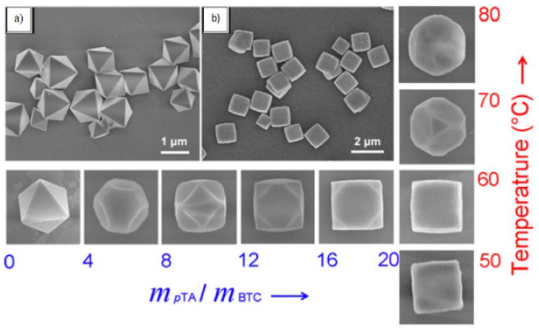

Fig. 11 SEM images of (a) octahedral o-NENU-3a without modulator and (b) cubic c-NENU-3a with a *p*TA/BTC mass ratio of 20. The morphology changes observed by changing the mass ratio *p*TA/BTC from 0 to 20 and the temperature from 50 to 80 °C for *p*TA/BTC of 20. Reproduced from ref. 117 with permission from the American Chemical Society, copyright 2015.

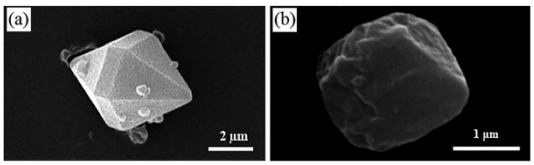

Fig. 12 (a) Diamond-like Fe-MIL-88A crystal with perfect faceted morphology, (b) Fe-MIL-88A crystal with a more spherical morphology. Reproduced from ref. 39 with permission from the Wiley-VCH Verlag GmbH & Co. KGaA, Weinheim, copyright 2018.

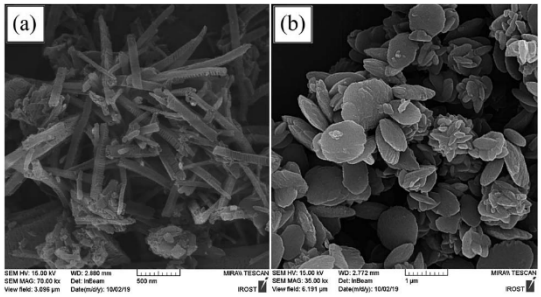

Fig. 13 FE-SEM images of nano-TMU-46 prepared by modulator (a) BA and (b) pyridine. Reproduced from ref. 118 with permission from the Elsevier B.V., copyright 2020.

preparation of MOFs with high porosity, without inducing defectivity. This was achieved through the use of oxidation modulation (utilizing various oxidation states of the metal ions) and a modulator simultaneously, resulting in the formation of a new phase and desired properties for the synthesized MOF. The oxidation of Fe^{2+} to Fe^{3+} impedes the self-assembly process and thus, in this case, the thermodynamic product is produced. Considering that Fe^{2+} is a softer Lewis acid, it increases ligand lability and coordination reversibility, thus reducing defects and increasing crystallinity in MOF products.[116]

Liu *et al.* achieved a transformation in the morphology of the new MOF NENU-3a, a copper and phosphotungstic acid (HPW) based MOF, during its synthesis by employing *p*-toluic acid (*p*TA) as a modulator. In the absence of the modulator, the MOF displayed an octahedral morphology. With an increasing amount of *p*TA, the appearance of the {100} facet became more prominent, while the {111} facet gradually diminished. This observation suggested that the modulator interacted more effectively with the {100} facet, particularly at temperatures below 50 °C. Further elevating the temperature to 80 °C resulted in a morphological transformation into spherical particles. This change occurred because the growth rates of the facets became nearly identical under these conditions (Fig. 11). Interestingly, the different morphologies show a different behavior in catalysis. A detailed investigation of these differences can be found in Section 5.1.[117]

Bagherzadeh *et al.* found that the absence or low concentrations of the modulators AA and FA in the synthesis of Fe-MIL-88A led to the formation of diamond-shaped particles with uniform size distribution and high crystallinity. Conversely, when high concentrations of the modulators were present, a spherical morphology with a rough surface was observed (Fig. 12). At high concentrations, the modulators acted as a structural unit and disrupted the assembly process such that the ligands could not be positioned properly.[39]

Solvothermal synthesis of the MOF $[Cu_2(OBA)_2(BPFB)]\cdot(DMF)_5$ (TMU-46), BPFB = *N*,*N*′-(1,4-phenylene) diisonicotinamide, was performed in the presence of benzoic acid and pyridine modulators, resulting in the formation of nanorod and nanoplate morphologies, respectively (Fig. 13); these morphologies exhibited distinct sensing performance (*cf.* Section 5.8).[118]

Safari *et al.* investigated the influence of various amino acids as modulators in the synthesis of the alkaline earth based MOF BaBTC. They found that among the amino acids alanine, glutamine, histidine, aspartic acid and proline, only the use of proline as a modulator led to the formation of the desired MOF. However, this was accompanied by a change in the morphology of the MOF with increasing concentration of proline from initially rod-shaped to a sheet-like morphology.[119]

Carmona *et al.* demonstrated that modulation of [Al(OH)(SDC)] (SDC = 4,4′-stilbenedicarboxylate) with AA can have a profound impact on both the size and morphology of the resulting MOF. This phenomenon can be elucidated by the capping of aluminum centers within the MOF structure, which selectively promotes the growth of specific crystallographic facets and directions, thus influencing the final size and shape of the MOF material (Fig. 14). Increasing the modulator amount favored the formation of one-dimensional channel structures. These modulated compounds are applied in the storage of ALF794 (Section 5.6).[120]

Rieter *et al.* used a microemulsion of water in surfactant to prepare nanorods of $[Gd(BDC)_{1.5}(H_2O)_2]$, BDC = 1,4-benzenedicarboxylate, which gave rise to nanoparticles under standard conditions. The morphology and size of the nanorods were

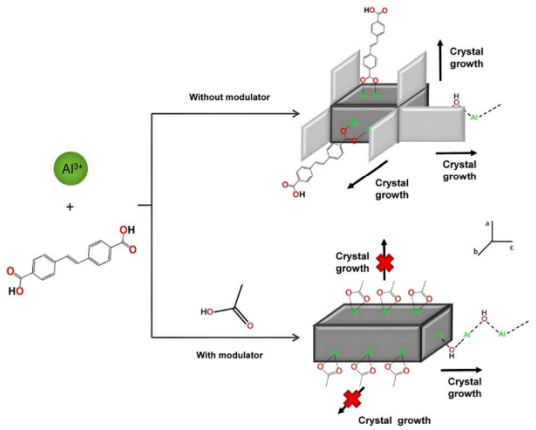

Fig. 14 Preparation of MOF with different features by coordination modulation. Reproduced from ref. 120 with permission from the American Chemical Society, copyright 2018.

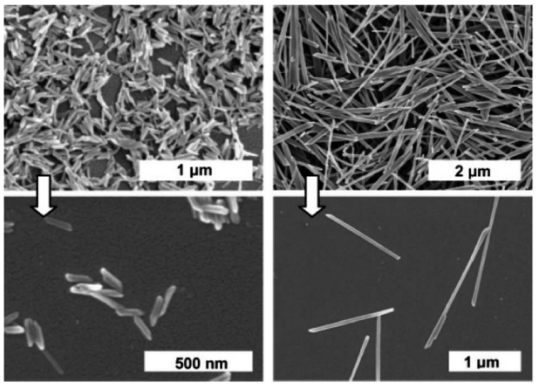

Fig. 15 SEM images of $[Gd(BDC)_{1.5}(H_2O)_2]$ nanorods synthesized with $w = 5$ (left) and $w = 10$ (right) (w: water/surfactant molar ratio). Reproduced from ref. 121 with permission from the American Chemical Society, copyright 2006.

affected by the molar ratio of water to CTAB surfactant in the microemulsion of water/CTAB/isooctane/1-hexanol. When the molar ratio of water/surfactant (w) was 5 (concentration of Gd^{3+}: 50 mM), the nanorods had a length of 100–125 nm and a diameter of 40 nm. When w increased to 10, the length of the nanorods increased to 1–2 μm and the diameter to about 100 nm (Fig. 15).[121]

Yang *et al.* investigated the effect of different concentrations of the surfactant CTAB on the morphology of IRMOF-3. They found that without the presence of CTAB, cubic MOF crystals formed with six {100} facets. The addition of CTAB first resulted in truncated cubes with small triangular faces corresponding to {111} facets. As the concentration of CTAB increased, the morphology changed so that the {111} facets grew while the {100} facets became smaller and eventually

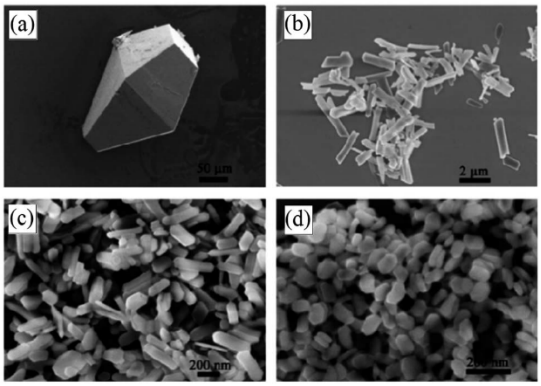

Fig. 16 SEM images of NMOF-1 synthesized by using various amounts of CTAB modulator; w is the molar ratio between CTAB and $Eu(NO_3)_3 \cdot 6H_2O$. (a) NMOF-1 with morphology of rhombus-truncated bipyramid synthesized without CTAB. (b) NMOF-1 crystals with elongated micrometer (2–4 μm) rod morphology prepared with CTAB at $w = 30$. (c) Elongated hexagonal nanorods (200–400 nm) synthesized with $w = 20$. (d) Hexagonal nanoplate morphology with $w = 15$. Reproduced from ref. 25 with permission from The Royal Society of Chemistry, copyright 2012.

disappeared, forming a perfect octahedron. This could be explained by the fact that the CTAB preferentially attaches to the {111} facets. Thus, these surfaces can grow more slowly than the {100} surfaces which then leads to the change in the morphology.[104]

According to a report by Qian *et al.*, the rhombus-truncated bipyramidal morphology and μm-size of $[Eu_2(FMA)_2(OX)(H_2O)_4] \cdot 4H_2O$ (NMOF-1), where FMA = fumarate and OX = oxalate (Fig. 16a), can be changed to smaller micrometer plates with sizes below 2 μm with different amounts of CTAB (Fig. 16b–d). Notably, the length of the rods or the length/width aspect ratio rises with increasing the amount of CTAB.[25]

Sarawade *et al.* demonstrated that through different charge densities of the cationic surfactants $C_{16}H_{33}N(CH_3)_3^+$, $C_{16}H_{33}N(C_2H_5)_3^+$, and $C_{16}H_{33}N(C_3H_7)_3^+$ together with the Br anion, Cu-meso-MOF (give formula with ligand abbreviation) could be synthesized in an aqueous solution using as spheres with the higher charge density of the trimethyl and regular cubes with the lower charge density of the tripropyl ammonium surfactant.[21]

A Co-MOF (from BIPYEN and 2,6-H_2NDC), Cu-MOF (from H_3BTC), and In-MOF (H_3IMDC) were obtained with different morphologies by employing the three surfactants CTAB, sodium dodecyl sulfate (SDS), and pluronic triblock copolymer (P-123) For the Co-MOF, nanosheets/nanoplates, nanosheets and nanorod-like morphologies were obtained with CTAB, SDS and P123, respectively. For the In-MOF, a nanorod and for the Cu-MOF, a nanocube morphology was derived.[21]

4.2 Size only

In numerous reports, it has been verified that as the nucleation rate of MOFs increases, the particle size decreases. Hence, when

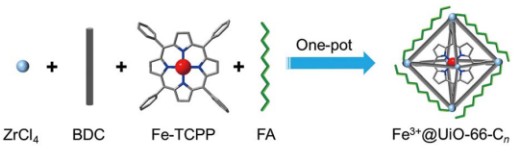

Fig. 17 Schematic illustration for the synthetic process of UiO-66 with Fe porphyrin as guest molecule in the presence of the fatty acid (FA) modulator. Reproduced from ref. 123 with permission from the Elsevier B.V., copyright 2023.

a modulator accelerates the rate of nucleation, *e.g.* through increased linker deprotonation, this leads to a particle size reduction. This is because more crystal seeds start to form and can only continue to grow until the solution is depleted of the starting materials. Conversely, a decrease in nucleation rate will give larger crystals Chem.[7,23,24]

Li *et al.* indicated that the size of ZIF-7 can be controlled from 40 nm to 140 nm by changing the molar ratio of polyethyleneimine (PEI) and also the reaction time. Three samples of compounds were prepared as ZIF-7@PEI-1, ZIF-7@PEI-2, and ZIF-7@PEI-3 with 0.140 g, 0.140 g, and 0.360 g PEI and 5 h, 24 h, and 1 h reaction time, respectively. The particle size of samples 1 to 2, with the same values of the modulator PEI, was observed to rise with increasing reaction time, while the particle size increases with decreasing time from 24 h to 1 h as well as by increasing the amount of modulator PEI from 0.14 g to 0.36 g.[122]

Sui *et al.* achieved the production of nano-sized UiO-66 crystals through the utilization of various fatty acids as modulators. The fatty acids thereby reduce the growth of UiO-66. Notably, they accomplished the encapsulation of Fe-porphyrin as a guest molecule within these nanostructures (Fig. 17). These nano UiO-66 crystals exhibit intriguing catalytic applications, which will be detailed in Section 5.1.[123]

Diring *et al.* found that a high concentration of *n*-dodecanoic acid as a modulator for the preparation of $[Cu_3(BTC)_2]$ led to the formation of larger crystals in comparison to solvothermal techniques with no modulators.[7]

By increasing the amount of sodium acetate modulator in the synthesis of $[Dy(BTC)H_2O]$, the crystal sizes were reduced from micro- to nanometers.[23]

In a study conducted by Pappas *et al.*, the impact of various monotopic modulators on the growth patterns of Co_2(DOBDC) nanorods was systematically explored. In this investigation, six distinct modulators, all derived from salicylic acid and characterized by differing pK_a values, were employed. They were able to show that with increasing pK_a value, the size of the formed rods also increases. At the same time, it was shown that with smaller pK_a values, higher capping takes place. This capping, in turn, acted as a suppressive factor against further growth of the nanorods.[124]

Guo *et al.* employed the organic base modulator triethyl amine (TEA) instead of sodium acetate in their attempt to synthesize $[Dy(BTC)H_2O]$, in which no MOF crystals were formed anymore.[66]

In the synthesis of MIL-101(Cr) the MOF particle size can be reduced to the nanometer scale (<100 nm) with increasing AA modulator to Cr–bdc ratio of up to 17.5 : 1 which is attributed to effective suppression of frame extension. With an average diameter of about 90 nm, MIL-101(Cr) can be prepared reproducibly in gram-scale, with high BET-surface areas (3200–3500 $m^2\ g^{-1}$) and fairly good yield (60–75%). Notably, at a slightly higher AA to Cr–bdc ratio of 20.4 : 1, the surface area, porosity, and yield are substantially reduced.[36]

MIL-101(Cr) nanoparticles were obtained by microwave heating of the reaction between chromium nitrate and 1,4-benzenedicarboxylic acid in heptane-in-water emulsions with the anionic surfactant sodium oleate as an emulsifier. The use of this emulsion with the phase inversion temperature (PIT) method offered the controlled nucleation and growth of nanoMIL-101 particles with an average size of less than 100 nm in 70 min, resulting in a high BET surface areas (2900 $m^2\ g^{-1}$) and a yield of 45%.[125] Phase inversion refers here to the conversion of oil-in-water to water-in-oil emulsion, which is achieved by carrying out the reaction at a temperature at which the phase transition occurs.

Webber *et al.* developed a two-stage synthetic protocol for the synthesis of NU-1000 that demonstrates the action of a modulator. The modulator biphenyl-4-carboxylic acid (H_2BPCA) first reacts with the metal ions to form metal-modulator clusters of the same nuclearity as the metal nodes in the MOF. The molecular clusters then react with the linker molecules 1,3,6,8-tetrakis(*p*-benzoic acid)pyrene (H_4TBAPy) to replace the modulator molecules. This competition of the carboxylate group for the metal coordination impedes the nucleation and growth of the MOF such that single crystals of NU-1000 were obtained. Based on this finding, by optimizing the reaction conditions and the amount of modulator used, they were able to produce NU-1000 crystals ranging in sizes from 300 nm to 9.3 mm.[126]

The synthesis of ZIF-8 and ZIF-67 was conducted using an ionic liquid microemulsions (ILMEs), wherein an H_2O/TX-100/BmimPF$_6$ mixture was applied to obtain a uniform particle size distribution. Additionally, the addition of ethanol to the reaction mixture was found to be essential in regulating the particle sizes of $[Cu_3(BTC)_2(H_2O)_3]$ (HKUST-1).[70]

4.3 Crystal phase

Yang *et al.* observed MIL-101-Cr nanocrystal formation at low BA concentration.[34] However, when the concentration of the

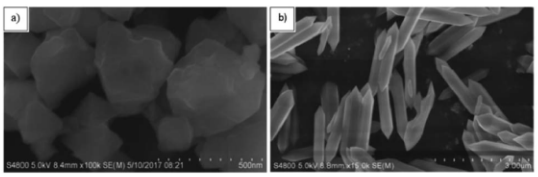

Fig. 18 SEM images on the effect of benzoic-acid (BA) modulation in the reaction of chromium nitrate with benzene-1,4-dicarboxylic acid. (a) MIL-101(Cr) sample for low BA amounts (scale bar 500 nm), (b) MIL-88B(Cr) sample at high BA amounts (scale bar 3 μm). Reproduced from ref. 34 with permission from The Royal Society of Chemistry, copyright 2019.

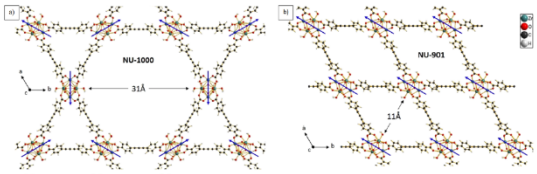

Fig. 19 Structure of (a) NU-1000, and (b) NU-901. Blue arrows indicate the angular or parallel orientations of the nodes in the frameworks. Reproduced from ref. 127 with permission from the American Chemical Society, copyright 2017.

modulator was increased under the same hydrothermal conditions, microparticulate MIL-88B(Cr) was formed (Fig. 18). This modulation enabled a new and efficient synthesis of MIL-88B(Cr).

The only structural difference between Zr-MOF polymorphs NU-1000 and NU-901 is in node orientation (Fig. 19). The angle between the Zr_6 nodes in NU-1000 is 120°, while NU-901 has all nodes parallel to each other. In the prevalent synthesis, NU-901 is formed with small pores. Webber *et al.* demonstrated that the modulator biphenyl-4-carboxylic acid favors the formation of the nodes with an angle of 120°, resulting in the production of the structure of NU-1000 with large pores when the modulator is replaced with the linker during the synthesis and framework growth (Fig. 19).[127]

In an effort to separate the two phases of NU-1000 and NU-901, Islamoglu *et al.* employed TFA as a co-modulator together with BA during the synthesis process, thereby preventing the formation of the NU-901 phase. As depicted in Fig. 20, NU-1000 crystals synthesized without TFA resulted in crystals with "rough" surfaces in the center (Fig. 20a). On the other hand, NU-1000 crystals, when modulated by TFA, showed well-shaped hexagonal rods with smooth surfaces without the presence of the NU-901 phase (Fig. 20b).[35]

In 2022 Gong *et al.* were able to prepare five new MOFs based on different [2,2]paracyclophane-based linkers. By exchanging AA with FA under the same synthesis conditions, two very different MOFs were synthesized, namely NU-405, which has a 3D structure and is connected with 12 linker molecules, and NU-700, which forms a 2D network structure with an unknown

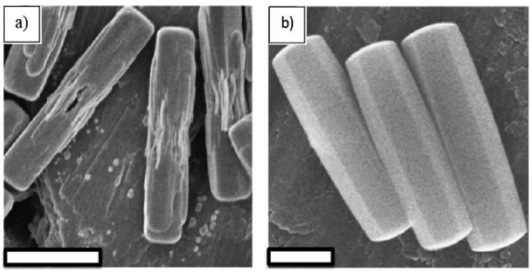

Fig. 20 SEM images of (a) NU-1000 and (b) NU-1000-TFA crystals. Scale bars are 2 μm. Reproduced from ref. 35 with permission from The Royal Society of Chemistry, copyright 2018.

9 linker structure. Three linker positions are occupied by FA. Furthermore, two more NU-MOFs, namely Nu-913 and NU-602 could be synthesized by simply exchanging the solvent DMF to DEF, using AA as modulator. This shows both the influence of the modulators on the formation of a particular crystal phase and the influence of the solvent on the crystal phase formation. NU-602 and NU-913 show interesting properties in the area of water sorption, discussed in Section 5.5.[128]

The use of a very high amount of the modulator mercaptoacetic acid (HMAc) in the synthesis of UiO-66 caused the formation of the hexagonally close-packed (hcp) crystal structure instead of the face-centered cubic (fcc) packing, which is normally observed in the formation of UiO-66. By using 100 eq HMAc to metal in the synthesis, a functionalized hcp-UiO-66 containing the thiol HMAc modulator was produced for the first time.[129]

Wang *et al.* demonstrated that varying the concentration of the BA modulator during the synthesis of Zr-MOFs induced the formation of three MOFs with distinct topologies as well as different pore sizes and structures. In this work, three Zr-MOFs (Zr-SXU-1, Zr-SXU-2, and Zr-SXU-3) were synthesized with the same ligands and metal clusters. The ligand used was tetratopic carboxylic 4,4′,4″,4‴-(1,4-phenylenebis(pyridine-4,2,6-triyl))tetrabenzoic acid (H_4PBPTTBA) of 1 eq. concentration, and the modulator was BA with concentrations of 110, 150 and 140 eq., respectively. These Zr-MOFs exhibited different connectivity of the Zr clusters from 8 in Zr-SXU-3 to 10 in Zr-SXU-1 and 12 in Zr-SXU-2.[33]

Hou *et al.* successfully synthesized five new thorium-based metal–organic frameworks (MOFs), namely NU-51 to NU-55, by employing the rigid tetratopic linker 1,3,5,7-adamantanetetracarboxylic acid (H_4ATC) in combination with various carboxylic acids (FA, AA, TFA, BA). Notably, the choice of different modulators and their respective concentrations played a pivotal role in this synthesis process. For instance, NU-51 and NU-52 could be obtained using FA at varying concentrations, highlighting the sensitivity of MOF formation to both the type and concentration of the modulator.[130]

4.4 Degree of crystallinity and defects

The degree of crystallinity is usually assessed only qualitatively by the width and sharpness of the reflexes in a powder X-ray diffractogram (PXRD). Thus, it is important to note that nanoparticles will also give broader reflexes.

MOFs based on metal ions with high oxidation states (Zr^{4+}, Cr^{3+}, Fe^{3+}), such as the Zr-MOFs UiO-66 and congeners possess high nucleation rates due to the strong bonds formed between the metal ions and the carboxylate-donor ligands. It has been shown that the presence of modulators is essential to produce UiO-MOFs with good crystallinity.[28]

Schaate *et al.* demonstrated that in the ordinary synthesis of a Zr-MOF (UiO-66, UiO-67, UiO-68) in the absence of a modulator (BA or AA), only an amorphous phase or micro-sized aggregates of the products are obtained. They showed that modulation synthesis of UiO-67 with increasing equivalents of BA or AA resulted in PXRD patterns with sharper reflexes (Fig. 21).[27]

Schaate *et al.* reported difficulty in reproducing the usual method of UiO-67 synthesis due to the formation of difficult-to-separate by-products with low crystallinity; however, in the presence of the modulator BA, the MOF nucleation process was slowed down, leading to UiO-67 products with higher crystallinity.[131]

Liu *et al.* added hydrophobic methyl groups in UiO-66 by using the linker 2,5-dimethylterephthalic acid to increase the hydrothermal stability in UiO-66-CH_3 films on a nickel support for the separation of N_2/CO_2 gases. It was found that the growth of UiO-66-CH_3 with an AA modulator enabled a facile secondary growth of the MOF on the support. Furthermore, the crystal growth can be controlled by tuning the modulator amount. For secondary crystal growth on the membrane, an optimal amount of acetic acid modulator is required to ensure that the membrane surface remains porous when using lower amounts of acetic acid.[132]

The engineering of defects in MOFs is an effective way for tuning the pore features, including the formation of open metal sites, alteration of the surface chemistry, modification of the properties, and improvement of applications in fields such as catalysis and gas storage. Ren *et al.* reviewed formation and detection methods and application details of structural defects of MOFs.[46,133,134] There are two types of defects: missing linker defects and missing metal cluster defects. When the linkers are replaced with terminal modulator ligands, missing linker defects occur.[85,135] Modulators create missing linker defects by competing with the linkers in coordination to the metal center during the framework formation.[85] Subsequently, post-synthetic elimination or replacement of the bound modulator can be performed (see Section 3.1).[136] To create an open metal site, modulator species are often removed from the structure by heating to a certain temperature.[137] Defect control can be an effective way to adjust the properties of MOFs for applications.[138] In the work of Epley *et al.*, the role of modulators including AA, FA and BA was investigated in the defect nature of UiO-AZB (AZB = 4,4′-azobenzenedicarboxylate). Generally, the highest surface area was obtained with AA modulator. Some testings of BET analysis were applied to evaluate the batch alteration of modulators over the concentration range. The results indicated that changes in the modulator concentrations and/or acidity formed more defects, which can be advantageous for applications such as gas adsorption (Fig. 22).[135]

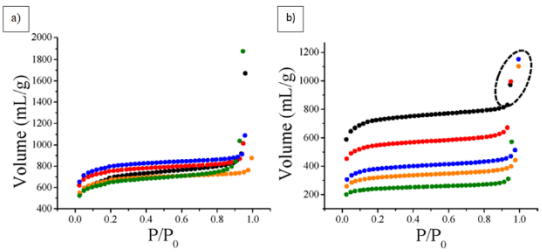

Fig. 22 (a) N_2 isotherms for MOFs synthesized with 30 equiv. (black), 40 equiv. (red), 50 equiv. (blue), 60 equiv. (orange), 70 equiv. (green) of AA (b) N_2 isotherms for MOFs synthesized with 10 equiv. (black), 15 equiv. (red), 20 equiv. (blue), 25 equiv. (orange), 30 equiv. (green) of BA. Reproduced from ref. 135 with permission from the American Chemical Society, copyright 2017.

Butova *et al.* employed the BA modulator in the synthesis of UiO-66-NDC. By altering the ratio of modulator to linker, the reaction kinetics are altered, resulting in the formation of crystals of different sizes. Additionally, the specific surface area changes through the formation of defects in the framework. A higher ratio of modulator to ligand resulted in larger crystal sizes and greater surface areas; however, this also caused a decrease in the thermal stability because of the formation of defects in the MOF structure.[138]

Olsbye *et al.* used BA as a modulator to produce a highly crystalline UiO-67 structure with varying degrees of defects. A crystalline and defect-free MOF was produced at a minimal amount of DMF and an optimized ratio of BA (Fig. 23 C-3_{BA}), while increasing the BA concentration to 15 equivalents resulted in no MOF formation. Defective MOFs were created at high-

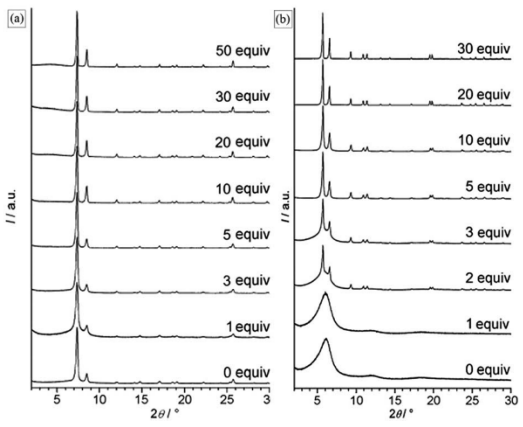

Fig. 21 Powder X-ray diffraction (PXRD) patterns of UiO-66 (a) and UiO-67 (b) synthesized with different proportions of BA modulator towards $ZrCl_4$. The same feature was obtained with AA as modulator. Reproduced from ref. 27 with permission from the Wiley-VCH Verlag GmbH & Co. KGaA, Weinheim, copyright 2011.

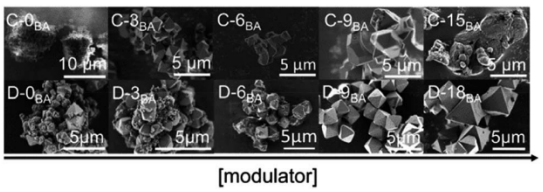

Fig. 23 SEM images of UiO-67 samples formed under concentrated (C-x_{BA}, where $x = 0$, 3, 6, 9, and 15 equivalent BA : Zr ratio) and diluted synthesis conditions (D-x_{BA}, where $x = 0$, 3, 6, 9, and 18 equivalent) (BA as a modulator, concentrated and diluted mean Zr : DMF ratios of 1 : 50 for C and 1 : 300 for D). Adapted from ref. 139 with permission from the American Chemical Society, copyright 2019.

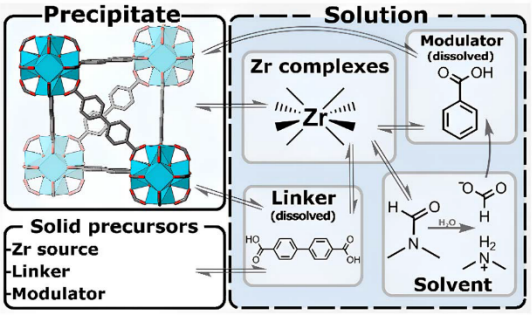

Fig. 24 Types of reversible reactions during the modulated synthesis of UiO-67. Reproduced from ref. 139 with permission from the American Chemical Society, copyright 2019.

dilution conditions (Fig. 23 D-3_{BA} to D-18_{BA}). Moreover, figures D-6_{BA} to D-18_{BA} show that with increasing ratio of BA, both shape and size of the crystals could be optimized. At diluted conditions, the crystallization process is affected in two additional ways: first, the hydrolysis of DMF produces formate and H^+ ions; the latter reduce the solubility of the linker molecules (H_2BDCA) by affecting the equilibrium reactions and second; the formate ions act as an additional modulator to further compete for the coordination bond between the linkers and metal centers (Fig. 24).[139]

In UiO-66 monocarboxylic acid modulators, such as difluoroacetic acid, allowed for an increase in the density of defects which resulted in increased surface area and pore volume compared with "defect-free" UiO-66. The extent of defects was observed to increase in proportion to the modulator amount.[43] Cai *et al.* used alkyl carboxylic acid modulators for the formation of meso- to macropore structural defects in UiO-66 (Fig. 25a–c). The diameter of the pore defect could be

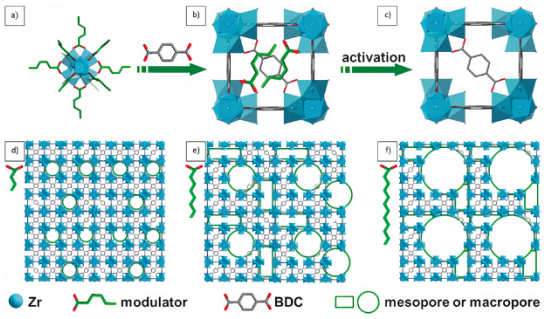

Fig. 25 Schematic representation of the synthesis of hierarchically porous UiO-66 with adjustable porosity by carboxylic acid modulators with different alkyl chain lengths. Steps (a)–(c) show the effect mechanism of alkyl carboxylic acid modulator in creating structural defects. The process of increasing size of the defect pores with the increase in the length of the alkyl chain of the modulator can be observed in the parts (d)–(f). Reproduced from ref. 40 with permission from the Wiley-VCH Verlag GmbH & Co. KGaA, Weinheim, copyright 2017.

increased with the alkyl chain length of the modulator and its concentration (Fig. 25d–f). By using an excess amount of the modulator and sub-stoichiometric amounts of the BDC linker, some coordination sites were occupied by the modulators. The large open pore defects were then formed as a result of the elimination of the modulator. These hierarchically porous UiO-66 MOFs (HP-UiO-66) were then tested in various applications (see Section 5).[40]

Bueken *et al.* synthesized a Zr-MOF by using the linker squaric acid (H_2SQA) which is therfore called ZrSQU. It has the smallest unit cell in the family of UiO-MOFs. Based on the crystal structure no porosity is expected. By using FA or AA as modulators, various defects could be incorporated into the structure. Depending on the modulator, 9.5 wt% acetate or 17.1 wt% formate ions were detected in the structure. By using the modulators, a sieve character could be incorporated into the structure, which will be discussed in more detail in Section 5.2.[85]

Chen *et al.* synthesized a new Ce-MOF called BIT-58, which exhibits excellent chemical and thermal stability. Hierarchical porous Ce-MOF (nano-BIT-58) could be synthesized by utilizing nitrogenous heterocyclic modulators, such as 1-methylimidazole (1-HMIM). The meso-pore volume in nano-BIT-58 significantly increased, approximately seven times more than native BIT-58, due to structural defects and led to an increase in acidic sites, including unsaturated open metal sites, allowing for easier mass transfer and exhibiting more catalytically active sites than BIT-58. Section 5.1 presents the catalytic properties in more detail.[41]

In synthesizing HKUST-1 films, Muller *et al.* used water as a modulator to control the amount of defects. Water slowed down and thereby controlled the coordinative bonding of the linkers to the metal centers by solvation. HKUST-1 films were obtained by stepwise growth with the coating method. Different amounts of water between 0 and 30% in solutions of water and ethanol were selected. The results demonstrated that the water content in the synthetic solutions has a great effect on the crystallinity of MOF thin films. The highest crystallinity and the least defect were gained for about 10% water in ethanolic synthesis solutions. A low-density of defects in these HKUST-1 films is ideal for application in semi-conductors.[140]

4.5 Surface area and porosity

The porosity control of MOFs is important for a variety of applications, such as magnetic,[141] catalytic,[142] adsorptive,[143] and chemical sensing purposes.[144] Most MOFs are microporous materials. Micropores (diameter <2 nm) engage in more effective interactions with the adsorbate and provide high surface areas. Yet micropores are not suitable for the adsorption of large molecules and also kinetically limit the diffusion of small molecules. In addition, their uptake capacity cannot be increased by factors such as increasing pressure. Mesopores (2 to 50 nm diameter) facilitates the diffusion of molecules and offer increased diffusion kinetics. Consequently, MOFs with both meso- and microporosity as hierarchical porous (HP-) MOFs can be provided, allowing for the utilization of the

benefits of both types of pores. Many synthesis methods have been suggested and applied for the design of hierarchical pore structures, including the ligand-extension method, surfactant templating, and ionic liquids as well as modulators.

With respect to the formation process, these mesopores differ from defects. Defect are created through missing linkers or metal units, best known for UiO-66, where linkers can be replaced, for example, by modulators.[40] Templates such as surfactants, on the other hand, form micelles in solution which serve as a site where the MOF can grow around.[23]

For example, Dissegna *et al.* synthesized UiO-66 structures using a series of monocarboxylic acid modulators. Through N_2 measurements, they demonstrated that the surface area of UiO-66 increased in response to increased modulator concentrations and enhanced acid strength. In addition, using water sorption measurements, their studies illuminated the changes in hydrophilicity and Lewis acidity that occur when different modulators are used. TFA as a modulator showed the strongest change in both cases.[145]

Prasetya *et al.* showed that, in addition to the conventional solvothermal synthesis with DMF, a more environmentally friendly "green" reaction approach also led to the desired MOF structure. In this alternative approach, water was used as solvent and various amounts of FA as modulator. After a reaction time of 24 hours at room temperature, MOF-801 was detected for all "green" approaches. It was found that the surface area of the synthesized MOFs decreased with increasing concentration of FA. Nevertheless, the resulting MOFs exhibited good adsorption capabilities for diclofenac from aqueous solutions (Section 5.7).[146]

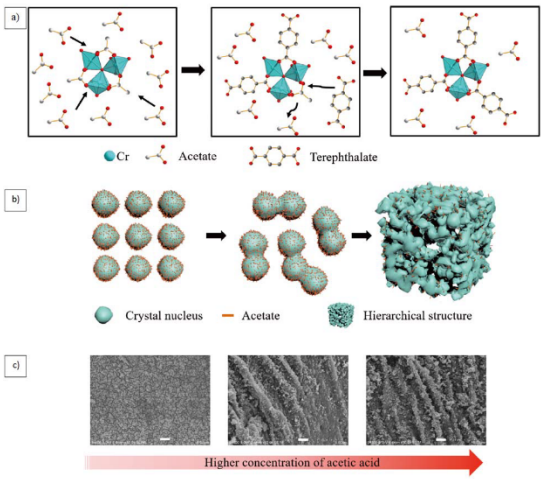

Fig. 26 Suggested mechanism for the synthesis of HP-MIL-101(Cr) with AA modulator. (a) Substitution of acetate with the terephthalate ligand. (b) Nanofusion of crystal nuclei. (c) Representation of microparticle-phase formation by increasing AA concentration at high temperature (scale bar is 1 μm). Reproduced from ref. 147 with permission from the Science China Press and Springer-Verlag GmbH Germany, part of Springer Nature, copyright 2020.

Hierarchical MIL-101(Cr) was obtained using high concentrations of AA as modulator under hydrothermal conditions. Moreover, by providing a particle size decrease due to growth limiting, the modulator caused the formation of an aggregated microparticle-phase with macropores (>50 nm), giving rise to a hierarchical micro–meso–macro-porous material which featured pores with ~3, 20–60, and 800–1000 nm sizes. The possible mechanism for the formation of HP-MIL-101(Cr) is presented in Fig. 26.[147]

An increase in both surface area and pore size was achieved in several shaped forms of MIL-101(Cr) prepared by using and increasing FA modulator to Cr ratio. The increasing porosity was tested for hydrogen adsorption (Fig. 27).[148]

UiO-67 with no modulator displayed a low surface area of only 270 $m^2\ g^{-1}$, while UiO-67 prepared with 30 equivalents of AA or BA modulator possessed high surface areas of 2400 and 3000 $m^2\ g^{-1}$, respectively.[27]

Kim *et al.* adopted an acetic acid-modulated strategy for the synthesis of HKUST-1. Through this approach, they deliberately introduced defects into the MOF structure. This deliberate defect incorporation led to the formation of a HP-MOF with a significantly enhanced surface area. Specifically, the surface area increased from 1787 $m^2\ g^{-1}$ to 2396 $m^2\ g^{-1}$. This substantial enhancement in surface area rendered the HP-MOF highly attractive for gas adsorption and storage applications (Section 5.2).[149] In addition to the use of monocarboxylic acids, polyprotonic acids can also be used as modulator. Liu *et al.* employed citric acid for the preparation of HP-HKUST-1, $[Cu_3(BTC)_2(H_2O)_3]$, with a pore size distribution in the range of 30–100 nm. Citric acid equivalent to less than 20% of the BTC linker was added to the reaction mixture. Despite the strong interaction of chelating citrate with Cu^{2+}, a hierarchical porous HKUST-1 was formed, which enabled HKUST-1 to be a host for the phosphomolybdic acid hydrate (HPMo) cluster, thereby constructing the composite HPMo@HP-HKUST-1 with excellent catalytic activity (see Section 5.1).[42]

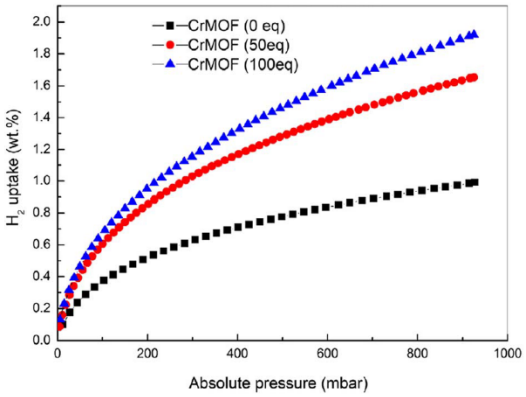

Fig. 27 H_2 sorption isotherms at 77 K for activated MIL-101(Cr) samples prepared with 0, 50 and 100 Fa/Cr equivalents. Reproduced from ref. 148 with permission from the Hydrogen Energy Publications, LLC. Published by Elsevier Ltd, copyright 2014.

One promising approach to modulation is the use of large organic molecules as modulator. Gau *et al.* introduced a modulator-based technique to prepare HP-MOF with pore size distributions in the range of 1 nm, 1.3 nm, 1.4 nm, 2 nm, 3.8 nm, and 10.5 nm, using RhB (Rhodamine B) as a modulator for the construction of a RhB@Al-MOF, where Al-MOF = amino-MIL-53. In the first step, RhB is weakly coordinated to Al^{3+} ions through the interaction of its –COOH group with Al^{3+}. Upon the addition of the linkers $H_2BDC\text{-}NH_2$ to the reaction mixture, the MOF formation begins. RhB with its approximate dimensions of $16 \times 10 \times 6$ Å^3 is larger than the channel cross-section in amino-MIL-53. Thus, the incorporation of the RhB molecules in the growing Al-MOF creates meso-pores in the framework. These meso-pores are created as the MOF grows around the templating guest molecules. The amount of mesoporous cavities created in RhB@Al-MOF depends directly on the RhB concentration. The presence of meso- and micro-pores in the HP-MOF framework makes MOF an interesting material for the uptake of various guest molecules (see Section 5 for applications).[150]

The work of Jin *et al.* also dealt with the modulation of MOFs with the aid of Rhodamine B. MIL-125-NH_2 was successfully transformed into a HP-MOF with the assistance of RhB (Fig. 28). Their investigations elucidated the mechanistic details of this modulation process, revealing that RhB coordinates with the Ti_8O_8 clusters formed during the MOF synthesis. In addition, the steric properties of RhB resulted in both missing linker and missing cluster defects within the MOF structure. Subsequently, RhB can be selectively removed from the MOF through washing and photodegradation processes, leaving behind a pure HP-MOF structure. This resulting HP-MOF exhibits intriguing properties, particularly in the realm of catalysis (detailed in Section 5.1). Furthermore, the study highlights that similar structural effects can also be achieved using the dye Eosin Y.[80]

In addition to using large organic molecules, whole organic scaffolds can also act as modulators. In their work, Li *et al.* show that porous styrene scaffolds can be used as structure-directing modulators in the synthesis of ZIF-8. Thus, after removal of the polystyrene, an increased porosity can be achieved.[81]

Surfactants, as another distinct group of large organic modulators, play a crucial role in MOF synthesis. They can engage with MOF formation through two primary mechanisms: micelle formation and direct interactions. He *et al.* employed the coordination competition between the BDC linker and the surfactant modulator lauric acid to generate mesopores in MOF-5.[151] The surfactant 4-(dodecyloxy)benzoic acid was found by Choi *et al.* to act as both a coordinating modulator ligand and templating agent (porogen) to form mesopores in MOF-5 with its alkyl chain.[152] Because of framework interpenetration, it is challenging to otherwise produce MOFs with permanent meso-porosity.[153]

The surfactant modulators CTAB, SDS, and pluronic triblock copolymer (P-123), increased the porosity in Co-MOF (from BIPYEN and 2,6-H_2NDC), Cu-MOF (from H_3BTC), and In-MOF (from H_3IMDC). In the presence of surfactants, the specific surface area in Cu-MOF increased by about two times (from 200 cm^3 g^{-1} to 400 cm^3 g^{-1}).[21]

To synthesize meso-$[Cu_3(BTC)_2(H_2O)_3]$, Qiu *et al.* used the surfactant CTAB, and adjusted the pore size from 4 to 31 nm by changing the Cu^{2+} : H_3BTC : CTAB : TMB molar ratio from 1 : 0.556 : 0.15 : 0 to 1 : 0.956 : 0.30 : 0.15 (TMB = 1,3,5-trimethylbenzene acts as an auxiliary agent to inflate the CTAB micelles).[154]

Peng *et al.* used the *N*-ethyl perfluorooctylsulfonamide surfactant as a directing agent for the crystal growth and template for the creation of the meso-porous $[Cu_3(BTC)_2(H_2O)_3]$ simultaneously. The surfactant concentrations determined the MOF morphologies and high surfactant concentration led to the formation of more meso-pores (Fig. 29).[155]

When the construction of mesoporous MOFs with surfactants does not work, Li *et al.* suggested to use ligands containing both weak and strong sites. Therefore, MOF walls are formed by bonding between metal-ion and active sites surrounding the meso-cavities. Weak sites cause surfactants to overcome lattice stability and form meso-spaces by the electrostatic interaction or the hydrogen bonding with MOF walls.[156]

In addition to the previously mentioned modulators, simple solvents like methanol or ethanol can also serve as modulators.

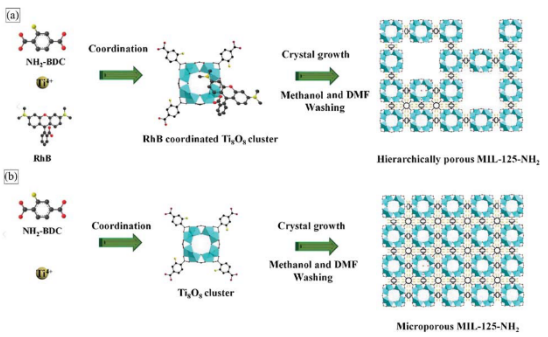

Fig. 28 Rhodamine B as a modulator in the synthesis of MIL-125-NH_2. Reproduced from ref. 80 with permission from the Wiley-VCH Verlag GmbH & Co. KGaA, Weinheim, copyright 2023.

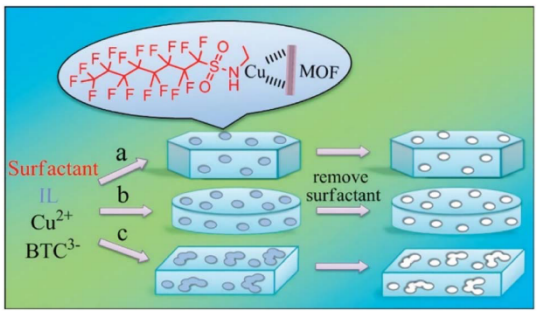

Fig. 29 Schematic representation for preparing meso-porous $[Cu_3(BTC)_2(H_2O)_3]$ nanoplates in surfactant-IL solutions at (a) low, (b) medium and (c) high surfactant concentrations. Reproduced from ref. 155 with permission from The Royal Society of Chemistry, copyright 2012.

An example of the use of alcohol as a modulator is demonstrated in the work of Wang *et al.* in the synthesis of MIL-88B. By varying the quantities of methanol used during synthesis, they were able to optimize the porosity of MIL-88B. The surface area of the MOF increased significantly from 28 $m^2 g^{-1}$ to 177 $m^2 g^{-1}$. In this context, methanol binds to the iron centers, leading to defects in the MOF structure. Interestingly, this defective MIL-88B structure exhibits excellent properties in the realm of sensing, which will be discussed in greater detail in Section 5.8.[44]

5. Application of modulated MOFs

Traditional MOFs often feature pores with dimensions smaller than 2 nm, which can impose limitations on their potential applications. These constraints can hinder the accommodation, separation, or transport of substrates within or through the MOF structure. Additionally, accessing catalytic or sensory active sites within such small pores can be challenging. In contrast, modulated MOFs, which exhibit various effects such as missing linkers defects, missing cluster defects, or other modulated properties, broaden the range of potential applications significantly. These modulated MOFs offer greater versatility and open up new possibilities in various fields by overcoming the limitations associated with traditional MOFs.

5.1 Catalysis

The catalytic performance of nano-sized MOF TMU-5 was studied by part of our us. Conventional synthesis without the presence of modulator led to the production of the MOF with undefined bulk morphology. Uniform and defined nanorod and nanoplate morphologies of this MOF were obtained through modulated synthesis with AA as modulator, which showed better catalytic activity in Knoevenagel condensation reaction due to high specific surface area and ease of substrate mass transfer in the structure. A comparison of the catalytic activity of modulated TMU-5 and original unmodulated TMU-5 can be seen in Fig. 30. The nanorod and nanoplate morphologies exhibited the highest yields.[60]

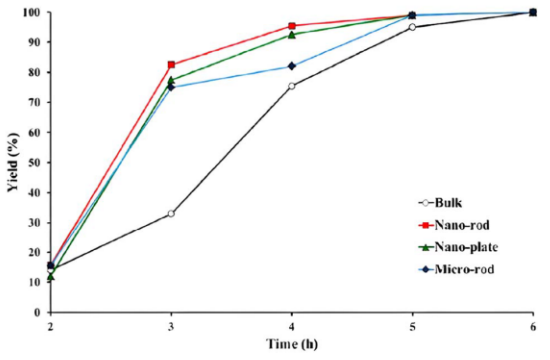

Fig. 30 Yield (%) *vs.* time (h) for Knoevenagel condensation reaction of benzaldehyde with malononitrile catalysed by bulk, nanorod, nanoplate, and microrod morphologies of TMU-5.

The work of Chen *et al.* also addresses the catalytic activity of nano-BIT-58 with respect to the Knoevenagel condensation reaction (Section 4.4). Here, Ce^{3+} centers act as Lewis acid catalysts. Due to the modulation with 1-HMIM, a hierarchical pore structure could be formed and a large number of free metal sites generated. This led to an increased catalytic effect compared to the non-modulated MOF BIT-58. A further advantage of the modulation becomes clear when larger molecules are used in the catalysis. For example, Chen *et al.* showed that the condensation of 9-anthraldehyde with malononitrile exhibited a 14-fold improvement in conversion efficiency.[41]

HP-MOF-5 nanosheets, hierarchical-pores (HPs), were prepared by He *et al.* with the aid of the modulator lauric acid as the substrate for the immobilization of Pd nanoparticles. Due to the high capacity of HP-MOF-5 for gas adsorption, Pd showed high-yield catalytic performance in the reduction of nitroarene by hydrogen which is a significant industrial reduction reaction.[151]

In the report of Jiang *et al.*, the influence of HCl modulator on the photocatalytic activity of MIL-53 was examined. HCl was able to generate more active sites for surface adsorption and catalysis. The photocatalytic activity was determined by the decomposition of tetracycline using visible light in aqueous solutions. The photocatalytic activity of MIL-53 with HCl modulator increased up to 1.5 times compared to unmodulated MIL-53. On the basis of recycling tests, it could be shown that the catalyst still shows good activity even after several cycles, which indicates good stability.[157]

Ly *et al.* used TFA modulators to enhance the catalytic hydrolysis of peptide bonds by UiO-66 through the formation of a defective missing-linker structure in the MOF. The catalytic activity was assessed by examining the cleavage of the peptide bond within the Gly–Gly molecule. The TFA-modulated UiO-66 showed a similar catalytic reaction rate as UiO-66-NH_2/NO_2. However, as expected, the UiO-66-NO_2/NH_2 MOFs demonstrated a higher adsorption capacity compared to the original UiO-66 structure due to the ability to form hydrogen bonds with peptide molecules. This result indicated a rise in active sites, including acidic centers, in the defective UiO-66.[158]

Dissegna *et al.* established a correlation between modulators and the presence of active Lewis acid centers by water sorption measurements. These Lewis acid centers are central to catalytic processes. To assess catalytic activity, they employed the cyanosilylation of benzaldehyde as a benchmark reaction. In this context, they observed that TFA-modulated UiO-66 exhibited significantly enhanced catalytic activity compared to unmodulated UiO-66. This result led to the conclusion that modulation introduces a greater number of defects, consequently increasing the availability of free metal sites. Notably, the UiO-66 catalyst employed exhibited robust stability, allowing for recyclability in catalytic processes.[145]

HP-UiO-66, synthesized by Cai *et al.* through the application of monocarboxylic acids of varying chain lengths as modulators, possessed high porosity that rendered it applicable across diverse fields. In catalysis, HP-UiO-66 demonstrated its efficacy in the [3 + 3] cycloaddition of 1,3-cyclohexanedione and various α,β-unsaturated aldehydes. The combination of its large pores

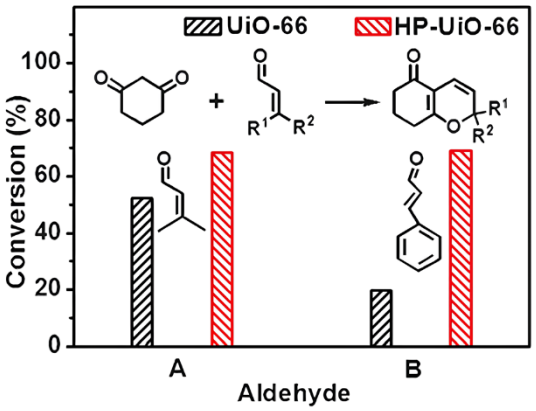

Fig. 31 Catalytic [3 + 3] cycloaddition reaction using Uio-66 and HP-UiO-66. Reproduced from ref. 40 with permission from the Wiley-VCH Verlag GmbH & Co. KGaA, Weinheim, copyright 2017.

and available open metal sites enhanced its catalytic performance, as demonstrated in several examples. While non-modulated UiO-66 and HP-UiO-66 showed nearly identical conversions for small substrates, HP-UiO-66 showed a distinct advantage for larger substrates due to its easier accessibility (Fig. 31).[40]

In their catalytic application research, Sui *et al.* employed a variety of fatty acids as modulators to synthesize nano-sized crystals of UiO-66. Within these nanostructures, they encapsulated Fe porphyrin (with Fe^{3+}) and the presence of hydrophobic fatty acids within the MOF generated catalytic properties reminiscent of enzymes. This system catalyzed the oxidation of CH_4 to CH_3OH (Fig. 32). The hydrophobic modulators played a dual role by regulating both the electronic states of the active Fe nuclei in the structure and the concentration of reactive oxygen species, in this case H_2O_2. Experimental data from both neat UiO-66 and mixtures of Fe-porphyrin with UiO-66 indicated either no conversion or extremely low conversion (2.9%). However, the most remarkable outcome was achieved with

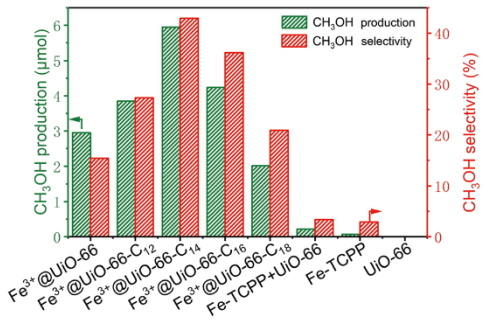

Fig. 32 Catalytic performance of Fe porphyrin with different modulator for CH_4 oxidation. Reproduced from ref. 123 with permission from the Elsevier B.V., copyright 2023.

tetradecanoic acid (C_{14}) as the modulator, yielding a substantial conversion of 42.9%. This underscores the critical role played by the modulator, which emulates the hydrophobic pocket found in enzymes and proves to be indispensable for the catalytic reaction.[123]

By using citric acid, Liu *et al.* were able to synthesize a HP-HUKST 1 MOF. This modulation process introduced defects, resulting in pores within the MOF capable of accommodating molecules such as phosphomolybdic acid hydrate cluster (HPMo), which possesses dimensions of approximately 10.5 × 10.5 × 7.4 Å. This guest molecule could be effectively stabilized within the MOF, making it suitable for applications in heterogeneous catalysis. As an illustrative example, they conducted the ring opening of styrene oxide with methanol. The composite's stability was substantiated through XRD measurements before and after the reaction, confirming its robust performance. Remarkably, the composite exhibited a high conversion of 99.6% achieved within just 20 minutes. This marked a significant improvement over the conversion observed for non-modulated HKUST-1 with HPMo, highlighting the catalytic efficiency of the modulated composite.[42]

By controlling the specific facet expansion in the phosphotungstic acid (HPW)-containing Cu-MOF NENU-3a, it could be grown in octahedral and cubic crystals, the latter with the modulator *p*TA. The catalytic activity was first tested with acetic acid and methanol. For small molecules, it could be shown that the esterification for both morphologies exhibit a high conversion. By increasing the alcohol or the carboxylic acid chain length, the activity of the octahedral crystals decreased strongly while the activity of the cubic crystals remained almost the same. The cubic morphology of Cu-MOF NENU-3a enabled a catalytic conversion of fatty acids (C12–C22) to biodiesel of 90%, whereas the octahedral crystals only achieved a conversion of 22%. In contrast to esterification reactions with acetic acid, which can occur both on the surface and within the pores of the MOF due to the small AA molecule size, the fatty acids employed in the study were unable to penetrate into the MOF pores. This observation suggested that the catalytic process in this context primarily takes place on the surface, and it is particularly favored by the presence of the {100} facet. The {100} facet facilitates the interaction of fatty acids with both the Lewis acid sites (free copper sites) and the Brønsted acid sites (HPW sites), promoting more efficient catalysis. Consequently, the cubic morphology, which exhibits a pronounced 100 facet, proves to be more advantageous for this specific catalytic process.[117]

Part of us investigated the catalytic properties of a zinc-based MOF using combinations of two different modulators. In one approach, mandelic acid was used as the sole modulator, while in three alternative approaches, mixtures of mandelic acid were used in combination with propanoic acid (Zn.Mand(PRA)), mercaptopropanoic acid (Zn.Mand(MPA)), and lauric acid (Zn.Mand(LA)) as modulator. We chose the enantioselective ring opening of styrene oxide with methanol as the benchmark reaction. From a mechanistic point of view, it can be deduced that catalysis occurs both through open metal sites within the MOF and through the Brønsted acidity of the modulators. This process involves the coordination and protonation of styrene

oxide by the respective MOF. Remarkably, the introduction of a second modulator at the same concentration resulted in a significant increase in conversion (48% *vs.* 98%). In comparison, unmodulated Zn-BDC only achieved a conversion of 21%. The most exceptional result was obtained when ethanol was used instead of methanol. In this case, Zn. Mand(MPA) achieved a complete conversion with a selectivity of 98% and an enantiomeric excess (ee) of 97% for the *S*-enantiomer.[159]

Yang *et al.* reported the modification of MIL-125 MOF by butyric acid as modulator to increase the catalytic activity of the MOF for oxidative desulfurization reaction of sulfur compounds. To investigate the catalytic performance of these different morphologies, dibenzothiophene (DBT) and 4,6-dimethyldibenzothiophene (4,6-DMDBT) in *n*-heptane, along with H_2O_2, were employed as example reactions. MIL-125 with {101} facets in greater abundance than pristine MIL-125 with predominant {001} facets displayed a better catalytic performance. The significantly higher turnover frequency (TOF) observed for 4,6-DMDBT in the presence of MIL-125 with {101} facets can be attributed to an increased number of available Ti sites. This enables the rapid formation of the necessary Ti-hydroperoxo species when reacting with H_2O_2, thus accelerating the overall reaction rate.[115]

Utilizing rhodamine B as a modulator, Jin *et al.* successfully synthesized HP-MIL-125-NH_2. Subsequent removal of the modulator resulted in pronounced porosity within the MOF structure and increased formation of open metal sites. This enhanced porosity facilitated the uptake of toluene. The unique feature of this modified MOF lies in its photocatalytic properties, particularly in its ability to decompose toluene under the influence of atmospheric oxygen. The excitation of the MOF linker initiates an electron transfer from the BDC-linker to the MOF cluster. This electron transfer process subsequently reduces an oxygen molecule to generate a superoxide anion radical. These highly reactive O_2^- radicals, in conjunction with the electron hole at the BDC-linker, function as potent agents for the oxidative transformation of toluene into CO_2 (Fig. 33).[80]

5.2 Gas sorption

The native Zr-MOF ZrSQA is not permeable to hydrogen and nitrogen gas; however, using the modulators AA and FA, Bueken *et al.* were able to synthesise the ZrSQU MOF with a type II isotherm, which is indicative of a non-porous material and a type I isotherm, with an uptake of 40 $cm^3\ g^{-1}$, for N_2 adsorption and an increased H_2 uptake (Fig. 34) which is explained by the formation of defects in the frameworks.[85]

Choi *et al.* reported that defected MOF-5, wich was formed by using surfactant 4-(dodecyloxy)benzoic acid as a modulator, to have a significantly higher adsorption capacity for CO_2 compared to original MOF-5. The increased adsorption of CO_2 was demonstrated by two different methods. First, by adsorption measurements, where the isotherm in the low-pressure micropore region was similar to that of non-modulated MOF-5. However, with increasing pressure, the modulated MOF showed a significant increase in CO_2 uptake. This trend indicated that the modulated MOF-5 effectively adsorbed CO_2 in its mesoporous and macroporous regions, unlike the non-modulated MOF-5. Second, the enhanced CO_2 adsorption was confirmed by synchrotron measurements.[152] Wu *et al.* reported that the introduction of defects into UiO-66 *via* the modulator acetic acid resulted in a porosity increase of up to 150%. This led to an enhanced adsorption of N_2, CH_4, and especially CO_2 gases. The –OH groups coordinated to Zr in UiO-66 have a significant impact on the adsorption of CO_2.[137]

Through the utilization of AA as a modulating agent, Kim *et al.* successfully synthesized a modified version of the HKUST-1, denoted as HP-HKUST-1 (Section 4.5). Remarkably, this material exhibited a 13% increase in methane storage

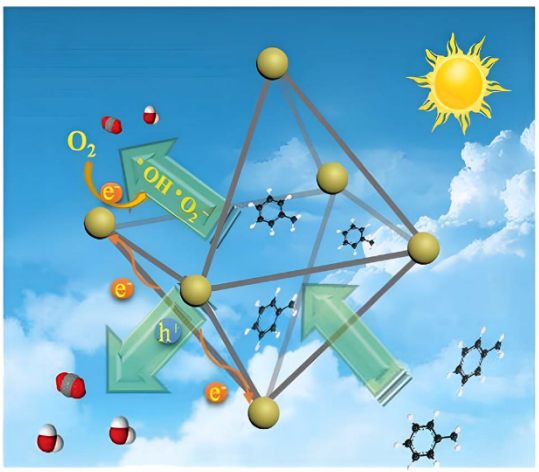

Fig. 33 Scheme for HP-MIL-125, synthesized with rhodamine B as modulator, and its photocatalytic degradation of toluene. Reproduced from ref. 80 with permission from the Wiley-VCH Verlag GmbH & Co. KGaA, Weinheim, copyright 2023.

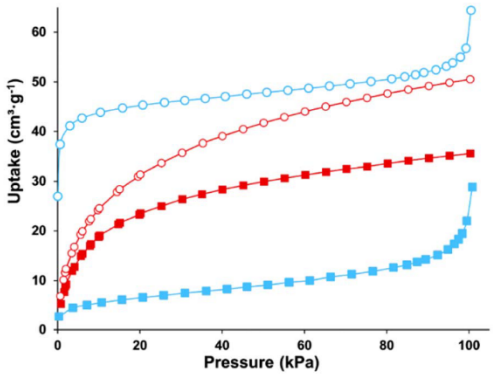

Fig. 34 N_2 (blue) and H_2 (red) adsorption isotherms measured at 77 K on $ZrSQU_A$ (square, AA modulator) and $ZrSQU_F$ (circle, FA modulator) outgassed at 10^{-4} bar at 373 K for 4 h. Reproduced from ref. 85 with permission from The Royal Society of Chemistry, copyright 2014.

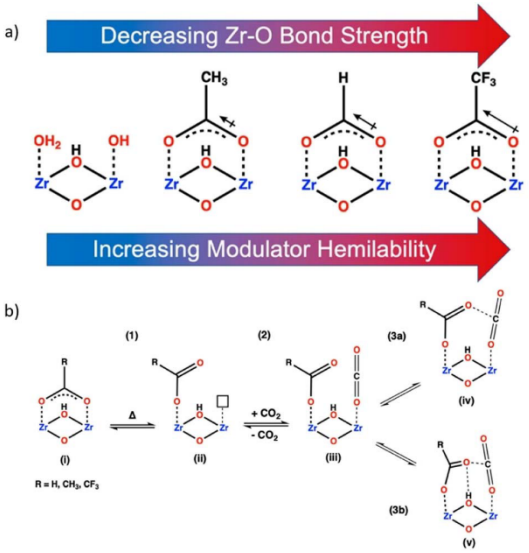

Fig. 35 (a) Increasing modulator hemilability. (b) Hypothesized modulator dynamics upon CO_2 adsorption. Reproduced from ref. 160 with permission from the American Chemical Society, copyright 2023.

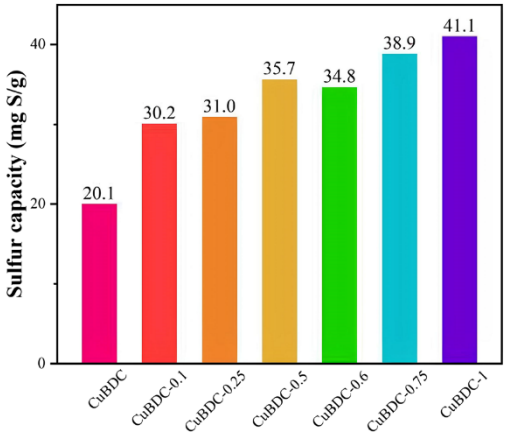

Fig. 36 Sulfur capacity of CuBDC with different concentration of AA modulator. Reproduced from ref. 163 with permission from the Elsevier B.V., copyright 2023.

capacity at a pressure of 65 bar and a 16% augmentation in deliverable capacity across the pressure range from 65 bar down to 5 bar when compared to its unmodified counterpart, HKUST-1.[149]

The behavior of zirconium-based MOFs with respect to CO_2 uptake was reexamined in 2023 by Rayder *et al.* from the perspective of dynamic interactions. For this purpose, MOF-808 was investigated with different modulators. Up to then, it was assumed that it is a static internal porous surface that interacts with gases such as CO_2 at their uptake. Through various investigations, Rayder *et al.* were able to show that it is a dynamic adsorption, depending on the modulator which was used as a capping agent and the resulting coverage of the open metal sides. The electron density at the carboxylate oxygen atoms is of particular importance as it influences the hemilability of the modulator and thus the access to the Zr center for the adsorbed CO_2 (Fig. 35).[160]

Thur *et al.* used modulators in the MOF-808 structure to enhance the uptake of CO_2 molecules. They incorporated a series of fluorinated carboxylic acid modulators as the CO_2-philic portions in the MOF-808 structure in place of the linkers. These MOFs were employed for CO_2/CH_4 separation and showed a much better performance compared to the native MOF-808.[161]

5.3 Separation

Slater *et al.* synthesized the defective MOF [Zn_2(BDC)(L-lac)(DMF)] (ZnBLD), using propanoic acid as a modulator and indicated that the enantioselective ability was increased in the enantiomeric excess for 1-phenylethanol of 35% compared to the non-defective MOF. The enhanced enantioselectivity was ascribed to size-matchable molecules with the pore size of the defective MOF. 1-Phenylethanol exhibited a superior response to enantiomeric separation compared to 2-butanol and pantolactone due to its molecules providing a better size-matching with the pores of the MOF.[162]

Zhang *et al.* conducted a study showcasing the significant impact of modulating CuBDC with AA on the desulfurization of gasoline. In their model fuel, they employed *n*-pentyl mercaptan for the reference reaction. The results of their study showed that an increased amount of the modulator followed by hot ethanol treatment resulted in an enhanced removal of the sulfur compound. This observation suggests an increased incidence of structural defects within the MOF. In addition, the study highlighted the critical role played by the oxidation state of free copper atoms. Zhang *et al.* demonstrated that the use of ethanol served to reduce copper from the 2+ to the 1+ oxidation state, which, notably, exhibits a heightened affinity for sulfur. As a result of modulation and subsequent reduction of the MOF, the total sulfur uptake capacity was substantially enhanced, achieving an impressive increase of 104.5% in comparison to non-modulated CuBDC (Fig. 36).[163]

5.4 Mechanical stability

MOFs with high mechanical stability are of great importance for industrial applications. Zr-MOFs often show a good mechanical stability due to several strong Zr–O bonds in their framework. Voorde *et al.* indicated that crystal defects can play an essential role in the mechanical stability of UiO-66 without altering its porosity. They used mono-coordinating modulators with different acidic property including trifluoroacetic acid, chloroacetic acid, and acetic acid. The mechanical stability of the modulated UiO-66 (physical stability under ball-milling) increases as the modulator pK_a decreases, due to electron withdrawing effect that strengthens the Zr–O bonds and increases the positive partial charge of the Zr^{4+} centers.[45,137]

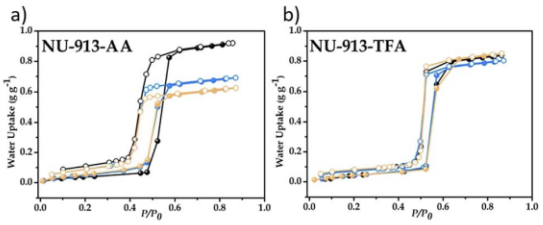

Fig. 37 Stability upon water uptake of (a) NU-913-AA and (b) Nu-913-TFA over three cycles. Black, blue, and yellow isotherms represent first, second, and third cycle, respectively. Reproduced from ref. 128 with permission from the American Chemical Society, copyright 2023.

5.5 Water sorption

Controlled adsorption and release of water by porous materials is widely used in fields such as water absorption from air,[164] dehumidification and thermal batteries.

Considering that zirconium-based MOFs are stable in water and easily recovered, they are suitable candidates for absorbing and releasing water. On the other hand, the synthesis of most crystals of zirconium MOFs is possible only in the presence of the modulator. Yaghi *et al.* showed that zirconium MOFs prepared with the modulating agents including formic acid or acetic acid are ideal materials for adsorption and release of water from the air.[165]

As mentioned in Section 4.3, the work of Gong *et al.* showed that different MOFs could be synthesized under the same conditions by changing the modulator. Furthermore, by changing the modulator from AA to TFA in the synthesis of Nu-913, an increased stability of the scaffold towards water sorption could be achieved due to the higher hydrophobicity introduced by the TFA modulator. The water uptake of AA and TFA Nu-913 was in the same range (0.88 g g^{-1} for AA and 0.85 g g^{-1} for TFA), showing that even over several cycles the uptake of the TFA-modulated MOF remained the same, while the uptake of the AA-modulated MOF decreased dramatically with the third cycle (Fig. 37).[128]

An investigation by Teo *et al.* highlighted the influence of modulation with varying quantities of FA on the water sorption behavior of Al-Fum. Their findings revealed that the most favorable outcome was achieved when 10 mL of FA were employed as the modulating agent. Under this condition, the water uptake capacity exhibited a noteworthy increase of 12.5% compared to the non-modulated Al-Fum.[166]

5.6 Storage of reactive gases

Storage and release of carbon monoxide (CO) at low concentrations have important therapeutic uses. The size and morphology of MOFs have an effective role in the loading of carbon monoxide containing and releasing molecules, known as CORMs. Carmona *et al.* showed that the MOF [Al(OH)(SDC)] (SDC = 4,4′-stilbenedicarboxylate) can be a suitable carrier for CORMs with controlled release of carbon monoxide in the physiological environment. The AA-modulated MOF was successfully loaded with the light-active photoCORM ALF794. Notably, this loading process could only be achieved with the modulated MOF, as the non-modulated MOF underwent decomposition during the loading procedure. Upon exposure to light, a gradual release of CO from the composite material was observed. It is worth noting that the release from the composite was marginally less efficient compared to the neat photoCORM, which may be attributed to the hindrance of CO release imposed by the MOF structure. Nevertheless, the composite still exhibited a substantial release, with approximately 35% of the loaded CO being released under the given conditions. In comparison, the neat photoCORM displayed a photo release efficiency of approximately 42%.[120]

Zhang *et al.* successfully improved the adsorption of sulfur-containing compounds in MOF-199 by using BA as a modulator. H_2S and dimethyl sulfide at different concentrations were used as test adsorbates. The results consistently showed that all modulated MOFs exhibited a better uptake of H_2S and dimethyl sulfide compared to the non-modulated MOF-199. The reason for using the modulator was the formation of structural defects in the MOF-199 lattice. These defects resulted in open copper sites that were more accessible for the interaction with sulfur-containing compounds. In addition, these defects facilitated the transport of H_2S and dimethyl sulfide through the MOF, which promoted enhanced uptake. The best value for the modulated MOF-199 was 20% higher than that of the non-modulated MOF for both adsorbates.[167]

Walton *et al.* used cyanoacetic acid as a modulator in the synthesis of UiO-66 in addition to AA, TFA, and acrylic acid. The reason for selecting these modulators was their ability to interact with SO_2 and consequently enhance its uptake. The results of their study showed that all modulated MOFs exhibited better SO_2 adsorption than their non-modulated counterparts. Moreover, the concentration of the modulator was found to be a crucial factor for SO_2 uptake. The strongest interaction, and consequently the highest uptake, was obtained when cyanoacetic acid was used as modulator at a ratio of 18 : 1 between modulator and linker. However, it should be noted that the crucial factor for SO_2 uptake is not the choice of modulator alone, but also the interaction between the modulator, the linker and the adsorbed SO_2 molecules within the MOF structure.[168]

Maddock *et al.* studied the uptake and storage of radioactive iodine with HP-UiO-66 modulated with FA. Using thermogravimetric measurements, they demonstrated that the modulated HP-UiO-66 had almost twice the uptake capacity for radioactive iodine compared to the unmodulated HP-UiO-66 (2.25 g g^{-1} *vs.* 1.17 g g^{-1}).[169]

5.7 Water decontamination

Contamination of drinking water by heavy metals or organic compounds such as benzene is a significant threat for the human health in many areas of the world.[170]

Prabhu *et al.* indicated that the surface charge of the MOF Zr-FMA can be controlled by the help of the modulator BA by affecting the colloid stability of the MOF. The resulting defect-free MOF showed a considerable enhancement in the

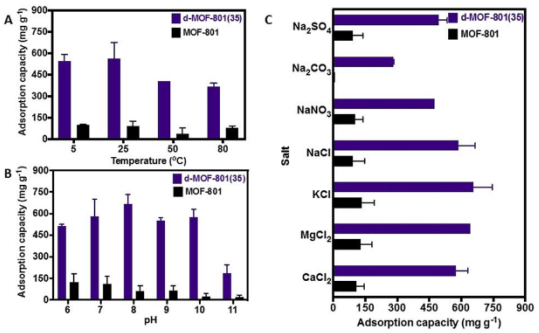

Fig. 38 The effect of temperature (A), pH (B) and the presence of various salts (C) on the diclofenac adsorption performance of d-MOF-801(35) and MOF-801. Reproduced from ref. 146 with permission from the Elsevier B.V., copyright 2022.

adsorption capacity of AsO_4^{3-} and AsO_3^{3-} ions from water that is attributed to the positive surface of the MOF.[171]

Li *et al.* demonstrated that the modulated yttrium MOF-76 showed better uptake of arsenate than the non-modulated MOF-76 under basic conditions. The high uptake was favored by the open metal sites formed during modulation. Uptake occurred in a basic environment (pH: 9–11) due to the formation of a Y–O–As bond. Furthermore, it was shown that ligand exchange in the MOF could also positively affect the uptake. Treating the MOF with HCl led to reactivation, and recycling tests achieved good uptake of arsenate even after several cycles.[113] Further, part of us synthesized Zr-based functionalized UiO-66 with a modulated synthesis for the removal of Ag(I) from wastewater.[129] By using the modifier mercaptoacetic acid (HMAc), an easy and economical way of incorporating a thiol group into the MOF was found. Despite the increasing amount of sulfur groups, the BET surface area of standard UiO-66 was maintained. The inclusion of ligands containing free thiol groups resulted in increased Ag^+ uptake when compared to the unfunctionalized (non-thiol) form. MOF-801 synthesized by Prasetya *et al.* showed good uptake of diclofenac from aqueous solutions, with the best results obtained with the lowest amount of FA as modulator. It should be mentioned that for all defective MOFs here, water was used as solvent and the reaction was carried out at room temperature. The modulated MOF d-MOF-801(35) showed a nearly four times higher uptake compared to non-modulated MOF-801, synthesised in DMF. Particularly noteworthy was the consistently high uptake under different temperature and pH conditions as well as in the presence of salts (Fig. 38). Recycling experiments showed a constant high uptake over several cycles.[146]

Assaad *et al.* synthesized UiO-66 in the presence of the modulators AA and TFA. The defects in the modulated Zr-MOFs provided avenues for entering arsenate ions into MOF to bind with the metal clusters. Therefore, modulated UiO-66 exhibited greater effective adsorption in comparison to the non-modulated one. UiO-66-36TFA (with a modulator ratio of 36 equivalents) presented the most defective sample and possessed the highest adsorption efficiency of 200 mg g^{-1} compared to 89.3 mg g^{-1} for unmodulated UiO-66.[172]

Li *et al.* were able to show that both the missing linker and the missing cluster approach for defective UiO-66 structures resulted in a higher uptake of selenium(VI) oxoanions. For the missing linker structure, HCl was used as a modulator, whereas for the missing cluster structure, TFA was employed. An uptake almost twice as high as that of the non-modulated MOF was achieved. The selenium(VI) oxoanions used bind to the open metal sites of the Zr clusters.[173]

Generally, MOFs consisting of defective structure facilitate the transfer of mass in the framework, which is important for catalysis and sensing applications.[174]

5.8 Sensing

The morphologies of the MOF $[Cu_2(OBA)_2(BPFB)]\cdot(DMF)_5$ (TMU-46) could be controlled by the benzoic acid and pyridine modulators as nanorods and nanoplates, respectively. The sensing experiments for trinitrophenol (TNP) and trinitrotoluene (TNT) showed that the plate morphology exhibits a better sensor performance (Fig. 39).[118]

Methanol was used as a modulating agent in the synthesis of MIL-88B-Fe, which is described in detail by Wang *et al.* in Section 4.5. This modified MIL-88B-Fe material exhibited exceptional sensitivity to hydrogen sulfide (H_2S), primarily due to the enhanced presence of open iron sites. Moreover, this modified material exhibited a remarkable long-term stability of more than 31 days. It also exhibited an impressive recovery time of only 88.5 seconds. When MIL-88B was modulated with 20% methanol (referred to as MIL-88B-20%), the response to H_2S was ten times higher than the non-modulated MIL-88B (Fig. 40).[44]

Li *et al.* used the HCl modulator, to form the defective MOF HCleNH$_2$-UiO-66 NPs which could be coated with a significant amount of iron nanoparticles due to its increased defects. The peroxidase-like activity of FeeHCleNH$_2$-UiO-66 NPs was found to be highly effective even at low concentrations of substrates, suggesting its potential application for detecting H_2O_2 in cancer cells.[175]

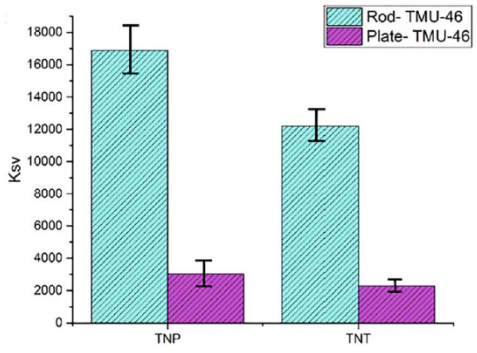

Fig. 39 Comparison of the fluorescence intensity of the rod and plate morphology of TMU-46 for TNT and TNP sensing. Reproduced from ref. 118 with permission from the Elsevier B.V., copyright 2020.

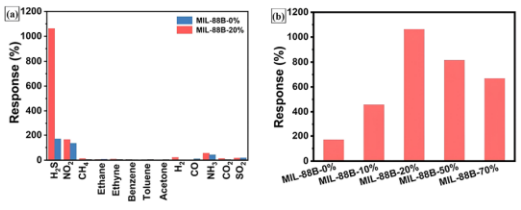

Fig. 40 (a) Selectivity tests of MIL-88B-20% and (b) sensitivity as a function of modulator amount. Reproduced from ref. 44 with permission from the Wiley-VCH Verlag GmbH & Co. KGaA, Weinheim, copyright 2023.

6. Conclusion and outlook

Coordination modulation is an easy and effective way for controlling the MOF properties. MOFs with high crystallinity, pure phases, good reproducibility, high porosity, desired morphology, and size can be produced by the coordination modulation method. Stability of the MOFs is one of the most important features not only for widespread applications, but also for easy pore engineering by creating defects in the MOFs. This is because the amount of defects is limited in the unstable MOFs due to the possibility of their structure collapsing. On the other hand, the existence of the modulators is necessary to synthesize some stable MOFs, such as zirconium-based MOFs, with suitable crystallinity. In addition, the post-synthesis process with the help of modulators can be conducted easily in mild conditions. The size and morphology characteristics of the MOFs are directly related to the type and quality of their application. For example, for catalytic applications and adsorption, both the shape and size of the MOFs should be optimized to maximize the mass transfer and adsorption capacity of the material. Self-assembly of MOFs can be controlled by using coordination modulators, paving the way for the preparation of MOFs with greater potential applications.

Generally, it appears that a suitable coordination modulator is a functional molecule with a weaker coordination bond affinity so that it can have a favorable performance to guide the self-assembly path towards the formation of MOF with the expected characteristics in terms of shape and size. In other words, in this case, the modulator can only intervene in the kinetic process of MOF synthesis and control the nucleation process without changing the chemical structure of MOF. On the other hand, the chemical nature and size of the modulator is the factor that determines the final properties of MOF, for example, MOF with a larger pore size can be synthesized by choosing a modulator with a long molecular chain size.

The synthesis of new modulators, to produce MOFs with various characteristics or the production of new MOFs whose crystal phase synthesis is not possible, can be the subject of researchers' research in the future. The effective steps can be taken in the design of the modulation procedure by using of computational chemistry, for example, by designing a suitable modulator, the growth of certain crystal faces of MOF can be controlled to produce nanoplates, nanosheets and other widely used morphologies.

Abbreviations

AA	Acetic acid
AZB	4,4′-Azobenzenedicarboxylate
4-BPDB	1,4-Bis(4-pyridyl)-2,3-diaza-1,3-butadiene
4-BPDH	2,5-Bis(4-pyridyl)-3,4-diaza-2,4-hexadiene
4-BPMB	N^1,N^4-Bis((pyridine-4-yl)methylene)benzene-1,4-diamine
BA	Benzoic acid
BBTA	1*H*,5*H*-Benzo(1,2-*d*:4,5-*d*′)bistriazole
BDC	1,4-Benzenedicarboxylate
BET	Brunauer–Emmett–Teller
BHC	The conjugate acid is also called mellitic acid
BIPYEN	*Trans*-1,2-bis(4-pyridyl)ethylene
BPFB	*N*,*N*′-(1,4-phenylene)diisonicotinamide
BTC	Benzene-1,3,5-tricarboxylate
CTAB	Cetyltrimethylammonium bromide
DABCO	1,4-Diazabicyclo[2.2.2]octane
DCA	Dichloroacetic acid
DGC	Dry gel conversion
DMF	*N*,*N*-dimethylformamide
FA	Formic acid
fcc	Face-centered cubic
FE-SEM	Field-emission scanning electron microscopy
FMA	Fumarate
Glu	Glutamate
H_2BDCA	Biphenyl-4-carboxylic acid
H_4TBAPy	1,3,6,8-Tetrakis(*p*-benzoic acid)pyrene
hcp	Hexagonal close packed
H_3IMDC	4,5-Imidazoledicarboxylic acid
1-HMIM	1-Methylimidazole
His	L-Histidine
HMAc	Mercaptoacetic acid
HP-MOF	Hierarchical-porous MOF
ILME	Ionic liquid microemulsion
L-Pro	L-Proline
MNA	6-Methoxy-2-naphtholate
MW	Microwave
NDC	Naphthalenedicarboxylate
NMOF	NanoMOF
NMR	Nuclear magnetic resonance
OBA	4,4-Oxybis(benzoate)
ORR	Oxygen reduction reaction
OX	Oxalate
P-123	Pluronic triblock copolymer
H_4PBPTTBA	4,4′,4″,4‴-(1,4-Phenylenebis(pyridine-4,2,6 triyl)) tetrabenzoic acid
PEI	Polyethyleneimine
*p*TA	*p*-Toluic acid
PVP	Poly(vinylpyrrolidone)
PXRD	Powder X-ray diffraction
RhB	Rhodamine B
SDBS	Sodium dodecylbenzenesulfonate
SDS	Sodium dodecyl sulfate
SEM	Scanning electron microscopy

H_2SQA	Squaric acid ($C_4O_4H_2$)
Tar	Tartrate
TCPP	Mesotetrakis(4-carboxyphenyl)porphyrin
TEA	Triethyl amine
TEM	Transmission electron microscopy
TFA	Trifluoroacetic acid
TMB	1,3,5-Trimethylbenzene
TNP	Trinitrophenol
TNT	Trinitrotoluene
TRO	Truncated octahedron
US	Ultrasonic

Conflicts of interest

There are no conflicts of interest to declare.

Acknowledgements

The authors gratefully appreciate the financial support of Tarbiat Modares University and the Heinrich-Heine-Universität Düsseldorf. Financial support by the Deutsche Forschungsgemeinschaft (DFG) within the Priority Program SPP 1928/2 COORNETs is gratefully acknowledged by C. J. (grant Ja466/43-1).

References

1 J. M. Chin, E. Y. Chen, A. G. Menon, H. Y. Tan, A. T. S. Hor, M. K. Schreyer and J. Xu, *CrystEngComm*, 2013, **15**, 654–657.
2 M. Ahmadi, M. Ebrahimnia, M.-A. Shahbazi, R. Keçili and F. Ghorbani-Bidkorbeh, *J. Ind. Eng. Chem.*, 2022, **115**, 1–11.
3 T. Tsuruoka, K. Mantani, A. Miyanaga, T. Matsuyama, T. Ohhashi, Y. Takashima and K. Akamatsu, *Langmuir*, 2016, **32**, 6068–6073.
4 W. Cho, H. J. Lee and M. Oh, *J. Am. Chem. Soc.*, 2008, **130**, 16943–16946.
5 T. Tsuruoka, S. Furukawa, Y. Takashima, K. Yoshida, S. Isoda and S. Kitagawa, *Angew. Chem.*, 2009, **121**, 4833–4837.
6 A. Umemura, S. Diring, S. Furukawa, H. Uehara, T. Tsuruoka and S. Kitagawa, *J. Am. Chem. Soc.*, 2011, **133**, 15506–15513.
7 S. Diring, S. Furukawa, Y. Takashima, T. Tsuruoka and S. Kitagawa, *Chem. Mater.*, 2010, **22**, 4531–4538.
8 R. J. Marshall, C. T. Lennon, A. Tao, H. M. Senn, C. Wilson, D. Fairen-Jimenez and R. S. Forgan, *J. Mater. Chem. A*, 2018, **6**, 1181–1187.
9 O. V. Gutov, S. Molina, E. C. Escudero-Adán and A. Shafir, *Chem.–Eur. J.*, 2016, **22**, 13582–13587.
10 M. Taddei, *Coord. Chem. Rev.*, 2017, **343**, 1–24.
11 A. K. P. Leite, B. S. Barros, J. Kulesza, J. F. S. d. Nascimento, D. M. d. A. Melo and A. A. S. d. Oliveira, *Mater. Res.*, 2017, **20**, 681–687.
12 E. Sanil, K.-H. Cho, S.-K. Lee, U.-H. Lee, S. G. Ryu, H. W. Lee, J.-S. Chang and Y. K. Hwang, *J. Porous Mater.*, 2015, **22**, 171–178.
13 M. H. Rosnes, F. S. Nesse, M. Opitz and P. D. Dietzel, *Microporous Mesoporous Mater.*, 2019, **275**, 207–213.
14 P. Pachfule, D. Shinde, M. Majumder and Q. Xu, *Nat. Chem.*, 2016, **8**, 718–724.
15 S. A. A. Razavi, M. Y. Masoomi and A. Morsali, *Ultrason. Sonochem.*, 2017, **37**, 502–508.
16 N. Varnaseri, F. Rouhani, A. Ramazani and A. Morsali, *Dalton Trans.*, 2020, **49**, 3234–3242.
17 Y. Lin, H. Wan, D. Wu, G. Chen, N. Zhang, X. Liu, J. Li, Y. Cao, G. Qiu and R. Ma, *J. Am. Chem. Soc.*, 2020, **142**, 7317–7321.
18 Y. Wan, J. Wan, J. R. Zhao, Y. Wang, T. Luo, S. Yang and Y. Liu, *Chemosphere*, 2020, **254**, 126798.
19 M. Qi, Y. Zhou, Y. Lv, W. Chen, X. Su, T. Zhang, G. Xing, G. Xu, O. Terasaki and L. Chen, *J. Am. Chem. Soc.*, 2023, **145**, 2739–2744.
20 L. Hu, P. Zhang, Q. Chen, H. Zhong, X. Hu, X. Zheng, Y. Wang and N. Yan, *Cryst. Growth Des.*, 2012, **12**, 2257–2264.
21 P. Sarawade, H. Tan and V. Polshettiwar, *ACS Sustain. Chem. Eng.*, 2013, **1**, 66–74.
22 P. Horcajada, T. Chalati, C. Serre, B. Gillet, C. Sebrie, T. Baati, J. F. Eubank, D. Heurtaux, P. Clayette and C. Kreuz, *Nat. Mater.*, 2010, **9**, 172–178.
23 H. Guo, Y. Zhu, S. Wang, S. Su, L. Zhou and H. Zhang, *Chem. Mater.*, 2012, **24**, 444–450.
24 J. Cravillon, R. Nayuk, S. Springer, A. Feldhoff, K. Huber and M. Wiebcke, *Chem. Mater.*, 2011, **23**, 2130–2141.
25 H. Xu, X. Rao, J. Gao, J. Yu, Z. Wang, Z. Dou, Y. Cui, Y. Yang, B. Chen and G. Qian, *Chem. Commun.*, 2012, **48**, 7377–7379.
26 X. Cheng, A. Zhang, K. Hou, M. Liu, Y. Wang, C. Song, G. Zhang and X. Guo, *Dalton Trans.*, 2013, **42**, 13698–13705.
27 A. Schaate, P. Roy, A. Godt, J. Lippke, F. Waltz, M. Wiebcke and P. Behrens, *Chem. Eur. J.*, 2011, **17**, 6643–6651.
28 Z. Hu, I. Castano, S. Wang, Y. Wang, Y. Peng, Y. Qian, C. Chi, X. Wang and D. Zhao, *Cryst. Growth Des.*, 2016, **16**, 2295–2301.
29 F. Drache, V. Bon, I. Senkovska, J. Getzschmann and S. Kaskel, *Philos. Trans. R. Soc., A*, 2017, **375**, 20160027.
30 J. J. Richardson, K. Liang, F. Lisi, M. Björnmalm, M. Faria, J. Guo and P. Falcaro, *Eur. J. Inorg. Chem.*, 2016, **2016**, 4499–4504.
31 Y. Ban, Y. Li, X. Liu, Y. Peng and W. Yang, *Microporous Mesoporous Mater.*, 2013, **173**, 29–36.
32 M. Vandichel, J. Hajek, F. Vermoortele, M. Waroquier, D. E. De Vos and V. Van Speybroeck, *CrystEngComm*, 2015, **17**, 395–406.
33 J.-H. Wang, M.-N. Li, S. Yan, Y. Zhang, C.-C. Liang, X.-M. Zhang and Y.-B. Zhang, *Inorg. Chem.*, 2020, **59**, 2961–2968.
34 L. Yang, T. Zhao, I. Boldog, C. Janiak, X.-Y. Yang, Q. Li, Y.-J. Zhou, Y. Xia, D.-W. Lai and Y.-J. Liu, *Dalton Trans.*, 2019, **48**, 989–996.
35 T. Islamoglu, K.-i. Otake, P. Li, C. T. Buru, A. W. Peters, I. Akpinar, S. J. Garibay and O. K. Farha, *CrystEngComm*, 2018, **20**, 5913–5918.
36 T. Zhao, L. Yang, P. Feng, I. Gruber, C. Janiak and Y. Liu, *Inorg. Chim. Acta*, 2018, **471**, 440–445.

37 L. Zhang, M. Li, H. Zhou, S. Zou, Z. Lin, S. Zhao, F. Fan, T. Wang, X. Zhang and Y. Fu, *Inorg. Chem. Commun.*, 2023, **150**, 110542.
38 P. Nian, H. Liu and X. Zhang, *CrystEngComm*, 2019, **21**, 3199–3208.
39 E. Bagherzadeh, S. M. Zebarjad and H. R. M. Hosseini, *Eur. J. Inorg. Chem.*, 2018, **2018**, 1909–1915.
40 G. Cai and H. L. Jiang, *Angew. Chem., Int. Ed.*, 2017, **56**, 563–567.
41 Y. Chen, S. Zhang, F. Chen, S. Cao, Y. Cai, S. Li, H. Ma, X. Ma, P. Li and X. Huang, *J. Mater. Chem. A*, 2018, **6**, 342–348.
42 T. Liu, Y. Liu, L. Yao, W. Yang, L. Tian, H. Liu, D. Liu and C. Wang, *Nanoscale*, 2018, **10**, 13194–13201.
43 G. C. Shearer, S. Chavan, S. Bordiga, S. Svelle, U. Olsbye and K. P. Lillerud, *Chem. Mater.*, 2016, **28**, 3749–3761.
44 C. Z. Wang, J. Chen, Q.-H. Li, G.-E. Wang, X.-L. Ye, L. Jia and G. Xu, *Angew. Chem.*, 2023, **135**, 1–6.
45 B. Van de Voorde, I. Stassen, B. Bueken, F. Vermoortele, D. De Vos, R. Ameloot, J.-C. Tan and T. D. Bennett, *J. Mater. Chem. A*, 2015, **3**, 1737–1742.
46 M. R. DeStefano, T. Islamoglu, S. J. Garibay, J. T. Hupp and O. K. Farha, *Chem. Mater.*, 2017, **29**, 1357–1361.
47 M. J. Katz, Z. J. Brown, Y. J. Colón, P. W. Siu, K. A. Scheidt, R. Q. Snurr, J. T. Hupp and O. K. Farha, *Chem. Commun.*, 2013, **49**, 9449–9451.
48 S. Dai, *Angew. Chem., Int. Ed.*, 2021, **60**, 4282–4288.
49 Y. Liu, P. Gao, C. Huang and Y. Li, *Sci. China: Chem.*, 2015, **58**, 1553–1560.
50 B. B. Kulkarni, K. S. Kanakikodi, D. A. Rambhia, S. B. Kalidindi and S. P. Maradur, *New J. Chem.*, 2022, **46**, 726–738.
51 G. Han, K. M. Rodriguez, Q. Qian and Z. P. Smith, *Ind. Eng. Chem. Res.*, 2020, **59**, 18139–18150.
52 Y. Han, M. Liu, K. Li, Y. Zuo, Y. Wei, S. Xu, G. Zhang, C. Song, Z. Zhang and X. Guo, *CrystEngComm*, 2015, **17**, 6434–6440.
53 S. Canossa, A. Gonzalez-Nelson, L. Shupletsov, M. del Carmen Martin and M. A. Van der Veen, *Chem.–Eur. J.*, 2020, **26**, 3564–3570.
54 X. Wang and A. J. Jacobson, *J. Solid State Chem.*, 2016, **236**, 230–235.
55 W. Mao, R. Huang, H. Xu, H. Wang, Y. Huang, S. Huang and J. Zhou, *Polymers*, 2022, **14**, 3826.
56 T. Zhao, F. Jeremias, I. Boldog, B. Nguyen, S. K. Henninger and C. Janiak, *Dalton Trans.*, 2015, **44**, 16791–16801.
57 H. R. Abid, H. M. Ang and S. Wang, *Nanoscale*, 2012, **4**, 3089.
58 A. T. A. Duong, H. V. Nguyen, M. V. Tran, Q. N. Ngo, L. C. Luu, T. L. H. Doan, H. N. Nguyen and M. V. Nguyen, *RSC Adv.*, 2023, **13**, 17370–17383.
59 Y. Li, L. Lin, M. Tu, P. Nian, A. J. Howarth, O. K. Farha, J. Qui and X. Zhang, *Nano Res.*, 2018, **11**, 1850–1860.
60 M. Y. Masoomi, S. Beheshti and A. Morsali, *Cryst. Growth Des.*, 2015, **15**, 2533–2538.
61 R. J. Marshall, C. L. Hobday, C. F. Murphie, S. L. Griffin, C. A. Morrison, S. A. Moggach and R. S. Forgan, *J. Mater. Chem. A*, 2016, **4**, 6955–6963.
62 M. W. Anjum, F. Vermoortele, A. L. Khan, B. Bueken, D. E. De Vos and I. F. Vankelecom, *ACS Appl. Mater. Interfaces*, 2015, **7**, 25193–25201.
63 K. Liang, R. Ricco, C. M. Doherty, M. J. Styles and P. Falcaro, *CrystEngComm*, 2016, **18**, 4264–4267.
64 T. Lu, L. Zhang, M. Sun, D. Deng, Y. Su and Y. Lv, *Anal. Chem.*, 2016, **88**, 3413–3420.
65 M. Taddei, G. M. Schukraft, M. E. Warwick, D. Tiana, M. J. McPherson, D. R. Jones and C. Petit, *J. Mater. Chem. A*, 2019, **7**, 23781–23786.
66 Y.-N. Guo, Y. Li, B. Zhi, D. Zhang, Y. Liu and Q. Huo, *RSC Adv.*, 2012, **2**, 5424–5429.
67 G. Zheng, Z. Chen, K. Sentosun, I. Pérez-Juste, S. Bals, L. M. Liz-Marzán, I. Pastoriza-Santos, J. Pérez-Just and M. Hong, *Nanoscale*, 2017, **9**, 16645.
68 X. Cai, J. Lin and M. Pang, *Cryst. Growth Des.*, 2016, **16**, 3565–3568.
69 S. Hartmann, D. Brandhuber and N. Hüsing, *Acc. Chem. Res.*, 2007, **40**, 885–894.
70 W. Zheng, X. Hao, L. Zhao and W. Sun, *Ind. Eng. Chem. Res.*, 2017, **56**, 5899–5905.
71 R. Ye, M. Ni, Y. Xu, H. Chen and S. Li, *RSC Adv.*, 2018, **8**, 26237–26242.
72 W. J. Rieter, K. M. L. Taylor, H. An, W. Lin and W. Lin, *J. Am. Chem. Soc.*, 2006, **128**, 9024–9025.
73 W. Sun, X. Zhai and L. Zhao, *Chem. Eng. J.*, 2016, **289**, 59–64.
74 R. Yu, X.-F. Kuang, X.-Y. Wu, C.-Z. Lu and J. P. Donahue, *Coord. Chem. Rev.*, 2009, **253**, 2872–2890.
75 S. S.-Y. Chui, S. M.-F. Lo, J. P. Charmant, A. G. Orpen and I. D. Williams, *Science*, 1999, **283**, 1148–1150.
76 X. Xu, Y. Lu, Y. Yang, F. Nosheen and X. Wang, *Sci. China Mater.*, 2015, **58**, 370–377.
77 X. Xu, S. Chen, Y. Chen, H. Sun, L. Song, W. He and X. Wang, *Small*, 2016, **12**, 2982–2990.
78 R. Monteagudo-Olivan, *J. Mater. Chem. A*, 2018, **6**, 14352.
79 N. Liedana, A. Galve, C. Rubio, C. Tellez and J. Coronas, *ACS Appl. Mater. Interfaces*, 2012, **4**, 5016–5021.
80 J. Jin, S. Wan, S. Lee, C. Oh, G. Y. Jang, K. Zhang, Z. Lu and J. H. Park, *Small*, 2023, e2302776, DOI: **10.1002/smll.202302776**.
81 H. Li, Z. Qin, X. Yang, X. Chen, Y. Li and K. Shen, *ACS Cent. Sci.*, 2022, **8**, 718–728.
82 N. Liedana, P. Lozano, A. Galve, C. Tellez and J. Coronas, *J. Mater. Chem. B*, 2014, **2**, 1144–1151.
83 A. K. Cheetham, G. Kieslich and H.-M. Yeung, *Acc. Chem. Res.*, 2018, **51**, 659–667.
84 W. P. Deleu, G. Rivero, R. F. Teixeira, F. E. Du Prez and D. E. De Vos, *Chem. Mater.*, 2015, **27**, 5495–5502.
85 B. Bueken, H. Reinsch, N. Reimer, I. Stassen, F. Vermoortele, R. Ameloot, N. Stock, C. E. Kirschhock and D. De Vos, *Chem. Commun.*, 2014, **50**, 10055–10058.
86 L. Huelsenbeck, K. S. Westendorff, Y. Gu, S. Marino, S. Jung, W. S. Epling and G. Giri, *Crystals*, 2018, **9**, 20.

87 G. Lu, C. Cui, W. Zhang, Y. Liu and F. Huo, *Chem.–Asian J.*, 2013, **8**, 69–72.
88 H. Embrechts, M. Kriesten, M. Ermer, W. Peukert, M. Hartmann and M. Distaso, *RSC Adv.*, 2020, **10**, 7336–7348.
89 R. Vakili, S. Xu, N. Al-Janabi, P. Gorgojo, S. M. Holmes and X. Fan, *Microporous Mesoporous Mater.*, 2018, **260**, 45–53.
90 S. Gökpinar, T. Diment and C. Janiak, *Dalton Trans.*, 2017, **46**, 9895–9900.
91 G. Wißmann, A. Schaate, S. Lilienthal, I. Bremer, A. M. Schneider and P. Behrens, *Microporous Mesoporous Mater.*, 2012, **152**, 64–70.
92 T. D. Bennett, A. K. Cheetham, A. H. Fuchs and F.-X. Coudert, *Nat. Chem.*, 2017, **9**, 11–16.
93 S. M. Shaikh, P. M. Usov, J. Zhu, M. Cai, J. Alatis and A. J. Morris, *Inorg. Chem.*, 2019, **58**, 5145–5153.
94 Ü. Kökçam-Demir, A. Goldman, L. Esrafili, M. Gharib, A. Morsali, O. Weingart and C. Janiak, *Chem. Soc. Rev.*, 2020, **49**, 2751–2798.
95 C. Ardila-Suárez, A. M. Díaz-Lasprilla, L. A. Díaz-Vaca, P. B. Balbuena, V. G. Baldovino-Medrano and G. E. Ramírez-Caballero, *CrystEngComm*, 2019, **21**, 3014–3030.
96 G. H. Albuquerque and G. S. Herman, *Cryst. Growth Des.*, 2017, **17**, 156–162.
97 E. Virmani, J. M. Rotter, A. Mähringer, T. Von Zons, A. Godt, T. Bein, S. Wuttke and D. D. Medina, *J. Am. Chem. Soc.*, 2018, **140**, 4812–4819.
98 G. Zahn, P. Zerner, J. Lippke, F. L. Kempf, S. Lilienthal, C. A. Schröder, A. M. Schneider and P. Behrens, *CrystEngComm*, 2014, **16**, 9198–9207.
99 G. Liu, H. Cui, S. Wang, L. Zhang and C.-Y. Su, *J. Mater. Chemi. A*, 2020, **8**, 8376–8382.
100 M. A. Alavi and A. Morsali, *CrystEngComm*, 2014, **16**, 2246–2250.
101 W. Lin, W. Lin, H. An, K. Taylor and W. Rieter, *J. Am. Chem. Soc.*, 2006, **128**, 9024–9025.
102 S. Wang, C. M. McGuirk, A. d'Aquino, J. A. Mason and C. A. Mirkin, *Adv. Mater.*, 2018, **30**, 1800202.
103 K. M. Taylor, W. J. Rieter and W. Lin, *J. Am. Chem. Soc.*, 2008, **130**, 14358–14359.
104 J. M. Yang, Q. Liu, Y. S. Kang and W. Y. Sun, *Dalton Trans.*, 2014, **43**, 16707–16712.
105 J. E. Mondloch, W. Bury, D. Fairen-Jimenez, S. Kwon, E. J. DeMarco, M. H. Weston, A. A. Sarjeant, S. T. Nguyen, P. C. Stair and R. Q. Snurr, *J. Am. Chem. Soc.*, 2013, **135**, 10294–10297.
106 F. Drache, V. Bon, I. Senkovska, C. Marschelke, A. Synytska and S. Kaskel, *Inorg. Chem.*, 2016, **55**, 7206–7213.
107 Y. Liu, W. Xuan and Y. Cui, *Adv. Mater.*, 2010, **22**, 4112–4135.
108 X.-J. Hu, G. Huang, S. Zhang, Z.-B. Fang, T.-F. Liu and R. Cao, *Chem. Commun.*, 2020, **56**, 7459–7462.
109 F. Drache, F. G. Cirujano, K. D. Nguyen, V. Bon, I. Senkovska, F. X. Llabres i Xamena and S. Kaskel, *Cryst. Growth Des.*, 2018, **18**, 5492–5500.
110 J. Duan, J. Bai, B. Zheng, Y. Li and W. Ren, *Chem. Commun.*, 2011, **47**, 2556–2558.
111 M.-H. Pham, G.-T. Vuong, F. d. r.-G. Fontaine and T.-O. Do, *Cryst. Growth Des.*, 2012, **12**, 3091–3095.
112 F. Wang, H. Guo, Y. Chai, Y. Li and C. Liu, *Microporous Mesoporous Mater.*, 2013, **173**, 181–188.
113 Z. Li, S. Ma, C. Chen, G. Qu, W. Jin and Y. Zhao, *Chem. Eng. J.*, 2020, **397**, 125292.
114 M. Li, H. Zhou, L. Zhang, J. Han, G. Wang, F. Fan, T. Wang, X. Zhang and Y. Fu, *Microporous Mesoporous Mater.*, 2023, **348**, 112379.
115 P. Yang, Y. Huang, Z.-W. Zhang, N. Li and Y. Fan, *Dalton Trans.*, 2020, **49**, 10052–10057.
116 D. Bara, C. Wilson, M. Mörtel, M. M. Khusniyarov, S. Ling, B. Slater, S. Sproules and R. S. Forgan, *J. Am. Chem. Soc.*, 2019, **141**, 8346–8357.
117 Y. Liu, S. Liu, D. He, N. Li, Y. Ji, Z. Zheng, F. Luo, S. Liu, Z. Shi and C. Hu, *J. Am. Chem. Soc.*, 2015, **137**, 12697–12703.
118 L. Esrafili, M. Gharib, A. Morsali and P. Retailleau, *Ultrason. Sonochem.*, 2020, **66**, 105110.
119 M. Safari, S. Sedghiniya, J. Soleimannejad and J. Janczak, *Acta Crystallogr., Sect. B: Struct. Sci., Cryst. Eng. Mater.*, 2023, **79**, 114–121.
120 F. J. Carmona, C. R. Maldonado, S. Ikemura, C. C. Romao, Z. Huang, H. Xu, X. Zou, S. Kitagawa, S. Furukawa and E. Barea, *ACS Appl. Mater. Interfaces*, 2018, **10**, 31158–31167.
121 W. J. Rieter, K. M. Taylor, H. An, W. Lin and W. Lin, *J. Am. Chem. Soc.*, 2006, **128**, 9024–9025.
122 Y. S. Li, H. Bux, A. Feldhoff, G. L. Li, W. S. Yang and J. Caro, *Adv. Mater.*, 2010, **22**, 3322–3326.
123 J. Sui, M.-L. Gao, B. Qian, C. Liu, Y. Pan, Z. Meng, D. Yuan and H. L. Jiang, *Sci. Bull.*, 2023, **68**(17), 112379.
124 N. S. Pappas and J. A. Mason, *Chem. Sci.*, 2023, **14**, 4647–4652.
125 I. Gruber, A. Nuhnen, A. Lerch, S. Nießing, M. Klopotowski, A. Herbst, M. Karg and C. Janiak, *Front. Chem.*, 2019, **7**, 777.
126 T. E. Webber, S. P. Desai, R. L. Combs, S. Bingham, C. C. Lu and R. L. Penn, *Cryst. Growth Des.*, 2020, **20**, 2965–2972.
127 T. E. Webber, W.-G. Liu, S. P. Desai, C. C. Lu, D. G. Truhlar and R. L. Penn, *ACS Appl. Mater. Interfaces*, 2017, **9**, 39342–39346.
128 W. Gong, H. Xie, K. B. Idrees, F. A. Son, Z. Chen, F. Sha, Y. Liu, Y. Cui and O. K. Farha, *J. Am. Chem. Soc.*, 2022, **144**, 1826–1834.
129 B. Moll, T. Müller, C. Schlüsener, A. Schmitz, P. Brandt, S. Öztürk and C. Janiak, *Mater. Adv.*, 2021, **2**, 804–812.
130 S. Hou, F. Liu, H. Xie, S. L. Hanna, K. B. Idrees, C. Zhang, X. Wang, Y. Chen, P. Li and O. K. Farha, *Inorg. Chem.*, 2023, **62**, 5479–5486.
131 A. Schaate, S. Dühnen, G. Platz, S. Lilienthal, A. M. Schneider and P. Behrens, *Eur. J. Inorg. Chem.*, 2012, 790–796.
132 J. Liu, N. Canfield and W. Liu, *Ind. Eng. Chem. Res.*, 2016, **55**, 3823–3832.
133 J. Ren, M. Ledwaba, N. M. Musyoka, H. W. Langmi, M. Mathe, S. Liao and W. Pang, *Coord. Chem. Rev.*, 2017, **349**, 169–197.

134 L. Zhou, X. Zhang and Y. Chen, *Mater. Lett.*, 2017, **197**, 167–170.
135 C. C. Epley, M. D. Love and A. J. Morris, *Inorg. Chem.*, 2017, **56**, 13777–13784.
136 F. Vermoortele, B. Bueken, G. Le Bars, B. Van de Voorde, M. Vandichel, K. Houthoofd, A. Vimont, M. Daturi, M. Waroquier and V. Van Speybroeck, *J. Am. Chem. Soc.*, 2013, **135**, 11465–11468.
137 H. Wu, Y. S. Chua, V. Krungleviciute, M. Tyagi, P. Chen, T. Yildirim and W. Zhou, *J. Am. Chem. Soc.*, 2013, **135**, 10525–10532.
138 V. V. Butova, A. P. Budnyk, A. A. Guda, K. A. Lomachenko, A. L. Bugaev, A. V. Soldatov, S. M. Chavan, S. Øien-Ødegaard, U. Olsbye and K. P. Lillerud, *Cryst. Growth Des.*, 2017, **17**, 5422–5431.
139 G. Kaur, S. Øien-Ødegaard, A. Lazzarini, S. M. Chavan, S. Bordiga, K. P. Lillerud and U. Olsbye, *Cryst. Growth Des.*, 2019, **19**, 4246–4251.
140 K. Müller, J. S. Malhi, J. Wohlgemuth, R. A. Fischer, C. Wöll, H. Gliemann and L. Heinke, *Dalton Trans.*, 2018, **47**, 16474–16479.
141 M. Kurmoo, *Chem. Soc. Rev.*, 2009, **38**, 1353–1379.
142 F. Bigdeli, S. Abedi, H. Hosseini-Monfared and A. Morsali, *Inorg. Chem. Commun.*, 2016, **72**, 122–127.
143 M. Y. Masoomi, K. C. Stylianou, A. Morsali, P. Retailleau and D. Maspoch, *Cryst. Growth Des.*, 2014, **14**, 2092–2096.
144 L. Aboutorabi, A. Morsali, E. Tahmasebi and O. Buyukgungor, *Inorg. Chem.*, 2016, **55**, 5507–5513.
145 S. Dissegna, R. Hardian, K. Epp, G. Kieslich, M.-V. Coulet, P. Llewellyn and R. A. Fischer, *CrystEngComm*, 2017, **19**, 4137–4141.
146 N. Prasetya and K. Li, *Sep. Purif. Technol.*, 2022, **301**, 122024.
147 T. Zhao, S. Li, Y.-X. Xiao, C. Janiak, G. Chang, G. Tian and X.-Y. Yang, *Sci. China Mater.*, 2021, **64**, 252–258.
148 J. Ren, N. M. Musyoka, H. W. Langmi, T. Segakweng, B. C. North, M. Mathe and X. Kang, *Int. J. Hydrogen Energy*, 2014, **39**, 12018–12023.
149 S.-Y. Kim, A.-R. Kim, J. W. Yoon, H.-J. Kim and Y.-S. Bae, *Chem. Eng. J.*, 2018, **335**, 94–100.
150 X. Gao, Y. Wang, G. Ji, R. Cui and Z. Liu, *CrystEngComm*, 2018, **20**, 1087–1093.
151 S. He, Y. Chen, Z. Zhang, B. Ni, W. He and X. Wang, *Chem. Sci.*, 2016, **7**, 7101–7105.
152 K. M. Choi, H. J. Jeon, J. K. Kang and O. M. Yaghi, *J. Am. Chem. Soc.*, 2011, **133**, 11920–11923.
153 R. J. Kuppler, D. J. Timmons, Q.-R. Fang, J.-R. Li, T. A. Makal, M. D. Young, D. Yuan, D. Zhao, W. Zhuang and H.-C. Zhou, *Coord. Chem. Rev.*, 2009, **253**, 3042–3066.
154 L. G. Qiu, T. Xu, Z. Q. Li, W. Wang, Y. Wu, X. Jiang, X. Y. Tian and L. D. Zhang, *Angew. Chem., Int. Ed.*, 2008, **47**, 9487–9491.
155 L. Peng, J. Zhang, J. Li, B. Han, Z. Xue and G. Yang, *Chem. Commun.*, 2012, **48**, 8688–8690.
156 Y. Li, D. Zhang, Y.-N. Guo, B. Guan, D. Tang, Y. Liu and Q. Huo, *Chem. Commun.*, 2011, **47**, 7809–7811.
157 D. Jiang, Y. Zhu, M. Chen, B. Huang, G. Zeng, D. Huang, B. Song, L. Qin, H. Wang and W. Wei, *Appl. Catal., B*, 2019, **255**, 117746.
158 H. G. T. Ly, G. Fu, F. de Azambuja, D. De Vos and T. N. Parac-Vogt, *ACS Appl. Nano Mater.*, 2020, **3**, 8931–8938.
159 Z. Sharifzadeh and A. Morsali, Multi-Modulator Incorporation in Metal-Organic Frameworks: an Efficient Approach for Water Purification and Promotion of Asymmetric Catalysis Reaction, 2023, submitted for publication.
160 T. M. Rayder, F. Formalik, S. M. Vornholt, H. Frank, S. Lee, M. Alzayer, Z. Chen, D. Sengupta, T. Islamoglu, F. Paesani, K. W. Chapman, R. Q. Snurr and O. K. Farha, *J. Am. Chem. Soc.*, 2023, **145**, 11195–11205.
161 R. Thür, N. Van Velthoven, V. Lemmens, M. Bastin, S. Smolders, D. De Vos and I. F. Vankelecom, *ACS Appl. Mater. Interfaces*, 2019, **11**, 44792–44801.
162 B. Slater, Z. Wang, S. Jiang, M. R. Hill and B. P. Ladewig, *J. Am. Chem. Soc.*, 2017, **139**, 18322–18327.
163 C. Zhang, X. Zhang, Z. Tao, B. Li, D. Zhao, H. Gao, Z. Zhu, G. Wang and X. Shu, *Chem. Eng. J.*, 2023, **455**, 140487.
164 M. J. Kalmutzki, C. S. Diercks and O. M. Yaghi, *Adv. Mater.*, 2018, **30**, 1704304.
165 H. Furukawa, F. Gandara, Y.-B. Zhang, J. Jiang, W. L. Queen, M. R. Hudson and O. M. Yaghi, *J. Am. Chem. Soc.*, 2014, **136**, 4369–4381.
166 H. W. B. Teo, A. Chakraborty and S. Kayal, *Microporous Mesoporous Mater.*, 2018, **272**, 109–116.
167 H.-Y. Zhang, R.-H. Shi, H.-L. Fan, C. Yang, C.-N. Zhang, Y.-S. Wang and Z. Tian, *Microporous Mesoporous Mater.*, 2020, **298**, 110070.
168 I. Walton, C. Chen, J. M. Rimsza, T. M. Nenoff and K. S. Walton, *Cryst. Growth Des.*, 2020, **20**, 6139–6146.
169 J. Maddock, X. C. Kang, L. F. Liu, B. X. Han, S. H. Yang and M. Schroder, *Chemistry*, 2021, **3**, 525–531.
170 E. Vunain, A. Mishra and B. Mamba, *Int. J. Biol. Macromol.*, 2016, **86**, 570–586.
171 S. M. Prabhu, S. Kancharla, C. M. Park and K. Sasaki, *CrystEngComm*, 2019, **21**, 2320–2332.
172 N. Assaad, G. Sabeh and M. Hmadeh, *ACS Appl. Nano Mater.*, 2020, **3**, 8997–9008.
173 J. Li, X. Wang, G. Zhao, Y. Ai, B. Han, T. We, T. Hayat, A. Alsaedi and X. Wang, *Chem. Eng. J.*, 2017, **330**, 1012–1021.
174 B. Liu, M. Tu and R. A. Fischer, *Angew. Chem.*, 2013, **125**, 3486–3489.
175 T. Li, Y. Bao, H. Qiu and W. Tong, *Anal. Chim. Acta*, 2021, **1152**, 338299.

3.3 Unlocking catalytic potential: a rhodium(II)-based coordination polymer for efficient carbene transfer reactions with donor/acceptor diazoalkanes

Diese Arbeit wurde veröffentlicht in

Claire Empel[+], Marcus N. A. Fetzer[+], Suman Sasmal, Till Strothmann, Christoph Janiak and Rene M. Koenigs, *Chemical Communications* **2024**, *60*, 7327-7330.

DOI: 10.1039/d4cc01386g; Ref.[96]

[+]Die Autoren haben zu gleichen Anteilen zu dieser Publikation beigetragen.

Kurzzusammenfassung

Hier berichten wir über die Verwendung eines molekular definierten Rhodium(II)-Koordinationspolymers (Rh-CP) als heterogener, recycelbarer Katalysator in Carben-Transferreaktionen. Wir zeigen die Anwendung dieses heterogenen Katalysators in einer Reihe von Carben-Transferreaktionen und schließen mit der Funktionalisierung von Naturstoffen und Wirkstoffmolekülen.

Anteile an der Publikation:

- Die Projektidee erfolgte durch Frau Dr. Claire Empel und Herrn Prof. Dr. Rene M. Koenigs.
- Die Synthese, Analytik wie REM, REM-EDX, DR-UV-Vis und Zersetzung-NMR sowie die Auswertung der IR-Messung und Charakterisierung des Katalysators erfolgte durch Marcus N. A. Fetzer.
- Till Strothmann führte die TGA-Messungen durch.
- Die katalytischen Untersuchungen des hergestellten Katalysators erfolgten durch Frau Dr. Claire Empel in Zusammenarbeit mit Suman Sasmal.
- Das Manuskript wurde in Zusammenarbeit mit Frau Dr. Claire Empel geschrieben.
- Die Überarbeitung und Korrektur erfolgte durch Herrn Prof. Dr. Rene M. Koenigs und Herrn Prof. Dr. Christoph Janiak.

ChemComm

ROYAL SOCIETY OF CHEMISTRY

COMMUNICATION

View Article Online
View Journal | View Issue

Cite this: *Chem. Commun.*, 2024, 60, 7327

Received 26th March 2024,
Accepted 15th June 2024

DOI: 10.1039/d4cc01386g

rsc.li/chemcomm

Unlocking catalytic potential: a rhodium(II)-based coordination polymer for efficient carbene transfer reactions with donor/acceptor diazoalkanes†

Claire Empel, ‡[a] Marcus N. A. Fetzer,‡[b] Suman Sasmal,[a] Till Strothmann, [b] Christoph Janiak [b] and Rene M. Koenigs *[a]

Herein, we report the use of a molecular-defined rhodium(II) coordination polymer (Rh-CP) as a heterogeneous, recyclable catalyst in carbene transfer reactions. We showcase the application of this heterogeneous catalyst in a range of carbene transfer reactions and conclude with the functionalization of natural products and drug molecules.

Rhodium(II) carboxylate paddlewheel complexes feature two rhodium centers, a rhodium–rhodium single bond and four bridging carboxylate ligands. They represent a privileged class of catalysts, primarily due to each rhodium center having a free coordination site, central for facilitating for example carbene or nitrene transfer reactions (Scheme 1A).[1–4] While the development of homogeneous rhodium paddlewheel catalysts has received significant attention,[3,4] the use of their heterogeneous counterparts has been much less explored.[5–8] Previous efforts primarily focused on the immobilization of homogeneous catalysts on a surface or polymer.[5] The catalytic activity of this material, however, is achieved through a single-molecule catalyst grafted onto the heterogeneous support (Scheme 1B). Studies on the application of heterogeneous rhodium-based carbene transfer catalysts, where the catalytically active site is an integral part of the heterogeneous material, however, received only little attention (Scheme 1C).[6–8] Studies on such heterogeneous catalysts are in high demand as these would allow facile catalyst recovery from the reaction mixture and may result in enhanced catalyst lifetime, which—given the low abundancy and high price of rhodium—would have a significant impact on the environmental footprint of rhodium-catalyzed reactions.[4]

Building on our interest in metal-catalyzed carbene transfer reactions using,[9] we considered that a Rh(II)-based coordination polymer (Rh-CP) could serve as a viable starting point to access a heterogeneous, molecular-defined rhodium catalyst with a repetitive paddlewheel structure (Scheme 1D). Such Rh-CP would differentiate from other approaches, where molecular-defined rhodium catalysts are heterogenized by immobilization to surfaces.[5] We got intrigued by a previous report by Buntkowsky and co-workers, who described a straightforward synthesis of such a Rh(II)-based coordination polymer by a ligand exchange reaction of $Rh_2(OAc)_4$ (Scheme 1C).[6] A related report by Furukawa *et al.* reports on the formation of octahedral clusters using benzene-1,3-dicarboxylic acid.[7] Very much to our surprise, only limited applications in catalysis were described, which focus on the reaction of ethyl diazoacetate.[6]

We commenced our studies by performing a ligand exchange reaction between $Rh_2(OAc)_4$ and terephthalic acid (H_2BDC) to obtain the Rh-CP as a green powder in excellent yield (Fig. 1A, 97%). The Rh-CP was authenticated to the literature[6] by PXRD analysis (see Fig. S1, ESI†), TGA analysis (Fig. S2 and S3, ESI†) ATR-IR (Fig. S4, ESI†), and diffuse reflectance spectra (Fig. 1B). Importantly, diffuse reflectance spectra in an Ulbricht sphere (Fig. 1B) indicate the persistence of the paddlewheel structure within the Rh-CP. This structural motif is crucial for the catalytic properties.[10]

^{1}H NMR measurements were carried out to determine the degree of ligand exchange. For this purpose, Rh-CP was digested in a mixture of DMSO-d_6 and D_2SO_4, whereby the integrals of the BDC linker and acetate gave a ratio of about 82 to 3 corresponding to a molar BDC : OAc ratio of 20 : 1 (Fig. S7 and S8, ESI†). Scanning electron microscopy (SEM) shows our Rh-CP as comparatively small agglomerates, which are characterized by a lamellar morphology at higher magnification (Fig. S5 and S6, ESI†). EDX elemental mapping indicates a homogeneous dispersion of rhodium throughout the synthesized Rh-CP, confirming a consistent elemental distribution within the compound (Fig. 1C).

[a] *Institute of Organic Chemistry, RWTH Aachen University, Landoltweg 1, 52074 Aachen, Germany. E-mail: rene.koenigs@rwth-aachen.de*
[b] *Institut für Anorganische Chemie und Strukturchemie, Heinrich-Heine-Universität Düsseldorf, Universitätsstraße 1, 40225 Düsseldorf, Germany*

† Electronic supplementary information (ESI) available. See DOI: https://doi.org/10.1039/d4cc01386g

‡ These authors contributed equally to this work.

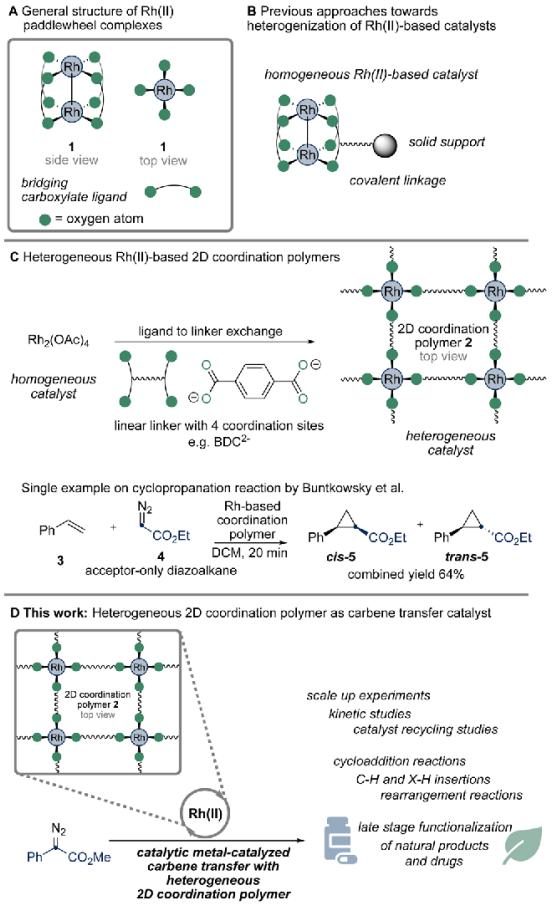

Scheme 1 Rh(II) paddlewheel complexes and Rh(II)-CP in carbene transfer reactions.

To evaluate the catalytic efficiency and stability in catalysis of the Rh-CP and to probe differences to homogeneous, achiral rhodium(II) catalysts, we investigated the model reaction of donor/acceptor diazoalkane **6** with styrene **3** to give cyclopropane **7** (Scheme 3). In a first step, we performed the reaction on 10 mmol scale of diazoalkane **6** (1.9 g) employing 0.5 mg Rh-CP (23.1% Rh-content) to evaluate stability and activity of Rh-CP. Complete consumption of the diazoalkane was observed and the desired cyclopropane was isolated in 92% yield (2.31 g) in high diastereoselectivity. The diastereoselectivity was comparable to achiral, homogeneous Rh(II) catalysts, which is suggestive that the coordination polymer backbone has little influence on the geometry of transition state in this cyclopropanation reaction. A further reduction of the Rh-CP catalyst loading to 0.236 mg gave the desired cyclopropane **7** in slightly reduced yield of 91% (2.29 g).

Recycling studies further showed that the first five cycles gave a relatively constant yield of >86% of cyclopropane **7**, while the amount of recovered Rh-CP constantly decreased to 60%. This reduction might be attributed to mechanical forces

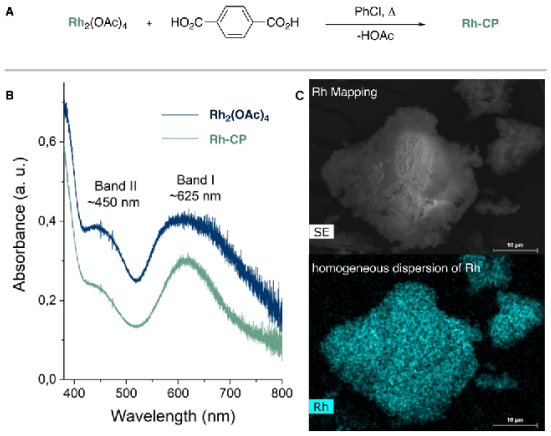

Fig. 1 (A) Synthesis of Rh-CP. (B) Optical Kubelka–Munk spectra of $Rh_2(OAc)_4$ and Rh-CP obtained from diffuse reflectance spectra. (C) EDX Rh mapping of Rh-CP.

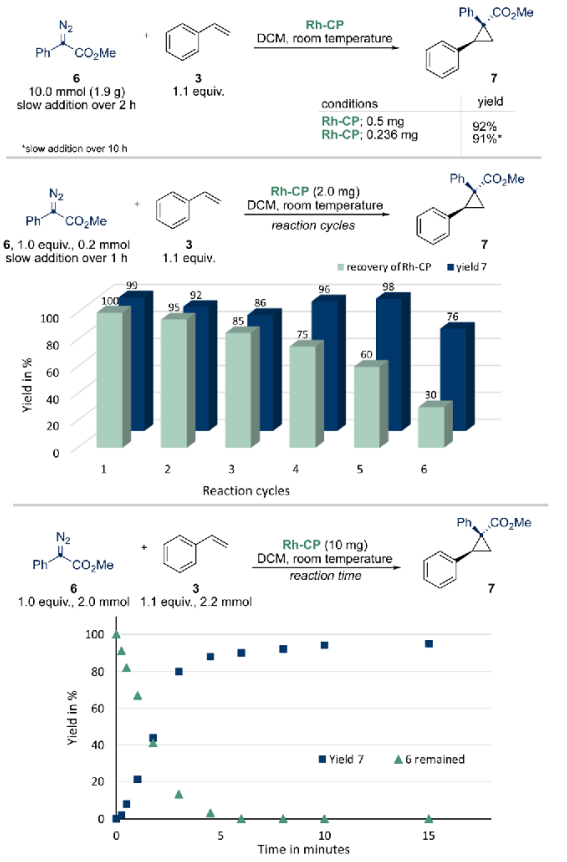

Scheme 2 Studies on Rh-CP catalyzed cyclopropanation of styrene.

on the Rh-CP catalyst during stirring the reaction mixture that results reduction of particle sizes and reduced catalyst recovery.

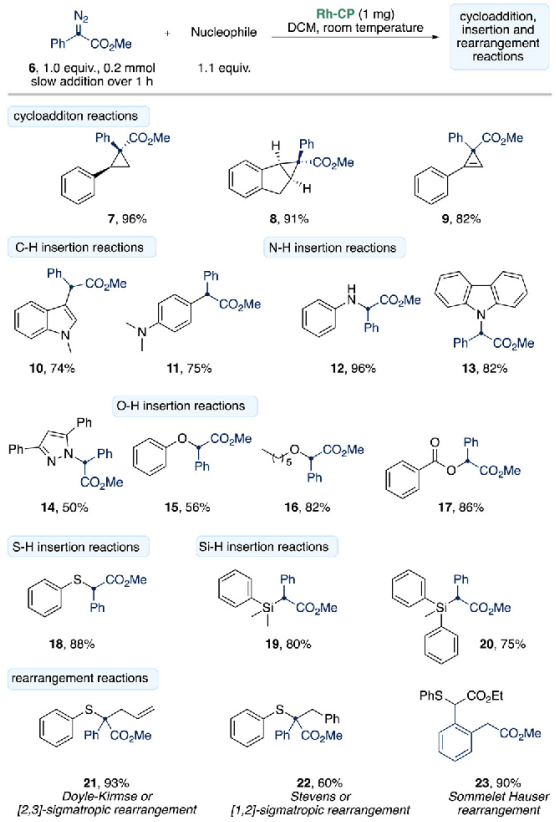

Scheme 3 Scope of different nucleophiles in Rh-CP catalyzed reactions.

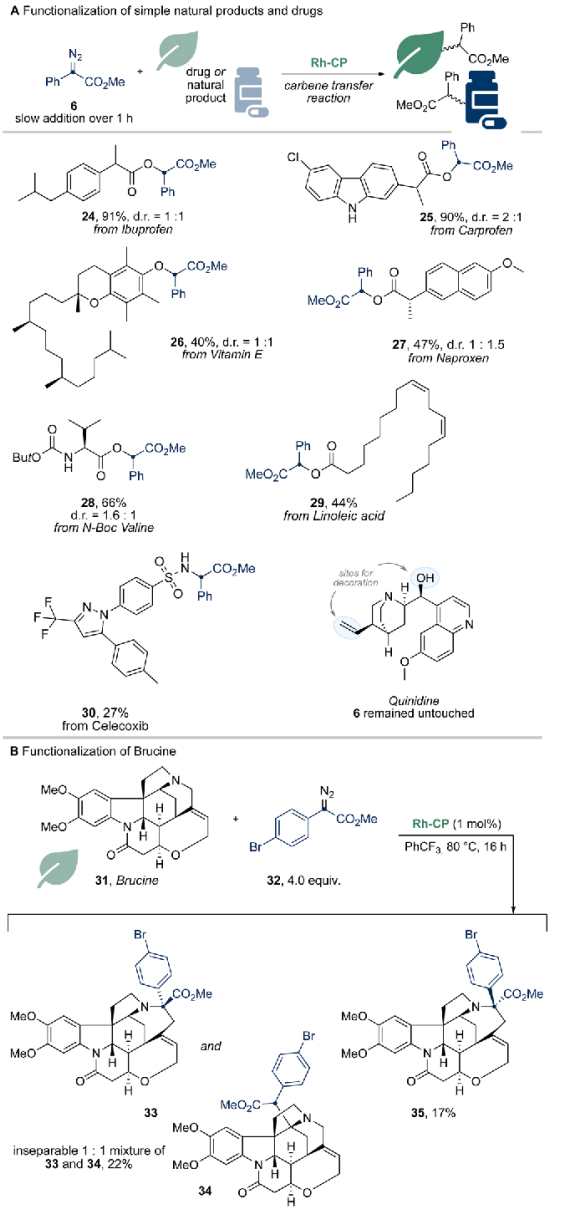

Scheme 4 Scope of natural products and drugs in Rh-CP catalyzed carbene transfer reactions.

The increase of product yield in the fourth and fifth catalytic cycle might result from this particle size reduction that would also result in an increased catalytically active surface of the heterogeneous catalyst. Notably, the amount of recovered Rh-CP significantly decreased after the fifth cycle (30%) resulting in a reduced yield of 76% of the desired cyclopropane. After the sixth cycle only traces of Rh-CP were recovered, and no further reactions were performed.[11] Kinetic studies of the Rh-CP were investigated next. Using 10 mg of Rh-CP a rapid and linear consumption of diazoalkane **6** was observed. The reaction rate only slowed down after a consumption of >90% of diazoalkane **6** (Scheme 2 and Table S1, ESI†).

In a next step, we investigated the applicability of the Rh-CP in the reaction of donor/acceptor diazoalkane **6** in carbene transfer reactions (Scheme 3). Only a minor excess of the corresponding nucleophile was used to emphasize the high efficiency of the Rh-CP. To our delight, the Rh-CP is compatible with a broad range of different substrates and performs excellent in cyclopropa(e)nation reactions (**7**–**9**). *N*-Methyl indole gave the product of C3-functionalization **10** in 74% yield and *N*,*N*-dimethyl aniline reacted smoothly in *para*-C–H functionalization to give **11** 75% yield.

X–H reactions (X = N, O, S, Si) gave the desired reaction products (**12**–**20**) in up to 96%. Yet, a longer reaction time of up to 24 h was required to achieve the full conversion of diazoalkane **6**. This observation could be explained by a potential catalyst poisoning as the desorption of products or reagents might be energetically disfavored. We further examined rearrangement reactions of sulfur ylides and were able to isolate the products of Doyle–Kirmse (**21**), Stevens rearrangement (**22**) and Sommelet–Hauser (**23**) rearrangement reactions in up to 93% yield (Scheme 3).

To further underline the applicability of Rh-CP, we studied more complex natural products and drugs in the reaction with donor/acceptor diazoalkanes (Scheme 4). Simple drug molecules such as Ibuprofen, Naproxen or Carprofen gave the desired O–H functionalization products (**24**, **25**, **27**) in high yield. Notably, only the O–H functionalization product of Carprofen was observed, while the free N–H function remained untouched.

We further explored natural products; vitamin E reacted in an O–H functionalization reaction to give the desired O–H functionalization product **26** in moderate yield. Derivatives of amino acids (**28**) and celecoxib (**30**) underwent X–H functionalization with Rh-CP catalyst. Quinidine, however, remained unreactive and no reaction was observed with the diazoalkane **6** staying untouched, which is indicative of catalyst poisoning (Scheme 4A).

In a last step, we studied the functionalization of brucine **31** in Rh-CP catalyzed reaction with diazoalkane **32**. Under similar reaction conditions as reported by Beckwith and co-workers,[12] we were able to obtain three different reaction products (**33**–**35**) in a total yield of 39% using 4 equivalents of diazoalkane **32** (Scheme 4B).[13]

In summary, we described here the application of a Rh(II)-based coordination polymer as a heterogeneous catalyst in carbene transfer reactions. Based on the IR and UV-Vis data, we were able to prove that the paddlewheel structure of the $Rh_2(OAc)_4$ precursor is also present in the synthesized Rh-based coordination polymer. Moreover, detailed studies on catalyst recycling and catalyst efficiency were performed. We were able to demonstrate the broad applicability ranging from X–H and C–H functionalization reactions towards rearrangement reactions and the functionalization of natural products and drugs.

R. M. K. thanks the Deutsche Forschungsgemeinschaft (DFG, for grant KO5659/2-1), C. J. for grant Ja466/43-1 within SPP 1928/2 COORNETs). C. E. thanks RWTH Aachen University for a Doctoral Scholarship. We thank Jun.-Prof. Dr Markus Suta for carrying out optical measurements.

Data availability

The data supporting this article have been included as part of the ESI.†

Conflicts of interest

There are no conflicts to declare.

Notes and references

1 (*a*) R. Hrdina, *Eur. J. Inorg. Chem.*, 2021, 501; (*b*) X. Tang, H. Noda and M. Shibasaki, *Angew. Chem., Int. Ed.*, 2023, **62**, e202311027; (*c*) A. Mang, M. Linseis and R. F. Winter, *Z. Anorg. Allg. Chem.*, 2022, **648**, e20220019.

2 Selected review articles: (*a*) A. Ford, H. Miel, A. Ring, C. N. Slattery, A. R. Maguire and M. A. McKervey, *Chem. Rev.*, 2015, **115**, 9981; (*b*) H. U. Reissig and R. Zimmer, *Chem. Rev.*, 2003, **103**, 1151; (*c*) H. M. L. Davies and J. R. Manning, *Nature*, 2018, **451**, 417; (*d*) M. P. Doyle, R. Duffy, M. Ratnikov and Z. Zhou, *Chem. Rev.*, 2010, **110**, 704; (*e*) Y. Xia, D. Qiu and J. Wang, *J. Chem. Rev.*, 2017, **117**, 13810; (*f*) H. M. L. Davies and J. R. Denton, *Chem. Soc. Rev.*, 2009, **38**, 3061; (*g*) J. Hansen and H. M. L. Davies, *Coord. Chem. Rev.*, 2008, **252**, 545; (*h*) R. Wu, D. Zhu and S. Zhu, *Org. Chem. Front.*, 2023, **10**, 2849; (*i*) Y. Luo, X. Zhang and Y. Xia, *Chin. Chem. Lett.*, 2024, **35**, 108778; (*j*) L. Mertens and R. M. Koenigs, *Org. Biomol. Chem.*, 2016, **14**, 10547; (*k*) Y. Xia, D. Qiu and J. Wang, *Chem. Rev.*, 2017, **117**, 13810; (*l*) M. Akter, K. Rupa and P. Anbarasan, *Chem. Rev.*, 2020, **122**, 13108.

3 Selected articles: (*a*) H. M. L. Davies and T. Hansen, *J. Am. Chem. Soc.*, 1997, **119**, 9075; (*b*) R. P. Reddy and H. M. L. Davies, *Org. Lett.*, 2006, **8**, 5013; (*c*) F. Xiao and J. Wang, *J. Org. Chem.*, 2006, **71**, 5789; (*d*) H. Wang, D. Guptill, A. Varela-Alveraz, D. G. Musaev and H. M. L. Davies, *Chem. Sci.*, 2013, **4**, 2844; (*e*) W. Liu, Z. Ren, A. T. Bosse, K. Liao, E. L. Goldstein, J. Basca, D. H. Musaev, B. M. Stoltz and H. M. L. Davies, *J. Am. Chem. Soc.*, 2018, **140**, 12247.

4 Selected examples: (*a*) F. P. Caló, A. Zimmer, G. Bistoni and A. Fürstner, *J. Am. Chem. Soc.*, 2022, **144**, 7465; (*b*) T. A. C. A. Bayrakda and C. Lescot, *ChemSusChem*, 2023, **16**, e202300596; (*c*) K. Makino, Y. Kumagai, T. Yoshino, M. Kojima and S. Masunaga, *Org. Lett.*, 2023, **25**, 3234; (*d*) J. E. Spangler and H. M. L. Davies, *J. Am. Chem. Soc.*, 2013, **135**, 6802; (*e*) M. Lee, G. D. Musaev and H. M. L. Davies, *ACS Catal.*, 2020, **10**, 6240; (*f*) Z. Zhang, Z. Sheng, W. Yu, G. Wu, R. Zhang, W.-D. Chu, Y. Zhang and J. Wang, *Nat. Chem.*, 2017, **9**, 970; (*g*) Z. Gao, D. Jiang, B. Li and B. Wang, *Chem. Commun.*, 2022, **58**, 1017.

5 Selected examples: (*a*) H. M. L. Davies and A. M. Walji, *Org. Lett.*, 2003, **5**, 479; (*b*) H. M. L. Davies and A. M. Walji, *Org. Lett.*, 2003, 7, 2941; (*c*) C.-J. Yoo, D. Rackl, W. Liu, C. B. Hoyt, B. Pimentel, R. P. Lively, H. M. L. Davies and C. Jones, *Angew. Chem., Int. Ed.*, 2018, **57**, 10923; (*d*) T. A. Hatridge, W. Liu, C.-J. Yoo, H. M. L. Davies and C. Jones, *Angew. Chem., Int. Ed.*, 2020, **59**, 19525; (*e*) K. T. T. Oohar, M. Anada, H. Nambu and S. A. Hashimoto, *Angew. Chem., Int. Ed.*, 2010, **49**, 6979; (*f*) Z. Li, H. Jiang, M. Zhu and F. Zhang, *ACS Appl. Mater. Interfaces*, 2024, **16**, 19003; (*g*) Z. Li, L. Rösler, H. Breitzke, T. Gutmann and G. Buntkowsky, *J. CO2 Util.*, 2021, **52**, 101682.

6 L. Liu, C. Fasel, P. Braga-Groszewicz, N. Rothermel, A. S. L. Thankamony, G. Sauer, Y. Xu, T. Gutmann and G. Buntkowsky, *Catal. Sci. Technol.*, 2016, **6**, 7830.

7 S. Furukawa, N. Horike, M. Kondo, Y. Hijikata, A. Carné-Sánchez, P. Larpent, N. Louvain, S. Diring, H. Sato, R. Matsuda, R. Kawano and S. Kitagawa, *Inorg. Chem.*, 2016, **55**, 10843.

8 G. Nickerl, U. Stoeck, U. Burkhardt, I. Senkovska and S. A. Kaskel, *J. Mater. Chem. A*, 2014, **2**, 144.

9 Selected examples: (*a*) F. Li, C. Pei and R. M. Koenigs, *Chem. Sci.*, 2021, **12**, 6362; (*b*) S. Jana, C. Empel, C. Pei, P. Aseeva, T. V. Nguyen and R. M. Koenigs, *ACS Catal.*, 2020, **362**, 5721; (*c*) K. J. Hock, A. Knorrscheidt, R. Hommelsheim, J. Ho, M. J. Weissenborn and R. M. Koenigs, *Angew. Chem., Int. Ed.*, 2019, **58**, 3630; (*d*) U. P. N. Tran, R. Hommelsheim, Z. Yang, C. Empel, K. J. Hock, T. V. Nguyen and R. M. Koenigs, *Chem. – Eur. J.*, 2020, **26**, 1254; (*e*) Z. Yang, M. Möller and R. M. Koenigs, *Angew. Chem., Int. Ed.*, 2020, **59**, 5572; (*f*) C. Empel, S. Jana, T. Langletz and R. M. Koenigs, *Chem. – Eur. J.*, 2022, **28**, e202104321; (*g*) C. Empel, S. Jana and R. M. Koenigs, *Molecules*, 2020, **25**, 880; (*h*) C. Empel, K. J. Hock and R. M. Koenigs, *Org. Biomol. Chem.*, 2018, **16**, 7129–7133.

10 (*a*) R. L. Firor and K. Seff, *J. Am. Chem. Soc.*, 1978, **100**, 978; (*b*) D. S. Martin, T. R. Webb, G. A. Robbins and P. E. Fanwick, *Inorg. Chem.*, 1979, **18**, 475; (*c*) J. Kitchens and L. J. Bear, *J. Inorg. Nucl. Chem.*, 1969, **31**, 2415.

11 The recycling may proof difficult due to the small reaction scale and an improved recovery of Rh-CP could be possible on a larger reaction scale.

12 J. He, L. G. Hamann, H. M. L. Davies and E. E. Beckwith, *Nat. Commun.*, 2015, **6**, 5943.

13 Structural assignment of **33**–**35** according to ref. 11.

Electronic Supplementary Material (ESI) for ChemComm.

Supporting Information

Unlocking catalytic potential: a rhodium(II)-based coordination polymer for efficient carbene transfer reactions with donor/acceptor diazoalkanes

Claire Empel,[a#] Marcus N. A. Fetzer,[b#] Suman Sasmal,[a] Till Strothmann,[b] Christoph Janiak[b] and Rene M. Koenigs[a*]

[a]Institute of Organic Chemistry, RWTH Aachen University, Landoltweg 1, 52074 Aachen, Germany.
[b]Institut für Anorganische Chemie und Strukturchemie, Heinrich-Heine-Universität Düsseldorf, Universitätsstr.1, 40225 Düsseldorf, Germany.
[#]denotes equal contribution

*rene.koenigs@rwth-aachen.de

Table of Contents

1. General Information

Unless otherwise noted, all commercially available compounds were used as provided without further purification. Chemicals used in this manuscript were purchased from Sigma Aldrich, Alfa Aesar, Chempur, Fluorochem, Activate Scientific and Carl Roth. Solvents used in reactions were p.A. grade. Solvents for chromatography were technical grade and distilled prior to use. Analytical thin-layer chromatography (TLC) was performed on Macherey-Nagel silica gel aluminium plates with F-254 indicator, visualized by irradiation with UV light. Column chromatography was performed using silica gel Merck 60 (particle size 0.063 – 0.2 mm). Solvent mixtures are understood as volume/volume. ^{1}H-NMR, ^{19}F-NMR and ^{13}C-NMR were recorded on a Varian AV600/AV400, an Agilent DD2 400 or a Bruker Avance III 300 MHz NMR spectrometer in $CDCl_3$ or DMSO-d_6 + D_2SO_4. Data are reported in the following order: chemical shift (δ) in ppm; multiplicities are indicated brs (broadened singlet), s (singlet), d (doublet), t (triplet), q (quartet), m (multiplet); coupling constants (J) are in Hertz (Hz). HRMS data were recorded on a ThermoFisher Scientific LTQ Orbitrap XL using ESI ionization or on a Finnigan MAT 95 using EI ionization at 70 eV. IR spectra were recorded on a Perkin Elmer-100 spectrometer and are reported in terms of frequency of absorption (cm^{-1}).
Powder X-ray diffraction (PXRD) analysis was conducted at ambient temperature on a Rigaku Miniflex 600 powder diffractometer (Rigaku, Tokyo, Japan) using Cu Kα1 radiation with λ = 1.5406 Å (40 kV, 15 mA, 600 W) and a flat silicon low background with a small indent in the range of 2 θ = 2 °–50 °. Scanning electron microscopy (SEM) images and energy dispersive X-ray (EDX) analysis were recorded on a Jeol JSM-6510LV QSEM electron microscope equipped with a LaB_6 filament and a Bruker XFlash 410-M EDX detector at an acceleration voltage of 20 kV. Prior to the measurement, samples were coated with gold using a Jeol JFC 1200 sputter coater. Fourier-transform infrared (FT-IR) spectra were recorded on a Bruker FT-IR Tensor 37 spectrometer in the attenuated total reflection (ATR) mode in the range of 4000–550 cm^{-1}. Thermogravimetric analyses (TGA) were performed on a Netzsch Tarsus TG 209 under synthetic air (20.5 ± 0.5% O_2 in N_2) from room temperature to 1000 °C with a heating rate of 5 °C min^{-1} in Al_2O_3-crucibles. Optical measurements were carried out on a FLS1000 photoluminescence spectrometer (Edinburgh Instruments) equipped with a 450 W Xe arc lamp, double grating monochromators (Czerny-Turner) in excitation and emission compartment and a thermoelectrically cooled PMT-980 detector (Hamamatsu). The diffuse reflectance was measured with an integrating sphere (Ulbricht sphere) lined on the inside with BenFlect and exhibiting R > 99% between 350 nm and 2500 nm.

2. Important Safety Note

Handling of diazo compounds should only be done in a well-ventilated fume cupboard using an additional blast shield. No incidents occurred handling of diazoalkanes during the preparation of this manuscript, yet the reader should be aware of carcinogenicity and explosiveness of the herein described diazo compounds. General safety precautions when working with diazomethane and its derivatives should be followed. Any reactions described in this manuscript should not be performed without strict risk assessment and proper safety precautions.

3. Catalyst Synthesis

Synthesis of $Rh_2(OAc)_4$[1]

The amount of 500 mg (1.06 mmol) of rhodium trichloride hydrate and 1 g (7.35 mmol) of sodium acetate trihydrate in a 1 : 1 mixture of glacial acetic acid and absolute ethanol (20 mL) were refluxed under nitrogen atmosphere for one hour to form a green solid. After cooling to room temperature, the green solid was collected by filtration and dissolved in boiling methanol (ca. 50 mL). The solution was filtered, concentrated to 20 mL and placed in a refrigerator overnight. The crystals formed were filtered off and dried in vacuum at 60 °C for 20 h to obtain 188 mg (71%) of green crystals.

Synthesis of Rh-CP[2]

In a 250 mL round bottom flask, $Rh_2(OAc)_4$ (150 mg, 0.34 mmol) and terephthalic acid (173 mg, 1.04 mmol) were dissolved in 150 mL of chlorobenzene. The flask was connected with a Soxhlet extractor. To remove the acetic acid, a cellulose filter tube with 3 g K_2CO_3 and 3 g activated molecular sieve (4 Å) was added to the Soxhlet extractor. The reaction was heated to 150 °C and extracted for 3 days. After 3 days of reaction, the obtained solid was filtered and washed for 5 days in a Soxhlet extractor with 100 mL of chlorobenzene. The product was dried at 80 °C under vacuum for 1 day. The product is a green powder. Yield 178 mg, 97% based on $Rh_2(OAc)_4$.

4. Powder XRD

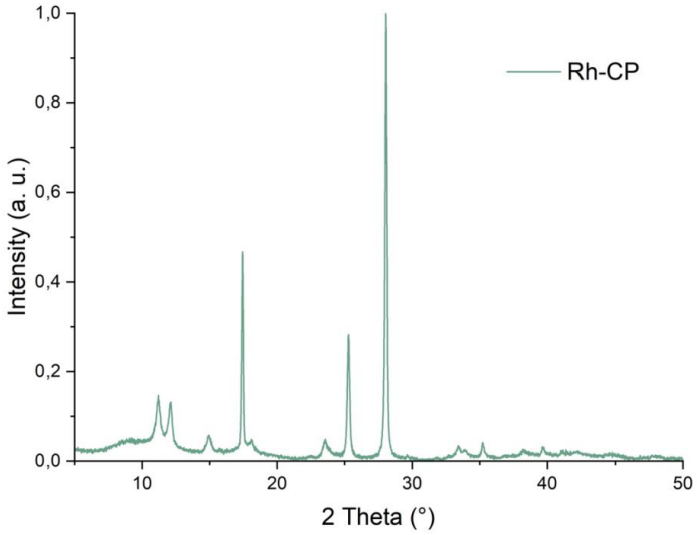

Fig. S1: PXRD of $Rh_2(OAc)_4$.

5. TGA Analysis

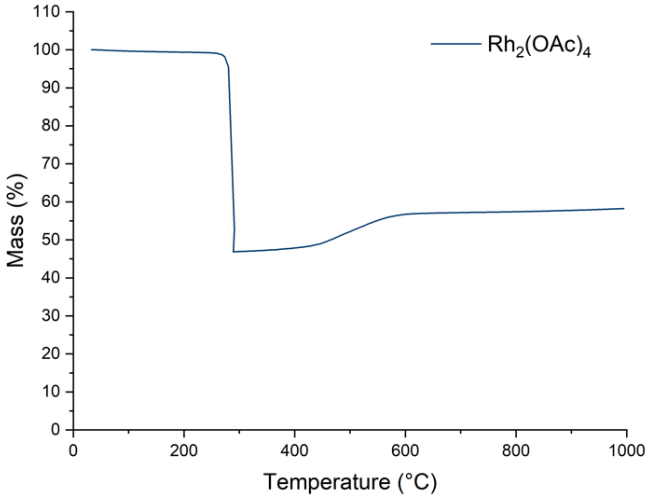

Fig. S2: TGA of $Rh_2(OAc)_4$ in the range of 20 to 1000 °C with a heating rate of 5 K min^{-1}.

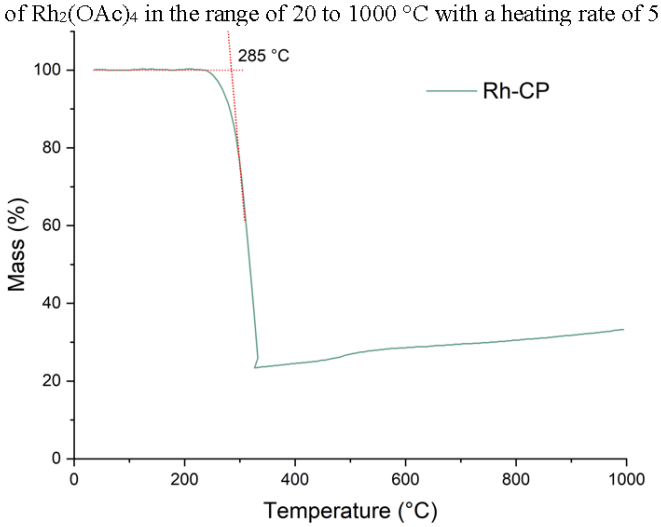

Fig. S3: TGA of Rh-CP in the range of 20 to 1000 °C with a heating rate of 5 K min^{-1}.

6. ATR-IR

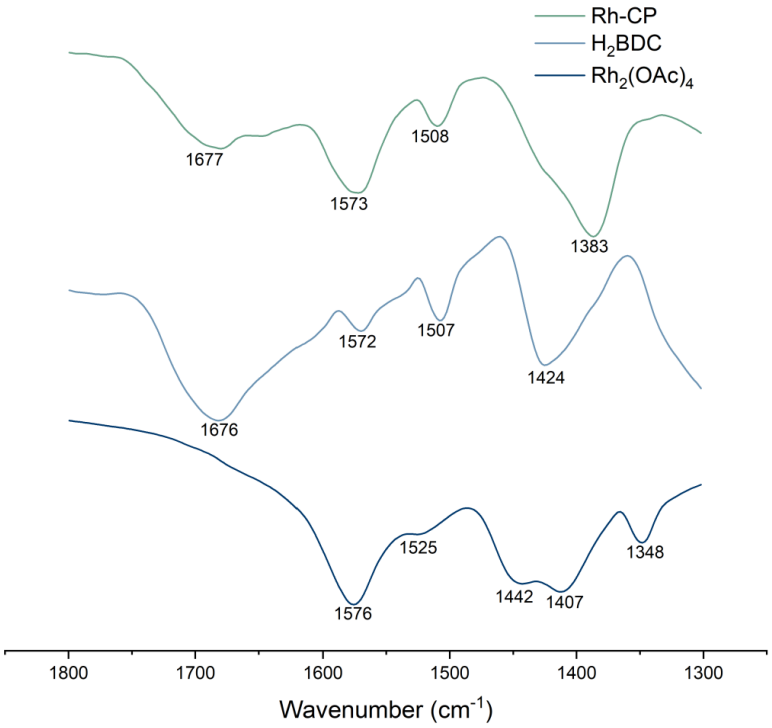

Fig. S4: ATR-IR of the synthesized Rh-CP, the pure linker H_2BDC, and the starting complex $Rh_2(OAc)_4$.

7. SEM

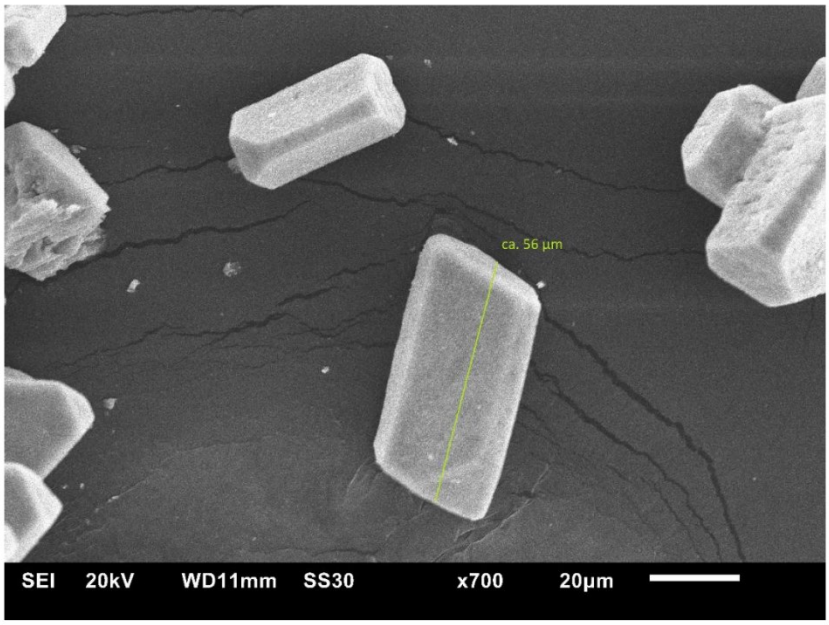

Fig. S5: SEM image of $Rh_2(OAc)_4$ crystal.

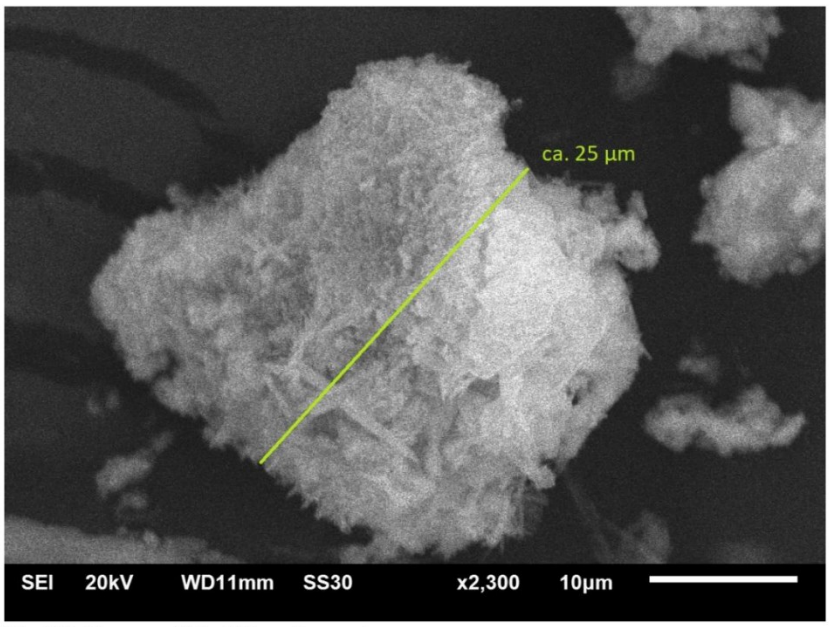

Fig. S6: SEM image of Rh-CP agglomerate.

8. Digestion NMR

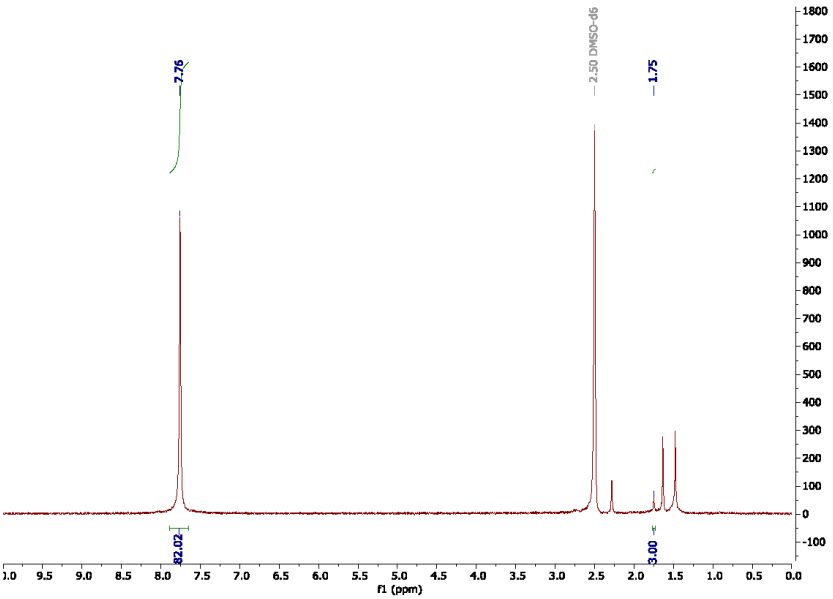

Fig. S7: ^{1}H NMR (300 MHz) of digested Rh-CP in DMSO-d_6 and D_2SO_4 to determine the linker, acetate ratio.

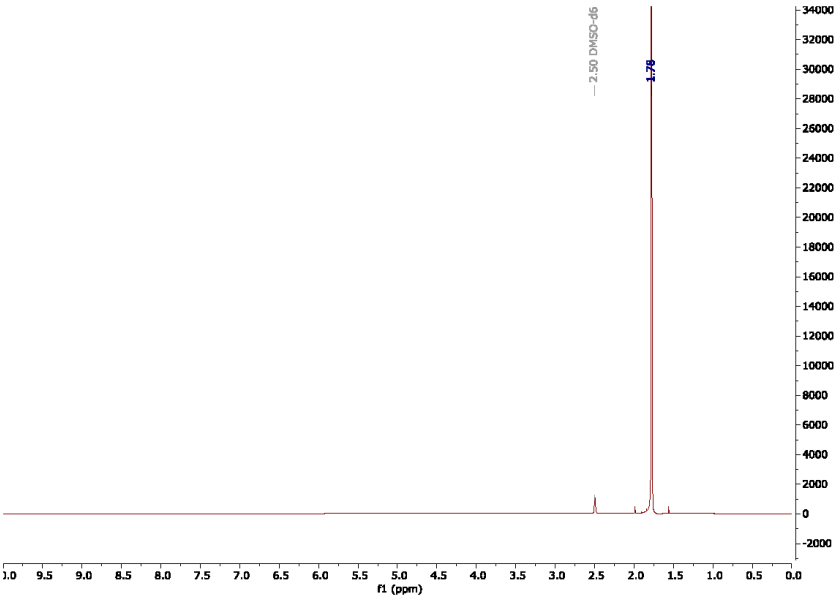

Fig. S8: ^{1}H NMR (300 MHz) of acetic acid as reference for determining the acetic acid chemical shift in DMSO-d_6 and D_2SO_4.

9. Scale Up Experiments

In an oven dried reaction flask Rh-CP or $Rh_2(OAc)_4$ was added. Then the flask was closed with septum and evacuated and backfilled with argon for three times. Then styrene (1.1 equiv., 11.0 mmol) and 10 mL dry, degassed DCM were added. The corresponding diazoalkane **6** (1.0 equiv., 10.0 mmol) was dissolved in a separate reaction test tube in 10 mL of dry and degassed DCM was added to the reaction tube via syringe over 2 h (or 10 h). After the completion of the addition of the diazoalkane, the reaction mixture was stirred until the orange color of the diazoalkane disappeared. The product **7** was purified by column chromatography on silica gel (*n*-hexane : ethyl acetate) to afford the desired pure product.

Rh-CP (0.5 mg)	92%	2.31 g	9.16 mmol
Rh-CP (0.236 mg)	91%	2.29 g	9.08 mmol
$Rh_2(OAc)_4$ (0.25 mg)	94%	2.43 g	9.63 mmol

10. Kinetic Studies

In an oven dried reaction flask Rh-CP (10.0 mg) was added. Then the flask was closed with septum and evacuated and backfilled with argon for three times. Then styrene (1.1 equiv., 2.2 mmol) and 10 mL dry, degassed DCM were added. The corresponding diazoalkane **6** (1.0 equiv., 2.0 mmol) was dissolved in a separate reaction test tube in 10 mL of dry and degassed DCM was added to the reaction tube via syringe in one portion. Then aliquots (0.5 mL each) were taken and quickly filtered through a pluck of silica to remove the Rh-CP. The solvent was removed under reduced pressure and the yield of **7** was determined by ^{1}H NMR spectroscopy using mesitylene as the internal standard. **6** indicates the remaining diazoalkane in the solution.

Table S1: Kinetic studies.

time	0	15 s	30 s	60 s	105 s	180 s	270 s	360 s	480 s	600 s	900s
Yield **7** [%]	0	2	8	21	44	80	88	90	92	94	95
6 [%]	100	91	82	67	41	13	0	0	0	0	0

11. Catalyst Recycling Studies

In an oven dried reaction tube Rh-CP (2.0 mg) was added. Then the tube was closed with septum and evacuated and backfilled with argon for three times. Then styrene (1.1 equiv., 0.22 mmol) and 1 mL dry, degassed DCM were added. The corresponding diazoalkane (1.0 equiv., 0.2 mmol) was dissolved in a separate reaction test tube in 1 mL of dry and degassed DCM was added to the reaction tube via syringe over 1 h. After the completion of the addition of the diazoalkane, the reaction mixture was stirred until the orange color of the diazoalkane disappeared. The catalyst was removed by centrifuge and the clear solution on top of the catalyst was transferred into a reaction flask. The solvent was removed under reduced pressure and the yield was determined by ^{1}H NMR spectroscopy using mesitylene as the internal standard. The remaining catalyst was transferred into a new reaction tube and weight after complete removal of solvent. Then the recycled catalyst was used in the next reaction step.

Table S2: Catalyst recycling studies.

Cycle	1	2	3	4	5	6
Yield 7 [%]	99	92	86	96	98	76
Recovered catalyst [mg]	2.0	1.9	1.7	1.5	1.2	0.6

12. General Procedure (GP-1) Rh-CP catalyzed reactions

In an oven dried reaction tube Rh-CP (1 mg) and the corresponding nucleophile (1.1 equiv., 0.22 mmol, if solid) were added. Then the tube was closed with septum and evacuated and backfilled with argon for three times. Then the corresponding nucleophile (1.1 equiv., 0.22 mmol, if liquid) and 1 mL dry, degassed DCM were added. The corresponding diazoalkane (1.0 equiv., 0.2 mmol) was dissolved in a separate reaction test tube in 1 mL of dry and degassed DCM was added to the reaction tube via syringe over 1 h. After the completion of the addition of the diazoalkane, the reaction mixture was stirred until the orange color of the diazoalkane disappeared. The product was purified by column chromatography on silica gel (*n*-hexane : ethyl acetate) to afford the desired pure product.

13. Physical Data

Methyl-1,2-diphenylcyclopropane-1-carboxylate (7)

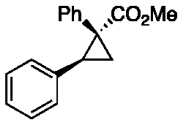

The title compound **7** was synthesized according to the general procedure (GP-1), and was obtained after silica column chromatography (*n*-hexane : ethyl acetate 20:1 → 10:1) as a colorless solid (96%, 40.5 mg).

^{1}H NMR (600 MHz, Chloroform-*d*): δ = 7.21 – 7.08 (m, 3H), 7.08 – 7.00 (m, 5H), 6.81 – 6.72 (m, 2H), 3.67 (s, 3H), 3.18 – 3.05 (m, 1H), 2.14 (ddd, *J* = 9.3, 4.9, 0.7 Hz, 1H), 1.93 – 1.83 (m, 1H) ppm.

^{13}C NMR (151 MHz, Chloroform-*d*): δ = 174.3, 136.3, 134.7, 131.9, 128.0, 127.68, 127.66, 127.0, 126.2, 52.6, 37.3, 33.1, 20.4 ppm.

The data is in accordance with the literature.[3]

Methyl -1-phenyl-1,1a,6,6a-tetrahydrocyclopropa[*a*]indene-1-carboxylate (8)

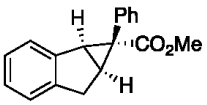

The title compound **8** was synthesized according to the general procedure (GP-1), and was obtained after silica column chromatography (*n*-hexane : ethyl acetate 20:1 → 10:1) as a colorless solid (91%, 39.9 mg).

^{1}H NMR (600 MHz, Chloroform-*d*): δ = 7.40 (d, *J* = 7.5 Hz, 1H), 7.13 – 7.01 (m, 5H), 6.96 – 6.85 (m, 3H), 6.74 – 6.68 (m, 1H), 3.63 (s, 3H), 3.50 – 3.42 (m, 1H), 3.27 – 3.17 (m, 1H), 2.86 (td, *J* = 6.8, 0.7 Hz, 1H), 2.75 (d, *J* = 17.9 Hz, 1H) ppm.

^{13}C NMR (151 MHz, Chloroform-*d*): δ = 174.0, 142.9, 141.4, 132.2, 127.3, 126.5, 126.3, 126.1, 125.0, 124.1, 52.5, 40.7, 38.2, 33.2, 32.0 ppm.

The data is in accordance with the literature.[3]

Methyl 1,2-diphenylcycloprop-2-ene-1-carboxylate (9)

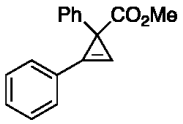

The title compound **9** was synthesized according to the general procedure (GP-1), and was obtained after silica column chromatography (*n*-hexane : ethyl acetate 20:1 → 10:1) as a colorless solid (82%, 41.1 mg).

^{1}H NMR (600 MHz, Chloroform-*d*): δ = 7.67 – 7.60 (m, 2H), 7.51 – 7.34 (m, 5H), 7.35 – 7.26 (m, 2H), 7.24 – 7.20 (m, 2H), 3.72 (s, 3H) ppm.

^{13}C NMR (151 MHz, Chloroform-*d*): δ = 175.0, 140.8, 130.0, 129.9, 128.8, 128.2, 128.0, 126.5, 125.4, 117.3, 100.3, 52.2, 33.5 ppm.

The data is in accordance with the literature.[4]

Methyl 2-(1-methyl-1*H*-indol-3-yl)-2-phenylacetate (10)

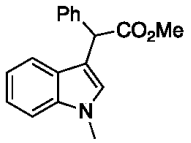

The title compound **10** was synthesized according to the general procedure (GP-1), and was obtained after silica column chromatography (*n*-hexane : ethyl acetate 20:1 → 10:1) as a colorless oil (74%, 50.1 mg).

^{1}H NMR (400 MHz, Chloroform-*d*): δ = 7.59 – 7.41 (m, 3H), 7.41 – 7.19 (m, 5H), 7.14 – 6.99 (m, 2H), 5.29 (s, 1H), 3.78 (s, 3H), 3.78 (s, 3H) ppm.

^{13}C NMR (101 MHz, Chloroform-*d*): δ = 173.5, 138.7, 137.0, 128.5, 128.4, 127.8, 127.2, 127.0, 121.8, 119.2, 119.0, 112.0, 109.3, 52.3, 48.8, 32.8 ppm.

The data is in accordance with the literature.[3]

Methyl 2-(4-(dimethylamino)phenyl)-2-phenylacetate (11)

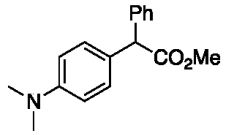

The title compound **11** was synthesized according to the general procedure (GP-1), and was obtained after silica column chromatography (*n*-hexane : ethyl acetate 20:1 → 10:1) as a colorless oil (75%, 40.1 mg).

^{1}H NMR (400 MHz, Chloroform-*d*): δ = 7.30 (d, *J* = 4.3 Hz, 4H), 7.27 – 7.19 (m, 1H), 7.17 (d, *J* = 8.7 Hz, 2H), 6.77 – 6.63 (m, 2H), 4.94 (s, 1H), 3.72 (s, 3H), 2.91 (s, 6H) ppm

^{13}C NMR (101 MHz, Chloroform-*d*): δ = 173.5, 149.7, 139.3, 129.2, 128.4, 126.9, 126.3, 112.5, 56.1, 52.1, 40.5 ppm.

The data is in accordance with the literature.[5]

Methyl 2-phenyl-2-(phenylamino)acetate (12)

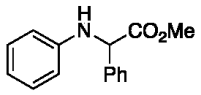

The title compound **12** was synthesized according to the general procedure (GP-1), and was obtained after silica column chromatography (*n*-hexane : ethyl acetate 20:1 → 10:1) as a colorless solid (96%, 46.6 mg).

^{1}H NMR (600 MHz, Chloroform-*d*): δ = 7.53 – 7.48 (m, 2H), 7.38 – 7.33 (m, 2H), 7.33 – 7.27 (m, 1H), 7.17 – 7.10 (m, 2H), 6.71 (tt, *J* = 7.3, 1.1 Hz, 1H), 6.61 – 6.54 (m, 2H), 5.10 (d, *J* = 4.4 Hz, 1H), 4.97 (s, 1H), 3.74 (s, 3H) ppm.

^{13}C NMR (151 MHz, Chloroform-*d*): δ = 172.3, 145.9, 137.6, 129.2, 128.8, 128.3, 127.2, 118.1, 113.4, 60.7, 52.8 ppm.

The data is in accordance with the literature.[5]

Methyl 2-(9*H*-carbazol-9-yl)-2-phenylacetate (13)

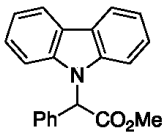

The title compound **13** was synthesized according to the general procedure (GP-1), and was obtained after silica column chromatography (*n*-hexane : ethyl acetate 20:1 → 10:1) as a colorless oil (82%, 43.1 mg).

^{1}H NMR (600 MHz, Chloroform-*d*): δ = 8.15 – 8.09 (m, 2H), 7.40 – 7.34 (m, 2H), 7.34 – 7.30 (m, 3H), 7.27 – 7.21 (m, 6H), 6.62 (s, 1H), 3.78 (s, 3H) ppm.

^{13}C NMR (151 MHz, Chloroform-*d*): δ = 169.8, 140.1, 133.9, 128.6, 128.3, 127.4, 125.7, 123.5, 120.2, 119.7, 119.4, 110.5, 110.1, 60.2, 52.7 ppm.

The data is in accordance with the literature.[5]

Methyl 2-(3,5-diphenyl-1*H*-pyrazol-1-yl)-2-phenylacetate (14)

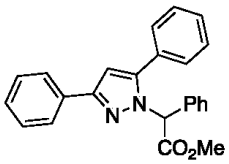

The title compound **14** was synthesized according to the general procedure (GP-1), and was obtained after silica column chromatography (*n*-hexane : ethyl acetate 20:1 → 10:1) as a colorless oil (50%, 36.6 mg).

^{1}H NMR (600 MHz, Chloroform-*d*): δ = 7.94 – 7.82 (m, 2H), 7.48 – 7.29 (m, 14H), 6.65 (s, 1H), 6.07 (s, 1H), 3.76 (s, 3H) ppm.

^{13}C NMR (151 MHz, Chloroform-*d*): δ = 169.0, 151.3, 146.0, 135.2, 133.2, 130.3, 129.1, 128.9, 128.8, 128.7, 128.5, 128.4, 127.8, 125.8, 103.7, 64.7, 53.0 ppm.

HRMS (ESI): m/z: $[M + K]^+$ Calcd. for $C_{24}H_{20}O_2N_2K^+$:407.11564; Found: 407.11559.

IR (KBr): 3061, 2952, 2323, 2083, 1893, 1749, 1603, 1552, 1484, 1455, 1304, 1257, 1204, 1109, 1077, 1002, 957, 919, 865, 805, 762, 735, 694 cm^{-1}.

Methyl 2-phenoxy-2-phenylacetate (15)

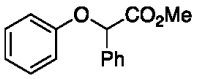

The title compound **15** was synthesized according to the general procedure (GP-1), and was obtained after silica column chromatography (*n*-hexane : ethyl acetate 20:1 → 10:1) as a colorless solid (56%, 26.9 mg).

^{1}H NMR (600 MHz, Chloroform-*d*): δ = 7.62 – 7.53 (m, 2H), 7.44 – 7.34 (m, 3H), 7.30 – 7.24 (m, 2H), 7.03 – 6.92 (m, 3H), 5.66 (s, 1H), 3.74 (s, 1H) ppm.

^{13}C NMR (151 MHz, Chloroform-*d*): δ = 170.4, 157.2, 135.4, 129.5, 128.9, 128.8, 127.0, 121.8, 115.4, 52.6 ppm.

The data is in accordance with the literature.[5]

Methyl 2-(hexyloxy)-2-phenylacetate (16)

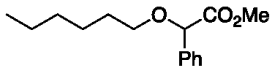

The title compound **16** was synthesized according to the general procedure (GP-1), and was obtained after silica column chromatography (*n*-hexane : ethyl acetate 20:1 → 10:1) as a colorless oil (82%, 43.3 mg).

^{1}H NMR (400 MHz, Chloroform-*d*): δ = 7.52 – 7.42 (m, 2H), 7.42 – 7.28 (m, 3H), 4.89 (s, 1H), 3.73 (s, 3H), 3.55 (dt, *J* = 9.0, 6.7 Hz, 1H), 3.45 (dt, *J* = 9.0, 6.8 Hz, 1H), 1.74 – 1.56 (m, 2H), 1.45 – 1.23 (m, 6H), 0.90 (t, *J* = 6.8 Hz, 3H) ppm.

^{13}C NMR (101 MHz, Chloroform-*d*): δ = 171.5, 136.7, 128.5, 127.1, 81.0, 70.0, 52.2, 31.6, 29.5, 25.6, 22.5, 14.0 ppm.

The data is in accordance with the literature.[6]

2-Methoxy-2-oxo-1-phenylethyl benzoate (17)

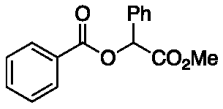

The title compound **17** was synthesized according to the general procedure (GP-1), and was obtained after silica column chromatography (*n*-hexane : ethyl acetate 20:1 → 10:1) as a colorless oil (86%, 46.6 mg).

^{1}H NMR (600 MHz, Chloroform-*d*): δ = 8.17 – 8.08 (m, 2H), 7.63 – 7.55 (m, 3H), 7.49 – 7.37 (m, 5H), 6.17 (s, 1H), 3.76 (s, 3H) ppm.

^{13}C NMR (151 MHz, Chloroform-*d*): δ = 169.3, 165.8, 133.9, 133.4, 129.9, 129.3, 129.2, 128.8, 128.4, 127.6, 74.8, 52.6 ppm.

The data is in accordance with the literature.[6]

Methyl 2-phenyl-2-(phenylthio)acetate (18)

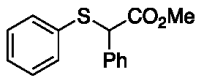

The title compound **18** was synthesized according to the general procedure (GP-1), and was obtained after silica column chromatography (*n*-hexane : ethyl acetate 20:1 → 10:1) as a colorless oil (88%, 45.5 mg).

^{1}H NMR (600 MHz, Chloroform-*d*): δ = 7.50 – 7.42 (m, 2H), 7.39 – 7.35 (m, 2H), 7.35 – 7.29 (m, 3H), 7.28 – 7.23 (m, 3H), 4.92 (s, 1H), 3.68 (s, 3H) ppm.

^{13}C NMR (151 MHz, Chloroform-*d*): δ = 170.8, 135.5, 133.6, 132.6, 128.9, 128.6, 128.5, 128.3, 128.0, 56.3, 52.7 ppm.

The data is in accordance with the literature.[7]

Methyl 2-(dimethyl(phenyl)silyl)-2-phenylacetate (19)

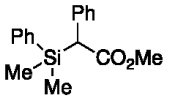

The title compound **19** was synthesized according to the general procedure (GP-1), and was obtained after silica column chromatography (*n*-hexane : ethyl acetate 20:1 → 10:1) as a colorless oil (80%, 54.3 mg).

^{1}H NMR (600 MHz, Chloroform-*d*): δ = 7.30 – 7.23 (m, 3H), 7.23 – 7.16 (m, 2H), 7.09 (d, *J* = 4.3 Hz, 4H), 7.02 (dt, *J* = 8.7, 4.2 Hz, 1H), 3.48 (s, 1H), 3.42 (s, 3H), 0.23 (s, 3H), 0.20 (s, 3H) ppm.

^{13}C NMR (151 MHz, Chloroform-*d*): δ = 173.1, 135.9, 135.5, 134.0, 129.6, 128.3, 128.0, 127.7, 125.6, 51.2, 46.0, -4.0, -4.5 ppm.

The data is in accordance with the literature.[8]

Methyl 2-(methyldiphenylsilyl)-2-phenylacetate (20)

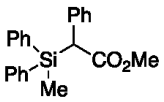

The title compound **20** was synthesized according to the general procedure (GP-1), and was obtained after silica column chromatography (*n*-hexane : ethyl acetate 20:1 → 10:1) as a colorless oil (75%, 63.0 mg).

^{1}H NMR (600 MHz, Chloroform-*d*): δ = 7.61 – 7.56 (m, 2H), 7.50 – 7.43 (m, 3H), 7.43 – 7.38 (m, 3H), 7.37 – 7.32 (m, 2H), 7.26 – 7.19 (m, 4H), 7.19 – 7.15 (m, 1H), 4.05 (s, 1H), 3.50 (s, 3H), 0.65 (s, 3H) ppm.

^{13}C NMR (151 MHz, Chloroform-*d*): δ = 173.0, 135.5, 135.08, 135.00, 134.0, 133.7, 129.8, 129.7, 128.8, 128.0, 127.8, 127.7, 125.8, 51.4, 44.8, -5.2 ppm.

The data is in accordance with the literature.[8]

Methyl 2-phenyl-2-(phenylthio)pent-4-enoate (21)

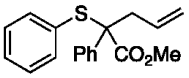

The title compound **21** was synthesized according to the general procedure (GP-1), and was obtained after silica column chromatography (*n*-hexane : ethyl acetate 20:1 → 10:1) as a colorless oil (92%, 55.3 mg).

^{1}H NMR (600 MHz, Chloroform-*d*): δ = 7.37 – 7.25 (m, 6H), 7.24 – 7.17 (m, 4H), 5.99 – 5.84 (m, 1H), 5.22 – 4.99 (m, 2H), 3.72 (s, 3H), 3.00 – 2.81 (m, 2H) ppm.

^{13}C NMR (151 MHz, Chloroform-*d*): δ = 172.3, 139.7, 136.8, 133.2, 130.7, 129.2, 128.5, 128.1, 127.5, 127.4, 118.8, 64.5, 52.6, 40.6 ppm.

The data is in accordance with the literature.[4]

Methyl 2,3-diphenyl-2-(phenylthio)propanoate (22)

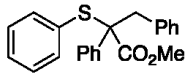

The title compound **22** was synthesized according to the general procedure (GP-1), and was obtained after silica column chromatography (*n*-hexane : ethyl acetate 20:1 → 10:1) as a colorless oil (60%, 42.0 mg).

^{1}H NMR (600 MHz, Chloroform-*d*): δ = 7.38 – 7.31 (m, 3H), 7.28 – 7.21 (m, 7H), 7.20 – 7.12 (m, 3H), 7.04 – 6.94 (m, 2H), 3.62 (s, 1H), 3.60 (d, *J* = 14.0, 1H), 3.44 (d, *J* = 13.7 Hz, 1H) ppm.

^{13}C NMR (151 MHz, Chloroform-*d*): δ = 171.9, 139.2, 136.4, 135.9, 131.3, 130.8, 129.2, 128.5, 128.2, 127.8, 127.6, 127.4, 126.7, 77.2, 65.8, 52.2, 44.5 ppm.

The data is in accordance with the literature.[9]

Ethyl 2-(2-(2-methoxy-2-oxoethyl)phenyl)-2-(phenylthio)acetate (23)

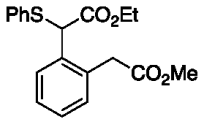

The title compound **23** was synthesized according to the general procedure (GP-1), and was obtained after silica column chromatography (*n*-hexane : ethyl acetate 20:1 → 10:1) as a colorless oil (90%, 62.3 mg).

^{1}H NMR (400 MHz, Chloroform-*d*): δ = 7.73 – 7.57 (m, 1H), 7.40 (dd, *J* = 6.6, 3.0 Hz, 2H), 7.35 – 7.18 (m, 6H), 5.21 (s, 1H), 4.19 – 3.99 (m, 2H), 3.71 (d, *J* = 4.1 Hz, 2H), 3.63 (s, 3H), 1.12 (t, *J* = 7.1 Hz, 3H) ppm.

^{13}C NMR (101 MHz, Chloroform-*d*): δ = 171.3, 170.3, 134.2, 133.7, 132.8, 132.5, 131.1, 129.1, 128.9, 128.4, 128.0, 127.9, 61.7, 52.4, 52.1, 38.8, 13.9 ppm.

The data is in accordance with the literature.[9]

2-Methoxy-2-oxo-1-phenylethyl 2-(4-isobutylphenyl)propanoate (24)

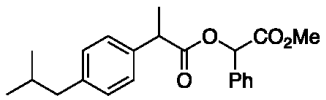

The title compound **24** was synthesized according to the general procedure (GP-1), and was obtained after silica column chromatography (*n*-hexane : ethyl acetate 20:1 → 10:1) as a colorless oil (91%, 64.3 mg), d.r. = 1 : 1

^{1}H NMR (400 MHz, Chloroform-*d*): δ = 7.43 – 7.29 (m, 4H), 7.29 – 7.19 (m, 3H), 7.18 – 7.00 (m, 2H), 5.91 (d, *J* = 1.9 Hz, 1H), 3.85 (dt, *J* = 14.1, 7.1 Hz, 1H), 3.70 (s, 1.50 H), 3.62 (s, 1.44 H), 2.44 (dd, *J* = 10.9, 7.2 Hz, 2H), 1.84 (dt, *J* = 10.5, 6.8 Hz, 1H), 1.56 (dd, *J* = 7.2, 5.3 Hz, 3H), 1.03 – 0.78 (m, 6H) ppm.

^{13}C NMR (101 MHz, Chloroform-*d*): δ = 174.0, 173.9, 169.2, 169.0, 140.6, 140.5, 137.0, 136.9, 133.8, 133.7, 129.27, 129.21, 129.08, 129.00, 128.68, 128.61, 127.4, 127.3, 74.5, 74.4, 52.5, 52.3, 45.04, 45.00, 44.9, 44.7, 30.1, 22.3, 18.5, 18.3 ppm.

HRMS (ESI): m/z: $[M + Na]^+$ Calcd. for $C_{22}H_{26}O_4Na^+$: 377.17233; Found: 377.17091.

IR (KBr): 3503, 3156, 3032, 2954, 2870, 2657, 2451, 2335, 2260, 2229, 2174, 2110, 1991, 1956, 1950, 1805, 1742, 1602, 1511, 1454, 1350, 1271, 1213, 1152, 1071, 1028, 967, 922, 848, 780, 733, 695 cm^{-1}.

2-Methoxy-2-oxo-1-phenylethyl 2-(6-chloro-9*H*-carbazol-2-yl)propanoate (25)

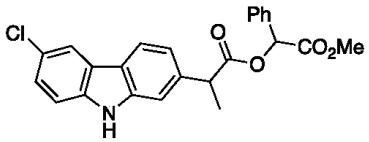

The title compound **25** was synthesized according to the general procedure (GP-1), and was obtained after silica column chromatography (*n*-hexane : ethyl acetate 20:1 → 10:1) as a colorless oil (90%, 75.2 mg), d.r. 2 : 1.

^{1}H NMR (400 MHz, Acetone): δ = 10.50 (s, 0.38H), 10.46 (s, 0.62H), 8.25 – 7.98 (m, 2H), 7.60 – 7.48 (m, 2H), 7.42 (dq, *J* = 7.3, 3.4 Hz, 2H), 7.39 – 7.30 (m, 4H), 7.24 (dt, *J* = 8.1, 1.0 Hz, 0.49H), 7.20 (dt, *J* = 8.2, 1.0 Hz, 0.81H), 5.92 (s, 1H), 4.09 (dd, *J* = 8.9, 7.0 Hz, 1H), 3.68 (d, *J* = 0.8 Hz, 2.31H), 3.57 (d, *J* = 0.7 Hz, 1.35H), 1.58 (t, *J* = 7.2 Hz, 3H) ppm.

^{13}C NMR (101 MHz, Acetone): δ = 173.49, 173.40, 168.9, 168.8, 140.9, 138.8. 134.1, 129.04, 129.00, 128.6, 128.5, 127.5, 127.4, 125.3, 125.2, 124.1, 123.8, 121.3, 120.4, 120.3, 119.6, 119.3, 119.1, 112.16, 112.11, 110.18, 110.10, 74.6, 74.5, 51.8, 51.6, 45.3, 18.6, 18.5 ppm.

HRMS (ESI): m/z: $[M + K]^+$ Calcd. for $C_{24}H_{20}O_4ClK^+$: 460.06960; Found: 460.07124.

IR (KBr): 3409, 3034, 2952, 2230, 2171, 2083, 1990, 1881, 1734, 1610, 1576, 1454, 1333, 1271, 1219, 1159, 1064, 1031, 970, 926, 867, 803, 732, 695 cm^{-1}.

Methyl 2-phenyl-2-(((*R*)-2,5,7,8-tetramethyl-2-((4*R*,8*R*)-4,8,12-trimethyltridecyl) chroman-6-yl)oxy)acetate (26)

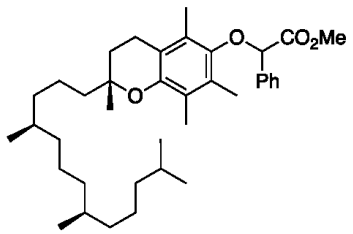

The title compound **26** was synthesized according to the general procedure (GP-1), and was obtained after silica column chromatography (*n*-hexane : ethyl acetate 20:1 → 10:1) as a colorless oil (40%, 44.8 mg), d.r. = 1 : 1.

^{1}H NMR (600 MHz, Chloroform-*d*): δ = 7.62 – 7.41 (m, 2H), 7.36 (dd, *J* = 4.9, 1.8 Hz, 3H), 5.05 (s, 1H), 3.73 (d, *J* = 1.3 Hz, 3H), 2.50 (td, *J* = 6.8, 4.3 Hz, 2H), 2.03 (s, 3H), 1.98 (s, 3H), 1.92 (d, *J* = 2.6 Hz, 3H), 1.85 – 1.70 (m, 2H), 1.66 – 1.48 (m, 3H), 1.43 – 1.33 (m, 2H), 1.33 – 1.23 (m, 5H), 1.22 (s, 3H), 1.18 – 1.10 (m, 2H), 1.09- 1.02 (m, 1H), 0.91 – 0.80 (m, 13H) ppm.

^{13}C NMR (151 MHz, Chloroform-*d*): δ = 171.2, 148.2, 147.9, 136.7, 128.7, 128.5, 127.7, 126.0, 122.9, 117.5, 84.1, 74.8, 52.2, 39.9, 39.3, 37.5, 37.4, 37.3, 37.2, 32.7, 32.6, 27.9, 24.8, 24.4, 23.8, 23.7, 22.7, 22.6, 21.0, 20.7, 19.7, 19.67, 19.60, 13.5, 12.6, 11.8 ppm.

HRMS (ESI): m/z: $[M + Na]^+$ Calcd. for $C_{38}H_{58}O_4Na^+$: 601.42273; Found: 601.42107.

IR (KBr): 3345, 2925, 2865, 2726, 2335, 2098, 1988, 1940, 1759, 1574, 1457, 1409, 1376, 1249, 1204, 1163, 1085, 916, 856, 814, 781, 729, 697 cm^{-1}.

2-Methoxy-2-oxo-1-phenylethyl (2*S*)-2-(6-methoxynaphthalen-2-yl)propanoate (27)

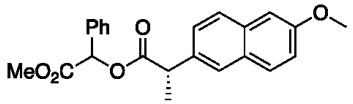

The title compound **27** was synthesized according to the general procedure (GP-1), and was obtained after silica column chromatography (*n*-hexane : ethyl acetate 20:1 → 10:1) as a colorless oil (47%, 35.5 mg) d.r. ~1.6:1.

^{1}H NMR (600 MHz, Chloroform-*d*): δ = 7.82 – 7.61 (m, 3H), 7.58 – 7.25 (m, 6H), 7.15 – 7.04 (m, 2H), 5.92 (s, 0.38H), 5.91 (s, 0.51H), 4.15 – 3.93 (m, 1H), 3.90 (s, 1.08H), 3.89 (s, 1.76H), 3.70 (s, 1.48H), 3.58 (s, 1.26fH), 1.89 – 1.49 (m, 3H).
ppm.

^{13}C NMR (151 MHz, Chloroform-*d*): δ = 174.0, 173.9, 169.2, 169.0, 157.6, 134.99, 134.93, 133.7, 133.6, 129.33, 129.30, 129.1, 129.0, 128.9, 128.8, 128.7, 128.6, 127.5, 127.4, 127.1, 127.0, 126.4, 126.3, 126.2, 126.1, 118.93, 118.90, 105.6, 105.5, 74.7, 74.5, 55.2, 52.6, 52.4, 45.2, 45.1, 18.6, 18.4 ppm.

HRMS (ESI): m/z: $[M + Na]^+$ Calcd. for $C_{23}H_{22}O_5Na^+$: 401.13594; Found: 401.13590.

IR (KBr): 2951, 2843, 2327, 2117, 1911, 1739, 1631, 1605, 1487, 1453, 1388, 1350, 1255, 1217, 1151, 1078, 1029, 969, 923, 892, 854, 812, 782, 763, 696 cm^{-1}.
, 1214, 1159, 1096, 1046, 979, 913, 849 cm^{-1}.

2-Methoxy-2-oxo-1-phenylethyl (*tert*-butoxycarbonyl)-*L*-valinate (28)

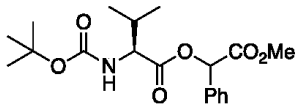

The title compound **28** was synthesized according to the general procedure (GP-1), and was obtained after silica column chromatography (*n*-hexane : ethyl acetate 20:1 → 10:1) as a colorless oil (72%, 41.8 mg) d.r. ~1.6:1.

^{1}H NMR (600 MHz, Chloroform-*d*): δ = 7.54 – 7.42 (m, 2H), 7.42 – 7.33 (m, 3H), 5.96 (s, 0.45H), 5.92 (s, 0.34H), 5.11 – 4.92 (m, 1H), 4.52 – 4.30 (m, 1H), 3.72 (s, 1.86H), 3.71 (s, 1.14H), 2.42 – 2.33 (m, 0.32H), 2.29 – 2.15 (m, 0.51H), 1.43 (s, 3.20H), 1.40 (s, 5.13H), 1.05 (d, *J* = 6.9 Hz, 1.31H), 1.01 (d, *J* = 6.9 Hz, 1.21H), 0.98 (d, *J* = 6.9 Hz, 1.86H), 0.87 (d, *J* = 6.9 Hz, 1.70H) ppm.

^{13}C NMR (151 MHz, Chloroform-*d*): δ = 172.0, 171.5, 168.9, 168.8, 155.6, 155.5, 133.5, 133.2, 129.38, 129.31, 128.8, 128.7, 127.6, 127.5, 79.8, 74.9, 74.8, 58.6, 58.2, 52.6, 52.5, 31.1, 28.29, 28.25, 19.03, 19.00, 17.3, 17.1 ppm.

HRMS (ESI): m/z: $[M + Na]^+$ Calcd. for $C_{19}H_{27}O_6NNa^+$: 388.17306; Found: 388.17306.

IR (KBr): 3387, 2969, 2160, 2022, 1747, 1711, 1499, 1456, 1364, 1310, 1217, 1155, 1089, 1039, 862, 736, 696 cm^{-1}.

2-Methoxy-2-oxo-1-phenylethyl (9*Z*,12*Z*)-octadeca-9,12-dienoate (29)

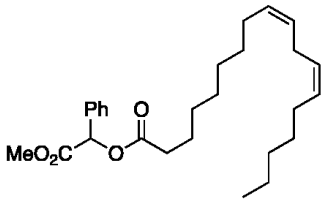

The title compound **29** was synthesized according to the general procedure (GP-1), and was obtained after silica column chromatography (*n*-hexane : ethyl acetate 20:1 → 10:1) as a colorless oil (44%, 37.8 mg).

^{1}H NMR (600 MHz, Chloroform-*d*): δ = 7.57 – 7.43 (m, 2H), 7.43 – 7.28 (m, 3H), 5.92 (s, 1H), 5.33 (tt, *J* = 11.2, 5.2 Hz, 4H), 3.70 (s, 3H), 2.75 (t, *J* = 6.5 Hz, 2H), 2.65 – 2.30 (m, 2H), 2.03 (q, *J* = 7.0 Hz, 4H), 1.67 (p, *J* = 7.4 Hz, 2H), 1.41 – 1.14 (m, 15H), 0.87 (t, *J* = 6.5 Hz, 3H) ppm.

^{13}C NMR (151 MHz, Chloroform-*d*): δ = 173.1, 169.3, 133.8, 130.2, 130.0, 129.1, 128.7, 128.0, 127.8, 127.5, 74.2, 52.5, 33.9, 31.5, 29.5, 29.3, 29.1, 29.0, 28.9, 27.1, 25.6, 24.7, 22.5, 14.0 ppm.

HRMS (ESI): m/z: $[M + Na]^+$ Calcd. for $C_{27}H_{40}O_4Na^+$: 451.28188; Found: 451.28188.

IR (KBr): 3481, 3067, 3009, 2926, 2855, 2664, 2329, 2118, 1992, 1960, 1746, 1649, 1588, 1496, 1456, 1349, 1269

Methyl 2-phenyl-2-((4-(5-(*p*-tolyl)-3-(trifluoromethyl)-1*H*-pyrazol-1-yl)phenyl)sulfonamido)acetate (30)

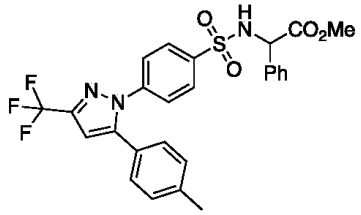

The title compound **30** was synthesized according to the general procedure (GP-1), and was obtained after silica column chromatography (*n*-hexane : ethyl acetate 10:1 → 4:1) as a colorless oil (27%, 28.7 mg).

^{1}H NMR (600 MHz, Chloroform-*d*): δ = 7.72 – 7.64 (m, 2H), 7.41 – 7.30 (m, 2H), 7.30 – 7.24 (m, 3H), 7.23 – 7.19 (m, 2H), 7.19 – 7.15 (m, 2H), 7.11 – 7.05 (m, 2H), 6.72 (s, 1H), 5.80 (d, *J* = 7.4 Hz, 1H), 5.08 (d, *J* = 7.4 Hz, 1H), 3.63 (s, 3H), 2.38 (s, 3H) ppm.

^{13}C NMR (151 MHz, Chloroform-*d*): δ = 170.3, 145.1, 144.0 (d, *J* = 38.6 Hz), 142.4, 139.6 (d, *J* = 51.6 Hz), 134.9, 129.7, 128.9, 128.8, 128.6, 128.0, 127.1, 125.6, 125.2, 121.0 (d, *J* = 269.5 Hz), 106.3, 59.3, 53.2, 21.3 ppm.

HRMS (ESI): m/z: $[M + Na]^+$ Calcd. for $C_{26}H_{22}O_4N_3F_3SNa^+$: 552.11753; Found: 552.11745.

IR (KBr): 3276, 3067, 3033, 2955, 2523, 2436, 2258, 2230, 2201, 2161, 2121, 2084, 2059, 2024, 1079, 1013, 1742, 1596, 1497, 1470, 1411, 1371, 1342, 1270, 1236, 1160, 1096, 1017, 974, 920, 842, 810, 760, 736, 697 cm^{-1}.

Reaction with Brucine

In an oven dried reaction tube Rh-CP (4 mg) and brucine (1.0 equiv., 0.2 mmol,) were added. Then the tube was closed with septum and evacuated and backfilled with argon for three times. Then 1 mL degassed $PhCF_3$ was added. The corresponding diazoalkane (4.0 equiv., 0.8 mmol) was dissolved in a separate reaction test tube in 1 mL of degassed $PhCF_3$ was added to the reaction tube and heated to 83 °C for 16 h. The corresponding products were obtained after column chromatography on silica gel using *n*-hexane : ethyl acetate as eluent.

Methyl (4a*R*,4a1*R*,5a*S*,8a*R*,8a1*S*,15a*S*,16*S*)-16-(4-bromophenyl)-10,11-dimethoxy-14-oxo-2,4a,4a1,5,5a,7,8,8a1,15,15a-decahydro-14*H*-6,4-ethanoindolo[3,2,1-*ij*]oxepino[2,3,4-*de*]pyrrolo[2,3-*h*]quinoline-16-carboxylate (33) & Methyl 2-(4-bromophenyl)-2-((4a*R*,4a1*R*,5a*R*,8a*S*,8a1*S*,15a*S*)-10,11-dimethoxy-14-oxo-4a,4a1,5,7,8,8a1,15,15a-octahydro-14*H*-4,6-methanoindolo[3,2,1-*ij*]oxepino[2,3,4-*de*]pyrrolo[2,3-*h*]quinolin-5a(2*H*)-yl)acetate (34)

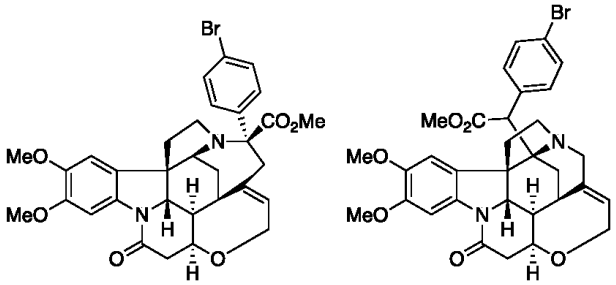

The title compound **33** and **34** were obtained as an inseparable 1 : 1 mixture after silica column chromatography (*n*-hexane : ethyl acetate 40:1 → 10:1) as a colorless solid (22%, 45.1 mg).

^{1}H NMR (600 MHz, Chloroform-*d*): δ = 7.92 (s, 1H), 7.82 (s, 1H), 7.53 (d, *J* = 8.6 Hz, 2H), 7.47 – 7.40 (m, 2H), 7.40 – 7.34 (m, 2H), 7.19 (d, *J* = 8.0 Hz, 2H), 6.91 (s, 1H), 6.71 (s, 1H), 5.89 – 5.80 (m, 1H), 5.64 (td, *J* = 6.6, 2.6 Hz, 1H), 4.37 (ddd, *J* = 16.1, 4.9, 1.8 Hz, 1H), 4.28 – 4.21 (m, 2H), 4.15 – 4.05 (m, 5H), 4.01 – 3.86 (m, 2H), 3.91 (d, *J* = 4.0 Hz, 1H), 3.89 (s, 3H), 3.88 (s, 3H), 3.87 (s, 3H), 3.82 (s, 3H), 3.62 (s, 3H), 3.49 (s, 3H), 3.27 (ddd, *J* = 10.2, 7.7, 5.8 Hz, 1H), 3.11 (dd, *J* = 17.7, 8.6 Hz, 1H), 3.08 – 3.00 (m, 4H), 3.00 – 2.94 (m, 1H), 2.91 (dd, *J* = 13.0, 6.5 Hz, 2H), 2.85 – 2.74 (m, 4H), 2.57 (dd, *J* = 17.7, 3.2 Hz, 1H), 2.31 (td, *J* = 12.7, 7.6 Hz, 1H), 2.27 (s, 2H), 2.03 (s, 2H), 1.99 (dt, *J* = 15.2, 3.6 Hz, 1H), 1.95 – 1.84 (m, 2H), 1.79 (dd, *J* = 13.1, 6.3 Hz, 1H), 1.69 (s, 2H), 1.64 – 1.55 (m, 2H), 1.40 (dt, *J* = 16.8, 3.5 Hz, 1H), 1.25 (t, *J* = 7.1 Hz, 3H) ppm.

^{13}C NMR (151 MHz, Chloroform-*d*): δ = 173.0, 172.1, 169.7, 167.4, 149.3, 149.2, 146.1, 145.1, 142.5, 139.3, 138.1, 136.2, 135.7, 135.0, 131.4, 130.3, 128.6, 128.1, 125.7, 123.6, 123.2, 121.4, 121.2, 108.7, 105.8, 100.9, 78.0, 75.6, 68.4, 67.8, 65.2, 65.0, 62.6, 61.5, 60.3, 59.4, 57.9, 56.66, 56.63, 56.3, 56.1, 55.9, 53.0, 52.80, 52.1, 51.8, 49.4, 49.2, 48.0, 46.79, 46.72, 42.4, 42.19, 42.17, 39.3, 35.1, 31.9, 31.5, 28.1 ppm.

The data is in accordance with the literature.[10]

Methyl (4a*R*,4a1*R*,5a*S*,8a*R*,8a1*S*,15a*S*,16*R*)-16-(4-bromophenyl)-10,11-dimethoxy-14-oxo-2,4a,4a1,5,5a,7,8,8a1,15,15a-decahydro-14*H*-6,4-ethanoindolo[3,2,1-*ij*]oxepino[2,3,4-*de*]pyrrolo[2,3-*h*]quinoline-16-carboxylate (35)

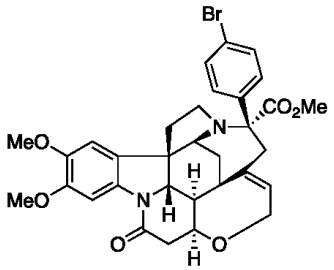

The title compound **35** was obtained after silica column chromatography (*n*-hexane : ethyl acetate 40:1 → 10:1) as a colorless solid (17%, 35.0 mg).

^{1}H NMR (400 MHz, Chloroform-*d*): δ = 7.79 (s, 1H), 7.45 (d, *J* = 8.3 Hz, 2H), 7.19 (s, 2H), 6.66 (s, 1H), 5.51 (s, 1H), 4.24 – 4.12 (m, 2H), 4.07 (d, *J* = 10.5 Hz, 1H), 4.02 – 3.94 (m, 1H), 3.91 (s, 3H), 3.87 (s, 3H), 3.85 (s, 3H), 3.76 – 3.67 (m, 1H), 3.52 – 3.38 (m, 1H), 3.07 (dd, *J* = 16.2, 8.2 Hz, 1H), 2.94 (s, 1H), 2.82 – 2.52 (m, 3H), 2.50 – 2.29 (m, 2H), 2.10 – 1.94 (m, 1H), 1.73 – 1.52 (m, 2H), 1.49 – 1.29 (m, 1H) ppm.

^{13}C NMR (101 MHz, Chloroform-*d*): δ = 173.6, 170.2, 149.0, 146.3, 136.3, 131.3, 128.1, 123.8, 121.4, 105.6, 101.0, 79.0, 68.3, 66.7, 64.2, 60.2, 56.5, 56.1, 52.7, 51.8, 48.9, 47.5, 45.6, 41.8, 40.5, 34.9, 29.0 ppm.

The data is in accordance with the literature.[10]

14. NMR Spectra

Methyl-1,2-diphenylcyclopropane-1-carboxylate (7)

^{1}H NMR (600 MHz, Chloroform-*d*)

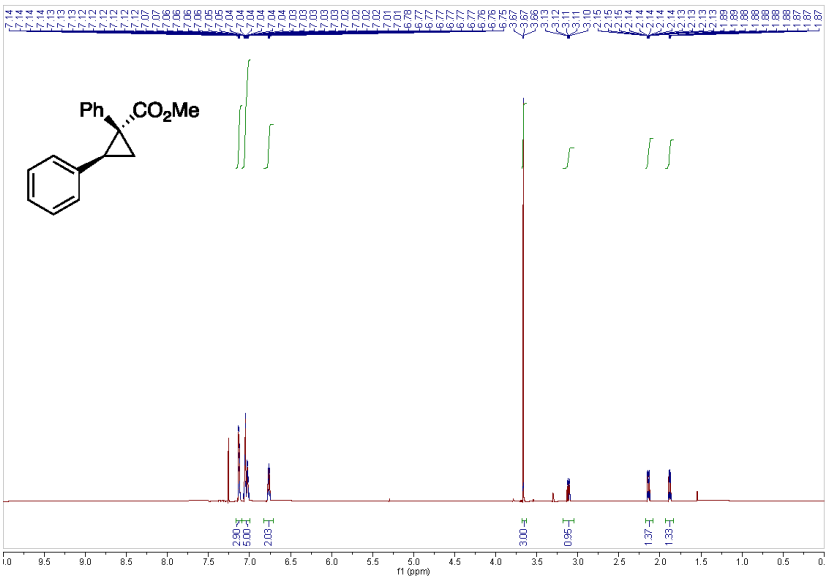

^{13}C NMR (151 MHz, Chloroform-*d*)

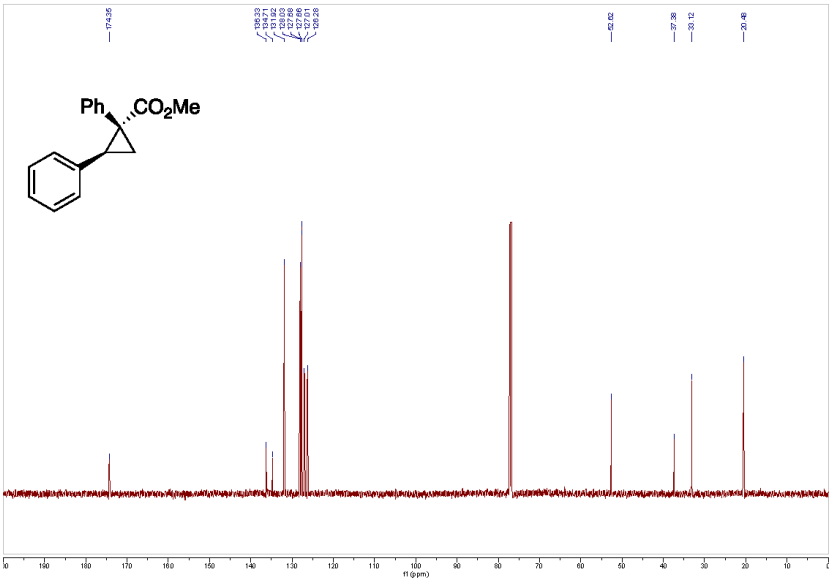

Methyl -1-phenyl-1,1a,6,6a-tetrahydrocyclopropa[*a*]indene-1-carboxylate (8)

^{1}H NMR (600 MHz, Chloroform-*d*)

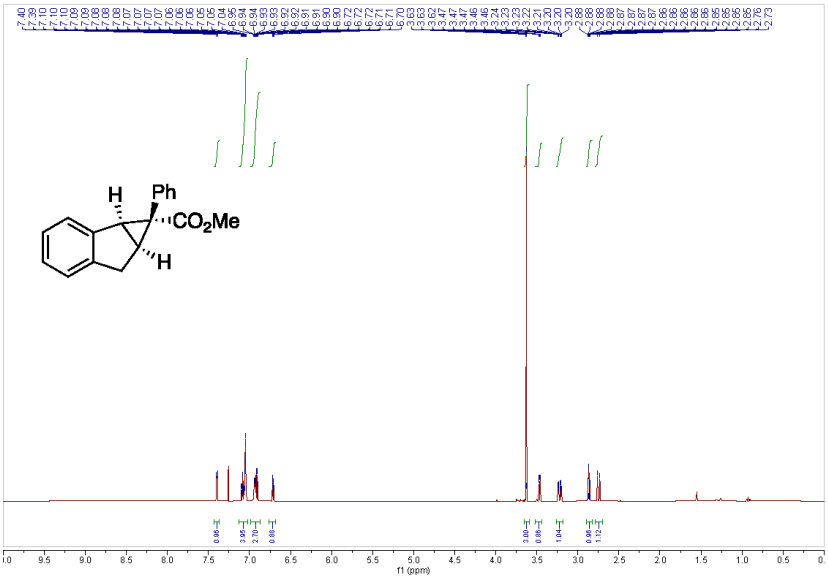

^{13}C NMR (151 MHz, Chloroform-*d*)

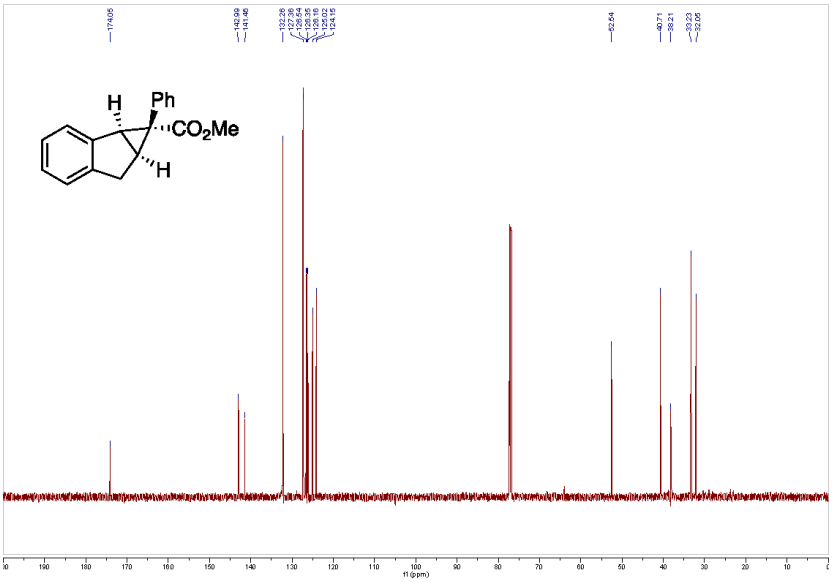

Methyl 1,2-diphenylcycloprop-2-ene-1-carboxylate (9)

^{1}H NMR (600 MHz, Chloroform-*d*)

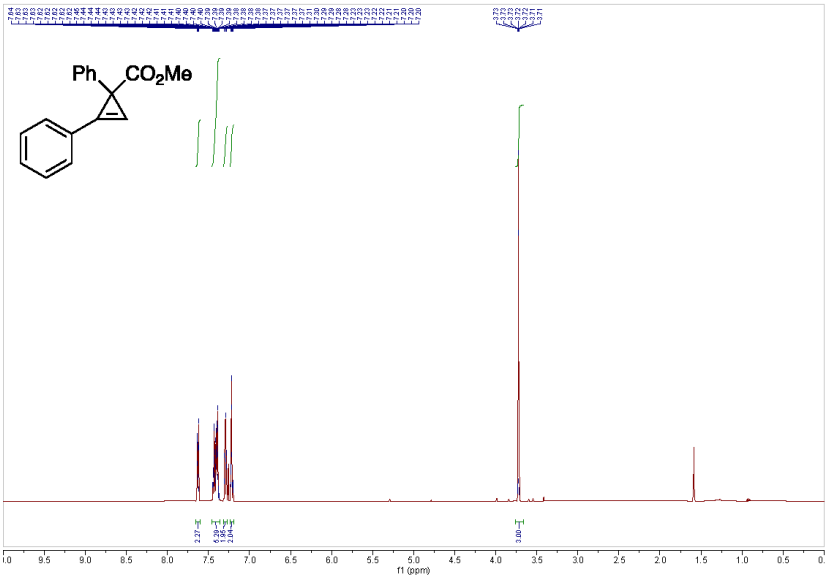

^{13}C NMR (151 MHz, Chloroform-*d*)

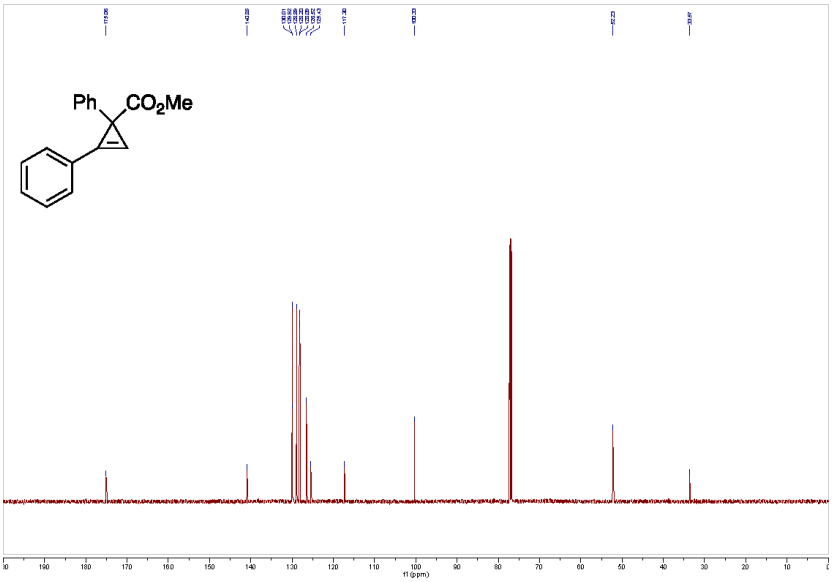

Methyl 2-(1-methyl-1*H*-indol-3-yl)-2-phenylacetate (10)

^{1}H NMR (400 MHz, Chloroform-*d*)

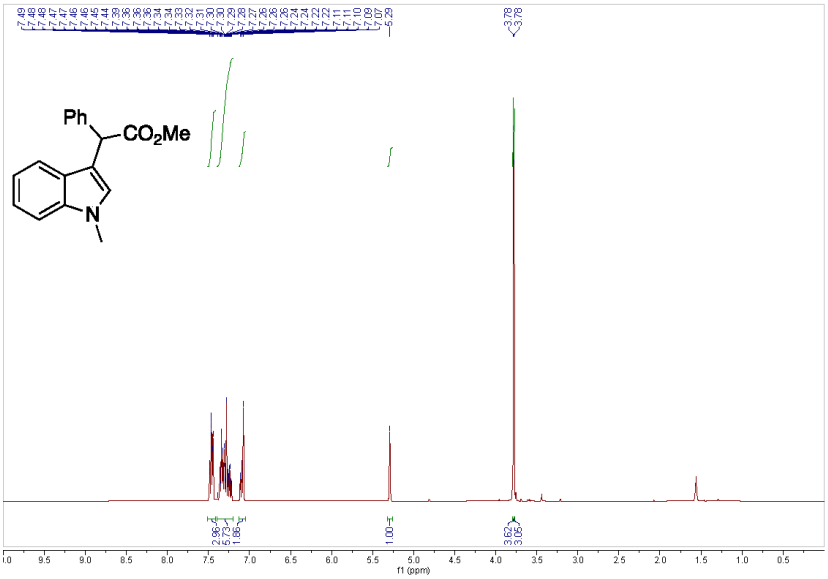

^{13}C NMR (101 MHz, Chloroform-*d*)

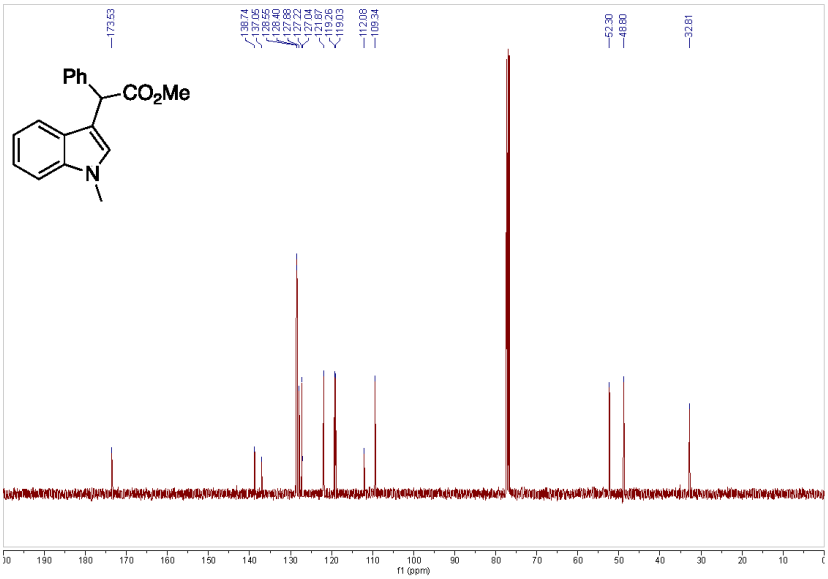

Methyl 2-(4-(dimethylamino)phenyl)-2-phenylacetate (11)

^{1}H NMR (400 MHz, Chloroform-*d*)

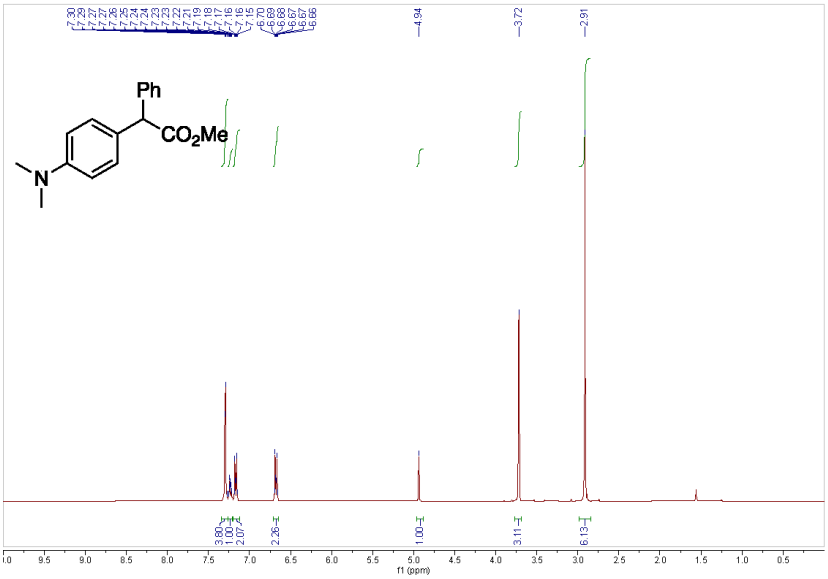

^{13}C NMR (101 MHz, Chloroform-*d*)

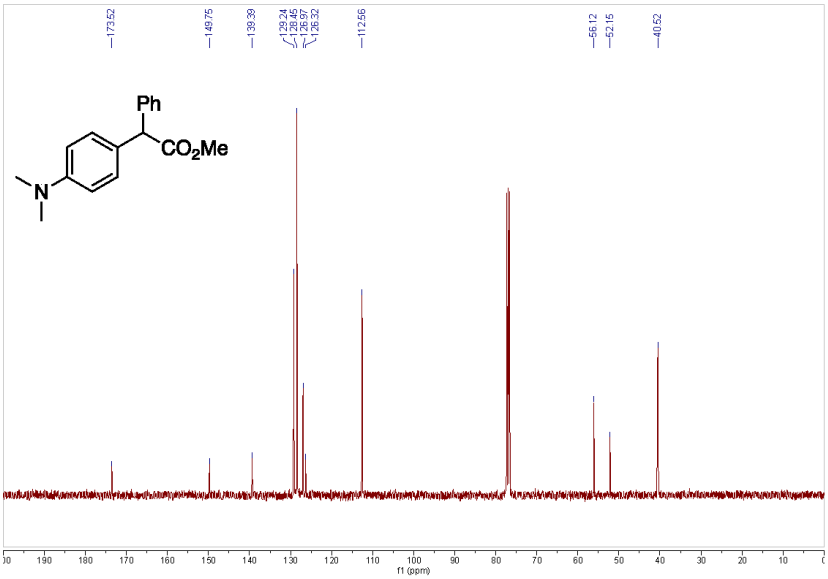

Methyl 2-phenyl-2-(phenylamino)acetate (12)

^{1}H NMR (600 MHz, Chloroform-*d*)

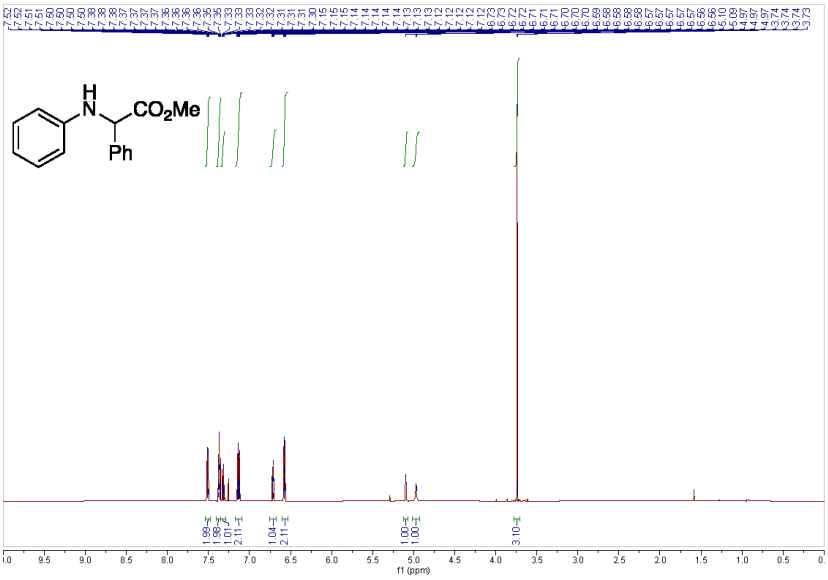

^{13}C NMR (151 MHz, Chloroform-*d*)

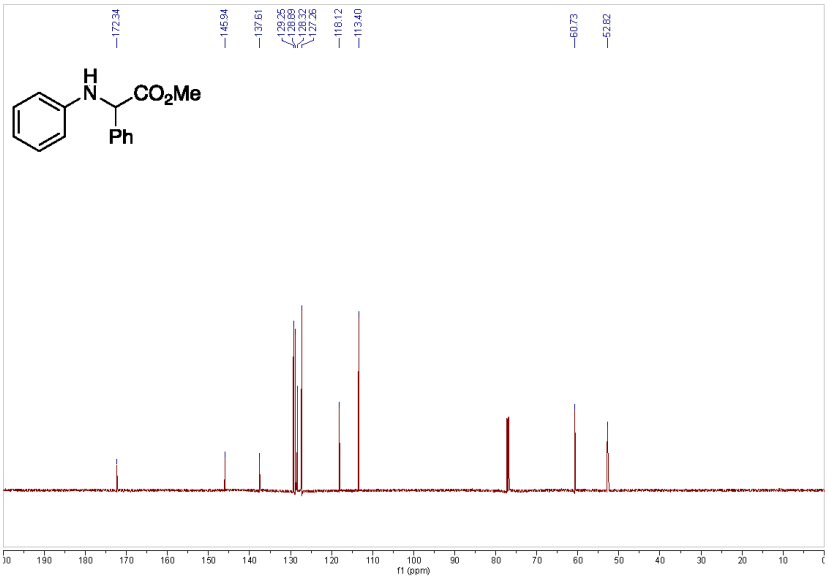

Methyl 2-(9*H*-carbazol-9-yl)-2-phenylacetate (13)

^{1}H NMR (600 MHz, Chloroform-*d*)

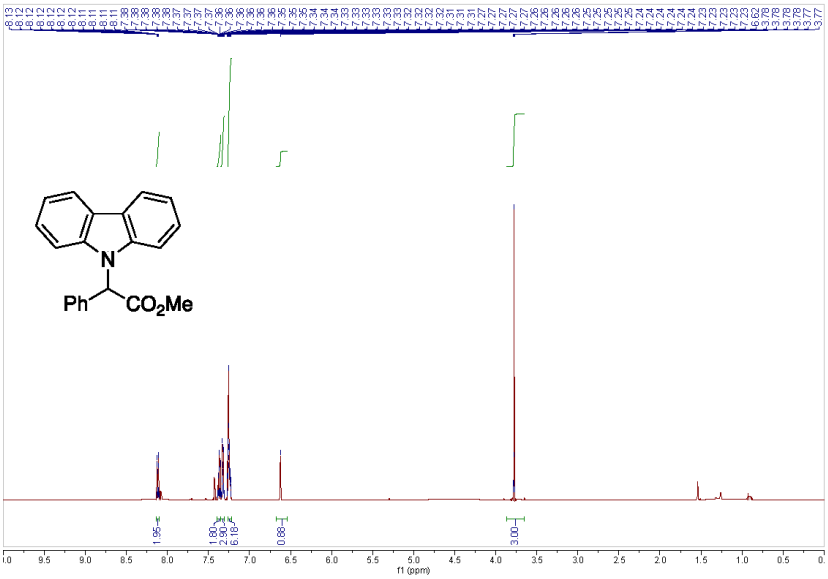

^{13}C NMR (151 MHz, Chloroform-*d*)

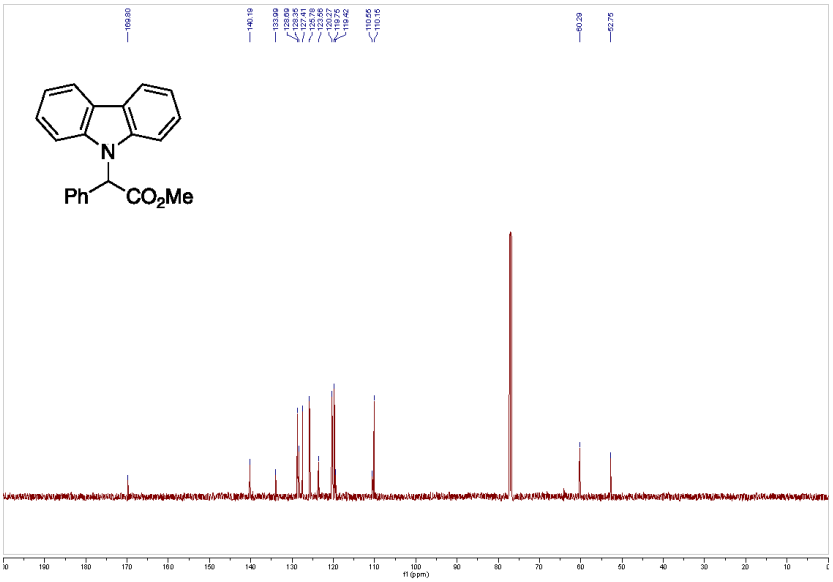

Methyl 2-(3,5-diphenyl-1*H*-pyrazol-1-yl)-2-phenylacetate (14)

^{1}H NMR (600 MHz, Chloroform-*d*)

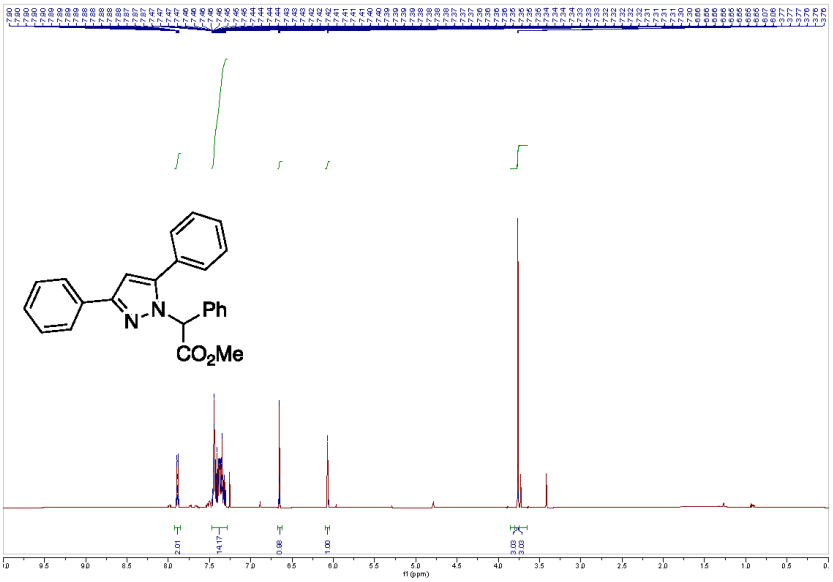

^{13}C NMR (151 MHz, Chloroform-*d*)

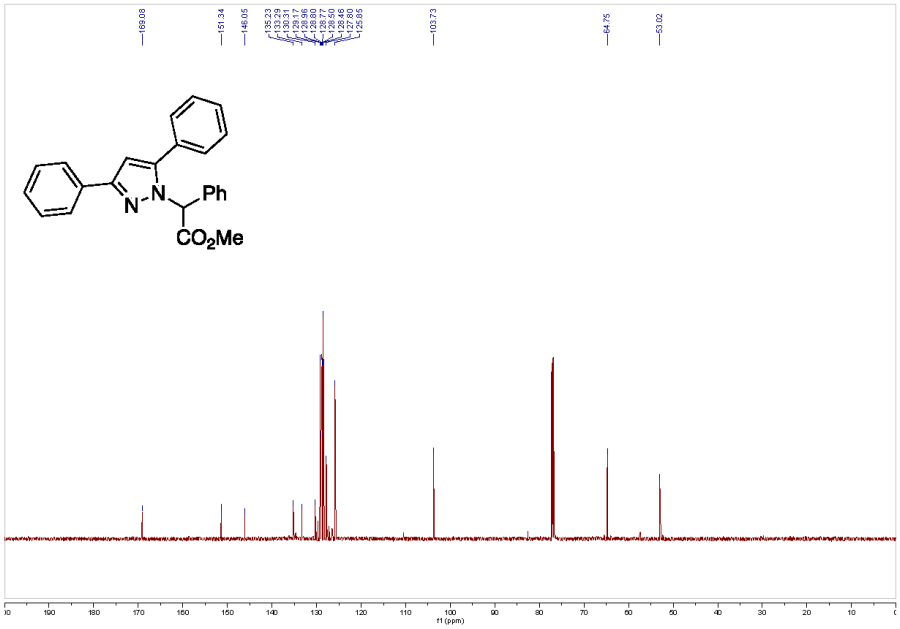

Methyl 2-phenoxy-2-phenylacetate (15)

^{1}H NMR (600 MHz, Chloroform-*d*)

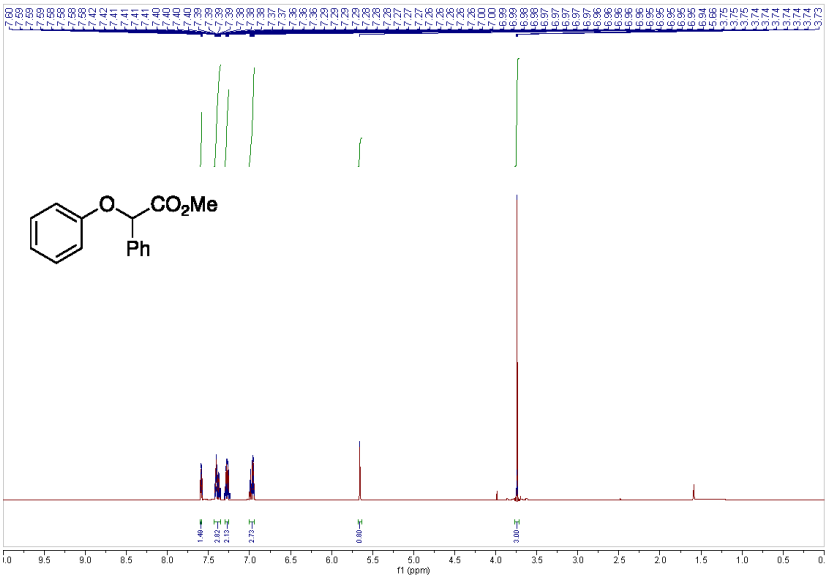

^{13}C NMR (151 MHz, Chloroform-*d*)

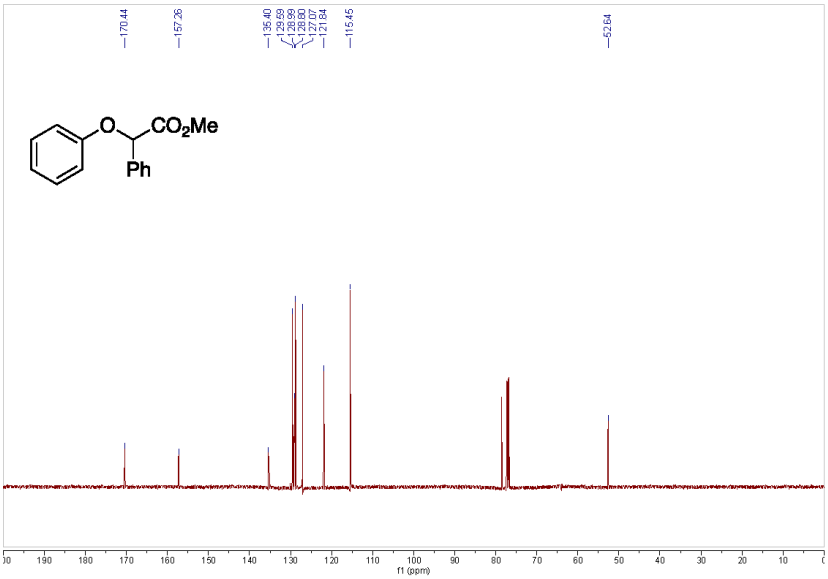

Methyl 2-(hexyloxy)-2-phenylacetate (16)

^{1}H NMR (400 MHz, Chloroform-*d*)

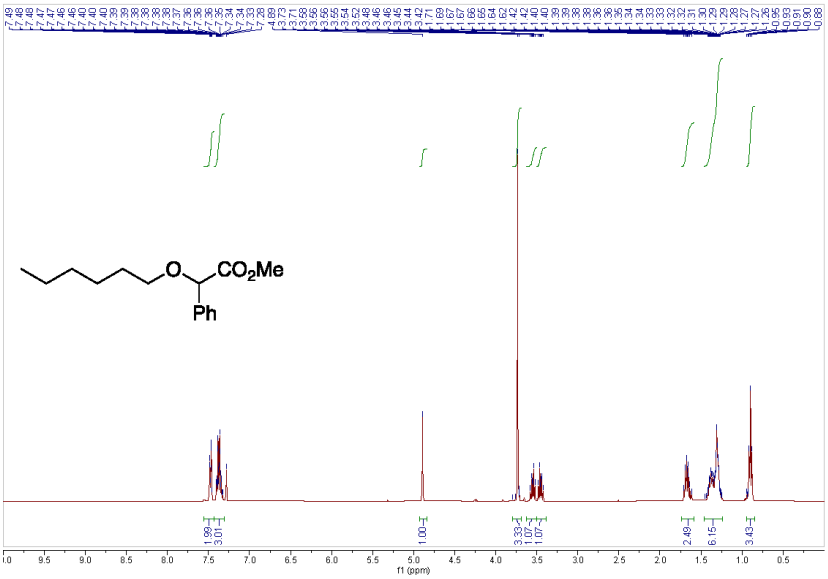

^{13}C NMR (101 MHz, Chloroform-*d*)

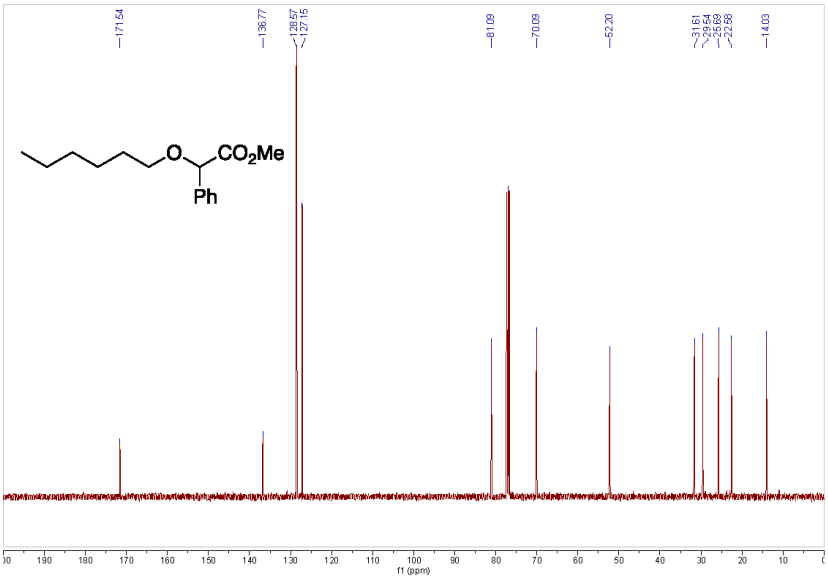

2-Methoxy-2-oxo-1-phenylethyl benzoate (17)

^{1}H NMR (600 MHz, Chloroform-*d*)

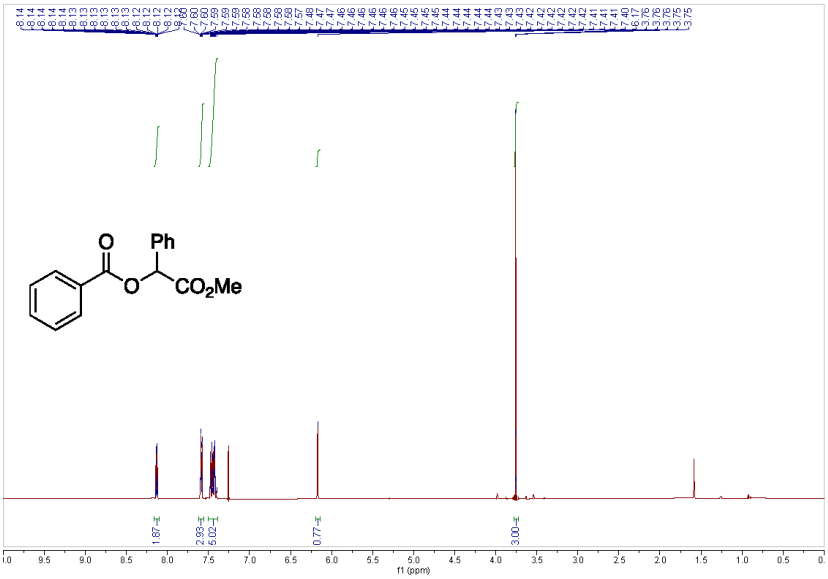

^{13}C NMR (151 MHz, Chloroform-*d*)

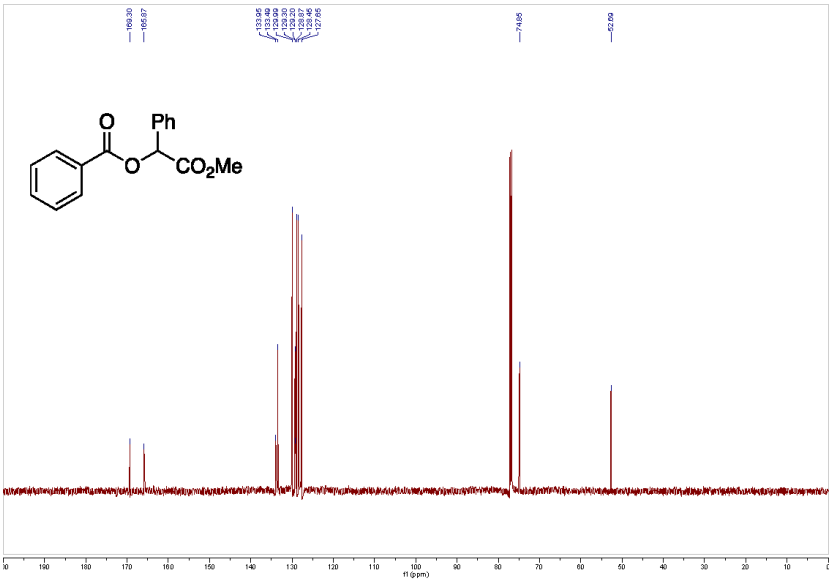

Methyl 2-phenyl-2-(phenylthio)acetate (18)

^{1}H NMR (600 MHz, Chloroform-*d*)

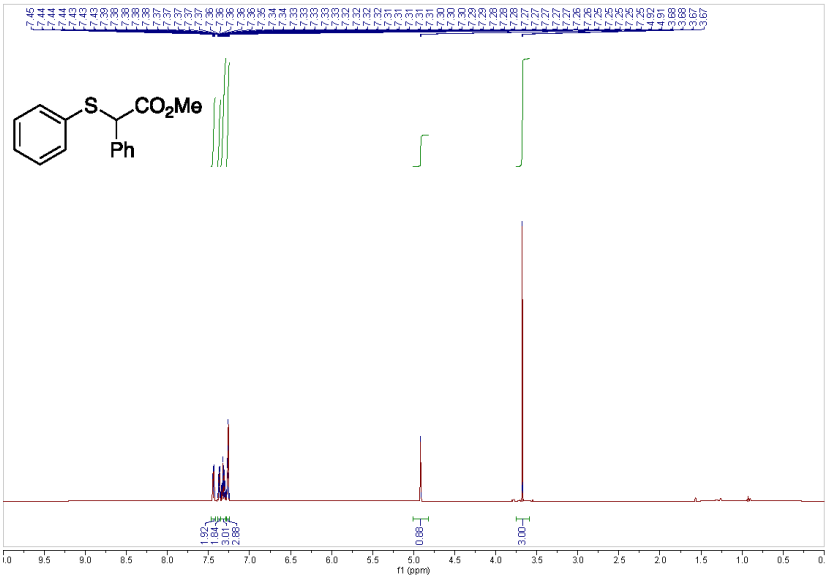

^{13}C NMR (151 MHz, Chloroform-*d*)

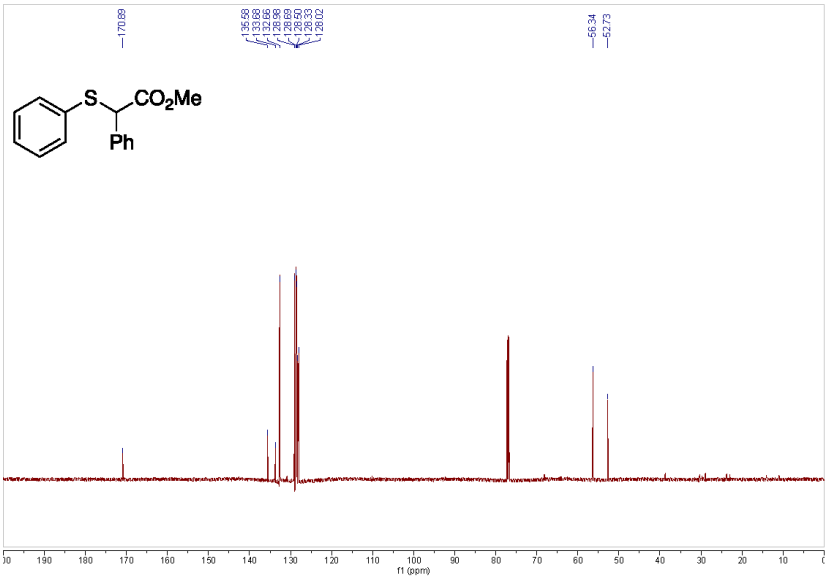

Methyl 2-(dimethyl(phenyl)silyl)-2-phenylacetate (19)

^{1}H NMR (600 MHz, Chloroform-*d*)

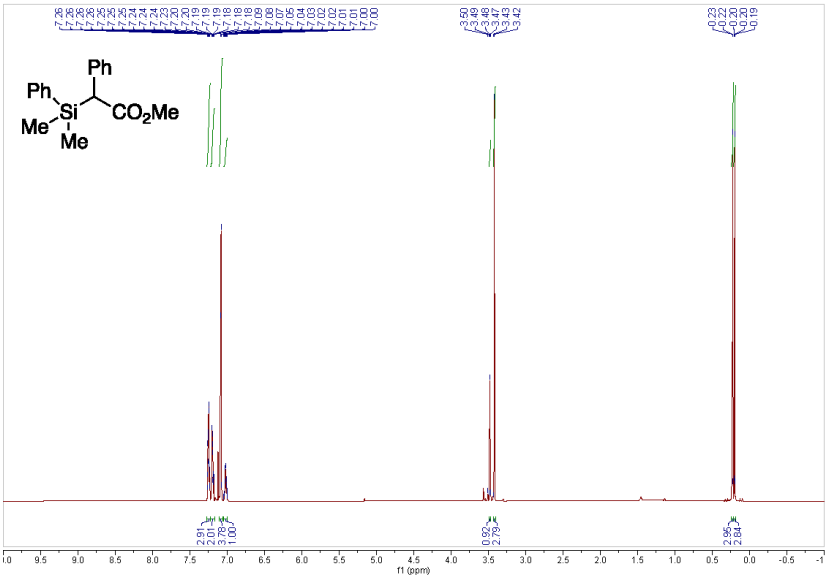

^{13}C NMR (151 MHz, Chloroform-*d*)

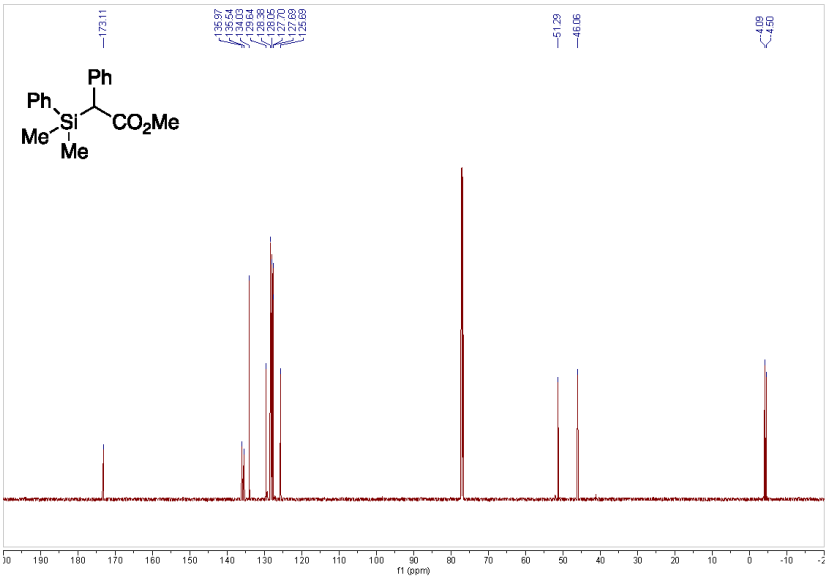

Methyl 2-(methyldiphenylsilyl)-2-phenylacetate (20)

^{1}H NMR (600 MHz, Chloroform-*d*)

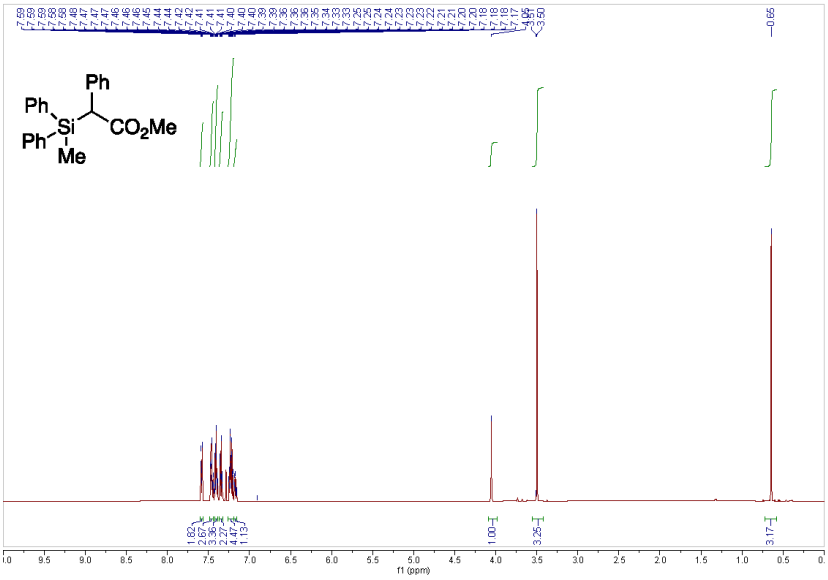

^{13}C NMR (151 MHz, Chloroform-*d*)

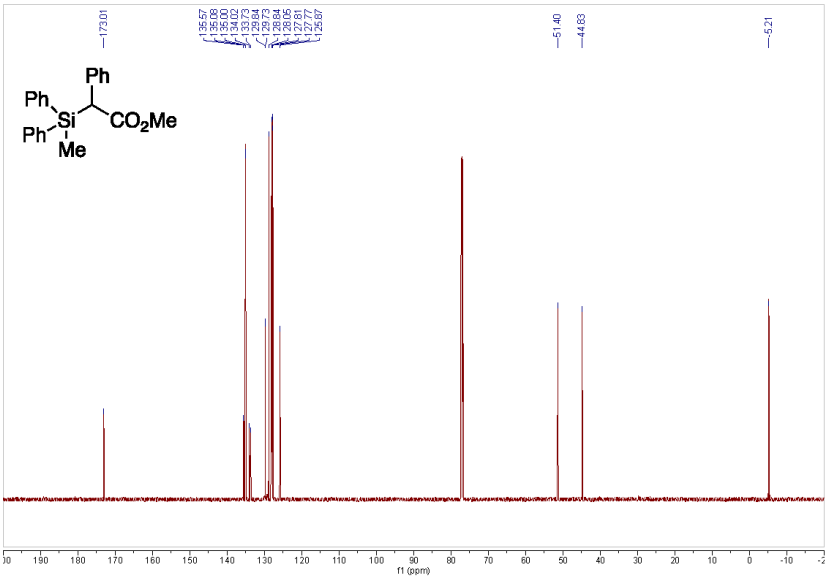

Methyl 2-phenyl-2-(phenylthio)pent-4-enoate (21)

^{1}H NMR (600 MHz, Chloroform-*d*)

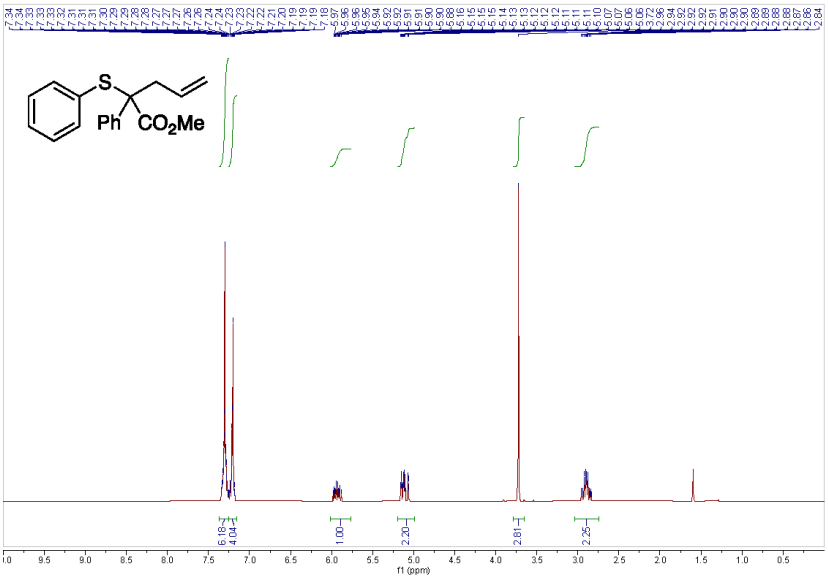

^{13}C NMR (151 MHz, Chloroform-*d*)

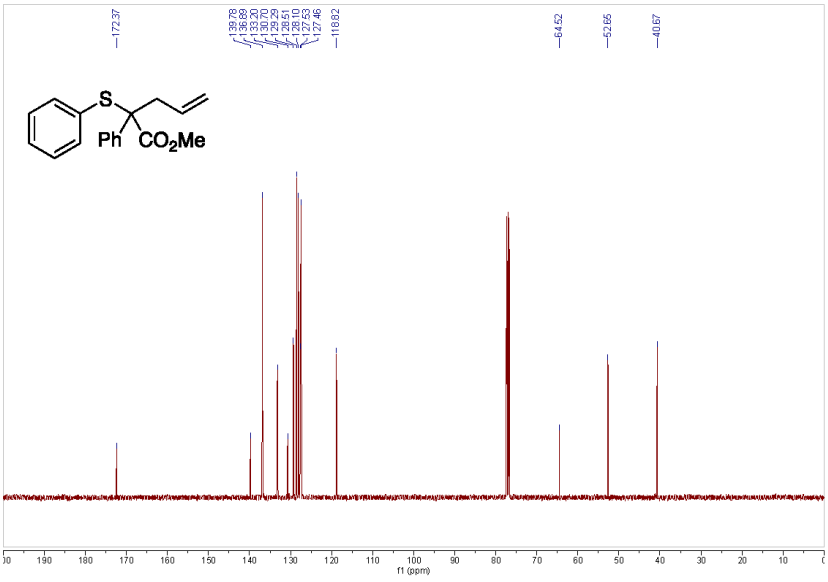

Methyl 2,3-diphenyl-2-(phenylthio)propanoate (22)

^{1}H NMR (600 MHz, Chloroform-*d*)

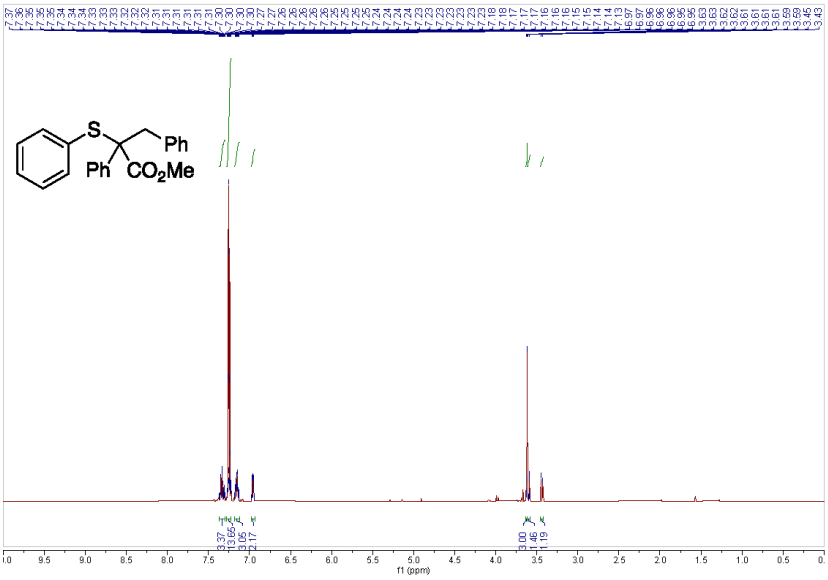

^{13}C NMR (151 MHz, Chloroform-*d*)

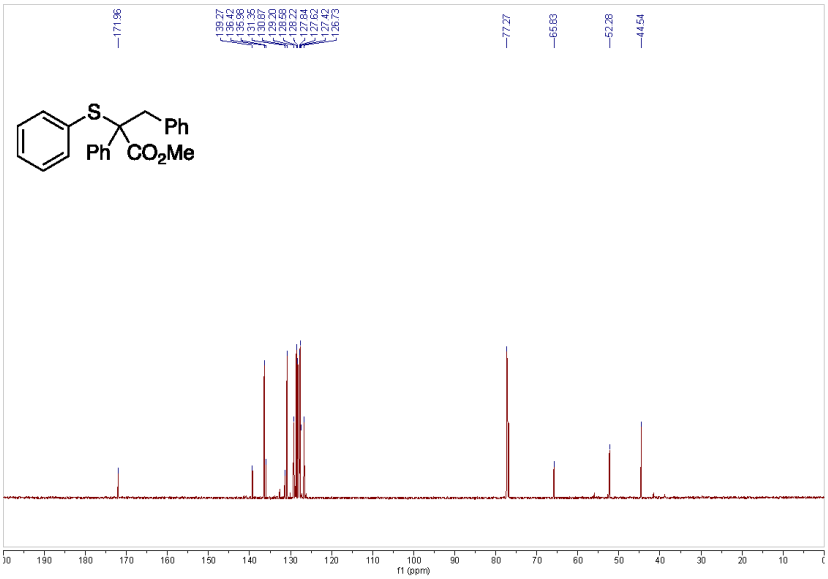

Ethyl 2-(2-(2-methoxy-2-oxoethyl)phenyl)-2-(phenylthio)acetate (23)

^{1}H NMR (400 MHz, Chloroform-*d*)

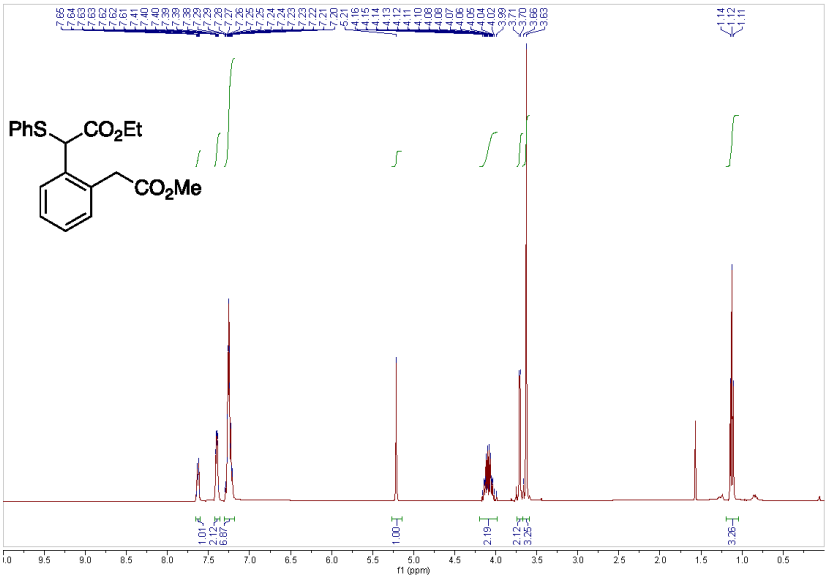

^{13}C NMR (101 MHz, Chloroform-*d*)

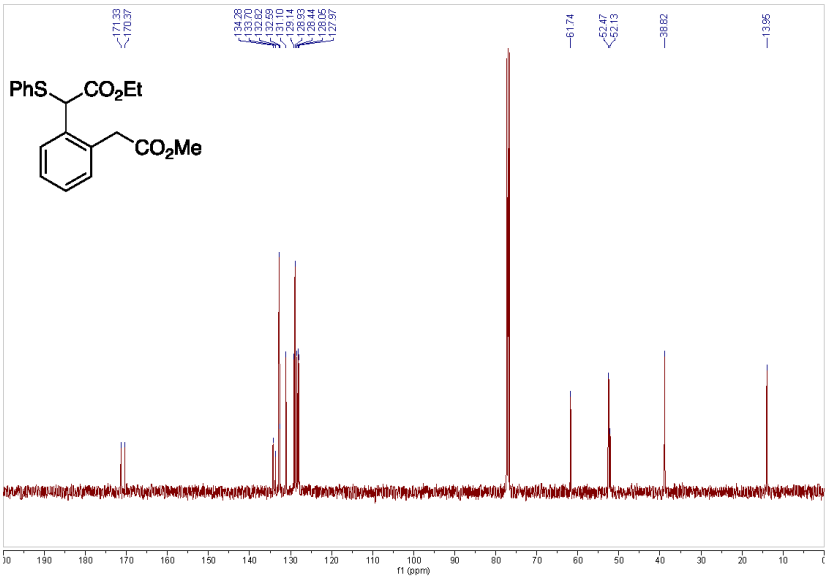

2-Methoxy-2-oxo-1-phenylethyl 2-(4-isobutylphenyl)propanoate (24)

^{1}H NMR (400 MHz, Chloroform-*d*)

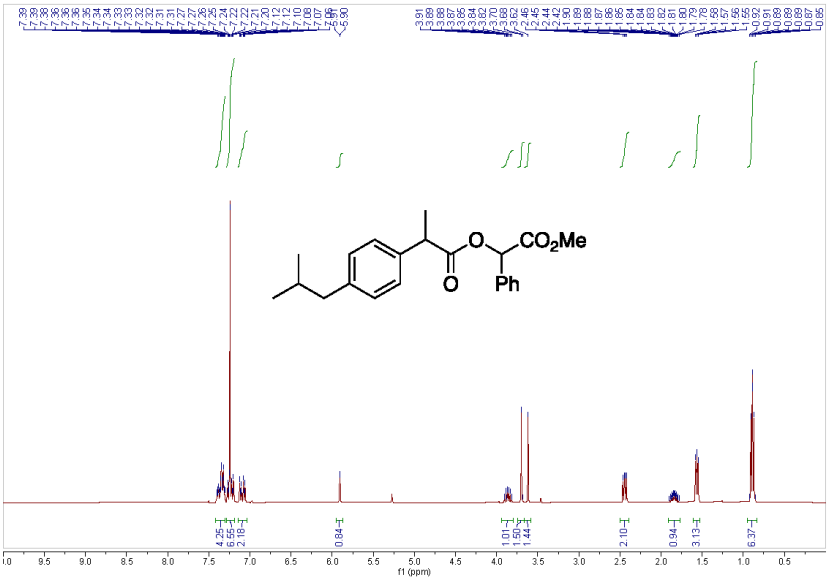

^{13}C NMR (101 MHz, Chloroform-*d*)

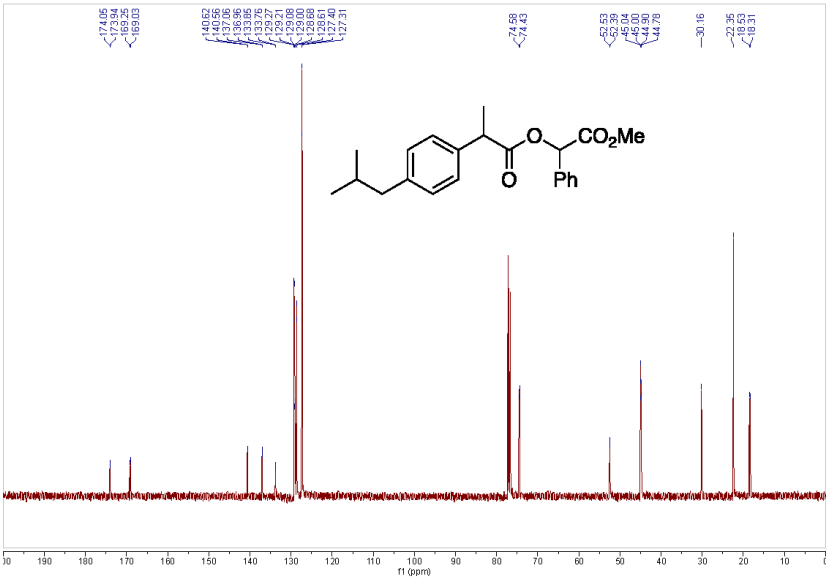

2-Methoxy-2-oxo-1-phenylethyl 2-(6-chloro-9*H*-carbazol-2-yl)propanoate (25)

^{1}H NMR (400 MHz, Acetone)

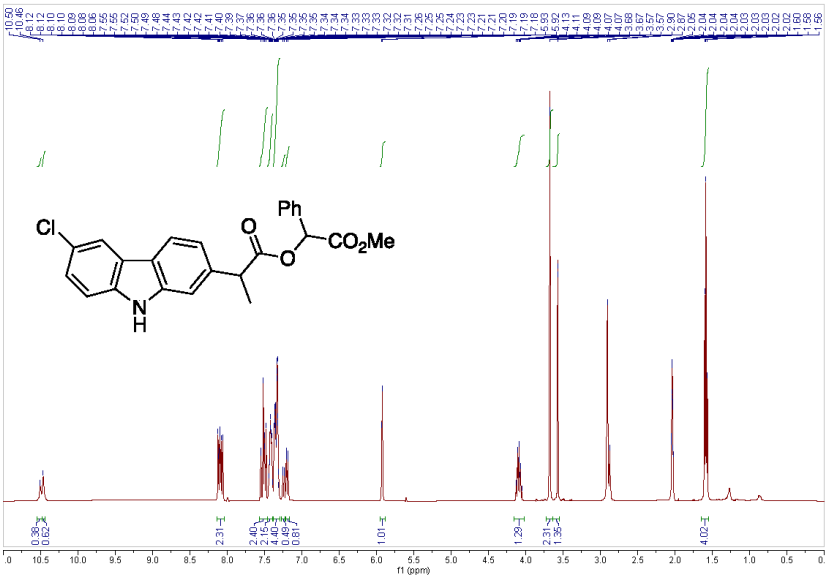

^{13}C NMR (101 MHz, Acetone)

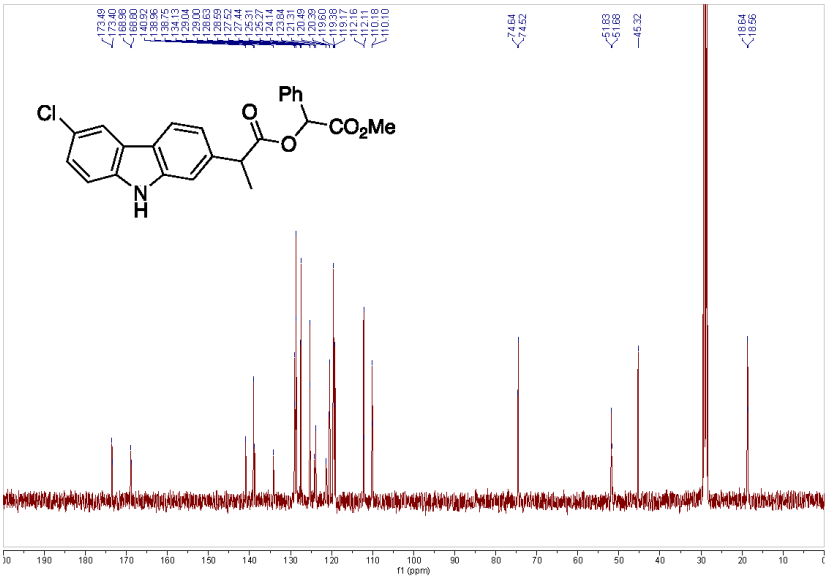

Methyl 2-phenyl-2-(((*R*)-2,5,7,8-tetramethyl-2-((4*R*,8*R*)-4,8,12-trimethyltridecyl) chroman-6-yl)oxy)acetate (26)

^{1}H NMR (400 MHz, Chloroform-*d*)

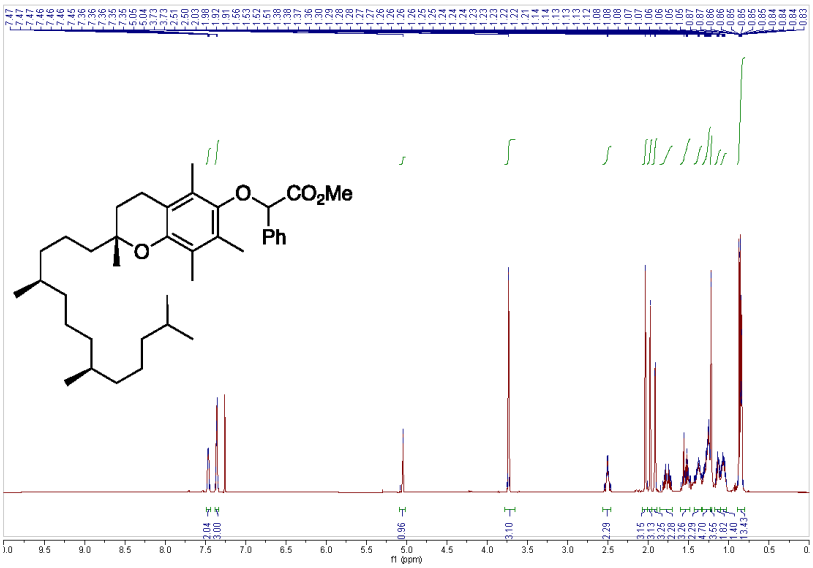

^{13}C NMR (101 MHz, Chloroform-*d*)

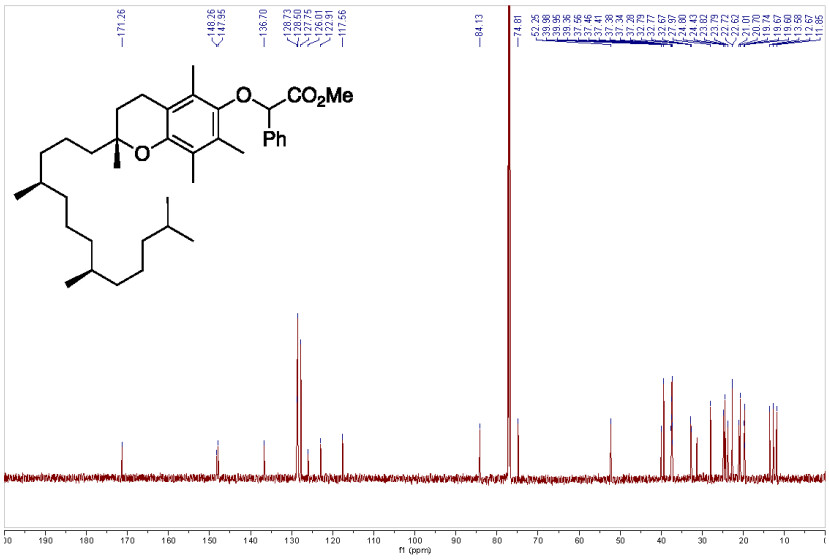

2-Methoxy-2-oxo-1-phenylethyl (2*S*)-2-(6-methoxynaphthalen-2-yl)propanoate (27)

^{1}H NMR (600 MHz, Chloroform-*d*)

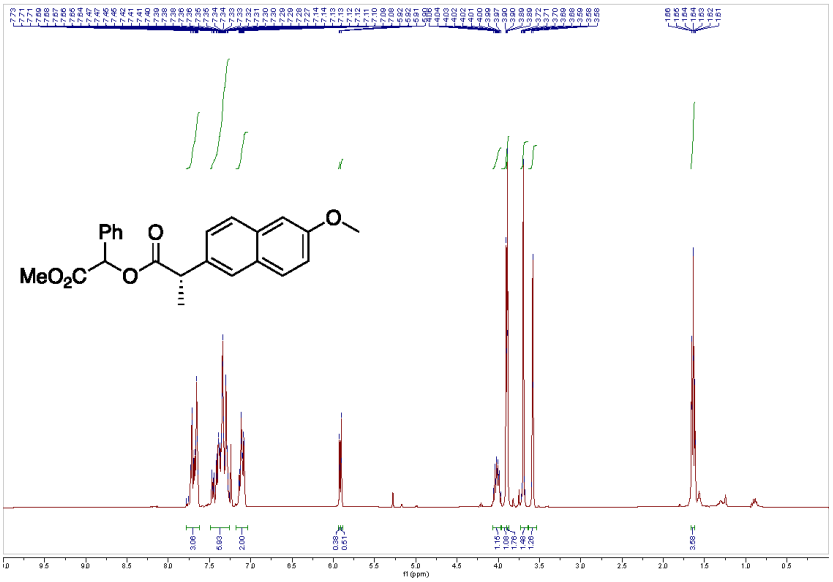

^{13}C NMR (151 MHz, Chloroform-*d*)

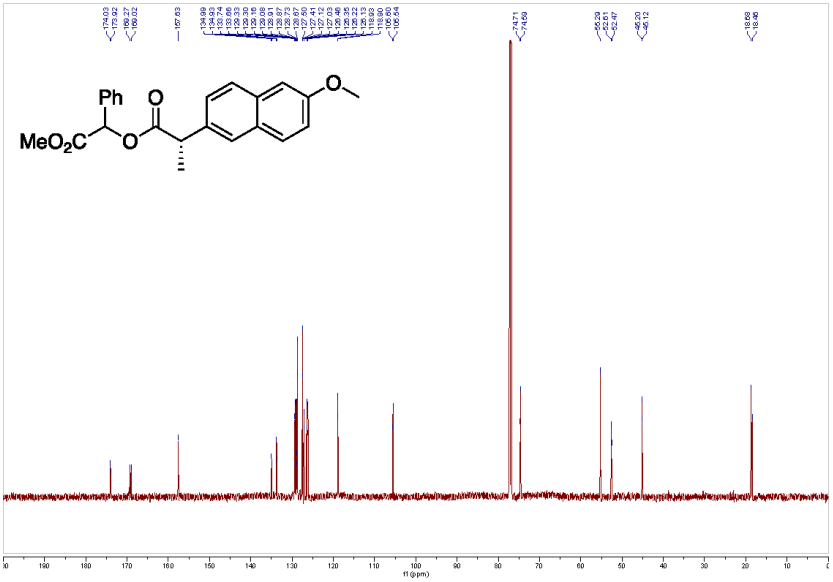

2-Methoxy-2-oxo-1-phenylethyl (*tert*-butoxycarbonyl)-*L*-valinate (28)

^{1}H NMR (600 MHz, Chloroform-*d*)

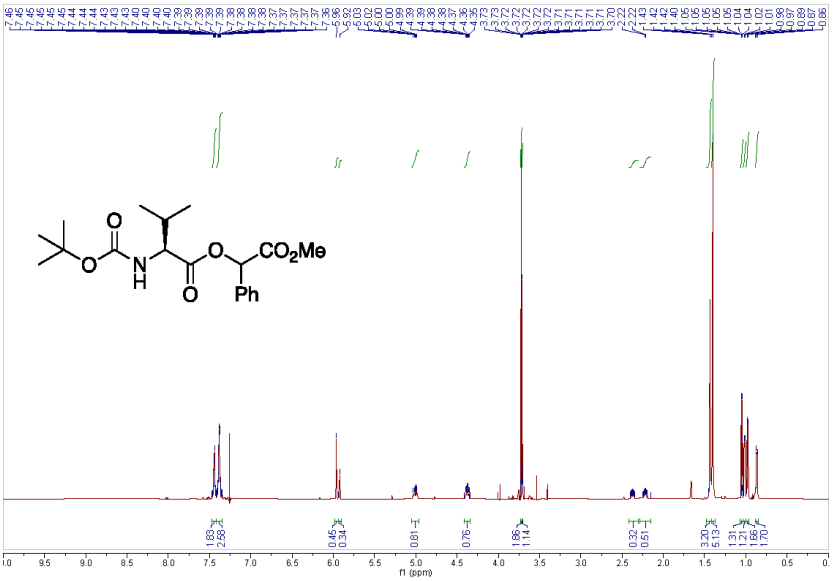

^{13}C NMR (151 MHz, Chloroform-*d*)

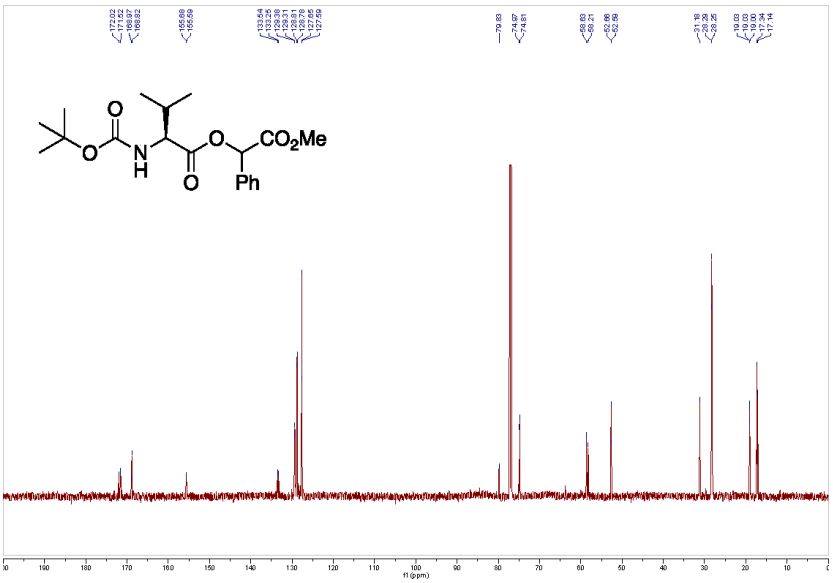

2-Methoxy-2-oxo-1-phenylethyl (9*Z*,12*Z*)-octadeca-9,12-dienoate (29)

^{1}H NMR (600 MHz, Chloroform-*d*)

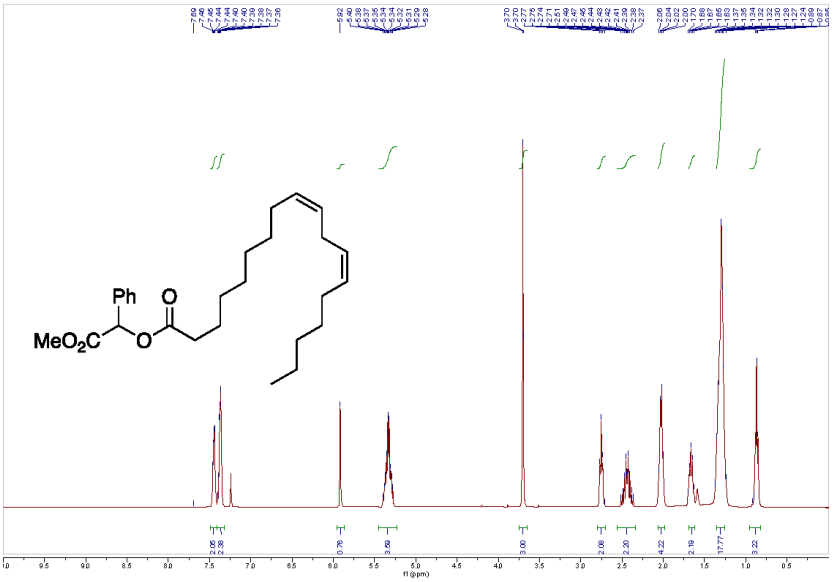

^{13}C NMR (151 MHz, Chloroform-*d*)

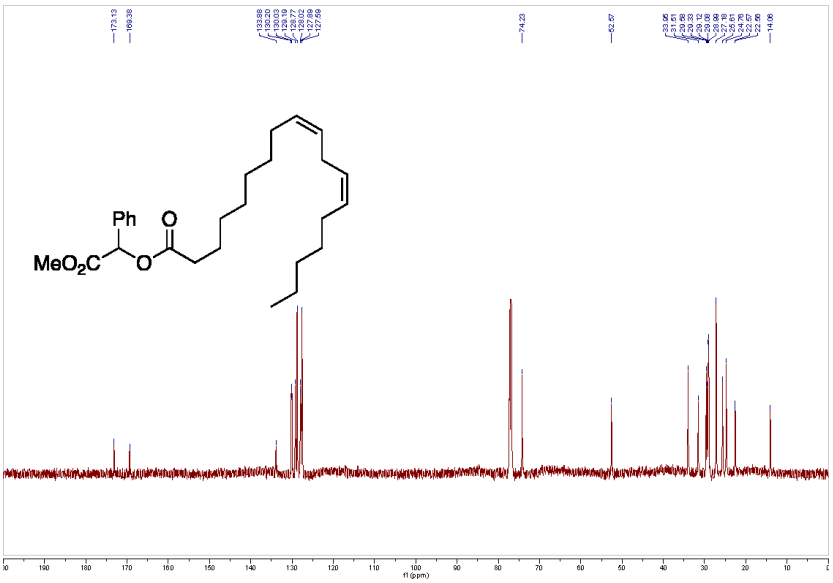

Methyl 2-phenyl-2-((4-(5-(*p*-tolyl)-3-(trifluoromethyl)-1*H*-pyrazol-1-yl)phenyl)sulfonamido)acetate (30)

^{1}H NMR (600 MHz, Chloroform-*d*)

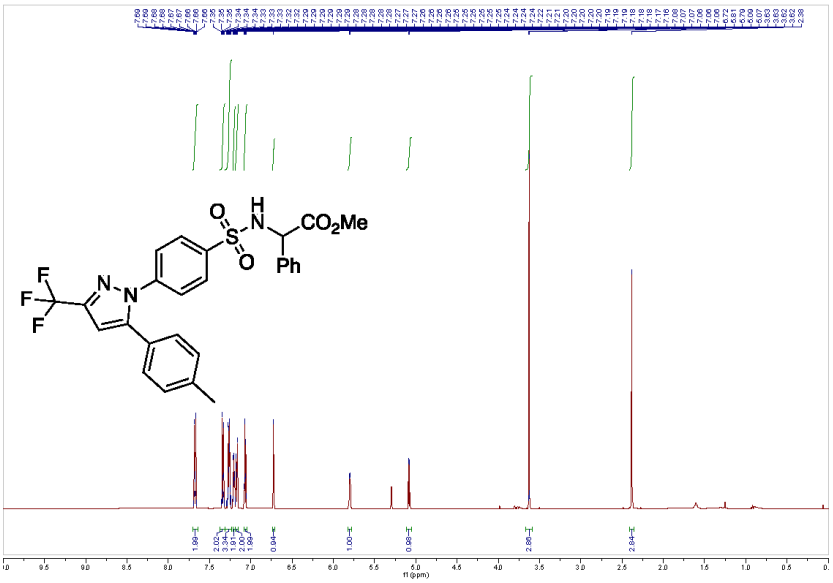

^{13}C NMR (151 MHz, Chloroform-*d*)

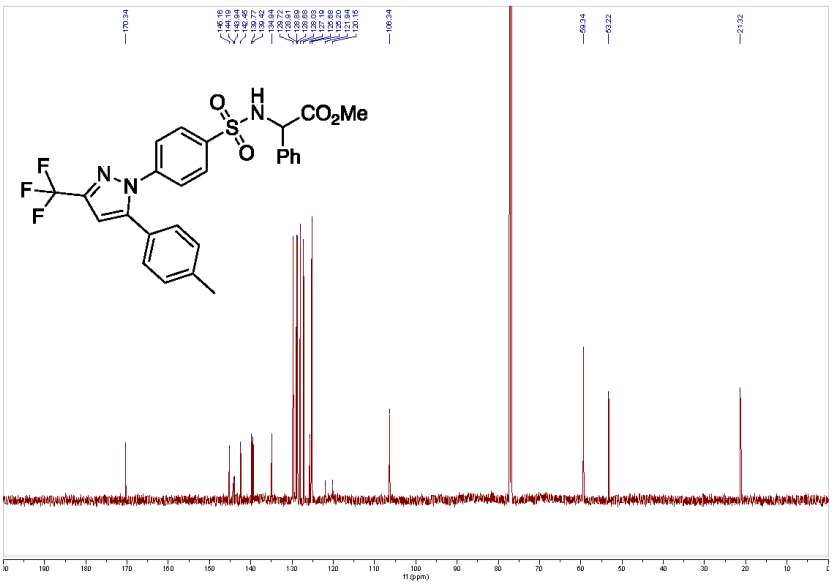

Methyl (4a*R*,4a1*R*,5a*S*,8a*R*,8a1*S*,15a*S*,16*S*)-16-(4-bromophenyl)-10,11-dimethoxy-14-oxo-2,4a,4a1,5,5a,7,8,8a1,15,15a-decahydro-14*H*-6,4-ethanoindolo[3,2,1-*ij*]oxepino[2,3,4-*de*]pyrrolo[2,3-*h*]quinoline-16-carboxylate (33) & Methyl 2-(4-bromophenyl)-2-((4a*R*,4a1*R*,5a*R*,8a*S*,8a1*S*,15a*S*)-10,11-dimethoxy-14-oxo-4a,4a1,5,7,8,8a1,15,15a-octahydro-14*H*-4,6-methanoindolo[3,2,1-*ij*]oxepino[2,3,4-*de*]pyrrolo[2,3-*h*]quinolin-5a(2*H*)-yl)acetate (34)

^{1}H NMR (400 MHz, Chloroform-*d*)

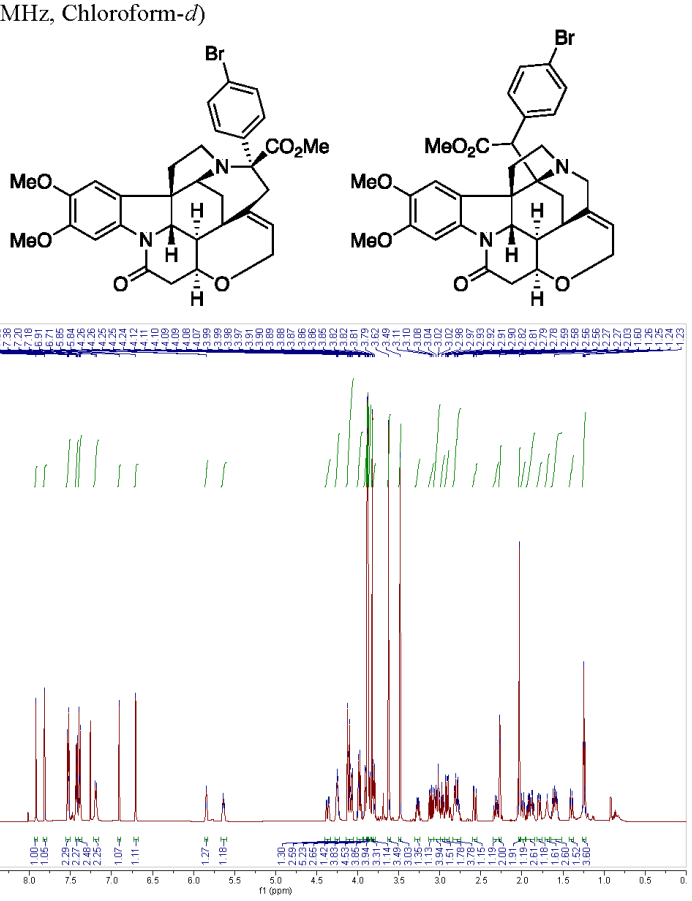

^{13}C NMR (101 MHz, Chloroform-*d*)

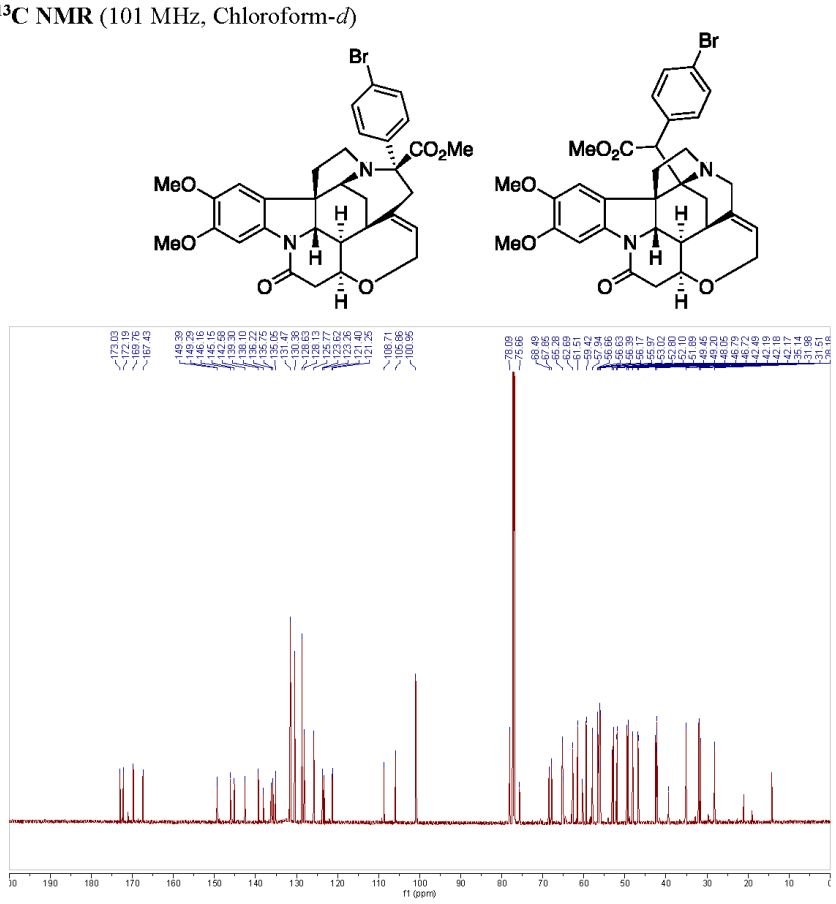

Methyl (4a*R*,4a1*R*,5a*S*,8a*R*,8a1*S*,15a*S*,16*R*)-16-(4-bromophenyl)-10,11-dimethoxy-14-oxo-2,4a,4a1,5,5a,7,8,8a1,15,15a-decahydro-14*H*-6,4-ethanoindolo[3,2,1-*ij*]oxepino[2,3,4-*de*]pyrrolo[2,3-*h*]quinoline-16-carboxylate (35)

^{1}H NMR (400 MHz, Chloroform-*d*)

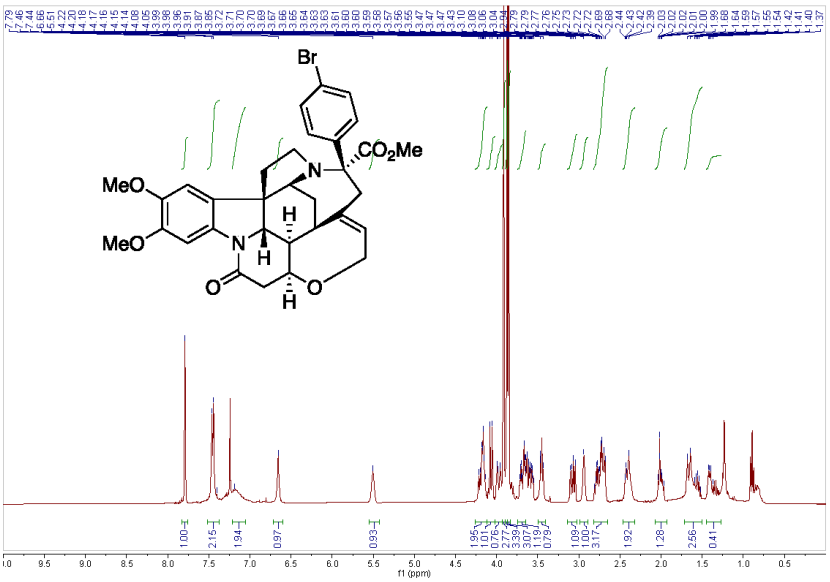

^{13}C NMR (101 MHz, Chloroform-*d*)

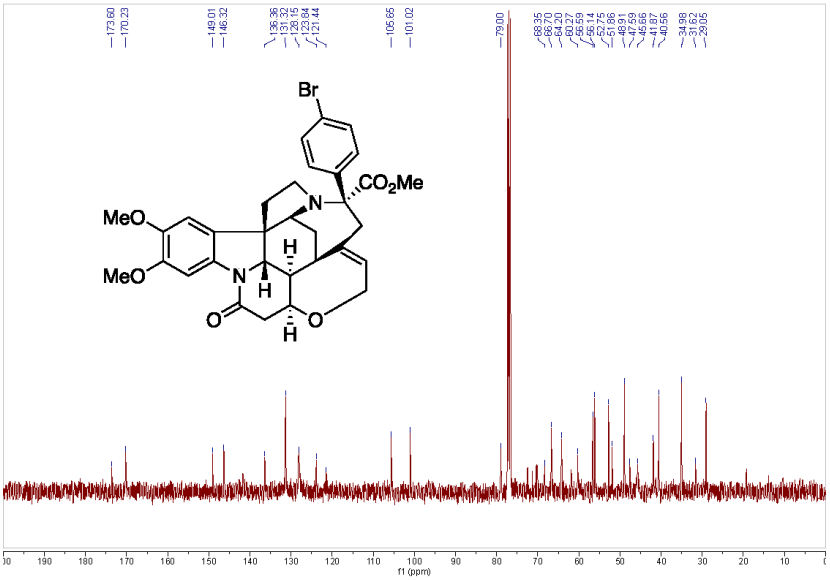

15. References

[1] G. A. Rempel, P. Legzdins, H. Smith, G. Wilkinson, and D. A. Ucko, *Inorg. Synth.,* 1972, **13**, 90-91.

[2] J. Liu, C. Fasel, P. Braga-Groszewicz, N. Rothermel, A. S. L. Thankamony, G. Sauer, Y. Xu, T. Gutmann and G. Buntkowsky, *Catal. Sci. Technol.,* 2016, **6**, 7830-7840.

[3] A. Dasgupta, R. Babaahmadi, B. Slater, B. F. Yates, A. Ariafard and R. L. Melen, *Chem,* 2020, **6**, 2364- 2381.

[4] R. Hommelsheim, Y. Guo, Z. Yang, C. Empel and R. M. Koenigs, *Angew. Chem. Int. Ed.,* 2019, **58**, 1203-1207.

[5] L. Wang, S. Perveen, Y. Ouyang, S. Zhang, J. Jiao, G. He, Y. Nie and P. Li, *Chem. Eur. J.,* 2021, **27**, 5754-5760.

[6] C. Empel, T. V. Nguyen and R. M. Koenigs, *Org. Lett.,* 2021, **23**, 548-553.

[7] H. Keipour, A. Jalba, N. Tanbouza, V. Carreras and T. Ollevier, *Org. Biomol. Chem.,* 2019, **17**, 3098-3102.

[8] F. He, F. Li and R. M. Koenigs, *J. Org. Chem.,* 2020, **85**, 1240-1246.

[9] Z. Yang, Y. Guo and R. M. Koenigs, *Chem. Eur. J.,* 2019, **25**, 6703-6706.

[10] J. He, L. G. Hamann, H. M. L. Davies and E. R. J. Beckwith, *Nat. Commun.,* 2015, **6**:5943.

3.4 Stable Ultramicroporous Metal–Organic Framework with Hydrophilic and Hydrophobic Domains for Selective Gas Adsorption

Diese Arbeit wurde veröffentlicht in

Robert Oestreich[+], Marcus N. A. Fetzer[+], Yifei Zhang, Andreas Schreiber, Alexander Knebel, Markus Suta, Christoph Janiak, Gabriel Hanna and Gündoğ Yücesan, *Angewandte Chemie-International Edition* **2025**, *64*, e202513788.

DOI: 10.1002/anie.202513788; Ref.[97]

[+]Die Autoren haben zu gleichen Anteilen zu dieser Publikation beigetragen.

Kurzzusammenfassung

In dieser Arbeit berichten wir über die thermische und chemische Stabilität und das Gasadsorptionsverhalten des Gemischtliganden-Phosphonat-MOFs [Cu(4,4´-bpy)$_{0.5}$(1,4-NDPAH$_2$)] (TUB41) (bpy = Bipyridin und NDPAH$_4$ = Naphthalindiphosphonsäure). TUB41 zeigt bemerkenswerte chemische Stabilität über einen weiten pH-Bereich (1-11). Es behält seine strukturelle Integrität über zwei Jahre mit wiederholten Adsorptionszyklen und Aktivierung bei 80 °C sowie Umgebungsluftfeuchtigkeit. Kryogene Adsorptionsexperimente zeigen, dass die Poren von TUB41 selektiv Gase mit größerem kinetischem Durchmesser, wie N_2 and Ar, ausschließen, aber zugänglich für kleinere Moleküle wie CO_2 and H_2O bei höheren Temperaturen sind. Die Adsorptionsenthalpie für CO_2 ist −41 kJ/mol bei einer Beladung von 0.01 mmol/g und für H_2O −38 kJ/mol bei einer Beladung von 0.7 mmol/g, was starke attraktive Wechselwirkungen mit TUB41 zeigt. Molekulardynamik-Simulationen legen nahe, dass die CO_2-Moleküle geordnete Positionen in den zentralen hydrophoben Regionen einnehmen, geleitet durch starke nichtbindende Interaktionen, wohingegen die H_2O-Moleküle bevorzugt an die hydrophilen SBUs binden. Analysen der mittleren quadratischen Verschiebung bestätigen, dass beide Gase in den Poren räumlich beschränkt werden. Diese Ergebnisse zeigen, dass TUB41 ein chemisch robustes und hochselektives MOF ist, mit potenziellen Anwendungen in Gastrennung, photokatalytischer Wasserspaltung und CO_2-Reduktion unter herausfordernden Bedingungen.

Anteile an der Publikation:

- Gassorptionen und optische Messungen wurden von Robert Oestreich in Zusammenarbeit mit Christoph Janiak und Markus Suta durchgeführt.
- Die Synthese des Linkers und die Synthese von TUB41 wurden von Marcus N. A. Fetzer durchgeführt.
- PXRD-Messungen, REM-Aufnahmen und Stabilitätstests wurden von Marcus N. A. Fetzer durchgeführt.
- Yifei Zhang hat die MD-Simulationen in Zusammenarbeit mit Gabriel Hanna durchgeführt.
- Andreas Schreiber hat Adsorptionsmessungen durchgeführt.
- Alexander Knebel hat die *in situ* temperaturvariablen PXRD-Messungen durchgeführt.
- Gündoğ Yücesan hat in Zusammenarbeit mit allen Autoren die den Autoren entsprechenden Abschnitte im Manuskript geschrieben.

GDCh Research Article Angewandte International Edition Chemie www.angewandte.org

How to cite: *Angew. Chem. Int. Ed.* **2025**, *64*, e202513788
doi.org/10.1002/anie.202513788

Metal-Organic Frameworks

Stable Ultramicroporous Metal–Organic Framework with Hydrophilic and Hydrophobic Domains for Selective Gas Adsorption

Robert Oestreich[+], *Marcus N. A. Fetzer*[+], *Yifei Zhang, Andreas Schreiber, Alexander Knebel, Markus Suta, Christoph Janiak,* Gabriel Hanna,* and Gündoğ Yücesan**

Abstract: Herein, we report the thermal and chemical stability, and the gas adsorption behavior, of a mixed-linker phosphonate MOF, [Cu(4,4′-bpy)$_{0.5}$(1,4-NDPAH$_2$)], namely TUB41 (where bpy = bipyridine and NDPAH$_4$ = naphthalenediphosphonic acid). TUB41 demonstrates remarkable chemical stability across a wide pH range (1–11) and retains its structural integrity after 2 years of repeated adsorption cycles and activation at 80 °C under ambient humidity. Cryogenic adsorption experiments reveal that TUB41's pores selectively exclude gases with larger kinetic diameters, such as N_2 and Ar, while accommodating smaller molecules like CO_2 and H_2O at elevated temperatures. The enthalpies of adsorption for CO_2 at a loading 0.01 mmol g^{-1} and H_2O at a loading of 0.7 mmol g^{-1} are −41 and −38 kJ mol^{-1}, respectively, reflecting their strongly attractive interactions with TUB41 under different conditions. Molecular dynamics simulations reveal that CO_2 molecules adopt ordered arrangements in the central hydrophobic regions of the pores, guided by strong nonbonding interactions, while H_2O molecules preferentially bind to the hydrophilic secondary building units. Mean-squared displacement analyses confirm that both gases remain spatially constrained within the pores. These findings highlight TUB41 as a chemically robust and highly selective MOF, with potential for applications in gas separation, photocatalytic water splitting, and CO_2 reduction under challenging conditions.

Introduction

Metal–organic frameworks (MOFs) have evolved as one of the most studied material classes with a wide range of potential industrial applications in medicine, food chemistry, catalysis, energy storage, and many others.[1–4] For each application, MOFs must possess unique chemical and thermal stabilities suitable for the desired application. For example, biodegradability is an essential requirement for MOFs to be used for applications such as drug delivery,[5–9] while MOFs intended for use in batteries, supercapacitors, electrocatalysis (including hydrogen evolution and oxygen evolution reactions), CO_2 capture, and water harvesting must demonstrate sufficient stability to survive in the presence of electrolytes, water, and acidic or basic environments.[10] Despite the rich structural diversity of MOFs and their vast potential applications,[2] there still is only a handful of MOFs in the literature, which are considered to be stable in the presence of water, acids, bases, and electrolytes.[11,12] Notably, UiO-66, which is known for its exceptional stability, has a shelf lifetime of ca. 2 months at room temperature and ambient humidity.[13,14] Therefore, the development of highly stable MOFs would finally open the way towards the wide-spread industrial use of MOFs. The secondary building units (SBUs) of conventional carboxylate MOFs are usually composed of water-labile metal carboxylate clusters, including Zr(IV) carboxylate clusters (as in UiO-66), which limit conventional MOF applications in aqueous media.[14] Furthermore, the CO_2 adsorption process also generates an acidic environment, which is challenging for conventional MOFs to survive for a

[*] R. Oestreich[+], M. N. A. Fetzer[+], C. Janiak, G. Yücesan
Institute for Inorganic and Structural Chemistry, Heinrich Heine University Düsseldorf, Universitätsstr. 1, D-40225 Düsseldorf, Germany
E-mail: janiak@hhu.de
guendog.yuecesan@hhu.de

M. Suta
Inorganic Photoactive Materials, Institute for Inorganic and Structural Chemistry, Heinrich Heine University Düsseldorf, Universitätsstr. 1, 40225 Düsseldorf, Germany

A. Schreiber
Microtrac Retsch GmbH, Retsch-Allee 1–5, D-42781 Haan, Germany

A. Knebel
Otto Schott Institute of Materials Research, Center for Energy and Environmental Chemistry II, Friedrich Schiller University Jena, Lessingstraße 12–14, D-07743 Jena, Germany

A. Knebel
Center for Energy and Environmental Chemistry, Friedrich Schiller University Jena, Philosophenweg 7a, D-07743 Jena, Germany

Y. Zhang, G. Hanna
Department of Chemistry, University of Alberta, Edmonton, Alberta, Canada
E-mail: gabriel.hanna@ualberta.ca

[+] Both authors contributed equally to this work.

Additional supporting information can be found online in the Supporting Information section

long period of time.[15] Phosphonic acid-based MOFs provide a promising route to achieving stability in acidic media.[16] Compared to conventional metal-binding functional groups, phosphonic acids are very robust organic linkers that survive in the presence of concentrated acids, and the P–C bond is known to be stable in the presence of UV-light and at high temperatures.[17,18] The formation of insoluble metal phosphonate SBUs is advantageous because it enhances the structural stability of the MOF in aqueous environments, unlike metal acetate SBUs, which are typically water-soluble and prone to degradation.[17,19,20]

While significant progress has been made in developing amine-functionalized MOFs for CO_2 capture via chemisorption (where CO_2 forms covalent bonds with amine groups), physisorptive capture remains a greater challenge.[15] This is largely due to the intrinsic hydrophilicity of many MOFs, which are often constructed from organic linkers bearing polar functional groups and SBUs that interact favorably with water vapor.[21] Although physisorption is technically simpler and more energy-efficient than chemisorption, especially when employing pressure swing adsorption, achieving selective CO_2 uptake in the presence of humidity has proven difficult.[22] Only a few MOFs have been reported to exhibit CO_2 selectivity under humid conditions.[15] Among them, CALF-20 shows promising performance at 10% RH but loses selectivity entirely at 40% RH.[15] Moreover, its chemical stability was tested only under gas-phase conditions in the original study. While amine-based systems and frameworks like MOF-74 demonstrate high CO_2 capacities, their chemical instability under humid or acidic/basic aqueous conditions severely limits practical applications.[23–27] Some well-studied MOFs, such as MOF-74 and DEF-2, decompose rapidly in air, and others lack reported stability data altogether.[23,25] Most chemical stability tests for CO_2-adsorbing MOFs rely on repeated adsorption-desorption cycles. As summarized in several review articles, only a few MOFs have demonstrated exceptional long-term stability in various chemical media. Notable examples include MIL-100(Cr), which remains stable in water for up to one year; $Ni(BTP)_2$, which retains its structural integrity for 14 days across a wide pH range (2 to 14); and ZIF-8, which is stable for 7 days in boiling organic solvents and water, and for 24 h in boiling NaOH.[11,28] One approach to overcoming this limitation involves designing chemically stable MOFs with unconventional organic linkers containing phosphonic acid functional groups.[29–31] These groups form strong coordination bonds with metal ions, leading to the formation of water-insoluble metal phosphonate SBUs that are highly resistant to hydrolysis in acidic/basic media.[29,31] Such MOFs offer a promising route towards physisorptive CO_2 capture that remain stable and selective in humid environments.

Our group and others have reported the stability of phosphonate MOFs in harsh environments, including strong acids, bases, and even aqua regia, making them highly promising candidates for diverse applications such as electrocatalysis, energy storage, and sequestration of greenhouse gases.[17,30–32] Additionally, our investigations into hydrogen-bonded organic frameworks (HOFs) and polyphosphonate covalent organic frameworks (COFs) constructed from phosphonic acids have shown exceptional stability in humid environments during and after proton conductivity experiments.[33–36] Although the short-term chemical stability of phosphonate MOFs is well-documented, their long-term stability over extended periods has, to the best of our knowledge, not been reported in the literature. It has been also shown that metal phosphonates might be electrically conductive.[4,37,38] Despite their inherent chemical stability and promising potential for applications in gas storage, energy storage, and catalysis, phosphonate MOFs remain relatively underexplored. Their development is largely hindered by the limited commercial availability of arylphosphonic acid linkers and fundamental phosphonate precursors.[29] Overcoming these challenges is essential for advancing the design of sustainable MOF families capable of operating in harsh chemical environments.

In this work, we focus on naphthalene as a linker core, which is a hydrophobic and polyaromatic moiety to create MOFs that could capture CO_2.[33] Previously, we published a structural report on TUB41, a mixed-linker MOF utilizing 1,4-naphthalenediphosphonic acid (1,4-NDPAH_4) and 4,4′-bipyridine (4,4′-bpy) (see Figure 1a).[39] However, due to its very low yield, we were not able to work on its applications previously. In this work, we synthesized TUB41 hydrothermally as a single product phase in high yield, and thus were able to study its chemical/thermal stability. Furthermore, since TUB41 has narrow and largely hydrophobic pores, which are suitable for sequestering molecules with small kinetic diameters (e.g., CO_2 and H_2O), we studied its ability to capture CO_2 and H_2O. Notably, TUB41 was found to have a shelf lifetime of beyond 2 years after repeated gas adsorption experiments and activation at 80 °C under vacuum, which is a major improvement over the 2 months for conventional carboxylate-based MOFs such as UiO-66.

In more detail, as shown in Figure 1b, TUB41 has a rod-shaped SBU composed of typical eight-membered Cu-O-P-O-Cu-O-P-O rings observed in phosphonate MOFs, which are bridged by the square pyramidal Cu(II) atoms. The hydrogen bonding between the Cu(II)-coordinating phosphonate groups defines the final shape of the SBU and provides a hydrophilic character to the SBU. The hydrophilic SBUs with hydrogen bonds are surrounded by hydrophobic naphthalene moieties, hypothetically limiting the noncovalent interactions of the SBU with hydrophilic gases and generating a more preferable environment for gases such as CO_2. Recently, MOF research has focused on frameworks with narrow pores to enhance gas adsorption selectivity.[40] The combination of narrow pores and a pronounced hydrophobicity in TUB41, along with its thermal and chemical stability, makes it highly desirable for the development of industrial MOF applications that can selectively capture or separate gases such as CO_2 in the presence of H_2O.[41,42]

Chemical Stability of TUB41

The crystals of TUB41 were reproduced in Fall 2022. Chemical stability tests on TUB41 were performed by suspending

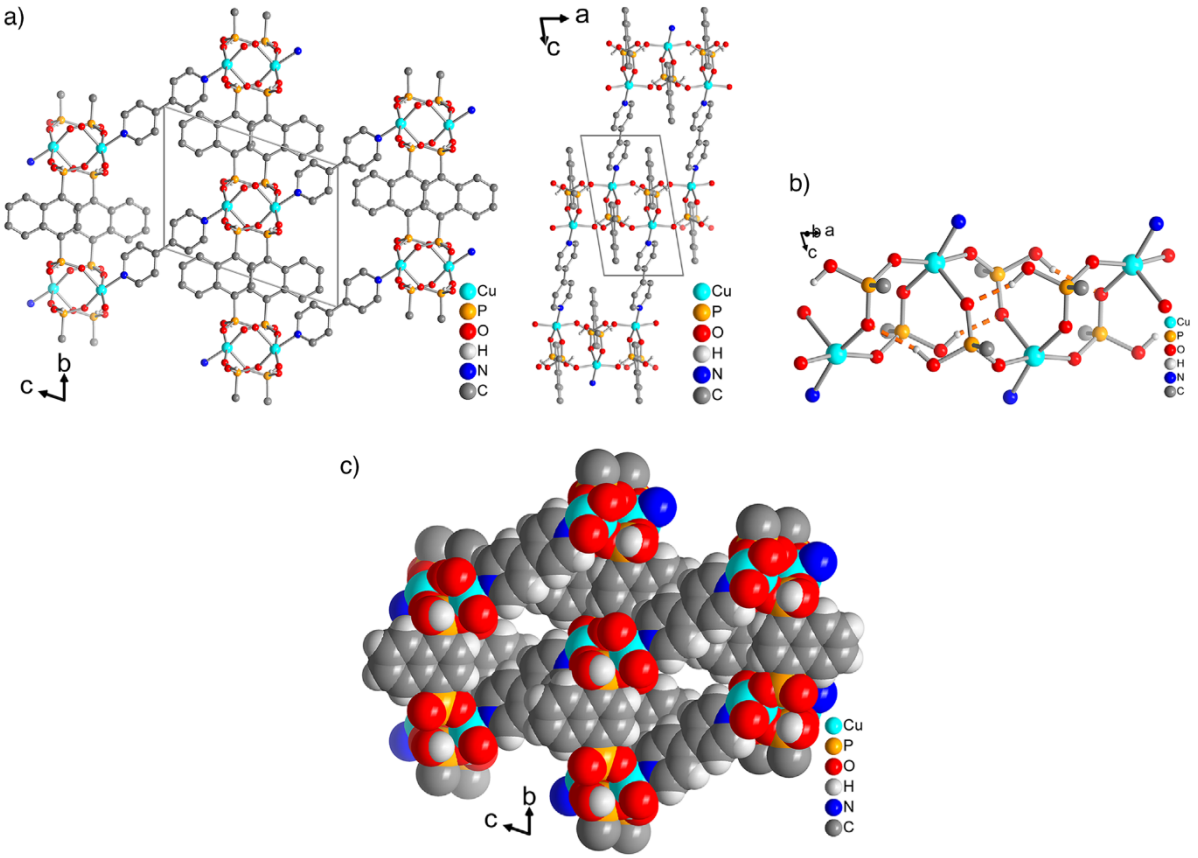

Figure 1. a) Section of the packing in the crystal structure of TUB41 along two different viewing directions (hydrogen atoms on carbon are omitted for clarity). b) SBU of TUB41 running along the *a* direction, showing the hydrogen bonds between the phosphonate groups. c) Space-filling representation to visualize the small ~4 × 2 Å^2 cross section of the slit-shaped channels along the *a* axis (cf. Figure S18 for a grid scale).

TUB41 crystals in aqueous HCl and NaOH solutions ranging in pH between 1 and 13 for 2 h. In addition, TUB41 samples were left in the hydrothermal reaction mixture (an aqueous medium of pH 2.5) for ca. 1 month before the purification of the crystals, pointing to its stability. As depicted in Figure 2a, the powder X-ray diffraction (PXRD) patterns of the acid- and base-treated samples of TUB41 retain their structures between pH 1 and pH 11 after 2 h, highlighting its stability in acidic and basic environments for this period of time. The sample treated at pH 13 starts to decompose, although it retains some of its original PXRD pattern. At this pH, it predominantly converts into CuOH species, indicating relatively slow decomposition. In addition, TUB41 was synthesized in Parr acid digestion reaction vessels in distilled water at pH 1.5 (pH 2.5 after the reaction) and 120 °C for 48 h, which also points to the intrinsic chemical stability of TUB41 in an acidic environment. As shown in Figure 3, the SEM images reveal that the crystals largely retain their morphology after 2 years of repeated adsorption experiments and storage under room temperature and ambient humidity conditions.

Thermal Stability of TUB41

To understand the thermal behavior of TUB41, we initially performed PXRD of samples that were heated up to 300 °C for 1 h periods, and collected the PXRD data after cooling them to room temperature (Figure 2b). Phosphonic acids condense at high temperatures to make P—O—P bonds, potentially leading to a crystalline metal polymeric framework at ca. 300 °C.[36] This is suggested by the MS-TGA results, which show that water evaporation gradually occurs above ca. 250 °C (see Figure 5 and Section 4).

To gain insight into the stability of the material after several years of cycling, we performed in situ variable temperature powder X-ray diffraction (VT-PXRD) on 2 year old crystals, which were repeatedly used in CO_2 and water vapor adsorption experiments (~20 cycles in total) and heated up to 330 °C. As can be seen in Figure 4a, the PXRD pattern remains very similar to the original phase until 330 °C, although some minor phase transformations can be observed. The phase transformation and thermal stability of the compound is better observed in contour plots of

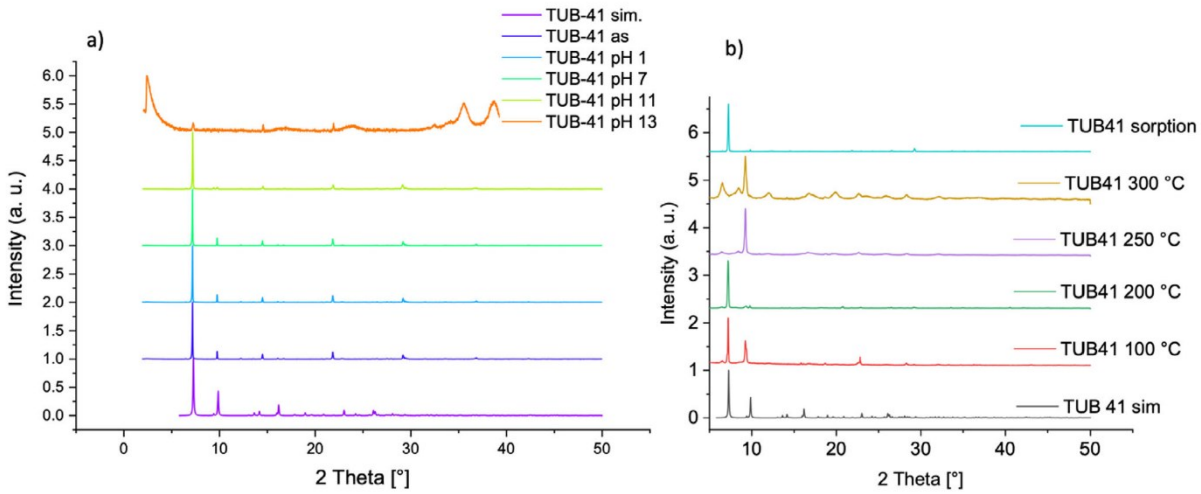

Figure 2. PXRD (Cu K_α radiation) of TUB41 at a) different pH's and b) different temperatures after adsorption experiments.

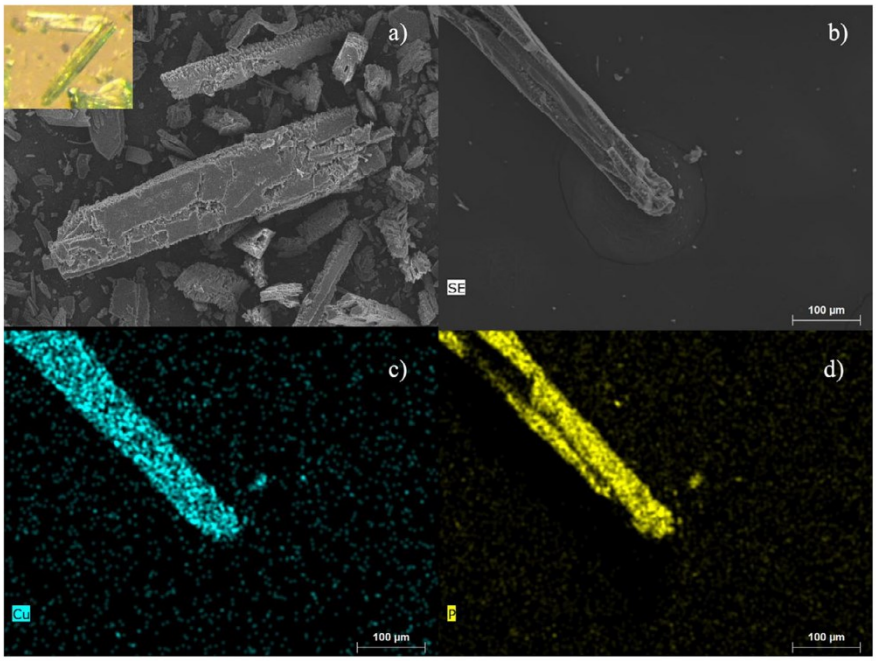

Figure 3. SEM pictures of TUB41 after adsorption experiments. Crystals of TUB41 are shown in panels a) and b), and the corresponding elemental mappings for Cu and P are shown in panels c) and d), respectively.

TUB41 in Figure 4b, with the dark areas showing crystalline, consistent Bragg reflections with varying intensity continuing until 330 °C. The most interesting reflex is observed at $2\theta = 7.2°$, which splits into two peaks above 120 °C and reverts to one peak above 250 °C, demonstrating the strongest phase transformation. Between 14° and 25°, many smaller but observable transformations occur. At $2\theta = 14.4°$, 20.5°, 21.8°, and 22.4°, reflections are sharpening from temperatures above 80 °C, demonstrating higher crystallinity of the sample until 330 °C (see Figure 4b). We previously summarized the conformational changes in flexible rod-shaped SBUs observed in phosphonate MOFs.[16] The observed phase transitions might be a result of the reversible conformational changes in the Cu–O–P–O–Cu–O–P–O rings up to 250 °C. Due to the observed condensation above 250 °C, the crystal data becomes more stable with the formation of new peaks and retains the major patterns observed at low temperatures (see Figures 2, 4 and 5). As depicted in Figure 1b, the

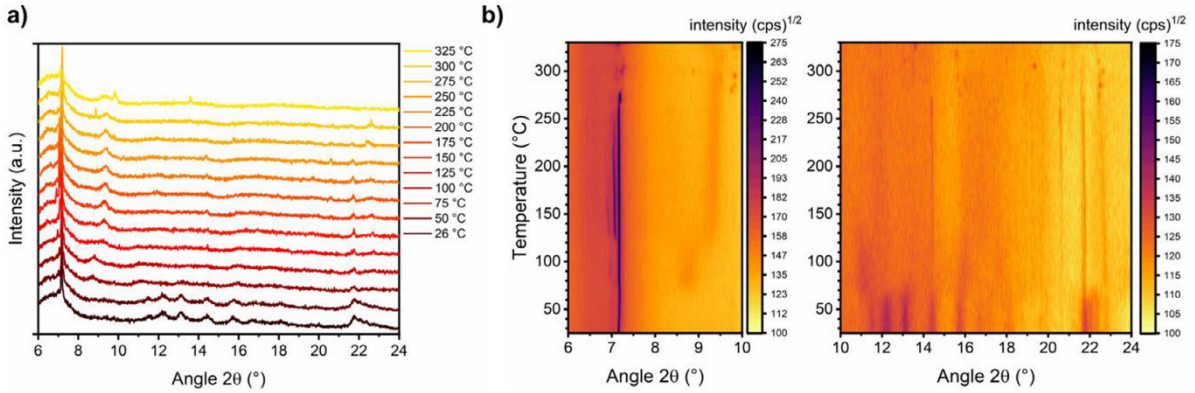

Figure 4. a) In situ VT-PXRD (Cu K_α radiation) in a staggered plot until 330 °C, showing no drastic changes in the patterns over a long 2θ range. b) Contour plots of TUB41 from 25–330 °C using square-root scaling of the intensity, allowing us to better follow changes in crystallinity and phase transformations. The dark areas correlate 2θ values to observed high intensity of reflections.

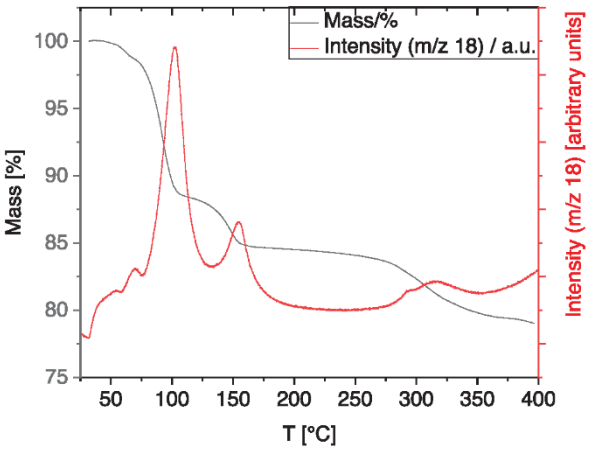

Figure 5. MS-TGA measurements in synthetic air for TUB41.

rod-shaped SBU of TUB41 has repeating hydrogen bonds between the mono-deprotonated phosphonate-based hydrogen atom and Cu(II)-coordinated phosphonate oxygen atoms. The thermal flexibility of TUB41 might be originating from the breaking and reforming of the hydrogen bonds leading to multiple SBU conformations and phase transitions at different temperatures.

MS-Coupled Thermogravimetric Analysis

We performed MS-coupled thermogravimetric analysis (MS-TGA) to understand the thermal behavior of TUB41 (see Supporting Information for instrumental details). As depicted in Figure 5, the MS-TGA results show two distinct steps of mass loss, occurring at around 100 °C (11.5 %) and around 150 °C (3.5%), which is identified as loss of water. After ca. 250 °C, decomposition is observed, which is accompanied by a loss of water, probably due to the condensation of phosphonic acid groups.[36,43] This transition is also confirmed by the in situ temperature variable PXRD showing peaks after 200 °C, and more intensely after keeping the TUB41 crystals at 250 and 300 °C for a longer period of time (see Figure 2b). At 400 °C, still more than 75 mass% of the sample remains, indicating appreciable thermal stability of the organic linker molecules. However, the structure has potentially changed to a less crystalline phase after condensation of the phosphonic acids, according to the PXRD results above 250 °C (see Figures 2b and 4).

Adsorption Studies

To characterize the surface area and porosity of TUB41, nitrogen and argon adsorption isotherms were measured at 77 K. As seen in Figure S4, they show very low adsorption and yield a BET surface area of only ca. 4 $m^2\ g^{-1}$ and a total pore volume of 0.04 $cm^3\ g^{-1}$, consistent with low porosity. In addition, nitrogen adsorption isotherms measured at 298 and 313 K (see Figure S4) also show very low adsorption, indicating that TUB41's pores continue to exclude gases with larger kinetic diameters even at elevated temperatures.

In contrast, the CO_2 adsorption isotherms (Figure 6a) show a higher adsorption and distinct hysteresis over the whole pressure range, indicating an attractive interaction between the adsorbent and adsorbate. The hysteresis looks closest to type H4,[44,45] further strengthening the hypothesis of small, narrow pores with a polar internal surface. BET calculations based on the CO_2 adsorption isotherm at 273 K yield a surface area of 60 $m^2\ g^{-1}$ and a total pore volume of 0.019 $cm^3\ g^{-1}$, consistent with low porosity. At low loadings (0.01 mmol g^{-1} CO_2), the enthalpy of adsorption was estimated to be −41 kJ mol^{-1}, indicative of a strong attractive interaction between CO_2 and the framework. (The details for calculating the enthalpy of adsorption, including model fitting and application of the Clausius–Clapeyron equation, are provided in the Supporting Information). This suggests the presence of high-affinity binding regions within the pores, making

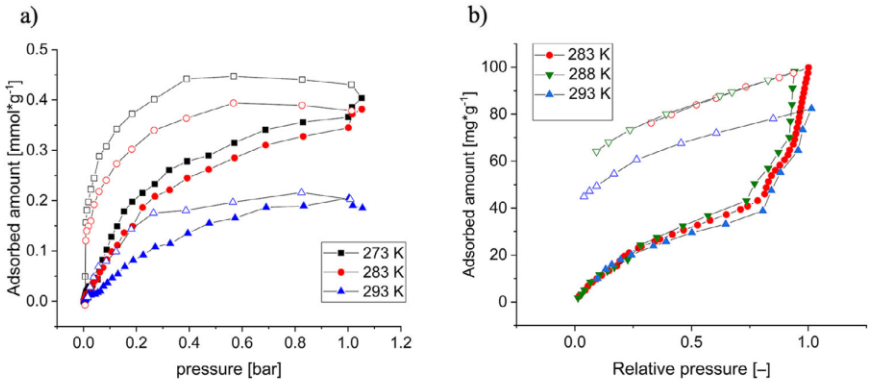

Figure 6. a) CO_2 adsorption isotherms at different temperatures (filled symbols–adsorption, empty symbols–desorption). b) Water vapor adsorption isotherms at different temperatures (filled symbols–adsorption, empty symbols–desorption).

TUB41 suitable for selective CO_2 capture in low-pressure environments. For comparison, TUB41's enthalpy of adsorption is comparable to that of CALF-20, which is −39 kJ mol^{-1}.

Water vapor isotherms measured at 283, 288, and 293 K exhibit a gradual uptake in the low-pressure region, followed by a sharp rise at ~0.8 relative pressure, a step at ~0.9, and another sharp rise at higher relative pressures (Figure 6b). This behavior matches a combination of type IV and type II isotherms at lower (up to ~0.8) and higher relative pressure, respectively. For water vapor sorption, type IV and type II isotherms are indicative of a hydrophilic material.[46] Importantly, the water uptake until ~0.8 relative pressure of 0.04 g g^{-1} matches very well with the pore volume of 0.04 cm^3 g^{-1} from N_2 gas sorption at 77 K (vide supra), thereby supporting the micropore filling with ("liquid") water (at a density of ~1 g cm^{-3}) until this relative pressure. Subsequently, at relative pressures between 0.7 and 0.8, inter-particle condensation in meso- and macro-pores begins, leading to a strong increase in the amount of adsorbed water in line with the type II branch starting at this relative pressure. The desorption measurements show a pronounced hysteresis, closest to type H2 behavior.[43,45] The incomplete desorption observed at all temperatures is indicative of strong interactions between the water molecules and polar groups within the pores. Since the same sample was used for all measurements, it was found that reactivation at 80 °C under vacuum for 2 h was sufficient to empty the pores. The total water uptake exceeds that of CO_2 and is much higher than that of nitrogen, underscoring the selectivity of the pores for molecules with sufficiently small kinetic diameters at elevated temperatures.

The enthalpy of adsorption of water vapor was estimated using the same procedure as for CO_2, focusing on the low-pressure region prior to the onset of condensation. At a loading of 0.7 mmol g^{-1} (corresponding to a pressure of 2×10^{-3} bar), the calculated enthalpy of adsorption is −38 kJ mol^{-1}. This higher loading, relative to the CO_2 case, was selected due to the lower accuracy in the low-pressure region of the water sorption and the available measurement points (Figure S2). The enthalpy of adsorption increases with increasing pressure (Figure S3), probably due to the formation of hydrogen bonds between adsorbed water molecules.

TUB41 exhibits a higher mass of water vapor adsorption (0.04 g g^{-1}) compared to CO_2 adsorption (0.017 g g^{-1}), which might be due to the smaller kinetic diameter of water molecules (2.65 Å) compared to CO_2 (3.3 Å) in the gaseous phase. Another reason for the higher water adsorption might be due to the condensation of water molecules between the TUB41 crystals, which usually happens at higher relative pressures. It should be noted that other MOFs, such as CALF-20, which capture CO_2 via physisorption, also adsorb a higher amount of H_2O compared to CO_2.[15] As discussed below, our MD simulations suggest that this phenomenon may be due to the formation of hydrogen bonds between water molecules, leading to more densely packed water molecules in the pores. On the other hand, gases like CO_2 interact weakly with each other via noncovalent interactions.

The total number of MOFs that are more selective for CO_2 in the presence of water vapor is very limited in the literature, as MOFs usually have higher affinity for water vapor due to the presence of hydrophilic moieties.[15,22] Although the amount of adsorbed CO_2 is limited in TUB41 due to its small surface area, it still has a unique place among MOFs with its narrow and selective pores limiting competition with gases having larger kinetic diameters, e. g., nitrogen (3.64 Å) under cryogenic conditions and methane (3.8 Å). Moreover, the naphthalene moieties impart a high hydrophobicity to the pores.

Altogether, the adsorption measurements confirm the existence of very small pores, which are not accessible to nitrogen (under both cryogenic and higher measurement temperatures) and argon (under the cryogenic measurement temperatures) due to their larger kinetic diameter (see Figure S4). Argon has a slightly larger kinetic diameter of 3.4 Å compared to CO_2 which has a kinetic diameter of 3.3 Å.[47] Therefore, TUB41 excludes gases with kinetic diameters exceeding approximately 3.3–3.4 Å.

Molecular Dynamics Studies

We performed molecular dynamics (MD) simulations on several TUB41 systems (12 × 4 × 4 supercells) containing varying concentrations of H_2O and CO_2, employing the flexible UFF4MOF force field for TUB41, rigid TIP4P model for water, and TraPPE model for CO_2. Specifically, four systems with different H_2O concentrations (containing 10, 30, 100, and 300 water molecules) and three systems with different CO_2 concentrations (containing 10, 30, and 100 CO_2 molecules) were constructed to investigate the distribution, adsorption, and diffusion properties of H_2O and CO_2 in TUB41. The full simulation details are provided in the Supporting Information.

To visualize the distribution of CO_2 and H_2O molecules within the pores of TUB41, atomic trajectory overlay maps were generated for each system. Specifically, the positions of all atoms in the supercell were saved at every 1000 frames of a trajectory. Then, for each unit cell, the positions of all atoms were re-calculated relative to a common reference point in the unit cell, and these relative positions were projected onto a two-dimensional plane perpendicular to a given axis. Finally, the atomic trajectory overlay map is generated by superimposing the projections for each unit cell in the supercell onto each other. An example of a trajectory overlay map for the system containing 30 H_2O and 30 CO_2 molecules (projected onto a plane perpendicular to the *x*-axis, i.e., channel direction) is shown in Figure 7. Atomic trajectory overlay maps for the remaining systems and projections are provided in the Supporting Information.

After analyzing the trajectory overlay maps for all systems and projections, several interesting conclusions can be drawn: the orientations and positions of the H_2O and CO_2 molecules are significantly constrained by the narrow channels, resulting in ordered arrangements. The H_2O molecules preferentially localize near the SBUs, whereas the CO_2 molecules predominantly occupy the centers of the channels (as seen in Figure 7). This distribution pattern is observed across all concentrations, suggesting distinct adsorption mechanisms for H_2O and CO_2 in the TUB41 framework.

To further investigate the distribution and interactions of the CO_2 and H_2O molecules with the TUB41 framework, radial distribution functions (RDFs) for select atomic pairs were calculated. The RDF for a pair of atoms *a* and *b*, $g_{ab}(r)$, is defined as[40,41]

$$g_{ab}(r) = (N_a N_b)^{-1} \sum_{i=1}^{N_a} \sum_{i=1}^{N_b} \langle \delta (|\boldsymbol{r}_i - \boldsymbol{r}_j| - r) \rangle \quad (1)$$

where *r* is the distance from atom *a*, N_a and N_b are the number of *a* and *b* atoms, respectively, $\boldsymbol{r}_i$ and $\boldsymbol{r}_j$ are the position vectors of particles *i* and *j*, respectively, and δ is the Dirac delta function.

Figure 8 presents RDFs between atoms in CO_2/H_2O and atoms in the TUB41 framework for all systems studied. The O (H_2O)–O (framework) RDF possesses a distinct peak at around 2.5 Å, indicating the presence of strong hydrogen bonding (see Figure 8a). In contrast, no significant peaks below 3.5 Å were observed between O (H_2O) atoms and other framework atoms (see Figure S29). The H (H_2O)–O (framework) RDF possesses two distinct peaks at around 1.5 and 2.7 Å, further supporting the presence of hydrogen bonding (see Figure 8b). Figure 8c shows two close peaks between 2.5–3.5 Å due to significant nonbonding interactions between the two O (CO_2) atoms and multiple H (framework) atoms; similarly, Figure 8d shows a single peak around 3 Å due to significant nonbonding interactions between the C (CO_2) atom and multiple H (framework) atoms. This explains the ordered arrangement of CO_2 molecules in the channel centers observed in Figure 7b. (For more RDF plots, the reader is referred to Figure S29 of the Supplementary Information.)

We next quantified the average number of hydrogen bonds between a H_2O molecule and the MOF framework for the water-containing systems.[42] Hydrogen bonds were assigned according to the following criteria: (1) donor–acceptor distance less than 3.0 Å, and (2) donor–hydrogen–acceptor angle greater than 150°. The results are shown in Figure 9. Across all investigated systems, each water molecule forms, on average, about one hydrogen bond with the MOF framework, consistent with the experimental hydration results. Based on the RDF results, this bond is a strong hydrogen bond. Additionally, no hydrogen bonds were identified between CO_2 molecules and the MOF framework (result not shown). We also analyzed the average number of hydrogen bonds between H_2O molecules for the water-containing systems. For the 30- and 100-water systems, this number is essentially zero; however, for the 300-water system, there are ~0.065 bonds, a small but significant number (see Figure S30). This is because, at higher concentrations, the binding sites of the framework become saturated, causing the additional water molecules to reside in the center of the channel where they have more opportunity to hydrogen bond with each other. This phenomenon is further supported by the atomic trajectory overlay map of the 300-water system (see Figure S28).

The mean-squared displacements (MSDs) of H_2O and CO_2 were computed according to:[43,44]

$$MSD(t) = \frac{1}{N} \sum_{i=1}^{N} |r_i - r_i(t)|^2 \quad (2)$$

where *N* is the number of particles averaged over and r_i is the position of particle *i*. They were calculated based on 5 ns NVT trajectories, started from the final frames of the previous production runs. The MSD results for the systems containing 30 H_2O and 30 CO_2 molecules are shown in Figure 10. Both the H_2O and CO_2 MSDs exhibit similar trends. Initially, the MSDs increase steadily up to about 0.3 ns. Beyond 0.3 ns, both MSDs cease to grow further and instead fluctuate around equilibrium values. The equilibrium MSD value is approximately 2.0 $Å^2$ for H_2O and 3.2 $Å^2$ for CO_2. These values are exceptionally small, indicating that both H_2O and CO_2 molecules are tightly confined in all three spatial dimensions near their equilibrium positions within the pores. This confinement arises from a combination of strong guest–host interactions and the ultramicroporous character

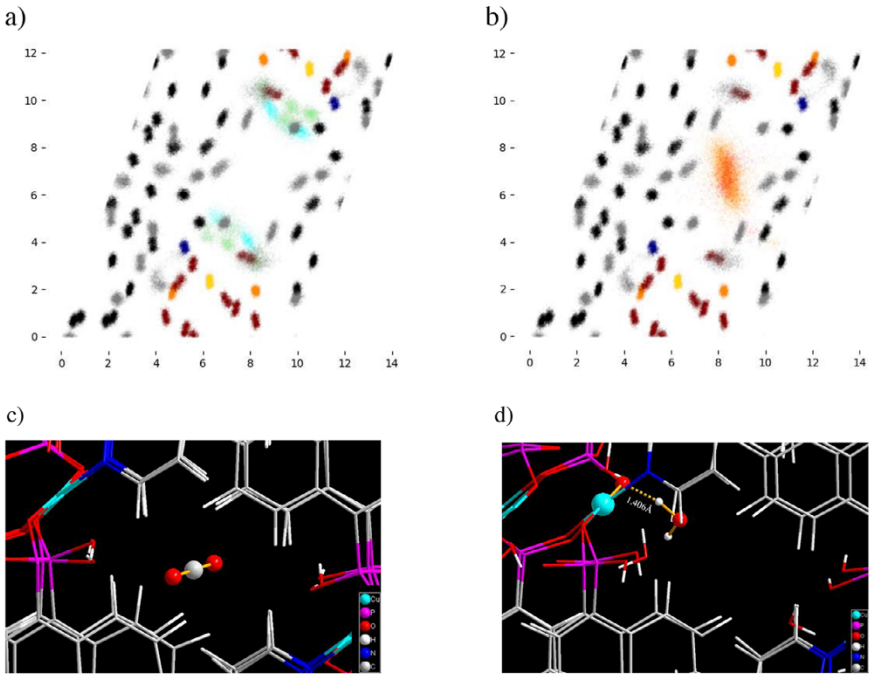

Figure 7. Atomic trajectory overlay maps of a TUB41 unit cell containing a) 30 H_2O molecules and b) 30 CO_2 molecules. The maps are projections onto a plane that is perpendicular to the channel direction. Cyan and green represent the oxygen and hydrogen atoms of H_2O, respectively; red and orange represent the carbon and oxygen atoms of CO_2, respectively; gold, dark blue, dark orange, dark red, black, and gray represent copper, nitrogen, phosphorus, oxygen, carbon, and hydrogen atoms, respectively, in the MOF framework. The *x* and *y* axes of the maps represent position, expressed in Ångströms (Å). A representative snapshot from the MD trajectory showing c) a typical position of a CO_2 molecule within a pore, and d) a typical hydrogen bond at the edge of a pore, formed between a H_2O molecule and an oxygen atom in the MOF's SBU.

of TUB41. For comparison, in another MOF currently under investigation, the MSDs of H_2O and CO_2 reach up to 1000 $Å^2$ within 5 ns. Given both the low MSD values observed in TUB41 and the small difference between them, it is not possible to draw meaningful conclusions about any preferential kinetic behavior between the two gases in this system.

In addition to MD simulations, we employed the random insertion algorithm in LAMMPS to estimate the maximum adsorption capacities of CO_2 and H_2O in the TUB41 supercell. For each gas, 1000 insertion attempts were made, with up to 10 000 placement attempts per molecule. If a suitable position is not found after 10 000 attempts, the algorithm proceeds to the next molecule. A minimum initial distance of 1.6 Å between all atoms was enforced to ensure stability, as values below this threshold resulted in unstable simulations. Parallel simulations were conducted using three different random number seeds. The number of CO_2 molecules successfully inserted into the TUB41 supercell was 254, 244, and 242, with an average of 247, while for H_2O, the counts were 762, 766, and 766, averaging 765. Thus, the calculated maximum adsorption capacities are 0.084 g g^{-1} for H_2O and 0.066 g g^{-1} for CO_2, which are consistent with the experimental observation that TUB41 possesses a higher mass of water vapor adsorption (0.04 g g^{-1}) compared to CO_2 adsorption (0.017 g g^{-1}).

Overall, the MD simulation results suggest that the pores of TUB41, which are lined predominantly with hydrophobic groups and only at select sites with hydrophilic phosphonate oxygen atoms from the SBUs, promote spatial separation between H_2O and CO_2, potentially enabling coadsorption while minimizing competitive interactions.

Optical Properties

Copper phosphonate MOFs, such as TUB1, TUB40, and TUB75 (sister compounds of TUB41), and other phosphonate MOFs are known for their semiconducting properties.[33,37,38,48] Thus, we measured the diffuse reflectance spectrum of TUB41 to estimate its optical band gap. Based on the Tauc plots generated from the diffuse reflectance spectra (see Figures S21a and S21b), we extracted an indirect band gap of 2.7 eV and direct band gap of 3.0 eV (see Supporting Information for experimental details).[49,50] The band centered at around 1.7 eV is likely due to a localized $3d^9 \leftarrow 3d^9$ transition of the Cu(II) centers ($^2E \leftarrow {}^2T_2$ in an approximately tetrahedral field). TUB41 has a very similar SBU compared to our previously reported MOF TUB1. The SBUs in both TUB1 and TUB41 have the same order of vertex-connected [Cu–O–P–O–Cu–O–P–O] eight-membered rings resulting in a rod-shaped SBU (see Figure 1b).[48] The

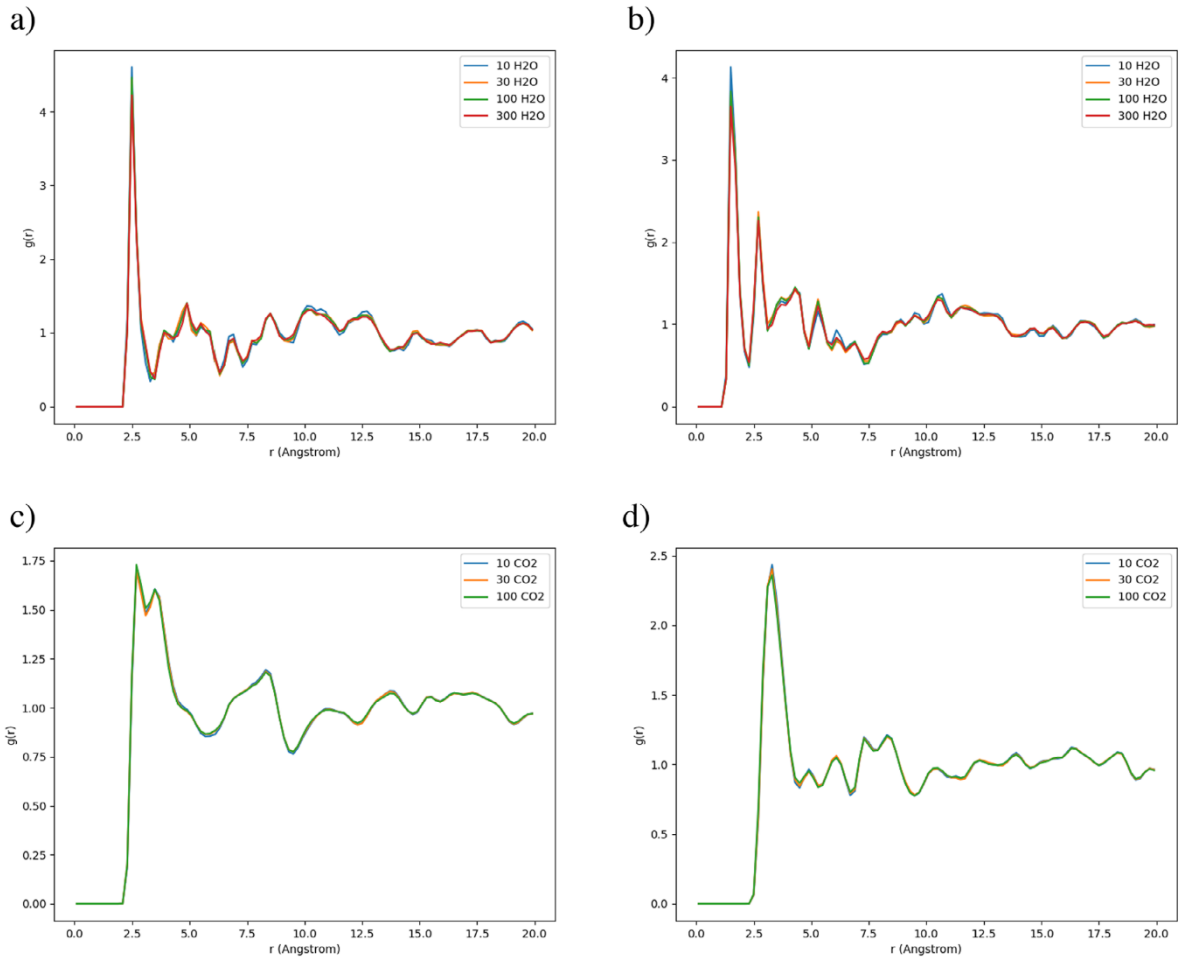

Figure 8. RDFs between atoms in CO_2/ H_2O and atoms in the TUB41 framework for all systems. a) O (H_2O)–O (framework). b) H (H_2O)–O (framework). c) O (CO_2)–H (framework). d) C (CO_2)–H (framework).

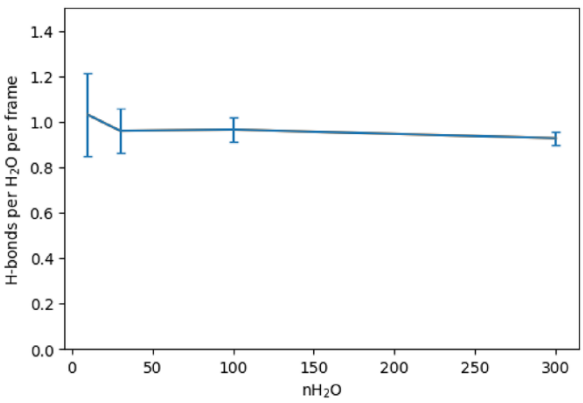

Figure 9. Average number of hydrogen bonds between a H_2O molecule and the MOF framework for the water-containing systems, normalized by both the number of trajectory frames and the number of H_2O molecules.

major difference between the SBUs of TUB41 and TUB1 is the first copper atom (Cu1) in TUB1, which is coordinated in a square-planar fashion, while the second copper atom (Cu2) is coordinated in a square-pyramidal fashion. In TUB41, all copper atoms show a square–pyramidal coordination sphere. Similar to TUB41, our previously published MOF TUB1 possesses an indirect band gap of 2.4 eV and a direct band gap of 2.7 eV, which was also confirmed by DOS calculations.[48] The slightly narrower band gap observed in TUB1 might be due to the presence of square planar coordinated Cu(II) ions as indicated by the calculations in the previous work. The indirect and direct band gaps of TUB41 are within the visible range, highlighting the potential of TUB41 in photocatalysis applications.

Conclusions

TUB41 stands out among MOFs for its narrow, selective pores, which effectively exclude gases with kinetic diameters

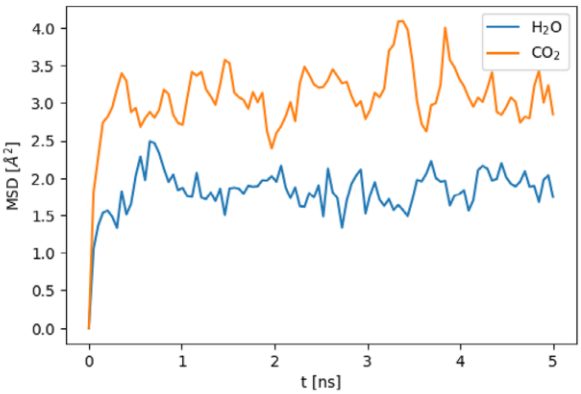

Figure 10. MSDs of H_2O and CO_2 in the TUB41 systems containing 30 H_2O and 30 CO_2 molecules, respectively.

larger than 3.3 Å, and for its remarkable stability, maintaining structural integrity over a two-year period. It remains stable for over a month at pH 2.5 and for at least 2 h across a broad pH range from 1 to 11. The crystals also retain their stability after repeated adsorption experiments and activation at 80 °C under vacuum. Compared to conventional MOFs, which are often hydrolyzed by water vapor, TUB41 shows superior chemical stability, particularly in acidic and basic environments within the pH 1–11 range. This exceptional stability enhances its suitability for industrial applications, especially in membrane-based coseparation of CO_2 and H_2O from other gases. In contrast, typical MOFs with metal-carboxylate SBUs, such as UiO-66, have relatively short shelf lives of approximately 2 months under ambient conditions.

A major challenge in CO_2 capture under humid conditions is the typically stronger affinity of MOFs for water, largely due to the presence of hydrophilic metal-binding groups. In TUB41, the presence of naphthalene moieties lining the pores imparts a predominantly hydrophobic character to the pores, creating a more favorable environment for CO_2 adsorption. The hydrophilic oxygen atoms of the phosphonate groups cover only a small fraction of the inner surface area (Figure 1a,c), which is sufficient to enable water adsorption while preserving the overall hydrophobic character of the pores. The slit-shaped channels along the *a* axis, with a cross-section of approximately 4 × 2 $Å^2$, provide a confined space well-suited for the selective adsorption of gases with small kinetic diameters. Additionally, the rod-shaped SBU imparts TUB41 with reversible phase transitions observable at different temperatures. In situ temperature-variable PXRD combined with MS-TGA points to the condensation of phosphonate groups, leading to the release of additional water molecules at elevated temperatures.

The MD simulations reveal distinct adsorption mechanisms for H_2O and CO_2 within TUB41. H_2O preferentially localizes near the SBUs through strong hydrogen-bonding interactions, while CO_2 predominantly occupies the central regions of the channels, driven by Coulombic and van der Waals forces. The RDFs and hydrogen-bond analysis confirm the specificity and strength of these interactions. The MSD results further demonstrate that both H_2O and CO_2 are spatially constrained within the pores, highlighting their strong affinity for the MOF framework. Despite the higher loading capacity of H_2O and its strong hydrogen-bonding interactions, which may impact CO_2 uptake, the largely hydrophobic nature of TUB41's pores and the spatial separation between CO_2 (in the center of the channels) and H_2O (near the SBUs) suggest that competitive adsorption could be partially mitigated. These characteristics enable the selective adsorption of CO_2 in humid environments, highlighting TUB41's potential for gas separation applications.

In summary, TUB41 represents a significant step forward in the design of robust MOFs, combining exceptional long-term thermal and chemical stability with selective gas adsorption and a visible-range band gap. Its unique combination of properties–including over 2 years of structural stability, resistance to harsh chemical environments, and molecular-level selectivity for CO_2 and water vapor–positions it as a promising candidate for applications such as photocatalytic water splitting, CO_2 reduction, and industrial gas separation. The development of phosphonate-based MOFs like TUB41, featuring insoluble SBUs and resilience in concentrated acids and bases, paves the way for the next generation of MOFs capable of operating in demanding aqueous and chemical environments.

Supporting Information

The Supporting Information contains details of the synthesis, gas and water adsorption, MD simulations, and optical spectroscopy.

Author Contributions

R.O. performed the gas sorption studies and optical measurements, and wrote the corresponding sections. M.F. resynthesized TUB41, developed a new method for the linker synthesis, and performed the stability experiments and took SEM pictures. Y.Z. set up and performed the MD simulations, generated the corresponding figures, and wrote the initial drafts of the computational parts of the manuscript. A.S. performed the N_2 and Ar adsorption measurements, A.K. performed the in situ temperature variable PXRD measurements and wrote the corresponding section, M.S. supervised the optical measurements, wrote the corresponding section, and edited the manuscript. C.J. supervised and interpreted the gas adsorption work, created the crystallographic figures, and edited the manuscript. G.H. supervised the work of Y.Z., provided critical feedback on several experimental sections of the manuscript, revised the computational parts of the manuscript, and edited the entire manuscript. G.Y. created the hypothesis, supervised the work of M.F. and R.O., and wrote the majority of the abstract, introduction, conclusion sections, and contributed experimental sections of the manuscript.

Acknowledgements

G.Y. would like to thank DFG for fundings DFG YU 267/2–1 and DFG YU 267/9–1. M.S. acknowledges funding from a materials cost allowance of the Fonds der Chemischen Industrie e.V. and a scholarship of the "Young College" of the North-Rhine Westphalian Academy of Sciences, Humanities, and the Arts. The authors would like to thank Microtrac Retsch GmbH to perform the N_2 and Ar adsorption work. G.H. acknowledges funding from the Natural Sciences and Engineering Research Council of Canada (NSERC). The MD simulations were enabled in part by support by the Digital Research Alliance of Canada (alliancecan.ca).

Open access funding enabled and organized by Projekt DEAL.

Conflict of Interests

The authors declare no conflict of interest.

Data Availability Statement

The data that support the findings of this study are available in the Supporting Information of this article.

Keywords: Chemically & thermally stable MOFs · CO_2 capture · Gas separation

[1] H. Furukawa, K. E. Cordova, M. O'Keeffe, O. M. Yaghi, *Science* **2013**, *341*, 1230444.
[2] O. M. Yaghi, M. J. Kalmutzki, C. S. Diercks, *Introduction to* Reticular Chemistry: Metal-Organic Frameworks and Covalent Organic Frameworks, Wiley, Hoboken, NJ **2019**.
[3] T. H. Y. Beglau, M. N. A. Fetzer, I. Boldog, T. Heinen, M. Suta, C. Janiak, G. Yücesan, *Chem. Eur. J.* **2024**, *30*, e202302765.
[4] P. Tholen, L. Wagner, J. G. A. Ruthes, K. Siemensmeyer, T. H. Y. Beglau, D. Muth, Y. Zorlu, M. Okutan, J. C. Goldschmidt, C. Janiak, V. Presser, Ö. Yavuzçetin, G. Yücesan, *Small* **2023**, *19*, 2304057.
[5] P. Horcajada, R. Gref, T. Baati, P. K. Allan, G. Maurin, P. Couvreur, G. Ferey, R. E. Morris, C. Serre, *Chem. Rev.* **2012**, *112*, 1232–1268.
[6] S. Rojas, A. Arenas-Vivo, P. Horcajada, *Coord. Chem. Rev.* **2019**, *388*, 202–226.
[7] M. W. Ambrogio, C. R. Thomas, Y. L. Zhao, J. I. Zink, J. F. Stoddart, *Acc. Chem. Res.* **2011**, *44*, 903–913.
[8] K. J. Hartlieb, D. P. Ferris, J. M. Holcroft, I. Kandela, C. L. Stern, M. S. Nassar, Y. Y. Botros, J. F. Stoddart, *Mol. Pharmaceutics* **2017**, *14*, 1831.
[9] R. A. Smaldone, R. S. Forgan, H. Furukawa, J. J. Gassensmith, A. M. Z. Slawin, O. M. Yaghi, J. F. Stoddart, *Angew. Chem. Int. Ed.* **2010**, *49*, 8630–8634.
[10] A. J. Howarth, Y. Liu, P. Li, Z. Li, T. C. Wang, J. T. Hupp, O. K. Farha, *Nat. Rev. Mater.* **2016**, *1*, 15018.
[11] M. Ding, X. Cai, H.-L. Jiang, *Chem. Sci.* **2019**, *10*, 10209–10230.
[12] C. Healy, K. M. Patil, B. H. Wilson, L. Hermanspahn, N. C. Harvey-Reid, B. I. Howard, C. Kleinjan, J. Kolien, F. Payet, S. G. Telfer, P. E. Kruger, T. D. Bennett, *Coord. Chem. Rev.* **2020**, *419*, 213388.
[13] M. Ding, X. Cai, H. L. Jiang, *Chem. Sci.* **2019**, *10*, 10209.
[14] D. Bu'žek, S. Adamec, K. Lang, J. Demel, *Inorg. Chem. Front.* **2021**, *8*, 720.
[15] J.-B. Lin, T. T. Nguyen Tai, R. Vaidhyanathan, J. Burner, M. Taylor Jared, H. Durekova, F. Akhtar, K. Mah Roger, O. Ghaffari-Nik, S. Marx, N. Fylstra, S. Iremonger Simon, W. Dawson Karl, P. Sarkar, P. Hovington, A. Rajendran, K. Woo Tom, K. H. Shimizu George, *Science* **2021**, *374*, 1464–1469.
[16] P. Tholen, Y. Zorlu, J. Beckmann, G. Yücesan, *Eur. J. Inorg. Chem.* **2020**, *2020*, 1542–1554.
[17] K. J. Gagnon, H. P. Perry, A. Clearfield, *Chem. Rev.* **2012**, *112*, 1034–1054.
[18] C. M. Sevrain, M. Berchel, H. Couthon, P.-A. Jaffrès, *Beilstein J. Org. Chem.* **2017**, *13*, 2186–2213.
[19] R. J. Motekaitis, I. Murase, A. E. Martell, *Inorg. Chem.* **1976**, *15*, 2303–2306.
[20] K. D. Demadis, N. Stavgianoudaki, *Metal Phosphonate Chemistry: From Synthesis to Applications*, RSC Publishing, Cambridge, UK **2012**.
[21] H. Deng, C. J. Doonan, H. Furukawa, R. B. Ferreira, J. Towne, C. B. Knobler, B. Wang, O. M. Yaghi, *Science* **2010**, *327*, 846–850.
[22] P. G. Boyd, A. Chidambaram, E. García-Díez, C. P. Ireland, T. D. Daff, R. Bounds, A. Gładysiak, P. Schouwink, S. M. Moosavi, M. M. Maroto-Valer, J. A. Reimer, J. A. R. Navarro, T. K. Woo, S. Garcia, K. C. Stylianou, B. Smit, *Nature* **2019**, *576*, 253–256.
[23] T. M. McDonald, W. R. Lee, J. A. Mason, B. M. Wiers, C. S. Hong, J. R. Long, *J. Am. Chem. Soc.* **2012**, *134*, 7056–7065.
[24] J. H. Choe, H. Kim, H. Yun, M. Kang, S. Park, S. Yu, C. S. Hong, *J. Am. Chem. Soc.* **2024**, *146*, 646–659.
[25] J. H. Choe, H. Kim, H. Yun, J. F. Kurisingal, N. Kim, D. Lee, Y. H. Lee, C. S. Hong, *J. Am. Chem. Soc.* **2024**, *146*, 19337–19349.
[26] O. I.-F. Chen, C.-H. Liu, K. Wang, E. Borrego-Marin, H. Li, A. H. Alawadhi, J. A. R. Navarro, O. M. Yaghi, *J. Am. Chem. Soc.* **2024**, *146*, 2835–2844.
[27] J. F. Kurisingal, J. H. Choe, H. Kim, J. Youn, G. Cheon, C. S. Hong, *Bull. Korean Chem. Soc.* **2024**, *45*, 675–688.
[28] Z. Chen, K. O. Kirlikovali, L. Shi, O. K. Farha, *Mater. Horiz.* **2023**, *10*, 3257–3268.
[29] G. Yücesan, Y. Zorlu, M. Stricker, J. Beckmann, *Coord. Chem. Rev.* **2018**, *369*, 105–122.
[30] R. K. Mah, M. W. Lui, G. K. H. Shimizu, *Inorg. Chem.* **2013**, *52*, 7311–7313.
[31] S.-S. Bao, G. K. H. Shimizu, L.-M. Zheng, *Coord. Chem. Rev.* **2019**, *378*, 577–594.
[32] P. Salcedo-Abraira, S. M. F. Vilela, A. A. Babaryk, M. Cabrero-Antonino, P. Gregorio, F. Salles, S. Navalón, H. García, P. Horcajada, *Nano Res.* **2021**, *14*, 450–457.
[33] C. A. Peeples, D. Kober, F.-J. Schmitt, P. Tholen, K. Siemensmeyer, Q. Halldorson, B. Çoşut, A. Gurlo, A. O. Yazaydin, G. Hanna, G. Yücesan, *Adv. Funct. Mater.* **2021**, *31*, 2007294.
[34] P. Tholen, C. A. Peeples, R. Schaper, C. Bayraktar, T. S. Erkal, M. M. Ayhan, B. Cosut, J. Beckmann, A. O. Yazaydin, M. Wark, G. Hanna, Y. Zorlu, G. Yucesan, *Nat. Commun.* **2020**, *11*, 3180.
[35] P. Tholen, C. A. Peeples, M. M. Ayhan, L. Wagner, H. Thomas, P. Imbrasas, Y. Zorlu, C. Baretzky, S. Reineke, G. Hanna, G. Yücesan, *Small* **2022**, *18*, 2204578.
[36] K. Xu, R. Oestreich, T. Haj Hassani Sohi, M. Lounasvuori, J. G. A. Ruthes, Y. Zorlu, J. Michalski, P. Seiffert, T. Strothmann, P. Tholen, A. Ozgur Yazaydin, M. Suta, V. Presser, T. Petit, C. Janiak, J. Beckmann, J. Schmedt auf der Günne, G. Yücesan, *Nat. Commun.* **2024**, *15*, 7862.
[37] C. Ribeiro, B. Tan, F. Figueira, R. F. Mendes, J. Calbo, G. Valente, P. Escamilla, F. A. A. Paz, J. Rocha, M. Dincă, M. Souto, *J. Am. Chem. Soc.* **2025**, *147*, 63–68.

[38] K. Siemensmeyer, C. A. Peeples, P. Tholen, F. Schmitt, B. Çoşut, G. Hanna, G. Yücesan, *Adv. Mater.* **2020**, *32*, 2000474.
[39] A. Bulut, Y. Zorlu, M. Wörle, A. Çetinkaya, H. Kurt, B. Tam, A. Ö. Yazaydın, J. Beckmann, G. Yücesan, *ChemistrySelect* **2017**, *2*, 7050–7053.
[40] S. Mukherjee, N. Sikdar, D. O'Nolan, D. M. Franz, V. Gascón, A. Kumar, N. Kumar, H. S. Scott, D. G. Madden, P. E. Kruger, B. Space, M. J. Zaworotko, *Sci. Adv.* **2019**, *5*, eaax9171.
[41] D.-X. Xue, Y. Belmabkhout, O. Shekhah, H. Jiang, K. Adil, A. J. Cairns, M. Eddaoudi, *J. Am. Chem. Soc.* **2015**, *137*, 5034–5040.
[42] O. Smirnova, S. Hwang, R. Sajzew, L. Ge, A. Reupert, V. Nozari, S. Savani, C. Chmelik, M. R. Reithofer, L. Wondraczek, J. Kärger, A. Knebel, *Nat. Mater.* **2024**, *23*, 262–270.
[43] L.-R. Guo, S.-S. Bao, Y.-Z. Li, L.-M. Zheng, *Chem. Commun.* **2009**, 2893.
[44] K. S. W. Sing, D. H. Everett, R. A. W. Haul, L. Moscou, R. A. Pierotti, J. Rouquerol, T. Siemieniewska, *Pure Appl. Chem.* **1985**, *57*, 603–619.
[45] M. Thommes, K. Kaneko, A. V. Neimark, J. P. Olivier, F. Rodriguez-Reinoso, J. Rouquerol, K. S. W. Sing, *Pure Appl. Chem.* **2015**, *87*, 1051–1069.
[46] E.-P. Ng, S. Mintova, *Microporous Mesoporous Mater.* **2008**, *114*, 1–26.
[47] S. Matteucci, Y. Yampolskii, B. D. Freeman, I. Pinnau, in *Materials Science of Membranes for Gas and Vapor Separation*, Wiley, Hoboken, NJ **2006**, pp. 1–47.
[48] C. A. Peeples, A. Çetinkaya, P. Tholen, F.-J. Schmitt, Y. Zorlu, K. Bin Yu, O. Yazaydin, J. Beckmann, G. Hanna, G. Yücesan, *Chem. Eur. J.* **2022**, *28*, e202104041.
[49] J. Tauc, *Mater. Res. Bull.* **1968**, *3*, 37.
[50] J. Tauc, R. Grigorovici, A. Vancu, *Phys. Status Solidi B* **1966**, *15*, 627–637.

Manuscript received: June 24, 2025
Revised manuscript received: July 17, 2025
Accepted manuscript online: July 21, 2025
Version of record online: August 23, 2025

Stable Ultramicroporous Metal-Organic Framework with Hydrophilic and Hydrophobic Domains for Selective Gas Adsorption

Robert Oestreich,[1#] Marcus N. A. Fetzer,[1#] Yifei Zhang[6], Andreas Schreiber,[3] Alexander Knebel,[4,5] Markus Suta,[2] Christoph Janiak[1]*, Gabriel Hanna[6]*, and Gündoğ Yücesan[1]*

1. Institute for Inorganic and Structural Chemistry, Heinrich Heine Universität Düsseldorf, Universitätsstr. 1, D-40225 Düsseldorf, Germany.
2. Inorganic Photoactive Materials, Institute for Inorganic and Structural Chemistry, Heinrich Heine University Düsseldorf, Universitätsstr. 1, 40225 Düsseldorf, Germany
3. Microtrac Retsch GmbH, Retsch-Allee 1-5, D-42781 Haan, Germany
4. Otto Schott Institute of Materials Research, Center for Energy and Environmental Chemistry II, Friedrich Schiller University Jena, Lessingstraße 12-14, D-07743 Jena, Germany.
5. Center for Energy and Environmental Chemistry, Friedrich Schiller University Jena, Philosophenweg 7a, D-07743 Jena, Germany
6. Department of Chemistry, University of Alberta, Edmonton, Alberta, Canada

# These authors contributed equally to this work.

Table of Contents

1. General information

Unless otherwise noted, all commercially available compounds were used as provided without further purification. Chemicals used in this study were purchased from Sigma Aldrich, Alfa Aesar, BLDpharm and Carl Roth. Solvents for chromatography were technical grade and distilled prior to use. Analytical thin-layer chromatography (TLC) was performed on Macherey-Nagel silica gel aluminium plates with F-254 indicator, visualized by irradiation with UV light. Column chromatography was performed using silica gel Merck 60 (particle size 0.063 – 0.2 mm). ^{1}H-NMR, ^{13}C-NMR and ^{31}P-NMR were recorded on a Bruker Avance III 300 MHz NMR spectrometer in $CDCl_3$ or DMSO-d_6. Data are reported in the following order: chemical shift (δ) in ppm; multiplicities are indicated brs (broadened singlet), s (singlet), d (doublet), t (triplet), q (quartet), m (multiplet); coupling constants (J) are in Hertz (Hz). Powder X-ray diffraction (PXRD) was performed on a Rigaku Miniflex powder diffractometer in θ/2θ geometry with Cu-Kα radiation (1.54184 Å) and equipped with a rotating low-background silicon sample holder. For thermogravimetric analysis (TGA) of the pure MOF a Netzsch TG 209 F3 Tarsus was used and operated with synthetic air atmosphere and a heating rate of 10 K min^{-1} . TGA curves were baseline corrected with a blank run. Gaseous products were analyzed with a GAM 200 mass spectrometer from InProcess Instruments. Gas and vapor sorption measurements were done on the BELSorp-max II by MicrotracBEL Corporation. The sample was heated to 80°C under vacuum for two hours for activation before every measurement to clear pores of residue gas. Diffuse reflectance and emission spectra were measured on an Edinburgh FLS1000 luminescence spectrometer with 450 W Xe arc lamp, double grating monochromators (Czerny-Turner configuration, blazed at 400 nm in excitation and 500 nm in emission) and a thermoelectrically cooled (-20 °C) PMT980 (Hamamatsu) photomultiplier tube as detection unit. All spectra were acquired at room temperature. Diffuse reflectance was measured using an integrating sphere (diameter 120 mm) setup with the inner surface coated with BenFlect (reflectance >99 % between 350 nm and 2500 nm). All spectra were corrected for the grating efficiency, the lamp intensity, and the wavelength-dispersive sensitivity of the detection unit.

2. Synthesis

Synthesis of tetraethyl naphthalene-1,4-diylbis(phosphonate)

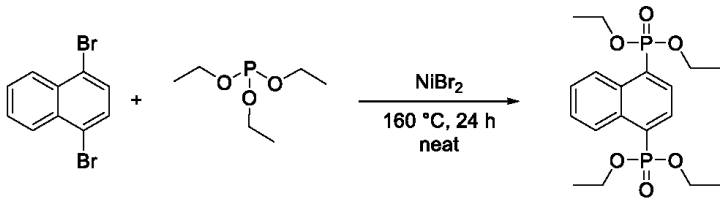

Under a nitrogen flow, 1,4-dibromonaphthalene (5,1 g, 17.8 mmol) was placed in a three-neck round-bottom flask equipped with a stirring bar. The flask was heated to 160 °C to melt the 1,4-dibromonaphthalene. To the melted 1,4-dibromonaphthalene, $NiBr_2$ (0.5 g, 2.2 mmol) was added. Finally, triethyl phosphite (7.8 g, 46.9 mmol) was added dropwise over a period of 7 h. The reaction was stirred at the same temperature for 24 h. The crude product, a dark brown to orange oil, was purified by column chromatography using a mixture of EtOAc and EtOH (9:1 v:v). The product was isolated as a colorless oil with a yield of 3.8 g (9.5 mmol, 53.3 %).

^{1}H NMR (300 MHz, $CDCl_3$) δ 8.63-8.59 (m, 2H), 8.29-8.22 (m, 2H), 7.68-7.64 (m, 2H), 4.27-4.07 (m, 8H), 1.32 (t, *J* = 7.1 Hz, 12H); ^{31}P{^{1}H} NMR (121 MHz, $CDCl_3$) δ 17.4 (s); ^{13}C{^{1}H} NMR (75 MHz, $CDCl_3$) δ 132.9-132.4, 131.6 (d, *J* = 3.6 Hz), 129.2 (d, *J* = 3.5 Hz), 127.6, 127.3, 62.5 (d, *J* = 3.0 Hz), 16.3.

Synthesis of naphthalene-1,4-diphosphonic acid (1,4-NDPA-H_4)

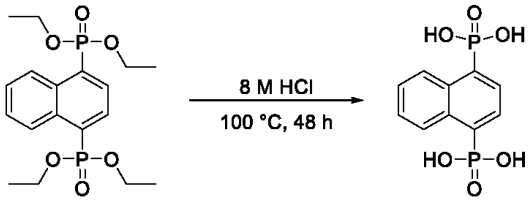

Tetraethyl naphthalene-1,4-diylbis(phosphonate) (3.8 g, 9.5 mmol) was mixed with 100 mL of 8 M hydrochloric acid and refluxed for 24 h. The white precipitate was filtered off and dried at 60 °C under reduced pressure to obtain 2.5 g (yield: 95 %) of pure acid.

^{1}H NMR (300 MHz, DMSO-d_6) δ 8.69-8.65 (m, 2H), 8.08-8.01 (m, 2H), 7.64 (dd, *J*=6.5, 3.4 Hz, 2H); ^{31}P{^{1}H} NMR (121 MHz, DMSO-d_6) δ 11.0 (s);

^{13}C{^{1}H} NMR (75 MHz, DMSO-d_6) δ 135.6 (d), 132.4 (d), 130.3-129.9 (m), 127.8 (s), 126.4 (s).

3. NMR spectra

Tetraethyl naphthalene-1,4-diylbis(phosphonate)

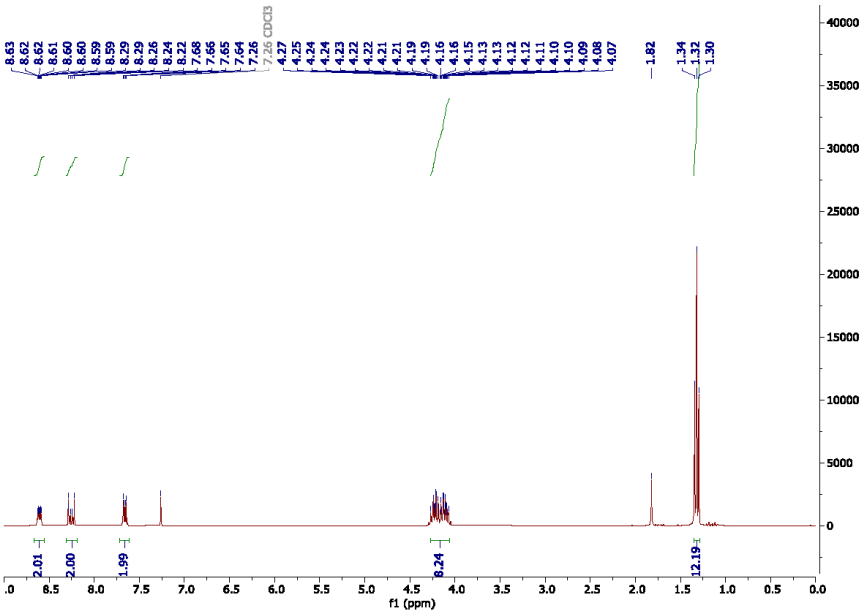

^{1}H NMR (300 MHz, $CDCl_3$)

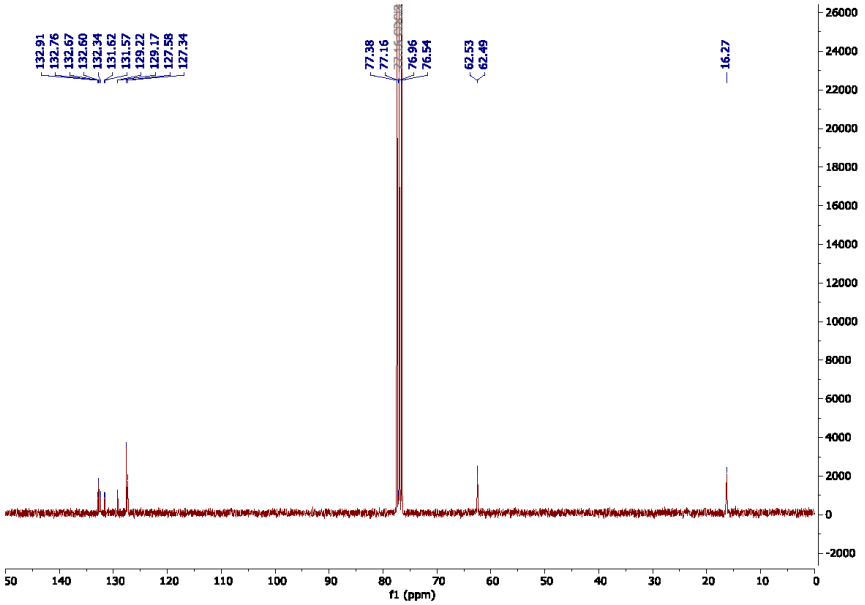

$^{13}C\{^{1}H\}$ NMR (75 MHz, $CDCl_3$)

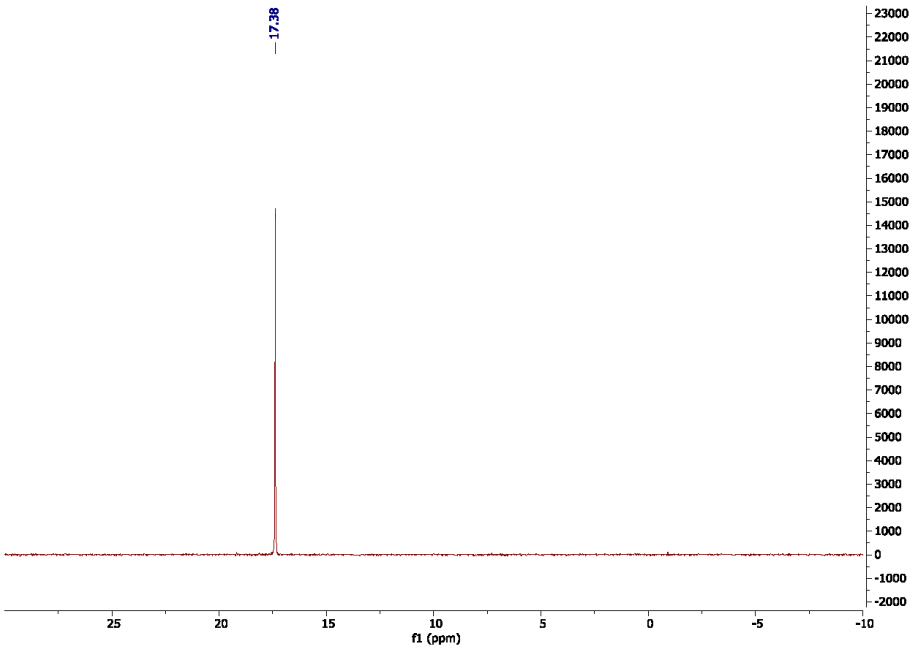

$^{31}P\{^{1}H\}$ NMR (121 MHz, $CDCl_3$)

Naphthalene-1,4-diphosphonic acid (1,4-NDPA-H_4)

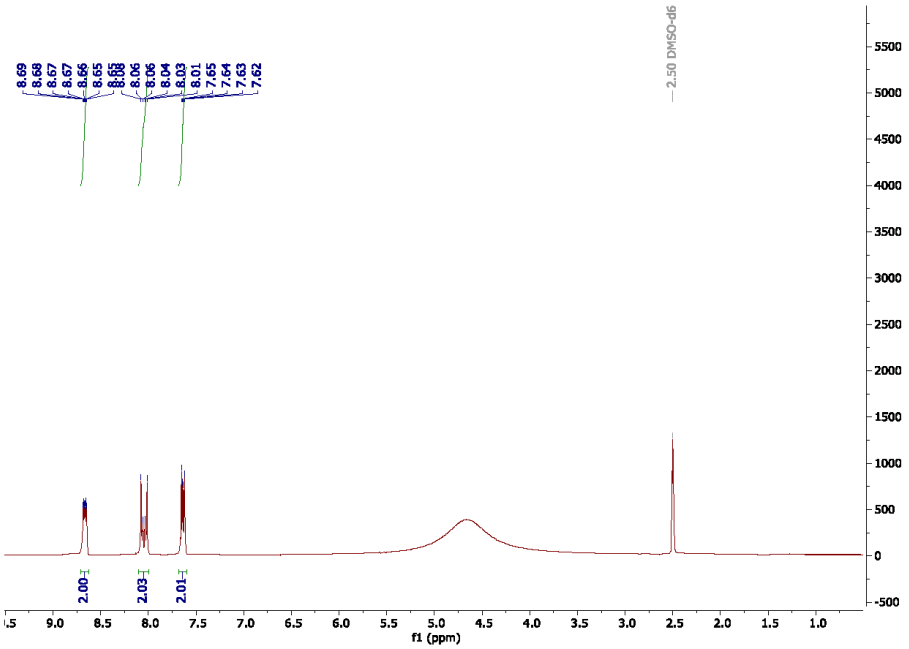

^{1}H NMR (300 MHz, DMSO-d_6)

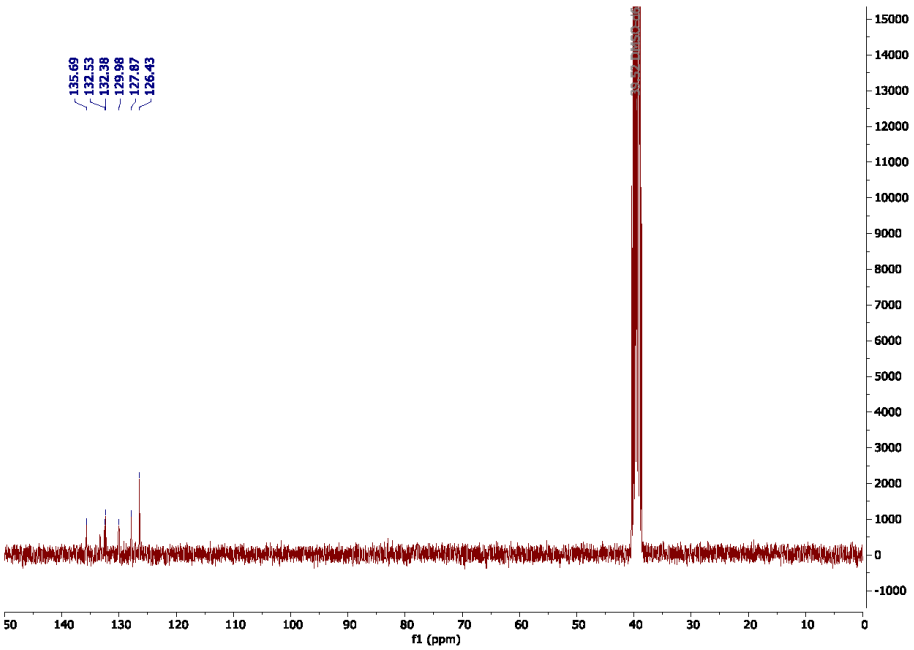

^{13}C{^{1}H} NMR (75 MHz, DMSO-d_6)

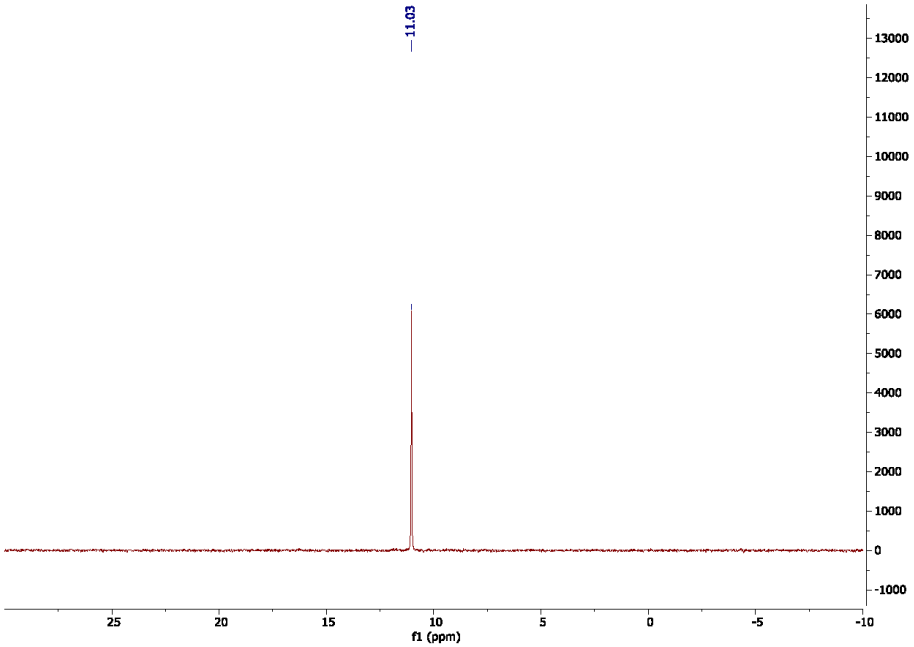

$^{31}P\{^{1}H\}$ NMR (121 MHz, DMSO-d_6)

4. Gas and water sorption

Enthalpy of adsorption was estimated by measuring adsorption isotherms at three temperatures (273, 283, and 293 K), fitting the data to a Freundlich-Langmuir model (Figures S1 and S2), and applying the Clausius-Clapeyron equation:[39]

$$\Delta H_{\text{ads}} = R \ln\left(\frac{p_2}{p_1}\right) \frac{T_1 T_2}{(T_2 - T_1)} \qquad (1)$$

where R = 8.314 J · K^{-1} · mol^{-1} is the gas constant, p_1 and p_2 are two reference pressures, and T_1 and T_2 are the respective reference temperatures.

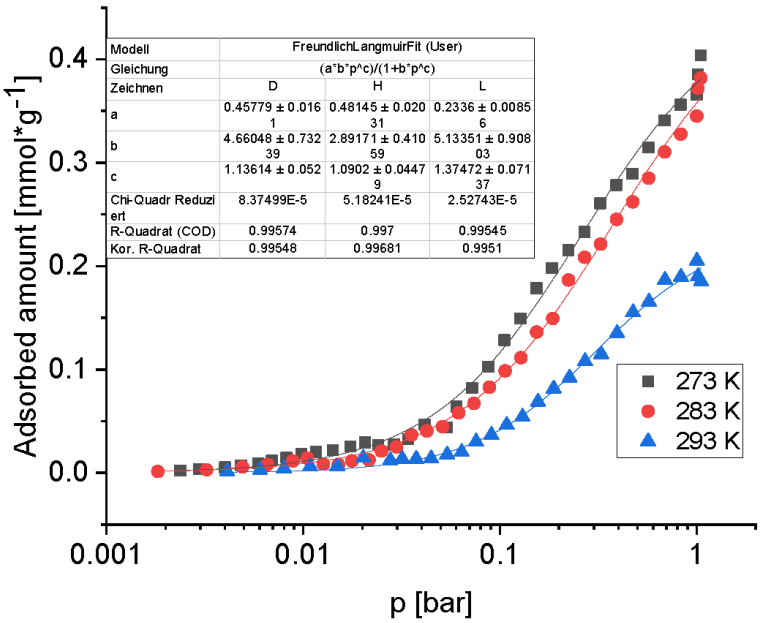

Figure S1: CO_2 adsorption isotherms at different temperatures (on a semi-logarithmic scale), fitted to a Freundlich-Langmuir model.

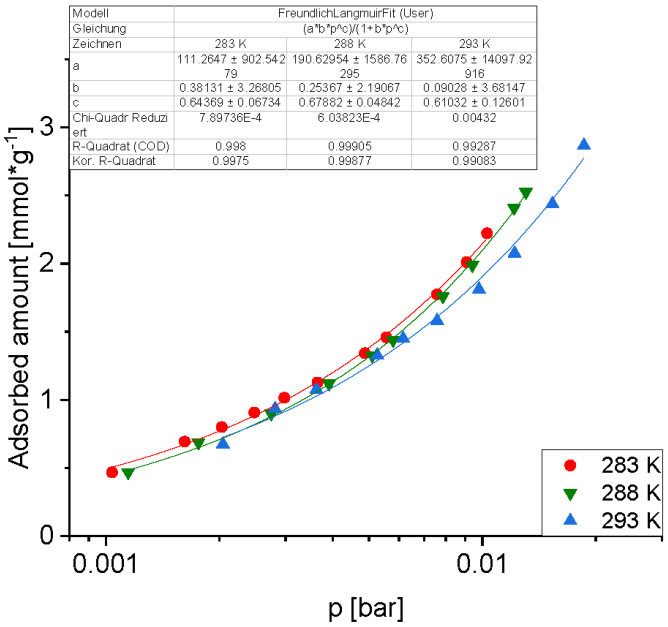

Figure S2: Water adsorption isotherms at different temperatures (on a semi-logarithmic scale), fitted to a Freundlich-Langmuir model.

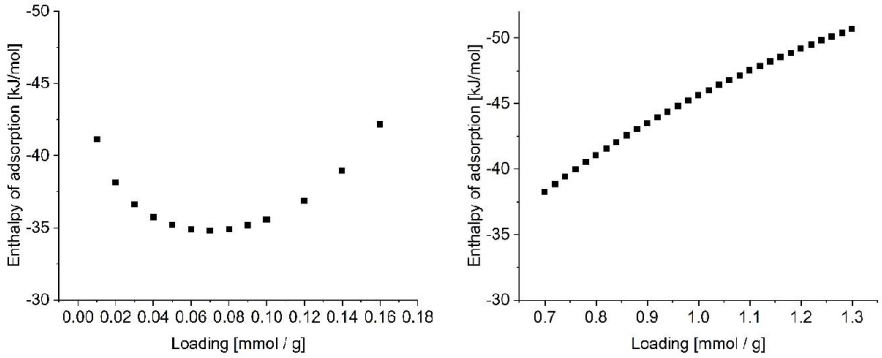

Figure S3: Enthalpy of adsorption against loading of CO_2 (left) and H_2O (right)

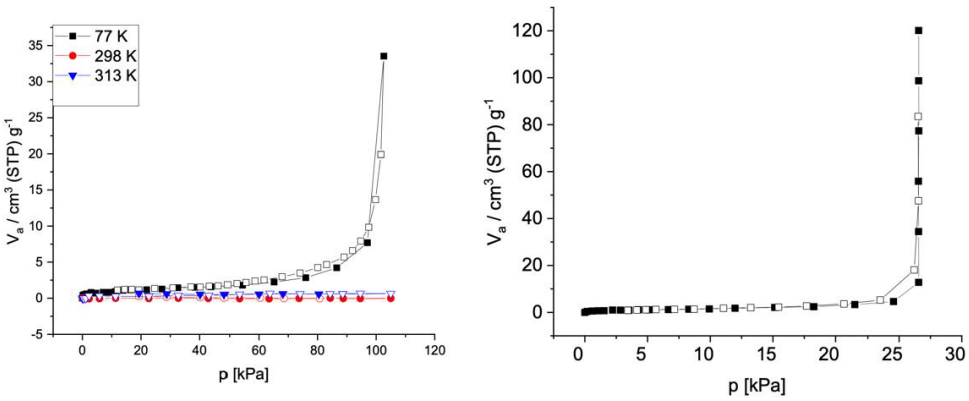

Figure S4: Nitrogen (left) and argon (right) adsorption isotherms for TUB41 (filled symbols – adsorption, empty symbols – desorption).

Below, we present the additional water and CO_2 adsorption isotherms collected over a two-year period.

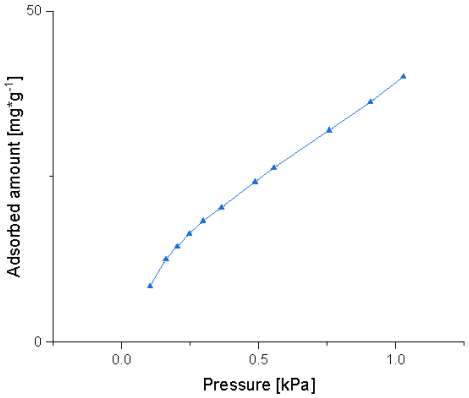

Figure S5: Water adsorption isotherm 1 at 283 K, before condensation

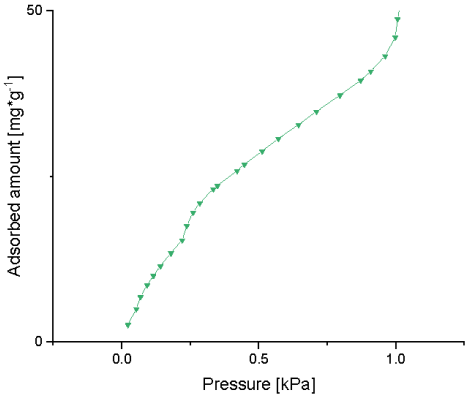

Figure S6: Water adsorption isotherm 2 at 283 K, before condensation

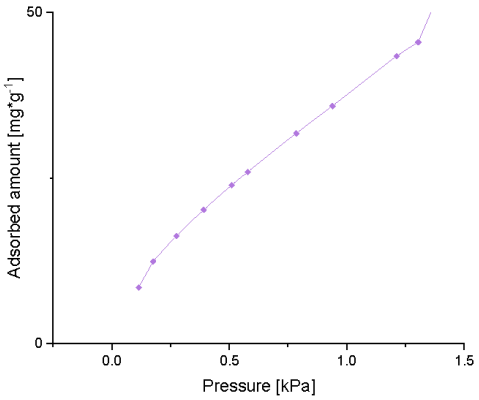

Figure S7: Water adsorption isotherm 1 at 288 K, before condensation

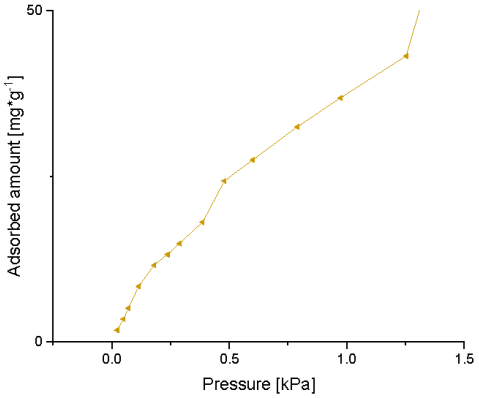

Figure S8: Water adsorption isotherm 2 at 288 K, before condensation

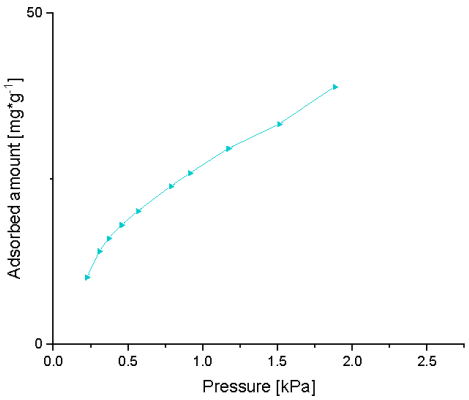

Figure S9: Water adsorption isotherm 1 at 293 K, before condensation

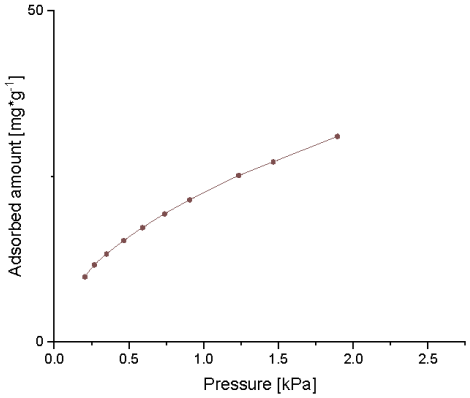

Figure S10: Water adsorption isotherm 2 at 293 K, before condensation

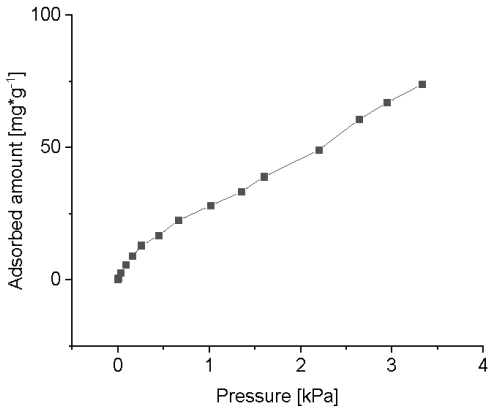

Figure S11: Water adsorption isotherm 1 at 298 K, before condensation

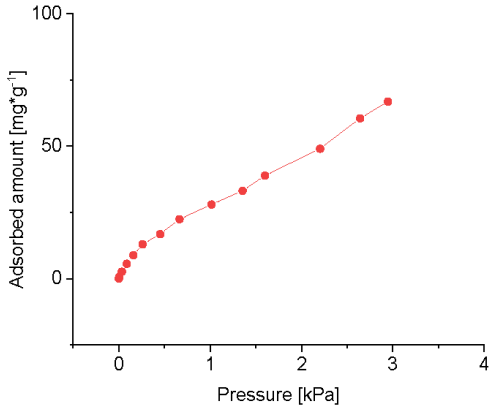

Figure S12: Water adsorption isotherm 2 at 298 K, before condensation

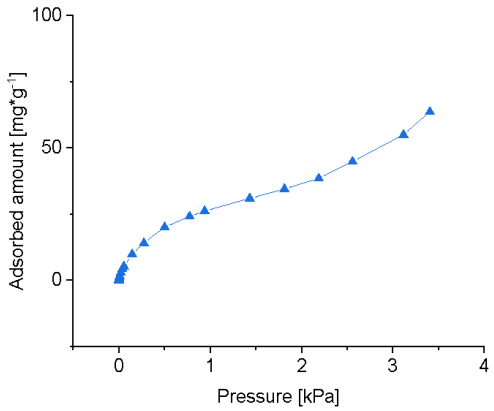

Figure S13: Water adsorption isotherm 1 at 303 K, before condensation

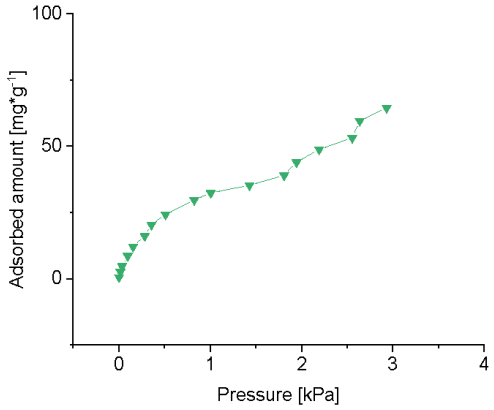

Figure S14: Water adsorption isotherm 2 at 303 K, before condensation

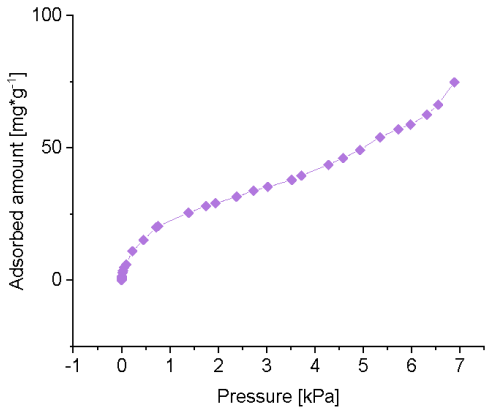

Figure S15: Water adsorption isotherm at 313 K, before condensation

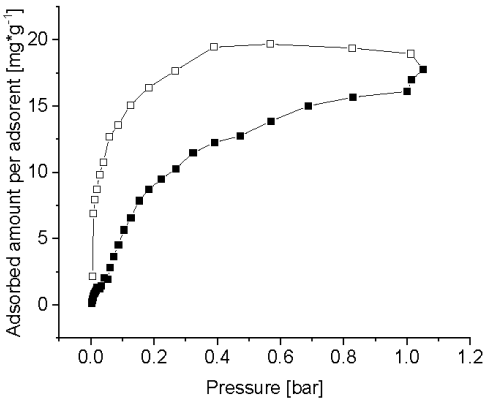

Figure S16: Carbon dioxide adsorption isotherm at 313 K

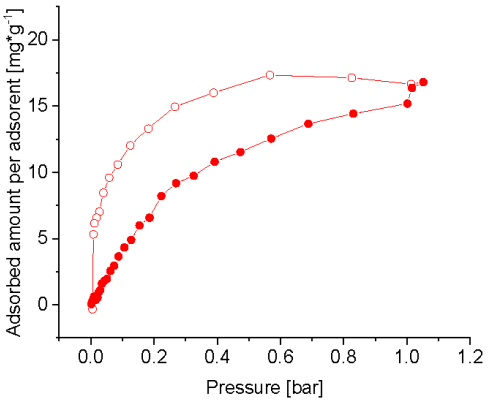

Figure S17: Carbon dioxide adsorption isotherm at 313 K

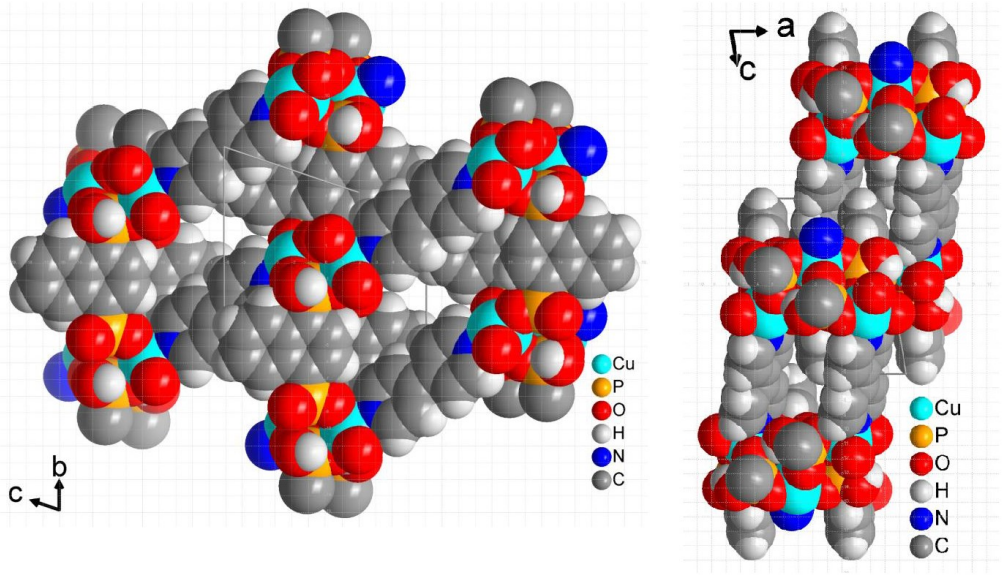

Figure S18: Section of the packing diagram in space-filling mode in two viewing directions to show the pore structure in the 3D network of [Cu(4,4'-bpy)$_{0.5}$(1,4-NDPAH$_2$)]. The edges of the grid-squares are 1 Å in length.

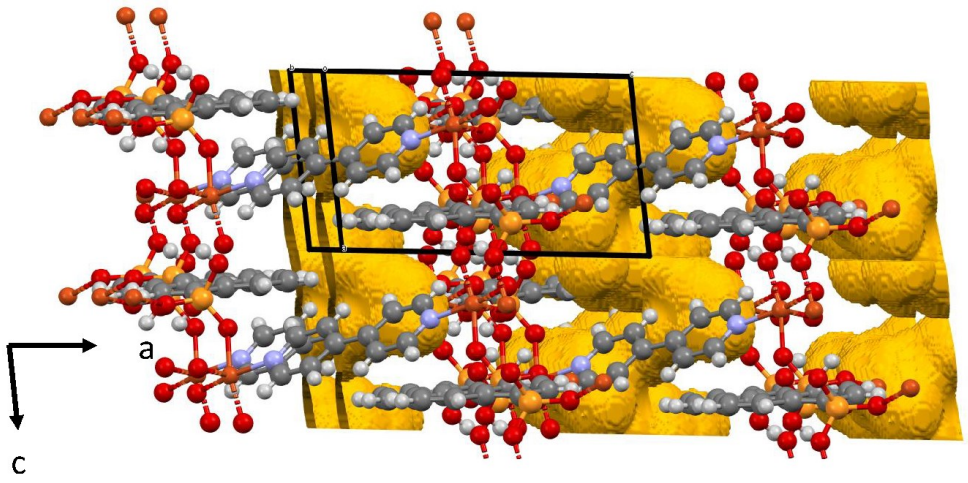

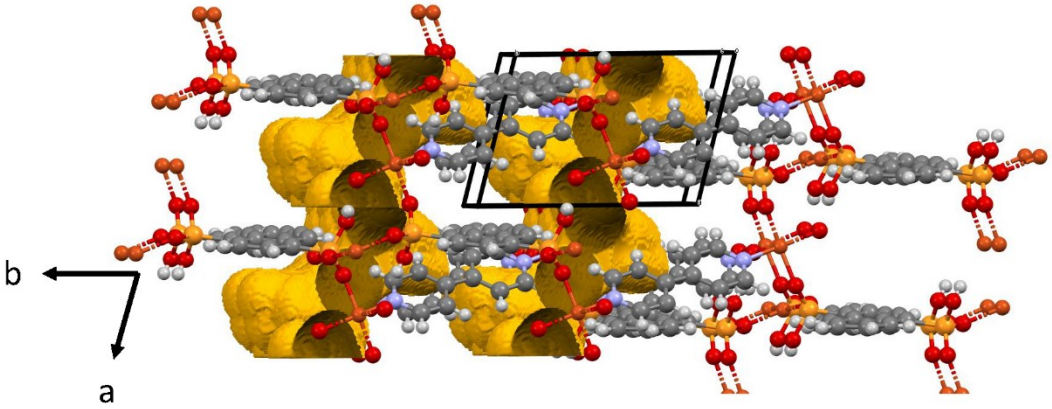

Figure S19: Voids in the MOF [Cu(4,4'-bpy)$_{0.5}$(1,4-NDPAH$_2$)], diameter 2.6 Å, suitable for water adsorption.

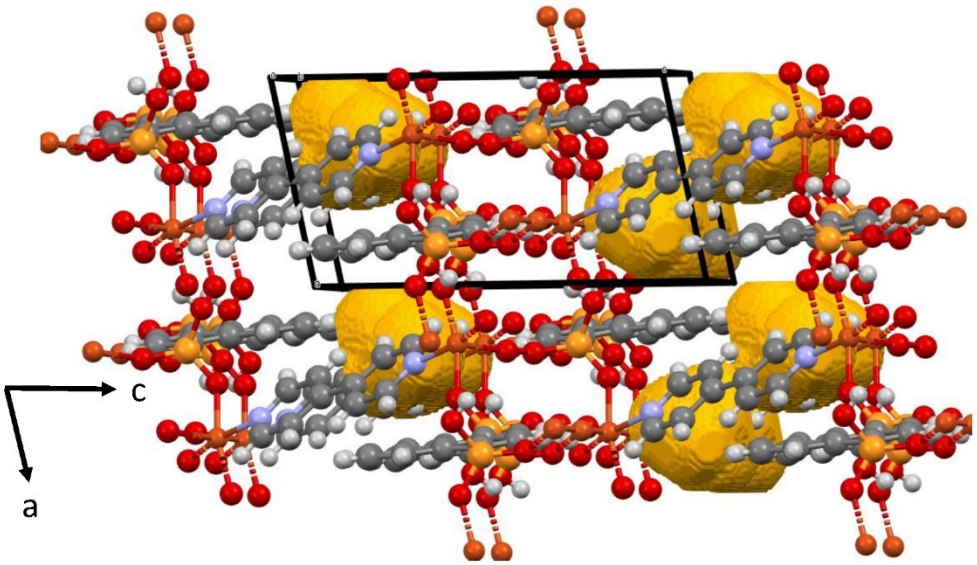

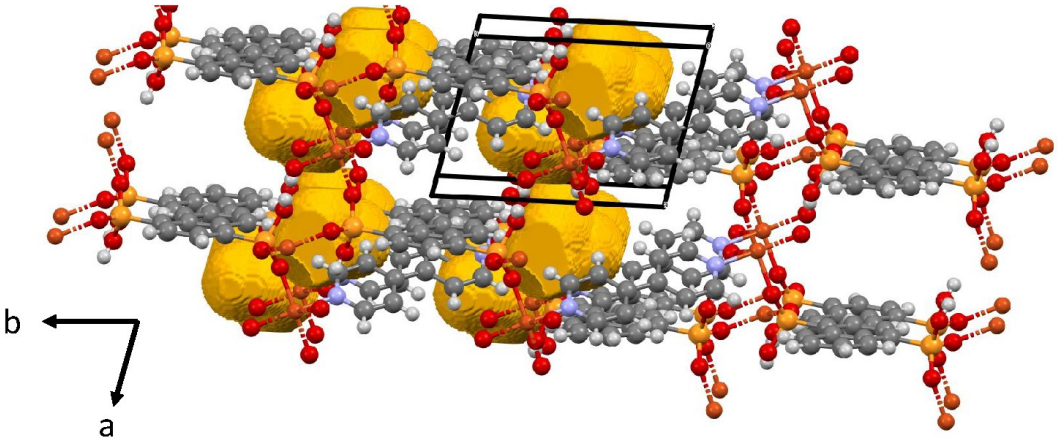

Figure S20: Voids in the MOF [Cu(4,4'-bpy)$_{0.5}$(1,4-NDPAH$_2$)], diameter 3.2 Å, suitable for CO_2 adsorption.

5. Optical spectroscopy

We measured diffuse reflectance spectra of TUB41 in an integrating sphere (diameter of 120 mm, internally coated with BenFlect® with a reflectance > 99% between 350 nm and 2500 nm) setup on a FLS1000 luminescence spectrometer equipped with a 450 W Xe arc lamp, double grating Czerny-Turner monochromators in both excitation and emission compartment and a thermoelectrically cooled (–20 °C) PMT-980 detector from Hamamatsu. All spectra were corrected for wavelength-dependent grating efficiency, detector sensitivity, and fluctuating lamp intensity. The diffuse reflectance, R_∞, was converted to the Kubelka-Munk function, K/S, given by equation (1), which is proportional to the effective absorbance, A, of the powdered sample,

$$\frac{K}{S} = f(R_\infty) = \frac{(1-R_\infty)^2}{2R_\infty} \propto A \qquad (1)$$

if the thickness of the powder slab is sufficiently high such that transmittance along the layer is negligible. Tauc plots were generated by plotting $(f(R_\infty) \cdot E)^{1/2}$ vs. incident photon energy $E = h\nu$ (with $h = 6.626 \cdot 10^{-34}$ Js as Planck's constant and ν as the frequency) for an indirect band gap and $(f(R_\infty) \cdot E)^2$ vs. incident energy E for a direct band gap.

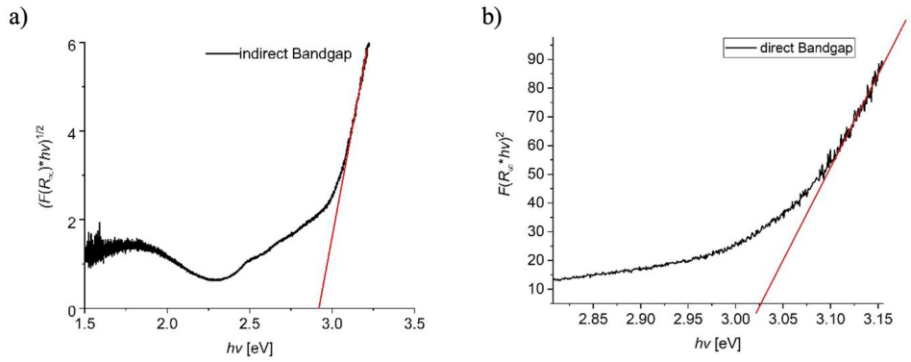

Figure S21: Tauc plots reflecting the a) indirect and b) direct band gap of TUB41.

6. SEM images

Scanning electron microscopy (SEM) images and element mapping analysis were recorded on a Jeol JSM-6510LV QSEM electron microscope equipped with a LaB6 filament and a Bruker XFlash 410-M EDX detector at an acceleration voltage of 20 kV. Prior to the measurement, samples were coated with gold using a Jeol JFC 1200 sputter coater.

7. In-situ variable temperature powder x-ray diffraction (VT-PXRD)

VT-XRD and isothermal XRD experiments were done using Rigaku Smartlab X-ray Diffractometer equipped with Cu K_α x-ray source (λ = 1.54059 Å) with a Hypix-3000 detector, measuring in 1D scanning mode with Bragg–Brentano geometry in horizontal position. The powder sample was prepared on a corundum sample holder and was mounted into a HTK1200N heating stage from Anton Paar. All measurements were performed under normal atmospheric conditions, no vacuum or inert gas was applied. Measurements were performed with an incident slit of 1 mm, 10 mm limiting slit combined with an incident soller slit of 5° and receiving slits #1 of 20 mm and #2 "open". A K_β filter was installed before the detector. Diffraction patterns were collected between 25°C to 350 °C heating rate of 2 K/min resulting

in 2 measurements within 5K. For isothermal XRD the target temperature was held for 3.5 min every 5K. Diffraction was measured from 6-24 °2θ with a step size of 0,01 ° and a speed of 10 °/min, resulting in a 3 min 1 s measurement.

8. Molecular dynamics (MD) simulation

Simulation details:

We adopted the experimentally determined unit cell dimensions and coordinates of the heavy atoms for TUB41, adding hydrogen atoms at appropriate positions. A DFT geometry optimization was subsequently performed in CP2K, employing the PBE functional along with GTH-PBE pseudopotentials, DZVP-MOLOPT-SR-GTH basis set, and DFT-D3(BJ) dispersion corrections. The optimized structure was then used to construct a 12 × 4 × 4 supercell as the initial structure for the MD simulations. Using the this supercell, we built several systems containing varying concentrations of H_2O and CO_2. Specifically, four systems with different H_2O concentrations (containing 10, 30, 100, and 300 H_2O molecules) and three systems with different CO_2 concentrations (containing 10, 30, and 100 CO_2 molecules) were constructed to investigate the distribution, adsorption, and diffusion properties of H_2O and CO_2 within the MOF.

The flexible UFF4MOF force field was employed for TUB41, with the atomic charges fitted using the restrained electrostatic potential–repeating electrostatic potential extracted atomic (RESP-REPEAT) method. The rigid TIP4P model was used for the water molecules, and the TraPPE model was selected for the CO_2 molecules. Interactions between different atom types were determined using the Lorentz–Berthelot mixing rules. A cutoff radius of 12.5 Å was applied for the van der Waals interactions, and the conversion radius between long-range and short-range Coulomb interactions was set to 12 Å. The particle–particle particle–mesh (PPPM) algorithm with a force accuracy set to $1e^{-5}$ was utilized to calculate the long-range electrostatic interactions. Long-range tail corrections were also applied to enhance the accuracy of pressure and energy calculations.

All systems were simulated using LAMMPS (version lammps-omp/20230802). An energy minimization was first performed, followed by a 100 ps NVT equilibration run during which the temperature was gradually increased from 10 K to 300 K. Subsequently, a 50 ns NVT

production run was conducted, with a time step of 0.5 fs. Temperature control was achieved using a Nosé–Hoover thermostat. During the production run, the trajectory data was recorded every 1 ps for further analysis. MDAnalysis (version 2.8.0) was used to calculate radial distribution functions (RDFs) and hydrogen bond numbers. In-house Python scripts were used to generate atomic trajectory overlay maps, and LAMMPS was used to compute mean-squared displacements.

Atomic trajectory overlay maps:

In all the figures shown below, cyan and green represent the oxygen and hydrogen atoms of H_2O, respectively; red and orange represent the carbon and oxygen atoms of CO_2, respectively; gold, dark blue, dark orange, dark red, black, and gray represent copper, nitrogen, phosphorus, oxygen, carbon, and hydrogen atoms, respectively, in the MOF framework. The *x* and *y* axes of the figures correspond to position, expressed in Ångstroms (Å).

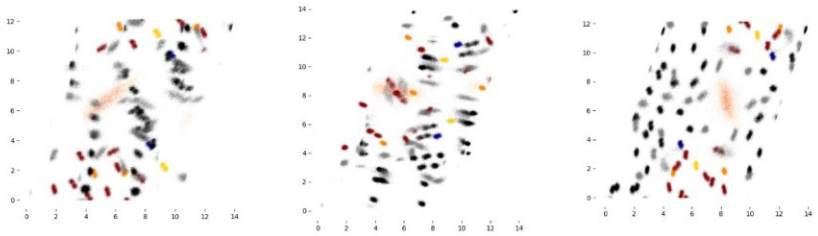

Figure S22: Atomic trajectory overlay maps for TUB41 with 10 CO_2 molecules. From left to right: Projections onto a plane perpendicular to the z, y, and x directions.

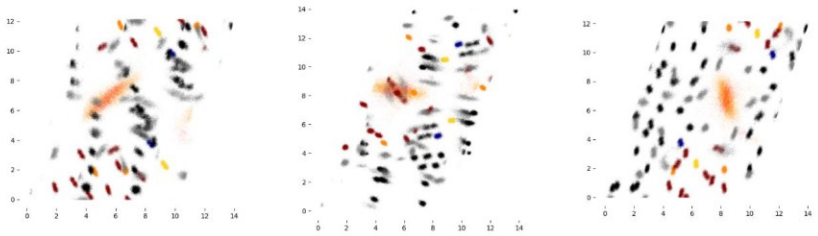

Figure S23: Atomic trajectory overlay maps for TUB41 with 30 CO_2 molecules. From left to right: Projections onto a plane perpendicular to the z, y, and x directions.

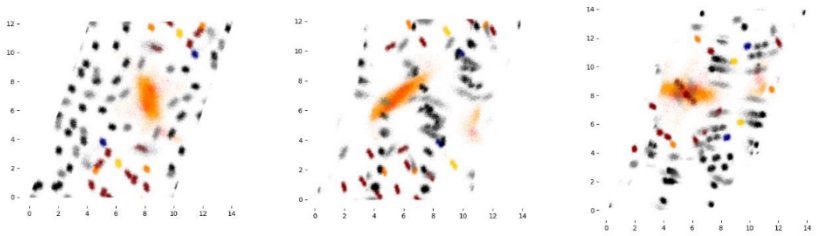

Figure S24: Atomic trajectory overlay maps for TUB41 with 100 CO_2 molecules. From left to right: Projections onto a plane perpendicular to the z, y, and x directions.

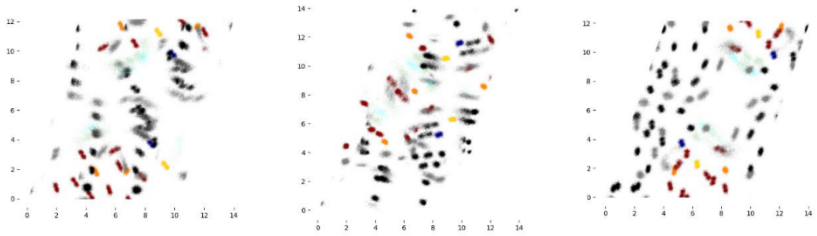

Figure S25: Atomic trajectory overlay maps for TUB41 with 10 H_2O molecules. From left to right: Projections onto a plane perpendicular to the z, y, and x directions.

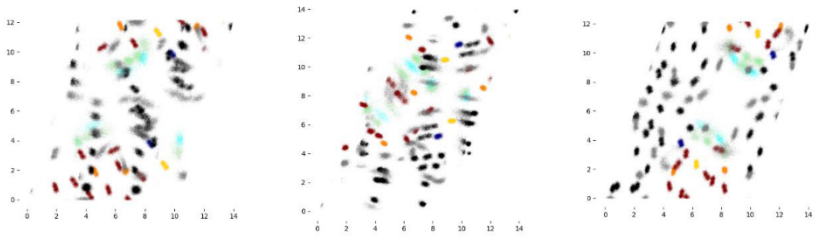

Figure S26: Atomic trajectory overlay maps for TUB41 with 30 H_2O molecules. From left to right: Projections onto a plane perpendicular to the z, y, and x directions.

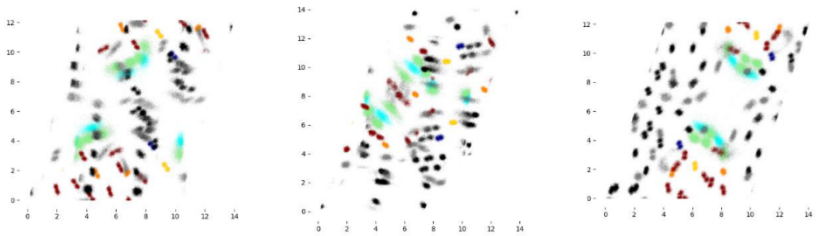

Figure S27: Atomic trajectory overlay maps for TUB41 with 100 H_2O molecules. From left to right: Projections onto a plane perpendicular to the z, y, and x directions.

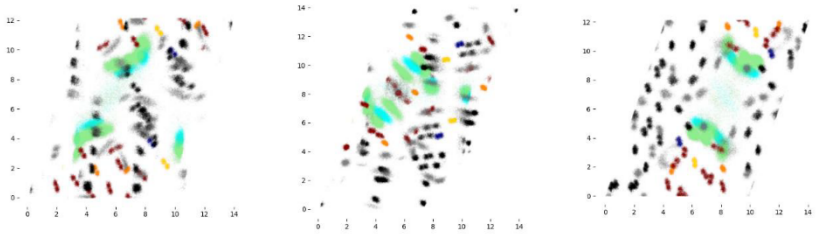

Figure S28: Atomic trajectory overlay maps for TUB41 with 300 H_2O molecules. From left to right: Projections onto a plane perpendicular to the z, y, and x directions.

RDF plots:

a)

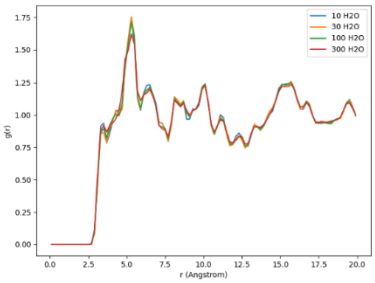

b)

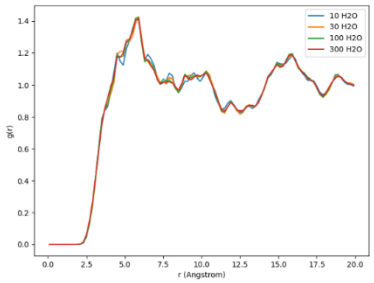

c)

d)

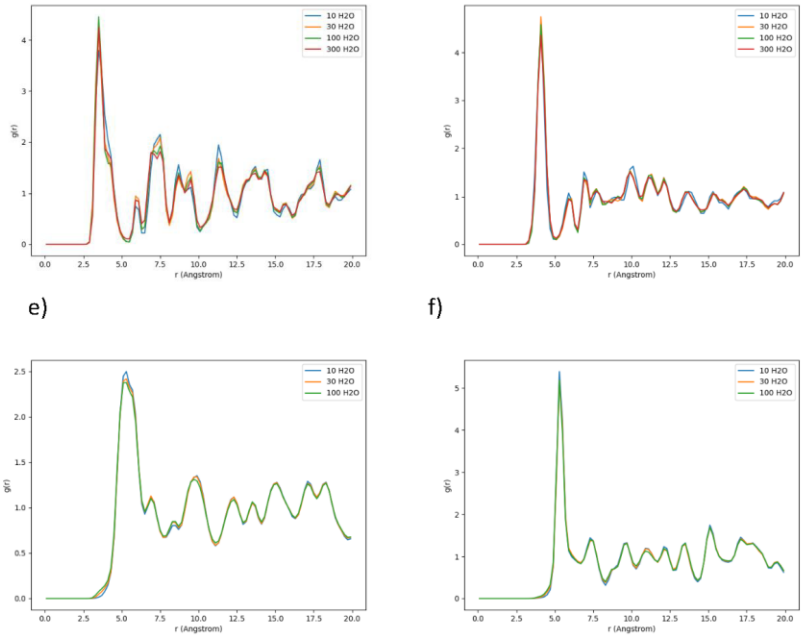

Figure S29: RDFs between atoms in CO_2/H_2O and atoms in the TUB41 framework for all systems. a) O (H_2O) – C (framework) b) H (H_2O) – C (framework) c) O (H_2O) – (framework) d) O (H_2O) – P (framework) e) O (CO_2) – C (framework) f) C (CO_2) – C (framework).

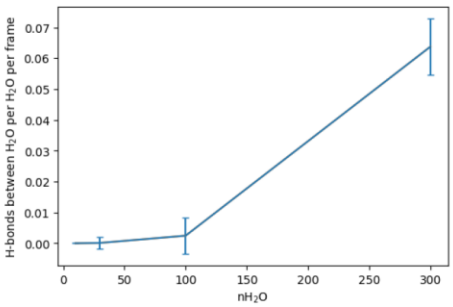

Figure S30: Average number of hydrogen bonds between H_2O molecules for the water-containing systems, normalized by both the number of trajectory frames and the number of H_2O molecules.

3.5 Encapsulation of a Highly Acid-Stable Dicyano-Bodipy in Zr-Based Metal–Organic Frameworks with Increased Fluorescence Lifetime and Quantum Yield Within the Solid Solution Concept

Diese Arbeit wurde veröffentlicht in

Marcus N. A. Fetzer, Maximilian Vieten, Aysenur Limon and Christoph Janiak, *Molecules* **2025**, *30*, 4151. DOI. 10.3390/molecules30214151; Ref.[98]

Kurzzusammenfassung

In dieser Arbeit haben wir eine säurestabilere Variante des klassischen Chromophors Difluor-Bodipy synthetisiert, indem wir die Difluorliganden am Bor durch Cyanogruppen ersetzt haben. Diese Dicyano-Bodipy-Variante ermöglichte die *in situ* Einlagerung während der MOF-Bildung unter sauren Bedingungen und wurde erstmals als Farbstoff@MOF-Verbundwerkstoff untersucht, wobei sowohl eine post-synthetische als auch eine *in situ* Einlagerung in die zirkoniumbasierten MOFs UiO-66, MOF-808, DUT-67 und MIP-206 verwendet wurde. Die erfolgreiche Einlagerung von Dicyano-Bodipy wurde durch PXRD, N_2-Sorption, Zersetzungs-UV–Vis und Fluoreszenzspektroskopie bestätigt. Je nach verwendeter Einlagerungsmethode konnten deutlich geringere BET-Oberflächen bestimmt werden. Die Lumineszenzeigenschaften der resultierenden Dicyano-Bodipy@MOF-Komposite aus den *in situ* Einlagerungen wiesen eine bis zu fast achtfach verlängerte Photolumineszenzlebensdauer von 9,0 ns auf, verglichen mit dem reinen Farbstoff in seinem festen Zustand mit 1,2 ns, was auf die Bildung einer Feststofflösung hindeutet, in der das eingebaute Bodipy vor äußeren Einflüssen innerhalb einer genau definierten MOF-Pore geschützt ist. Die Quantenausbeute konnte durch die post-synthetische Einlagerung in das MOF DUT-67 auf bis zu 77 % gesteigert werden, verglichen mit 9 % beim reinen Farbstoff im festen Zustand.

Anteile an der Publikation:

- Die Projektidee erfolgte durch Marcus N. A. Fetzer und Christoph Janiak.
- Marcus N. A. Fetzer synthetisierte die Bodipy-Verbindung, alle MOFs und alle Komposite.

- Marcus N. A. Fetzer entwickelte die Zersetzungs-UV-Vis-Methode und führte die gesamte Analytik außer der Quantenausbeuten-Messungen durch.
- Die Quantenausbeuten-Messungen wurden von Maximilian Vieten durchgeführt.
- Aysenur Limon führte vorbereitende Untersuchungen durch.
- Das Manuskript wurde von Marcus N. A. Fetzer geschrieben und in Zusammenarbeit mit Christoph Janiak überarbeitet.
- Die finale Korrektur wurde von allen Autoren durchgeführt.

molecules

MDPI

Article

Encapsulation of a Highly Acid-Stable Dicyano-Bodipy in Zr-Based Metal–Organic Frameworks with Increased Fluorescence Lifetime and Quantum Yield Within the Solid Solution Concept

Marcus N. A. Fetzer, Maximilian Vieten, Aysenur Limon and Christoph Janiak *

Institut für Anorganische Chemie und Strukturchemie, Heinrich-Heine-Universität Düsseldorf, Universitätsstraße 1, D-40225 Düsseldorf, Germany; marcus.fetzer@hhu.de (M.N.A.F.); mavie107@hhu.de (M.V.); aysenur.limon@hhu.de (A.L.)

* Correspondence: janiak@uni-duesseldorf.de

Abstract

In this work, we have synthesized a more acid-stable variant of the classic chromophore difluoro-Bodipy by substituting the difluoro ligands at boron with cyano groups. This dicyano-Bodipy variant allowed the in situ incorporation during the MOF formation under acidic conditions and was investigated for the first time as dye@MOF composites using both post-synthetic and in situ incorporation into the zirconium-based metal–organic frameworks (MOFs) UiO-66, MOF-808, DUT-67, and MIP-206. The successful incorporation of dicyano-Bodipy was confirmed by PXRD, N_2 sorption, digestion UV–Vis, and fluorescence spectroscopy. Depending on the incorporation method used, significant lower BET surface areas could be determined. The luminescence properties of the resulting dicyano-Bodipy@MOF composites from the in situ incorporation had up to almost eight-fold extended photoluminescent lifetimes of 9.0 ns, compared to the neat dye in its solid state with 1.2 ns, which suggests the formation of a solid solution in which the incorporated Bodipy is protected from external influences within a well-defined MOF pore. The quantum yield could be enhanced to as high as 77% through post-synthetic incorporation into the MOF DUT-67, compared to the neat dye in its solid state, with 9%.

Keywords: dicyano-Bodipy; metal–organic framework (MOF); UiO-66; MOF-808; DUT-67; MIP-206; dye@MOF; fluorescence; solid solution

Academic Editor: Michal Szostak

Received: 24 September 2025
Revised: 15 October 2025
Accepted: 18 October 2025
Published: 22 October 2025

Citation: Fetzer, M.N.A.; Vieten, M.; Limon, A.; Janiak, C. Encapsulation of a Highly Acid-Stable Dicyano-Bodipy in Zr-Based Metal–Organic Frameworks with Increased Fluorescence Lifetime and Quantum Yield Within the Solid Solution Concept. *Molecules* **2025**, *30*, 4151. https://doi.org/10.3390/molecules30214151

1. Introduction

Metal–organic frameworks (MOFs) represent a unique class of hybrid compounds in which metal atoms or metal clusters as secondary building units (SBUs) are connected by organic linkers [1]. The resulting frameworks often exhibit high crystallinity and porosity, with specific surface areas of several thousand square meters per gram [2]. Compared to traditional porous materials, such as activated carbon, zeolites, or silica gel, the properties of MOFs, such as defined pores and pore sizes [3,4], surface areas, morphology [5–8], defects [9,10], or stability, can be designed by the use of different SBUs or organic linkers [11–16]. For these reasons, MOFs are investigated for a wide range of applications, such as heterogeneous catalysis [17,18], drug transport [19,20], gas and liquid adsorption and separation [21–23], heat transformation [24–26], or for the post-synthetic or in situ encapsulation of dyes to modulate their photophysical properties [27–30]. For example, Chen et al.

were able to optimize the emission maximum of composites obtained by post-synthetic encapsulation of different rhodamine dyes in bio-MOF-1 [31]. Tang et al. produced white light-emitting composites by simultaneous encapsulation of different dyes in the MOF ZJU-28 [32]. An important aspect of dye encapsulation is the stability of the resulting composites. Zirconium-based MOFs have proven to be particularly robust compounds in this regard [33,34], making them suitable for the encapsulation of various dyes and their application in different fields. The class of Bodipy dyes is of particular interest in this context [35,36].

Bodipy is the abbreviation for boron dipyrromethene and was first synthesized and characterized by Treibs and Kreuzer in 1968 [37]. Bodipy represents a class of boron complexes formed by a dipyrromethene ligand and two other anionic ligands, usually fluorine (Scheme 1). Due to their chemical and photophysical properties, such as fluorescence with a high quantum yield and narrow emission band width, high thermal and photochemical stability, as well as good solubility in a wide range of solvents, interest in this class of dyes is constantly increasing [38,39]. It is widely used as a fluorescent sensor [40,41] in photothermal and photodynamic therapy for the treatment of cancer [42,43], as well as in the development of lasers [44] and for the labelling of proteins and nucleic acids [45]. It is also of great interest for catalysis research in various fields, such as selective oxidation or the coupling of a wide range of compounds [46,47]. In addition to the most widely used difluoro variant **1**, a large number of other Bodipy compounds have been prepared and analyzed in recent years by substitution of the fluorine atoms at the boron nucleus with other groups (Scheme 1) [48]. With several new dipyrromethene-based ligands, which form the backbone of the Bodipy compounds, the variety of different Bodipy compounds is constantly increasing, demonstrating the continuing interest in this class of dyes [49].

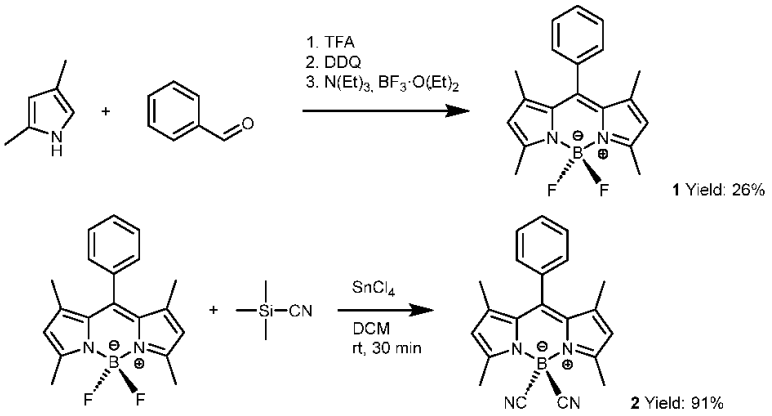

Scheme 1. Synthesis of 5,5-difluoro-1,3,7,9-tetramethyl-10-phenyl-Bodipy **1** and 5,5-dicarbonitril-1,3,7,9-tetramethyl-10-phenyl-Bodipy **2**.

A problem with Bodipy dyes is that their exceptional photophysical properties are usually only observed in solution. In the solid state, strong intermolecular interactions such as π–π stacking and aggregation often lead to fluorescence quenching and spectral shifts. This limitation restricts their applicability in various fields that require stable and efficient solid-state emitters, such as LED technology or sensors. To preserve their luminescent properties in the solid state, formulation strategies such as the incorporation of Bodipy into solid matrices are necessary. We expect that the encapsulation or incorporation of Bodipy into MOFs will give the photophysical properties of the dye as in solution. This should enable us to produce composites for a wide range of applications, such as

heterogeneous catalysis, cancer therapy, or sensing. Another interesting approach for such dye composites comes from LED technology, where interactions between the molecules, such as π-π stacking or aggregation-induced quenching, can be suppressed by targeted separation of the dye molecules in the individual MOF pores. The increased stability is highly beneficial for all types of applications. For these reasons, we present here the synthesis of a variety of zirconium-based Bodipy@MOF composites, both by post-synthetic and in situ encapsulation of Bodipy in the MOF.

2. Results and Discussion

The synthesis and analysis of the Bodipy dyes and the MOFs used in this work are described in detail in the Supplementary Materials. In short, the Bodipy syntheses in Scheme 1 were carried out according to Caruso et al. [50] and Nguyen et al. [51]. For the MOFs, we chose Zr-based MOFs because of their high hydrothermal stability compared to other MOFs. In addition, Zr-MOFs typically form colorless, crystalline compounds, which makes it easier to detect the color changes caused by the incorporation of Bodipy (see the in situ produced **2**@UiO-66 composites in Figure S13). The MOFs were prepared according to the synthesis described in the literature. For the synthesis of UiO-66, the procedure described by Katz et al. was used with minor modifications [52]. The MOFs MOF-808 and DUT-67 were both synthesized according to Reinsch et al. [53]. MIP-206 was prepared according to a procedure by Wang et al. [54].

The successful synthesis and identity of the Bodipy derivatives **1** and **2** were verified by NMR and high-resolution mass spectrometry. The neat MOFs were prepared by the synthesis routes reported in the literature and characterized by powder X-ray diffraction (PXRD) together with N_2 gas sorption for BET surface area and porosity determination.

Initial encapsulation experiments with the zirconium-based MOFs UiO-66 and UiO-67, using the difluoro variant **1,** gave no detectable luminescence, probably due to the acidity of the inherently defective UiO structures [55]. This confirms the statement by Wang et al. that the dye cannot be effectively stabilized under strongly acidic conditions. In their study on the stability of Bodipy compounds, it was found that the addition of trifluoroacetic acid led to the degradation of the Bodipy structure [56]. Since the dicyanide variants exhibited increased stability under acidic conditions, we decided to use the less studied but more stable dicyano-Bodipy **2**. Another advantage of this dicyano-Bodipy **2** is, in addition to the increased stability against acids, the increased quantum yield compared to difluoro-Bodipy **1**. By going from the difluoro species **1** to the dicyano species **2**, the quantum yield of the Bodipy dye in THF solution could be increased from approximately 37% for **1** [57] to 89% for **2** [51].

Luminescence studies in solution show that both the difluoro and dicyano species **1** and **2** have narrow excitation and emission bands (Figure 1a,b) and are similar in their photophysical properties. The emission maxima at 514.4 nm for **1** and 510.0 nm for **2** in highly diluted chloroform solution correspond to the values given in the literature [51,57]. The Stokes shifts are 7.7 nm (295 cm^{-1}) for **1** and 9.7 nm (381 cm^{-1}) for **2,** and their full width at half-maximum (FWHM) values are 19 nm (720 cm^{-1}) for **1** and 22 nm (850 cm^{-1}) for **2**, making both species very narrow band emitters. Lifetime measurements of both compounds in chloroform yielded an average lifetime value of 5.7 ns for **1** and 4.8 ns for **2** (Figure S6, Supplementary Materials). Investigations of compound **2** in different solvents at the same concentration showed that the emission maxima are almost unaffected by the polarity of the solvent. All maxima were consistently in the range of 525 nm ± 2 nm (Figure S7, Supplementary Materials). This indicates that the photophysical behavior of compound **2** is largely independent of the solvent environment, suggesting minimal interaction between the solvent and the emission states of the compound. However, a

concentration-dependent bathochromic shift of the emission maxima was observed in $CHCl_3$ solution (Figure 1c).

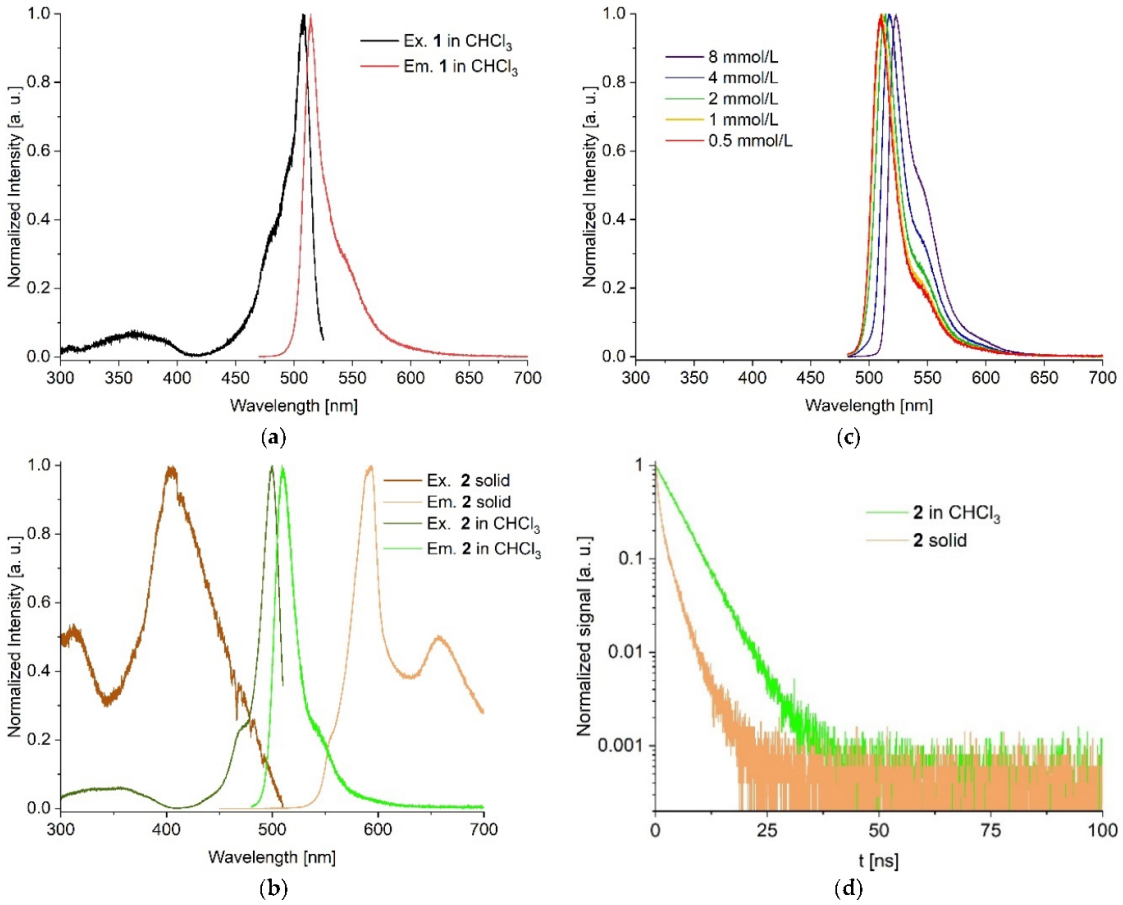

Figure 1. (**a**) Excitation and emission spectra of **1** in $CHCl_3$. Emission spectra were measured with an excitation at 360 nm. Excitation spectra were measured at an emission of 540 nm. (**b**) Excitation and emission spectra of **2** in $CHCl_3$ and neat Bodipy in the solid state in a reflective setup. Emission spectra in solution were measured with an excitation at 360 nm and as a solid with an excitation at 400 nm. Excitation spectra in solution were measured at an emission of 540 nm and as a solid at an emission of 600 nm. (**c**) Concentration-dependent bathochromic shift of **2** in $CHCl_3$. Emission maxima: 510 nm (0.5 mmol/L), 511 nm (1 mmol/L), 514 nm (2 mmol/L), 517 nm (4 mmol/L), and 523 nm (8 mmol/L). Emission spectra were measured with an excitation at 360 nm. (**d**) Lifetime measurements of **2** in solution (0.5 mmol/L) and neat **2** in the solid state at the respective emission maxima of 510 nm and 594 nm (λ_{exc} = 375 nm).

The wavelength increases for the emission maxima with increasing concentration of compound **2,** which implies the presence of concentration-dependent aggregation phenomena such as π-π interactions and an associated reduction in free rotation. This assumption is also supported by the increasing intensity of the shoulder at 540 nm. These interactions can change the electronic environment of the emission states, which, in our case, leads to a bathochromic shift of the fluorescence.

As a solid, neat Bodipy **2** is a red crystalline powder, while the $CHCl_3$ solution has a green color (Figure S8). We used a reflective setup for all solid-state measurements.

For this purpose, both neat Bodipy in the solid state and all composites were placed as solids in a brass sample holder. Under UV light excitation with λ_{exc} = 400 nm, solid **2** emits an orange to red luminescence with emission maxima at 594 nm and 659 nm Figures 1b and S8). The formation of two emission maxima and the clear bathochromic shift are discussed in the literature and can be attributed mainly to the formation of J-aggregates [58,59]. The excitation maximum for the solid occurs at 404 nm (Figure 1b), corresponding to Stokes shifts of 190 nm (7917 cm^{-1}) and 255 nm (9577 cm^{-1}) for the two emission peaks, respectively. A comparison of these values with those of the $CHCl_3$ solution shows the influence of aggregation effects in **2**. While Bodipy molecules are surrounded by solvent molecules in solution, allowing for dynamic solvation, molecular motion, and minimal intermolecular interactions, they are densely packed in the solid state, promoting the formation of aggregates. These aggregates significantly influence molecular mobility, the local electronic environment, and the strength of intermolecular interactions. As a result, new electronic states with lower energy levels can arise in the solid state, often accompanied by enhanced π–π interactions between neighboring chromophores. These effects collectively lead to a bathochromic shift compared to the monomeric species in solution.

In addition to the clear differences in the steady-state luminescence measurements, there is also a significant change in luminescence lifetime and quantum yield for neat **2** in the solid state versus **2** in solution. Solid **2** had a lifetime of only 1.2 ns and an average quantum yield of only 9% compared to a lifetime of 4.8 ns in $CHCl_3$ and an average quantum yield of 89% in THF solution (Figures 1d, S6 and S9) [51]. The increased quantum yield of **2,** when going from the solid to the solution state, and the drastically improved stability against organic and inorganic acids, make compound **2** in solution very interesting for various applications. With the concept of solid solutions for dye@MOF composites, the embedding or encapsulation of non-aggregated Bodipy in the defined pores of MOFs could open up interesting future applications in areas such as optoelectronic devices or chemical sensors.

The inclusion of dyes in MOFs can be carried out post-synthetically by wet infiltration in the already prepared MOF or in situ, that is, during the MOF synthesis [60]. Furthermore, the presence of defects, such as missing linkers or missing cluster defects, can facilitate the incorporation of the dye molecules and enable the production of composites with both higher dye loadings and high N_2 uptake. We chose the MOFs UiO-66, MOF-808, DUT-67, and MIP-206. All MOFs are colorless, microcrystalline powders with BET surface areas as reported in the literature. All of them show only a weak linker-based luminescence in the range between 350 and 440 nm, depending on the linkers used. We were able to perform both post-synthetic and in situ encapsulations for **2** in all MOFs except for MIP-206. For comparison purposes, the same initial concentration of Bodipy was used for both the post-synthetic and in situ approaches for MOF-808 and DUT-67.

2.1. Composite **2***@UiO-66*

We started our studies on the encapsulation of **2** in MOFs with the zirconium MOF UiO-66. The encapsulation was carried out in a post-synthetic approach over a period of 5 days at a concentration of 1.0 mmol/L Bodipy in dichloromethane (CH_2Cl_2) with activated UiO-66 (see Section S5, Supplementary Materials for details). With pore sizes of about 8 Å for the tetrahedral pore and 11 Å for the octahedral pore in UiO-66, it is clear that the post-synthetic encapsulation of the Bodipy dye **2**, with molecular dimensions of about 10 Å, is restricted to the larger octahedral pores of UiO-66 (see Section S7, Supplementary Materials for details) [61,62]. Up to 0.44 wt% (4.4 mg of **2** per g of UiO-66 or 21.7 mmol of **2** per mol of UiO-66) could be embedded, based on the UiO-66 formula of $[Zr_6O_4(OH)_4(BDC)_6]$

(1664.01 g/mol), denoting the composite as **2**@UiO-66$_{0.44}$. No structural change could be detected by powder X-ray diffraction (PXRD, Figure 2a). The loading of all composites was determined post-synthetically by UV–Vis digestion analysis (Section S6, Supplementary Materials) [63] after extended washing procedures with dimethylformamide (DMF) until we could no longer detect any luminescence in the washing solution. This allowed us to assume that all Bodipy molecules attached to the outside of the MOF had been removed. The dye@MOF samples were then digested under strong basic (1 mol/L KOH for UiO-66, MOF-808, and MIP-206) or acidic conditions (conc. HCl for DUT-67) in order to determine the loading of **2** in the MOFs by UV–Vis spectroscopy. After the noted washing procedures, the thus determined Bodipy could only originate from the MOF-incorporated dye molecules.

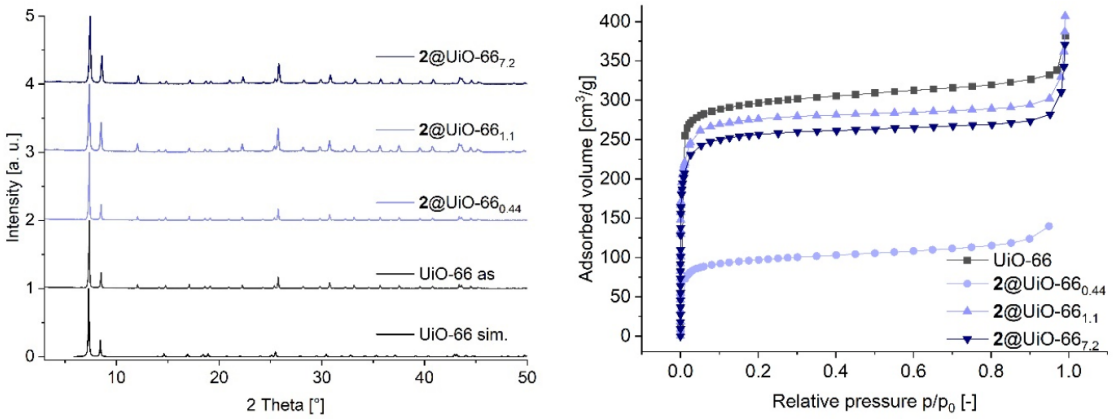

Figure 2. (**a**) PXRD of UiO-66, **2**@UiO-66$_{0.44}$ (post-synthetic encapsulated) and the in situ encapsulated **2**@UiO-66$_{1.1}$ and **2**@UiO-66$_{7.2}$ composites. Simulated diffractogram of UiO-66 from CCDC No. 752051 [64]. (**b**) Nitrogen adsorption isotherms at 77 K of neat UiO-66 (1192 m^2/g), **2**@UiO-66$_{1.1}$ (1115 m^2/g), **2**@UiO-66$_{7.2}$ (916 m^2/g), and **2**@UiO-66$_{0.44}$ (381 m^2/g). For the desorption isotherms, see Figures S11 and S12 in Supplementary Materials.

The apparent low post-synthetic loading results from only a short diffusion path of the dye molecules into the crystal lattice, slightly beneath the surface layer [29]. This is in line with the significant decrease in the BET surface area from 1192 m^2/g for neat UiO-66 down to 381 m^2/g for **2**@UiO-66$_{0.44}$ due to pore blocking (Figure 2b). Even these small amounts of **2** resulted in a composite with strong emission in the green wavelength range.

Further, the dye was also incorporated in situ into the MOF structure of UiO-66. Four different concentrations of **2** in DMF were used in the MOF reaction mixture of H_2BDC and $ZrCl_4$ (see Table S1, Supplementary Materials). Noteworthy, the synthesis of UiO-66 was carried out at 80 °C with hydrochloric acid as a modulator (see Section S5, Supplementary Materials for details) [52]. The improved stability of dicyano-Bodipy **2** versus difluoro-Bodipy **1** allowed us to use acids as modulators, giving acidic reaction conditions. The resulting **2**@UiO-66 composites were washed with DMF until the solution no longer showed any residual luminescence. The recorded PXRDs in Figure 2a show no differences compared to the reference sample or the simulation of neat UiO-66. This indicates that the presence of **2** does not affect the MOF structure, and face-centered cubic UiO-66 is the only crystalline product that is formed (see Figure S10, Supplementary Materials for all PXRDs). Scanning electron microscope (SEM) images of both the neat UiO-66 and the

synthesized composites show a homogeneous distribution of MOF particles of similar size and unchanged morphology (see Figure S21, Supplementary Materials).

The amount of Bodipy incorporated in situ in each composite was determined by UV–Vis digestion analysis (see above) between 1.1 and 7.2 wt% (11.1 to 77.5 mg of **2** per g of UiO-66 or 54.7 to 381 mmol of **2** per mol of UiO-66, see Section S6 for details), denoting the composites as **2**@UiO-66$_{1.1}$ to **2**@UiO-66$_{7.2}$, respectively. This corresponds to an average octahedral pore filling (n_{av}(Bodipy/pore)) of 5.5 to 37.5%, taking into account the number of octahedral pores and asymmetric units in the unit cell of UiO-66 (For a detailed description of the pore calculation, see Section S7 in Supplementary Materials). A higher concentration of **2** in the reaction mixture resulted in a higher loading in the in situ method, also in comparison to the post-synthetic incorporation. While the low loading from post-synthetic encapsulation of **2** in UiO-66 still gave a colorless composite akin to the color of neat UiO-66, the higher amounts of **2** through in situ encapsulations were also evident from an increasingly pinkish color of **2**@UiO-66 (Figures 3a and S13).

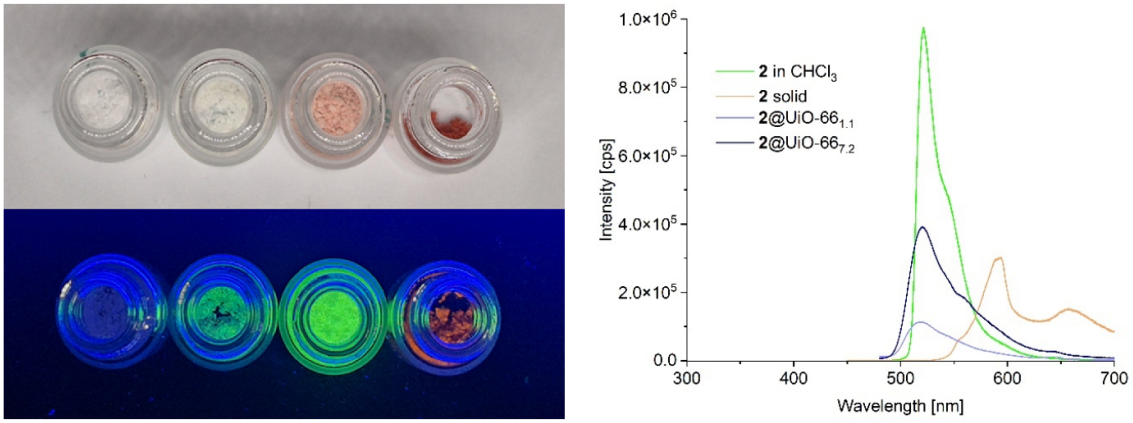

Figure 3. (**a**) From left to right: Neat UiO-66, post-synthetically encapsulated **2**@UiO-66$_{0.44}$ (0.44 wt%), in situ prepared **2**@UiO-66$_{2.3}$ (2.3 wt%), and neat **2** in the solid state, both under daylight (top) and under UV-light (λ_{exc} = 365 nm, bottom). (**b**) Emission spectra (λ_{exc} = 330 nm) of the **2**@UiO-66 in situ composites with the lowest (1.1 wt%) and highest (7.2 wt%) achieved loading together with the emission spectra of **2** in $CHCl_3$ solution (8 mmol/L, λ_{exc} = 360 nm) and the emission spectra of neat **2** in the solid state (λ_{exc} = 400 nm) in a reflective setup.

Nitrogen sorption measurements and BET surface area determinations of the activated in situ **2**@UiO-66 composites listed in Table 1 showed a decrease in surface area with increasing Bodipy loading compared to neat UiO-66 (for all isotherms, see Figures S11 and S12). This trend supports the successful incorporation of the dye into the MOF structure, as higher loadings of Bodipy reduce the number of accessible pores available for N_2 adsorption. The determined BET surface areas of the composites range from 1115 m^2/g for the least in situ loaded composite **2**@UiO-66$_{1.1}$ to 916 m^2/g for the composite with the highest Bodipy loading **2**@UiO-66$_{7.2}$. The even lower N_2 uptake and concomitant lower surface area of only 381 m^2/g for the post-synthetically prepared sample with only 0.44 wt% dye loading is interpreted through pore blocking by the dye molecules, which diffuse only slightly beneath the outer surface [29]. In situ incorporation results in a more homogeneous distribution of the Bodipy across the entire MOF. This generally leads to better pore accessibility and thus to a larger pore volume for in situ composites compared to post-synthetically produced composites. The similar or even slightly larger pore volume in the

in situ composites compared to neat UiO-66 (Table 1) can be explained by the encapsulation of the Bodipy molecules and the resulting formation of defects due to the Bodipy molecules. These defects lead to larger pores with an expanded pore volume.

Table 1. Results of nitrogen sorption measurements for neat UiO-66 and **2**@UiO-66 composites.

Compound	Bodipy Loading [wt%] [a]	S_{BET} [m^2/g]	$V_{pore(total)}$ [cm^3/g] [b]	$V_{pore(micro)}$ [cm^3/g] [c]
UiO-66 literature	-	1580 [52]	-	-
	-	1175 [65]	0.63	-
UiO-66 synthesized	-	1192	0.55	0.55
2@UiO-$66_{0.44}$ (post-synth.)	0.44	381	0.19	0.19
2@UiO-$66_{1.1}$ (in situ)	1.1	1115	0.63	0.63
2@UiO-$66_{2.3}$ (in situ)	2.3	1096	0.6	0.61
2@UiO-$66_{4.7}$ (in situ)	4.7	1022	0.57	0.59
2@UiO-$66_{7.2}$ (in situ)	7.2	916	0.56	0.53

[a] Calculated by UV–Vis digestion analysis. [b] Total pore volume at $p/p_0 = 0.9$. [c] Micropore volume calculated from NLDFT method using the N_2 adsorption isotherm at 77 K for cylindrical pores $\leq$ 2 nm.

Photophysical measurements show that all **2**@UiO-66 composites exhibit a strong green emission, as seen for the $CHCl_3$ solutions of **2** (Figures 3a and S8), hence indicating solid solution behavior and is in contrast to the red emission characteristics of solid **2** (emission maxima at 594 nm and 659 nm, cf. Figure 1b). This behavior can be attributed to the spatial separation of individual Bodipy molecules within the porous structure of the MOF. Within the individual pores, the Bodipy molecules can behave more like molecules in solution than molecules in the solid state. The MOF framework effectively prevents the aggregation of Bodipy molecules in the solid and dry composite material, causing them to exhibit emission behavior similar to Bodipy in solution.

The **2**@UiO-66 composites exhibit emission maxima at 521 nm $\pm$ 2 nm and are thus all comparable to **2** in solution (8 mmol/L), which shows its emission maximum at 523 nm. Figure 3b illustrates the emission intensities of the lowest and highest in situ loaded **2**@UiO-66 composites together with **2** in $CHCl_3$ (8 mmol/L) and **2** as a solid (for the emission spectra of all UiO-66 composites, see Figure S25). The observed broadening of the emission band of the composites shown in Figure 3b can be attributed to the heterogeneous and rigid environment of the MOF matrix. As already described, the Bodipy molecules in solution are uniformly solvated by $CHCl_3$, which allows free rotational and translational motion. As a result, all molecules emit with nearly identical energies and produce a narrow emission band. In contrast, the confinement within the MOF restricts molecular mobility and exposes the Bodipy molecules to different microenvironments depending on their orientation within the pore. This leads to different emission energies and slight shifts in the emission maxima of individual molecules. In addition, intermolecular interactions such as aggregation further disrupt the energies in the excited state. The cumulative effect of all these changes leads to an experimentally observed broadening of the entire emission band. The intensity of this band increases with higher Bodipy loading, yet without any bathochromic shift being observed for higher concentrations in $CHCl_3$ solutions of **2** (cf. Figure 1c). However, the emission maximum of 521 nm is already as seen for the higher-concentrated Bodipy $CHCl_3$ solution of 8 mmol/L, which can be attributed to the suppression of the rotation of **2** within the MOF pore [66,67].

We assume that the compact structure of the MOF composites causes a primary inner filter effect, whereby the excitation light is absorbed before it reaches molecules located deeper within the framework. Consequently, these internal molecules remain unexcited. However, the observed linear correlation between emission intensity and dye loading and

the absence of a significant redshift between the individual composites indicate that our composites are in a concentration range in which the secondary inner filter effect due to self-quenching or reabsorption phenomena plays a minor role, if any (see Figure S25f).

The constant emission maxima of the **2**@UiO-66 composites with different loadings strongly suggest that the encapsulation of **2** into the MOF structure effectively limits the interactions and aggregation of Bodipy molecules. All composites show, by their emission behavior, a desired separation of the Bodipy molecules, similar to that in the 8 mmol/L solution. However, it can be assumed that as the load increases, the probability of finding more than one Bodipy molecule in a pore also increases. This assumption is based on the shoulder at 550 nm, which is most prominent for the **2**@UiO-66$_{7.2}$ composite with the highest loading. It indicates some formation of J-aggregates between two or more Bodipy molecules in the same pore. The emission maximum remains unchanged at this low degree of aggregation. Based on the above loading, we calculated the probability p of multiple occupations in a random distribution of Bodipy in UiO-66 and listed this probability in Table 2 (for a more detailed description of the calculation, see Section S7, Supplementary Materials). The same behavior was observed and discussed in the work of Püschel et al. [68].

Table 2. Probability p of multiple occupations of Bodipy molecules in a pore of the **2**@UiO-66 composites [a].

	2@UiO-66$_{1.1}$	**2@UiO-66$_{2.3}$**	**2@UiO-66$_{4.7}$**	**2@UiO-66$_{7.2}$**
n_{av}(Bodipy/pore)	0.055	0.12	0.243	0.375
p(one) [%]	96.4	94	86.7	78.1
p(two) [%]	3.6	5.7	12.1	18.4
p(≥three) [%]	0	0.2	1.1	3.5

[a] Calculations are based on the UiO-66 formula of $[Zr_6O_4(OH)_4(BDC)_6]$, the amount of Bodipy in mol per mol MOF, and the ratio of pores per formula unit (1:1). Pore refers to the octahedral pore in UiO-66.

The probability calculations confirmed our assumptions of some J-aggregate formation already at low loadings. At the same time, we were able to determine that the majority of the Bodipy molecules are embedded separately, which explains the solution-like luminescence behavior of the composites. Furthermore, based on the measured emission wavelengths and increasing intensities with loading, we assume that there is no strong interaction of the dye molecules with the MOF pore surface that would affect the wavelength of the emission maxima. Time-resolved fluorescence spectroscopy of the **2**@UiO-66 composites shows that a tri-exponential decay of the post-synthetically prepared **2**@UiO-66$_{0.44}$ composite and bi-exponential decay of all in situ prepared composites were needed to describe the luminescence lifetimes and decays of all composites (for the decay plots of all UiO-66 composites, see Figure S26). The difference in decay can be explained by the presence of different luminescent species. These species can be attributed to the presence of different J-aggregates, which are formed by the multiple loading of pores with two or more Bodipy molecules within the MOF structure. This aggregation depends on the loading and the probability of several Bodipy molecules within a pore (cf. Table 2). Such an aggregate exhibits its own decay, whereby its respective properties significantly influence the lifetimes of the composite materials. Furthermore, the environment formed by the MOF can also affect the luminescence lifetime decay. This can result in either a prolongation or a shortening of the lifetime [69–71]. The lifetimes of **2**@UiO-66 were significantly extended compared to the lifetime of solid **2** (Table 3).

The average lifetimes τ_x of the composites are comparable to the lifetime of **2** in solution, with the lowest loadings of 0.44 and 1.1 wt% showing slightly increased lifetimes of 5.3 and 5.1 ns, respectively. Interestingly, the lifetimes show an inverse relationship to the Bodipy loading in the composites (Table 3). The sample with the highest loading of

7.2 wt% gave the shortest lifetime, measured at 4.0 ns. This trend is consistent with the observed quantum yields, which also decrease with increasing loading. In particular, the composites with the lowest loadings exhibited average quantum yields of around 30%, while the composite with the highest loading exhibited a reduced quantum yield of 19%. The presence of π-π interactions between neighboring Bodipy molecules can influence the lifetime. However, it is mainly explained by the presence and increase of J-aggregates in higher loaded composites (cf. Table 2) [72]. In addition to the increased aggregation, Bodipy-to-MOF wall interactions play a decisive role, as the excited state loses its energy more quickly through a Bodipy contact with the MOF pore wall. This can contribute to both a reduced quantum yield and a reduced lifetime. Although the quantum yields of **2**@UiO-66 are lower than the quantum yield of **2** in THF solution, they are significantly improved over the quantum yield of solid **2**, which is only 9%.

Table 3. Photophysical data for **2** as a solid, in solution, and for the **2**@UiO-66 composites.

Compound	$\lambda_{F,\,max}$ [nm] [a]	τ_1 (x_1), τ_2 (x_2), τ_3 (x_3) [ns] [b]	τ_x [ns] [b]	Φ_F [%] [c]
2 solid	594/659	0.6 (0.74), 2.8 (0.29)	1.2	9
2 in $CHCl_3$ (0.5 mmol/L)	510	4.8 (1)	4.8	89 [d]
2@UiO-66$_{0.44}$ (post-synth.)	519	0.7 (0.10), 5.3 (0.8), 11.1 (0.09)	5.3	29
2@UiO-66$_{1.1}$ (in situ)	521	1.0 (0.08), 5.4 (0.91)	5.1	32
2@UiO-66$_{2.3}$ (in situ)	523	0.6 (0.09), 5.1 (0.89)	4.6	28
2@UiO-66$_{4.7}$ (in situ)	519	1.4 (0.21); 4.8 (0.8)	4.2	21
2@UiO-66$_{7.2}$ (in situ)	520	0.9 (0.14), 4.6 (0.85)	4.0	19

[a] Wavelength of the fluorescence maximum; λ_{exc} = 400 nm for solid **2**; λ_{exc} = 360 nm for **2** in $CHCl_3$; λ_{exc} = 330 nm for **2**@UiO-66. [b] Fluorescence lifetime (λ_{exc} = 375 nm): τ_i (x_i) species i lifetime (fraction), τ_x species-weighted average lifetime. [c] Fluorescence quantum yield. [d] Measured in THF taken from the literature [51].

2.2. *Composites* **2**@*MOF-808,* **2**@*DUT-67 and* **2**@*MIP-206*

To investigate the influence of the MOF host on the photophysical properties of **2**@MOF composites, a post-synthetic and an in situ composite were synthesized for MOF-808 and DUT-67, and a post-synthetic composite for MIP-206. The same MOF to Bodipy ratio was used in the preparation of both the post-synthetic and in situ composites. Due to the increased stability of **2**, we were able to use glacial acetic acid in a large excess in the in situ syntheses of the **2**@MOF-808 and **2**@DUT-67 composites. However, due to the extremely harsh synthesis conditions required for MIP-206, with formic acid as the sole solvent at temperatures of 180 °C, the in situ encapsulations of **2** could not be successfully carried out for MIP-206.

MOF-808 contains a hierarchical pore structure of large, interconnected hexagonal channels with diameters of approximately 18 Å (1.8 nm) and isolated tetrahedral cages with internal pore diameters of around 4.8 Å (or 0.48 nm); the latter being unaccessible for Bodipy [73]. DUT-67 has a hierarchical porous structure that contains cuboctahedral pores with a diameter of 14.2 Å (1.42 nm) and an octahedral pore with a diameter of 11.7 Å (1.17 nm) [74]; both of which can encapsulate Bodipy, and we took both pores into account when calculating pore filling. The structure of MIP-206 has uniform meso-voids with a diameter of ca. 26 Å (2.6 nm) [54].

The post-synthetic **2**@MOF-808 and **2**@DUT-67 composites show no detectable changes in their PXRD patterns in Figure 4, indicating that the crystalline structures of the MOFs were unchanged.

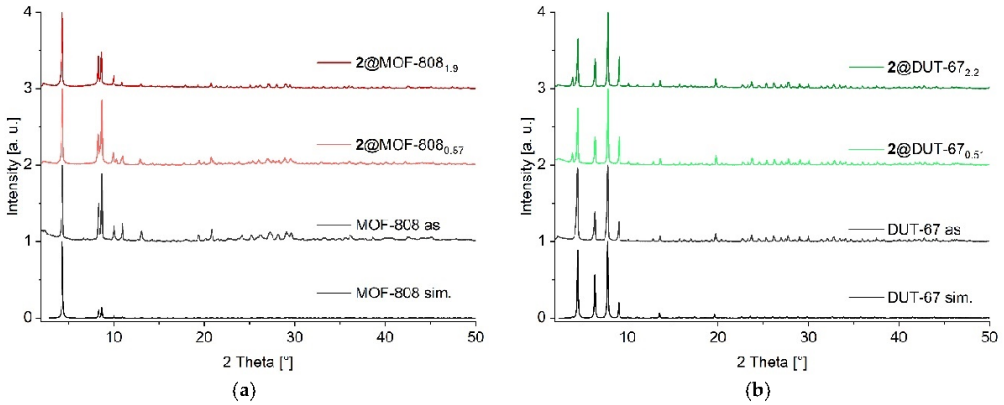

Figure 4. (**a**) PXRD of MOF-808, post-synthetic **2**@MOF-808$_{0.57}$ and in situ encapsulated **2**@MOF-808$_{1.9}$ composites. Simulated diffractogram of MOF-808 from CCDC No. 1002672 [73]. (**b**) PXRD of DUT-67, post-synthetic **2**@DUT-67$_{0.51}$, and in situ encapsulated **2**@DUT-67$_{2.2}$ composites. Simulated diffractogram of DUT-67 from CCDC No. 921644 [74]. For the PXRDs of MIP-206 and **2**@MIP-206$_{0.3}$, see Figure S20a.

From the UV–Vis digestion analysis, the post-synthetic loadings were determined to be 0.57 wt% for MOF-808 and 0.51 wt% for DUT-67 (see Table S2) [75,76]. The resulting composites are designated as **2**@MOF-808$_{0.57}$ and **2**@DUT-67$_{0.51}$. This corresponds to a molar ratio of 22.1 mmol Bodipy per mol of MOF-808 and 23.3 mmol Bodipy per mol of DUT-67. The formulas for MOF-808 [$Zr_6O_4(OH)_{10}(BTC)_2(H_2O)_6$] (1303.7 g/mol) and DUT-67 [$Zr_6O_4(OH)_8(TDC)_4(H_2O)_6$] (1536.1 g/mol) were used for the calculation [53].

In agreement with such a low loading, we observed only very slight changes in the color of both post-synthetic composites, which were almost colorless, microcrystalline powders (see Section S10, Figures S27c and S29c). However, a significant decrease in the determined BET surface area was observed for the **2**@MOF-808$_{0.57}$ composite, with a reduction of up to 65% versus neat MOF-808. By comparison, only a 31% reduction of the BET surface area was observed for the **2**@DUT-67$_{0.51}$ composite compared to neat DUT-67 (Figure 5, Table 4).

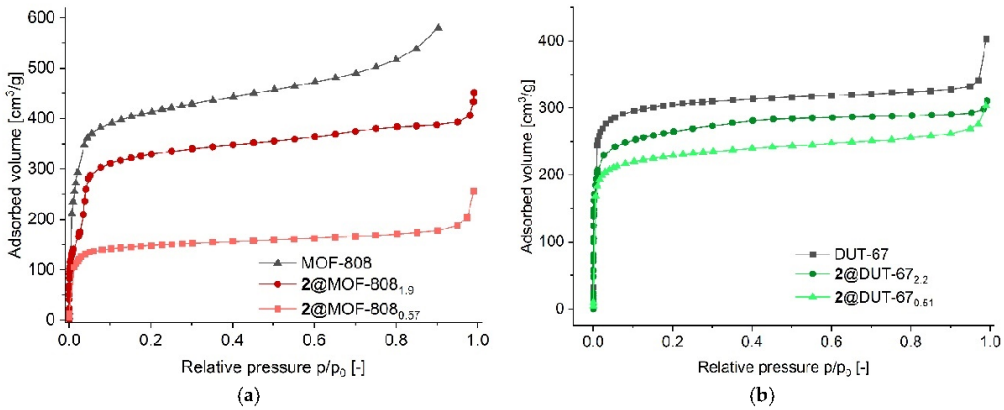

Figure 5. (**a**) Nitrogen adsorption isotherms at 77 K of neat MOF-808 (1683 m^2/g), **2**@MOF-808$_{1.9}$ (1200 m^2/g, in situ), and **2**@MOF-808$_{0.57}$ (596 m^2/g, post-synthetic) composites. (**b**) Nitrogen adsorption isotherms at 77 K of neat DUT-67 (1207 m^2/g), **2**@DUT-67$_{2.2}$ (1020 m^2/g, in situ), and **2**@DUT-67$_{0.51}$ (840 m^2/g, post-synthetic) composites. For the desorption isotherms, see Figures S18 and S19, for the isotherms of **2**@MIP-206$_{0.3}$, see Figure S20b.

Table 4. Results of nitrogen sorption measurements for neat MOF-808, **2**@MOF-808 composites, neat DUT-67, **2**@DUT-67 composites, neat MIP-206, and **2**@MIP-206$_{0.3}$.

Compound	Bodipy Loading [wt%] [a]	S_{BET} [m^2/g]	$V_{pore(total)}$ [cm^3/g] [b]	$V_{pore(micro)}$ [cm^3/g] [c]
MOF-808 literature	-	2060 [73]	0.84	-
	-	1210 [53]	0.53	-
MOF-808 synthesized	-	1683	0.8	0.76
2@MOF-808$_{0.57}$ (post-synth.)	0.57	596	0.27	0.27
2@MOF-808$_{1.9}$ (in situ)	1.9	1200	0.68	0.24
DUT-67 literature	-	1171 [77]	-	-
	-	1150 [53]	-	-
DUT-67 synthesized	-	1207	0.56	0.52
2@DUT-67$_{0.51}$ (post-synth.)	0.51	840	0.4	0.37
2@DUT-67$_{2.2}$ (in situ)	2.2	1020	0.47	0.51
MIP-206 literature	-	1059 [54]	0.45	-
MIP-206 synthesized	-	1062	0.42	0.41
2@MIP-206$_{0.3}$ (post-synth.)	0.3	701	0.39	0.37

[a] Calculated by UV–Vis digestion analysis. [b] Total pore volume at $p/p_0 = 0.9$. [c] Micropore volume calculated from the NLDFT method using the N_2 adsorption isotherm at 77 K for cylindrical pores $\leq$ 2 nm.

The BET surface area reductions for the two post-synthetic composites compared to the in situ prepared composites (see below) can be attributed to the accumulation predominantly in the outer layers of the MOF crystallites rather than uniformly penetrating the entire porous network [29]. Thereby, access to the inner dye-free pore structure is restricted by pore blocking, which leads to reduced N_2 adsorption and, consequently, lower BET surface areas.

The in situ encapsulations of **2** into MOF-808 and DUT-67 resulted in the composites **2**@MOF-808$_{1.9}$ and **2**@DUT-67$_{2.2}$ with loadings of 1.9 wt% and 2.2 wt%, corresponding to 74.7 and 102 mmol Bodipy per mol of MOF-808 and DUT-67, respectively. The in situ prepared composites **2**@MOF-808$_{1.9}$ and **2**@DUT-67$_{2.2}$ showed a slight color change to pale yellow compared to the neat MOFs (see Figures S27c and S29c, Supplementary Materials). The PXRD analysis of the in situ prepared composites, which are shown in Figure 4, revealed no differences from the simulated patterns of MOF-808 and DUT-67. These observations indicate the formation of the neat MOF structure and a crystalline phase-pure synthesis of the composites produced in situ. SEM images of neat MOF-808, DUT-67, and MIP-206, as well as the synthesized composites, each show a homogeneous distribution of MOF particles with a uniform size and unchanged morphology (see Figures S22–S24, Supplementary Materials).

Their N_2 adsorption measurements, shown in Figure 5, yielded BET surface areas of 1200 m^2/g for **2**@MOF-808$_{1.9}$ and 1020 m^2/g for **2**@DUT-67$_{2.2}$. These values are comparable to those reported in the literature. We assume that the in situ encapsulation enables homogeneous distribution of the Bodipy dye within the MOF frameworks. This results in better pore availability compared to post-synthetic loading.

Steady-state luminescence measurements showed that both the post-synthetically loaded and in situ fabricated composites of MOF-808 and DUT-67 exhibit the characteristic luminescence of **2** in solution with emission maxima in the region of 521 nm $\pm$ 2 nm, with a shoulder at 550 nm (Figure 6). The observed broadening of the emission bands of the **2**@MOF-808 and **2**@DUT-67 composites shown in Figure 6 can be explained by the different microenvironments, as for the **2**@UiO-66 composites. Due to the higher loading in the composites produced in situ, a significant increase in luminescence intensity can be measured (for MIP-206 see Supplementary Materials, Section S10). We expect only a primary inner filter effect, just as for the **2**@UiO-66 composites, as the **2**@MOF-808 and **2**@DUT-67 com-

posites are in the same concentration range. Again, as for **2**@UiO-66, the shoulder around 550 nm indicates multiple occupancy of some pores and thus the formation of aggregates between two or more Bodipy molecules in the same pore. The probability p of a multiple pore occupation of **2** in both MOFs is listed in Table 5, taking into account that the pores are formed with the molecular formula units of $[Zr_6O_4(OH)_{10}(BTC)_2(H_2O)_6]$ for MOF-808 and $[Zr_6O_4(OH)_8(TDC)_4(H_2O)_6]$ for DUT-67 (for a more detailed description of the structures and the ratios of pore-to-molecular formula units, see Supplementary Materials Section S7).

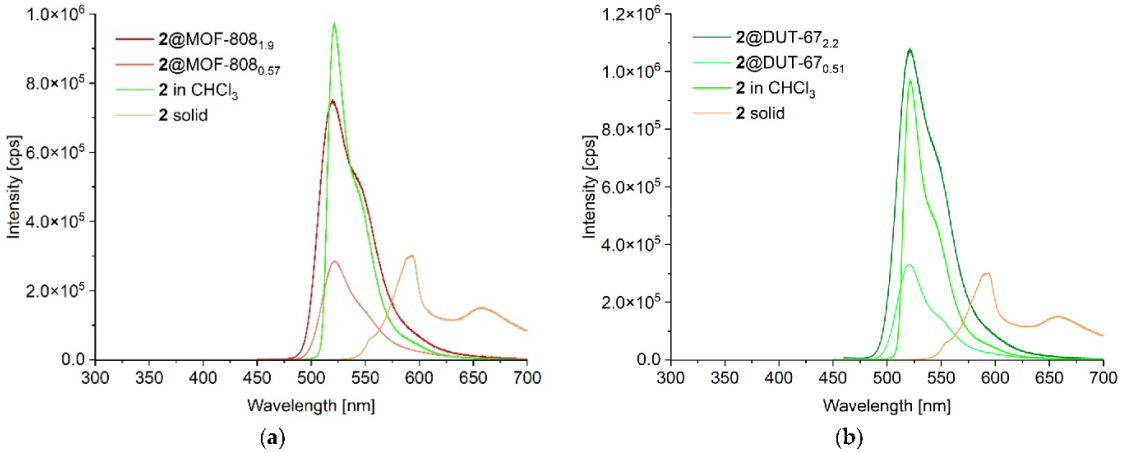

Figure 6. (**a**) Luminescence spectra of in situ and post-synthetic **2**@MOF-808 composites together with **2** in $CHCl_3$ solution (8 mmol/L) and neat **2** in the solid state. (**b**) Luminescence spectra of in situ and post-synthetic **2**@DUT-67 composites together with **2** in $CHCl_3$ solution (8 mmol/L) and neat **2** in the solid state. Emission spectra were measured with excitation at 360 nm for all composites and the $CHCl_3$ solution and at 400 nm for neat **2** in the solid state in a reflective setup. For the luminescence spectra of post-synthetic **2**@MIP-206, see Figure S31a.

Table 5. Probability p of multiple occupations of **2** in the in situ prepared **2**@MOF-808 and **2**@DUT-67 composite materials [a].

	2@MOF-808$_{1.9}$	**2@DUT-67$_{2.2}$**
n_{av}(Bodipy/pore)	0.298	0.155
p(one) [%]	83.4	91.7
p(two) [%]	14.7	7.7
p(≥three) [%]	1.9	0.6

[a] The calculations are based on encapsulated 74.7 and 102 mmol Bodipy per mol of MOF-808 and DUT-67, respectively, and the ratio of pores per formula unit of each MOF. The latter ratio for MOF-808 is 0.25:1, and for DUT-67, it is 0.66:1. For more details about the calculation, see Supplementary Materials Section S7.

Looking at the lifetimes of the prepared composites in Table 6, the post-synthetic composites gave tri-exponential decays, and the in situ composites bi-exponential ones, as seen in the **2**@UiO-66 composites. The observed tri-exponential and bi-exponential decays suggest the coexistence of different emitting species—a property often associated in the literature with the formation of J-aggregates (cf. Table 5)—similar to what was seen in the **2**@UiO-66 composites [69]. Compared to the lifetime of **2** in solution (4.8 ns for 0.5 mmol/L) and as a solid (1.2 ns), all composites show significantly longer lifetimes. For the post-synthetic composites of MOF-808, DUT-67, and MIP-206, average lifetimes τ_x of 6.5 ns to 7.9 ns were measured. The in situ synthesized composites **2**@MOF-808$_{1.9}$ and **2**@DUT-67$_{2.2}$ showed a further significant increase in average lifetimes, with values of 9.0 ns and 8.5 ns, respectively (see Section S10, Supplementary Materials for the decay

plots of all **2**@MOF composites). The average lifetime of these composites represents a doubling compared to **2** in solution (0.5 mmol/L) and an eight-fold increase compared to neat **2** in the solid state. For the **2**@UiO-66 composites, the average lifetime τ_x was close to the lifetime of **2** in solution (0.5 mmol/L) (cf. Table 3).

Table 6. Photophysical data for **2** as a solid and in solution, and the **2**@MOF-808 and **2**@DUT-67 composites.

Compound	$\lambda_{F,\,max}$ [nm] [a]	τ_1 (x_1), τ_2 (x_2), τ_3 (x_3) [ns] [b]	τ_x [ns] [b]	Φ_F [%] [c]
2 solid	594/659	0.6 (0.74), 2.8 (0.29)	1.2	9
2 in $CHCl_3$	510	4.8 (1)	4.8	89 [d]
2@MOF-808$_{0.57}$ (post-synth.)	523	6.5 (0.85), 0.8 (0.09), 13.2 (0.07)	6.5	48
2@MOF-808$_{1.9}$ (in situ)	519	6.6 (0.44), 11.3 (0.54)	9.0	35
2@DUT-67$_{0.51}$ (post-synth.)	519	6.2 (0.78), 1.6 (0.07), 10.8 (0.16)	6.8	77
2@DUT-67$_{2.2}$ (in situ)	521	8.4 (0.97), 19.8 (0.02)	8.5	41

[a] Wavelength of the fluorescence maximum (λ_{exc} = 360 nm). [b] Fluorescence lifetime (λ_{exc} = 375 nm): τ_i (x_i) species i lifetime (fraction), τ_x species-weighted average lifetime. [c] Fluorescence quantum yield. [d] Measured in THF taken from the literature [51]. For the fluorescence lifetime of post-synthetic **2**@MIP-206, see Table S6.

Compared to the UiO-66 composites, the extended lifetimes in MOF-808 and DUT-67 reveal the influence of both pore size and pore environment. The latter two MOFs have pores that are significantly larger than the embedded dye molecules. This results in a larger distance and better separation of the Bodipy molecules within the pores and fewer interactions, such as π-π interactions or aggregation, both between individual Bodipy molecules and the pore walls and between neighboring Bodipy molecules. Lower interactions between both the Bodipy molecules themselves and the Bodipy molecules and the MOF walls are evident when comparing the aggregation (cf. Tables 2 and 5) and respective lifetimes (cf. Tables 3 and 6) of UiO-66 vs. MOF-808 and UiO-66 vs. DUT-67. At comparable degrees of aggregation of **2**@MOF-808$_{1.9}$ (τ_x = 9.0 ns) vs. **2**@UiO-66$_{4.7}$ (τ_x = 4.2 ns), and of **2**@DUT-67$_{2.2}$ (τ_x = 8.5 ns) vs. **2**@UiO-66$_{2.3}$ (τ_x = 4.6 ns), the lifetime increases with the pore size. The largest pore sizes in MOF-808 are about 18 Å, both in DUT-67 14 Å and in UiO-66 11 Å (see Section S7, Supplementary Materials). Thus, the distance between two Bodipy molecules as well as the distance between Bodipy molecules and the MOF walls also increases. In other words, the larger pores lead to weaker interactions of the Bodipy molecules, both with each other and with the MOF walls.

The presence of such monomers has already been described in the work of Xiong et al. using rhodamine B in ZIF-8 [70]. However, the significant increase in lifetime in the **2**@MOF-808 and **2**@DUT-67 composites compared to the lifetime in solution is not only due to the formation of such isolated monomers through enlarged pores, but also to the pore-forming MOF environment. Studies such as those by Liu et al. demonstrate the significant impact that changes in the MOF environment due to the introduction of functional groups can have on the photophysical properties of dyes [78]. In their work, they modified ZIF-8 by introducing 1,2,4-benzenetricarbonic acid with carboxyl functional groups, which significantly increased the quantum yield of the dye@MOF composite.

In addition to the extended lifetimes of **2** in **2**@MOF-808 and **2**@DUT-67, good quantum yields were observed. The composites prepared in situ had average quantum yields of 35% for MOF-808 and 41% for DUT-67. Significantly higher quantum yields were obtained for the post-synthetically encapsulated composites. For **2**@MOF-808$_{0.57}$, we measured an average quantum yield of 48% and for **2**@DUT-67$_{0.51}$, it was an impressive 77%. These high quantum yields derive from the Bodipy concentration in the outer MOF layer, which

enables efficient molecule excitation. The inner Bodipy molecules of the in situ composites may not be reached by the photons, and their emission is also more readily absorbed within the MOF. Furthermore, the decreased dye-to-wall interactions between Bodipy in MOF-808 and DUT-67, with their larger pores, compared to UiO-66, result in less quenching. The quantum yield for **2**@DUT-67$_{0.51}$ of 77% is comparable to the quantum yield of 89% for **2** in the THF solution reported in the literature [51].

All composites far exceed the quantum yield of the solid dye. The **2**@MOF-808 and **2**@DUT-67 composites also gave higher quantum yields than the **2**@UiO-66 composites. The UiO-66 composites ranged from 31% for **2**@UiO-66$_{1.1}$, which had the highest quantum yield, to 19% for **2**@UiO-66$_{7.2}$, which had the lowest quantum yield (cf. Table 3). Overall, the improved photophysical emission lifetimes and quantum yields make the Bodipy@MOF composites interesting for applications in solid-state devices.

3. Conclusions

In conclusion, we have shown that by substituting the well-known and well-studied difluoro groups of Bodipy with the less-investigated cyano groups, an acid-stable variant of Bodipy can be synthesized and used for both post-synthetic and in situ incorporation into zirconium-based MOFs under highly acidic synthesis conditions. The **2**@MOF composites show a distinct emission at 521 nm ± 2 nm, comparable to the emission of **2** in solution (8 mmol/L), in line with the solid solution concept for dyes@MOFs. From N_2 adsorption measurements with surface area determinations, it could be inferred that the post-synthetic encapsulation method leads to a dye loading predominantly in the outer layers of the MOF crystallites. On the contrary, the in situ encapsulation method yields a more homogeneous distribution of the Bodipy molecules over the entire MOF crystallite. By means of distribution calculations and by fluorescence spectroscopic measurements, it is suggested that isolated J-aggregates are formed as the loadings increase. Yet, the post-synthetic concentration of the dye in the outer layer was found advantageous to increase the quantum yield in the case of large-pore MOFs. Through the choice of a MOF with a pore size larger than the dye molecule, composites with a high quantum yield close to the quantum yield of **2** in solution could be obtained due to decreased dye-to-wall interactions, and thereby, reduced quenching. The advantage of the solid **2**@MOF composites was their increased fluorescence lifetime and quantum yield, both up to eight-fold, compared to solid **2**. These results provide a starting point for the targeted development of solid Bodipy@MOF composites with specific optical and structural properties so that they could also be used for sensing as other dye@MOF composites [79–81].

Supplementary Materials: The following supporting information can be downloaded at: https://www.mdpi.com/article/10.3390/molecules30214151/s1, Section S1: General information; Section S2: Sources of chemicals; Section S3: Synthesis of Bodipy compounds **1** and **2** (Schemes S1 and S2); Section S4: Photophysical properties of Bodipy **2**; Section S5: Synthesis of UiO-66 and **2**@UiO-66 composites (Scheme S3); Section S6: Digestion UV–Vis; Section S7: Calculation of pore filling and the probability p of multiple occupations; Section S8: Synthesis of MOF-808, DUT-67, and MIP-206 and their composites (Schemes S4 and S5); Section S9: Scanning electron microscopy images of MOFs and composites; Section S10: Photophysical properties of all composites; Section S11: References. References [82,83] are cited in the Supplementary Materials.

Author Contributions: Conceptualization, C.J. and M.N.A.F.; methodology, M.N.A.F.; validation, M.N.A.F.; formal analysis, M.N.A.F. and M.V.; investigation, M.N.A.F., M.V., and A.L.; resources, C.J.; data curation, M.N.A.F.; writing—original draft preparation, M.N.A.F.; writing—review and editing, C.J.; visualization, M.N.A.F. and C.J.; supervision, C.J.; project administration, C.J.; funding acquisition, C.J. All authors have read and agreed to the published version of the manuscript.

Funding: C. J. thanks the Deutsche Forschungsgemeinschaft (DFG, German Research Foundation) for grant 396890929/GRK 2482.

Institutional Review Board Statement: Not applicable.

Informed Consent Statement: Not applicable.

Data Availability Statement: The original contributions presented in this study are included in the article/Supplementary Material. Further inquiries can be directed to the corresponding author(s).

Acknowledgments: We thank the Center for Molecular and Structural Analytics at Heinrich Heine University (CeMSA@HHU) for recording the mass spectrometric and NMR-spectrometric data. M.N.A.F. would like to thank István Boldog for his helpful suggestions and discussions.

Conflicts of Interest: The authors declare no conflicts of interest.

References

1. Gangu, K.K.; Maddila, S.; Mukkamala, S.B.; Jonnalagadda, S.B. A review on contemporary Metal–Organic Framework materials. *Inorganica Chim. Acta* **2016**, *446*, 61–74. [CrossRef]
2. Honicke, I.M.; Senkovska, I.; Bon, V.; Baburin, I.A.; Bonisch, N.; Raschke, S.; Evans, J.D.; Kaskel, S. Balancing Mechanical Stability and Ultrahigh Porosity in Crystalline Framework Materials. *Angew. Chem. Int. Ed.* **2018**, *57*, 13780–13783. [CrossRef]
3. Schaate, A.; Roy, P.; Godt, A.; Lippke, J.; Waltz, F.; Wiebcke, M.; Behrens, P. Modulated synthesis of Zr-based metal-organic frameworks: From nano to single crystals. *Chem. Eur. J.* **2011**, *17*, 6643–6651. [CrossRef] [PubMed]
4. Ren, J.; Musyoka, N.M.; Langmi, H.W.; Segakweng, T.; North, B.C.; Mathe, M.; Kang, X. Modulated synthesis of chromium-based metal-organic framework (MIL-101) with enhanced hydrogen uptake. *Int. J. Hydrogen Energy* **2014**, *39*, 12018–12023. [CrossRef]
5. Bagherzadeh, E.; Zebarjad, S.M.; Hosseini, H.R.M. Morphology Modification of the Iron Fumarate MIL—88A Metal–Organic Framework Using Formic Acid and Acetic Acid as Modulators. *Eur. J. Inorg. Chem.* **2018**, *2018*, 1909–1915. [CrossRef]
6. Li, M.; Zhou, H.; Zhang, L.; Han, J.; Wang, G.; Fan, F.; Wang, T.; Zhang, X.; Fu, Y. Size and morphology control of two-dimensional metal-organic frameworks through coordination modulation. *Microporous Mesoporous Mater.* **2023**, *348*, 112379. [CrossRef]
7. Yang, P.; Huang, Y.; Zhang, Z.W.; Li, N.; Fan, Y. Shape-controlled synthesis of the metal-organic framework MIL-125 towards a highly enhanced catalytic performance for the oxidative desulfurization of 4,6-dimethyldibenzothiophene. *Dalton Trans.* **2020**, *49*, 10052–10057. [CrossRef]
8. Liu, Y.; Liu, S.; He, D.; Li, N.; Ji, Y.; Zheng, Z.; Luo, F.; Liu, S.; Shi, Z.; Hu, C. Crystal Facets Make a Profound Difference in Polyoxometalate-Containing Metal-Organic Frameworks as Catalysts for Biodiesel Production. *J. Am. Chem. Soc.* **2015**, *137*, 12697–12703. [CrossRef]
9. Cai, G.; Jiang, H.L. A Modulator-Induced Defect-Formation Strategy to Hierarchically Porous Metal-Organic Frameworks with High Stability. *Angew. Chem. Int. Ed.* **2017**, *56*, 563–567. [CrossRef]
10. Epley, C.C.; Love, M.D.; Morris, A.J. Characterizing Defects in a UiO-AZB Metal-Organic Framework. *Inorg. Chem.* **2017**, *56*, 13777–13784. [CrossRef]
11. Chung, Y.G.; Camp, J.; Haranczyk, M.; Sikora, B.J.; Bury, W.; Krungleviciute, V.; Yildirim, T.; Farha, O.K.; Sholl, D.S.; Snurr, R.Q. Computation-Ready, Experimental Metal–Organic Frameworks: A Tool To Enable High-Throughput Screening of Nanoporous Crystals. *Chem. Mater.* **2014**, *26*, 6185–6192. [CrossRef]
12. Eddaoudi, M.; Kim, J.; Rosi, N.; Vodak, D.; Wachter, J.; O'Keeffe, M.; Yaghi, O.M. Systematic design of pore size and functionality in isoreticular MOFs and their application in methane storage. *Science* **2002**, *295*, 469–472. [CrossRef] [PubMed]
13. Yuan, S.; Feng, L.; Wang, K.; Pang, J.; Bosch, M.; Lollar, C.; Sun, Y.; Qin, J.; Yang, X.; Zhang, P.; et al. Stable Metal-Organic Frameworks: Design, Synthesis, and Applications. *Adv. Mater.* **2018**, *30*, 1704303. [CrossRef] [PubMed]
14. Lu, W.; Wei, Z.; Gu, Z.Y.; Liu, T.F.; Park, J.; Park, J.; Tian, J.; Zhang, M.; Zhang, Q.; Gentle, T., 3rd; et al. Tuning the structure and function of metal-organic frameworks via linker design. *Chem. Soc. Rev.* **2014**, *43*, 5561–5593. [CrossRef] [PubMed]
15. Mai, Z.; Liu, D. Synthesis and Applications of Isoreticular Metal–Organic Frameworks IRMOFs-n (n = 1, 3, 6, 8). *Cryst. Growth Des.* **2019**, *19*, 7439–7462. [CrossRef]
16. Fan, W.; Zhang, X.; Kang, Z.; Liu, X.; Sun, D. Isoreticular chemistry within metal–organic frameworks for gas storage and separation. *Coord. Chem. Rev.* **2021**, *443*, 213968. [CrossRef]
17. Empel, C.; Fetzer, M.N.A.; Sasmal, S.; Strothmann, T.; Janiak, C.; Koenigs, R.M. Unlocking catalytic potential: A rhodium(II)-based coordination polymer for efficient carbene transfer reactions with donor/acceptor diazoalkanes. *Chem. Commun.* **2024**, *60*, 7327–7330. [CrossRef]
18. Jin, J.; Wan, S.; Lee, S.; Oh, C.; Jang, G.Y.; Zhang, K.; Lu, Z.; Park, J.H. Tailoring the Nanoporosity and Photoactivity of Metal-Organic Frameworks with Rigid Dye Modulators for Toluene Purification. *Small* **2023**, *19*, 2302776. [CrossRef]

19. Vasconcelos, I.B.; Silva, T.G.d.; Militão, G.C.G.; Soares, T.A.; Rodrigues, N.M.; Rodrigues, M.O.; Costa, N.B.d.; Freire, R.O.; Junior, S.A. Cytotoxicity and slow release of the anti-cancer drug doxorubicin from ZIF-8. *RSC Adv.* **2012**, *2*, 9437–9442. [CrossRef]
20. Javanbakht, S.; Pooresmaeil, M.; Namazi, H. Green one-pot synthesis of carboxymethylcellulose/Zn-based metal-organic framework/graphene oxide bio-nanocomposite as a nanocarrier for drug delivery system. *Carbohydr. Polym.* **2019**, *208*, 294–301. [CrossRef]
21. Wu, X.; Bao, Z.; Yuan, B.; Wang, J.; Sun, Y.; Luo, H.; Deng, S. Microwave synthesis and characterization of MOF-74 (M = Ni, Mg) for gas separation. *Microporous Mesoporous Mater.* **2013**, *180*, 114–122. [CrossRef]
22. Dechnik, J.; Nuhnen, A.; Janiak, C. Mixed-Matrix Membranes of the Air-Stable MOF-5 Analogue $[Co_4(\mu_4\text{-}O)(Me_2pzba)_3]$ with a Mixed-Functional Pyrazolate-Carboxylate Linker for CO_2/CH_4 Separation. *Cryst. Growth Des.* **2017**, *17*, 4090–4099. [CrossRef]
23. Adil, K.; Belmabkhout, Y.; Pillai, R.S.; Cadiau, A.; Bhatt, P.M.; Assen, A.H.; Maurin, G.; Eddaoudi, M. Gas/vapour separation using ultra-microporous metal-organic frameworks: Insights into the structure/separation relationship. *Chem. Soc. Rev.* **2017**, *46*, 3402–3430. [CrossRef]
24. Gökpinar, S.; Ernst, S.-J.; Hastürk, E.; Möllers, M.; El Aita, I.; Wiedey, R.; Tannert, N.; Nießing, S.; Abdpour, S.; Schmitz, A.; et al. Air-Con Metal–Organic Frameworks in Binder Composites for Water Adsorption Heat Transformation Systems. *Ind. Eng. Chem. Res.* **2019**, *58*, 21493–21503. [CrossRef]
25. Hanikel, N.; Pei, X.; Chheda, S.; Lyu, H.; Jeong, W.; Sauer, J.; Gagliardi, L.; Yaghi, O.M. Evolution of water structures in metal-organic frameworks for improved atmospheric water harvesting. *Science* **2021**, *374*, 454–459. [CrossRef] [PubMed]
26. Terzis, A.; Ramachandran, A.; Wang, K.; Asheghi, M.; Goodson, K.E.; Santiago, J.G. High-Frequency Water Vapor Sorption Cycling Using Fluidization of Metal-Organic Frameworks. *Cell Rep. Phys. Sci.* **2020**, *1*, 100057. [CrossRef]
27. Zhang, N.; Zhang, D.; Zhao, J.; Xia, Z. Fabrication of a dual-emitting dye-encapsulated metal-organic framework as a stable fluorescent sensor for metal ion detection. *Dalton Trans.* **2019**, *48*, 6794–6799. [CrossRef] [PubMed]
28. Knedel, T.O.; Buss, S.; Maisuls, I.; Daniliuc, C.G.; Schlusener, C.; Brandt, P.; Weingart, O.; Vollrath, A.; Janiak, C.; Strassert, C.A. Encapsulation of Phosphorescent Pt(II) Complexes in Zn-Based Metal-Organic Frameworks toward Oxygen-Sensing Porous Materials. *Inorg. Chem.* **2020**, *59*, 7252–7264. [CrossRef]
29. Ma, M.; Gross, A.; Zacher, D.; Pinto, A.; Noei, H.; Wang, Y.; Fischer, R.A.; Metzler-Nolte, N. Use of confocal fluorescence microscopy to compare different methods of modifying metal–organic framework (MOF) crystals with dyes. *CrystEngComm* **2011**, *13*, 2828–2832. [CrossRef]
30. Yin, J.C.; Chang, Z.; Li, N.; He, J.; Fu, Z.X.; Bu, X.H. Efficient Regulation of Energy Transfer in a Multicomponent Dye-Loaded MOF for White-Light Emission Tuning. *ACS Appl. Mater. Interfaces* **2020**, *12*, 51589–51597. [CrossRef]
31. Chen, W.; Zhuang, Y.; Wang, L.; Lv, Y.; Liu, J.; Zhou, T.L.; Xie, R.J. Color-Tunable and High-Efficiency Dye-Encapsulated Metal-Organic Framework Composites Used for Smart White-Light-Emitting Diodes. *ACS Appl. Mater. Interfaces* **2018**, *10*, 18910–18917. [CrossRef]
32. Tang, Y.; Xia, T.; Song, T.; Cui, Y.; Yang, Y.; Qian, G. Efficient Energy Transfer within Dyes Encapsulated Metal–Organic Frameworks to Achieve High Performance White Light—Emitting Diodes. *Adv. Opt. Mater.* **2018**, *6*, 1800968. [CrossRef]
33. He, T.; Kong, X.J.; Li, J.R. Chemically Stable Metal-Organic Frameworks: Rational Construction and Application Expansion. *Acc. Chem. Res.* **2021**, *54*, 3083–3094. [CrossRef]
34. Kim, J.Y.; Kang, J.; Cha, S.; Kim, H.; Kim, D.; Kang, H.; Choi, I.; Kim, M. Stability of Zr-Based UiO-66 Metal-Organic Frameworks in Basic Solutions. *Nanomaterials* **2024**, *14*, 110. [CrossRef]
35. Glembockyte, V.; Frenette, M.; Mottillo, C.; Durantini, A.M.; Gostick, J.; Strukil, V.; Friscic, T.; Cosa, G. Highly Photostable and Fluorescent Microporous Solids Prepared via Solid-State Entrapment of Boron Dipyrromethene Dyes in a Nascent Metal-Organic Framework. *J. Am. Chem. Soc.* **2018**, *140*, 16882–16887. [CrossRef]
36. Oh, J.S.; Park, K.C.; Gupta, G.; Lee, C.Y. Complementary Chromophore Decoration in NU-1000 via Solvent-Assisted Ligands Incorporation: Efficient Energy Transfer within the Metal-Organic Frameworks. *Bull. Korean Chem. Soc.* **2019**, *40*, 128–133. [CrossRef]
37. Treibs, A.; Kreuzer, F.H. Difluorboryl-Komplexe von Di- und Tripyrrylmethenen. *Justus Liebigs Ann. Chem.* **1968**, *718*, 208–223. [CrossRef]
38. Duan, C.; Zhou, Y.; Shan, G.-G.; Chen, Y.; Zhao, W.; Yuan, D.; Zeng, L.; Huang, X.; Niu, G. Bright solid-state red-emissive BODIPYs: Facile synthesis and their high-contrast mechanochromic properties. *J. Mater. Chem. C* **2019**, *7*, 3471–3478. [CrossRef]
39. Gibbs, J.H.; Robins, L.T.; Zhou, Z.; Bobadova-Parvanova, P.; Cottam, M.; McCandless, G.T.; Fronczek, F.R.; Vicente, M.G. Spectroscopic, computational modeling and cytotoxicity of a series of meso-phenyl and meso-thienyl-BODIPYs. *Bioorganic Med. Chem.* **2013**, *21*, 5770–5781. [CrossRef] [PubMed]
40. Tang, F.K.; Zhu, J.; Kong, F.K.; Ng, M.; Bian, Q.; Yam, V.W.; Tse, A.K.; Tse, Y.C.; Leung, K.C. A BODIPY-based fluorescent sensor for the detection of Pt2+ and Pt drugs. *Chem. Commun.* **2020**, *56*, 2695–2698. [CrossRef] [PubMed]
41. Dorh, N.; Zhu, S.; Dhungana, K.B.; Pati, R.; Luo, F.T.; Liu, H.; Tiwari, A. BODIPY-Based Fluorescent Probes for Sensing Protein Surface-Hydrophobicity. *Sci. Rep.* **2015**, *5*, 18337. [CrossRef]

42. Guan, Q.; Fu, D.D.; Li, Y.A.; Kong, X.M.; Wei, Z.Y.; Li, W.Y.; Zhang, S.J.; Dong, Y.B. BODIPY-Decorated Nanoscale Covalent Organic Frameworks for Photodynamic Therapy. *iScience* **2019**, *14*, 180–198. [CrossRef]
43. Schneider, L.; Kalt, M.; Koch, S.; Sithamparanathan, S.; Villiger, V.; Mattiat, J.; Kradolfer, F.; Slyshkina, E.; Luber, S.; Bonmarin, M.; et al. BODIPY-Based Photothermal Agents with Excellent Phototoxic Indices for Cancer Treatment. *J. Am. Chem. Soc.* **2023**, *145*, 4534–4544. [CrossRef]
44. Mack, J.; Kubheka, G.; May, A.; Ngoy, B.P.; Nyokong, T. BODIPY dyes for optical limiting applications on the nanosecond timescale. *Dalton Trans.* **2024**, *53*, 17766–17771. [CrossRef]
45. Karaman, O.; Almammadov, T.; Emre Gedik, M.; Gunaydin, G.; Kolemen, S.; Gunbas, G. Mitochondria-Targeting Selenophene-Modified BODIPY-Based Photosensitizers for the Treatment of Hypoxic Cancer Cells. *ChemMedChem* **2019**, *14*, 1879–1886. [CrossRef]
46. Wang, X.F.; Yu, S.S.; Wang, C.; Xue, D.; Xiao, J. BODIPY catalyzed amide synthesis promoted by BHT and air under visible light. *Org. Biomol. Chem.* **2016**, *14*, 7028–7037. [CrossRef] [PubMed]
47. Liras, M.; Iglesias, M.; Sánchez, F. Conjugated Microporous Polymers Incorporating BODIPY Moieties as Light-Emitting Materials and Recyclable Visible-Light Photocatalysts. *Macromolecules* **2016**, *49*, 1666–1673. [CrossRef]
48. Stachelek, P.; Alsimaree, A.A.; Alnoman, R.B.; Harriman, A.; Knight, J.G. Thermally-Activated, Delayed Fluorescence in O,B,O- and N,B,O-Strapped Boron Dipyrromethene Derivatives. *J. Phys. Chem. A* **2017**, *121*, 2096–2107. [CrossRef]
49. Fan, Y.; Zhang, J.; Hong, Z.; Qiu, H.; Li, Y.; Yin, S. Architectures and Applications of BODIPY-Based Conjugated Polymers. *Polymers* **2020**, *13*, 75. [CrossRef]
50. Caruso, E.; Gariboldi, M.; Sangion, A.; Gramatica, P.; Banfi, S. Synthesis, photodynamic activity, and quantitative structure-activity relationship modelling of a series of BODIPYs. *J. Photochem. Photobiol. B* **2017**, *167*, 269–281. [CrossRef]
51. Nguyen, A.L.; Wang, M.; Bobadova-Parvanova, P.; Do, Q.; Zhou, Z.; Fronczek, F.R.; Smith, K.M.; Vicente, M.G.H. Synthesis and properties ofB-cyano-BODIPYs. *J. Porphyr. Phthalocyanines* **2016**, *20*, 1409–1419. [CrossRef]
52. Katz, M.J.; Brown, Z.J.; Colon, Y.J.; Siu, P.W.; Scheidt, K.A.; Snurr, R.Q.; Hupp, J.T.; Farha, O.K. A facile synthesis of UiO-66, UiO-67 and their derivatives. *Chem. Commun.* **2013**, *49*, 9449–9451. [CrossRef]
53. Reinsch, H.; Waitschat, S.; Chavan, S.M.; Lillerud, K.P.; Stock, N. A Facile "Green" Route for Scalable Batch Production and Continuous Synthesis of Zirconium MOFs. *Eur. J. Inorg. Chem.* **2016**, *2016*, 4490–4498. [CrossRef]
54. Wang, S.; Chen, L.; Wahiduzzaman, M.; Tissot, A.; Zhou, L.; Ibarra, I.A.; Gutiérrez-Alejandre, A.; Lee, J.S.; Chang, J.-S.; Liu, Z.; et al. A Mesoporous Zirconium-Isophthalate Multifunctional Platform. *Matter* **2021**, *4*, 182–194. [CrossRef]
55. Jiang, J.; Yaghi, O.M. Bronsted acidity in metal-organic frameworks. *Chem. Rev.* **2015**, *115*, 6966–6997. [CrossRef] [PubMed]
56. Wang, M.; Vicente, M.G.H.; Mason, D.; Bobadova-Parvanova, P. Stability of a Series of BODIPYs in Acidic Conditions: An Experimental and Computational Study into the Role of the Substituents at Boron. *ACS Omega* **2018**, *3*, 5502–5510. [CrossRef] [PubMed]
57. Zhang, G.; Wang, M.; Fronczek, F.R.; Smith, K.M.; Vicente, M.G.H. Lewis-Acid-Catalyzed BODIPY Boron Functionalization Using Trimethylsilyl Nucleophiles. *Inorg. Chem.* **2018**, *57*, 14493–14496. [CrossRef] [PubMed]
58. Manzano, H.; Esnal, I.; Marqués-Matesanz, T.; Bañuelos, J.; López-Arbeloa, I.; Ortiz, M.J.; Cerdán, L.; Costela, A.; García-Moreno, I.; Chiara, J.L. Unprecedented J-Aggregated Dyes in Pure Organic Solvents. *Adv. Funct. Mater.* **2016**, *26*, 2756–2769. [CrossRef]
59. Marfin, Y.S.; Banakova, E.A.; Merkushev, D.A.; Usoltsev, S.D.; Churakov, A.V. Effects of Concentration on Aggregation of BODIPY-Based Fluorescent Dyes Solution. *J. Fluoresc.* **2020**, *30*, 1611–1621. [CrossRef]
60. Ryu, U.; Lee, H.S.; Park, K.S.; Choi, K.M. The rules and roles of metal-organic framework in combination with molecular dyes. *Polyhedron* **2018**, *154*, 275–294. [CrossRef]
61. Slawek, A.; Jajko, G.; Ogorzaly, K.; Dubbeldam, D.; Vlugt, T.J.H.; Makowski, W. The Influence of UiO-66 Metal-Organic Framework Structural Defects on Adsorption and Separation of Hexane Isomers. *Chem. Eur. J.* **2022**, *28*, e202200030. [CrossRef]
62. Bárcia, P.S.; Guimarães, D.; Mendes, P.A.P.; Silva, J.A.C.; Guillerm, V.; Chevreau, H.; Serre, C.; Rodrigues, A.E. Reverse shape selectivity in the adsorption of hexane and xylene isomers in MOF UiO-66. *Microporous Mesoporous Mater.* **2011**, *139*, 67–73. [CrossRef]
63. D'Amato, R.; Bondi, R.; Moghdad, I.; Marmottini, F.; McPherson, M.J.; Naïli, H.; Taddei, M.; Costantino, F. "Shake 'n Bake" Route to Functionalized Zr-UiO-66 Metal-Organic Frameworks. *Inorg. Chem.* **2021**, *60*, 14294–14301. [CrossRef] [PubMed]
64. Guillerm, V.; Gross, S.; Serre, C.; Devic, T.; Bauer, M.; Ferey, G. A zirconium methacrylate oxocluster as precursor for the low-temperature synthesis of porous zirconium(IV) dicarboxylates. *Chem. Commun.* **2010**, *46*, 767–769. [CrossRef]
65. Shearer, G.C.; Chavan, S.; Bordiga, S.; Svelle, S.; Olsbye, U.; Lillerud, K.P. Defect Engineering: Tuning the Porosity and Composition of the Metal–Organic Framework UiO-66 via Modulated Synthesis. *Chem. Mater.* **2016**, *28*, 3749–3761. [CrossRef]
66. Grabowski, Z.R.; Dobkowski, J. Twisted Intramolecular Charge-Transfer (Tict) Excited-States—Energy and Molecular-Structure. *Pure Appl. Chem.* **1983**, *55*, 245–252. [CrossRef]
67. Sasaki, S.; Drummen, G.P.C.; Konishi, G. Recent advances in twisted intramolecular charge transfer (TICT) fluorescence and related phenomena in materials chemistry. *J. Mater. Chem. C* **2016**, *4*, 2731–2743. [CrossRef]

68. Puschel, D.; Hede, S.; Maisuls, I.; Hofert, S.P.; Woschko, D.; Kuhnemuth, R.; Felekyan, S.; Seidel, C.A.M.; Czekelius, C.; Weingart, O.; et al. Enhanced Solid-State Fluorescence of Flavin Derivatives by Incorporation in the Metal-Organic Frameworks MIL-53(Al) and MOF-5. *Molecules* **2023**, *28*, 2877. [CrossRef]
69. Rodrigues, A.C.B.; Wetterling, D.; Scherf, U.; Seixas de Melo, J.S. Tuning J-aggregate Formation and Emission Efficiency in Cationic Diazapentacenium Dyes. *Chem. Eur. J.* **2021**, *27*, 7826–7830. [CrossRef]
70. Xiong, T.; Zhang, Y.; Amin, N.; Tan, J.C. A Luminescent Guest@MOF Nanoconfined Composite System for Solid-State Lighting. *Molecules* **2021**, *26*, 7583. [CrossRef]
71. Gutierrez, M.; Zhang, Y.; Tan, J.C. Confinement of Luminescent Guests in Metal-Organic Frameworks: Understanding Pathways from Synthesis and Multimodal Characterization to Potential Applications of LG@MOF Systems. *Chem. Rev.* **2022**, *122*, 10438–10483. [CrossRef]
72. Schrimpf, W.; Jiang, J.C.; Ji, Z.; Hirschle, P.; Lamb, D.C.; Yaghi, O.M.; Wuttke, S. Chemical diversity in a metal-organic framework revealed by fluorescence lifetime imaging. *Nat. Commun.* **2018**, *9*, 1647. [CrossRef] [PubMed]
73. Furukawa, H.; Gandara, F.; Zhang, Y.B.; Jiang, J.; Queen, W.L.; Hudson, M.R.; Yaghi, O.M. Water adsorption in porous metal-organic frameworks and related materials. *J. Am. Chem. Soc.* **2014**, *136*, 4369–4381. [CrossRef] [PubMed]
74. Bon, V.; Senkovska, I.; Baburin, I.A.; Kaskel, S. Zr- and Hf-Based Metal–Organic Frameworks: Tracking Down the Polymorphism. *Cryst. Growth Des.* **2013**, *13*, 1231–1237. [CrossRef]
75. Valverde, A.; Tovar, G.I.; Rio-López, N.A.; Torres, D.; Rosales, M.; Wuttke, S.; Fidalgo-Marijuan, A.; Porro, J.M.; Jiménez-Ruiz, M.; García Sakai, V.; et al. Designing Metal-Chelator-like Traps by Encoding Amino Acids in Zirconium-Based Metal–Organic Frameworks. *Chem. Mater.* **2022**, *34*, 9666–9684. [CrossRef]
76. Winters, W.M.W.; Zhou, C.; Hou, J.; Diaz-Lopez, M.; Bennett, T.D.; Yue, Y. Order-to-Disorder Transition in a Zirconium-Based Metal–Organic Framework. *Chem. Mater.* **2024**, *36*, 8400–8411. [CrossRef]
77. Drache, F.; Bon, V.; Senkovska, I.; Marschelke, C.; Synytska, A.; Kaskel, S. Postsynthetic Inner-Surface Functionalization of the Highly Stable Zirconium-Based Metal-Organic Framework DUT-67. *Inorg. Chem.* **2016**, *55*, 7206–7213. [CrossRef]
78. Liu, Q.; Chen, X.; Wu, J.; Zhang, L.; He, G.; Tian, S.; Zhao, X. Enhanced Luminescence of Dye-Decorated ZIF-8 Composite Films via Controllable D-A Interactions for White Light Emission. *Langmuir* **2023**, *39*, 3656–3667. [CrossRef]
79. Yu, J.; Cheng, Y.; Zhang, X.; Zhou, L.; Song, Z.; Nezamzadeh-Ejhieh, A.; Huang, Y. Application progress of nano-platforms based on metal-organic frameworks (MOFs) in modern agriculture. *J. Environ. Chem. Eng.* **2025**, *13*, 116870. [CrossRef]
80. Zhang, Y.; Tan, H.; Zhu, J.; Duan, L.; Ding, Y.; Liang, F.; Li, Y.; Peng, X.; Jiang, R.; Yu, J.; et al. A Fluorine-Functionalized Tb(III)-Organic Framework for Ba^{2+} Detection. *Molecules* **2024**, *29*, 5903. [CrossRef]
81. Ma, D.; Chen, C.; Chen, M.; Zhu, S.; Wu, Y.; Li, Z.; Li, Y.; Zhou, L. A hydrostable Cadmium-Organic Framework for Highly Selective and Sensitive Luminescence Sensing of Al^{3+} Ion. *J. Inorg. Organomet. Polym. Mater.* **2019**, *29*, 1829–1837. [CrossRef]
82. Valenzano, L.; Civalleri, B.; Chavan, S.; Bordiga, S.; Nilsen, M.H.; Jakobsen, S.; Lillerud, K.P.; Lamberti, C. Disclosing the Complex Structure of UiO-66 Metal Organic Framework: A Synergic Combination of Experiment and Theory. *Chem. Mater.* **2011**, *23*, 1700–1718. [CrossRef]
83. Garai, M.; Yavuz, C.T. Robust Mesoporous Zr-MOF with Pd Nanoparticles for Formic-Acid-Based Chemical Hydrogen Storage. *Matter* **2021**, *4*, 10–12. [CrossRef]

Supplementary Material

Encapsulation of a Highly Acid-stable Dicyano-Bodipy in Zr-based Metal–organic Frameworks with Increased Fluorescence Lifetime and Quantum Yield within the Solid solution Concept

Marcus N. A. Fetzer, Maximilian Vieten, Aysenur Limon, and Christoph Janiak*

Institut für Anorganische Chemie und Strukturchemie, Heinrich-Heine-Universität Düsseldorf, 40204 Düsseldorf, Germany

E-Mail: Christoph Janiak* - janiak@uni-duesseldorf.de * Corresponding author

Fax: +49-211-81-12287; Tel: +49-211-81-12286

Emails: Marcus N. A. Fetzer – fetzer@uni-düsseldorf.de; Maximilian Vieten – mavie107@uni-düsseldorf.de; Aysenur Limon – aysenur.limon@uni-düsseldorf.de

Table of Contents

S1. General Information

Unless otherwise noted, all commercially available compounds were used as provided without further purification. Solvents used in reactions were p. A. grade. Solvents for ambient pressure column chromatography for the preparative purification of synthesis products were technical grade and distilled prior to use. Column chromatography was performed using silica gel Merck 60 (particle size 0.063 – 0.2 mm, Merck KGaA, Darmstadt, Germany). Solvent mixtures are understood as volume/volume. Analytical thin-layer chromatography (TLC) was performed on Macherey-Nagel silica gel aluminium plates (Macherey-Nagel GmbH & Co. Kg, Düren, Germany) with the F-254 indicator, and was visualized by irradiation with UV light (λ_{exc} = 254 or 360 nm). ^{1}H-NMR, ^{13}C-NMR, and ^{19}F-NMR were recorded on a Bruker Avance III 300 MHz NMR spectrometer in $CDCl_3$ (Bruker, Billerica, MA, USA). NMR data are reported as a chemical shift (δ) in ppm with multiplicities indicated as s (singlet), d (doublet), t (triplet), q (quartet), and m (multiplet). ^{1}H-NMR chemical shifts are referenced to the residual proton solvent signal versus TMS (δ($CHCl_3$ = 7.26). ^{13}C-NMR chemical shifts are referenced to the carbon solvent signal versus TMS (δ($CHCl_3$ = 77.2). ESI-MS was measured on a Bruker Daltonics UHR-QTOF maXis 4G (Bruker Daltonics GmbH & Co. KG, Bremen, Germany). All MS measurements were done on positive ion mode, and species can appear as protonated (m/z $[M+H]^+$), sodium adduct (m/z $[M+Na]^+$), or ammonium adduct (m/z $[M+NH_4]^+$). Powder X-ray diffraction (PXRD) analysis was conducted at an ambient temperature on a Rigaku Miniflex 600 powder diffractometer (Rigaku, Tokyo, Japan) using Cu Kα1 radiation with λ = 1.5406 Å (40 kV, 15 mA, 600 W) in the range of 2 θ = 2°– 50° and a flat silicon holder with low background and with a small indent for sample placement. N_2 sorption isotherms were obtained with a Belsorp MAXII high-precision gas/vapor adsorption measurement instrument (Microtrac MRB, Haan, Germany) or a Quantachrome Autosorb-6 at 77 K (Anton Paar QuantaTec, Boynton Beach, FL, USA). Scanning electron microscopy images were taken using a Jeol JSM-6510LV QSEM equipped with a LAB_6 cathode. The acceleration voltage was 20 kV. Before the measurement, the samples were coated with gold using a Jeol JFC 1200 Fine Coater (Jeol Ltd., Akishima, Tokyo, Japan). Optical measurements were carried out using a reflective setup on a FS5 photoluminescence spectrometer (Edinburgh Instruments, Livingston, UK) equipped with a 450 W Xe arc lamp. For this purpose, all solid samples were placed as solids in a brass sample holder. The quantum yield was measured with an integrating sphere (Ulbricht sphere) lined on the inside with BenFlect and exhibiting R > 99% between 350 nm and 2500 nm. All measurements were performed in ambient air.

S2. Sources of chemicals

Reagent	Manufacturer
2,4-Dimethyl-1H-pyrrole	BLDpharm
Benzaldehyde	ACROS Organics
Trifluoroacetic acid (TFA)	ACROS Organics
2,3-Dichloro-5,6-dicyano-1,4-benzoquinone (DDQ)	Sigma-Aldrich
Triethylamine	Fisher Chemical
Boron trifluoride etherate	TCI Chemicals
Magnesium sulfate	VWR Chemicals
Tin tetrachloride	ACROS Organics
Trimethylsilyl cyanide	Thermo Scientific
Sodium bicarbonate	Alfa Aesar
Zirconyl chloride octahydrate	Alfa Aesar
Zirconium(IV) chloride	Alfa Aesar
Dimethylformamide	Honeywell
Terephthalic acid	Alfa Aesar
Methanol	Sigma-Aldrich
Chloroform	Fisher Chemical
Dichloromethane	Sigma-Aldrich
2,5-Thiophenedicarboxylic acid	BLDpharm
Trimesic acid	BLDpharm
HCl (37%)	Sigma-Aldrich
Formic acid	Honeywell

S3. Synthesis of Bodipy compounds 1 and 2 (Scheme S1 and S2)

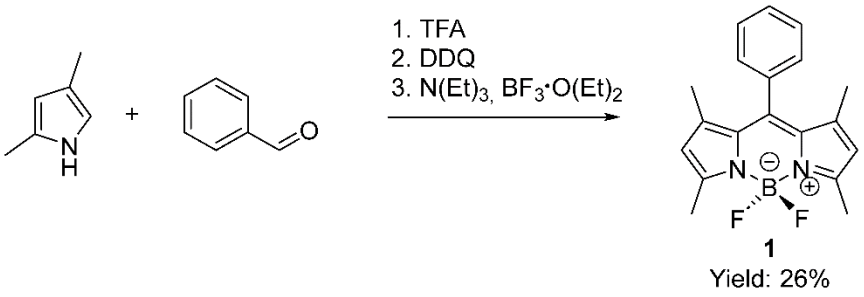

1
Yield: 26%

Scheme S1. Synthesis of 5,5-difluoro-1,3,7,9-tetramethyl-10-phenyl-Bodipy **1** according to Caruso et al. [1].

Under a nitrogen atmosphere, 1.13 mL of 2,4-dimethyl-1H-pyrrole (11 mmol) and 505.4 µL of benzaldehyde (5 mmol) were placed in dry dichloromethane (40 mL). Three drops of trifluoroacetic acid (TFA) were added to the solution. The reaction mixture was stirred for 4 h at room temperature. The progress of the reaction was monitored by TLC. After the benzaldehyde was completely consumed, 1.25 g of 2,3-dichloro-5,6-dicyano-1,4-benzoquinone (DDQ) (5.5 mmol) was added to the reaction, and the mixture was stirred for another 1.5 h. Subsequently, 4 mL of triethylamine and 4 mL of boron trifluoride diethyl etherate were added and stirred for 16 h. The mixture was washed three times with water (3 × 100 mL), and the organic layer was dried over $MgSO_4$. The solvent was removed under reduced pressure, and the crude product was purified by column chromatography on silica (cyclohexane/CH_2Cl_2 1:1) to afford 420 mg of difluoro-Bodipy **1** as a red solid.

Yield: 26%

^{1}H NMR (300 MHz, $CDCl_3$): δ = 7.49-7.47 (m, 3H), 7.30-7.26 (m, 2H), 5.98 (s, 2H), 2.56 (s, 6H), 1.37 (s, 6H) ppm (Figure S1).

^{19}F NMR (282 MHz, $CDCl_3$): δ = -146.31 (q, $^1J_{F\text{-}B}$ = 33.1 Hz) ppm (Figure S2).

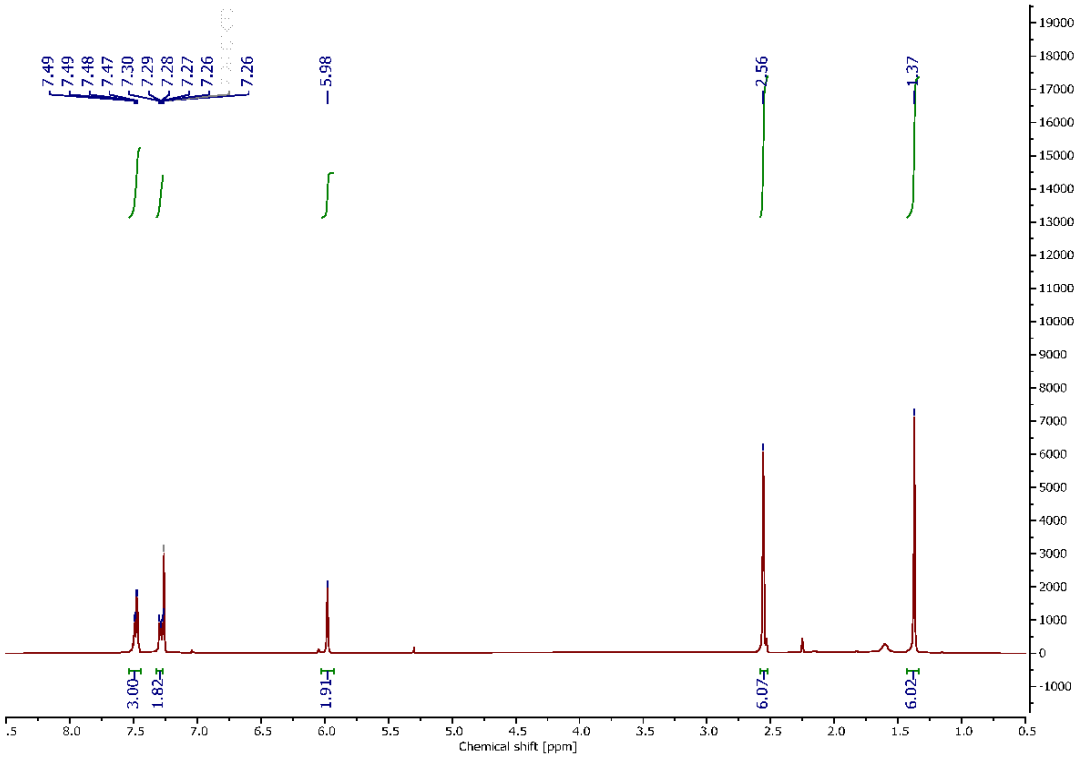

Figure S1. ^{1}H NMR spectrum (300 MHz) of difluoro-Bodipy **1** in $CDCl_3$.

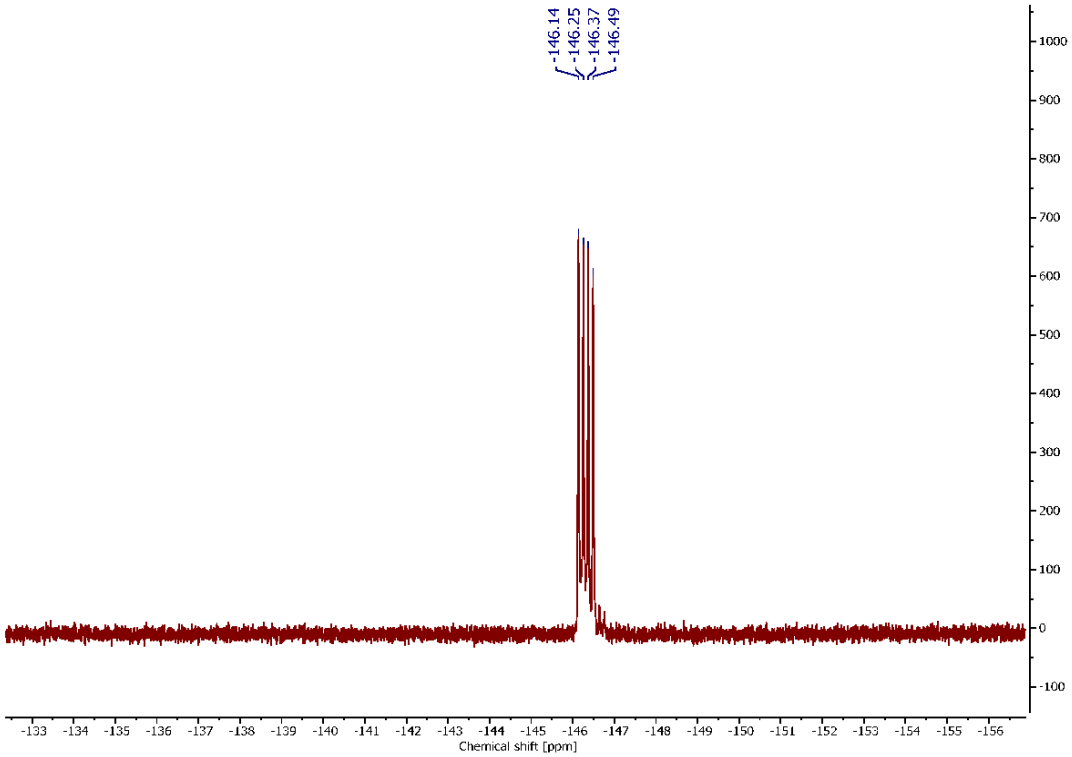

Figure S2. ^{19}F NMR (282 MHz) spectrum of difluoro-Bodipy **1** in $CDCl_3$.

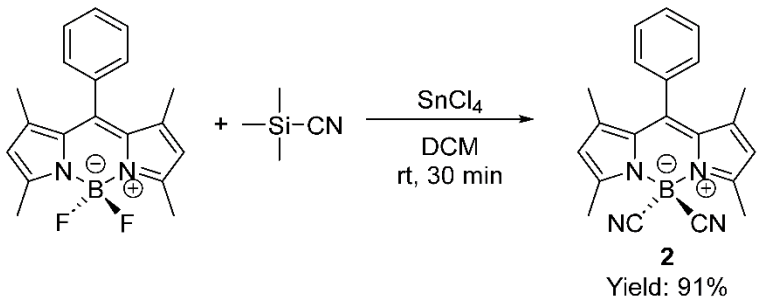

Scheme S2. Synthesis of 5,5-dicarbonitril-1,3,7,9-tetramethyl-10-phenyl-Bodipy **2** according to Nguyen et al. [2].

The amount of 200 mg of **1** (0.62 mmol) was dissolved in anhydrous dichloromethane (30 mL). Tin tetrachloride (36 µL, 0.31 mmol) in 5 mL of dichloromethane was added dropwise, followed by 388 µL of trimethylsilyl cyanide (3.1 mmol). After 30 min, the reaction was quenched with water and extracted three times with dichloromethane (3 × 50 mL). The organic phase was washed with a saturated aqueous $NaHCO_3$ solution (30 mL) and dried over $MgSO_4$. The solvent was removed under reduced pressure, and the crude product was purified by column chromatography on silica (cyclohexane/EtOAc 5:1) to afford 190 mg of dicyano-Bodipy **2** as a red to orange solid.

Yield: 91%

^{1}H NMR (300 MHz, $CDCl_3$): δ = 7.54-7.52 (m, 3H), 7.30-7.27 (m, 2H), 6.16 (s, 2H), 2.73 (s, 6H), 1.41 (s, 6H) ppm (Figure S3).

^{13}C NMR (75 MHz, $CDCl_3$): δ = 156.1, 144.6, 143.7, 134.1, 130.3, 129.8, 129.6, 127.8, 122.7, 122.5, 15.6, 14.7 ppm (Figure S4).

HRMS $[M+H]^+$ calculated ($^{12}C_{21}$ $^{1}H_{20}$ ^{11}B $^{14}N_4$) 339.1776; found: 339.1784 (Figure S5).

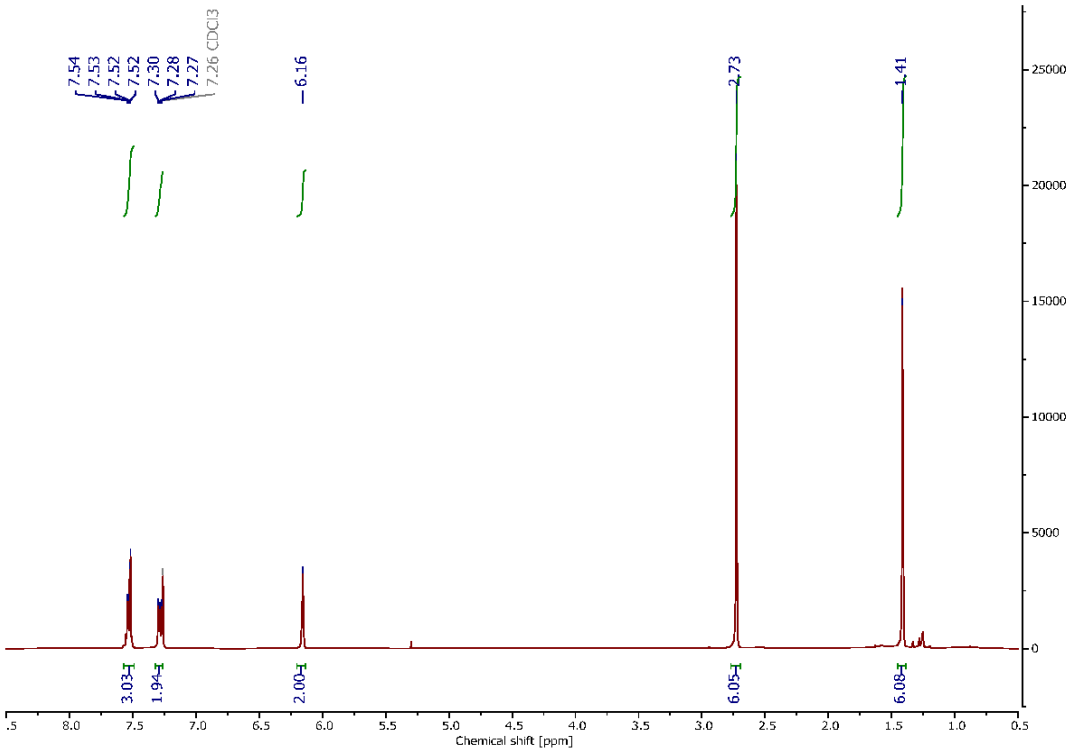

Figure S3. ^{1}H NMR (300 MHz) of dicyano-Bodipy **2** in $CDCl_3$.

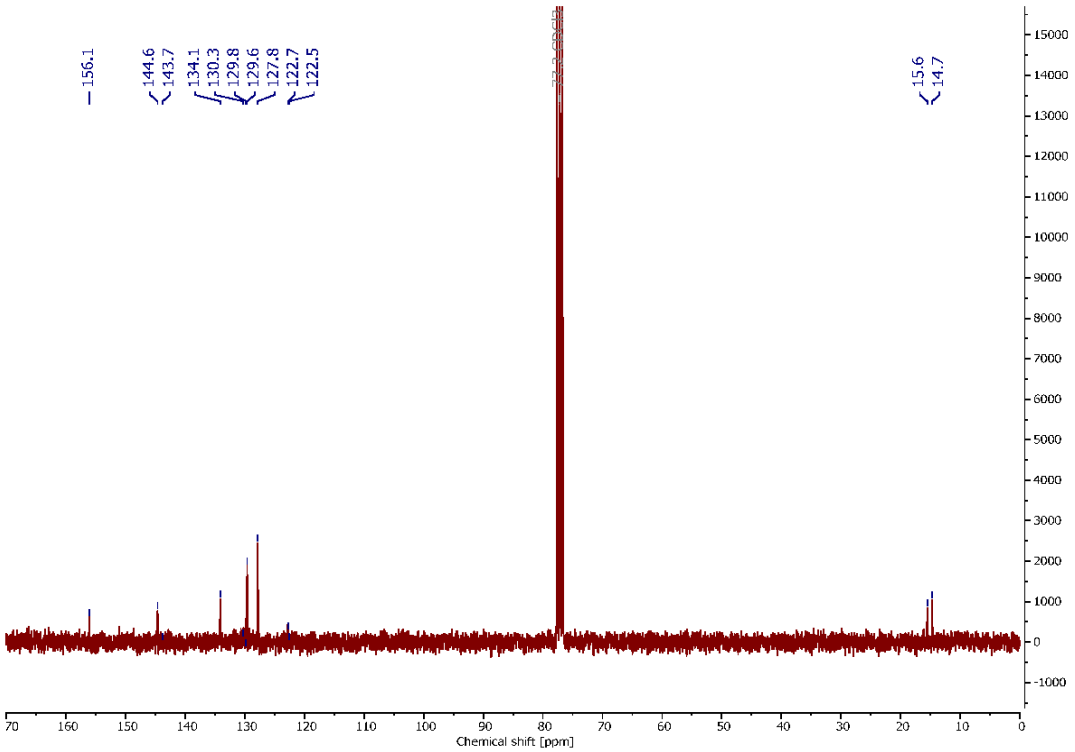

Figure S4. ^{13}C NMR (75 MHz) of dicyano-Bodipy **2** in $CDCl_3$.

Mass Spectrum SmartFormula Report

Analysis Info

Analysis Name	D:\Data\Spektren 2024\JAN24HR000011.d	Acquisition Date	9/24/2024 10:19:56 AM
Method	tune_low_new.m	Operator	PT
Sample Name	Fetzer MF400 Fr.4-12 in CHCl3 (CH3OH)	Instrument	maXis 288882.20213
Comment			

Acquisition Parameter

Source Type	ESI	Ion Polarity	Positive	Set Nebulizer	0.3 Bar
Focus	Not active	Set Capillary	4000 V	Set Dry Heater	180 °C
Scan Begin	50 m/z	Set End Plate Offset	-500 V	Set Dry Gas	4.0 l/min
Scan End	1500 m/z	Set Collision Cell RF	600.0 Vpp	Set Divert Valve	Source

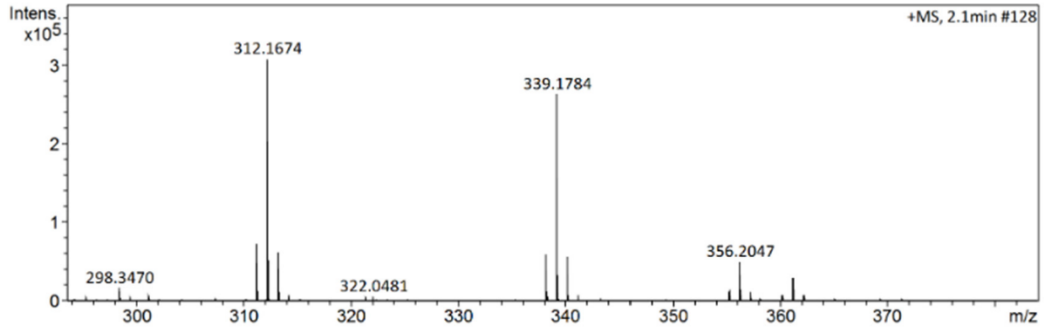

Meas. m/z	#	Ion Formula	m/z	err [ppm]	mSigma	# mSigma	Score	rdb	e⁻ Conf	N-Rule
312.1674	1	C20H19BN3	312.1667	-1.2	11.9	1	100.00	13.5	even	ok
339.1784	1	C21H20BN4	339.1776	-1.3	12.1	1	100.00	14.5	even	ok
356.2047	1	C20H27BNO4	356.2028	-4.4	6.7	1	48.38	8.5	even	ok
	2	C21H23BN5	356.2041	-0.6	7.9	2	100.00	13.5	even	ok
361.1601	1	C21H19BN4Na	361.1595	-0.5	8.6	1	100.00	14.5	even	ok
	2	C20H23BNaO4	361.1582	-4.3	14.8	2	42.42	9.5	even	ok

Figure S5. High-resolution ESI-MS of dicyano-Bodipy **2**.

S4. Photophysical properties of dicyano-Bodipy 2

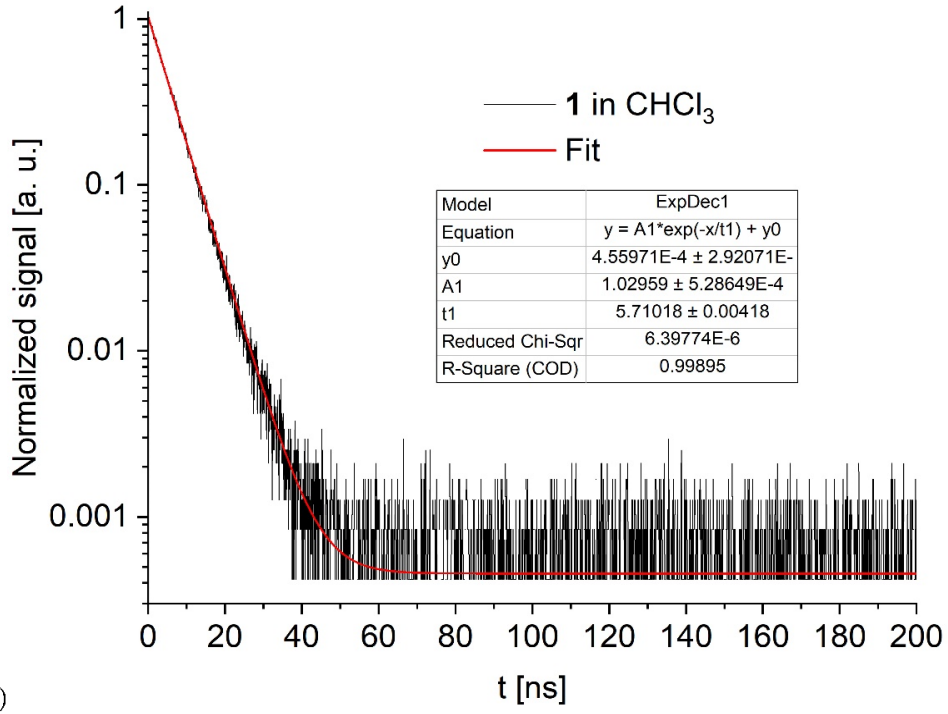

a)

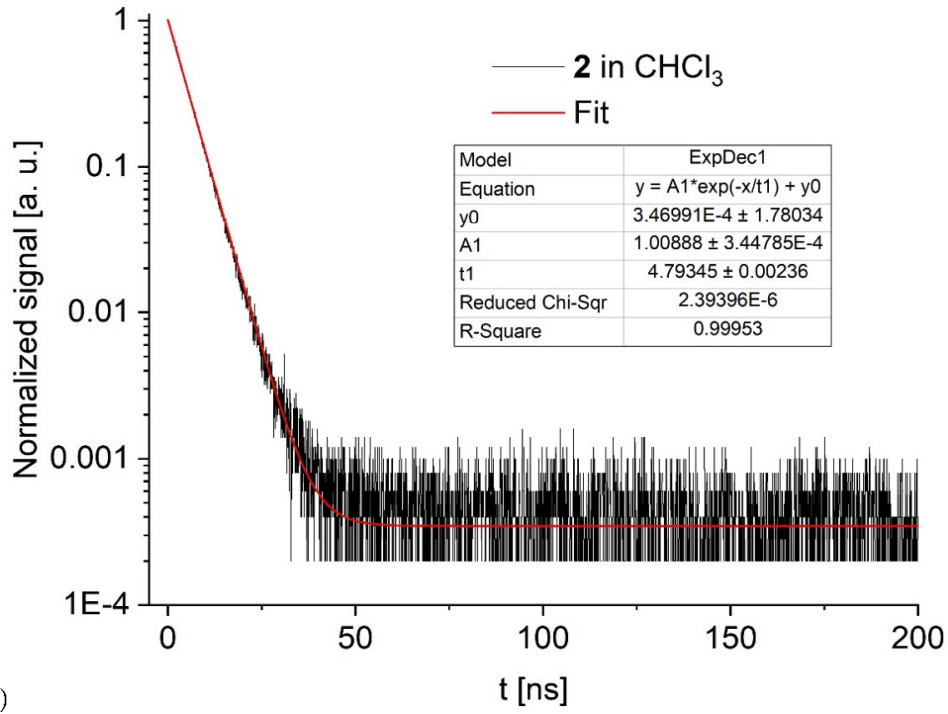

b)

Figure S6. Time-resolved photoluminescence decay (black) of the emission of a) **1** at 514.4 nm and b) **2** at 510 nm after excitation at 375 nm, both in chloroform solution (c = 0.5 mmol/L) with the respective exponential fitting parameters, including the pre-exponential factors A_1, lifetimes t_1, and confidence limits.

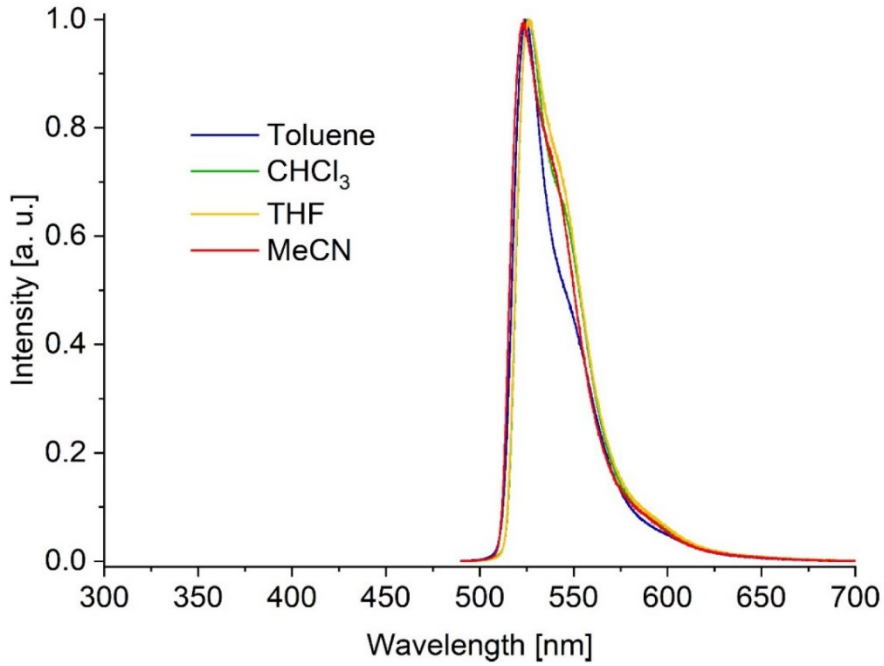

Figure S7. Emission spectra of **2** in different solvents. Excitation at 360 nm.

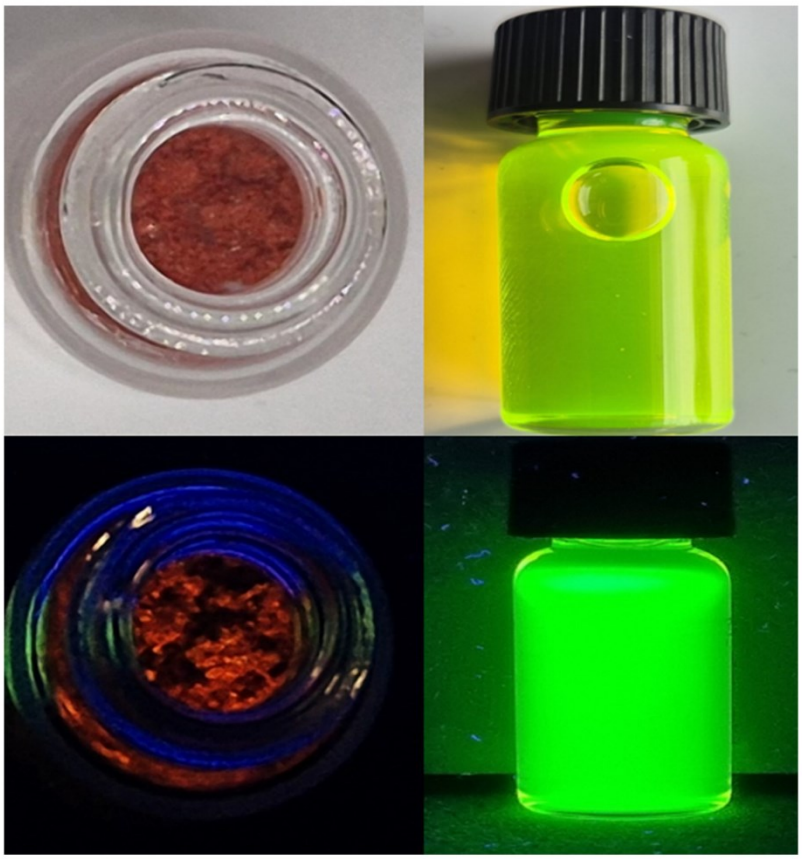

Figure S8. Neat dicyano-Bodipy **2** in the solid state (left) and dicyano-Bodipy **2** solution in $CHCl_3$ (8 mmol/L right) under daylight (top) and UV-light (λ_{exc} = 365 nm, bottom).

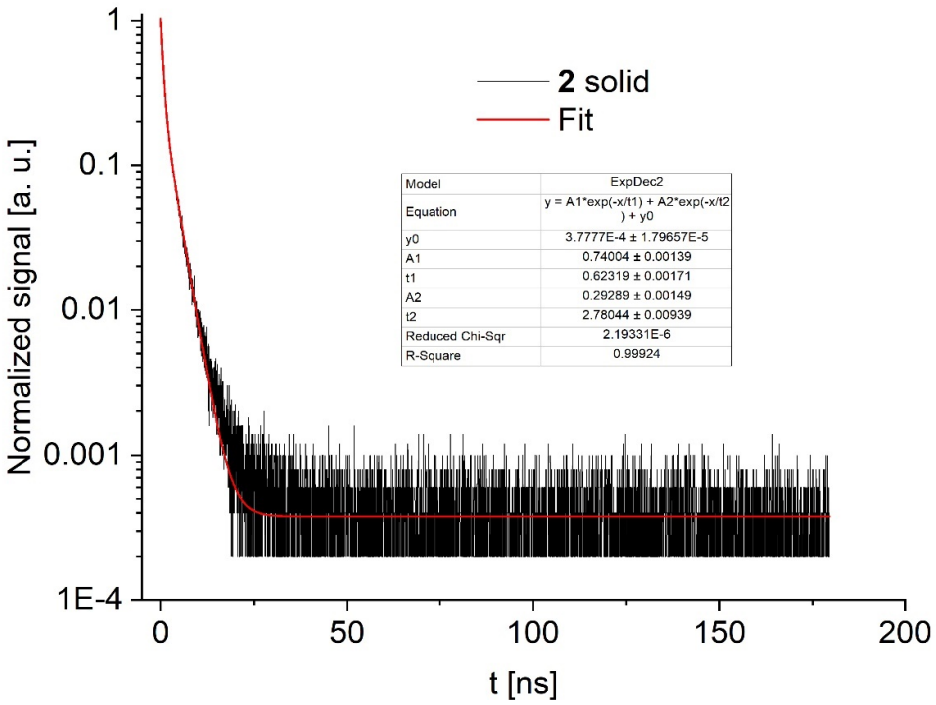

Figure S9. Time-resolved photoluminescence decay (black) of the emission of neat **2** in the solid state at 594 nm after excitation at 375 nm with the respective two-exponential fitting parameters, including the pre-exponential factors A_1 and A_2, lifetimes t_1 and t_2, and confidence limits.

S5. Synthesis of UiO-66 and 2@UiO-66 composites (Scheme S3)

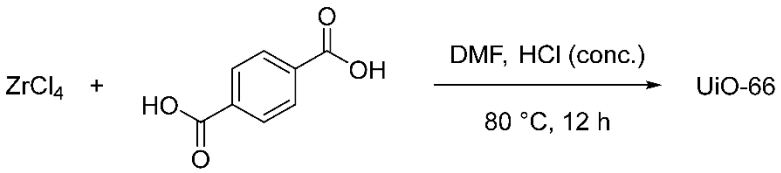

Scheme S3. Synthesis of UiO-66 according to the synthesis of Katz et al. with slight modifications [3].

A 16 mL Pyrex tube was loaded with 125 mg of $ZrCl_4$, 125 mg of H_2BDC, 1 mL of concentrated HCl (37 %), and 15 mL of DMF. The reaction mixture was sonicated for 20 minutes until all solids were dissolved. The reaction mixture was then heated to 80 °C for 12 hours. The white solid obtained was filtered off and washed with DMF (3 × 30 mL) and MeOH (3 × 30 mL). The sample was dried in a vacuum oven at 60 °C for 24 hours and then activated under high vacuum at 150 °C for 16 hours.

The post-synthetic wet infiltration was carried out with stirring for a period of 5 days in a 6 mL solution with a concentration of 1.0 mmol/L of **2** in dichloromethane with 80 mg of activated UiO-66, which led to the composite **2**@UiO-66$_{0.44}$. For the in situ synthesis of the composites, the above-described synthesis protocol was used. Thereby, a defined part of the 15 mL of neat DMF was replaced by a DMF solution of **2** with a concentration of 15 mmol/L (see Table S1), resulting in concentrations of **2** in the reaction mixtures of 3, 7, 10, and 15 mmol/L. The reactions, depending on the increasing concentration, led to the composites **2**@UiO-66$_{1.1}$, **2**@UiO-66$_{2.3}$, **2**@UiO-66$_{4.7}$, and **2**@UiO-66$_{7.2}$.

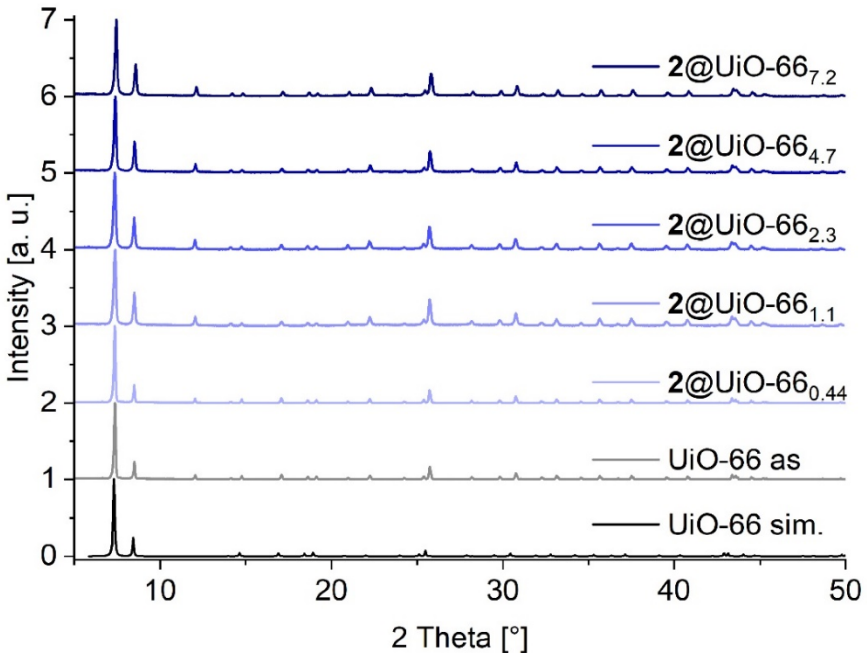

Figure S10. PXRD of UiO-66 and all UiO-66 composites. Simulation of UiO-66 from CCDC No. 752051 [4].

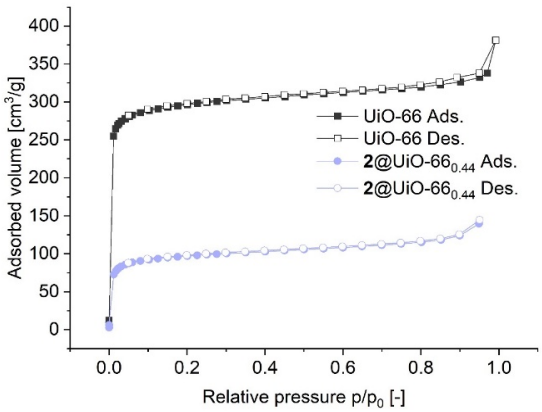

Figure S11. Nitrogen sorption isotherms at 77 K of UiO-66 and the post-synthetic composite with S_{BET} = 1196 m^2/g and 381 m^2/g, respectively (filled symbols: adsorption; empty symbols: desorption).

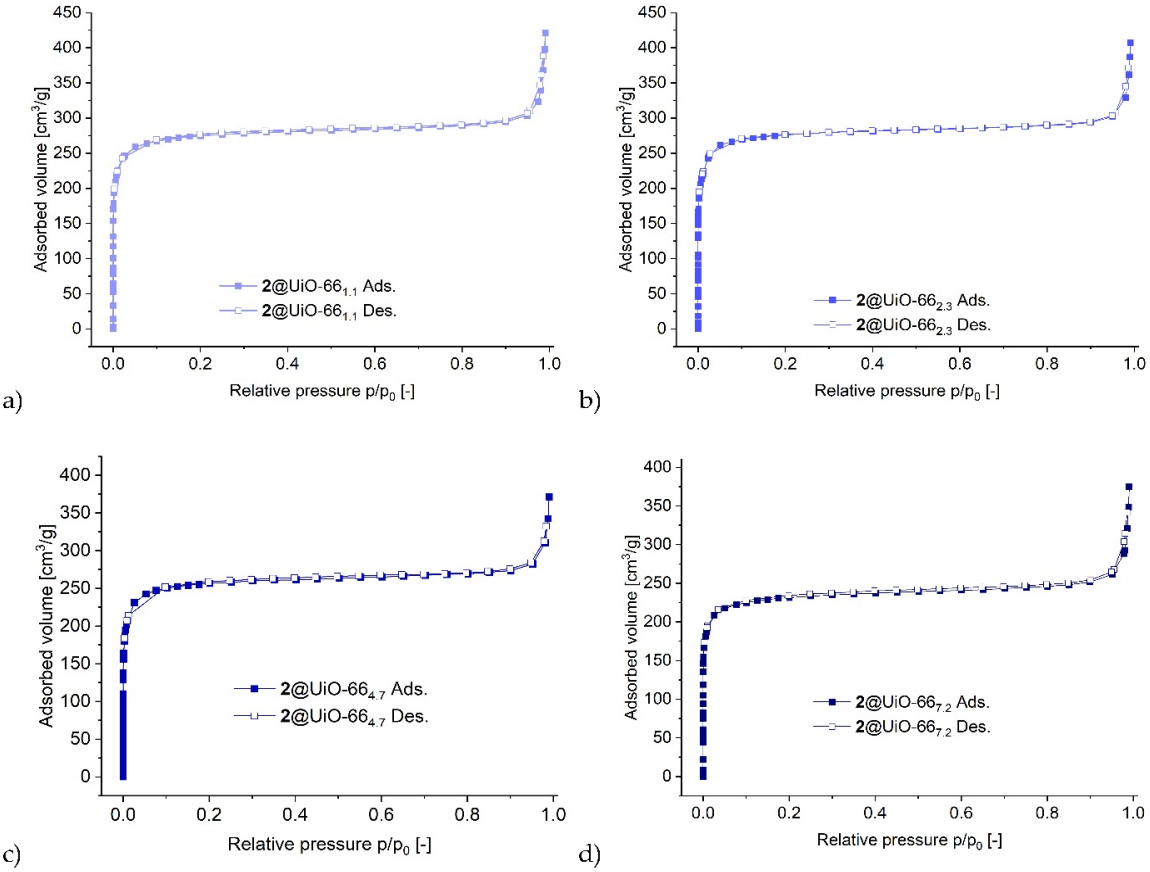

Figure S12. Nitrogen sorption isotherms at 77 K of in situ synthesized **2**@UiO-66 composites with S_{BET} = 1115 m^2/g (a), 1096 m^2/g (b), 1022 m^2/g (c), and 916 m^2/g (d) (filled symbols: adsorption; empty symbols: desorption).

Table S1. Concentrations and BET surface area determinations of the in situ prepared composites.

Compound	Volume of DMF solution of 2 [a] [mL]	Concentrations of 2 in the reaction mixtures [mmol/L]	S_{BET} [m²/g]
UiO-66 synthesized	-	-	1192
a) 2@UiO-66$_{1.1}$	3	3	1115
b) 2@UiO-66$_{2.3}$	7	7	1096
c) 2@UiO-66$_{4.7}$	10	10	1022
d) 2@UiO-66$_{7.2}$	15	15	916

[a] DMF solution of **2** with a concentration of 15 mmol/L.

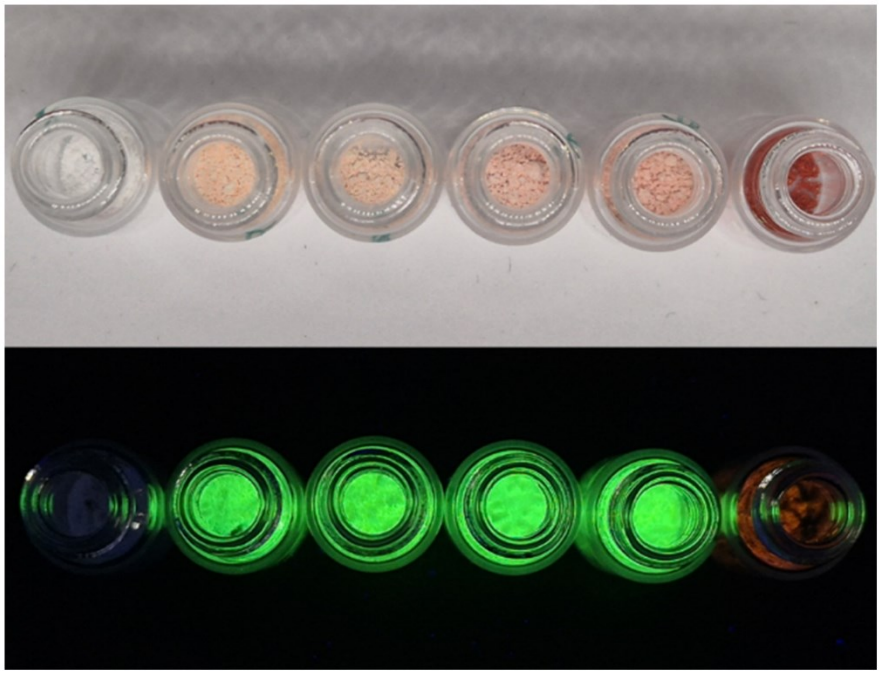

Figure S13. From left to right, neat UiO-66, the four in situ prepared UiO-66 composites **2**@UiO-66$_{1.1}$, **2**@UiO-66$_{2.3}$, **2**@UiO-66$_{4.7}$, **2**@UiO-66$_{7.2}$, and neat **2** as a solid under daylight (top) and UV-light (λ_{exc} = 365 nm, bottom).

S6. Digestion UV–Vis spectroscopy

Carefully weighted aliquots (see example below and Table S2) of all post-synthetic and in situ samples of **2**@MOF were digested under strong acidic (conc. HCl for DUT-67) or basic (1 mol/L KOH for UiO-66, MOF-808, and MIP-206) conditions in order to determine the loading of **2** in the MOF. Dicyano-Bodipy **2** was extracted from the aqueous phase with dichloromethane, the solvent was removed under reduced pressure using a rotary evaporator, the solid residue was dried under high vacuum, and it was then dissolved in a defined amount of 3.0 mL of chloroform for the post-synthetic composites and 5.0 mL of chloroform for the in situ composites. The amount of **2** in each MOF could be determined using the previously generated calibration curve (Figure S14) [5-8].

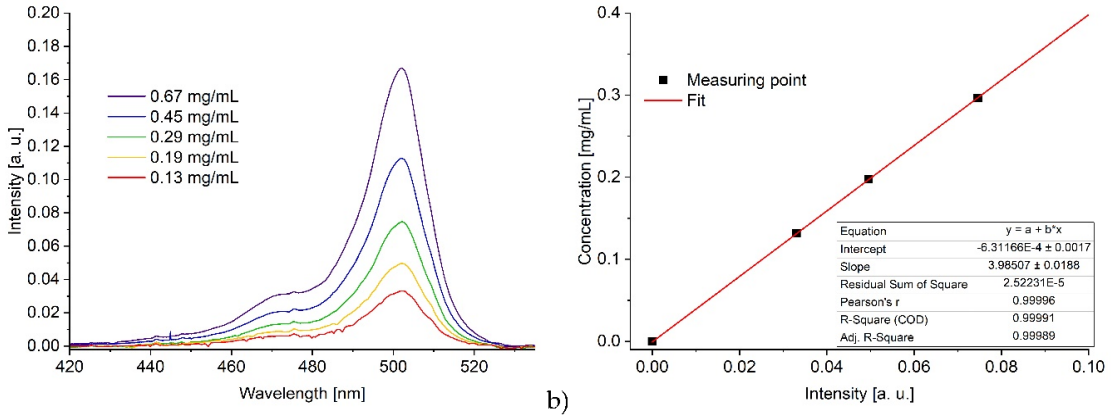

a) b)

Figure S14. a) UV–Vis spectra of different concentrated solutions of **2** in chloroform. b) Calibration line with fit and R-values. Values were taken at a wavelength of 502 nm.

The mass of Bodipy **2** in the analytical sample (weight of incorporated Bodipy) is obtained by multiplying the absorption intensity by the slope of the calibration curve and the volume of chloroform. The loading of Bodipy in MOFs can then be calculated using the following equation (1):

$$loading\ (wt\%) = \frac{weight\ of\ incorporated\ \boldsymbol{Bodipy}}{weight\ of\ \boldsymbol{Bodipy}@MOF} \times 100 \qquad (1)$$

For example, for post-synthetic **2**@UiO-66$_{0.44}$ (eq. (2)), 16.3 mg of the composite was digested and the extracted Bodipy dissolved in 3.0 mL of chloroform, resulting in a rounded intensity of 0.006 at λ_{em} = 502 nm.

$$loading\ (0.44\ wt\%) = \frac{0.006 \times 3.985 \times 3}{16.3} \times 100 \qquad (2)$$

For example, for in situ **2**@UiO-66$_{4.7}$ (eq. (3)), 16.1 mg of the composite was digested, and the extracted Bodipy was dissolved in 5.0 mL of chloroform, resulting in a rounded intensity of 0.038 at λ_{em} = 502 nm.

$$loading\ (4.7\ wt\%) = \frac{0.038 \times 3.985 \times 5}{16.1} \times 100 \qquad (3)$$

Table S2. Determination of the Bodipy **2** loading in the in situ prepared UiO-66 composites using the UV–Vis digestion method. All in situ prepared UiO-66 composites were dissolved in 5 mL of chloroform.

Bodipy 2 concentration in synthesis [mmol/L]	Mass of composite digested [mg]	Intensity at λ_{em} = 502 nm	Concentration from UV–Vis calibration curve [mg/mL]	Loading [wt%]	Sample name
0	14.2	0	0	0	UiO-66
3	14.8	0.008	0.03	1.1	**2**@UiO-66$_{1.1}$
7	14.4	0.016	0.07	2.3	**2**@UiO-66$_{2.3}$
10	16.1	0.038	0.15	4.7	**2**@UiO-66$_{4.7}$
15	15.8	0.057	0.23	7.2	**2**@UiO-66$_{7.2}$

Table S3. Determination of the Bodipy **2** loading of individual composites for MOF-808, DUT-67, and MIP-206 using the UV–Vis method described.

MOF	Mass of composite digested [mg]	Intensity at λ_{em} = 502 nm	Concentration from UV–Vis calibration curve [mg/mL]	Loading [wt%]
2@MOF-808$_{0.57}$[a]	16.9	0.008	0.03	0.57
2@MOF-808$_{1.9}$[b]	16.2	0.016	0.06	1.9
2@DUT-67$_{0.51}$[a]	16.3	0.007	0.03	0.51
2@DUT-67$_{2.2}$[b]	12.4	0.018	0.07	2.2
2@MIP-206$_{0.3}$[a]	17.4	0.004	0.02	0.30

[a] Extract after digestion was dissolved in 3.0 mL of chloroform. [b] Extract after digestion was dissolved in 5.0 mL of chloroform.

S7 Calculation of pore filling and the probability p of multiple occupations

We used the crystal structures of the respective MOFs to visualize the pores. It is crucial that only pores capable of accommodating the dye molecule are considered.

Structure of UiO-66:

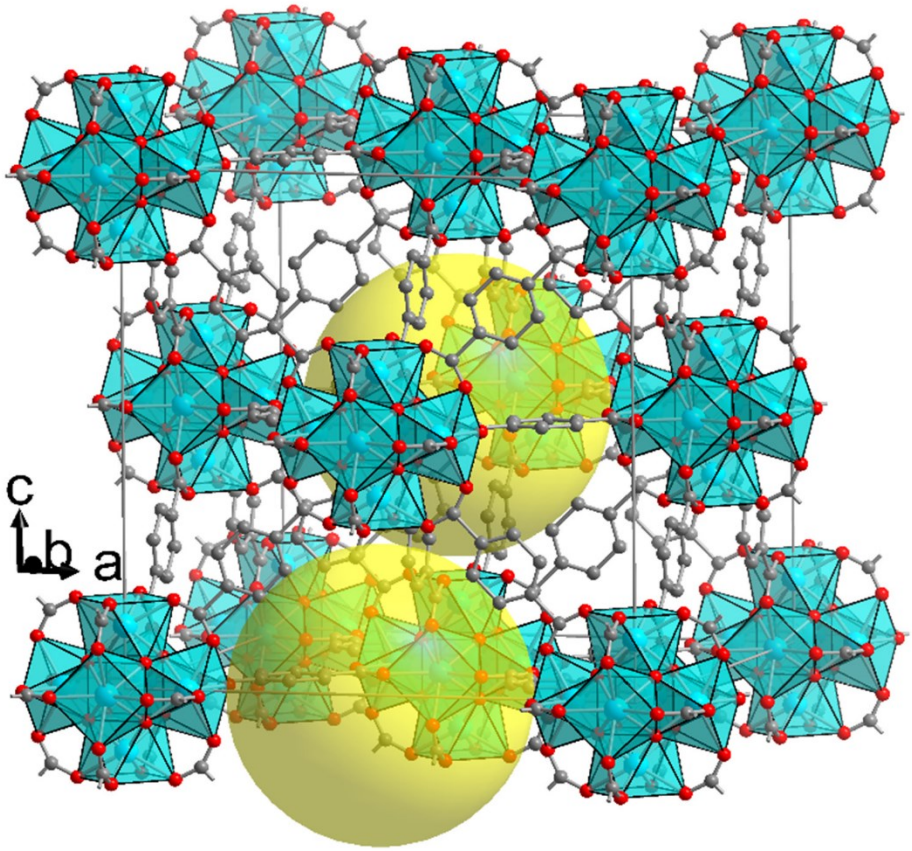

Figure S15. Structure of zirconium terephthalate UiO-66, with the formula unit 3D-$[Zr_6O_4(OH)_4(BDC)_6]$ in the face-centered cubic **fcu** structure, showing the octahedral pore in yellow in the center and on one of the edges. The diameter of the yellow sphere is 12 Å. The UiO-66 structure was drawn from the deposited CIF files under CCDC 837796 [9]. Hydrogen atoms are omitted for clarity.

UiO-66 contains two main types of pores: tetrahedral pores with diameters of approximately 8 Å (0.8 nm) and octahedral pores with a diameter of 11 Å (1.1 nm). Only the latter is capable of absorbing Bodipy. There are four formula units per unit cell. Two of the octahedral pores are indicated as yellow spheres. There is one octahedral pore in the center of the cubic unit cell and one on each of the 12 edges of the cube, counting as ¼, giving an additional three octahedral pores or four in total per unit cell. Thus, there is one octahedral pore per formula unit of $[Zr_6O_4(OH)_4(BDC)_6]$ (1664.01 g/mol).

Based on the number of pores per formula unit (1:1), the formula unit of **2** (338.22 g/mol), and the UV–Vis analysis for **2**@UiO-66 from Table S2, we can calculate the ratio of **2** to octahedral pores (eq. (4)). This will be illustrated using the example **2**@UiO-66$_{7.2}$.

2@UiO-66$_{7.2}$ contains 72 mg of **2** per gram of composite, which then contains 1–0.072 = 0.928 mg of UiO-66. This corresponds to 0.21 mmol of **2** and 0.56 mmol of UiO-66, which equals 0.56 mmol of pores because of the 1:1 ratio (eq. (5)).

$$n\left(\frac{Bodipy}{pore}\right) = filled\ pores \tag{4}$$

$$n\left(\frac{Bodipy}{pore}\right) = \frac{0.21\ mmol}{0.56\ mmol} = 0.375 \tag{5}$$

The result is a pore filling of 37.5% of the existing octahedral pores, leaving 62.5% of the pores empty. Based on this result, we were able to calculate the probability p of multiple occupancy. For this, we used a Poisson distribution (eq. (6) and (7)).

$$p(n) = \frac{\alpha^n \times e^{-\alpha}}{n!} \tag{6}$$

$$\alpha = -\ln(unoccupied\ pores) \tag{7}$$

In the case of **2**@UiO-66$_{7.2}$ $\alpha = -\ln(0.625) = 0.47$

Table S4. Calculations of the probability p of multiple occupancy for **2**@UiO-66$_{7.2}$.

2@UiO-66$_{7.2}$	**Calculated probability**	**Probability in %**
p(one)	0.293	78.1
p(two)	0.069	18.4
p(≥three)	0.013	3.5
Sum	0.375	100

The sum of all probabilities must equal 1 (when adding p(zero) = 0.625). Additionally, the expected value of α should equal the sum of all probabilities p multiplied by the number of occupations n (eq. (8)).

$$\alpha = \sum p(n) \times n \tag{8}$$

Thus, from the above calculated probabilities. $\alpha = 0.47 = 0.293 \times 1 + 0.069 \times 2 + 0.013 \times 3$

Structure of MOF-808:

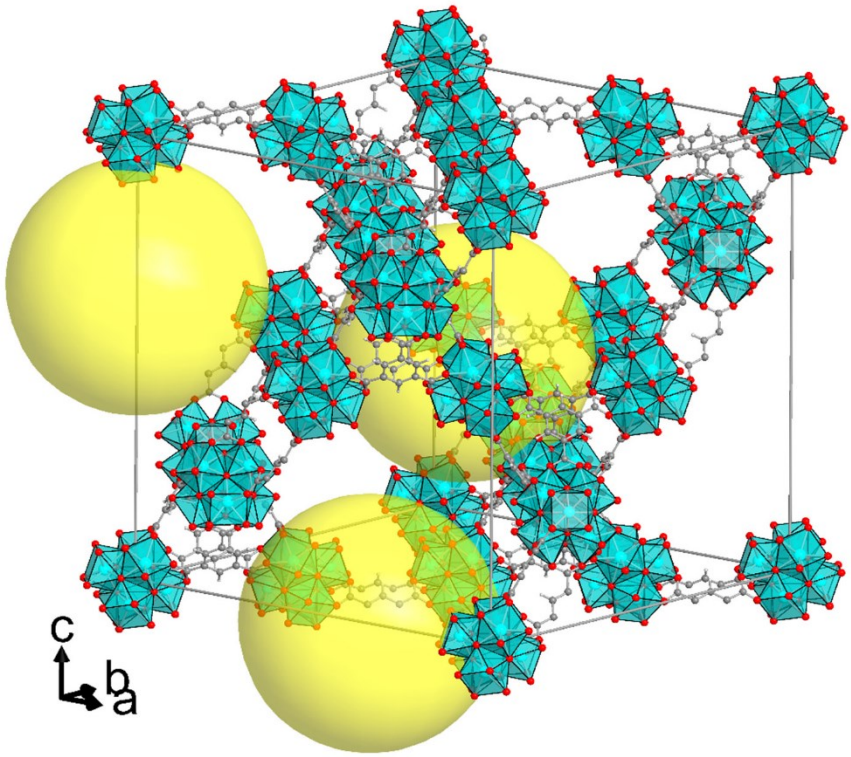

Figure S16. Structure of zirconium benzene-1,3,5-tricarboxylate MOF-808, with the formula unit 3D-$[Zr_6O_4(OH)_{10}(BTC)_2(H_2O)_6]$ and an expanded diamond (dia-a) net, consisting of 6-connected Zr-based clusters (SBUs) and trimesate linkers. Its structure features two types of interconnected voids: small, isolated tetrahedral cages (not highlighted) and large, adamantane-shaped pores. The latter in yellow are shown in the center, and two exemplarily on two of the edges (at 0,0,0.66 and at 0.66,0,0). The diameter of the yellow sphere is 20 Å. The MOF-808 structure was drawn from the deposited CIF file under CCDC 1002627 [10]. Note that in this CIF file, there are bridging and terminal formiate linkers at the Zr_6 clusters, giving a formula unit of -$[Zr_6O_4(OH)_4(BTC)_2(HCOO)_6]$ [10]. We followed the synthesis of Reinsch et al. [11], who did not provide a CIF file but had given a formula unit of $[Zr_6O_4(OH)_{10}(BTC)_2(H_2O)_6]$, and we used this formula unit in our subsequent calculations here.

MOF-808 contains two main types of pores: large, interconnected hexagonal channels with diameters of approximately 18 Å (1.8 nm), and isolated tetrahedral cages with internal pore diameters around 4.8 Å (or 0.48 nm). Thus, this hierarchical pore structure of MOF-808 consists of both micropores (tetrahedral cages) and mesopores (hexagonal channels). Only the latter are accessible for Bodipy **2**.

There are 16 formula units per unit cell. There is one pore in the center of the cubic unit cell and one on each of the 12 edges of the cube, counting as ¼, giving an additional three pores or four in total per unit cell. Thus, there is ¼ = 0.25 pores per formula unit of $[Zr_6O_4(OH)_{10}(BTC)_2(H_2O)_6]$ (1303.7 g/mol).

Using the number of pores per formula unit (0.25:1), the formula unit of **2** (338.22 g/mol), and the digestion UV–Vis analysis for the in situ **2**@MOF-808 from Table S3, we can calculate the ratio of **2** to the pores. This will be illustrated using the example **2**@MOF-808$_{1.9}$.

2@MOF-808$_{1.9}$ contains 19 mg of **2** per gram of composite, which then contains 1–0.019 = 0.981 mg of MOF-808. This corresponds to 0.056 mmol of **2** and 0.75 mmol of MOF-808, which equals 0.25 × 0.75 mmol of pores because of the 0.25:1 ratio.

$$n\left(\frac{Bodipy}{pore}\right) = \frac{0.056\ mmol}{0.188\ mmol} = 0.298 \tag{9}$$

The result is a pore filling of 29.8% of the existing pores (eq. (9)), leaving 70.2% of the pores empty. Based on this result, we calculated the probability p of multiple occupancy using the above Poisson distribution.

In the case of **2**@MOF-808$_{1.9}$ $\alpha = -\ln(0.702) = 0.354$

The results of the calculation are listed in Table S5.

The sum of all probabilities must equal 1 (when adding p(zero) = 0.702). Additionally, the expected value of α should equal the sum of all probabilities p multiplied by the number of occupations n (eq. (10)).

$$\alpha = \sum p(n) \times n \tag{10}$$

Thus, from the subsequent calculated probabilities. $\alpha = 0.354 = 0.2484 \times 1 + 0.044 \times 2 + 0.0058 \times 3$

Structure of DUT-67:

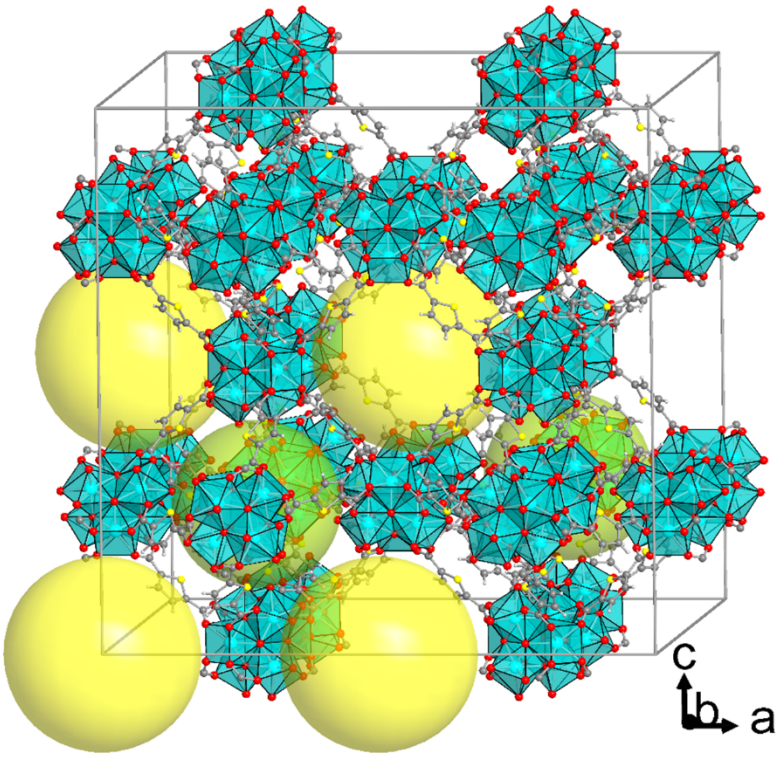

Figure S17. Structure of zirconium thiophenedicarboxylate DUT-67, with the formula unit 3D-$[Zr_6O_4(OH)_8(TDC)_4(H_2O)_6]$ in the reo topology, featuring cuboctahedral cages (yellow) and octahedral cages (light green). The cuboctahedral cages in yellow (sphere diameter 14 Å) are shown in the center, and one each exemplarily on one of the face centers, edge centers, and vertices. Two octahedral cages in light green (sphere diameter 12 Å) are exemplarily given at 0.25,0.25,0.25 and at 0.75,0.75,0.25. The DUT-67 structure was drawn from the deposited CIF file under CCDC 921644 [12].

DUT-67 has a hierarchical porous structure containing two types of pores: A cuboctahedral pore with a diameter of 14.2 Å (1.42 nm), and an octahedral pore with a diameter of 11.7 Å (1.17 nm). Both of which can encapsulate Bodipy, and we took both pores into account when calculating the occupation.

In DUT-67, there are 24 formula units of $[Zr_6O_4(OH)_8(TDC)_4(H_2O)_6]$ (1536.1 g/mol)per unit cell. There is one cuboctahedral pore in the center of the cubic unit cell, one on each center of the six faces, counting ½, one on the midpoint of each of the 12 edges of the cube, counting as ¼, and one on each of the eight vertices, counting 1/8, giving in total eight cuboctahedral pores per unit cell. Further, there are eight octahedral pores per unit cell. Combined, this gives 16 accessible pores per unit cell with its 24 formula units. We expect an even distribution across both types of pores. This results in a ratio of 0.66 pores per formula unit of DUT-67.

Using the number of pores per formula unit (0.66:1), the formula unit of **2** (338.22 g/mol), and the digestion UV–Vis analysis for the in situ **2**@DUT-67 from Table S3, we can calculate the ratio of **2** to the pores. This will be illustrated using the example **2**@DUT-67$_{2.2}$.

2@DUT-67$_{2.2}$ contains 22 mg of **2** per gram of composite, which then contains 1–0.022 = 0.978 mg of DUT-67. This corresponds to 0.065 mmol of **2** and 0.637 mmol of DUT-67, which equals 0.66 × 0.637 mmol of pores because of the 0.66:1 ratio.

$$n\left(\frac{Bodipy}{pore}\right) = \frac{0.065\ mmol}{0.42\ mmol} = 0.155 \tag{11}$$

The result is a pore filling of 15.5% of the existing cuboctahedral and octahedral pores (eq. (11)), leaving 84.5% of the pores empty. Based on this result, we calculated the probability p of multiple occupancy using the above Poisson distribution.

In the case of **2**@DUT-67$_{2.2}$ $\alpha = -\ln(0.845) = 0.168$

The results of the calculation are listed in Table S5.

The sum of all probabilities must equal 1 (when adding p(zero) = 0.845). Additionally, the expected value of α should equal the sum of all probabilities p multiplied by the number of occupations n (eq. (12)).

$$\alpha = \sum p(n) \times n \tag{12}$$

Thus, from the subsequent calculated probabilities. $\alpha = 0.168 = 0.1421 \times 1 + 0.012 \times 2 + 0.0007 \times 3$

Table S5. Calculations of the probability p of multiple occupancy for **2**@MOF-808$_{1.9}$ and **2**@DUT$_{2.2}$.

	2@MOF-808$_{1.9}$		2@DUT-67$_{2.2}$	
n_{av}(Bodipy/pore)	0.298		0.155	
	Calc. probability	Probability in %	Calc. probability	Probability in %
p (one)	0.2484	83.4	0.1421	91.7
p (two)	0.044	14.7	0.012	7.7
p (≥three)	0.0058	1.9	0.0007	0.6
Sum	0.298	100	0.155	100

S8. Synthesis of MOF-808, DUT-67, and MIP-206 and their composites (Scheme S4 and S5)

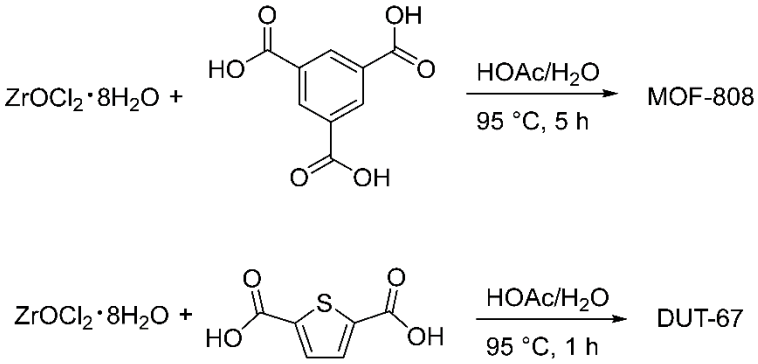

Scheme S4. Synthesis of MOF-808 and DUT-67 in a microwave oven according to a procedure by Reinsch et al. [11].

For MOF-808, 280 mg (1.33 mmol) of 1,3,5-benzenetricarboxylic acid, and for DUT-67, 458 mg (2.66 mmol) of 2,5-thiophenedicarboxylic acid were heated together with 1.288 g (4 mmol) of $ZrOCl_2 \cdot 8H_2O$ in a mixture of 10 mL of water and 10 mL of acetic acid while stirring to 95 °C. The reaction time for MOF-808 was set to 5 h. The reaction time for DUT-67 was set to 1 h. Both MOFs were then separated by centrifugation and washed twice with 15 mL of aqueous sodium acetate solution and once with 15 mL of ultrapure water. The centrifuged products were dried in a vacuum oven at 60 °C for 24 hours and then activated under high vacuum at 150 °C for 16 hours. The respective in situ composites with **2** were prepared in the same way with a concentration of 6 mmol/L of **2** in acetic acid.

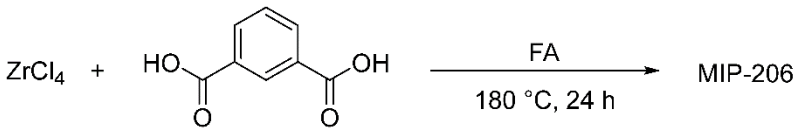

Scheme S5. Synthesis of MIP-206 according to the literature by Wang et al. [13].

MIP-206 was synthesized according to the literature by Wang et al. [13]. 1.1 g (6.6 mmol) of isophthalic acid was added to a Teflon reactor together with 5 mL of formic acid and stirred for 5 minutes. Then 2.0 g of $ZrCl_4$ (8.6 mmol) was added, and the mixture was stirred again for 10 minutes. The reactor was then sealed and heated to 180 °C over a period of two hours. This temperature was maintained for 24 h. The reaction was allowed to cool under ambient conditions to room temperature. The resulting white solid was separated by centrifugation and was washed three times with 20 mL of acetone each and dried in air. It was activated under high vacuum at 150 °C for 16 hours.

Only pores larger than 10 Å can be considered for the incorporation of **2** into the respective MOFs. MOF-808 contains only one type of pore larger than 10 Å (18.4 Å for the adamantane pore; the tetrahedral pore has a size of 4.8 Å), while DUT-67 features two types of pores, both with diameters exceeding 10 Å (14.2 Å for cuboctahedral and 11.7 Å for octahedral pores). Compared to all the other MOFs, MIP-206 has a channel structure with a diameter of 26 Å.

The post-synthetic wet infiltrations were carried out with stirring 80 mg of activated MOF for a period of 5 days in a 6 mL solution of **2** in dichloromethane with a concentration of 1.0 mmol/L, which led to the composites **2**@MOF-808$_{0.57}$, **2**@DUT-67$_{0.51}$, and **2**@MIP-206$_{0.3}$.

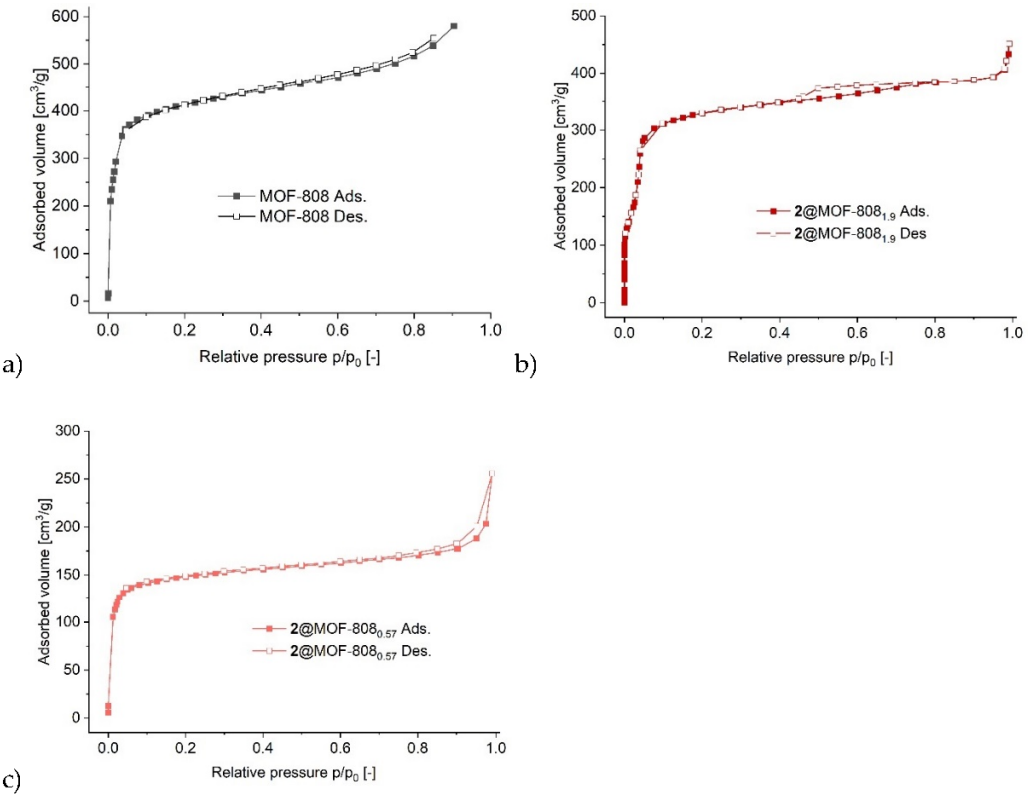

Figure S18. Nitrogen sorption isotherms at 77 K of a) neat MOF-808, b) **2**@MOF-808$_{1.9}$, and c) **2**@MOF-808$_{0.57}$ (filled symbols: adsorption; empty symbols: desorption).

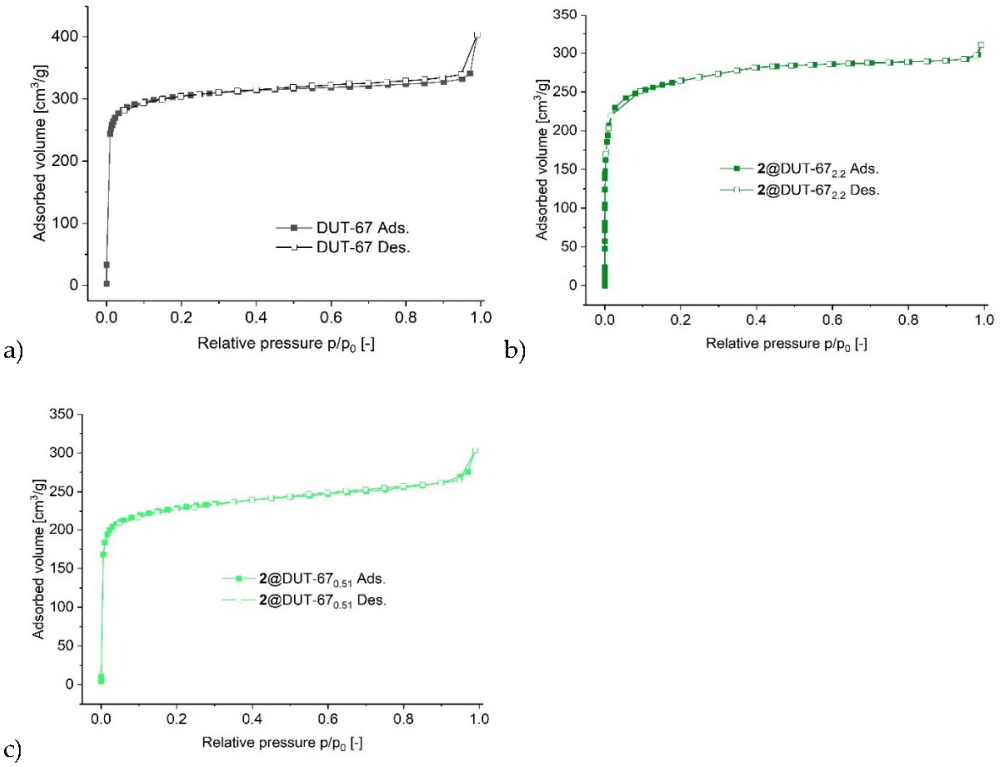

Figure S19. Nitrogen sorption isotherms at 77 K of a) neat DUT-67, b) **2**@DUT-67$_{2.2}$, and c) **2**@DUT-67$_{0.51}$ (filled symbols: adsorption; empty symbols: desorption).

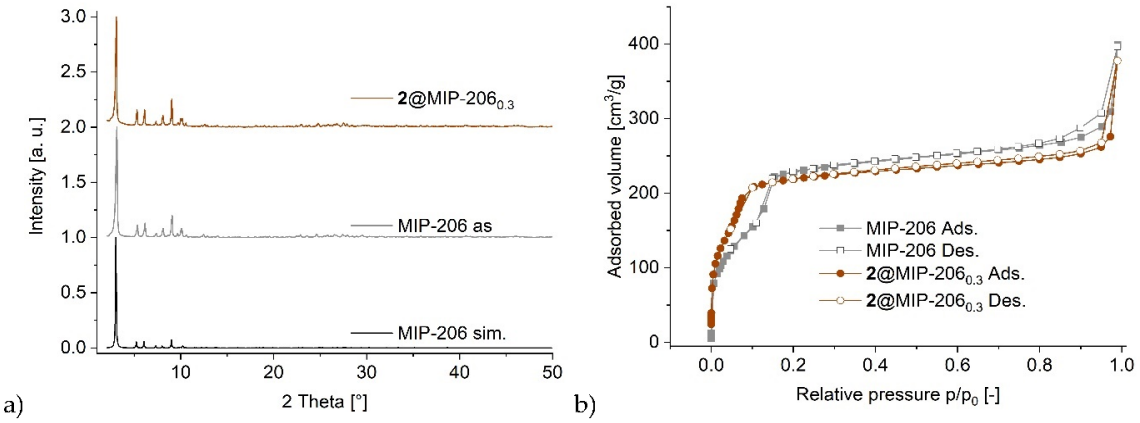

Figure S20. a) PXRD of MIP-206 and post-synthetic **2**@MIP-206$_{0.3}$ composite. Simulation of MIP-206 from CCDC No. 2005237 [13]. b) Nitrogen sorption isotherms at 77 K of MIP-206 (1062 m^2/g) and **2**@MIP-206$_{0.3}$ post-synthetic (701 m^2/g) composites (filled symbols: adsorption; empty symbols: desorption).

S9. Scanning electron microscopy images of MOFs and composites

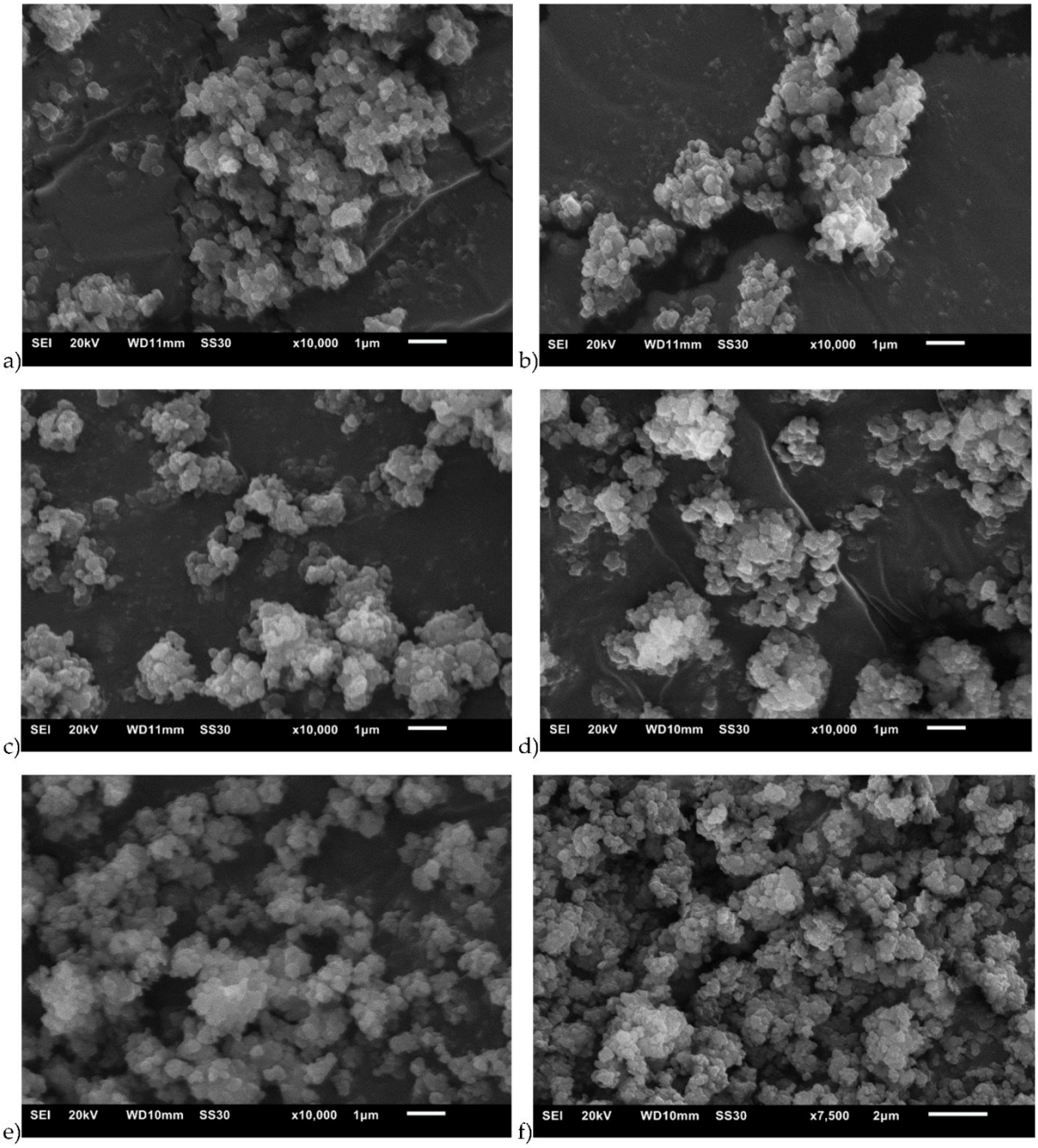

Figure S21. Scanning electron microscopy images of a) neat UiO-66, b) **2**@UiO-66$_{0.44}$ (post-synth.), c) **2**@UiO-66$_{1.1}$ (in situ), d) **2**@UiO-66$_{2.3}$ (in situ), e) **2**@UiO-66$_{4.7}$ (in situ), and f) **2**@UiO-66$_{7.2}$ (in situ).

a)

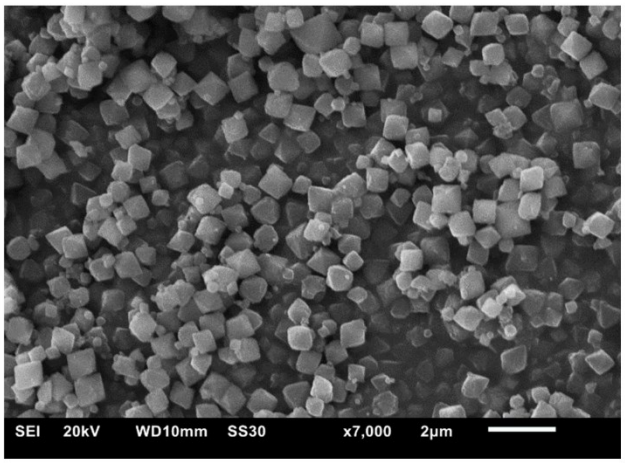

b)

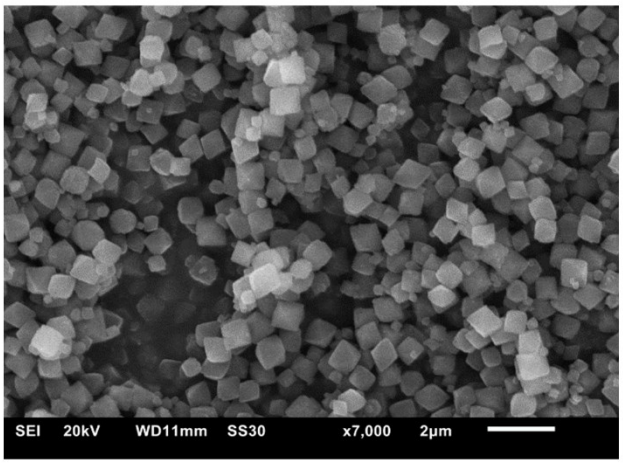

c)

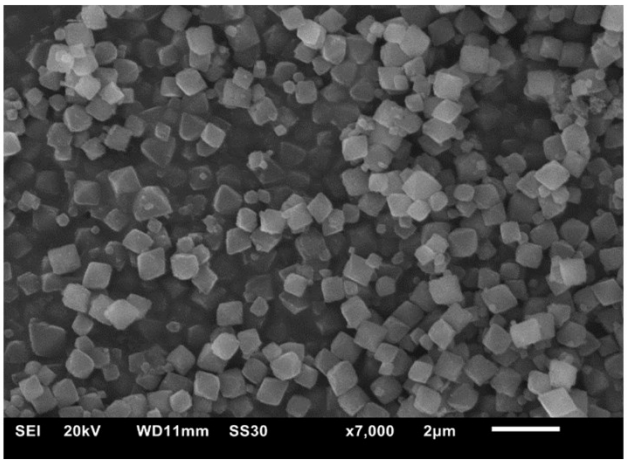

Figure S22. Scanning electron microscopy images of a) neat MOF-808, b) **2**@MOF-808$_{0.57}$ (post-synth.), and c) **2**@MOF-808$_{1.9}$ (in situ).

a)

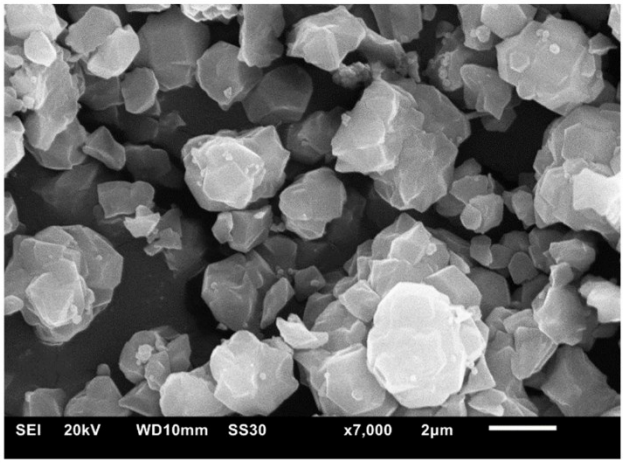

b)

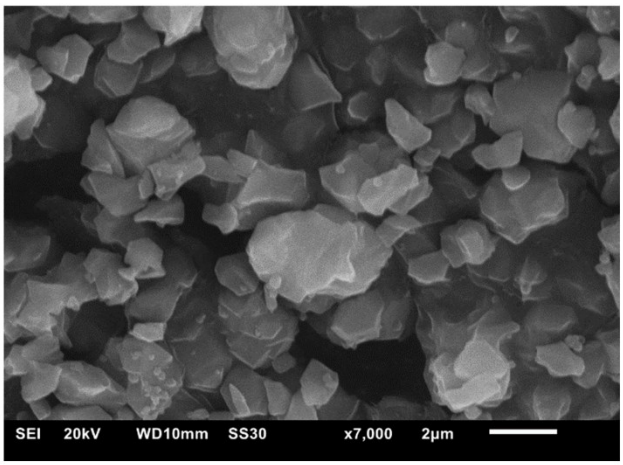

c)

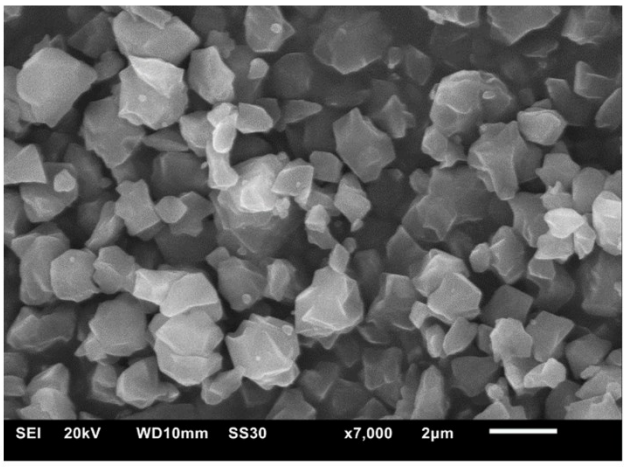

Figure S23. Scanning electron microscopy images of a) neat DUT-67, b) **2**@DUT-67$_{0.51}$ (post-synth.), and c) **2**@DUT-67$_{2.2}$ (in situ).

a)

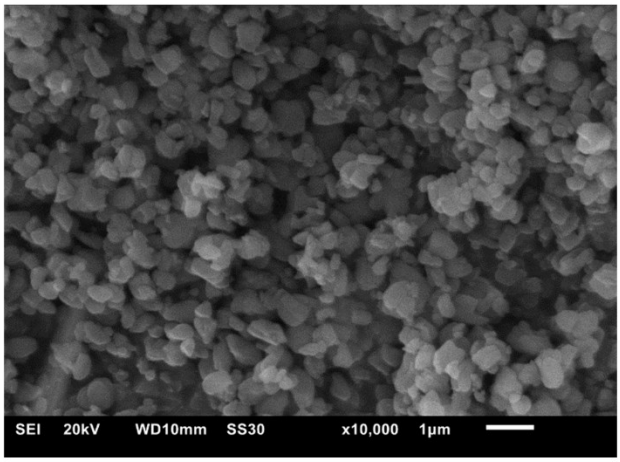

b)

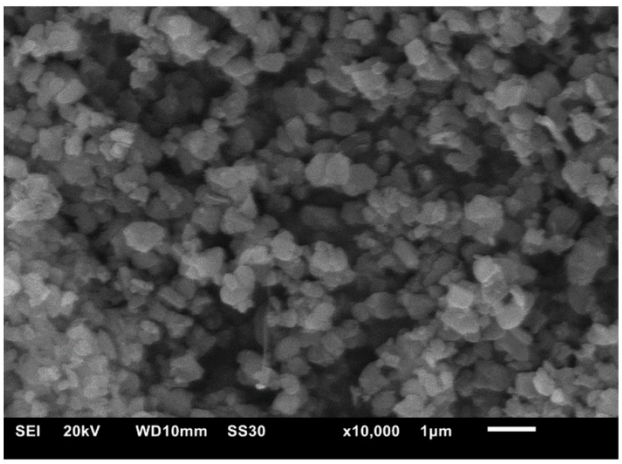

Figure S24. Scanning electron microscopy images of a) neat MIP-206 and b) **2**@MIP-206$_{0.3}$ (post-synth.).

S10. Photophysical properties of all composites

2@UiO-66: Luminescence spectra and emission lifetimes

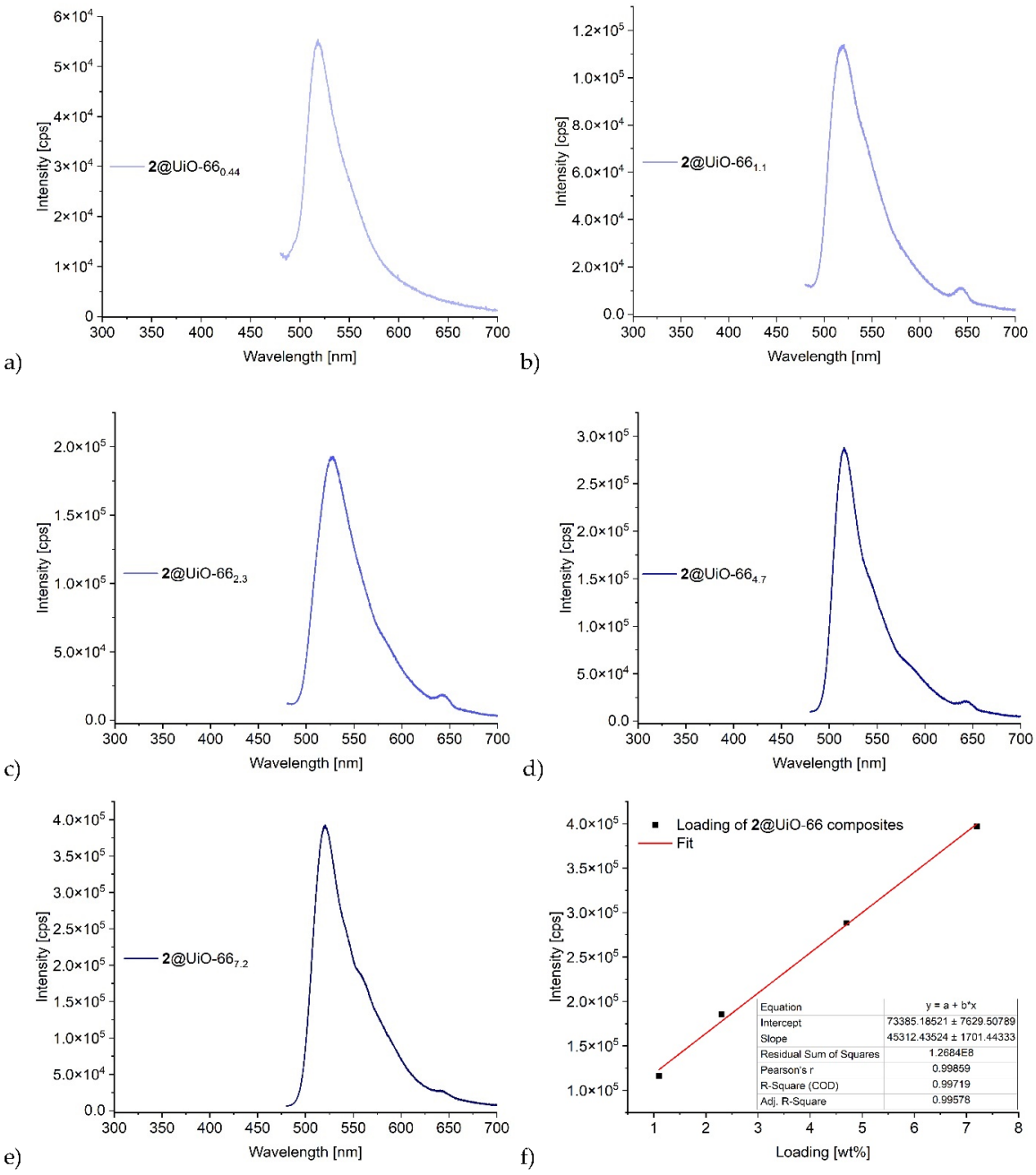

Figure S25. Emission spectra of the **2**@UiO-66 composites: a) 0.44 wt%, b) 1.1 wt%, c) 2.3 wt%, d) 4.7 wt%, and e) 7.2 wt% loading (λ_{exc} = 330 nm) (solid state, reflective setup). f) Linear relationship between intensity and loading of the UiO-66 composites produced in situ.

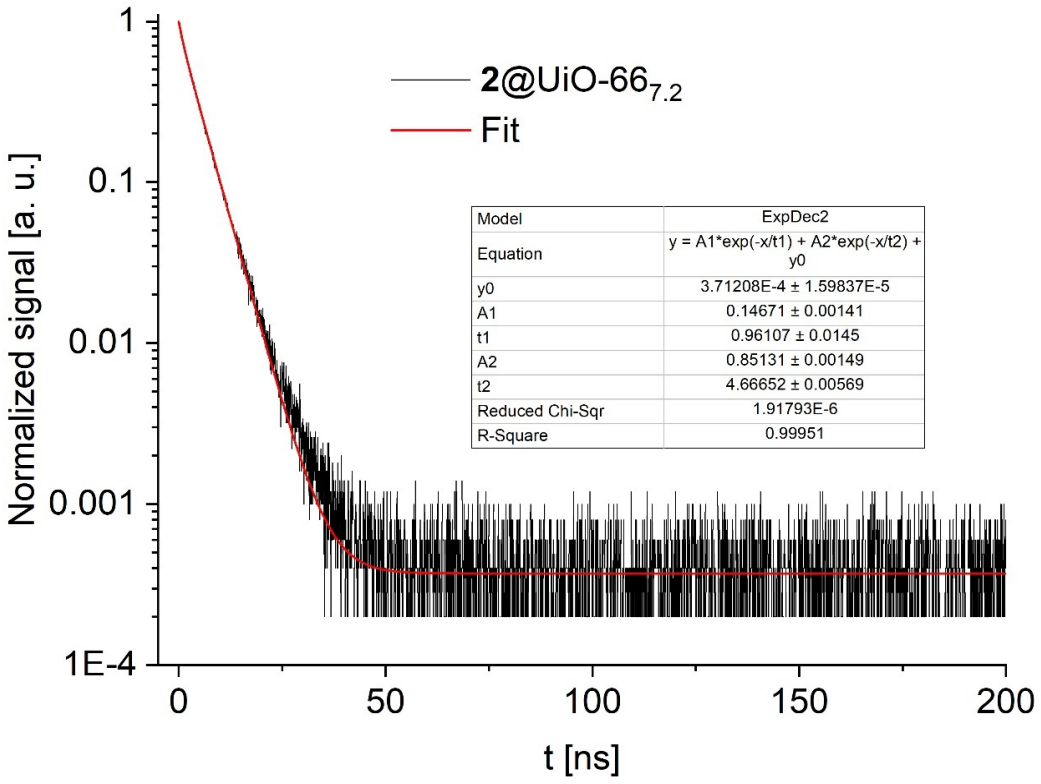

e)

Figure S26. Time-resolved photoluminescence decay (black) of the emission of **2**@UiO-66 composites at 521 nm ± 2 nm. (a) 0.44 wt%, (b) 1.1 wt%, (c) 2.32 wt%, (d) 4.7 wt%, and (e) 7.2 wt% with the respective two- and three-exponential fitting parameters, including pre-exponential factors A_i, lifetimes t_i, and confidence limits (λ_{exc} = 375 nm).

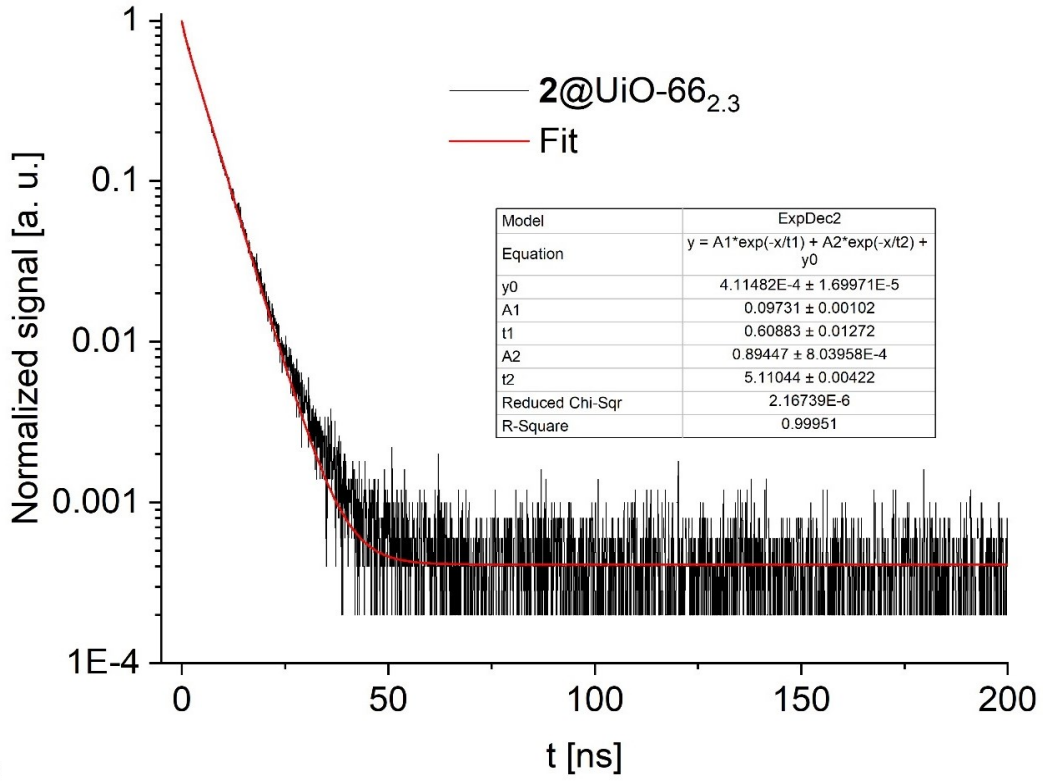
2@UiO-66$_{2.3}$
Fit
Model ExpDec2
Equation y = A1*exp(-x/t1) + A2*exp(-x/t2) + y0
y0 4.11482E-4 ± 1.69971E-5
A1 0.09731 ± 0.00102
t1 0.60883 ± 0.01272
A2 0.89447 ± 8.03958E-4
t2 5.11044 ± 0.00422
Reduced Chi-Sqr 2.16739E-6
R-Square 0.99951
Normalized signal [a. u.]
t [ns]
1
0.1
0.01
0.001
1E-4
0
50
100
150
200

c)

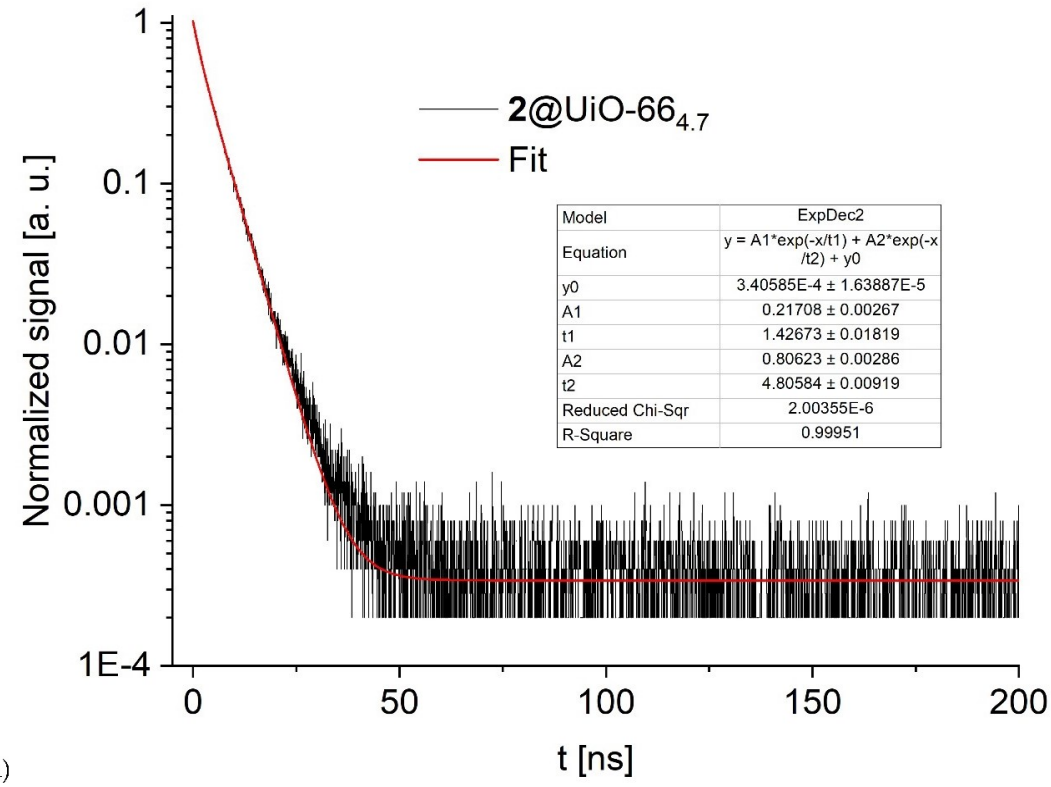
2@UiO-66$_{4.7}$
Fit
Model ExpDec2
Equation y = A1*exp(-x/t1) + A2*exp(-x/t2) + y0
y0 3.40585E-4 ± 1.63887E-5
A1 0.21708 ± 0.00267
t1 1.42673 ± 0.01819
A2 0.80623 ± 0.00286
t2 4.80584 ± 0.00919
Reduced Chi-Sqr 2.00355E-6
R-Square 0.99951
Normalized signal [a. u.]
t [ns]
1
0.1
0.01
0.001
1E-4
0
50
100
150
200

d)

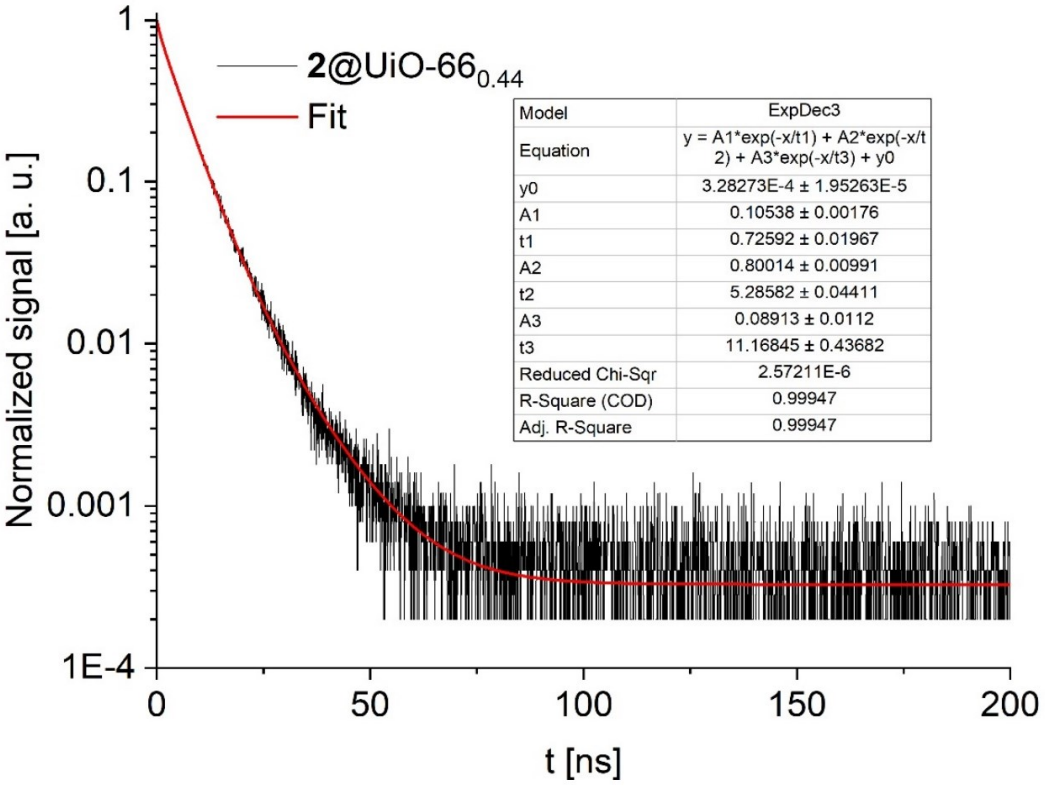
2@UiO-66$_{0.44}$
Fit
Model ExpDec3
Equation y = A1*exp(-x/t1) + A2*exp(-x/t2) + A3*exp(-x/t3) + y0
y0 3.28273E-4 ± 1.95263E-5
A1 0.10538 ± 0.00176
t1 0.72592 ± 0.01967
A2 0.80014 ± 0.00991
t2 5.28582 ± 0.04411
A3 0.08913 ± 0.0112
t3 11.16845 ± 0.43682
Reduced Chi-Sqr 2.57211E-6
R-Square (COD) 0.99947
Adj. R-Square 0.99947
Normalized signal [a. u.]
1
0.1
0.01
0.001
1E-4
0
50
100
150
200
t [ns]

a)

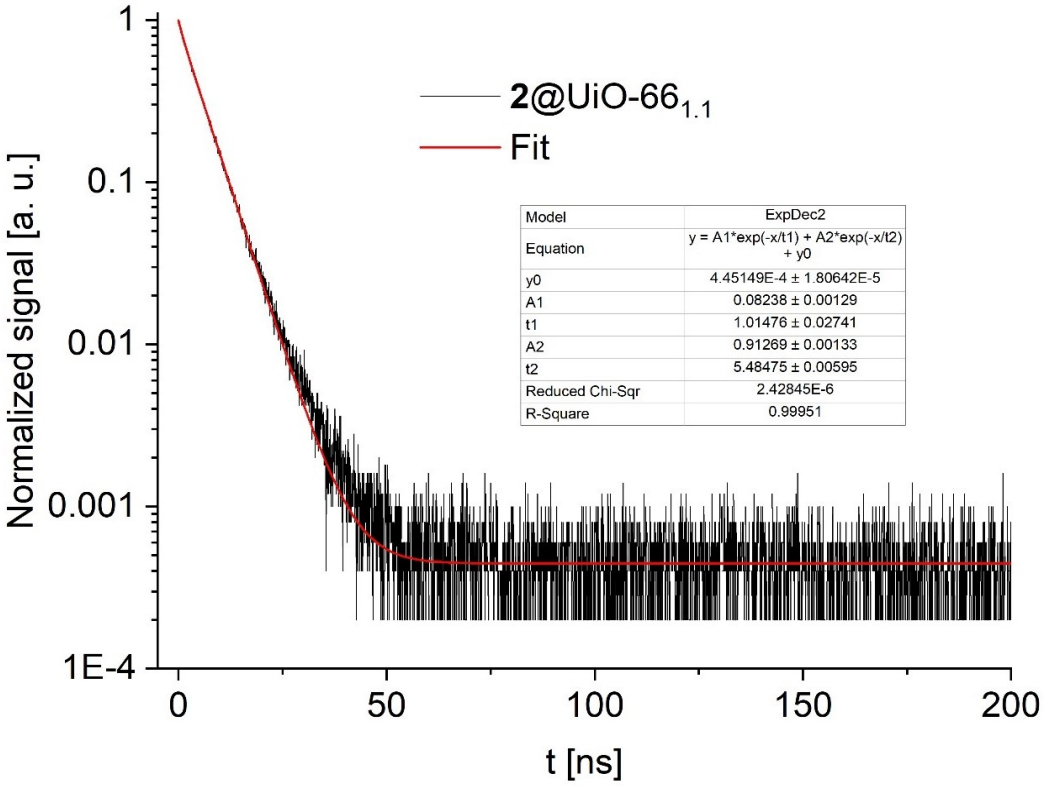
2@UiO-66$_{1.1}$
Fit
Model ExpDec2
Equation y = A1*exp(-x/t1) + A2*exp(-x/t2) + y0
y0 4.45149E-4 ± 1.80642E-5
A1 0.08238 ± 0.00129
t1 1.01476 ± 0.02741
A2 0.91269 ± 0.00133
t2 5.48475 ± 0.00595
Reduced Chi-Sqr 2.42845E-6
R-Square 0.99951
Normalized signal [a. u.]
1
0.1
0.01
0.001
1E-4
0
50
100
150
200
t [ns]

b)

2@MOF-808: Luminescence spectra and emission lifetimes:

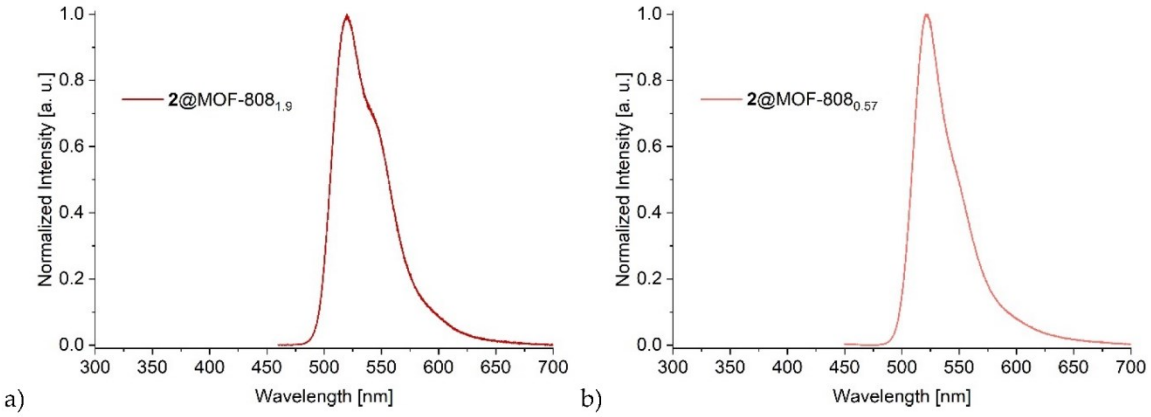

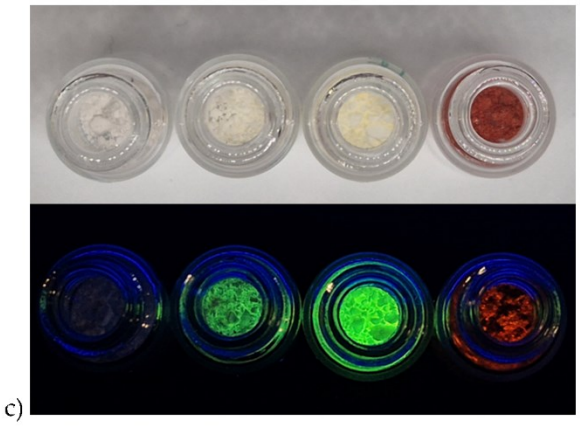

Figure S27. Emission spectra of a) **2**@MOF-808$_{1.9}$ and b) **2**@MOF-808$_{0.57}$ (λ_{exc} = 360 nm) (solid state, reflective setup). c) From left to right: Neat MOF-808, **2**@MOF-808$_{0.57}$, **2**@MOF-808$_{1.9}$ composites and **2** as a solid under daylight (top) and UV-light (λ_{exc} = 365 nm, bottom).

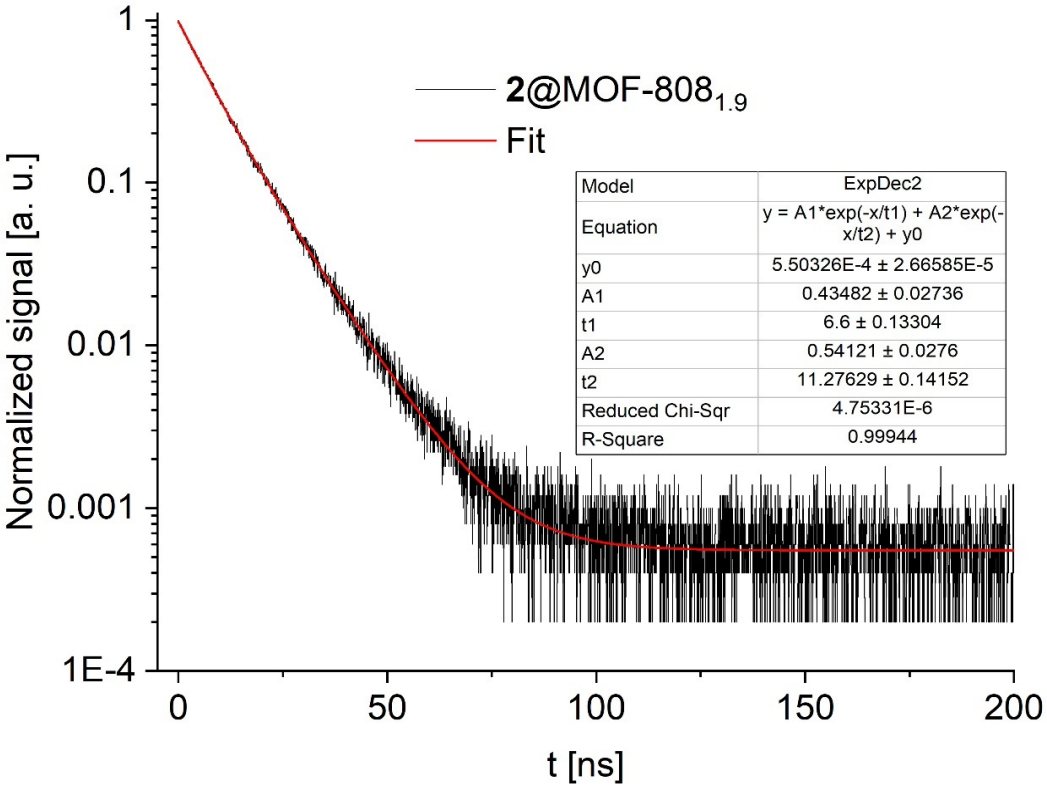

a)

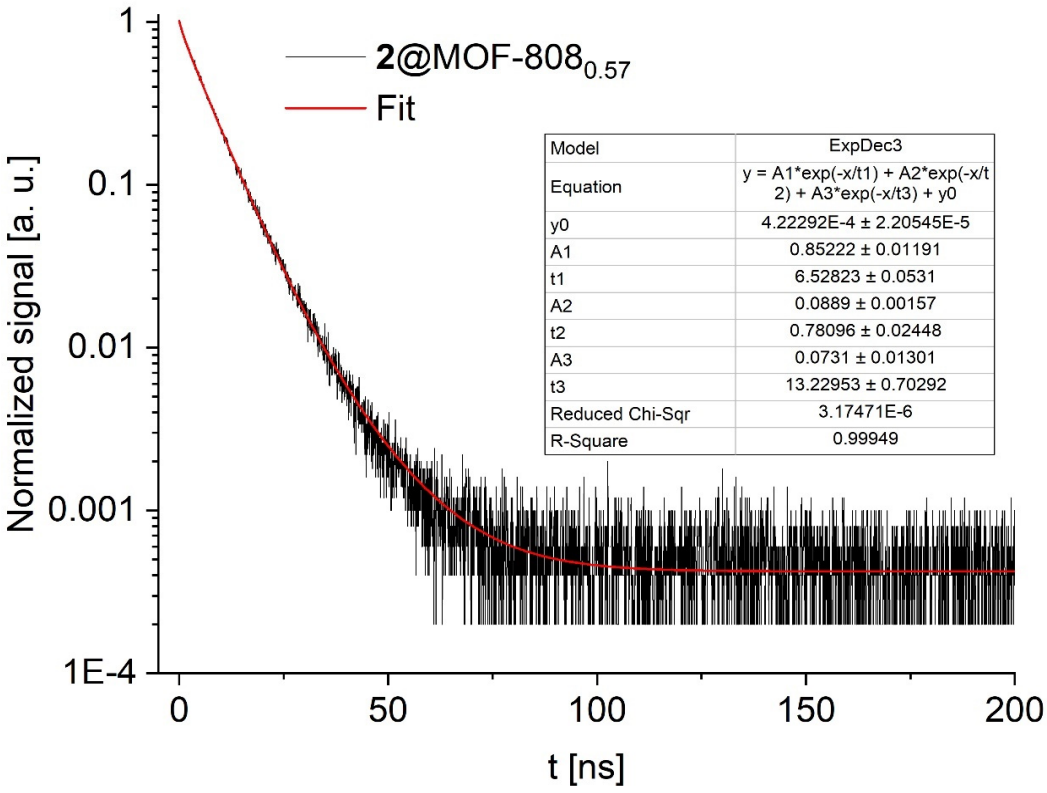

b)

Figure S28. Time-resolved photoluminescence decay (black) of the **2**@MOF-808$_{1.9}$ (a) and **2**@MOF-808$_{0.57}$ (b) composite with the respective two- and three-exponential fitting parameters, including pre-exponential factors A_i, lifetimes t_i, and confidence limits (λ_{exc} = 375 nm).

2@DUT-67: Luminescence spectra and emission lifetimes

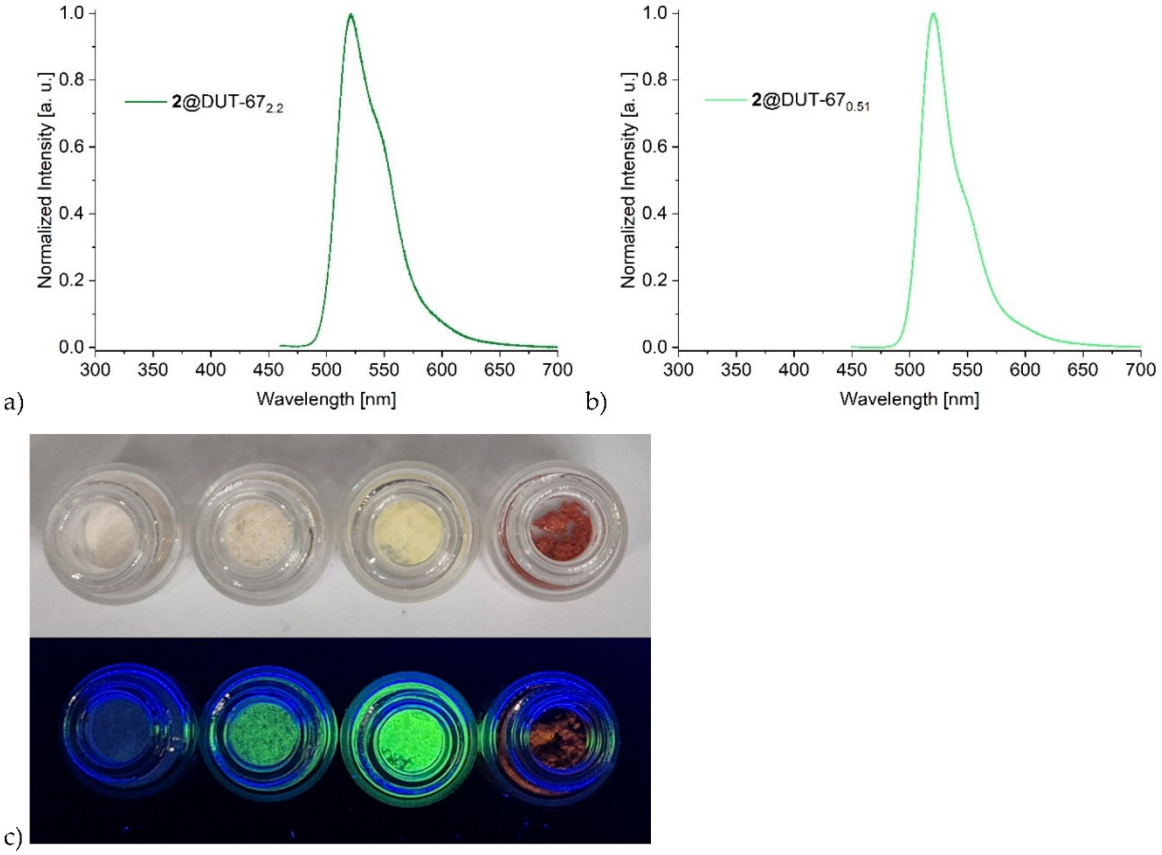

Figure S29. Emission spectra of a) **2**@DUT-67$_{2.2}$ and b) **2**@DUT-67$_{0.51}$ (λ_{exc} = 360 nm) (solid state, reflective setup). c) From left to right: Neat DUT-67, **2**@DUT-67$_{0.51}$, **2**@DUT-67$_{2.2}$ composites and **2** as a solid under daylight (top) and UV-light (λ_{exc} = 365 nm, bottom).

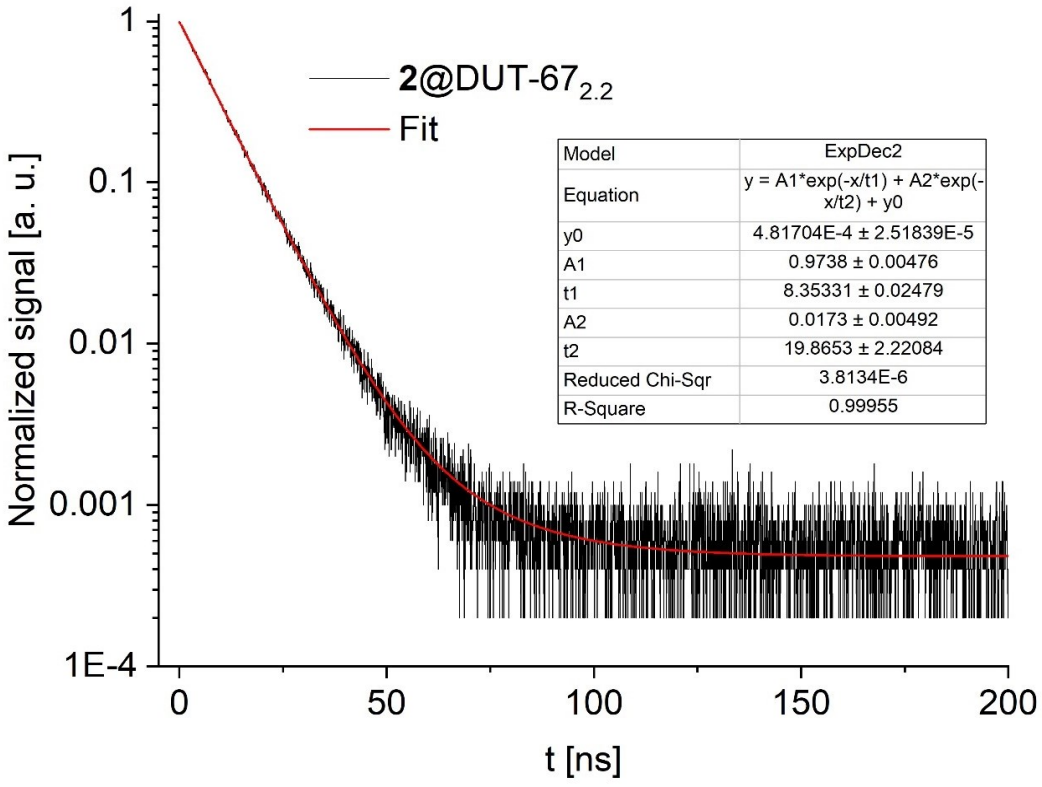

a)

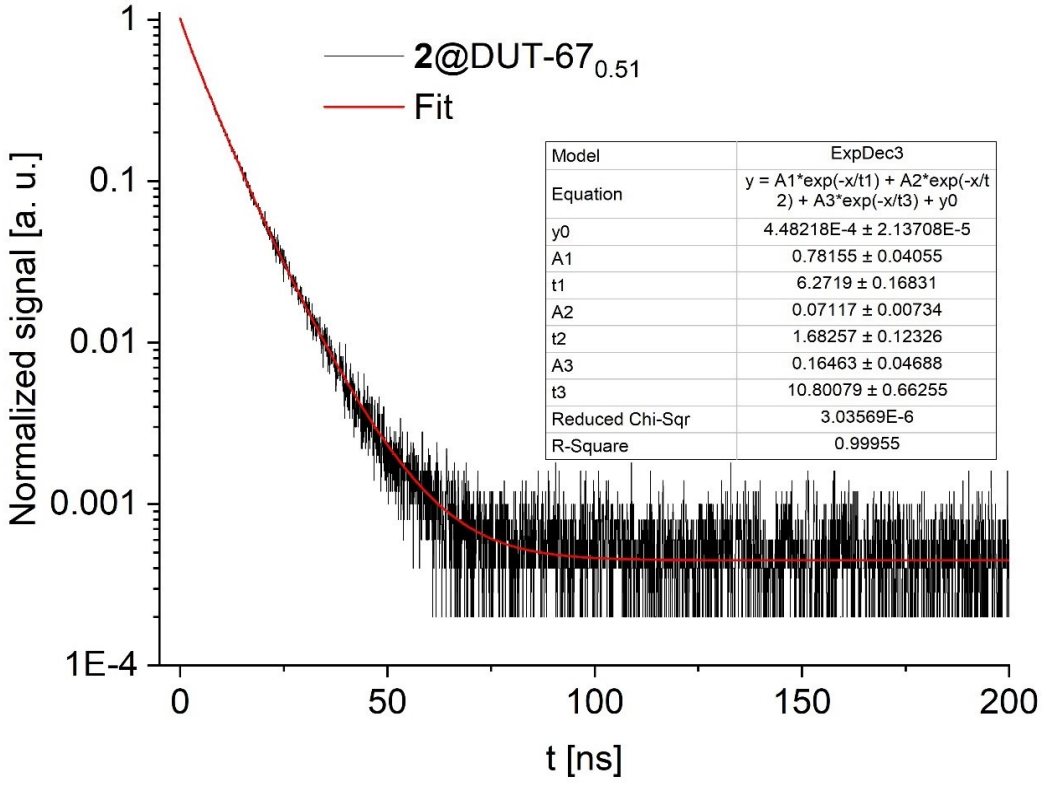

b)

Figure S30. Time-resolved photoluminescence decay (black) of the **2**@DUT-67$_{2.2}$ (a) and **2**@DUT-67$_{0.51}$ (b) composite with the respective two- and three-exponential fitting parameters, including pre-exponential factors A_i, lifetimes t_i, and confidence limits (λ_{exc} = 375 nm).

2@MIP-206: Luminescence spectra and emission lifetimes

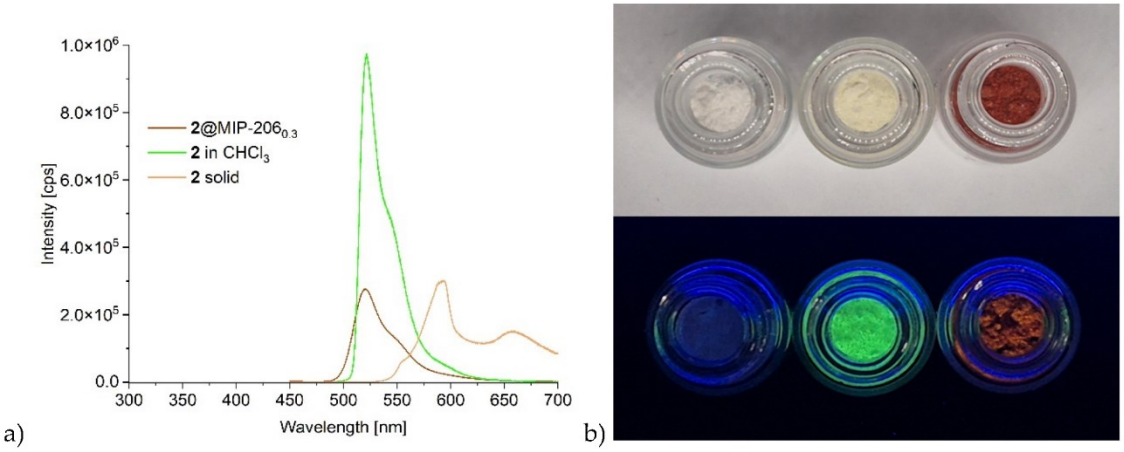

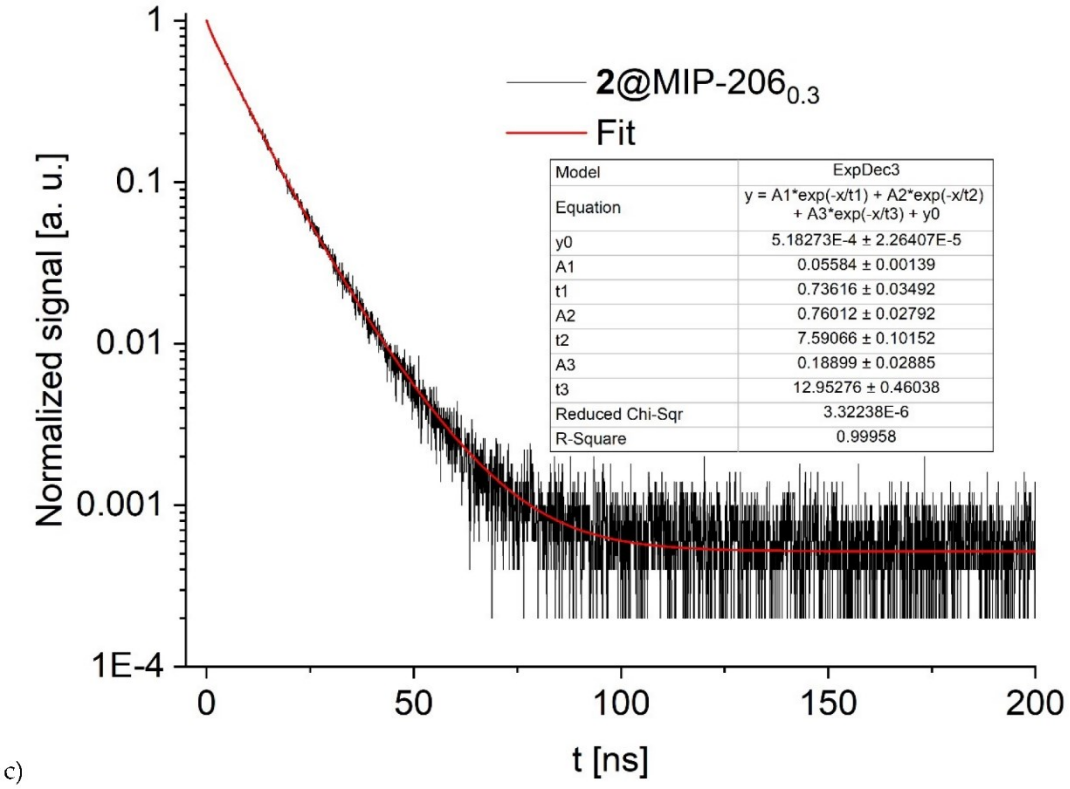

Model	ExpDec3
Equation	y = A1*exp(-x/t1) + A2*exp(-x/t2) + A3*exp(-x/t3) + y0
y0	5.18273E-4 ± 2.26407E-5
A1	0.05584 ± 0.00139
t1	0.73616 ± 0.03492
A2	0.76012 ± 0.02792
t2	7.59066 ± 0.10152
A3	0.18899 ± 0.02885
t3	12.95276 ± 0.46038
Reduced Chi-Sqr	3.32238E-6
R-Square	0.99958

Figure S31. a) Normalized emission spectra of **2**@MIP-206$_{0.3}$, **2** in $CHCl_3$ solution, and **2** as a solid (solid state in a reflective setup). Emission spectra were measured with excitation at 360 nm for **2**@MIP-206$_{0.3}$ and the $CHCl_3$ solution, and at 400 nm for **2** as a solid. b) From left to right: neat MIP-206, post-synthetic encapsulated **2**@MIP-206$_{0.3}$, and **2** as a solid both under daylight (top) and under UV-light (λ_{exc} = 365 nm, bottom). c) Time-resolved photoluminescence decay (black) of the emission of the **2**@MIP-206$_{0.3}$ composite at 521 nm with the respective three-exponential fitting parameters, including pre-exponential factors A_1, A_2, and A_3, lifetimes t_1, t_2, and t_3, and confidence limits (λ_{exc} = 375 nm).

Table S6. Photophysical data for **2** as a solid and in solution, and the **2**@MIP-206 composite.

Compound	$\lambda_{F,max}$ [nm] [a]	τ_1 (x_1), τ_2 (x_2), τ_3 (x_3) [ns] [b]	τ_x [ns] [b]	Φ_F [%] [c]
2 solid	594/659	0.6 (0.74), 2.8 (0.29)	1.2	9
2 in $CHCl_3$ (0.5 mmol/L)	510	4.8 (1)	4.8	89 [d]
2@MIP-$206_{0.3}$ (post-synth.)	521	0.7 (0.05), 7.6 (0.7), 12.9 (0.2)	7.9	47

[a] Wavelength of the fluorescence maximum (λ_{exc} = 360 nm). [b] Fluorescence lifetime (λ_{exc} = 375 nm): τ_i (x_i) species i lifetime (fraction), τ_x species-weighted average lifetime. [c] Fluorescence quantum yield. [d] Measured in THF taken from the literature [2].

S11. References

1. Caruso, E.; Gariboldi, M.; Sangion, A.; Gramatica, P.; Banfi, S. Synthesis, photodynamic activity, and quantitative structure-activity relationship modelling of a series of BODIPYs. *J. Photochem. Photobiol. B* **2017**, *167*, 269-281, doi:10.1016/j.jphotobiol.2017.01.012.
2. Nguyen, A.L.; Wang, M.; Bobadova-Parvanova, P.; Do, Q.; Zhou, Z.; Fronczek, F.R.; Smith, K.M.; Vicente, M.G.H. Synthesis and properties ofB-cyano-BODIPYs. *J. Porphyr. Phthalocyanines* **2017**, *20*, 1409-1419, doi:10.1142/s108842461650125x.
3. Katz, M.J.; Brown, Z.J.; Colon, Y.J.; Siu, P.W.; Scheidt, K.A.; Snurr, R.Q.; Hupp, J.T.; Farha, O.K. A facile synthesis of UiO-66, UiO-67 and their derivatives. *Chem. Commun.* **2013**, *49*, 9449-9451, doi:10.1039/c3cc46105j.
4. Guillerm, V.; Gross, S.; Serre, C.; Devic, T.; Bauer, M.; Ferey, G. A zirconium methacrylate oxocluster as precursor for the low-temperature synthesis of porous zirconium(IV) dicarboxylates. *Chem. Commun.* **2010**, *46*, 767-769, doi:10.1039/b914919h.
5. Garai, M.; Yavuz, C.T. Robust Mesoporous Zr-MOF with Pd Nanoparticles for Formic-Acid-Based Chemical Hydrogen Storage. *Matter* **2021**, *4*, 10-12, doi:10.1016/j.matt.2020.12.011.
6. Valverde, A.; Tovar, G.I.; Rio-López, N.A.; Torres, D.; Rosales, M.; Wuttke, S.; Fidalgo-Marijuan, A.; Porro, J.M.; Jiménez-Ruiz, M.; García Sakai, V.; et al. Designing Metal-Chelator-like Traps by Encoding Amino Acids in Zirconium-Based Metal–Organic Frameworks. *Chem. Mater.* **2022**, *34*, 9666-9684, doi:10.1021/acs.chemmater.2c02431.
7. Winters, W.M.W.; Zhou, C.; Hou, J.; Diaz-Lopez, M.; Bennett, T.D.; Yue, Y. Order-to-Disorder Transition in a Zirconium-Based Metal–Organic Framework. *Chem. Mater.* **2024**, *36*, 8400-8411, doi:10.1021/acs.chemmater.4c01460.
8. D'Amato, R.; Bondi, R.; Moghdad, I.; Marmottini, F.; McPherson, M.J.; Naïli, H.; Taddei, M.; Costantino, F. "Shake 'n Bake" Route to Functionalized Zr-UiO-66 Metal-Organic Frameworks. *Inorg. Chem.* **2021**, *60*, 14294-14301, doi:10.1021/acs.inorgchem.1c01839.
9. Valenzano, L.; Civalleri, B.; Chavan, S.; Bordiga, S.; Nilsen, M.H.; Jakobsen, S.; Lillerud, K.P.; Lamberti, C. Disclosing the Complex Structure of UiO-66 Metal Organic Framework: A Synergic Combination of Experiment and Theory. *Chem. Mater.* **2011**, *23*, 1700-1718, doi:10.1021/cm1022882.
10. Furukawa, H.; Gandara, F.; Zhang, Y.B.; Jiang, J.; Queen, W.L.; Hudson, M.R.; Yaghi, O.M. Water adsorption in porous metal-organic frameworks and related materials. *J. Am. Chem. Soc.* **2014**, *136*, 4369-4381, doi:10.1021/ja500330a.
11. Reinsch, H.; Waitschat, S.; Chavan, S.M.; Lillerud, K.P.; Stock, N. A Facile "Green" Route for Scalable Batch Production and Continuous Synthesis of Zirconium MOFs. *Eur. J. Inorg. Chem.* **2016**, *2016*, 4490-4498, doi:10.1002/ejic.201600295.
12. Bon, V.; Senkovska, I.; Baburin, I.A.; Kaskel, S. Zr- and Hf-Based Metal–Organic Frameworks: Tracking Down the Polymorphism. *Cryst. Growth Des.* **2013**, *13*, 1231-1237, doi:10.1021/cg301691d.
13. Wang, S.; Chen, L.; Wahiduzzaman, M.; Tissot, A.; Zhou, L.; Ibarra, I.A.; Gutiérrez-Alejandre, A.; Lee, J.S.; Chang, J.-S.; Liu, Z.; et al. A Mesoporous Zirconium-Isophthalate Multifunctional Platform. *Matter* **2021**, *4*, 182-194, doi:10.1016/j.matt.2020.10.009.

3.6 Beiträge an weiteren Veröffentlichungen als Co-Autor

Die in diesem Kapitel vorgestellten Publikationen werden in der gleichen Reihenfolge wie in der Publikationsliste angegeben vorgestellt. Die Co-Autorenschaften wurden durch das Mitwirken an verschiedenen Publikationen während der Promotion erlangt. Der Großteil davon bezieht sich auf Bildaufnahmen mittels Rasterelektronenmikroskopie (REM) aber auch Elementanalyse durch energiedispersive Röntgenspektroskopie (EDX). Weitere Co-Autorenschaften wurden für die Unterstützung bei der Linker- oder Materialsynthese vergeben, sowie für die Messung von Pulverröntgendiffraktogrammen (PXRD).

3.6.1 Engineering and structural properties of compressed earth blocks (CEB) stabilized with a calcined clay-based alkali-activated binder

Eguekeng Idriss, Sylvain Tome, Tchouateu Kamwa Rolande Aurelie, Achile Nana, Juvenal G. Deutou Nemaleu, Chongouang Judicaël, Alex Spieß, Markus N. A. Fetzer, Christoph Janiak and Marie-Annie Etoh, *Innovative Infrastructure Solutions* **2022**, *7*, 157.

Kurzzusammenfassung

Die chemische Stabilisierung von gepressten Erdziegeln (CEB) mit geopolymeren Bindemitteln stellt eine ökologische und effiziente Technik zur Herstellung beständiger Lehmziegel dar. Ziel dieser Arbeit ist es, die Machbarkeit der Stabilisierung von Lehmbausteinen mit kalziniertem Kaolinit als alkaliaktiviertem Bindemittel zu untersuchen. Dieses wurde aus kalziniertem Kaolinit, Natriumhydroxid (8 M) und Natriumsilikatlösung synthetisiert. Die CEB-Matrix bestand aus lehmhaltigem Boden und Sand. Die Erdziegel mit 5–20 % Geopolymer zur Stabilisierung wurden bei 25 und 70 °C hergestellt und 14 bzw. 28 Tage ausgehärtet. Anschließend wurden sie hinsichtlich Dichte, Druck- und Biegefestigkeit sowie mittels Röntgenbeugung und FT-IR analysiert. Die Biegefestigkeit steigt mit zunehmendem Stabilisatoranteil von 0,3 auf 3,0 MPa (25 °C) bzw. 1,2 auf 3,6 MPa (70 °C). Die Druckfestigkeit erhöhte sich ebenfalls von 5,6 auf 18,1 MPa bei 25 °C und von 7,7 auf 20,0 MPa bei 70 °C. In feuchter Umgebung sinkt die Festigkeit um etwa 55 %. Das kalzinierte Tonbindemittel erweist sich als energieeffiziente und nachhaltige Lösung für die Stabilisierung von

CEBs. Besonders Ziegel mit 15 und 20 % Stabilisator zeigten interessante Eigenschaften für den Einsatz in Gebieten mit starker Witterung.

Eigenanteil an der Veröffentlichung:

- Aufnahmen von PXRDs der einzelnen Proben.
- REM-Aufnahmen der einzelnen Proben.
- Revision des Manuskripts.

3.6.2 Stabilization of compressed earth blocks (CEB) by pozzolana based phosphate geopolymer binder: Physico-mechanical and microstructural investigations

Rolande Aurelie Tchouateu Kamwa, Sylvain Tome, Judicael Chongouang, Idriss Eguekeng, Alex Spieß, Markus N. A. Fetzer, Kamseu Elie, Christoph Janiak and Marie-Annie Etoh, *Cleaner Materials* **2022**, *4*, 100062.

Kurzzusammenfassung

In dieser Arbeit wird das Poly(phospho-ferro-siloxo)-Bindemittel, das aus der Phosphorsäureaktivierung von Puzzolan (PZ) resultiert, als Stabilisator für gepresste Erdziegel (CEBs) vorgeschlagen. Anteile von Puzzolan (5, 10, 15 und 20 Gew. %) wurden in den Lehmboden eingearbeitet. Die CEBs wurden bei 25 °C und bei 70 °C ausgehärtet. Durch Pulverröntgendiffraktometrie (PXRD), Fourier-Transformierte-Infrarot-Spektroskopie (FTIR), Wasseraufnahme sowie mechanische Festigkeitsprüfungen wurden die 28 Tage gealterten CEBs charakterisiert. Die Druckfestigkeit der CEBs liegt im Bereich von 9,2 bis 20,6 MPa bei 25 °C und 10,2 bis 42,8 MPa bei 70 °C. Die Wasseraufnahme liegt zwischen 6 und 11 % bzw. zwischen 8 und 12 % bei 25 °C und 70 °C. Diese Ergebnisse weisen auf die Möglichkeit hin, Phosphatgeopolymerbindemittel auf Puzzolanbasis als wirksame Stabilisatoren für die Entwicklung von CEBs zu verwenden. Phosphatgeopolymerbindemittel auf Puzzolanbasis scheinen eine energieeffiziente und nachhaltige Lösung für die Stabilisierung von CEBs zu sein.

Eigenanteil an der Veröffentlichung:

- Aufnahmen von PXRDs der einzelnen Proben.
- REM-Aufnahmen der einzelnen Proben.

- Revision des Manuskripts.

3.6.3 A caveat on the effect of modulators in the synthesis of the aluminum furandicarboxylate metal-organic framework MIL-160

Dominik Moritz Steinert, Alexa Schmitz, Marcus Fetzer, Philipp Seiffert and Christoph Janiak, *Zeitschrift für anorganische und allgemeine Chemie* **2022**, *648*, e202100380.

Kurzzusammenfassung

Modulatoren werden häufig bei der Synthese von metallorganischen Gerüsten (MOFs) eingesetzt, um die Porosität und Morphologie zu verbessern. Für Aluminium-MOFs wurde bisher nur selten über Modulation berichtet und, wie hier am Beispiel des Aluminiumfurandicarboxylat-MOF MIL-160 gezeigt wird, sind die positiven Effekte von Modulatoren gering und nachteilige Effekte eher wahrscheinlich. Ameisensäure als Modulator kann die BET-Oberfläche und das Porenvolumen von MIL-160 bis zu einem Modulator:Linker-Verhältnis von 1,25:1 leicht erhöhen. Essigsäure zeigt nur bei dem kleinsten getesteten Verhältnis von 0,125:1 eine gewisse Zunahme sowohl der Oberfläche als auch des Porenvolumens. Die stärkeren Säuren Oxalsäure und Salzsäure mit den ebenfalls stärker aluminiumkoordinierenden Anionen haben keinen positiven Porositätseffekt und verringern bereits in geringen Mengen die Oberfläche und das Porenvolumen. Bei einem Modulator:Linker-Verhältnis von 1:1 für Oxalsäure und von 0,75:1 für Salzsäure bildet sich laut der Analyse mittels Pulver-Röntgendiffraktometrie und Stickstoffsorption kein poröses MOF mehr. Darüber hinaus deuten thermogravimetrische Analysen und Rasterelektronenmikroskopie darauf hin, dass keiner der getesteten Modulatoren einen nennenswerten positiven Effekt auf die Einführung von Linker-Defekten oder die Verbesserung der Kristallinität oder Kristallgröße hat.

Eigenanteil an der Veröffentlichung:

- REM-Aufnahmen der modulierten MIL-160 Proben.
- Analyse der modulierten MIL-160 Proben mit EDX.
- Revision des Manuskripts.

3.6.4 Iron-Containing Nickel Cobalt Sulfides, Selenides, and Sulfoselenides as Active and Stable Electrocatalysts for the Oxygen Evolution Reaction in an Alkaline Solution

Soheil Abdpour, Lars Rademacher, Marcus N. A. Fetzer, Thi Hai Yen Beglau and Christoph Janiak, *Solids* **2023**, *4*, 181–200.

Kurzzusammenfassung

Eisenhaltige Nickelsulfide, Selenide und Sulfoselenide wurden mittels einer einfachen zweistufigen hydrothermalen Reaktion (Temperatur 160 °C) für ihre Anwendung als Elektrokatalysatoren in der Sauerstoffentwicklungsreaktion (OER) in einer alkalischen Lösung (1 mol/L KOH) synthetisiert. Die Studie zeigte, dass eisenhaltige Nickelkobalt-Sulfide und -Selenide im Vergleich zu eisenfreien Nickelkobalt-Sulfiden und -Seleniden eine überlegene OER-Leistung mit geringeren Überpotenzialen aufweisen, was die bedeutende Rolle von Eisen bei der Verbesserung von OER-Nickelkobalt-Elektrokatalysatoren unterstreicht: $Fe_{0,1}Ni_{1,4}Co_{2,9}(S_{0,87}O_{0,13})_4$, η_{50} = 318 mV; $Fe_{0,2}Ni_{1,5}Co_{2,8}(S_{0,9}O_{0,1})_4$, η_{50} = 294 mV; $Fe_{0,6}Ni_{1,2}Co_{2,5}(S_{0,83}O_{0,17})_4$, η_{50} = 294 mV; $Fe_{0,4}Ni_{0,7}Co_{1,6}(Se_{0,81}O_{0,19})_4$, η_{50} = 306 mV im Vergleich zu $Ni_{1,0}Co_{2,1}(S_{0,9}O_{0,1})_4$, η_{50} = 346 mV; und $Ni_{0,7}Co_{1,4}(Se_{0,85}O_{0,15})_4$, η_{50} = 355 mV (alle Werte bei einer Stromdichte η_{50} von 50 mA/cm²). Darüber hinaus zeigte das eisenhaltige Nickelkobalt-Sulfoselenid $Fe_{0,5}Ni_{1,0}Co_{2,0}(S_{0,57}Se_{0,25}O_{0,18})_4$ eine außergewöhnliche OER-Leistung mit η_{50} = 277 mV und übertraf damit die Referenzelektrode RuO_2 mit η_{50} = 299 mV. Die überlegene Leistung des Sulfoselenids wurde auf seinen geringen Ladungsübertragungswiderstand (Rct) von 0,8 W bei 1,5 V gegenüber der reversiblen Wasserstoffelektrode (RHE) zurückgeführt. Darüber hinaus zeigte das Sulfoselenid eine bemerkenswerte Stabilität mit nur einem minimalen Anstieg der Überspannung (η_{50}) von 277 mV auf 279 mV nach 20-stündigen Chronopotentiometrietest. Diese Ergebnisse deuten darauf hin, dass trimetallische Eisen-, Nickel- und Kobaltsulfid-, Selenid- und insbesondere Sulfoselenid-Materialien vielversprechende, leistungsstarke, kostengünstige und langlebige Elektrokatalysatoren für nachhaltige OER-Reaktionen sind. Diese Studie liefert einen wertvollen Ansatz für die Entwicklung effizienter elektrokatalytischer Materialien und trägt damit zur Weiterentwicklung von Technologien für erneuerbare Energien bei.

Eigenanteil an der Veröffentlichung:

- Aufnahme von REM-Bildern der hergestellten Proben.
- Bestimmung der jeweiligen Verhältnisse aller Elemente durch EDX-Messungen.
- Revision des Manuskripts.

3.6.5 The efficient removal of ibuprofen, caffeine, and bisphenol A using engineered egusi seed shells biochar: adsorption kinetics, equilibrium, thermodynamics, and mechanism

René Blaise Ngouateu Lekene, Tobie Matemb Ma Ntep, Marcus N. A. Fetzer, Till Strothmann, Julius Ndi Nsami and Christoph Janiak, *Environmental Science and Pollution Research* **2023**, *30*, 100095–100113.

Kurzzusammenfassung

Besonders besorgniserregende Schadstoffe (Contaminants of Emerging Concern, CEC), auch bekannt als Mikroverunreinigungen, wurden in den letzten Jahren als erhebliche Wasserverschmutzung erkannt, da sie eine potenzielle Bedrohung für die Umwelt und die menschliche Gesundheit darstellen. Ziel dieser Studie war die Herstellung von Biokohle (BC) auf der Basis von Egusi-Samenschalen (ESS) mit gut entwickelter Porosität und hervorragender Adsorptionskapazität für CECs wie Ibuprofen (IBP), Koffein (CAF) und Bisphenol A (BPA). Die BC-Proben wurden durch Pyrolyse bei verschiedenen Temperaturen (400 bis 800 °C) hergestellt und mittels Stickstoffsorption, FT-IR, PXRD, REM/EDX, Elementaranalyse und Thermoanalyse charakterisiert. Die Ergebnisse der Stickstoffsorption und der REM-Aufnahmen zeigten, dass die texturellen Eigenschaften mit steigender Pyrolysetemperatur stärker ausgeprägt waren. Die bei 800 °C erhaltene BC-Probe, die die größte spezifische Oberfläche (688 m^2/g) und das größte Porenvolumen (0,320 cm^3/g) aufwies, wurde für die Adsorptionsstudie von CECs ausgewählt. Die kinetische Studie zeigt, dass das Adsorptionsgleichgewicht von CAF und BPA schneller eintrat als das von IBP. Die kinetischen Modelle pseudo-erster und pseudo-zweiter Ordnung passten am besten zu den Adsorptionsdaten. Die maximalen Langmuir-Adsorptionskapazitäten von Biokohle betrugen ~ 180, 121 bzw. 73 mg/g für IBP, CAF und BPA. Die thermodynamische Studie zeigt, dass der Adsorptionsprozess für die drei CECs spontan und endotherm verlief. Die Ergebnisse der Adsorption und die Analyse der

BC nach der Adsorption zeigten, dass Wasserstoffbrückenbindungen, van der Waals-Wechselwirkungen, π-π- und n-π-Wechselwirkungen sowie die Porenfüllung am Adsorptionsmechanismus beteiligt waren. Die aus ESS hergestellte Biokohle wies eine große Oberfläche und eine gute Morphologie auf und förderte die Adsorption von CECs. Abschließend bietet sie eine kostengünstige und saubere Produktionsmethode.

Eigenanteil an der Veröffentlichung:

- Aufnahme von REM-Bildern der unterschiedlichen Biokohleansätze.
- Revision des Manuskripts.

3.6.6 Impregnation of textile cotton material with Cymbopogon citratus-mediated silver nanoparticles and investigations by light, electron and hyperspectral microscopies

Jean Yves Sikapi Fouda, Agnes Antoinette Ntoumba, Philippe Belle Ebanda Kedi, Thi Hai Yen Beglau, Marcus Fetzer, Till Strothmann, Tchangou Armel Florian, Sone Enone Bertin, Vandi Deli, Emmanuel Jean Teinkela Mbosso, Gustave Leopold Lehman, Emmanuel Albert Mpondo Mpondo, Gisele Etame Loe, Francois Eya'ane Meva and Christoph Janiak, *Journal of Pharmacognosy and Phytochemistry* **2023**,*12(5)*:135-146.

Kurzzusammenfassung

Die vorliegende Studie zielt darauf ab, ein kostengünstiges und umweltfreundliches Baumwolltextil zu entwickeln, das mit grün synthetisierten Silbernanopartikeln aus Cymbopogon citratus-Blättern imprägniert ist. Die Silbernanopartikel wurden durch Ultraviolett-Spektroskopie und Pulver-Röntgenbeugung charakterisiert. Die analytischen Unterschiede zwischen imprägnierten und nicht imprägnierten Baumwolltextilien wurden mittels Licht- und Transmissionselektronenmikroskopie (TEM) untersucht. Die Hyperspektralmikroskopie zeigt das Vorhandensein von Silbernanopartikeln in *in situ* imprägniertem Baumwollmaterial und wurde mit der Emissionsspektroskopie gekoppelt, um Baumwollgewebe zu unterscheiden, was einen Einblick in die Qualitätskontrolle des Materials ermöglicht. Die TEM-Untersuchung zeigt eine hochdichte Dispersion von Silber-Nanopartikeln in den Baumwollmaterialien und die geringsten Größen für das *in situ* imprägnierte Baumwollmaterial. Das *in situ* Nanomaterial zeigt Unterschiede in der maximalen

Emission im Vergleich zum Baumwollgewebe und die Partikel konnten durch Dunkelfeldmikroskopie sichtbar gemacht werden. Das Rückhaltevermögen der Baumwollgewebe für Wasser und Nanopartikel wurde bestimmt. Das Experiment legt nahe, dass der *in situ* imprägnierte Baumwollstoff eine hervorragende Waschbeständigkeit aufweist.

Eigenanteil an der Veröffentlichung:

- Aufnahme von REM-Bildern der modifizierten Textilproben.
- Revision des Manuskripts.

3.6.7 Efficient Electrochemical Lead Detection by a Histidine-Grafted Metal–Organic Framework MOF-808 Electrode Material

Sherman Lesly Zambou Jiokeng, Tobie J. Matemb Ma Ntep, Marcus N. A. Fetzer, Till Strothmann, Cyrille G. Fotsop, Ignas Kenfack Tonle and Christoph Janiak, *ACS Applied Materials & Interfaces* **2024**, *16*, 2, 2509–2521.

Kurzzusammenfassung

Da das übermäßige Vorhandensein von Schwermetallen in der Umwelt die menschliche Gesundheit erheblich beeinträchtigt, ist es notwendig, effiziente, selektive und empfindliche Methoden für deren Nachweis zu entwickeln. In dieser Studie wird ein neuartiger elektrochemischer Sensor für den Nachweis von Pb^{2+}-Ionen beschrieben. Der vorgeschlagene Sensor basiert auf einer Glaskohlenstoffelektrode (GCE), die mit einem dünnen Film aus einem mit Histidin versehenen metallorganischen Gerüst (MOF-808-His) modifiziert wurde. Das MOF-808 wurde solvothermal hergestellt und dann post-synthetisch modifiziert, indem das koordinierte Acetat durch Histidinat ersetzt wurde. In der Elektrochemie zeigte die MOF-808-His-modifizierte GCE eine hohe Ladungsselektivität, während die elektrochemische Impedanzspektroskopie (EIS) und kinetische Studien einen geringeren Ladungstransferwiderstand (4196 Ω) und eine bessere heterogene Standard-Elektronentransfer-Ratenkonstante ($1{,}80 \times 10^{-5}$ cm s^{-1}) für MOF-808-modifizierte GCE ergaben. Diese Ergebnisse deuten auf eine schnelle und direkte Elektronenübertragungsrate von $[Fe(CN)_6]^{3-/4-}$ auf die Elektrodenoberfläche hin. Mit Hilfe der anodischen Inversvoltammetrie (SWASV) wurde die schnelle und hochempfindliche Bestimmung von Pb^{2+} durch MOF-808-His-modifizierter GCE

erreicht. Durch Optimierung der Akkumulations-Detektions-Parameter, einschließlich des pH-Werts des Detektionsmediums, der Ablagerungszeit und des Potenzials sowie der Konzentration, wurde eine bemerkenswerte Nachweisgrenze (LoD, basierend auf einem Signal-Rausch-Verhältnis von 3) von ($1{,}12 \times 10^{-10} \pm 0{,}10 \times 10^{-10}$) mol L^{-1} mit einer Empfindlichkeit von (9,6 ± 0,1) µA L µmol^{-1} erreicht. Nach Interferenz- und Stabilitätsstudien wurde die MOF-808-His-modifizierte GCE für den Nachweis von Pb^{2+} in einer Leitungswasserprobe mit einer Konzentration von 10 µmol L^{-1} Pb^{2+} eingesetzt.

Eigenanteil an der Veröffentlichung:

- Aufnahme von REM-Bildern der MOF-808 und MOF-808-His Proben.
- Revision des Manuskripts.

3.6.8 Bimetallic CPM-37(Ni,Fe) metal-organic framework: enhanced porosity, stability and tunable composition

Soheil Abdpour, Marcus N. A. Fetzer, Robert Oestreich, Thi Hai Yen Beglau, István Boldog and Christoph Janiak, *Dalton Transactions* **2024**, *53*, 4937.

Kurzzusammenfassung

Eine neu synthetisierte Serie von bimetallischen CPM-37(Ni,Fe)-Metallorganischen Gerüsten mit unterschiedlichem Eisengehalt (Ni/Fe ≈ 2, 1, 0,5, genannt CPM-37(Ni_2Fe), CPM-37(NiFe) und CPM-37($NiFe_2$)) zeigte hohe N_2-basierte spezifische BET-Oberflächen von 2039, 1955 und 2378 $m^2\ g^{-1}$ für CPM-37(Ni_2Fe), CPM-37(NiFe) und CPM-37($NiFe_2$), die im Vergleich zu den monometallischen CPM-37(Ni) und CPM-37(Fe) mit nur 87 und 368 $m^2\ g^{-1}$ wesentlich höhere Werte aufweisen. Es wird vermutet, dass die Mischmetallnatur der Materialien die strukturelle Robustheit aufgrund des besseren Ladungsausgleichs an den koordinativ gebundenen Clustern erhöht, was interessante anwendungsorientierte Möglichkeiten für CPM-37 und andere weniger stabile MOFs eröffnet. In dieser Arbeit zeigten die CPM-37-abgeleiteten α,β-$Ni(OH)_2$, γ-NiO(OH) und, plausiblerweise, γ-FeO(OH)-Phasen, die durch Zersetzung im alkalischen Medium erhalten wurden, eine starke elektrokatalytische Aktivität in der Sauerstoffentwicklungsreaktion (OER). Das Verhältnis Ni: Fe ≈ 2 aus CPM-37(Ni_2Fe) zeigte die beste OER-Aktivität mit einer geringen Überspannung von 290 mV bei 50 mA cm^{-2}, einer niedrigen Tafel-Steigung

von 39 mV dez^{-1} und einer stabileren OER-Leistung im Vergleich zu RuO_2 nach 20 Stunden Chronopotentiometrie bei 50 mA cm^{-2}.

Eigenanteil an der Veröffentlichung:

- Aufnahme von REM-Bildern der CPM-37 Proben.
- Analyse der CPM-37 Proben mit EDX.
- Linkersynthese.
- Revision des Manuskripts.

3.6.9 Anti-inflammation Study of Cellulose-Chitosan Biocomposite-Based *Tetrapleura tetraptera* (Taub) Dried Fruits Aqueous Extract

Jean Baptiste Hzounda Fokou, Annick Christianne Nsegbe, Beglau Thi Hai Yen, Marcus N. A. Fetzer, Elise Nadia Mbogbe, Maeva Jenna Chameni Nkouankam, Pamela Ngadie Mponge, Marie Tryphene Magaly Ngo Yomkil Baleng, Sylvie Pascale Songue, Chris Rosaire Ninpa Kuissi, Juliette Koube, Bertin Sone Enone, Agnes Antoinette Ntoumba, Francois Eya'ane Meva and Christoph Janiak, *BioNanoScience* **2024**, *14*, 699–709.

Kurzzusammenfassung

Die Nanotechnologie macht außergewöhnliche Fortschritte im medizinischen Bereich. Die Entwicklung neuer Systeme für die Verabreichung pflanzlicher Inhaltsstoffe bringt Vorteile wie gute Bioverfügbarkeit, Löslichkeit, verzögerte Freisetzung und verbessertes Potenzial mit sich. Nach unserem Kenntnisstand gibt es keine Berichte über Nanokomposite aus *Tetrapleura tetraptera*, obwohl diese Pflanze in der Ethnopharmakologie vielfältige Verwendung findet, unter anderem zur Behandlung von Entzündungskrankheiten. Ziel dieser Studie war es, Nanokomposite auf Chitosan- und Cellulose-Basis mit entzündungshemmendem Potenzial herzustellen. Die Biokomposite zeigten eine Einkapselungseffizienz von 69,4 %. Ihre Bildung wurde durch einen Peak bei 290 nm im UV-Vis-Spektrum bestätigt. Die Infrarotspektroskopie bestätigte die Bildung eines gemischten Polysaccharid- und Polyphenolsystems. Es wurden keine Anzeichen von Toxizität und keine Todesfälle festgestellt; daher liegt die letale Dosis 50 (LD_{50}) über 2000 mg/kg. Das Biokomposit weist in vitro eine entzündungshemmende Wirkung mit einer maximalen Hemmung von 99,5 % und in

vivo eine entzündungshemmende Wirkung mit einer maximalen Hemmung von 98,7 % bei einer Dosis von 200 mg/kg auf. Die aus dem wässrigen Extrakt der Früchte von *Tetrapleura tetraptera* synthetisierten Biokomposite zeigten eine entzündungshemmende Eigenschaft mit zufriedenstellender Sicherheit.

Eigenanteil an der Veröffentlichung:

- Aufnahme von REM-Bildern der jeweiligen Proben.
- Revision des Manuskripts.

3.6.10 Structural properties and thermal decomposition of three heteroleptic coordination polymers with oxalate, 2-aminomethylpyridine and metal = Zn^{2+}, Ni^{2+} and Cu^{2+}

Patrice Kenfack Tsobnang, Christelle Ivane Azambou, Roussin Lontio Fomekong, Tobie Junior Matemb Ma Ntep, Marcus N.A. Fetzer, Arnaud Kamdem Tamo and Christoph Janiak, *Journal of Solid State Chemistry* **2025**, *346*, 125282.

Kurzzusammenfassung

Drei heteroleptische eindimensionale (1D) (2-Aminomethylpyridin-κ^2N,N′)(μ-Oxalato-κ^2O,O'':κ^2O',O''') Metallkoordinationspolymere 1D-[Zn(ampy)(μ-ox)]·H_2O (1), 1D-[Ni(ampy)(μ-ox)]·H_2O (2) und 1D-[Cu(ampy)(μ-ox)H_2O (3) wurden synthetisiert und das Produkt ihrer Kalzinierung untersucht. Die Verbindungen 1 und 2 sind neu und isomorph. In ihrer Packung bilden die Metall-Oxalat-Einheiten durch die bis-bidentate Chelatbildung und Brückenbildung des Oxalats Zickzackketten entlang der *a*-Richtung. Diese Ketten bilden durch C–H···π-Wechselwirkungen zwischen den Aminomethylpyridin-Liganden supramolekulare Schichten in der *ab*-Ebene. Die Schichten sind mit Wassermolekülen verbunden und bilden Doppelschichten, die entlang der *c*-Achse verlaufen. Der thermische Zersetzungsprozess der drei Materialien in der Luft ist bei etwa 500 °C abgeschlossen und ergibt ZnO, NiO bzw. CuO, während unter N_2 der Zersetzungsmechanismus anders ist und bei etwa 600 °C ZnO, Ni bzw. Cu erzeugt. Eine weitere Zersetzung dieses ZnO in dieser sauerstofffreien Atmosphäre wird bei 800 °C beobachtet, und das verbleibende Material weist eine geringere durchschnittliche scheinbare Kristallitgröße auf und ist stärker dispergiert als das in Luft erhaltene ZnO, bei dem kein solcher Massenverlust

beobachtet wird. Beide ZnO weisen jedoch die gleiche Menge an Defekten auf. Diese Arbeit zeigt die Bedeutung der Atomabsorptionsspektroskopie-Messungen von Oxidmaterialien, die Defekte aufweisen könnten.

Eigenanteil an der Veröffentlichung:

- Aufnahme von REM-Bildern der jeweiligen Proben.
- EDX-Analysen der unterschiedlichen Proben.

3.6.11 Synthesis and Characterization of Covalent Triazine Frameworks Based on 4,4′-(Phenazine-5,10-diyl)dibenzonitrile and Its Application in CO_2/CH_4 Separation

Hanibal Othman, Robert Oestreich, Vivian Küll, Marcus N. A. Fetzer and Christoph Janiak, *Molecules* **2025**, *30*(15), 3110.

Kurzzusammenfassung

Kovalente Triazin-Gerüste (CTFs) haben sich als stabile poröse organische Polymere, beispielsweise für die CO_2-Abscheidung, etabliert. Ausgehend vom Monomer 4,4′-(Phenazin-5,10-diyl)dibenzonitril (pBN) wurden neue pBN-CTFs unter Verwendung des ionothermischen Verfahrens mit unterschiedlichen Temperaturen (400 und 550 °C) und unterschiedlichen $ZnCl_2$-zu-Monomer-Verhältnissen (10 und 20) synthetisiert. Die N_2-Adsorption ergab BET-Oberflächen von bis zu 1460 $m^2\,g^{-1}$. Die pBN-CTFs sind vielversprechende CO_2-Adsorbentien und mit anderen Referenz-CTFs wie CTF-1 vergleichbar, wobei die CO_2-Aufnahme von pBN-CTF-10-550 bei 293 K bis zu 54 $cm^3\,g^{-1}$ oder 96 mg g^{-1} beträgt und die CO_2/CH_4-IAST-Selektivität bei einer 50-prozentigen CO_2/CH_4-Mischung 22 beträgt. pBN-CTF-10-400 hat im Vergleich zu anderen CTFs eine sehr hohe Adsorptionswärme von 79 kJ mol^{-1} für CO_2 bei einer Bedeckung nahe Null und bleibt aufgrund seiner hohen Mikroporosität von 50 % des gesamten Porenvolumens deutlich über der Verflüssigungswärme von CO_2.

Eigenanteil an der Veröffentlichung:

- Aufnahme von REM-Bildern der jeweiligen CTFs.
- EDX-Analysen der jeweiligen CTFs.

3.6.12 Magnesium Hydroxide Nanoneedles Derived from *Anthocleista schweinfurthii* Gilg (Loganiaceae) Support Mesenchymal Stromal Cell Proliferation and Wound Healing

Francois Eya'ane Meva, A. Rita Pereira, Sandrine Elodie Ngnihamye, Armel Florian Tchangou Njiemou, Agnes Antoinette Ntoumba, Jean Baptiste Hzounda Fokou, Thi Hai Yen Beglau, Marcus N. A. Fetzer, Marilyn Kaul, Bianca Schlierf, Ulrich Armel Mintang Fongang, Phillipe Belle Ebanda Kedi, Simone Veronique Fannang, Marietta Herrmann and Christoph Janiak, *Journal of Inorganic and Organometallic Polymers and Materials* 2025. DOI: 10.1007/s10904-025-03833-1.

Kurzzusammenfassung

Diese Studie untersucht das Wundheilungs- und Knochenreparaturpotenzial von nanoskaligem Magnesiumhydroxid [nano$Mg(OH)_2$], das aus den Blättern von *Anthocleista schweinfurthii* Gilg (Loganiaceae) gewonnen wird, einer in Afrika heimischen Pflanze, die traditionell zur Behandlung von Verletzungen verwendet wird. $Mg(OH)_2$-AS Nanonadeln wurden aus wässrigen Extrakten der Blätter von *Anthocleista schweinfurthii* Gilg (Loganiaceae) (AS) und Magnesiumnitrat synthetisiert. Die Verbindung wurde mittels UV-Vis, DLS, FT-IR, PXRD, REM-EDX und TEM untersucht. Die Sicherheit der topischen Anwendung wurde anhand eines akuten Hauttoxizitätstests an einem Tiermodell untersucht. Es wurden In-vitro-Experimente zum entzündungshemmenden Potenzial und In-vivo-Wundheilungsassays an Wistar-Ratten durchgeführt. Um die Auswirkungen von $Mg(OH)_2$-AS auf zellulärer Ebene zu untersuchen, wurden mesenchymale Stromazellen aus dem Knochenmark (BM-MSCs) verwendet. Die $Mg(OH)_2$-Grenzfläche enthält sekundäre Metaboliten wie Polyphenole. Das PXRD konnte mit dem $Mg(OH)_2$-Muster abgeglichen werden und die Scherrer-Gleichung ergab Korngrößen < 50 nm nach verschiedenen Temperaturbedingungen. Die Pulver bilden Aggregate, die C-, O- und Mg-Elemente enthalten. Es wurden Nadeln mit einer Länge von 33 ± 9 nm und einer Breite von 4 ± 2 nm von $Mg(OH)_2$-AS abgebildet. $Mg(OH)_2$-AS wurde als sicher für die topische Anwendung befunden. $Mg(OH)_2$-AS hat entzündungshemmendes Potenzial und kann die Wundheilung verbessern. Im Gegensatz zu reinem $Mg(OH)_2$ oder AS wurden die Lebensfähigkeit und Proliferation der Zellen durch $Mg(OH)_2$-AS nicht beeinträchtigt. Die Zellmorphologie blieb nach Zugabe von $Mg(OH)_2$-AS zum Medium unverändert. Es wurde eine Verbesserung der osteogenen Differenzierung von BM-MSCs

beobachtet. Diese Ergebnisse motivieren zu weiteren Forschungen zur Einbeziehung des Materials, das sekundäre Pflanzenmetaboliten in Implantaten für die Knochenheilung antreibt.

Eigenanteil an der Veröffentlichung:

- Aufnahme von REM-Bildern der jeweiligen Proben.
- EDX-Analysen der jeweiligen Proben.
- Revision des Manuskripts.

3.6.13 Apoptosis-Inducing Fe^{2+}/*β*-Cyclodextrin Supramolecular Nano–Particulate Complex as an Anticancer Drug Platform and Cancer-Diagnostic Tool Prototype

Sheta M. Sheta, Said M. El-Sheikh, Mahmoud T. Abo-Elfadl, Ahmed Younis, Mohkles M. Abd-Elzaher, Hanibal Othman, Till Strothmann, Marcus N. A. Fetzer, Istvan Boldog, and Christoph Janiak, *ChemMedChem* **2025**, *0*, e202500665.

Kurzzusammenfassung

Beta-Cyclodextrin (*β*-CD)-Metallkomplexe und ihre biomedizinischen Anwendungen stellen insbesondere in der Medizin ein sich aktiv entwickelndes Forschungsgebiet dar. Hier wird ein bei Raumtemperatur synthetisierter Eisen/β-Cyclodextrin (Fe(II)-*β*-CD)-Nanokomplex mittels verschiedener analytischer Techniken charakterisiert. Der Komplex weist eine Morphologie aus unregelmäßigen Partikeln mit einer durchschnittlichen Größe von 4–10 nm auf und zeigt eine poröse Struktur. In vitro sind die Partikel im Kulturmedium, bei dem es sich in der Regel um eine wässrige Lösung mit einem pH-Wert von 7,4 handelt, gut dispergierbar. Die Partikel sind unter physiologischen Bedingungen stabil und mit lebenden Zellen biokompatibel, was sie zu einem vielversprechenden Kandidaten für eine Plattform zur Wirkstoffabgabe macht. Das Fe(II)-*β*-CD wird auf sein Antikrebs-Potenzial gegen vier Arten von malignen Zelllinien untersucht: Leber (HepG2), Brust (A549), Lunge (MCF7) und Prostata (PC3), um die potenziellen zytotoxischen Eigenschaften zu bewerten. Die Ergebnisse zeigen, dass der Nanokomplex keine zytotoxische Wirkung aufweist. Die Dosis-Wirkungs-Kurven und die IC_{50} der Probe auf jeder Zelllinie werden bei unterschiedlichen Inkubationszeitintervallen bewertet. Der apoptotische Zelltod ist nach 24 und 48 Stunden der vorherrschende Modus. Darüber hinaus wird das

molekulare Docking des Nanokomplexes als Krebsmedikament gegen die aktive Stelle des CD44-Glykoproteins (PDB-ID-1poz) untersucht. Basierend auf den erzielten Ergebnissen ebnet der hergestellte Komplex den Weg für ähnliche Biomarker in der Krebsbehandlung.

Eigenanteil an der Veröffentlichung:

- Aufnahme von REM-Bildern der jeweiligen Proben.
- EDX-Analysen der jeweiligen Proben.
- Revision des Manuskripts.

4. Zusammenfassung

Im ersten Teil dieser Arbeit wurde die Entwicklung zweier neuer Metallphosphonat-Gerüste, Co_2[1,4-NDPA] und Zn_2[1,4-NDPA], besprochen. Hierbei zeigten beide Verbindungen, besonders aber das Co_2[1,4-NDPA] ein Halbleiterverhalten und präkatalytische Eigenschaften in der OER. Ziel dieser Arbeit war es, kostengünstige Alternativen zu den etablierten Edelmetall-Katalysatoren zu entwickeln. Die beiden Materialien wurden durch die Reaktion von Naphthalendiphosphonsäure (1,4-NDPAH_4) mit den entsprechenden Metallsalzen hydrothermal hergestellt. Aus den diffusen Reflexionsspektren und den sich daraus ergebenden optischen Kubelka-Munk-Spektren konnten für beide Verbindungen die Bandlücken bestimmt werden. Dabei zeigen beide Verbindungen bei ca. 2,5 eV ihre jeweiligen Absorptionsanfänge. Das Co_2[1,4-NDPA] zeigt eine weitere Absorption bei ca. 1,7 eV, welche als Ligandenfeldübergang identifiziert werden kann. Die elektrochemischen Untersuchungen sowohl auf einer Glas-Kohlenstoff-Elektrode als auch auf einer Nickelschaum-Elektrode zeigen die besonders interessanten Eigenschaften des Co_2[1,4-NDPA]. Hierfür konnten in Abhängigkeit zur verwendeten Elektrode für das Co_2[1,4-NDPA] Überpotenziale von 374 mV bzw. 312 mV erreicht werden. Anhand der Tafelsteigung ließen sich Rückschlüsse auf die Reaktionskinetik ziehen. Mit einem Wert von 43 mV/dec in 1 molarer Kaliumhydroxid-Lösung übertraf sie sogar die Kinetik von RuO_2, das heute als Standard gilt. Auch die Aktivität des Co_2[1,4-NDPA] für die Wasserspaltung zeigt mit einer Stromdichte von 200 mA/cm^2 bei 1,63 V eine deutliche Verbesserung gegenüber RuO_2. Langzeitstudien über einen Zeitraum von 30 Stunden bei 50 mA/cm^2 demonstrieren die hohe Stabilität der aktiven Spezies durch das Verwenden von Co_2[1,4-NDPA] als Präkatalysator. Die Ergebnisse dieser Publikation zeigen, welches Potenzial in der Anwendung von MOFs als Halbleiter bzw. als Präkatalysator in der industriellen Anwendung steckt und unterstreichen das Interesse an diesem Forschungsbericht.

Die zweite Publikation beschäftigte sich mit dem Einfluss von Modulatoren auf die Synthese und Eigenschaften der herzustellenden MOFs. Dabei konnte mittels einer ausgiebigen Literaturrecherche anhand unterschiedlicher Beispiele der Effekt verschiedener Modulatoren verdeutlicht werden. Dabei zeigte sich, dass Modulatoren aktiv an der Ausbildung der MOFs und ihrer Eigenschaften beteiligt sind. Die Verwendung unterschiedlicher Modulatoren hat dabei nicht nur Einfluss auf die

Porosität der hergestellten MOFs, sondern kann auch die Partikelgröße, Länge und sogar die gesamte Form des sich bildenden MOFs durch bevorzugte Wechselwirkungen mit den gebildeten Flächen stark beeinflussen. Dies führt dazu, dass durch unterschiedliche Modulatoren eine räumliche Orientierung bevorzugt wird, was eine Abgrenzung zum Templateffekt schwierig macht. Neben den strukturellen Änderungen nehmen Modulatoren auch auf die chemischen und physikalischen Eigenschaften einen bedeutenden Einfluss. So kann durch die Verwendung von Modulatoren das Sorptionsverhalten, die katalytische Aktivität oder auch die Stabilität der gebildeten Strukturen verändert werden. Die Ergebnisse der Literaturrecherche im Zusammenhang mit dieser Publikation verdeutlichen, dass Modulatoren in der MOF-Synthese durch ihre Wechselwirkungen mit den sich bildenden Partikeln ein zentrales Werkzeug für eine gezielte Anwendung sind. Durch die Verwendung von Modulatoren lassen sich Materialien anwendungsspezifisch designen.

In der dritten Publikation konnte durch die Synthese eines auf Rhodium basierenden Koordinationspolymers eine sonst homogene Katalyse an einem heterogenen Katalysator durchgeführt werden. Dafür wurde die Schaufelrad-Struktur von $Rh_2(OAc)_4$ ausgenutzt und das gesuchte Koordinationspolymer durch die Verwendung von Terephthalsäure hergestellt. Dabei konnte mittels unterschiedlicher Analysemethoden wie PXRD, Zersetzungs-NMR, REM in Kombination mit EDX, thermogravimetrische Analyse (TGA) oder Infrarotspektroskopischen-Messungen (IR) die gesuchte Struktur bestätigt werden. Anhand einer Modellreaktion zwischen einem Diazoalkan und Styrol wurde dann die katalytische Aktivität und Stabilität bestimmt. Während die katalytische Aktivität konstant hoch blieb, nahm die Stabilität mit jedem Katalysezyklus ab, so dass nach sechs Zyklen nur noch 30 % des ursprünglichen Katalysators zurückgewonnen werden konnte. Um die breite Anwendbarkeit des hergestellten Katalysators zu überprüfen, wurden über 25 unterschiedliche Verbindungen getestet. Die meisten Reaktionen führten zu einem hohen Umsatz in die gewünschten Produkte, wobei die Ausbeuten nahezu 90 % betrugen. Besonders sollen hier die Tests mit Medikamenten und Naturstoffen hervorgehoben werden. Dies zeigt, dass die heterogene Katalyse mit dem hergestellten Koordinationspolymer auch mit komplizierten Molekülen möglich ist. Diese Publikation verdeutlicht, dass durch die gezielte Synthese von katalytisch aktiven Feststoffen neue Anwendungsbereiche, die sonst nur der homogenen Katalyse vorbehalten waren, erschlossen werden können.

Die vierte Publikation beschäftigt sich mit der Synthese und den Sorptionseigenschaften des Metallphosphonat-Gerüsts TUB41. Dieses konnte hier zum ersten Mal phasenrein synthetisiert werden. Seine überragende thermische als auch chemische Stabilität wurde durch verschiedene Untersuchungen wie Säure-Base-Tests oder temperaturabhängige PXRD-Messungen bestätigt. Seine Langzeitstabilität konnte über zwei Jahre nachgewiesen werden. Durch die Verwendung von Bipyridin und 1,4-Naphthalindiphosphonsäure als Linker ergibt sich eine auf Kupfer basierende Struktur mit der Summenformel $[Cu(4,4´\text{-bpy})_{0.5}(1,4\text{-}NDPAH_2)]$, die über Kanäle mit den Maßen 4×2 Å verfügt. Durch das Vorhandensein der Napthalin-Reste, welche die Poren auskleiden, wird eine vorwiegend hydrophobe Struktur erzeugt. Dies macht TUB41 besonders interessant in der CO_2-Sorption und -Abtrennung. Trotzdem können Wassermoleküle in den Poren mit den hydrophilen Sauerstoffatomen der Phosphonatgruppen wechselwirken. Molekulardynamische Berechnungen zeigen, dass es sich bei H_2O und CO_2 um verschiedene Adsorptionsmechanismen handelt. Während sich CO_2 bevorzugt in der Mitte der einzelnen Poren aufhält, sitzen die Wassermoleküle in der direkten Umgebung der SBUs. Die Berechnung der mittleren quadratischen Verschiebung weist darauf hin, dass sowohl die Wasser- als auch die CO_2-Moleküle in der Pore stark eingeschränkt sind, was sowohl auf den kleinen Porendurchmesser als auch auf starke Wirt-Gast-Wechselwirkungen zurückzuführen ist. Die weitestgehend hydrophoben Poren und die räumliche Trennung der aufgenommenen Wasser- bzw. CO_2-Moleküle deuten auf eine gemilderte kompetitive Adsorption hin, wodurch TUB41 in der Lage ist, selektiv CO_2 in feuchten Umgebungen zu adsorbieren.

Die fünfte Publikation beschäftigt sich mit der Einlagerung eines säurestabilen Bodipy-Farbstoffs. Hierbei wurde durch Vortests festgestellt, dass die ursprüngliche Difluoro-Spezies des verwendeten Bodipy-Farbstoffs unter sauren Bedingungen eine geringere Stabilität aufweist. Durch das Einbringen von Cyano-Gruppen am Borzentrum konnte sowohl die Stabilität als auch die Quantenausbeute deutlich gesteigert werden. Dieser Farbstoff wurde dann in ersten Ansätzen sowohl post-synthetisch als auch *in situ* in das MOF UiO-66 eingelagert. Die so hergestellten Bodipy@UiO-66-Komposite zeigten, unabhängig von der Einlagerungsmethode, eine für Bodipy typische grüne Fluoreszenz unter UV-Licht. Stickstoffsorptionsmessungen zeigten hingegen einen deutlichen Unterschied zwischen den verwendeten Einlagerungsmethoden. Während

alle *in situ* hergestellten Komposite eine UiO-66 entsprechende BET-Oberfläche zeigten, wurde in dem post-synthetischen Ansatz eine deutliche Verringerung der Oberfläche festgestellt. Die Abnahme der Oberfläche konnte durch das Blockieren der Poren aufgrund der hohen Farbstoffkonzentrationen in den äußeren MOF-Bereichen erklärt werden. Durch Zersetzungs-UV-Vis-Messungen konnte die genaue Beladung aller UiO-66-Komposite bestimmt werden. Diese Beladungen ermöglichten es, das Verhältnis zwischen unbesetzten, einfach und mehrfach besetzten Poren für die homogen verteilten *in situ* hergestellten Komposite zu errechnen. Diese Rechnungen zeigen, dass mit zunehmender Beladung auch die Anzahl an mehrfach beladenen Poren zunimmt, was direkten Einfluss auf die photophysikalischen Eigenschaften der Komposite hat. So nimmt mit höherer Beladung sowohl die Lebenszeit als auch die Quantenausbeute der *in situ* Komposite ab. Neben den UiO-66-Kompositen wurden auch jeweils ein post-synthetisches und ein *in situ* Komposit mit den beiden MOFs MOF-808 und DUT-67 hergestellt. Auch diese Komposite zeigen die charakteristische Bodipy-Fluoreszenz. In beiden Fällen zeigen die post-synthetischen Komposite die geringste BET-Oberfläche, während die PXRDs aller MOF-808- und DUT-67-Komposite keine Unterschiede zur jeweiligen Simulation zeigen. Auch hier konnte für die *in situ* hergestellten Komposite die Mehrfachbeladung berechnet werden. Durch die größeren Poren in MOF-808 und DUT-67 im Vergleich zu UiO-66 kann davon ausgegangen werden, dass die eingelagerten Bodipy-Moleküle eine höhere Beweglichkeit und eine geringere Wechselwirkung sowohl untereinander als auch mit den MOF-Wänden aufweisen. Diese Annahme kann durch eine deutlich verlängerte Lebenszeit bei gleicher Porenbeladung im Vergleich mit den entsprechenden UiO-66-Kompositen belegt werden. Für MOF-808 wurde eine Lebenszeit von 9,0 Nanosekunden gemessen. Diese ist nahezu doppelt so lange wie bei UiO-66 unter vergleichbarer Beladung und etwa acht Mal länger als bei dem festen Farbstoff. Bei den Quantenausbeuten wurde der höchste Wert von 77 % für das post-synthetisch hergestellte DUT-67-Komposit erreicht. Dieser Wert entspricht eher der Quantenausbeute in Lösung mit 89 % als der im festen Farbstoff, die bei 9 % liegt. Anhand dieser Publikation kann der Einfluss der unterschiedlichen Einlagerungsmethoden verdeutlicht werden.

5. Publikationsentwürfe unveröffentlichter Ergebnisse

Alle gezeigten Abbildungen, Tabellen und Schemata in den Publikationsentwürfen folgen nicht dem Haupttext dieser Dissertation. Ebenso wird die verwendete Literatur in jeweils separaten Verzeichnissen am Ende jedes Entwurfs aufgelistet, wodurch es zu einer mehrfachen Zitation einiger Quellen kommen kann. Alle Publikationsentwürfe werden mit einer kurzen Zusammenfassung beschrieben. Eine Benennung der jeweiligen Anteile an den Entwürfen kann hier nicht erfolgen, da es sich um nicht publizierte Entwürfe handelt und es zu Änderungen in der fertigen Publikation kommen kann.

5.1 Luminescent Crystals: MR-TADF emitter DiKTa inside of metal-organic framework MOF-5

Marcus N. A. Fetzer,‡ Annette Vollrath,‡ Jennifer Kremper,‡ Benedikt Bendel, Ralf Kühnemuth, Markus Suta, Oliver Weingart,* Jan Meisner,* and Christoph Janiak*.

‡: Die Autoren haben zu gleichen Anteilen zu dieser Publikation beigetragen.

Kurzzusammenfassung

Hier berichten wir über den ersten Versuch, ein hoch emittierendes mikroporöses metallorganisches Gerüst (MOF) durch Einschluss eines multiresonanten, thermisch aktivierten verzögerten Fluoreszenzemitters namens DiKTa (Chinolino-[3,2,1-de]acridin-5,9-dion) zu synthetisieren, der erstmals von Hellwinkel *et al.* synthetisiert wurde. Dieses Molekül ist für seine schmalbandige Emission bekannt, was es zu einem interessanten Kandidaten für die Anwendung in organischen Leuchtdioden (OLEDs) macht. Aufgrund seiner geeigneten Porengröße haben wir MOF-5 als MOF ausgewählt, basierend auf den Abmessungen der DiKTa-Moleküle. Die MOF-Synthesen sowie das Einlagern wurden durch eine solvothermale *in situ* Synthese ausgehend von kostengünstigen Materialien durchgeführt. Wir haben uns bei der Synthese auf die Herstellung von MOF-5-Einkristallen konzentriert. Vier DiKTa@MOF-5-Komposite mit unterschiedlicher DiKTa-Beladung wurden erfolgreich als Einkristalle synthetisiert. Die photophysikalischen und strukturellen Eigenschaften dieser Komposite wurden umfassend analysiert und mit denen von reinem DiKTa sowohl im festen Zustand als auch in Lösung verglichen. Die beschriebenen DiKTA@MOF-5-

Komposite zeigen je nach Beladung gute Emissionen und im Vergleich zu DiKTa in Lösung etwas breitere Werte für die Halbwertsbreite (FWHM). Die Lebensdauermessungen der Komposite lieferten Ergebnisse, die mit denen für DiKTa in Lösung vergleichbar sind, wobei die Werte je nach Konzentration von DiKTa im Komposit variieren. Die gemessenen Lebensdauern umfassten sowohl prompte als auch verzögerte Komponenten, was das Konzept einer Feststofflösung bestätigt. Mithilfe von Fluoreszenzanisotropiemessungen konnten wir die bevorzugte Ausrichtung einzelner DiKTa-Moleküle in der MOF-Matrix bestimmen. Zusätzlich zur Verringerung der jeweiligen BET-Oberflächen lieferten die PXRD-Messungen jedes Komposits wertvolle Erkenntnisse darüber, wie sich unterschiedliche DiKTa-Beladungen auf die strukturelle Integrität und Stabilität der MOF-5-Matrix auswirkten. Dies zeigt, wie sich Farbstoff und MOF gegenseitig beeinflussen.

Luminescent Crystals: MR-TADF emitter DiKTa inside of metal-organic framework MOF-5

Marcus N. A. Fetzer,‡[a] Annette Vollrath,‡[a] Jennifer Kremper,‡[d] Benedikt Bendel,[b] Ralf Kühnemuth,[c] Markus Suta,[b] Oliver Weingart,*[d] Jan Meisner,*[d] and Christoph Janiak*[a]

[a]Inorganic and Structural Chemistry, Heinrich Heine University Düsseldorf, Universitätsstraße 1, D-40225 Düsseldorf, Germany

[b]Inorganic Photoactive Materials, Heinrich Heine University Düsseldorf, Universitätsstraße 1, D-40225 Düsseldorf, Germany

[c]Molecular Physical Chemistry, Heinrich Heine University Düsseldorf, Universitätsstraße 1, D-40225 Düsseldorf, Germany

[d]Theoretical and Computational Chemistry, Heinrich Heine University Düsseldorf, Universitätsstraße 1, D-40225 Düsseldorf, Germany

‡ These authors contributed equally to this work.

* Corresponding authors

Abstract:

In here we report the first attempt to synthesize a highly emissive microporous metal-organic framework (MOF) by entrapment of a multi-resonant thermally activated delayed fluorescence emitter called DiKTa (quinolino-[3,2,1-*de*]acridine-5,9-dione) which was first synthesized by Hellwinkel *et al.*[1] This molecule is known for its narrowband emission, which makes it an interesting candidate for the application in organic light-emitting diodes (OLED's). Due to its suitable pore size, we chose MOF-5 as the MOF, based on the dimensions of DiKTa molecules. The MOF syntheses as well as the entrapment were carried out by a solvothermal in situ synthesis starting from inexpensive materials. We focused the synthesis on the production of MOF-5 single crystals. Four **DiKTa**@MOF-5 composites with different DiKTa loading were successfully synthesized as single crystals. The photophysical and structural

properties of these composites were comprehensively analyzed and compared with those of pure DiKTa in both solid-state and solution. The reported **DiKTA@**MOF-5 composites show good emissions depending on their loading and slightly broader full width at half maximum (FWHM) values compared to DiKTa in solution. Lifetime measurements of the composites yielded results comparable to those observed for DiKTa in solution, with values varying depending on the concentration of DiKTa in the composite. The measured lifetimes included both prompt and delayed components, confirming the concept of a solid solution. Using fluorescence anisotropy measurements, we were able to determine the preferred orientation of individual DiKTa molecules in the MOF matrix. In addition to the decrease in the respective BET surface areas, the powder X-ray diffraction (PXRD) of each composite provided valuable insights into how different DiKTa loadings affected the structural integrity and stability of the MOF-5 matrix. This shows how dye and MOF affect each other.

1. Introduction:

Over the last few decades, the interest in new organic chromophores has increased significantly, due to their potential application in OLEDs in electronic devices such as smart phones, TVs or other types of displays.[2] These new compounds provide a simple, efficient and cost-effective alternative to the commonly used noble-metal complex emitters.[3] One of the major problems is the low emission efficiency of only 25% from the excited singlet state and the associated loss of 75% from the excited triplet states. To overcome this problem, the concept of thermally activated delayed fluorescence (TADF) emitters, known since the beginning of the 20th century, is of great interest.[4] The fundamental principle of TADF emitters is based on the prompt emission of light from the singlet (S_1) and the delayed emission from the lower-energy triplet (T_1) states by reverse intersystem crossing (rISC). A key requirement for this mechanism is a minimal energy gap (ΔE_{ST}) between these states, which is typically less than 0.1 eV and is largely determined by the overlap between the highest occupied molecular orbital (HOMO) and the lowest unoccupied molecular orbital (LUMO).[5] The small S_1-T_1 energy gap allows efficient reverse intersystem crossing (rISC) at or near room temperature, where a significant part of the triplet excitons can be converted to the emitting singlet state. As a result, TADF materials have the potential to achieve internal quantum efficiencies approaching 100%.[6] The first molecules to be

investigated are based on a donor-acceptor architecture, where the HOMO is located on the donor and the LUMO on the acceptor. This type of structure exploits the clear separation of HOMO and LUMO but has the disadvantage of a certain flexibility and thus a strong broadening of the emission band with FWHM values in the range of 80-200 nm. In these cases, the color fastness required for industrial applications can only be achieved by using different filters.[7] To overcome the limitations of conventional TADF emitters, Hatakeyama *et al.*[8] introduced the class of multi-resonant TADF (MR-TADF) emitters in 2016 with the synthesis of DABNA-1. Molecules within this class exhibit high structural rigidity due to their extended π-conjugated backbone. The precise positioning of electron-donating atoms (e.g., N, O, P, S) and electron-deficient elements (e.g., B, C=O) leads to a unique luminescent interaction.[9] This allows both small ΔE_{ST} values and smaller FWHM of less than 30 nm to be achieved, resulting in narrowband emission with high color purity.[10] However, these conditions are typically observed only in solutions, where intermolecular interactions such as aggregation effects can be effectively controlled by adjusting concentration or solvent polarity. In the solid state, many organic emitters often exhibit significantly different photophysical behavior due to enhanced π–π stacking, aggregation-induced quenching, or excitonic interactions. This makes their use as a solid in most optoelectronic areas uninteresting.

MOFs represent a new class of hybrid compounds, combining metals or metal clusters, also known as SBUs, and organic linker molecules.[11] The materials obtained in this way are mostly crystalline three-dimensional coordination networks with high porosity and surface areas of several thousand square meters per gram.[12] By using different metal salts or linkers, they can be designed for the desired application in terms of pore size porosity and surface area,[13] stability,[14] or morphology.[15] These properties make MOFs significantly more interesting compared to traditional porous materials such as zeolites or activated carbon. Thanks to their high level of adaptability, MOFs are used in a wide variety of areas. In addition to the encapsulation of guest molecules such as enzymes,[16] pharmaceuticals or nanoparticles,[17] MOFs are widely used in heterogeneous catalysis,[18] gas adsorption and separation,[19] thermal energy conversion,[20] water decontamination,[21] and sensor technology.[22] In the field of dye encapsulation, research is mainly focused on the development of advanced optoelectronic devices such as LEDs and sensors.[22d, 23] For example, Cui *et al.* successfully synthesized a white light-emitting composite by incorporating two different

dyes into the MOF ZJU-28.[24] Similarly, Zhang *et al*. developed an MOF-based sensor for metal ion detection by encapsulating the dye fluorescein into bio-MOF-1.[25]

Our work focused on the incorporation of the MR-TADF emitter DiKTa and the resulting photophysical properties of the obtained composites. To the best of our knowledge, the incorporation of MR-TADF emitters into MOFs remains largely unexplored. Therefore, in this study, we investigate the behavior of the MR-TADF emitter DiKTa in MOF-5 as a solid solution, aiming to understand its structural integrity, emission properties, and potential advantages conferred by the MOF matrix. The comparison between pore size (12 Å) and DiKTa size (10-11 Å) led us to conclude that successful incorporation into defined pores without defects is possible.[26] The photophysical results obtained for the composites were compared with the results in solution and as a solid. Furthermore, we focused on the exact incorporation and the associated change in the MOF parameters. These should show that the DiKTa molecules have been successfully incorporated into MOF-5.

2. Results:

2.1 Synthesis and photophysical properties of DiKTa

For our investigations, DiKTa was synthesized following the work of J. E. Field *et al*.[27] and Hall *et al*.[28] (see Scheme 1). In a Jordan-Ullmann coupling, aniline was reacted with methyl 2-iodobenzoate using copper iodide and powdered copper as catalysts. The product obtained could be re-functionalized to the corresponding acyl chloride and then converted to a closed DiKTa in a Friedel-Craft acylation reaction using $AlCl_3$ as Lewis acid catalyst. The products obtained were synthesized with high yields of 76 % and 82 %. The overall yield was 62 %. These values are in good agreement with the literature.[27-28]

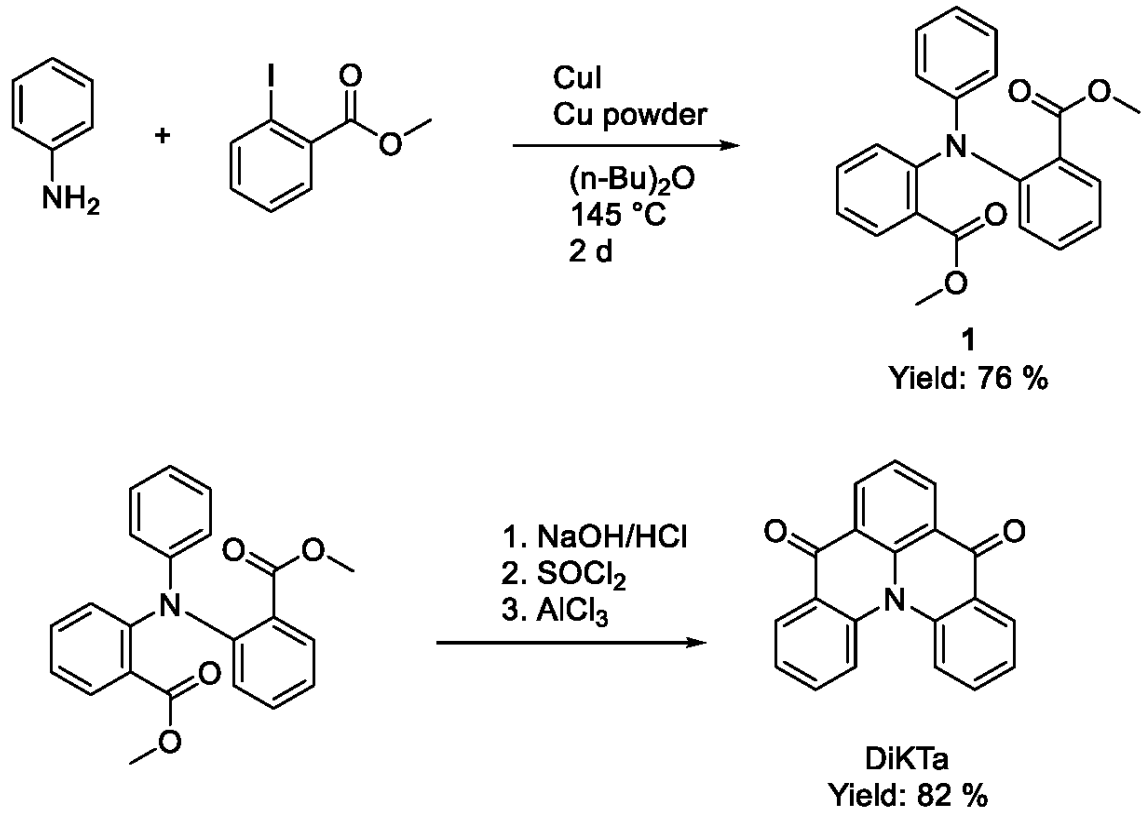

Scheme 1. Synthesis of DiKTa.

The successful synthesis was confirmed by NMR and mass spectroscopy (see Section S3, ESI). The pure solid DiKTa is a yellow crystalline powder which shows a strong yellow luminescence under UV light (Figure 1a). The excitation spectrum of the pure solid shows a broad excitation band with a maximum at 380 nm. The emission has its maximum at 541 nm with a full width at half maximum (FWHM) of 98 nm (3199 cm^{-1}) (Figure 1b). This value does not correspond to the classic MR-TADF emitters, which have a much narrower emission band. In solution, depending on the concentration, DiKTa forms a pale-yellow color. Under UV light it shows an emission in the blue-turquoise region (Figure 1c). Steady state measurements in *n*-hexane show a narrow band emission at 436 nm and an overlapping absorption with a maximum at 426 nm (Figure 1d).

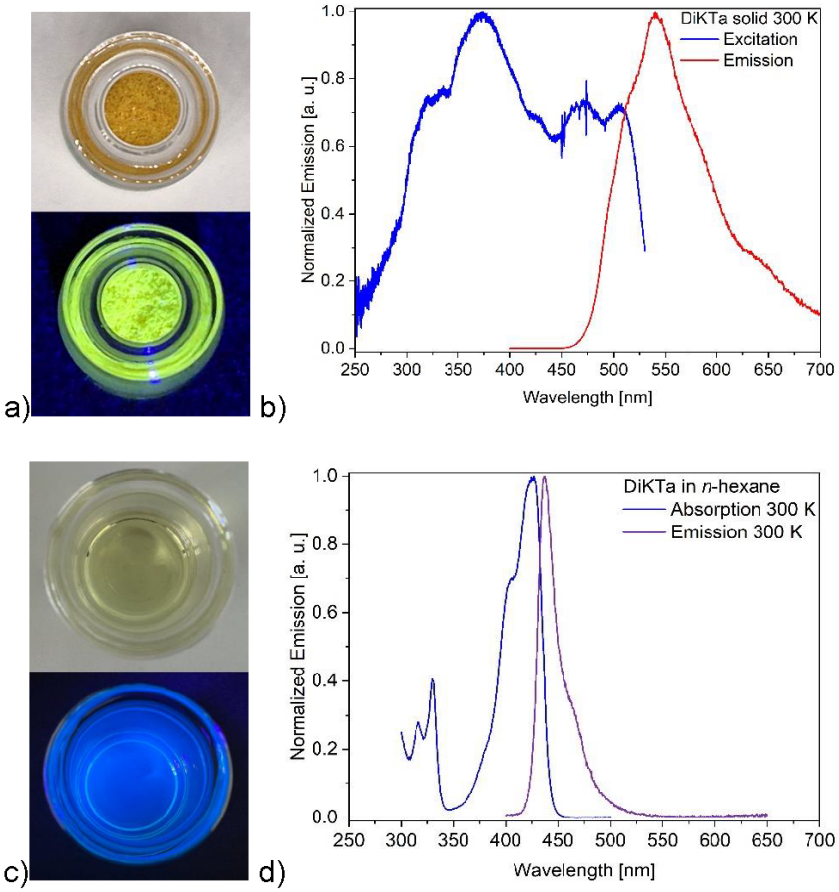

Figure 1. a) Solid DiKTa under daylight (top) and UV-light (λ_{exc} = 365 nm). b) Excitation (λ_{em} = 540 nm) and emission (λ_{exc} = 360 nm) spectra of solid DiKTa. c) DiKTa in *n*-hexane under daylight (top) and UV-light (λ_{exc} = 365 nm). d) Absorption and emission (λ_{exc} = 360 nm) spectra of DiKTa in *n*-hexane.

The resulting Stokes shift is 10 nm (538.4 cm^{-1}). In addition to the literature-known positive solvatochromic shift of the emission maxima as a function of the polarity of the solvent used for DiKTa and DiKTa-based compounds (Figure 2a), concentration-dependent bathochromic shifts in solution could also be measured here.[28] Figure 2b shows the bathochromic shift of the emission maxima for different concentrations of DiKTa in chloroform from 458 nm for a 0.003 mol/l solution to 483 nm for a concentration of 16.82 mol/l (Figure S7 shows DiKTa in $CHCl_3$ with different concentrations).

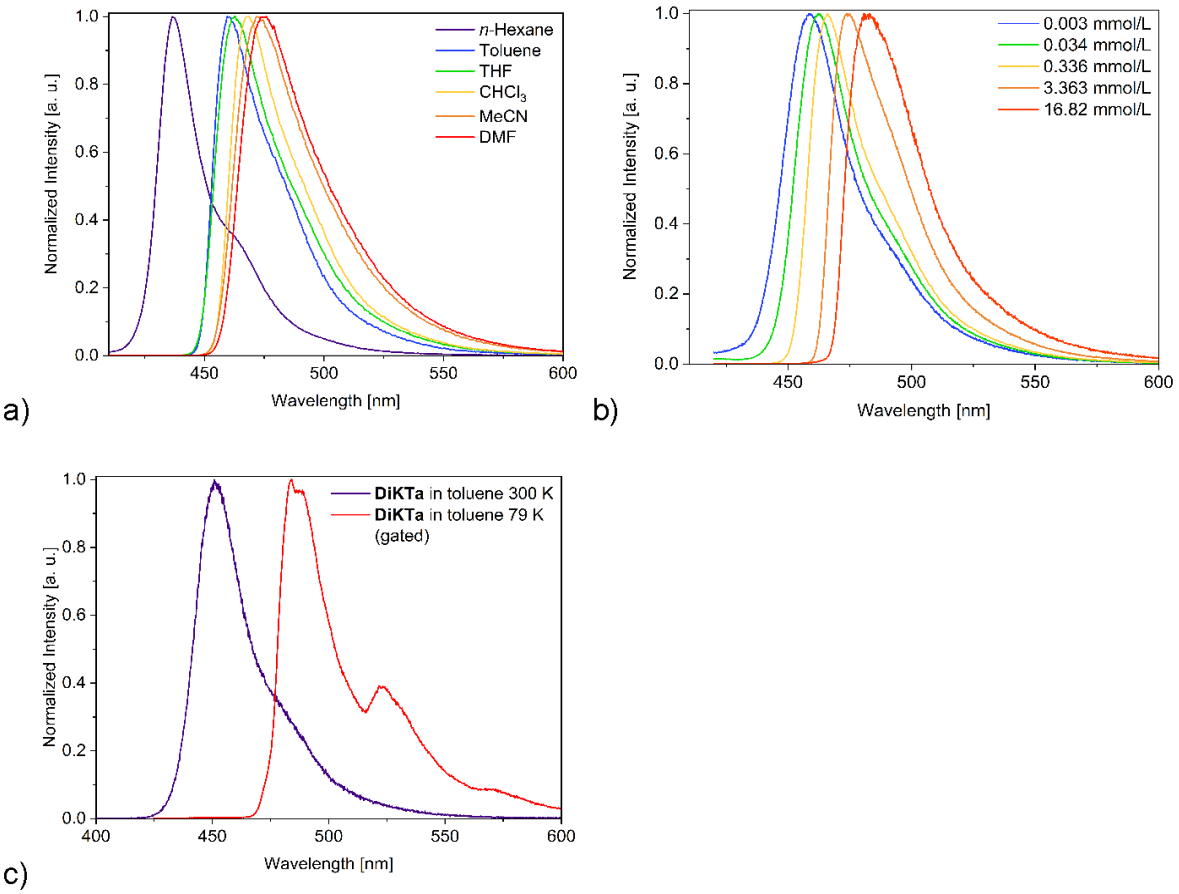

Figure 2. a) Solvatochromic shift with different solvents (λ_{exc} = 360 nm). b) Concentration-dependent shift in chloroform (λ_{ex} = 360 nm). c) DiKta in toluene at 300 K (λ_{exc} = 335 nm) and 79 K. after 10 ms for 10 ms (λ_{exc} = 420 nm).

We did not detect any broadening of the emission bands. All FWHM values remain almost constant in a range of 30 to 34 nm with increasing concentration. Steady state measurements at 79 K revealed a pronounced red-shift of the emission maximum to 484 nm (see Figure 2c and Figure S8a). At this low temperature, the rISC is effectively suppressed, resulting in predominant luminescence from the excited triplet state. This allowed the determination of ΔE_{ST}, which was calculated to be 0.19 eV (see Figure 8b, ESI). Lifetime measurements of DiKTa as a polymer film at room temperature showed both a prompt fluorescence component with a lifetime of 5.7 ns and a delayed fluorescence component of 22 µs. Upon cooling to 79 K, a significant elongation of the delayed fluorescence component was observed, indicating a greatly reduced rISC rate at lower temperatures. The measured lifetimes in a polymer film at 79 K was 8.4 ns for the prompt fluorescence and 120 ms for the delayed component. These results are in good agreement with the literature (see ESI, Figures 9 and 10 for lifetime plots).[28] Compared to the lifetime measurements in the polymer film, DiKTa shows clear

differences as a solid. We were able to determine a lifetime for solid DiKTa of 799 ns at room temperature and 882 µs at 79 K from the measurements shown in Figure S11. These results indicate that DiKTa exhibits MR-TADF emitter properties exclusively in solution or as a polymer film, but not in the solid state.

2.2 Encapsulation of DiKTa

The encapsulation of the DiKTa molecules into the MOF-5 matrix was carried out as *in situ* approaches according to Han *et al.* with different concentrations, starting from 0.06 mmol/L to 0.5 mmol/L.[29] In addition to the encapsulation of DiKTa, we also synthesized pure MOF-5 in the same way as a reference (for more details, see Section 5, ESI). All compounds were washed with DCM to remove non-incorporated dye and educt residues. In this way, we were able to produce cubic single crystals with an edge length of up to 1.5 mm. With increasing concentration of DiKTa used in the reaction, an increasing color change of the composites obtained could be observed, starting from colorless crystals for neat MOF-5 to an intensifying yellow with increasing concentration. Figure 3 shows the color change in the MOF-5 single crystals under both daylight and UV light. All composites emit in the wavelength range from blue to turquoise under UV light (λ_{exc} = 365 nm), while pure DiKTa as a solid exhibits strong yellow fluorescence (cf. Figure 1a).

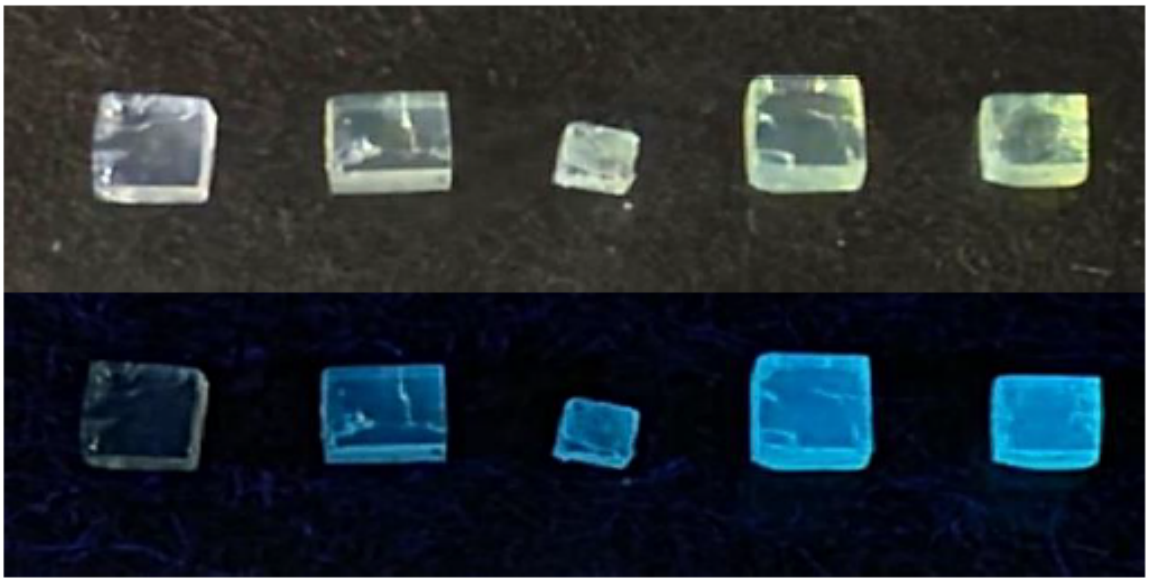

Figure 3. From left to right: neat MOF-5, **DiKTa@MOF-5**$_{0.03}$, **DiKTa@MOF-5**$_{0.05}$, **DiKTa@MOF-5**$_{0.09}$, and **DiKTa@MOF-5**$_{0.13}$. Both under daylight (top) and UV-light (λ_{exc} = 365 nm).

All composites show that the syntheses were successful, based on powder X-ray diffraction (PXRD) measurements shown in Figure 4a and ESI Figure S12.

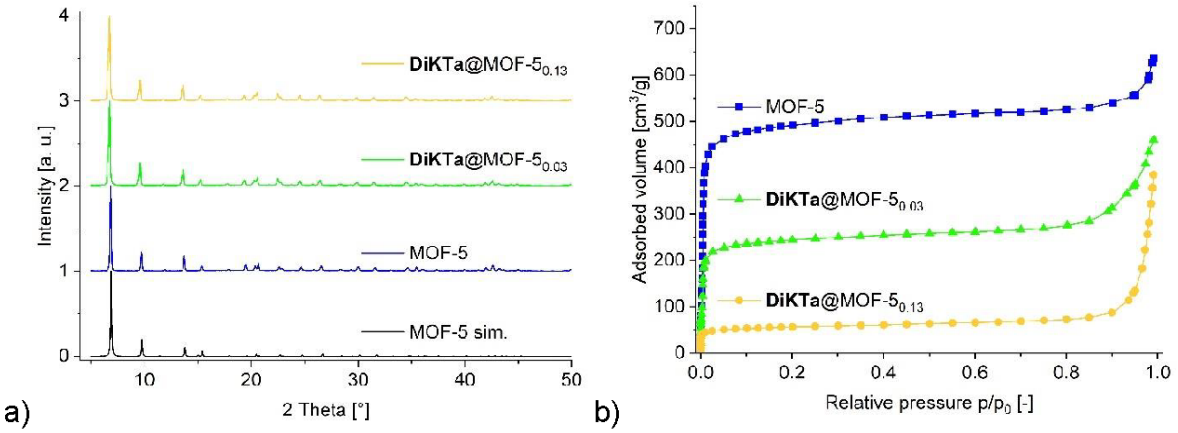

Figure 4. a) PXRD of MOF-5 and the lowest and highest loaded **DiKTa**@MOF-5 composite. Simulated diffractogram of MOF-5 (CCDC No. 819641). b) Nitrogen adsorptions isotherms at 77 K of neat MOF-5 (1973 m^2/g) and the lowest (965 m^2/g) and highest (213 m^2/g) loaded **DiKTa**@MOF-5 composite.

No suitable PXRD reflections of the starting materials used could be measured. Therefore, we assumed that the neat MOF-5 and all the composites were formed as phase pure material. The exact DiKTa loading of the synthesized composites was determined by digestion UV-Vis. Depending on the initial concentration, loadings of 0.03 wt% up to 0.13 wt% were found, denoting the composites as **DiKTa**@MOF-$5_{0.03}$ to **DiKTa**@MOF-$5_{0.13}$, respectively (for more details see ESI, Section S6). Based on these results, we calculated the molar ratio of DiKTa molecules to MOF-5 pores, which falls within the range of 0.0008 and 0.0034 DiKTa molecules per pore for **DiKTa**@MOF-$5_{0.03}$ to **DiKTa**@MOF-$5_{0.13}$, respectively (for a detailed description, see Section S7, ESI).

A more detailed analysis of the PXRD data, shown in Figure 5, shows a consistent and concentration-dependent shift and broadening of the diffraction peaks to lower 2θ angles with increasing DiKTa loading. This systematic change in the diffraction pattern serves as a indication of the successful encapsulation of DiKTa molecules within the porous structure of the MOF-5 framework.

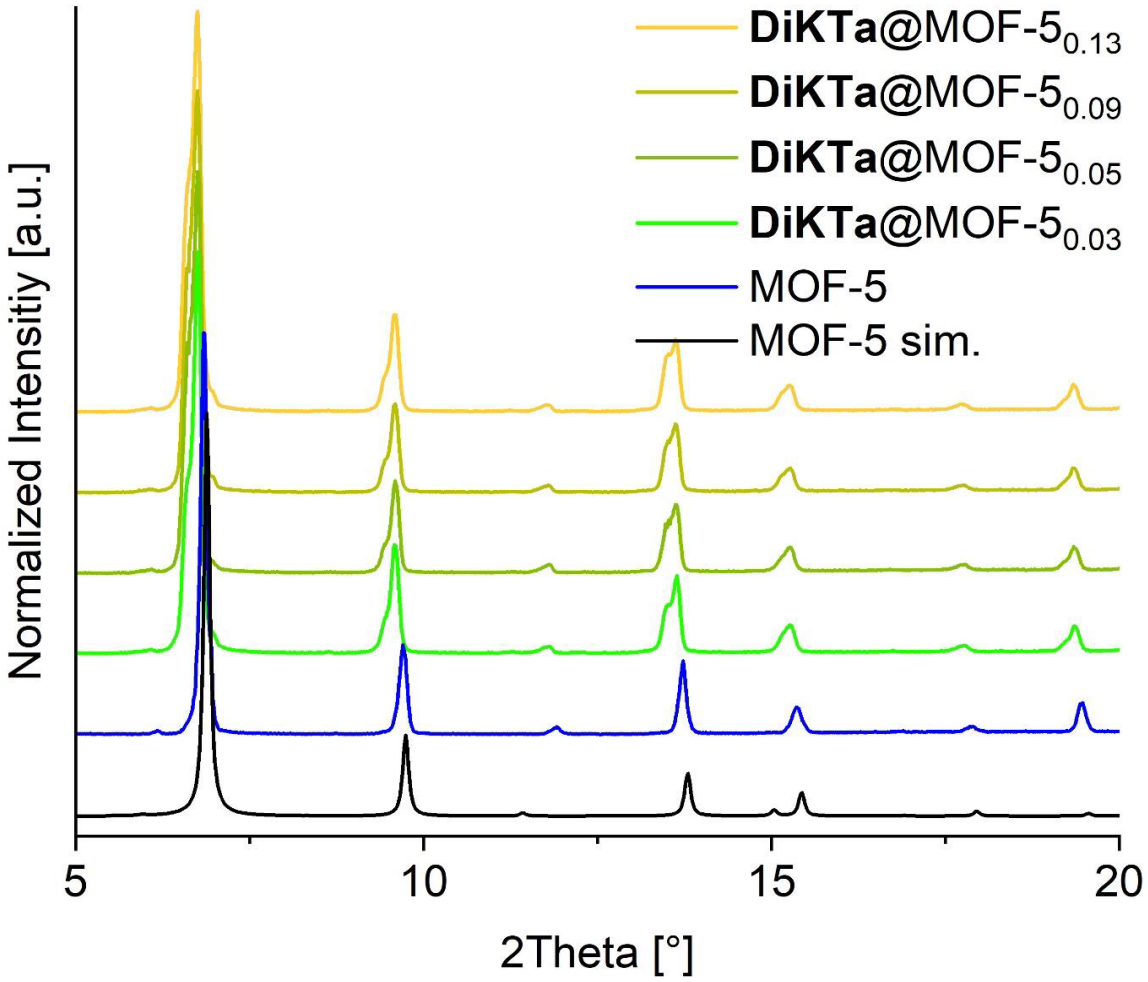

Figure 5. PXRD of MOF-5 and the **DiKTa@**MOF-5 composites produced in the range of 2 θ = 5° to 20°.

The observed shifts indicate small but measurable changes in the lattice parameters, which can be most plausibly explained by direct host-guest interactions between the incorporated DiKTa molecules and the MOF framework. These interactions appear to generate localized mechanical tension, which in turn causes a slight expansion of the pore size of the framework. The resulting increase in interplanar spacing is directly responsible for the observed shift of the diffraction peaks to lower angles. This structural change caused by the incorporation of guest molecules into the MOF framework can be described as analogous to the gate-opening mechanism in ZIF-8 or the breathing behavior characteristic of MIL-53. In all cases, the respective framework reacts to the presence of guest species by subtle or pronounced adjustments in pore size or geometry.[30] The concomitant peak broadening may be attributed to increasing structural disorder or microstrain within the MOF lattice as more DiKTa molecules are

incorporated. This disorder likely arises from the uneven occupancy of the pores, some being filled while others remain empty, which disrupts the uniformity of the framework. These observations further support the conclusion that DiKTa encapsulation involves true structural integration into the host matrix rather than mere surface adsorption. Overall, these diffraction-based observations emphasize the incorporation of guest molecules into the MOF-5 matrix and give us further indication that the encapsulation method used is a success.

Despite this low pore loading, we were able to detect significant effects of the differently loaded composites, which can be seen in Figure 4b. On the basis of N_2 adsorption measurements, it can be seen that with increasing concentration of incorporated DiKTa, the determined surface areas and pore volumes decrease drastically. For pure MOF-5 single-crystals, we were able to determine a surface area of 1973 m^2g^{-1}. However, for the highest loading of DiKTa in MOF-5, we only determined a surface area of 213 m^2g^{-1}.

Table 1. Results of nitrogen sorption measurements for MOF-5 and DiKTa@MOF-5 composites.

Compound	**DiKTa Loading [wt%]**[a]	S_{BET} **[m^2/g]**	$V_{pore\ (total)}$ **[cm^3/g]**[b]
MOF-5 literature	-	240 to 4400[31]	
MOF-5 synthesized	-	1973	0.98
DiKTa@MOF-$5_{0.03}$	0.03	965	0.71
DiKTa@MOF-$5_{0.05}$	0.05	540	0.62
DiKTa@MOF-$5_{0.09}$	0.09	499	0.58
DiKTa@MOF-$5_{0.13}$	0.13	213	0.57

[a] Calculated by UV-Vis digestion analysis. [b] Total pore volume at p/p_0 = 0.9.

The observed low nitrogen uptake indicates successful incorporation of DiKTa molecules into the MOF-5 structure. The reduced nitrogen adsorption can be attributed to the pore occupancy by the DiKTa molecules, which restrict the access of nitrogen gas to the surface. This gives us a further indication of the successful encapsulation of the dye in the MOF-5 structure (for all nitrogen sorption measurements, see ESI Figure 13).

2.3 Photophysical properties of **DiKTa**@MOF-5 composites

Photophysical properties of the composites were determined by excitation and emission measurements. As shown in Figure 5b, all synthesized composites exhibit luminescence under UV excitation that is characteristic of DiKTa at elevated concentrations or when dissolved in highly polar solvents (cf. Figure 2a and b). The recorded emission maxima are in the range of 487 to 494 nm at an ambient temperature, shown in Figure 6a.

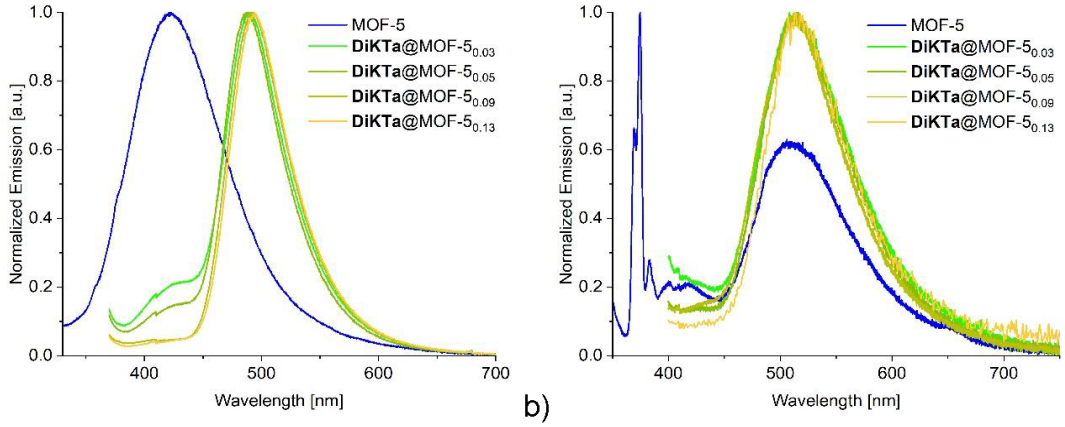

Figure 6. a) Emission spectra of MOF-5 (λ_{exc} = 290) and the **DiKTa**@MOF-5 composites (λ_{exc} = 345 nm). b) Emission spectra of MOF-5 (λ_{exc} = 325) and the **DiKTa**@MOF-5 composites at 79 K (λ_{exc} = 345 nm).

Notably, a systematic bathochromic shift of the emission maximum is observed with increasing DiKTa concentration in the composite. This concentration-dependent spectral shift, which is consistent with the behavior of DiKTa in solution, suggests the presence of intermolecular interactions between the encapsulated DiKTa molecules. Furthermore, with increasing DiKTa loading, a relative decrease in the emission contribution from the MOF-5 framework, evident in the shoulder around 420 nm, is observed. This spectral feature, typically attributed to the intrinsic luminescence of pure MOF-5, serves as an internal reference and highlights the growing dominance of DiKTa emission within the composite. The progressive reduction in the relative intensity of this MOF-5-associated emission shoulder, combined with the simultaneous increase in DiKTa emission intensity, provides clear evidence for successful incorporation and increasing concentration of DiKTa within the composite materials.

Compared to the emission maxima recorded at room temperature (cf. Figure 6a), a pronounced red shift of the emission maximum was observed at 79 K, as shown in

Figure 6b, with all composites exhibiting maxima at 515 nm, regardless of the dye concentration. This temperature-dependent shift is indicative of phosphorescence originating from the excited triplet state due to the suppression of thermal activation of reverse intersystem crossing at low temperatures. These results suggest that the photophysical behavior of DiKTa within the composites is very similar to that of the dye in solution, supporting the conclusion that the dye molecules are distributed within the MOF matrix. The resulting materials can be described by the concept of solid solution for dyes@MOFs.

We computed the probability *p* for the incorporation of a given number of DiKTa molecules per pore in MOF-5, assuming a random distribution of dyes (see Section S7). Based on the average occupation numbers estimated in the Supporting Information (Section S7), our calculations indicate that the probability *p(>1)*, of more than one DiKTa molecule per pore is consistently close to zero across all studied loading levels. This suggests that multiple occupancy per pore is highly unlikely. As a consequence, it can be inferred that DiKTa molecules are predominantly distributed as isolated guests within the MOF-5 matrix rather than forming clusters, which may favor uniform guest-host interactions and minimize excitonic coupling or self-quenching effects.

To gain a more comprehensive understanding of the integration and spatial distribution of DiKTa molecules within the MOF-5 framework, confocal laser scanning microscopy (CLSM) was performed on the synthesized single-crystal composites. The fluorescence microscope images shown in Figure 7 clearly show that the characteristic emission signal of the DiKTa dye, here in green, is present throughout the crystal structure (for all composites, see Figure 16 and 17, ESI).

a) 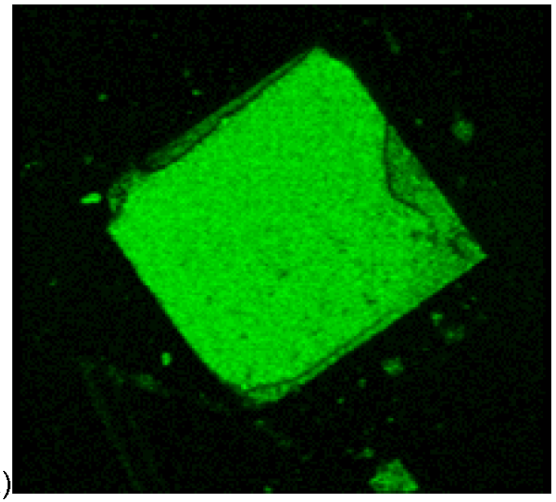 b) 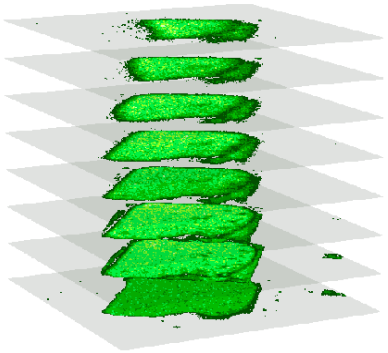

Figure 7. Confocal images of **DiKTa**@MOF-5. a) Measured single crystal viewed from above. b) stack of sectional planes of **DiKTa**@MOF-5 (cw excitation at λ_{exc} = XXX nm, λ_{em} = XXX nm). Each sectional plane represents a measurement thickness of 9.6 µm.

The uniform green coloration of the individual layers, which is visible both in the inner and outer regions of the crystals, strongly indicates a homogeneous distribution of the dye within the MOF matrix. This observation is particularly interesting because an uneven distribution or distribution limited to the surface would typically lead to irregular or peripheral fluorescence. This phenomenon is often observed in post-synthetic dye loading processes.[22d] In such cases, the dye molecules are often quickly immobilized on the outer surface or in the pores near the surface of the framework, resulting in inhomogeneous loading and incomplete penetration of the MOF material. This can have a significant impact on their photophysical properties. However, the continuous emission observed here confirms that the DiKTa molecules were successfully embedded throughout the entire crystal volume during the formation of the MOF-5 structure. This homogeneous distribution indicates that the DiKTa molecules find a consistent microenvironment within the MOF-5 pores, which is essential for the observed solid solution-like photophysical properties of the composite materials. To learn more about the spatial orientation and rotational freedom of the DiKTa dye molecules within the MOF-5 framework, we performed anisotropy measurements (Figure 8a and Figure S18). For reference, DiKTa dissolved in toluene was also investigated under identical conditions. As expected for a molecular dye in a freely diffusing liquid environment, the measurements in the solution phase, given in Figure 8b, showed no measurable anisotropy, since the unrestricted rotational movement of the DiKTa molecules leads to immediate depolarization of the emitted fluorescence. In

contrast, the anisotropy decay curves recorded for the **DiKTa**@MOF-5 composites showed a significantly slower depolarization behavior, indicating a considerably restricted freedom of rotation of the encapsulated dye molecules. Since the initial anisotropy correlates with the orientation of the crystal, the measurements also show that the dipole moment of DiKTa has a preferred orientation within the MOF pore, which is approximately 45°.

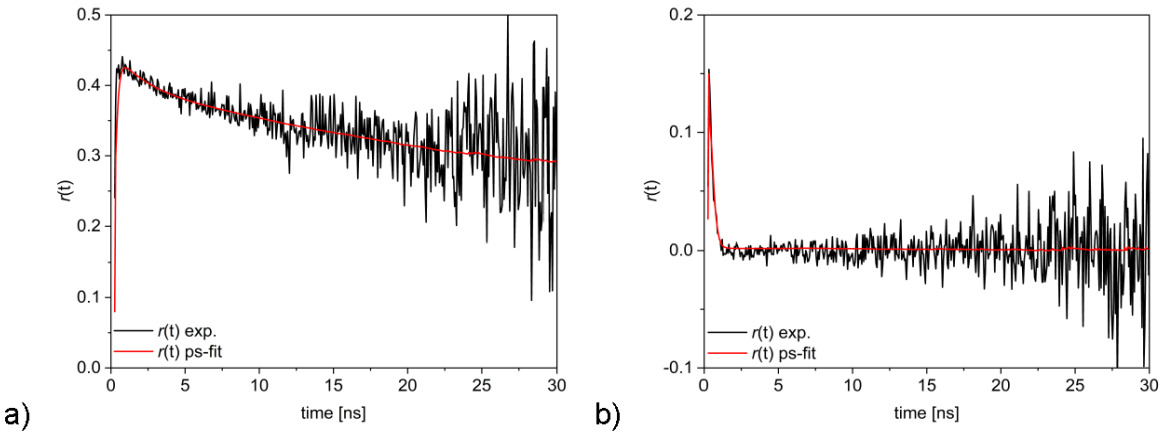

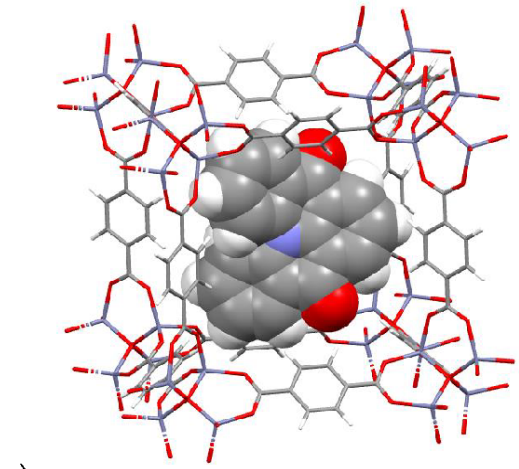

Figure 8. Time-resolved fluorescence anisotropy curves *r*(t) to resolve the fundamental anisotropy r_0 of a) **DiKTa**@MOF-$5_{0.13}$, b) DiKTa in toluene and c) Visualization of one possible structure of **DiKTA**@MOF-5. Positioning of the complex was calculated with DFT methods.

This pronounced difference strongly suggests that DiKTa molecules adopt a spatially defined, preferred orientation within the MOF-5 pore structure and that the rotational movement is sterically hindered by the restriction in the rigid, crystalline framework. This experimental observation is further supported by DFT calculations. The resulting simulation in Figure 8c shows the optimized geometry of the **DiKTa**@MOF-5 composite. It can be seen that the spatial dimensions of a single defect-free MOF-5

pore only allow the encapsulation of one single DiKTa molecule. Furthermore, the calculated optical properties—in particular the absorption and emission spectra—show a slight blue shift compared to the experimentally recorded spectra, which could be attributed to the idealized nature of the simulation model and the neglect of dynamic lattice effects and weak intermolecular interactions.

As already mentioned, a significant shift in the emission maxima was observed in all materials investigated when cooled to 79 K. It is noteworthy that even neat MOF-5 showed significant spectral changes under these conditions, with two emission maxima occurring at 380 nm and 506 nm (cf. Figure 6b). To further elucidate the photophysical behavior of DiKTa molecules in the MOF-5 matrix, we performed time-resolved luminescence measurements in addition to stationary emission spectroscopy and compared these with those of a 2 wt% DiKTa-doped PMMA polymer film, which served as a reference. The results are summarized in Table 2 (for more Information see Figures S19-S27, ESI).

Table 2. Photophysical data for DiKTa polymer film and the **DiKTa**@MOF-5 composites with λ_{exc} = 375 nm or 420 nm for the lifetime measurements at room temperature and 79 K, respectively.

Compound	λ_{exc} **[nm]**[a]	λ_{em} **[nm]**[b]	τ_p **[ns]**[c]	τ_d **[µs]**[d]	τ_p **[ns]**[e]	τ_d **[ms]**[f]
DiKTa solid	330	540 / 534	4.2	0.8	6.3	0.9
2 wt% DiKTa in PMMA	335 / 420	472 / 505	5.7	22	8.4	120
Neat MOF-5	290 / 325	422 / 506	0.65	[g]	3.7	[h]
DiKTa@MOF-$5_{0.03}$	345	487 / 514	6.1	23	5.1	151
DiKTa@MOF-$5_{0.05}$	345	488 / 514	4.9	11	4.6	93
DiKTa@MOF-$5_{0.09}$	345	492 / 515	4.7	27	4.1	48
DiKTa@MOF-$5_{0.13}$	345	494 / 513	5.7	16	5.9	19

[a] Excitation wavelength at room temperature / 79 K. [b] Wavelength of the fluorescence maximum at room temperature / 79 K. [c] Measured at 300 K (λ_{exc} = 375 nm). [d] Measured at 300 K (λ_{exc} = 420 nm). [e] Measured at 79 K (λ_{exc} = 375 nm). [f] Measured at 79 K (λ_{exc} = 420 nm). [g] Due to the emission maximum, we were unable to measure a lifetime. [h] No delayed components could be detected.

In the polymer matrix, both prompt and delayed fluorescence components were resolved at room temperature and at 79 K. Under ambient conditions, the prompt emission showed a lifetime of 5.7 ns, while the delayed component was measured at 22 µs. These values are in good agreement with the measurements from toluene solution reported in the literature.[28] A similar photophysical behavior was observed for the **DiKTa**@MOF-5 composites, with prompt fluorescence lifetimes between 4.7 and

6.1 ns. In the delayed fluorescence range, the measured lifetimes were between 11 and 27 ms, with no consistent trend with respect to the loading amount. These values are in the typical range for prompt and delayed fluorescence of DiKTa, confirming that the molecule retains its emitting properties after incorporation. The intrinsic photophysical behavior of the DiKTa molecules in both polymeric and MOF-based matrices indicates the absence of strong specific interactions, such as π–π stacking or matrix-induced quenching, between the embedded emitters and their respective host frameworks. However, a comparison of the delayed emission of the composite materials and the polymer film with that of solid DiKTa clearly shows that aggregation phenomena significantly influence the photophysical reaction in the solid state. In particular, the delayed fluorescence in the microsecond range characteristic of DiKTa is completely absent in the solid form. This suggests that strong intermolecular interactions and aggregation-induced quenching occur here, which have a significant influence on the MR-TADF behavior. At 79 K, solid DiKTa exhibits significant phosphorescence, but the observed delayed emission is characterized by a relatively short lifetime of approximately 1 ms. This contrasts sharply with the prolonged delayed fluorescence lifetime of approximately 120 ms measured for DiKTa in a PMMA polymer matrix. A comparative analysis between the 2 wt% DiKTa-doped PMMA film and the **DiKTa@**MOF-5 composites shows that all composites exhibit a significantly delayed luminescence at 79 K. It is noteworthy that the duration of the delayed emission is inversely proportional to the dye loading. With increasing loading, the lifetime of the delayed component decreases systematically. This trend, which can already be observed here at relatively low concentrations, is well known and well researched in the literature for both, MOFs and polymer films.[32] The comparison of the photophysical data of polymer films, **DiKTA@**MOF-5 composites, and DiKTa in the solid state supports the conclusion that the DiKTa molecules were successfully embedded in the MOF matrix. The observed emission properties are consistent with those of a polymer film and confirm the assumption of a solid solution. The embedded dye molecules are spatially isolated from each other within the MOF pores. To our knowledge, these results show for the first time that the concept of solid solution can be effectively extended to MR-TADF emitters in MOF environments, enabling their use in solid-state optoelectronics without the typical disadvantages of dye aggregation.

3. Conclusion

In this study, we report, to the best of our knowledge, the first successful incorporation of an MR-TADF called DiKTa into MOF-5 single crystals. Structural characterizations using PXRD and N_2 adsorption measurements showed that the presence of DiKTa leads to a slight expansion of the MOF lattice and a significant reduction in surface area, indicating partial pore occupation and a guest-host interaction. Photophysical investigations, including steady-state spectroscopy and time-resolved spectroscopy, showed a homogeneous distribution of DiKTa in the MOF crystals as well as restricted rotational freedom and a preferred spatial orientation within the framework. These experimental results were further supported by a DFT simulation, which provided insights into the spatial confinement of the emitter and the MOF matrix. Comparison of the photophysical behavior of the MOF composites with DiKTa-doped polymer films revealed analogous emission characteristics, particularly with regard to delayed fluorescence, supporting the conclusion that DiKTa behaves as a solid solution within the MOF matrix. This work not only establishes a framework for embedding MR-TADF materials in crystalline porous host materials but also highlights the potential of such composites for integration into next-generation optoelectronic solid-state devices.

References

[1] D. Hellwinkel and M. Melan, *Chemische Berichte-Recueil* **1971**, *104*, 1001-+.

[2] a) C. W. Tang and S. A. Vanslyke, *Applied Physics Letters* **1987**, *51*, 913-915; b) G. Mandal, J. Bauri and R. B. Choudhary, *Materials Science and Engineering B-Advanced Functional Solid-State Materials* **2024**, *303*; c) M. A. Baldo, S. Lamansky, P. E. Burrows, M. E. Thompson and S. R. Forrest, *Applied Physics Letters* **1999**, *75*, 4-6.

[3] a) M. Cocchi, J. Kalinowski, D. Virgili and J. A. G. Williams, *Applied Physics Letters* **2008**, *92*; b) T. Fleetham, G. J. Li and J. Li, *Acs Applied Materials & Interfaces* **2015**, *7*, 16240-16246; c) D. H. Kim, N. S. Cho, H. Y. Oh, J. H. Yang, W. S. Jeon, J. S. Park, M. C. Suh and F. H. Kwon, *Advanced Materials* **2011**, *23*, 2721-2726.

[4] a) C. A. Parker and C. G. Hatchard, *Transactions of the Faraday Society* **1961**, *57*, 1894-&; b) A. Maciejewski, M. Szymanski and R. P. Steer, *Journal of Physical Chemistry* **1986**, *90*, 6314-6318; c) A. Endo, M. Ogasawara, A. Takahashi, D. Yokoyama, Y. Kato and C. Adachi, *Adv Mater* **2009**, *21*, 4802-4806; d) A. Endo, K. Sato, K. Yoshimura, T. Kai, A. Kawada, H. Miyazaki and C. Adachi, *Applied Physics Letters* **2011**, *98*; e) Q. Wei, N. N. Fei, A. Islam, T. Lei, L. Hong, R. X. Peng, X. Fan, L. Chen, P. Q. Gao and Z. Y. Ge, *Advanced Optical Materials* **2018**, *6*.

[5] a) Y. Gao, T. Su, L. Zhao, Y. Geng, Y. Wu, M. Zhang and Z. M. Su, *Organic Electronics* **2017**, *50*, 70-76; b) Y. Gao, C. L. Sun and T. Su, *Journal of Molecular Structure* **2023**, *1272*; c) Y. Yuan, Y. Hu, Y. X. Zhang, J. D. Lin, Y. K. Wang, Z. Q. Jiang, L. S. Liao and S. T. Lee, *Advanced Functional Materials* **2017**, *27*; d) H. Uoyama, K. Goushi, K. Shizu, H. Nomura and C. Adachi, *Nature* **2012**, *492*, 234-+.

[6] a) G. Mehes, H. Nomura, Q. Zhang, T. Nakagawa and C. Adachi, *Angew Chem Int Ed Engl* **2012**, *51*, 11311-11315; b) H. Nakanotani, Y. Tsuchiya and C. Adachi, *Chemistry Letters* **2021**, *50*, 938-948.

[7] a) P. Data, P. Pander, M. Okazaki, Y. Takeda, S. Minakata and A. P. Monkman, *Angewandte Chemie-International Edition* **2016**, *55*, 5739-5744; b) D. Püschel, J. Wiefermann, S. Hédé, T. Heinen, L. Pfeifer, O. Weingart, M. Suta, T. J. J. Müller and C. Janiak, *Journal of Materials Chemistry C* **2023**, *11*, 8982-8991; c) D. Y. Chen, W. Liu, C. J. Zheng, K. Wang, F. Li, S. L. Tao, X. M. Ou and X. H. Zhang, *Acs Applied Materials & Interfaces* **2016**, *8*, 16791-16798.
[8] T. Hatakeyama, K. Shiren, K. Nakajima, S. Nomura, S. Nakatsuka, K. Kinoshita, J. Ni, Y. Ono and T. Ikuta, *Adv Mater* **2016**, *28*, 2777-2781.
[9] a) X. Qiu, G. J. Tian, C. W. Lin, Y. Y. Pan, X. Y. Ye, B. H. Wang, D. G. Ma, D. H. Hu, Y. Luo and Y. G. Ma, *Advanced Optical Materials* **2021**, *9*; b) S. M. Suresh, L. Zhang, D. Hall, C. F. Si, G. Ricci, T. Matulaitis, A. M. Z. Slawin, S. Warriner, Y. Olivier, I. D. W. Samuel and E. Zysman-Colman, *Angewandte Chemie-International Edition* **2023**, *62*; c) S. Wu, L. Zhang, J. Wang, A. Kumar Gupta, I. D. W. Samuel and E. Zysman-Colman, *Angew Chem Int Ed Engl* **2023**, *62*, e202305182.
[10] a) E. Hamzehpoor and D. F. Perepichka, *Angewandte Chemie-International Edition* **2020**, *59*, 9977-9981; b) X. Liang, Z. P. Yan, H. B. Han, Z. G. Wu, Y. X. Zheng, H. Meng, J. L. Zuo and W. Huang, *Angewandte Chemie-International Edition* **2018**, *57*, 11316-11320; c) S. Nakatsuka, H. Gotoh, K. Kinoshita, N. Yasuda and T. Hatakeyama, *Angewandte Chemie-International Edition* **2017**, *56*, 5087-5090; d) Y. Tsuchiya, Y. Ishikawa, S. H. Lee, X. K. Chen, J. L. Brédas, H. Nakanotani and C. Adachi, *Advanced Optical Materials* **2021**, *9*.
[11] a) C. Janiak and J. K. Vieth, *New Journal of Chemistry* **2010**, *34*, 2366-2388; b) A. Kirchon, L. Feng, H. F. Drake, E. A. Joseph and H. C. Zhou, *Chemical Society Reviews* **2018**, *47*, 8611-8638; c) H. C. Zhou, J. R. Long and O. M. Yaghi, *Chemical Reviews* **2012**, *112*, 673-674.
[12] I. M. Hönicke, I. Senkovska, V. Bon, I. A. Baburin, N. Bönisch, S. Raschke, J. D. Evans and S. Kaskel, *Angewandte Chemie-International Edition* **2018**, *57*, 13780-13783.
[13] a) J. Lippke, B. Brosent, T. von Zons, E. Virmani, S. Lilienthal, T. Preusse, M. Hulsmann, A. M. Schneider, S. Wuttke, P. Behrens and A. Godt, *Inorg Chem* **2017**, *56*, 748-761; b) I. Senkovska, F. Hoffmann, M. Fröba, J. Getzschmann, W. Böhlmann and S. Kaskel, *Microporous and Mesoporous Materials* **2009**, *122*, 93-98; c) M. Eddaoudi, J. Kim, N. Rosi, D. Vodak, J. Wachter, M. O'Keeffe and O. M. Yaghi, *Science* **2002**, *295*, 469-472; d) J. H. Cavka, S. Jakobsen, U. Olsbye, N. Guillou, C. Lamberti, S. Bordiga and K. P. Lillerud, *J Am Chem Soc* **2008**, *130*, 13850-13851.
[14] a) K. S. Park, Z. Ni, A. P. Cote, J. Y. Choi, R. Huang, F. J. Uribe-Romo, H. K. Chae, M. O'Keeffe and O. M. Yaghi, *Proc Natl Acad Sci U S A* **2006**, *103*, 10186-10191; b) W. Gong, H. M. Xie, K. B. Idrees, F. A. Son, Z. J. Chen, F. R. Sha, Y. Liu, Y. Cui and O. K. Farha, *Journal of the American Chemical Society* **2022**, *144*, 1826-1834.
[15] a) X. B. Xu, Y. Lu, Y. Yang, F. Nosheen and X. Wang, *Science China-Materials* **2015**, *58*, 370-377; b) Y. Liu, S. Liu, D. He, N. Li, Y. Ji, Z. Zheng, F. Luo, S. Liu, Z. Shi and C. Hu, *J Am Chem Soc* **2015**, *137*, 12697-12703.
[16] a) W. Q. Fan, K. Liang and J. Y. Liang, *Journal of Materials Chemistry A* **2024**, *12*, 30318-30328; b) T. O. Knedel, E. Ricklefs, C. Schlusener, V. B. Urlacher and C. Janiak, *ChemistryOpen* **2019**, *8*, 1337-1344; c) Y. L. Weng, R. Chen, Y. Hui, D. Chen and C. X. Zhao, *Chem & Bio Engineering* **2024**, *1*, 99-112.
[17] a) S. L. Li, Z. X. Zhou, G. Q. Liu, Q. Zhang, Y. F. Gao, H. Zhu and S. P. Zhu, *Chemical Engineering Journal* **2024**, *493*; b) X. C. Li, Z. H. Zhang, W. M. Xiao, S. J. Deng, C. Chen and N. Zhang, *Journal of Materials Chemistry A* **2019**, *7*, 14504-14509; c) S. Rojas, F. J. Carmona, C. R. Maldonado, P. Horcajada, T. Hidalgo, C. Serre, J. A. R. Navarro and E. Barea, *Inorganic Chemistry* **2016**, *55*, 2650-2663; d) H. Q. Zheng, Y. N. Zhang, L. F. Liu, W. Wan, P. Guo, A. M. Nyström and X. D. Zou, *Journal of the American Chemical Society* **2016**, *138*, 962-968.
[18] a) C. C. Cao, C. X. Chen, Z. W. Wei, Q. F. Qiu, N. X. Zhu, Y. Y. Xiong, J. J. Jiang, D. W. Wang and C. Y. Su, *Journal of the American Chemical Society* **2019**, *141*, 2589-2593; b) C. Empel, M. N. A. Fetzer, S. Sasmal, T. Strothmann, C. Janiak and R. M. Koenigs, *Chemical Communications* **2024**, *60*, 7327-7330; c) G. Cai and H. L. Jiang, *Angew Chem Int Ed Engl* **2017**, *56*, 563-567.
[19] a) X. Wu, Z. Bao, B. Yuan, J. Wang, Y. Sun, H. Luo and S. Deng, *Microporous and Mesoporous Materials* **2013**, *180*, 114-122; b) J. Dechnik, A. Nuhnen and C. Janiak, *Crystal Growth & Design* **2017**,

17, 4090-4099; c) F. Wang, Z. Wang, J. J. Yu, S. Han, X. W. Li and Y. Wang, *Separation and Purification Technology* **2024**, *333*.
[20] a) S. Gökpinar, S. J. Ernst, E. Hastürk, M. Möllers, I. El Aita, R. Wiedey, N. Tannert, S. Niessing, S. Abdpour, A. Schmitz, J. Quodbach, G. Füldner, S. K. Henninger and C. Janiak, *Industrial & Engineering Chemistry Research* **2019**, *58*, 21493-21503; b) H. Babaei, A. J. H. McGaughey and C. E. Wilmer, *Chemical Science* **2017**, *8*, 583-589; c) H. Babaei, M. E. DeCoster, M. Jeong , Z. M. Hassan, T. Islamoglu, H. Baumgart, A. J. H. McGaughey, E. Redel, O. K. Farha, P. E. Hopkins, J. A. Malen and C. E. Wilmer, *Nature Communications* **2020**, *11*.
[21] a) Y. Gao, F. Wang, J. Tang, C. C. Wang, X. H. Yi, Y. W. Wei, G. C. Liu, P. Wang, H. F. Fu, C. Zhao, X. C. Qiu and S. L. Yi, *Chemical Engineering Journal* **2024**, *495*; b) N. Prasetya and C. Wöll, *Rsc Advances* **2023**, *13*, 22998-23009; c) K. L. Shi, H. H. Su, K. K. Liu, Y. T. Zhang and J. Y. Zhu, *Separation and Purification Technology* **2025**, *357*.
[22] a) C. Z. Wang, J. Chen, Q. H. Li, G. E. Wang, X. L. Ye, J. Lv and G. Xu, *Angewandte Chemie-International Edition* **2023**, *62*; b) M. B. Kanakala, S. A. Bhat, A. Kumar and C. V. Yelamaggad, *Acs Applied Optical Materials* **2025**; c) S. L. Z. Jiokeng, T. J. M. M. Ntep, M. N. A. Fetzer, T. Strothmann, C. G. Fotsop, I. K. Tonle and C. Janiak, *Acs Applied Materials & Interfaces* **2024**, *16*, 2509-2521; d) T. O. Knedel, S. Buss, I. Maisuls, C. G. Daniliuc, C. Schlusener, P. Brandt, O. Weingart, A. Vollrath, C. Janiak and C. A. Strassert, *Inorg Chem* **2020**, *59*, 7252-7264.
[23] a) Z. Wang, C. Y. Zhu, J. T. Mo, P. Y. Fu, Y. W. Zhao, S. Y. Yin, J. J. Jiang, M. Pan and C. Y. Su, *Angewandte Chemie-International Edition* **2019**, *58*, 9752-9757; b) X. Y. Liu, K. Xing, Y. Li, C. K. Tsung and J. Li, *Journal of the American Chemical Society* **2019**, *141*, 14807-14813; c) U. Ryu, H. S. Lee, K. S. Park and K. M. Choi, *Polyhedron* **2018**, *154*, 275-294.
[24] Y. J. Cui, T. Song, J. C. Yu, Y. Yang, Z. Y. Wang and G. D. Qian, *Advanced Functional Materials* **2015**, *25*, 4796-4802.
[25] N. Zhang, D. Zhang, J. Zhao and Z. Xia, *Dalton Trans* **2019**, *48*, 6794-6799.
[26] C. S. Tsao, M. S. Yu, T. Y. Chung, H. C. Wu, C. Y. Wang, K. S. Chang and H. L. Chen, *J Am Chem Soc* **2007**, *129*, 15997-16004.
[27] J. E. Field and D. Venkataraman, *Chemistry of Materials* **2002**, *14*, 962-+.
[28] D. Hall, S. M. Suresh, P. L. dos Santos, E. Duda, S. Bagnich, A. Pershin, P. Rajamalli, D. B. Cordes, A. M. Z. Slawin, D. Beljonne, A. Köhler, I. D. W. Samuel, Y. Olivier and E. Zysman-Colman, *Advanced Optical Materials* **2020**, *8*.
[29] S. B. Han, Y. H. Wei, C. Valente, I. Lagzi, J. J. Gassensmith, A. Coskun, J. F. Stoddart and B. A. Grzybowski, *Journal of the American Chemical Society* **2010**, *132*, 16358-16361.
[30] a) T. Chokbunpiam, S. Fritzsche, C. Chmelik, J. Caro, W. Janke and S. Hannongbua, *Chemical Physics Letters* **2016**, *648*; b) F. Salles, A. Ghoufi, G. Maurin, R. G. Bell, C. Mellot-Draznieks and G. Ferey, *Angew Chem Int Ed Engl* **2008**, *47*, 8487-8491.
[31] a) K. K. Gangu, S. Maddila and S. B. Jonnalagadda, *Rsc Advances* **2022**, *12*, 14282-14298; b) M. Eddaoudi, H. L. Li, T. Reineke, M. Fehr, D. Kelley, T. L. Groy and O. M. Yaghi, *Topics in Catalysis* **1999**, *9*, 105-111.
[32] a) M. H. Ni, M. Gong, X. Li, J. L. Gu, B. Li and Y. Chen, *Applied Materials Today* **2021**, *23*; b) V. Glembockyte, M. Frenette, C. Mottillo, A. M. Durantini, J. Gostick, V. Strukil, T. Friscic and G. Cosa, *Journal of the American Chemical Society* **2018**, *140*, 16882-16887; c) R. Luchowski, S. Sabnis, M. Szabelski, P. Sarkar, S. Raut, Z. Gryczynski, J. Borejdo, P. Bojarski and I. Gryczynski, *Journal of Luminescence* **2010**, *130*, 2446-2451.

Electronic Supporting Information

Luminescent Crystals: MR-TADF emitter DiKTa inside of metal-organic framework MOF-5

Marcus N. A. Fetzer,‡[a] Annette Vollrath,‡[a] Jennifer Kremper,‡[d] Benedikt Bendel,[b] Ralf Kühnemuth,[c] Markus Suta,[b] Oliver Weingart,*[d] Jan Meisner,*[d] and Christoph Janiak*[a]

[a]Inorganic and Structural Chemistry, Heinrich Heine University Düsseldorf, Universitätsstraße 1, D-40225 Düsseldorf, Germany

[b]Inorganic Photoactive Materials, Heinrich Heine University Düsseldorf, Universitätsstraße 1, D-40225 Düsseldorf, Germany

[c]Molecular Physical Chemistry, Heinrich Heine University Düsseldorf, Universitätsstraße 1, D-40225 Düsseldorf, Germany

[d]Theoretical and Computational Chemistry, Heinrich Heine University Düsseldorf, Universitätsstraße 1, D-40225 Düsseldorf, Germany

‡ These authors contributed equally to this work.

* Corresponding authors

Table of Contents

S1. General Information

Unless otherwise noted, all commercially available compounds were used as provided without further purification. Solvents used in reactions were p. A. grade. Solvents for ambient pressure column chromatography for the preparative purification of synthesis products were technical grade and distilled prior to use. Column chromatography was performed using silica gel Merck 60 (particle size 0.063 – 0.2 mm). Solvent mixtures are understood as volume/volume. Analytical thin-layer chromatography (TLC) was performed on Macherey-Nagel silica gel aluminium plates with F-254 indicator, visualized by irradiation with UV light (λ_{exc} = 254 or 365 nm). ^{1}H-NMR and ^{13}C-NMR were recorded on a Bruker Avance III 300 MHz NMR spectrometer in $CDCl_3$. Data are reported in the following order: chemical shift (δ) in ppm; multiplicities are indicated s (singlet), d (doublet), t (triplet), q (quartet), m (multiplet). ^{1}H-NMR chemical shifts are referenced to the residual proton solvent signal versus TMS (δ($CHCl_3$ = 7.26)). ^{13}C-NMR chemical shifts are referenced to the carbon solvent signal versus TMS (δ($CHCl_3$ = 77.2)). EI-MS was measured on a JOEL JMS-Q1600GC. HR-ESI-MS was measured on a Bruker Daltonics UHR-QTOF maXis 4G. All measurements were done on positive ion mode. Powder X-ray diffraction (PXRD) analysis was conducted at ambient temperature on a Rigaku Miniflex 600 powder diffractometer using Cu Kα1 radiation with λ = 1.5406 Å (40 kV, 15 mA, 600 W) in the range of 2 θ = 2°– 50° and a flat silicon low background with a small indent. N_2 sorption isotherms were obtained with a Belsorp MAXII high-precision gas/vapor adsorption measurement instrument at 77 K. Optical measurements were carried out on a FS5 photoluminescence spectrometer (Edinburgh Instruments) or on a FLS1000 photoluminescence spectrometer (Edinburgh Instruments) equipped with a 450 W Xe arc lamp, double grating monochromators (Czerny-Turner) in excitation and emission compartment and a thermoelectrically cooled PMT-980 detector (Hamamatsu).

S2. Sources of chemicals

Reagent	Manufacturer
Aniline	ACROS Organics
Methyl 2-iodobenzoate	BLDpharm
Copper(I) iodide	Alfa Aesar
Potassium carbonate	Fisher Chemical
Copper powder	Laboratory stock
Dibutyl ether	Sigma-Aldrich
Dimethyldormamide (DMF)	Fisher Chemical
Magnesium sulfate	VWR Chemicals
Sodium hydroxide	Fisher Chemical
HCl (37%)	Sigma-Aldrich
Thionyl chloride	Thermo Scientific
Aluminium chloride	TCI Chemicals
Dichloromethane (DCM)	Sigma-Aldrich
Diethylformamide (DEF)	TCI Chemicals
Zinc nitrate hexahydrate	Roth
Terephthalic acid (H_2BDC)	Alfa Aesar

S3. Synthesis of DiKTa

3.1 Synthesis of dimethyl 2,2'-(phenylazanediyl)dibenzoate 1

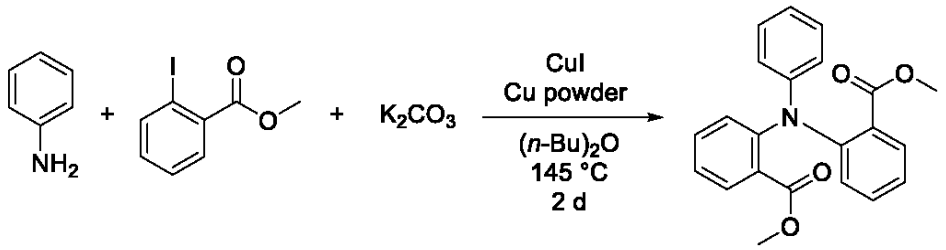

1 Yield: 76 %

Freshly distilled aniline was used for the synthesis. The synthesis was carried out according to the instructions of J. E. Field *et al.*[1]

In a 100 ml three-necked round-bottom flask equipped with a stirring bar and a reflux condenser, 2.28 mL of aniline (25 mmol), 11.2 mL of methyl 2-iodobenzoate (76.2 mmol), 10.5 g of K_2CO_3 (76.2 mmol), 500 mg of Cu powder (7.87 mmol), and 320 mg of CuI (1.68 mmol) were placed under a nitrogen atmosphere. 40 mL of dibutyl ether were added and the reaction mixture was heated to 145 °C for 48 h. The mixture was filtered through celite and the remaining product was washed from the filter with 500 mL of DCM. The filtrate was concentrated under vacuum. The crude product was purified by column chromatography on silica using a 4:1 mixture of cyclohexane and ethyl acetate as eluent. The resulting solid was washed with hot ethanol to yield 6.87 g (76 %) of pure product.

^{1}H-NMR (300 MHz, $CDCl_3$): δ = 7.65 (dd, *J* = 7.7, 1.2 Hz, 2H), 7.41 (ddd, J = 8.1, 7.3, 1.7 Hz, 2H), 7.20-7.10 (m, 6H), 6.90-6.82 (m, 1H), 6.78-6.74 (m, 2H), 3.39 (s, 6H) ppm (Figure S1).

^{13}C-NMR (75 MHz, $CDCl_3$): δ = 168.0, 148.6, 146.6, 132.8, 131.1, 129.1, 128.8, 128.0, 124.1, 121.9, 120.8, 51.9 ppm (Figure S2).

The data is in accordance with the literature.[1-2]

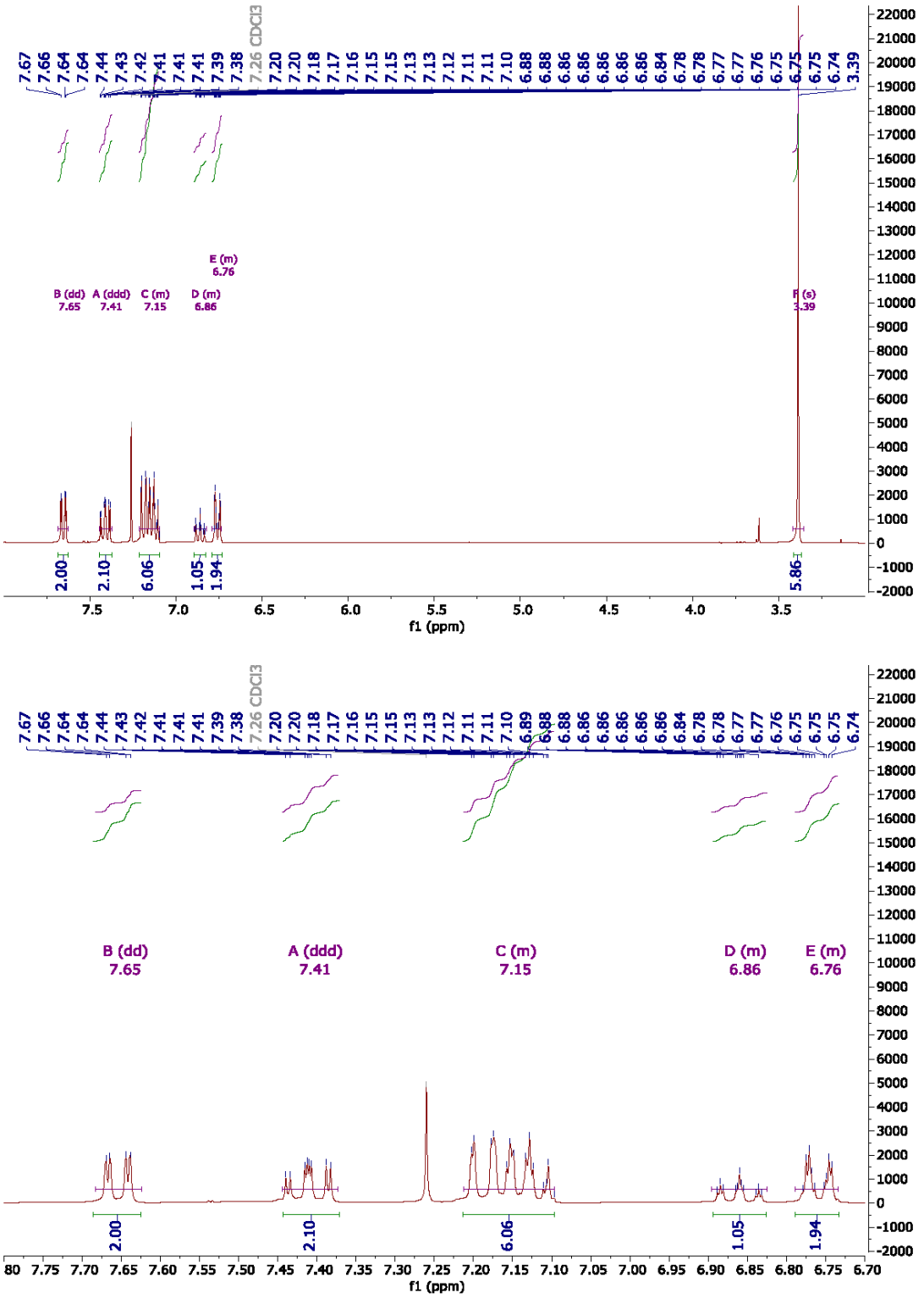

Figure S1. ^{1}H-NMR (300 MHz) of **1** in $CDCl_3$.

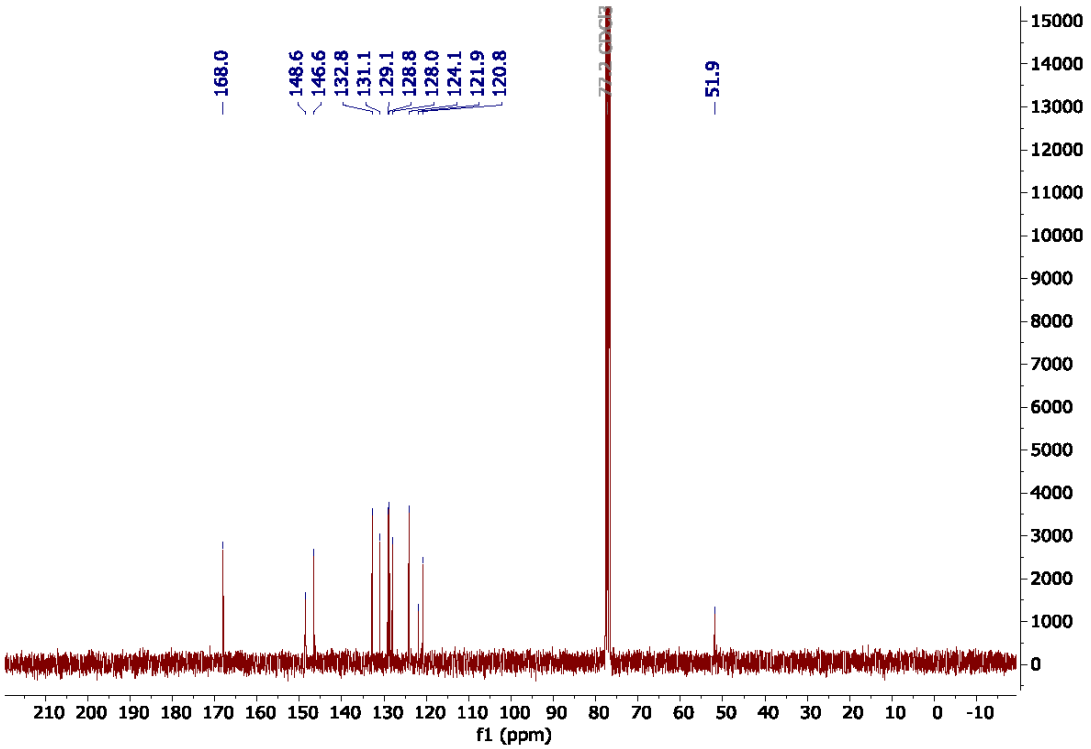

Figure S2. ^{13}C-NMR (75 MHz) of **1** in $CDCl_3$.

3.2 Synthesis of DiKTa

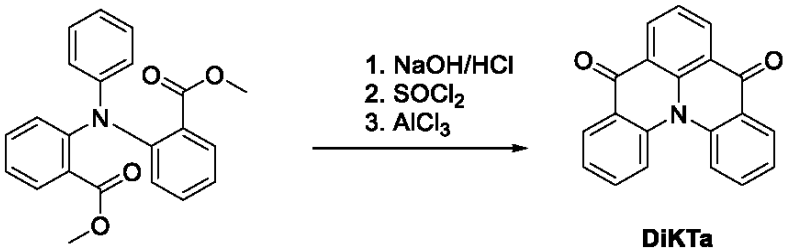

DiKTa
Yield: 82 %

The synthesis was carried out according to the instructions of D. Hall *et al.*[2]

Product **1** (5.0 g, 13.8 mmol) was combined with an excess of sodium hydroxide in a mixture of ethanol and water (1:1) with a total volume of 60 ml. The reaction was heated under reflux for 16 hours. After cooling to room temperature, the mixture was acidified with hydrochloric acid to precipitate the diacid. After filtration, the product was washed three times with 25 ml of distilled water and dried overnight in a vacuum oven at 60 °C (4.34 g, 94% yield). The product was used for the next step without further purification or characterization.

Under a nitrogen atmosphere, the diacid (2.0 g, 6 mmol) was dispersed in 50 mL DCM and 1.0 mL of thionyl chloride (13.7 mmol) and 4 drops of DMF were added successively. The reaction

mixture was refluxed for 3 hours and then cooled to room temperature. Under a nitrogen counterflow, 8 g of aluminum chloride (60 mmol) was slowly added and refluxed for another 4 hours. The reaction mixture was then cooled to 0 °C in an ice bath and the reaction was quenched by adding water dropwise under vigorous stirring. The reaction was extracted with 50 mL DCM, the organic phase was washed three times with 50 mL water, and then dried over magnesium sulfate. After removing the excess solvent, the crude product was purified by column chromatography using a 1:1 mixture of cyclohexane and ethyl acetate. The resulting product is a yellow crystalline solid (1.55 g, 87% yield). Yield from product **1**: 82%, overall: 62%.

^{1}H-NMR (300 MHz, $CDCl_3$): δ = 8.74 (d, *J* = 7.6 Hz, 1H), 8.49 (dd, *J* = 7.9, 1.2 Hz, 1H), 8.14 (d, *J* = 8.0 Hz, 0H), 7.74 – 7.61 (m, 2H), 7.49 (ddd, *J* = 8.0, 7.1, 1.0 Hz, 1H) ppm (Figure S3).

^{13}C-NMR (75 MHz, $CDCl_3$): δ = 178.7, 139.9, 139.4, 133.0, 132.8, 127.9, 126.6, 125.3, 123.7, 120.4 ppm (Figure S4).

EI-MS: m/z = 297 $[M]^+$, 269 $[M\text{-}CO]^+$, 241 $[M\text{-}C_2O_2]^+$ (Figure S5).

HR-ESI-MS: $[M+H]^+$ Calculated ($C_{20}H_{12}NO_2$) 298.0863; Found 298.0859 (Figure S6).

The data is in accordance with the literature.[1-2]

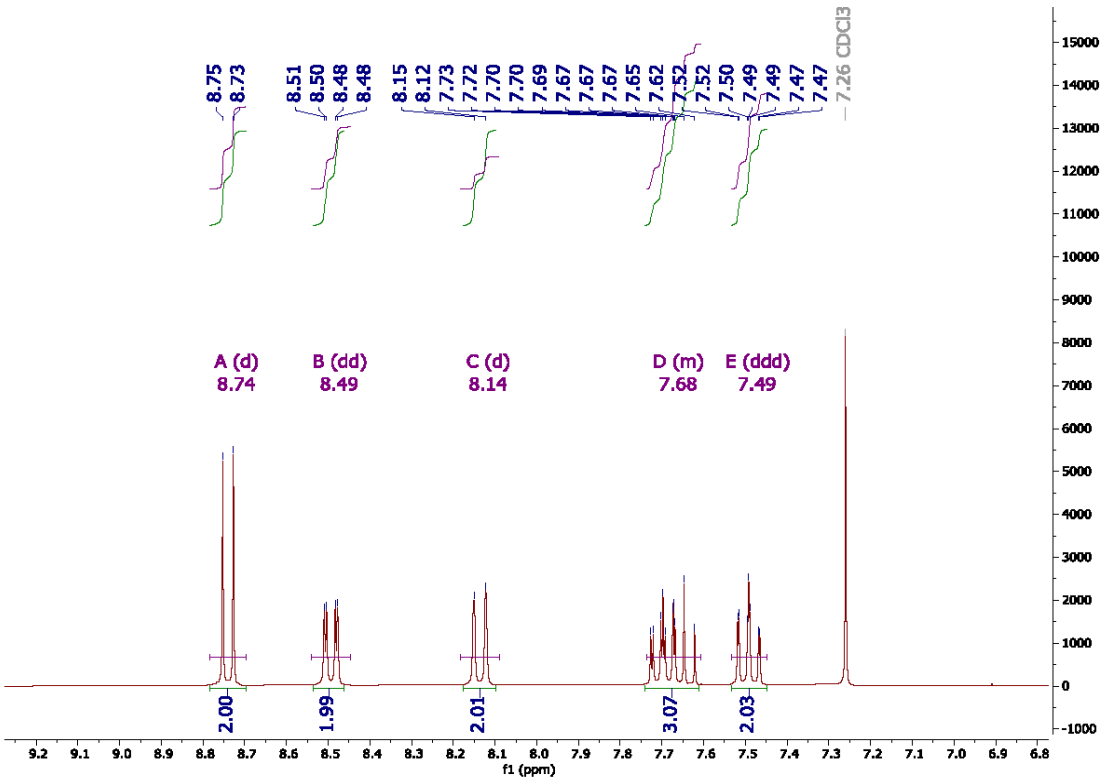

Figure S3. ^{1}H-NMR (300 MHz) of DiKTa in $CDCl_3$.

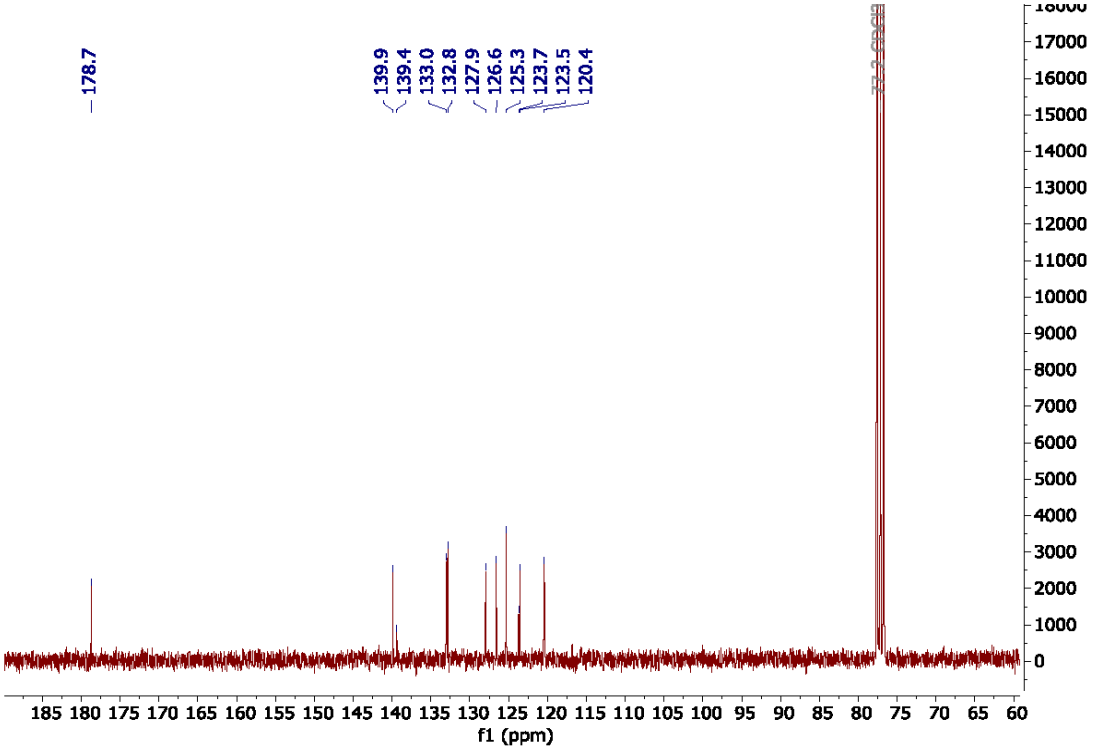

Figure S4. ^{13}C-NMR (75 MHz) of DiKTa in $CDCl_3$.

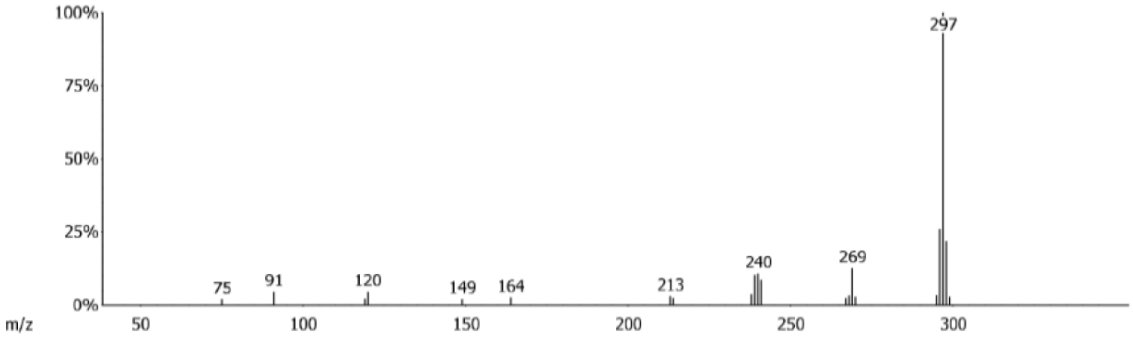

Figure S5. EI-MS of DiKTa.

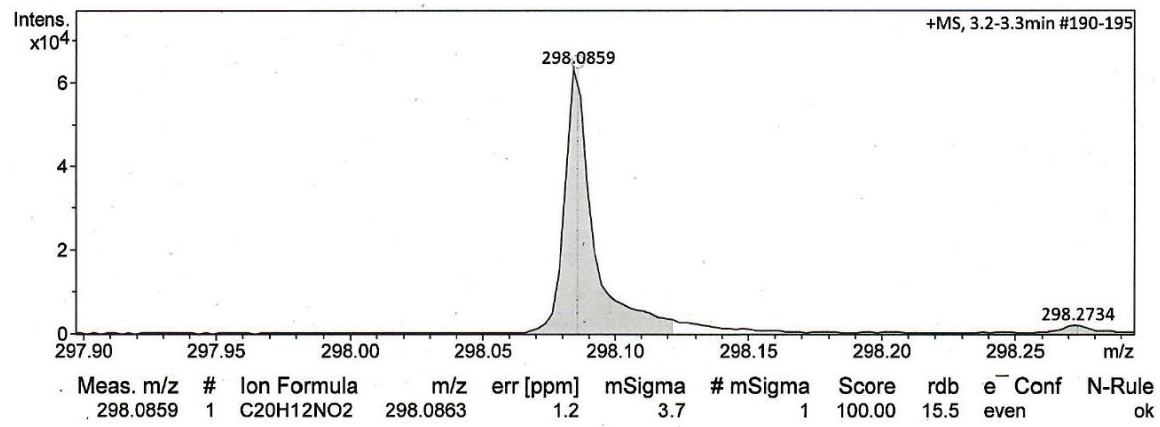

Figure S6. HR-ESI-MS of DiKTa.

S4. Photophysical properties of DiKTa

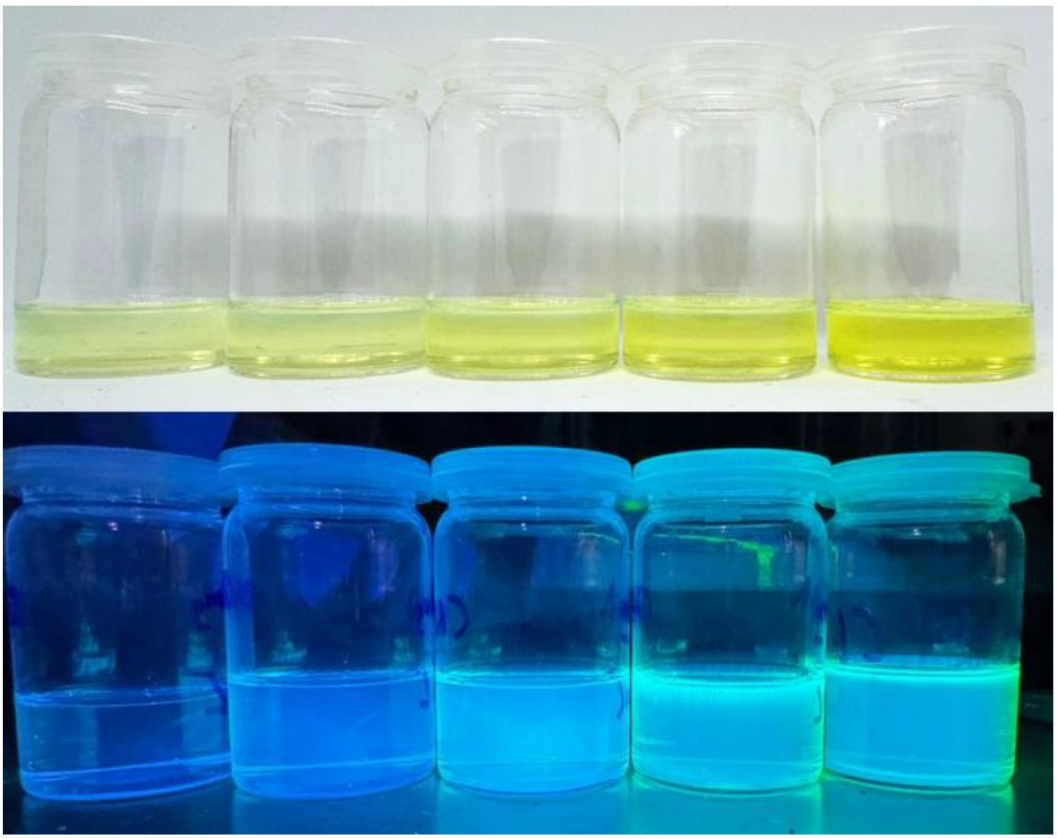

Figure S7. Increasing concentrations of DiKTa in $CHCl_3$ under daylight (top) and UV-light (λ_{exc} = 365 nm, bottom). Concentration from left to right 0.001 g/L, 0.01 g/L, 0.1 g/L, 1 g/L, and 5 g/L.

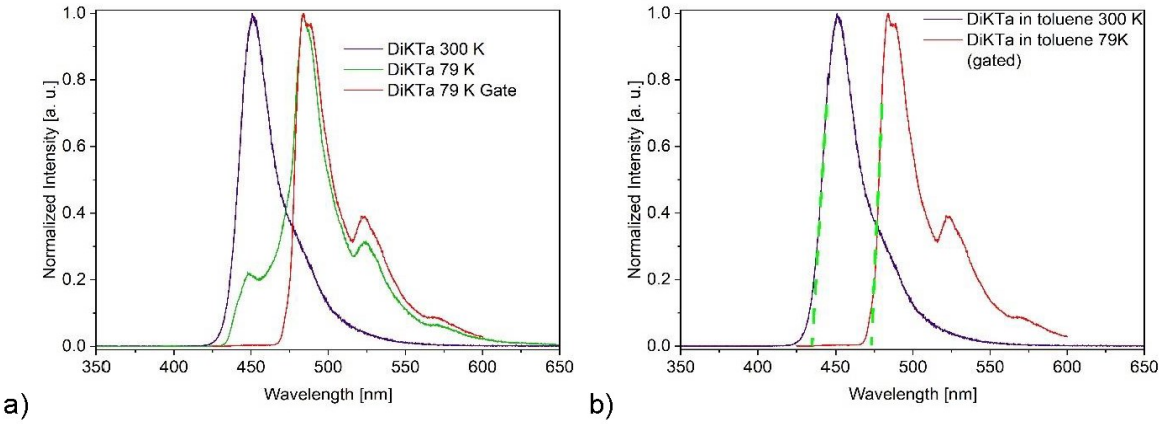

a) b)

Figure 8. a) DiKta in toluene at 300 K (λ_{exc} = 335 nm), 79 K (λ_{exc} = 335 nm), and 79 K. after 10 ms for 10 ms (λ_{exc} = 420 nm). b) Onset (green dotted line) of the steady state spectrum at 300 K and 79 K for the determination of ΔE_{ST}.

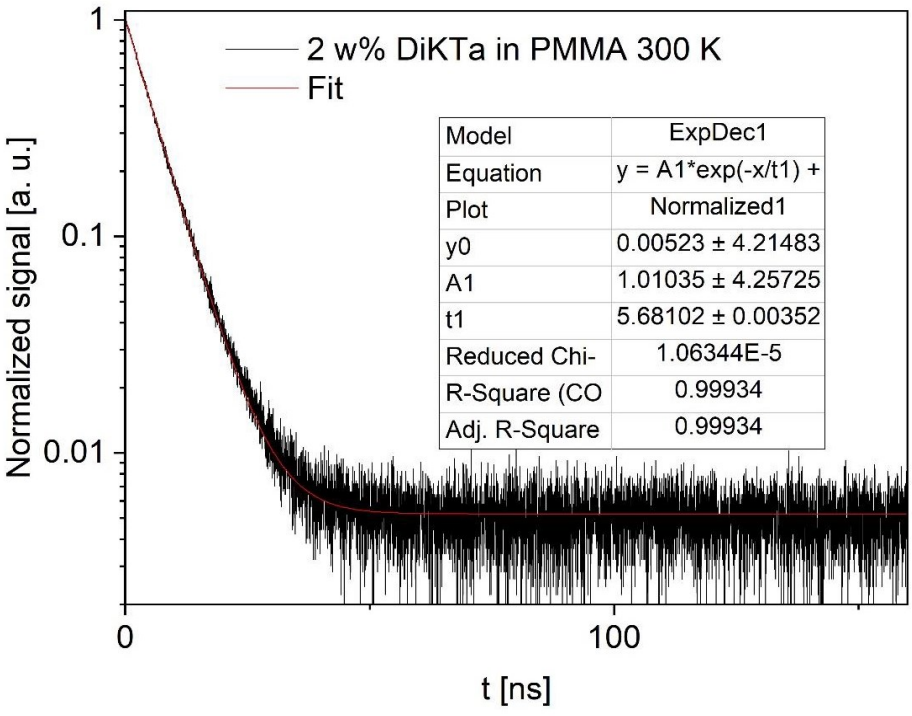

a)

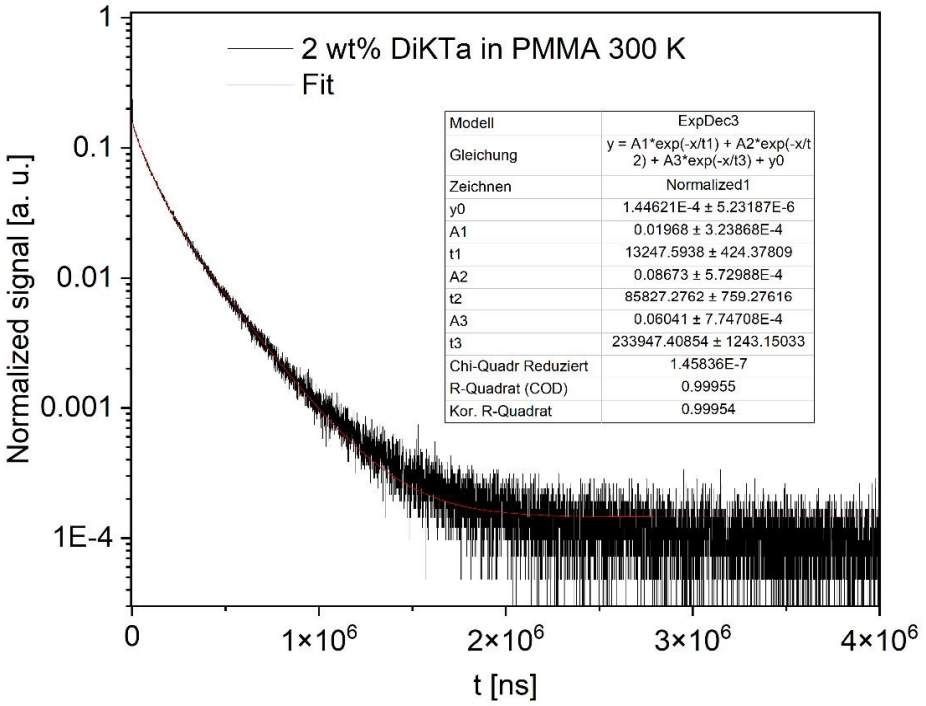

b)

Figure S9. a) prompt and b) delayed time-resolved photoluminescence decay (black) of the DiKTa in PMMA at 300 K with the respective exponential fitting parameters including pre-exponential factors A_i, lifetimes t_i, and confidence limits.

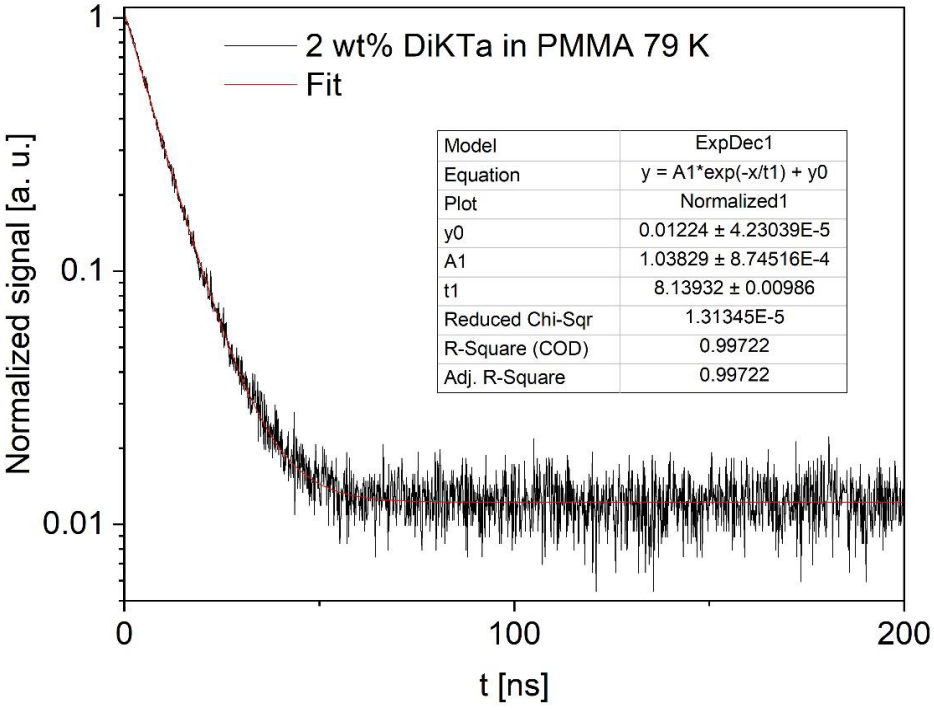

a)

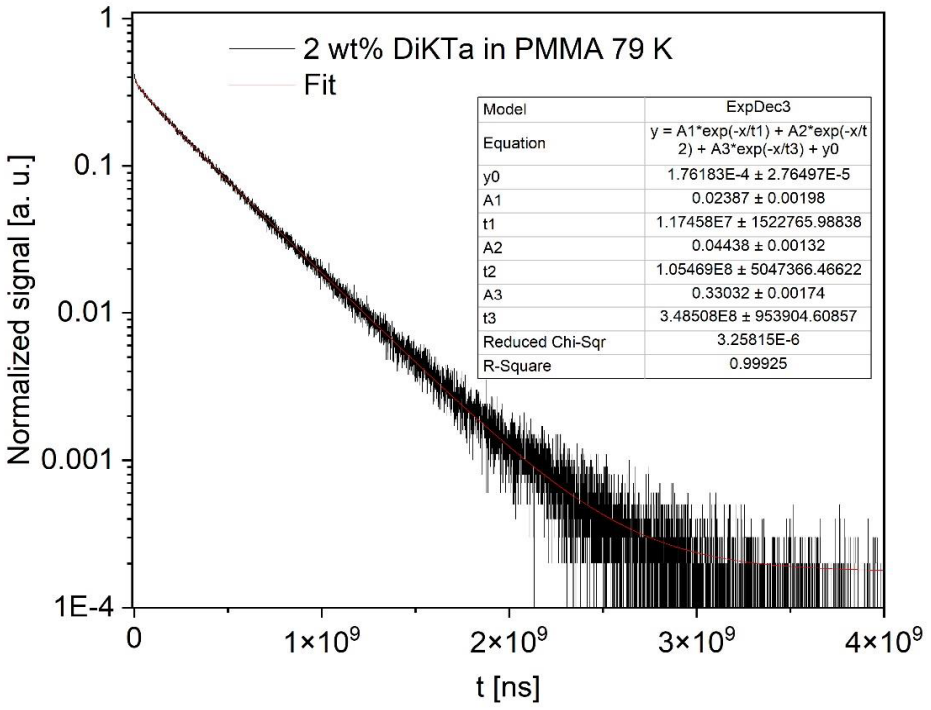

b)

Figure S10. a) prompt and b) delayed time-resolved photoluminescence decay (black) of the DiKTa in PMMA at 79 K with the respective exponential fitting parameters including pre-exponential factors A_i, lifetimes t_i, and confidence limits.

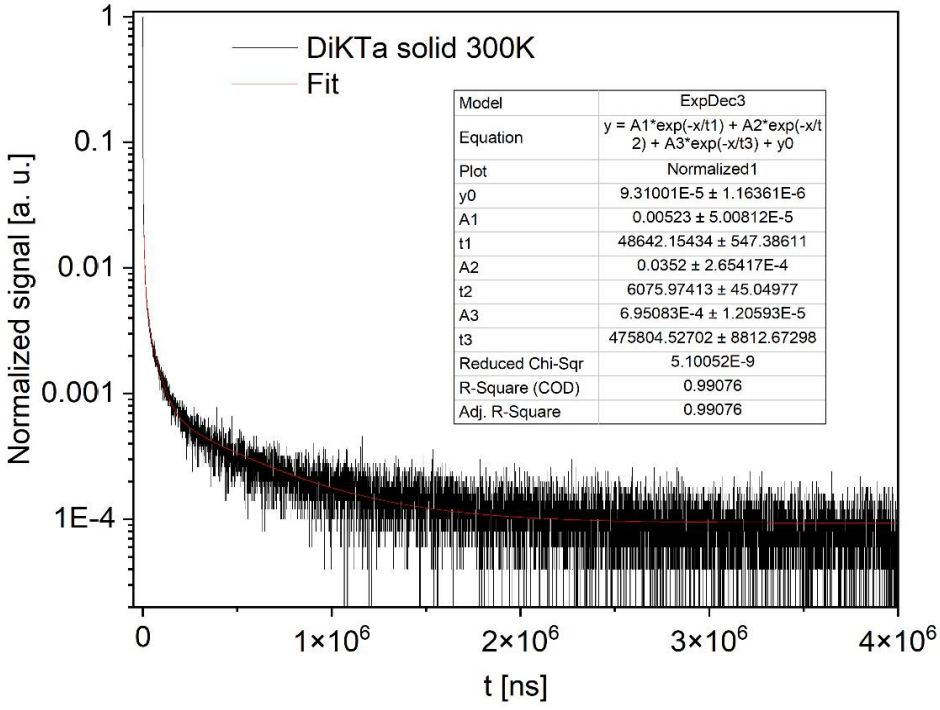

a)

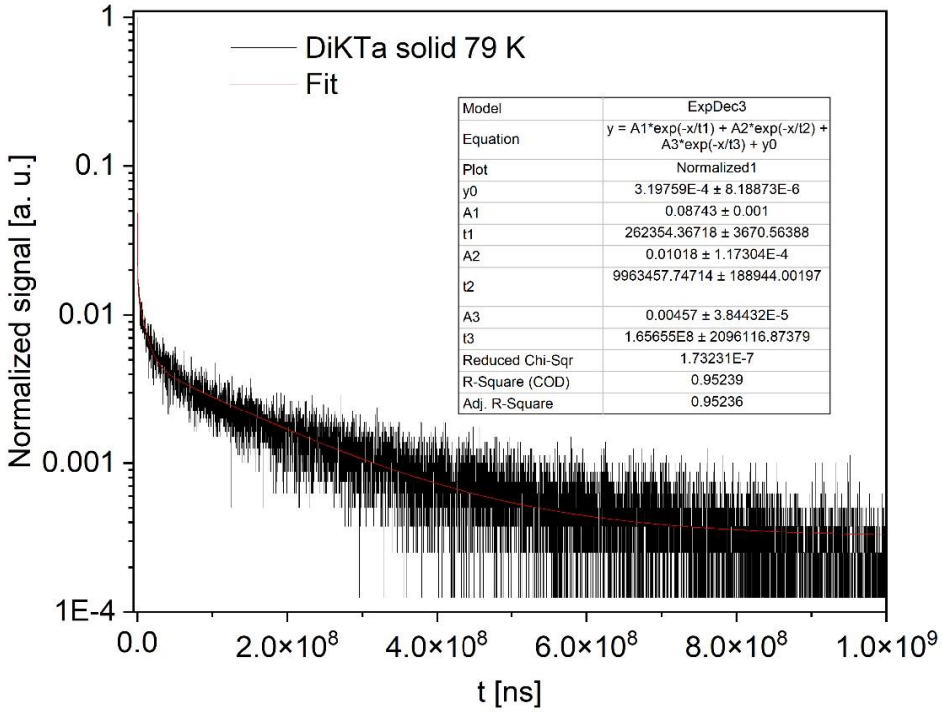

b)

Figure S11. Time-resolved photoluminescence decay (black) of solid DiKTa at a) 300 K and b) 79 K with the respective exponential fitting parameters including pre-exponential factors A_i, lifetimes t_i, and confidence limits.

S5. DiKTa@MOF-5 Synthesis and characterization

In this work, we used the optimized synthesis of Han *et al.* with slight modifications.[3]

8 mL of DEF was placed in a test tube together with 308 mg of $Zn(NO_3)_2 \cdot 6H_2O$ and 58 mg of H_2BDC. The mixture was treated in an ultrasonic bath until all solids were dissolved. The reaction solution was filled into a 16 mL Pyrex tube via a syringe filter (0.2 µm PTFE membrane) and sealed. The tube was stored in an oven at 85 °C for 72 hours and then cooled back to room temperature. The crystals obtained were washed three times with 5 mL DEF and stored in solution. For N_2 adsorption, the crystals were activated super critically with CO_2.

The same synthesis procedure was used for the synthesis of the composites. In this process, pure DEF was gradually replaced by a 0.5 mmol/L concentrated solution of DiKTa in DEF (see Table S1), resulting in concentrations of DiKTa in the reaction mixtures of 0.06, 0.12, 0.25, and 0.5 mmol/L. Depending on the increasing

concentration, the composite materials **DiKTa**@MOF-$5_{0.03}$, **DiKTa**@MOF-$5_{0.05}$, **DiKTa**@MOF-$5_{0.09}$, and **DiKTa**@MOF-$5_{0.13}$ could be produced.

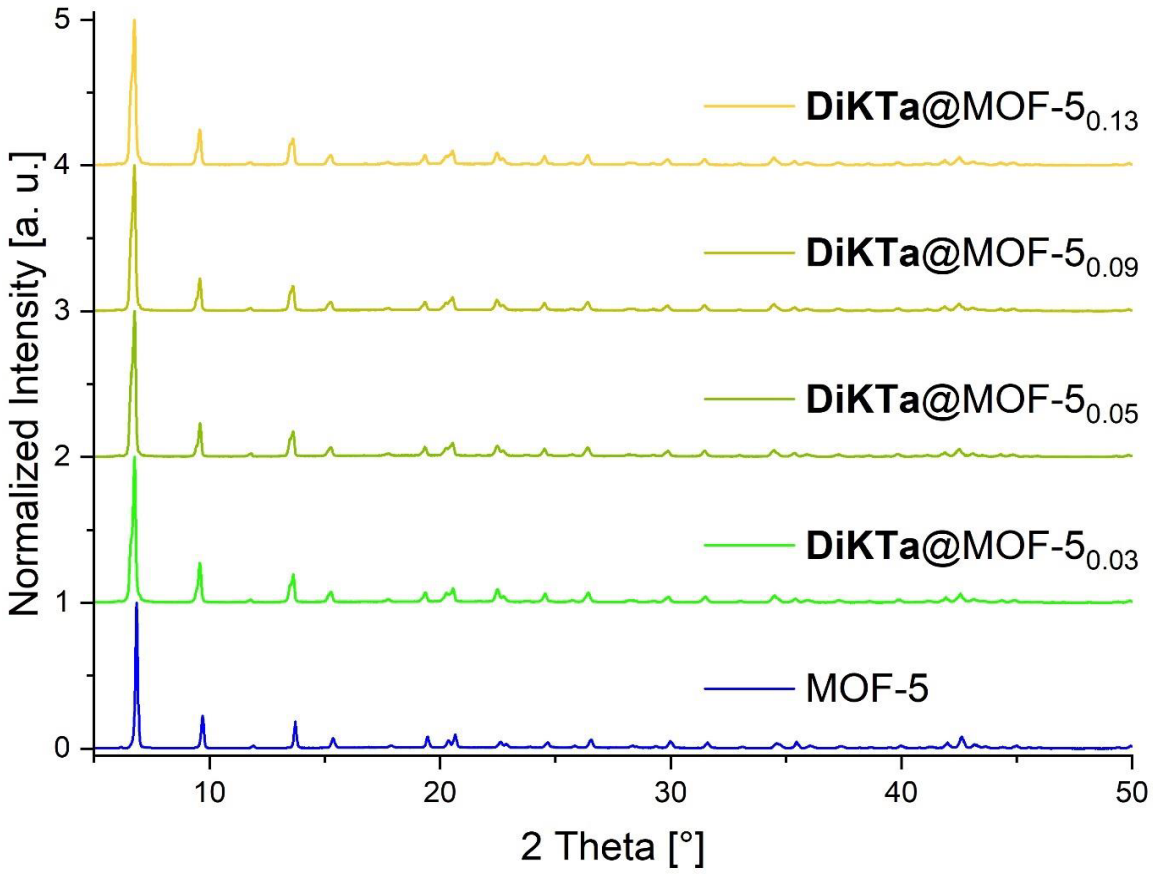

Figure S12. PXRD of MOF-5 and all composites prepared.

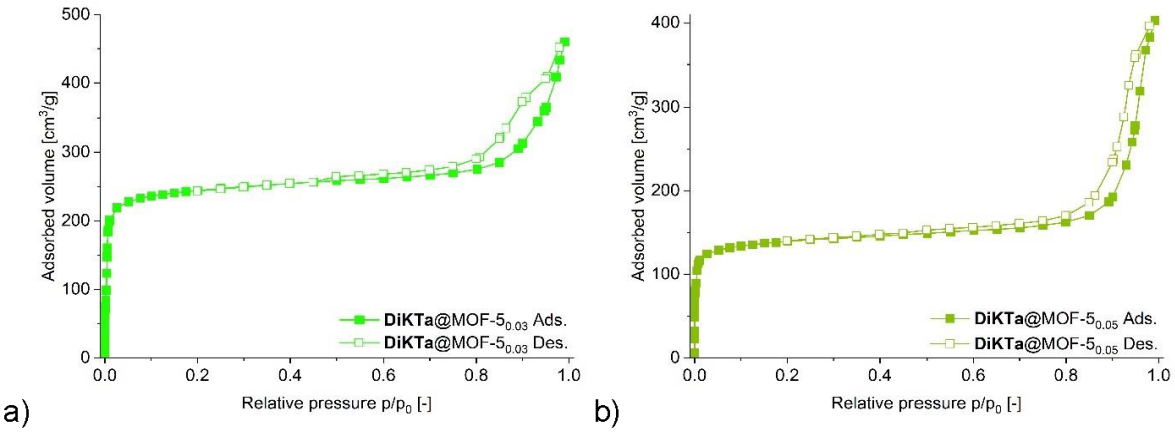

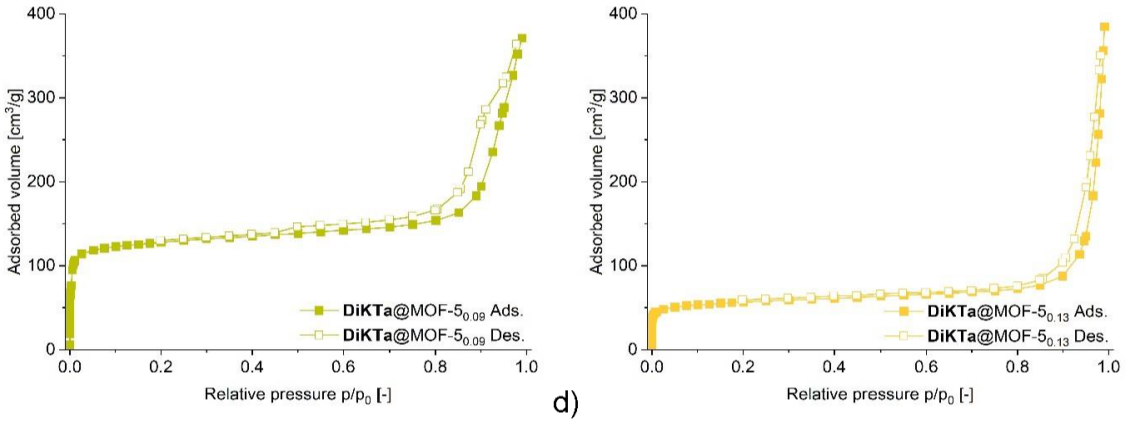

Figure S13. Nitrogen sorption isotherms at 77 K of a) **DiKTa**@MOF-$5_{0.03}$ (965 m^2/g), b) **DiKTa**@MOF-$5_{0.05}$ (540 m^2/g), c) **DiKTa**@MOF-$5_{0.09}$ (499 m^2/g), and d) **DiKTa**@MOF-$5_{0.13}$ (213 m^2/g) (filled symbols adsorption, empty symbols desorption).

Table S1. Concentrations and BET surface area determinations of the prepared DiKTa@MOF-5 composites.

Compound	Volume of DEF solution of DiKTa[a] [mL]	Concentrations of DiKTa in the reaction mixtures [mmol/L]	S_{BET} [m^2/g]
DiKTa@MOF-$5_{0.03}$	1	0.06	965
DiKTa@MOF-$5_{0.05}$	2	0.12	540
DiKTa@MOF-$5_{0.09}$	4	0.25	499
DiKTa@MOF-$5_{0.13}$	8	0.5	213

[a] DEF solution of DiKTa with a concentration of 0.5 mmol/L

S6. Digestion UV-Vis spectroscopy

All samples were digested under acidic conditions. DiKTa was extracted from the aqueous phase with DCM, the solvent was removed under reduced pressure using a rotary evaporator, the solid residue was dried at high vacuum, and then dissolved in a defined amount of chloroform. The amount of DiKTa in each MOF could be determined using the previously generated calibration curve (Figure S14).

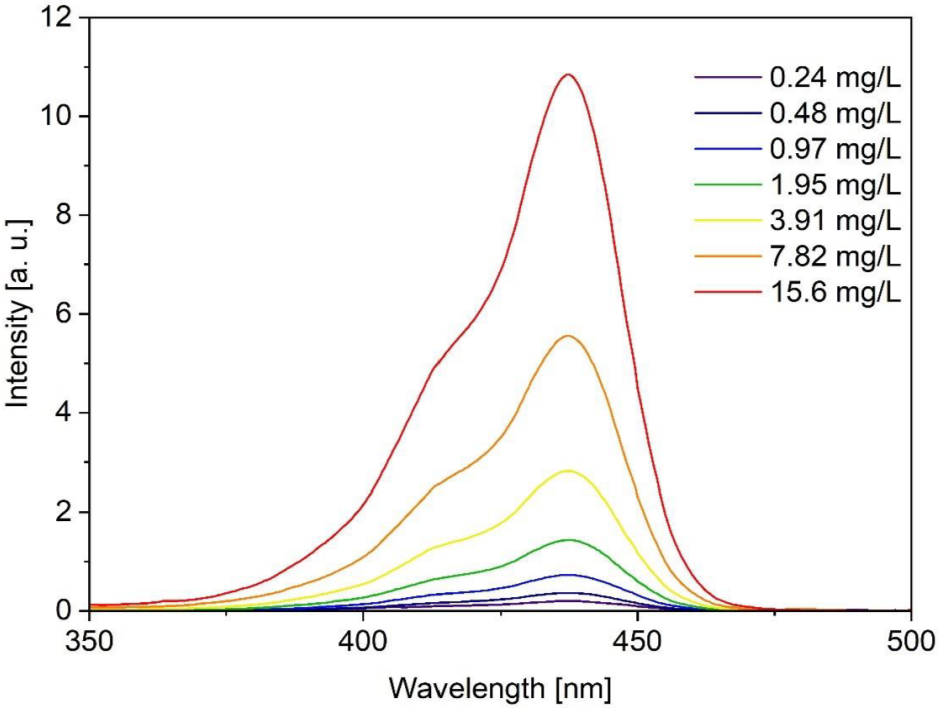

a)

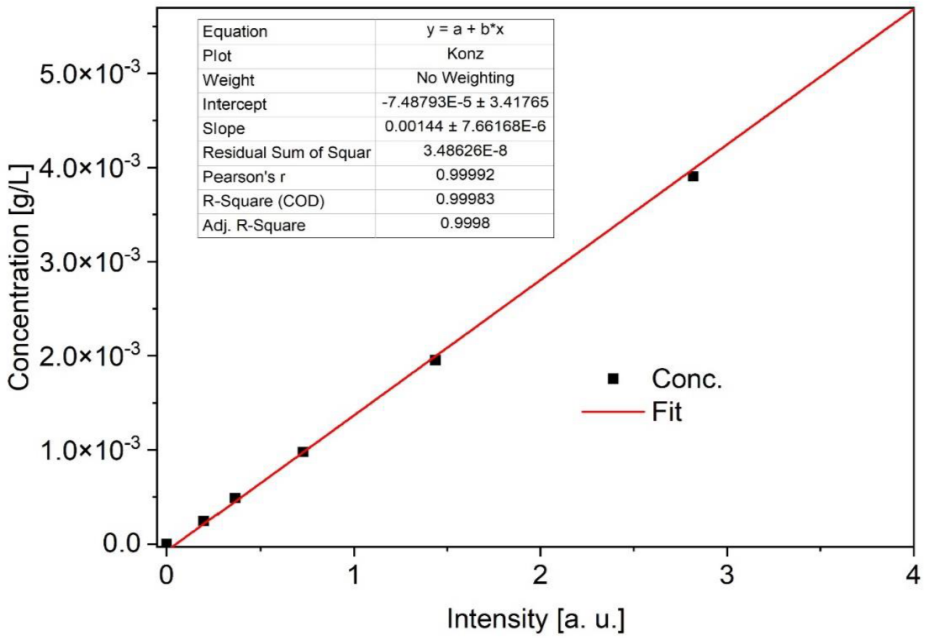

b)

Figure S14. a) UV-Vis spectra of differently concentrated solutions of DiKTa in chloroform. b) Calibration line with fit and R-values. Values were taken at a wavelength of 437 nm.

The weight of incorporated DiKTa can be calculated by multiplying the intensity by the slope of the calibration curve and the amount of chloroform. The loading of DiKTa in MOF-5 could be calculated using the following formula:

$$loading\ (wt\%) = \frac{weight\ of\ incorporated\ \boldsymbol{DiKTa}}{weight\ of\ \boldsymbol{DiKTa}@MOF} \times 100$$

All MOF-5 composites were dissolved with 4 mL chloroform. E. g. for the determination of DiKTa@MOF-$5_{0.13}$: 8.3 mg of composite were digested, resulting in an intensity of 1.873 at $\lambda_{abs.}$ = 437 nm.

$$loading\ (0.13\ wt\%) = \frac{1.873 \times 0.00144 \times 4}{8.3} \times 100$$

Table S2. Determination of the DiKTa loading in the prepared MOF-5 composites using the UV-Vis digestion method.

Initial concentration	mg digested	Intensity at λ_{em} = 426 nm	Concentration from UV-Vis	Loading [wt%]	Name
0 mmol/L	4.2	0	0	0	MOF-5
0.06 mmol/L	6.5	0.338	0.41 mg/L	0.03	**DiKTa**@MOF-$5_{0.03}$
0.12 mmol/L	10.1	0.877	1.21 mg/L	0.05	**DiKTa**@MOF-$5_{0.05}$
0.25 mmol/l	7.1	1.109	1.52 mg/L	0.09	**DiKTa**@MOF-$5_{0.09}$
0.5 mmol/L	8.3	1.873	2.62 mg/L	0.13	**DiKTa**@MOF-$5_{0.13}$

S7. Calculation of pore filling and the probability p of multiple occupations

We analyzed the crystallographic structure of MOF-5 to calculate the pore loading. The framework consists of cubic pores, each defined by eight SBUs at the corner points. Each SBU contributes one-eighth of its volume to a specific pore. The pore edges are bridged by linker molecules (here BDC), with each link contributing a quarter of its length to the pore structure. This arrangement allows us to directly relate the atomic composition of a single pore to the molecular formula of the MOF-5 repeating unit (see Figure S15). Based on the molecular formulas and the loadings from section S6, the ratio of occupied to unoccupied pores could be calculated. However, it is assumed that there is only one DiKTa molecule in each pore. For this purpose, the molar mass of MOF-5, which corresponds to 769.87 g/mol, and the molar mass of DiKTa, which corresponds to 297.31 g/mol, were used. It can be calculated that for a loading of 0.13 wt% **DiKTa**@MOF-5, 0.0013 g DiKTa (4.37 µmol) are contained in 0.9987 g MOF-5 (1.29 mmol). This results in a ratio of 0.0044:1.3. This corresponds to 295 pores per DiKTa molecule or 0.0034 DiKTa molecules per pore for the largest loading. For all composites, see Table S3

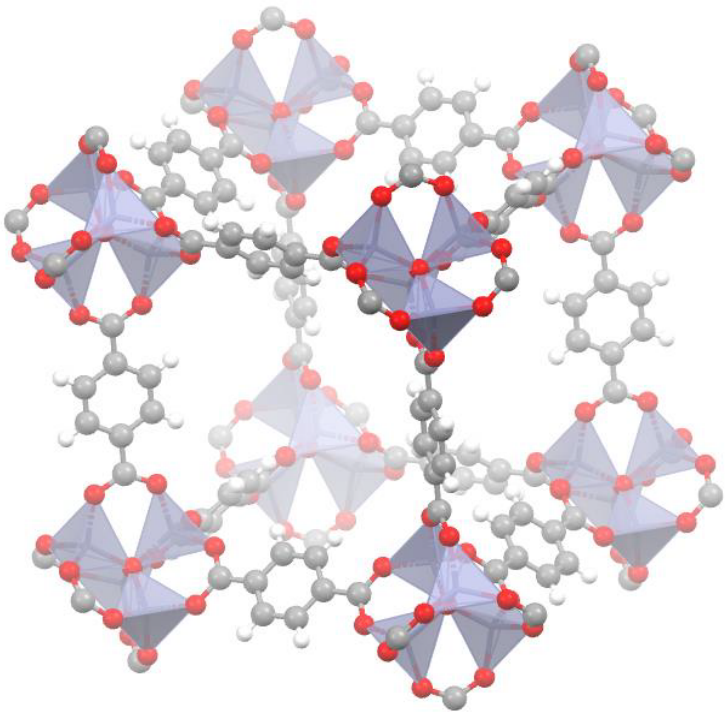

Figure S15: Structure of MOF-5 from CCDC No.256965.[4]

Table S3. Calculations for pore filling

Compound	DiKTa / MOF-5 [g]	DiKTa / MOF-5 [mmol]	Pores per DiKTa ratio	DiKTa per pore ratio
DiKTa@MOF-5$_{0.03}$	0.0003 / 0.9997	0.001 / 1.3	1300	0.0008
DiKTa@MOF-5$_{0.05}$	0.0005 / 0.9995	0.0017 / 1.3	765	0.0013
DiKTa@MOF-5$_{0.09}$	0.0009 / 0.9991	0.003 / 1.3	433	0.0023
DiKTa@MOF-5$_{0.13}$	0.0013 / 0.9987	0.0044 / 1.3	295	0.0034

Based on this results, we were able to calculate the probability p of multiple occupancy. For this, we used a Pearson distribution. The results are listed in Table S4.

$$P(n) = \frac{\alpha^n \times e^{-\alpha}}{n!}$$

$$\alpha = -\ln\left(unoccupied\ pores\right)$$

Table 4. Probability *p* of multiple occupation of DiKTa in a MOF-5 pore.

	DiKTa@MOF-$5_{0.03}$	**DiKTa**@MOF-$5_{0.05}$	**DiKTa**@MOF-$5_{0.09}$	**DiKTa**@MOF-$5_{0.13}$
DiKTa per pore	0.0008	0.0013	0.0023	0.0034
α	0.0008	0.001301	0.002303	0.003405
p (one) [%]	99.96	99.93	99.89	99.83
p (two) [%]	0.04	0.07	0.11	0.17

S8. Photophysical properties of DiKTa@MOF-5 composites

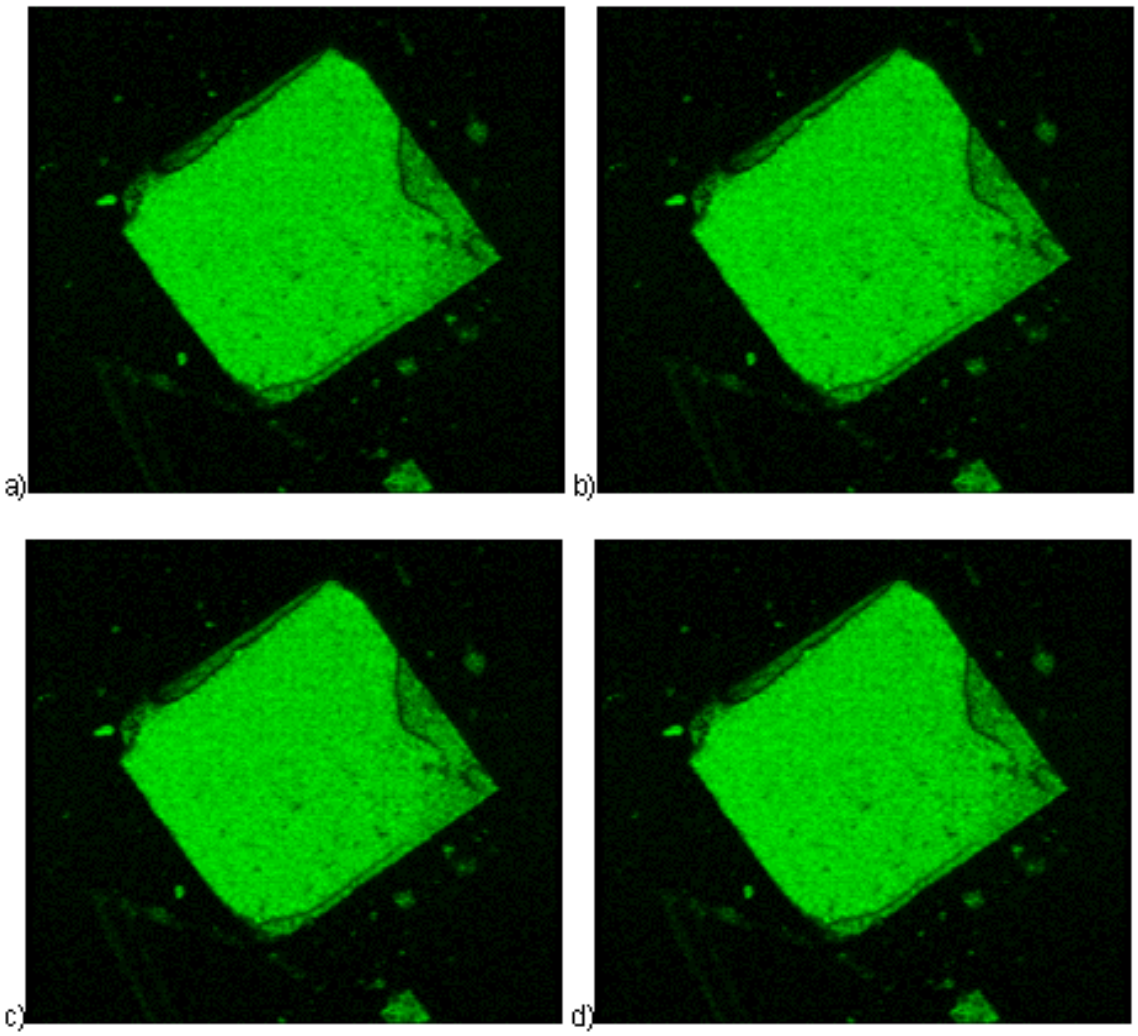

Figure S16. Confocal images of single crystals of all **DiKTa**@MOF-5 composite viewed from above a) **DiKTa**@MOF-$5_{0.03}$, b) **DiKTa**@MOF-$5_{0.05}$, c) **DiKTa**@MOF-$5_{0.09}$, and d) **DiKTa**@MOF-$5_{0.13}$.

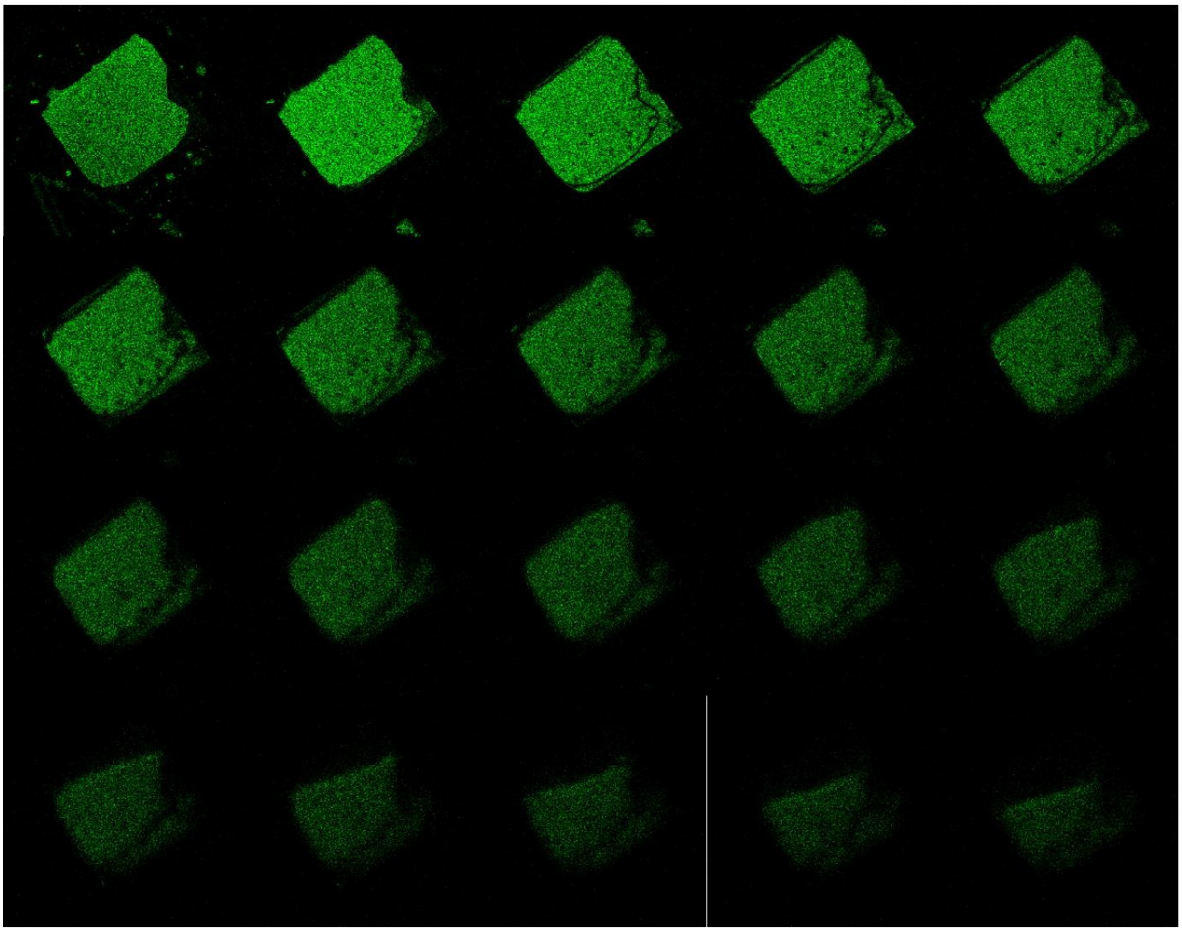

Figure S17. Confocal images of one single crystal of a **DiKTa**@MOF-5 composite. The crystal was scanned in z-direction in steps of XX µm. The obtained images are shown from the bottom of the crystal (top left picture) to the top of the crystal (bottom right picture). λ_{exc} = XXX nm, λ_{em} = XXX nm

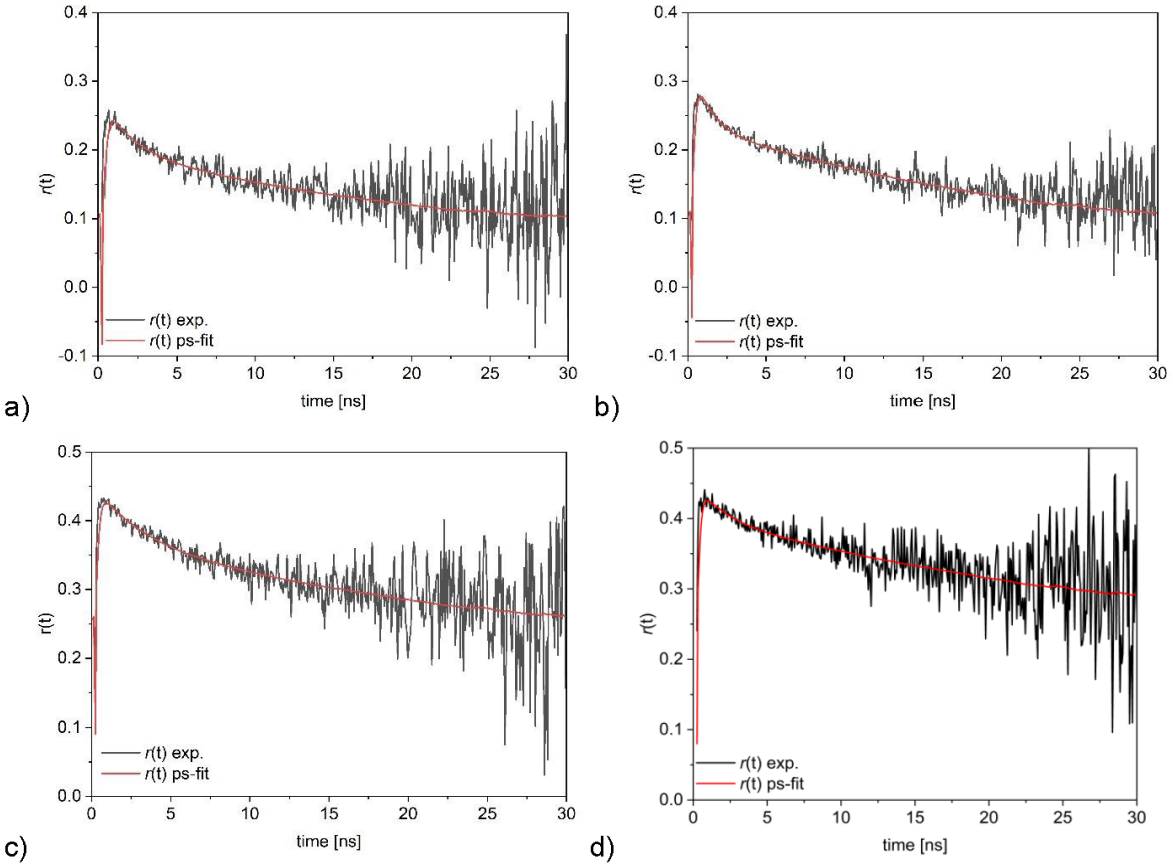

Figure S18. Time-resolved fluorescence anisotropy curves *r*(t) to resolve the fundamental anisotropy r_0 of a) **DiKTa**@MOF-$5_{0.03}$, b) **DiKTa**@MOF-$5_{0.05}$, c) **DiKTa**@MOF-$5_{0.09}$, and d) **DiKTa**@MOF-$5_{0.13}$.

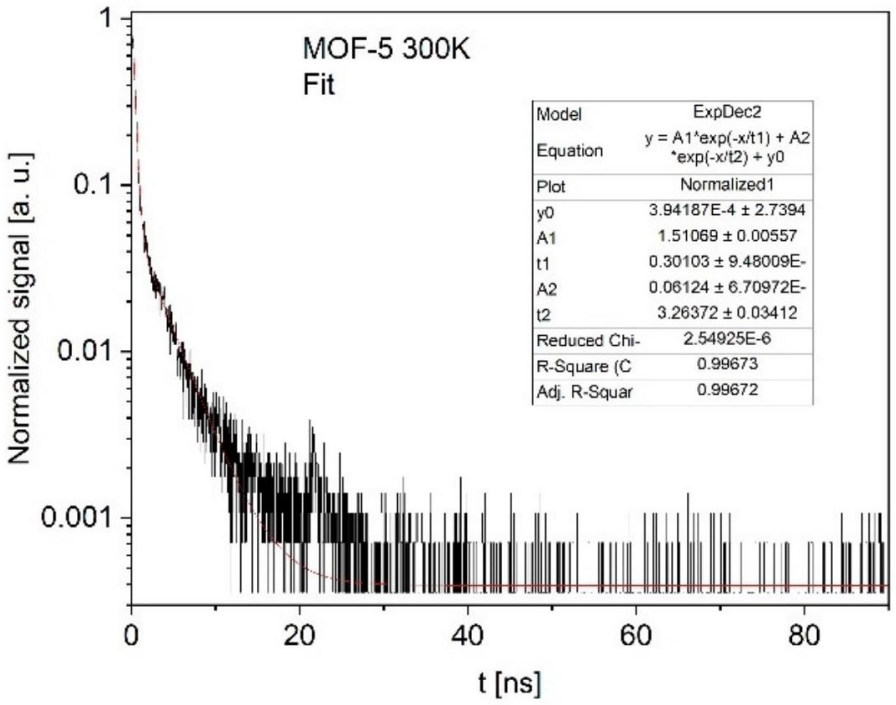

a)

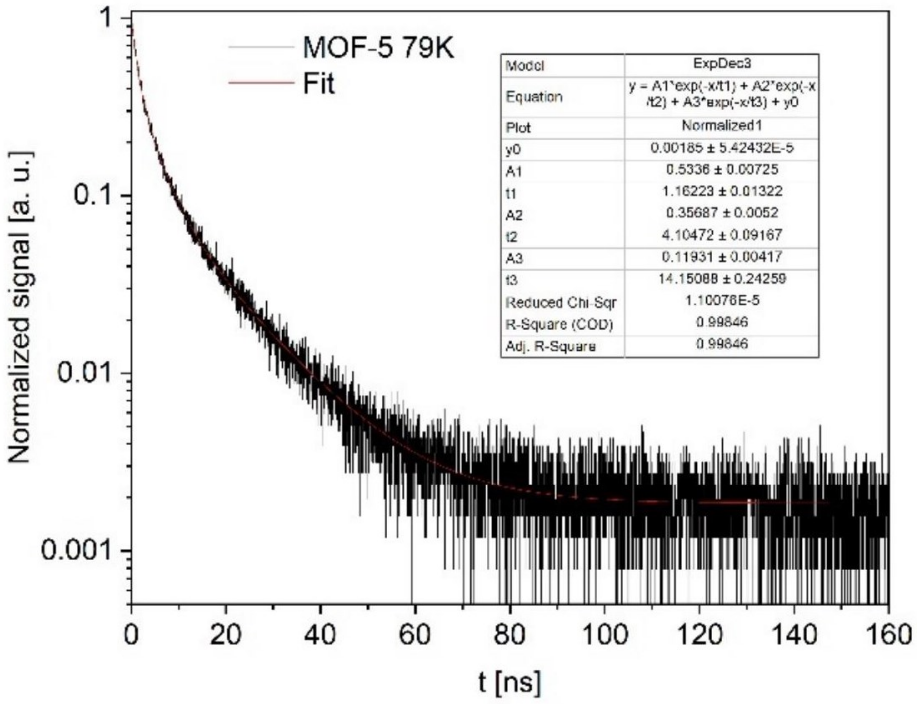

b)

Figure S19. Time-resolved photoluminescence decay (black) of the MOF-5 at a) 300 K and b) 79 K with the respective exponential fitting parameters including pre-exponential factors A_i, lifetimes t_i, and confidence limits.

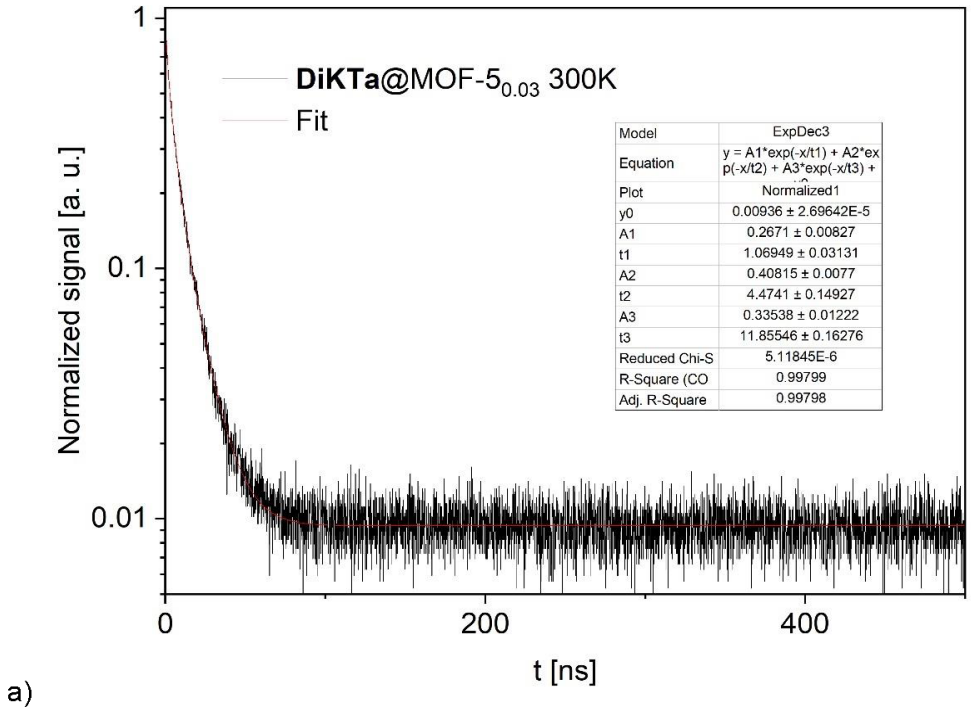

a)

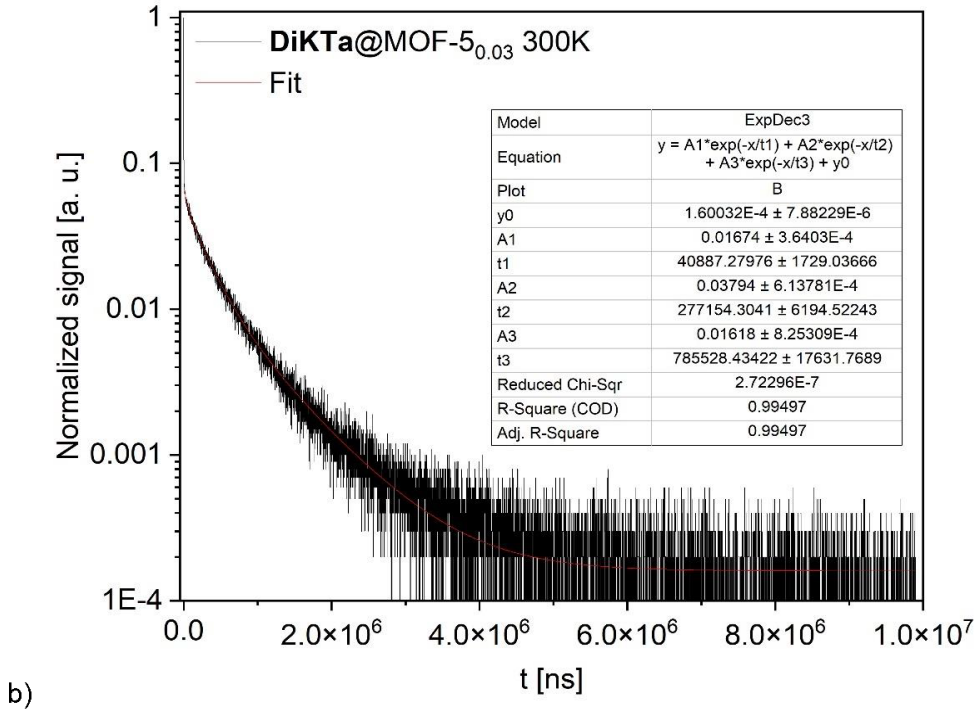

b)

Figure S20. a) prompt and b) delayed time-resolved photoluminescence decay (black) of **DiKTa**@MOF-5$_{0.03}$ at 300 K with the respective exponential fitting parameters including pre-exponential factors A_i, lifetimes t_i, and confidence limits.

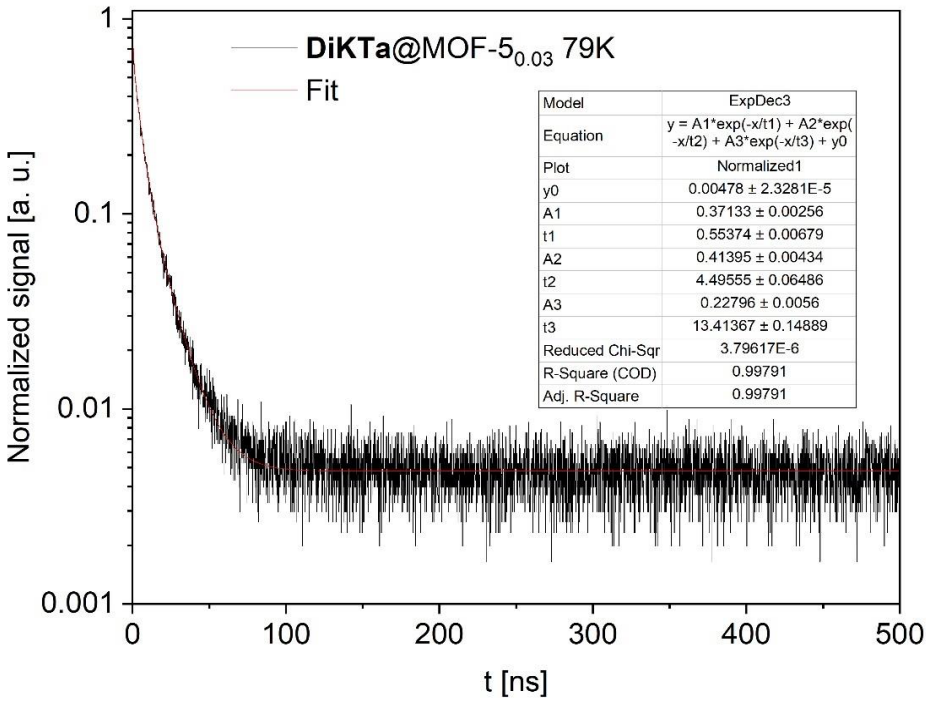

a)

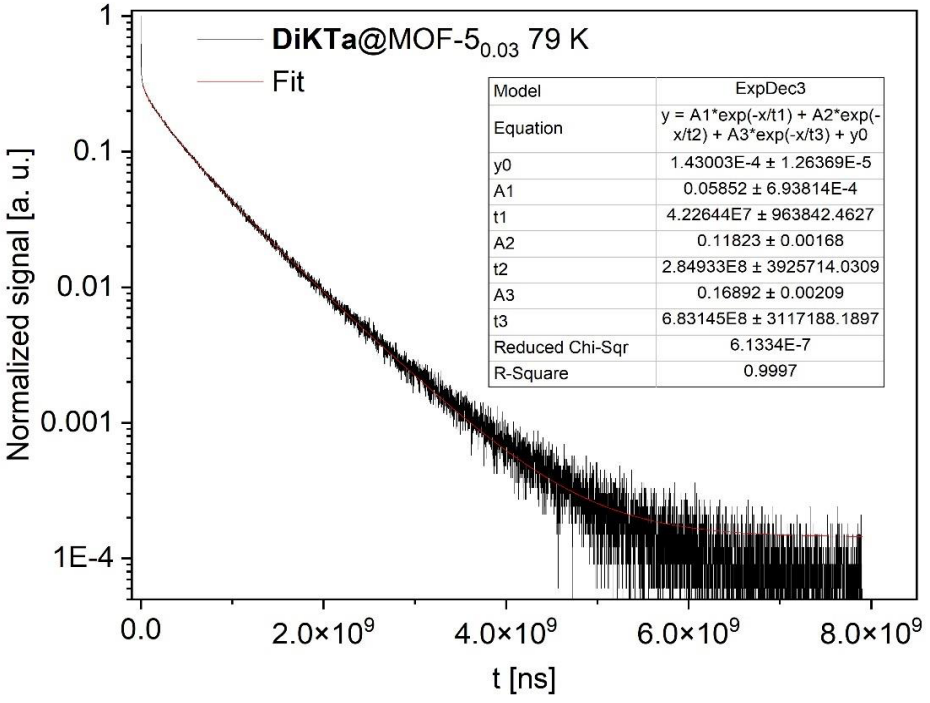

b)

Figure S21. a) prompt and b) delayed time-resolved photoluminescence decay (black) of **DiKTa**@MOF-5$_{0.03}$ at 79 K with the respective exponential fitting parameters including pre-exponential factors A_i, lifetimes t_i, and confidence limits.

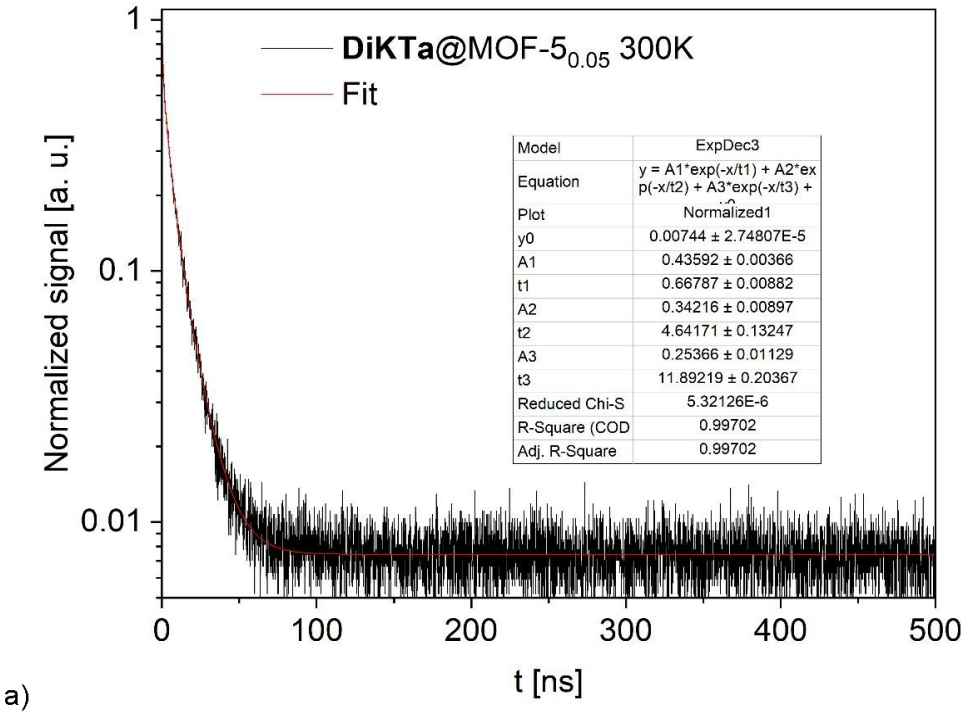

a)

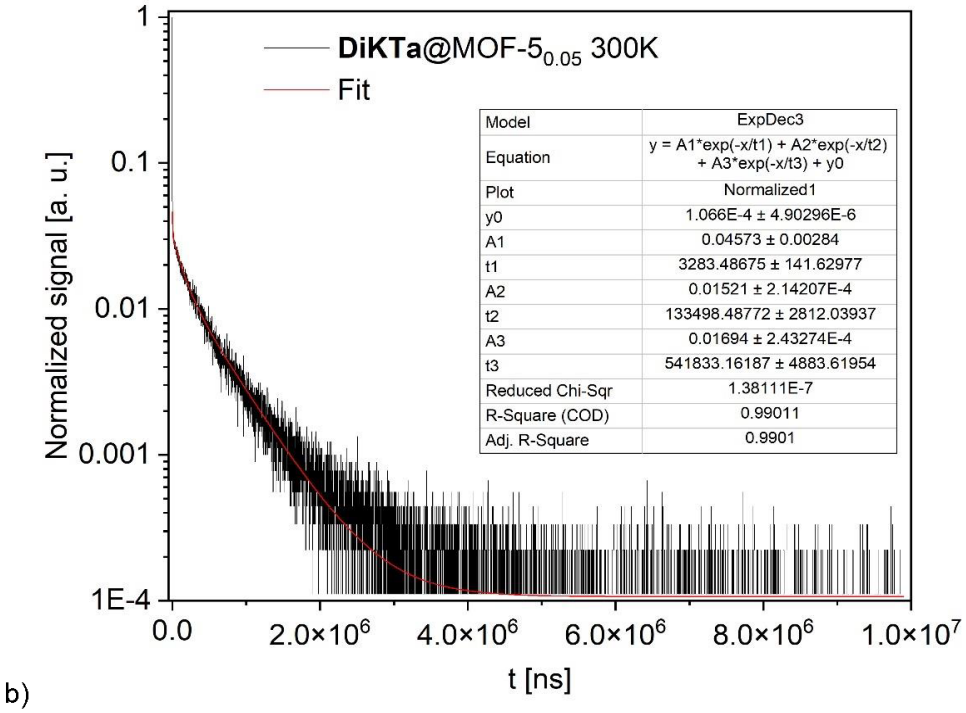

b)

Figure S22. a) prompt and b) delayed time-resolved photoluminescence decay (black) of **DiKTa**@MOF-5$_{0.05}$ at 300 K with the respective exponential fitting parameters including pre-exponential factors A_i, lifetimes t_i, and confidence limits.

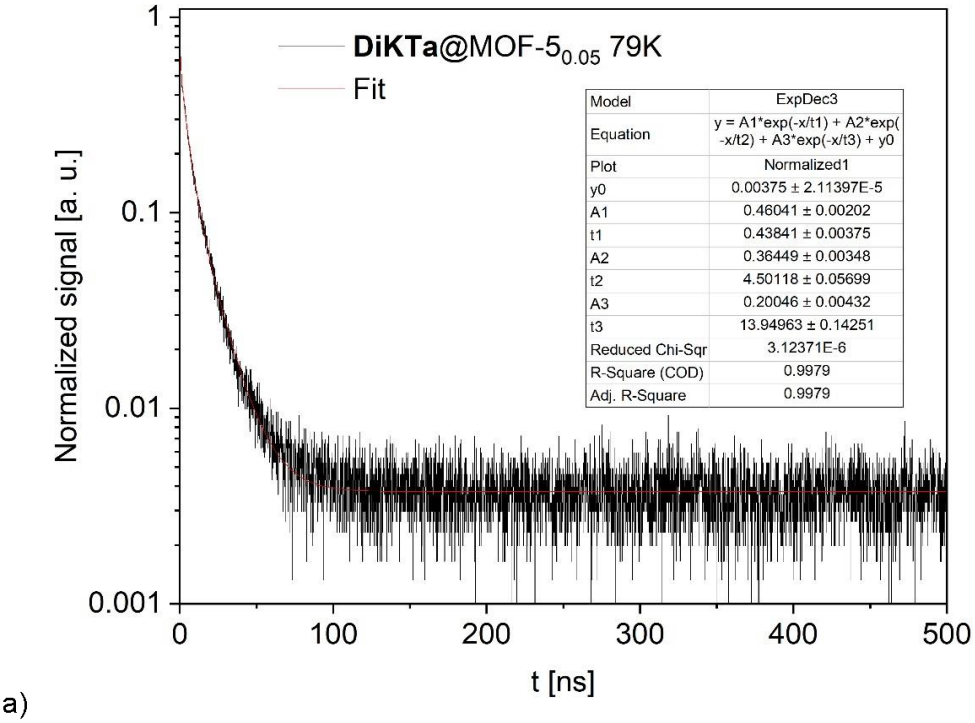

a)

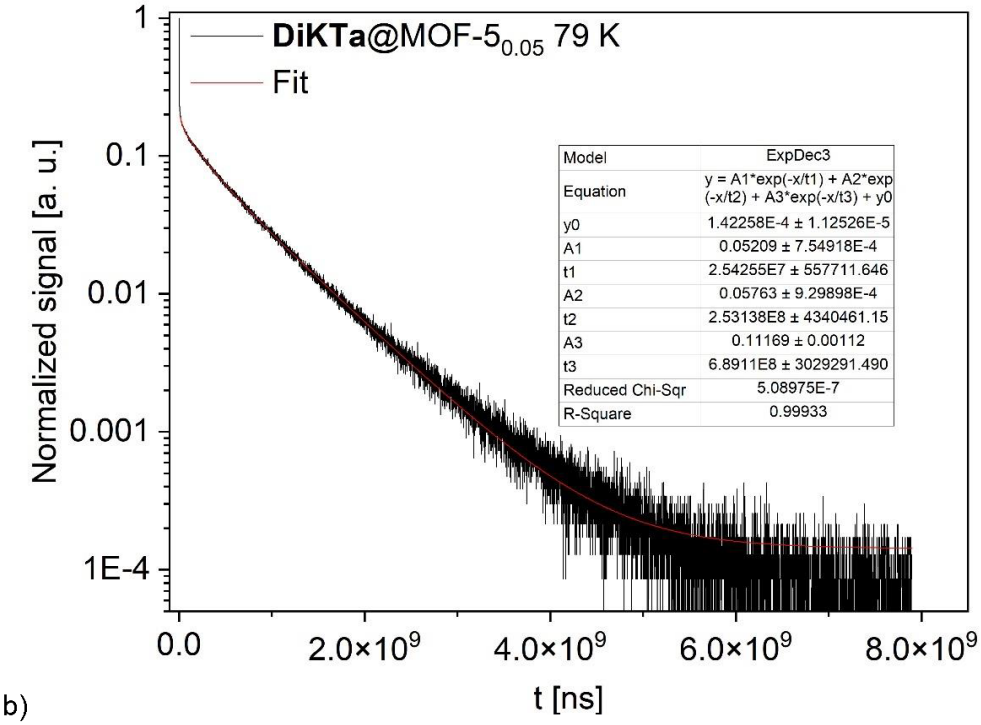

b)

Figure S23. a) prompt and b) delayed time-resolved photoluminescence decay (black) of **DiKTa**@MOF-5$_{0.05}$ at 79 K with the respective exponential fitting parameters including pre-exponential factors A_i, lifetimes t_i, and confidence limits.

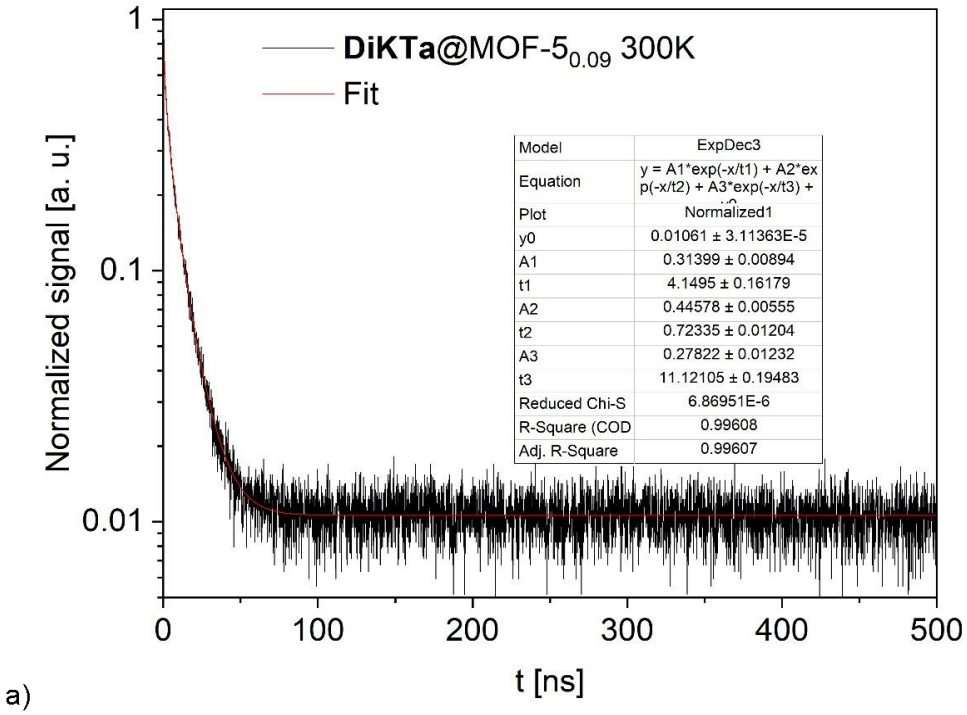

a)

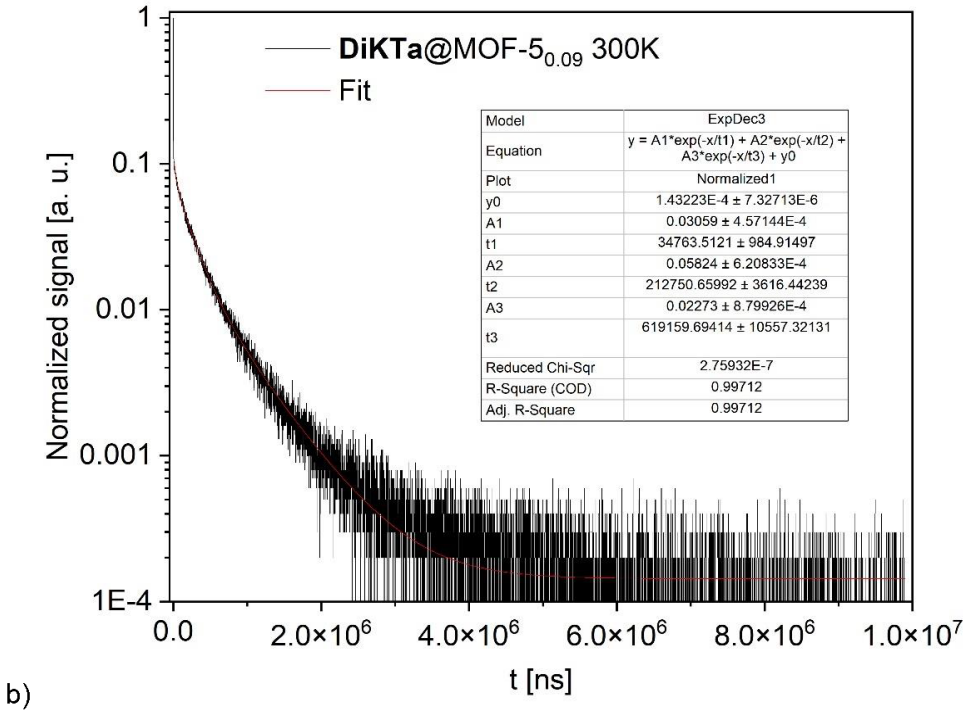

b)

Figure S24. a) prompt and b) delayed time-resolved photoluminescence decay (black) of **DiKTa**@MOF-5$_{0.09}$ at 300 K with the respective exponential fitting parameters including pre-exponential factors A_i, lifetimes t_i, and confidence limits.

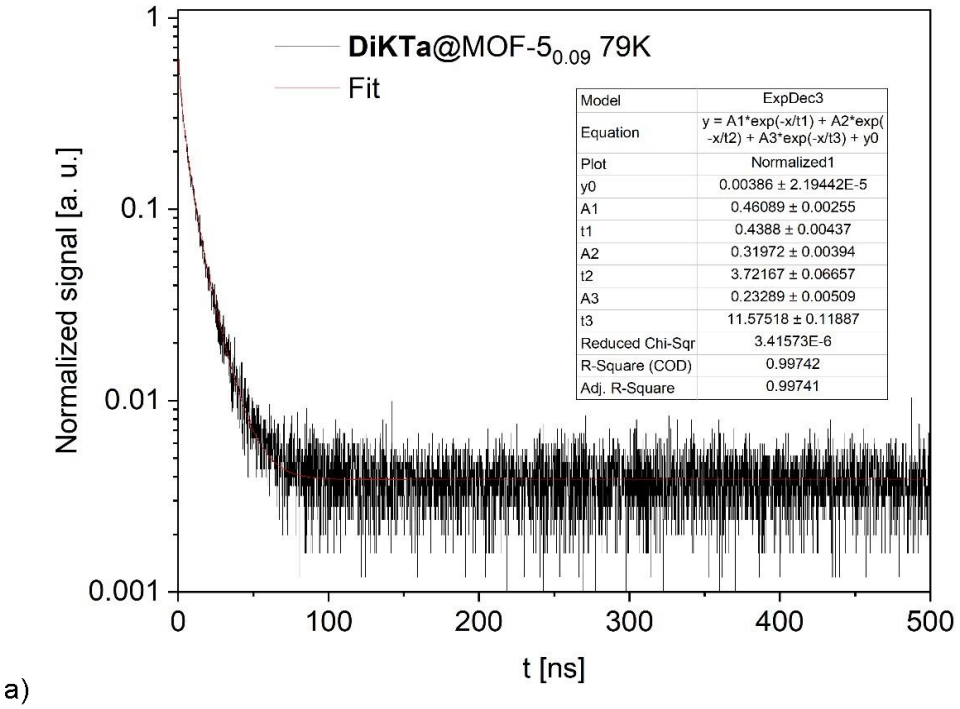

a)

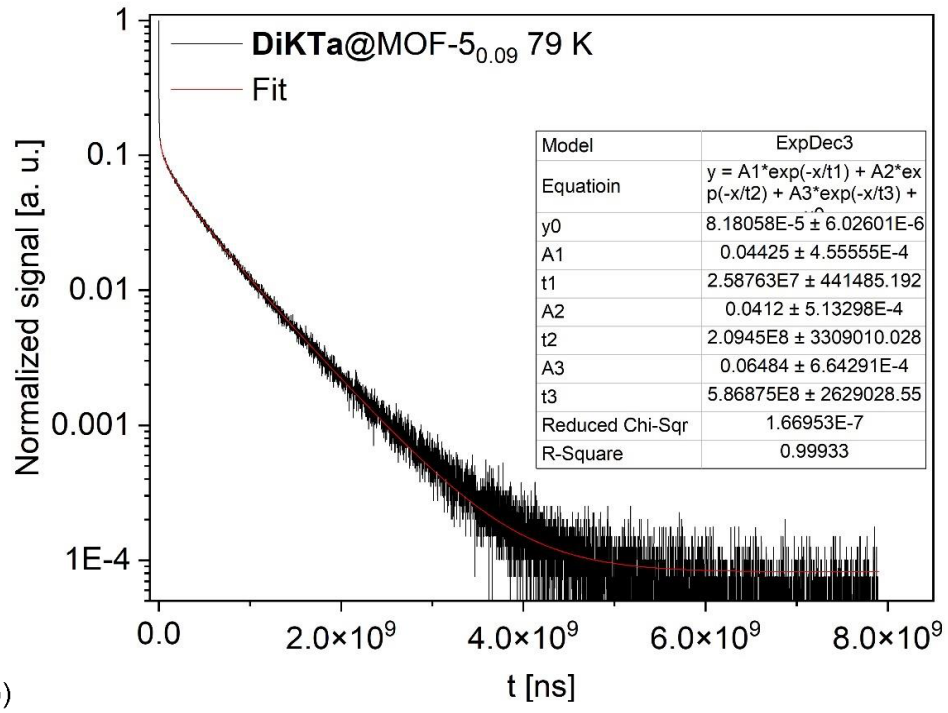

b)

Figure S25. a) prompt and b) delayed time-resolved photoluminescence decay (black) of **DiKTa**@MOF-5$_{0.09}$ at 79 K with the respective exponential fitting parameters including pre-exponential factors A_i, lifetimes t_i, and confidence limits.

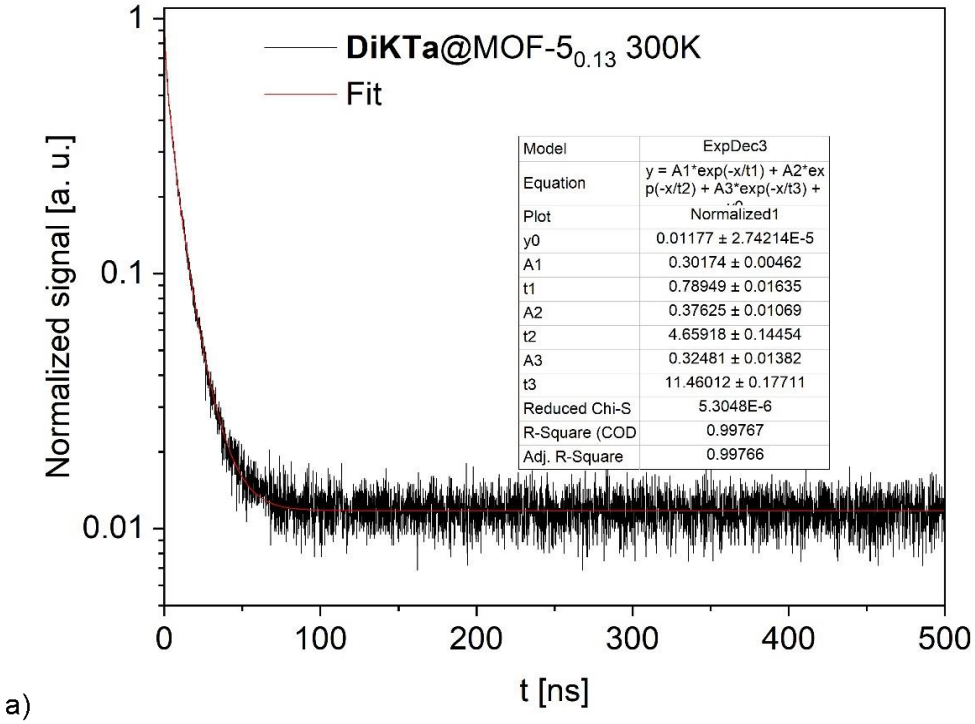

a)

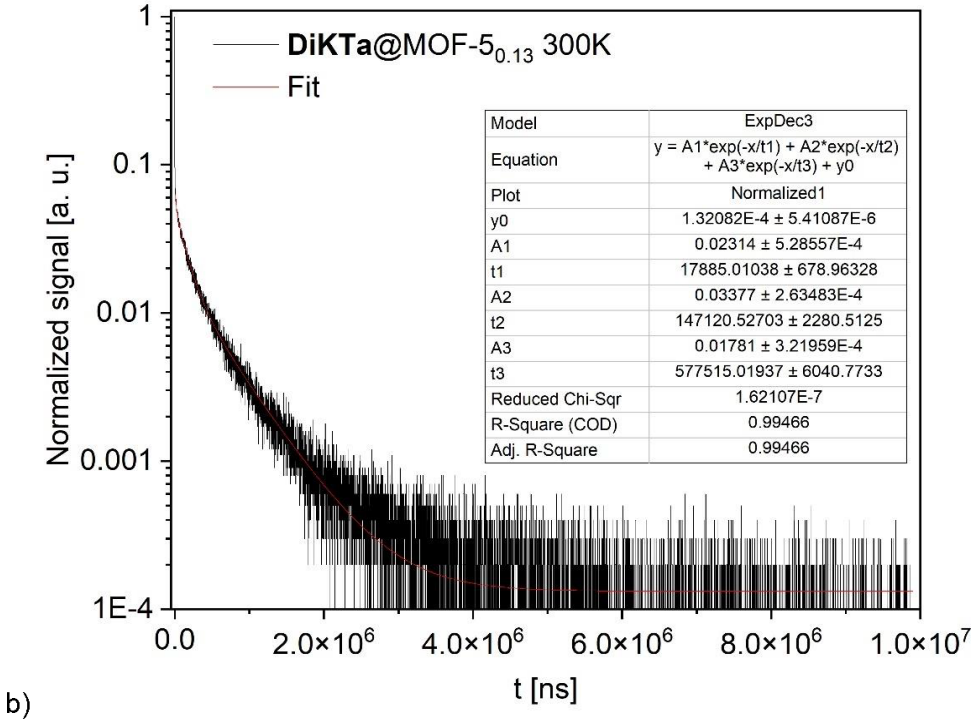

b)

Figure S26. a) prompt and b) delayed time-resolved photoluminescence decay (black) of **DiKTa**@MOF-5$_{0.13}$ at 300 K with the respective exponential fitting parameters including pre-exponential factors A_i, lifetimes t_i, and confidence limits.

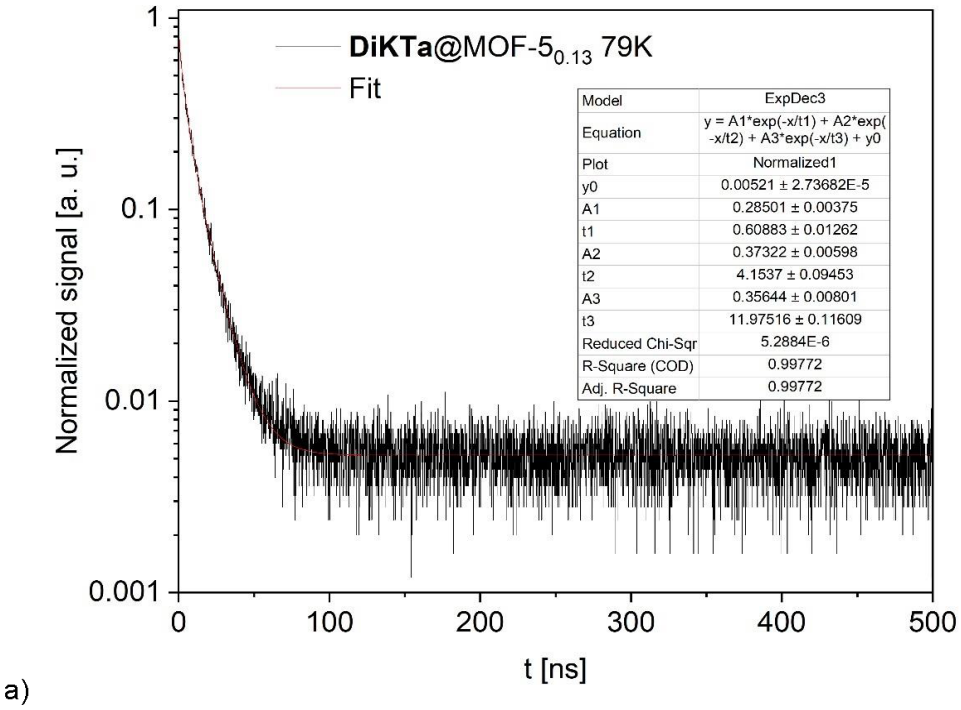

a)

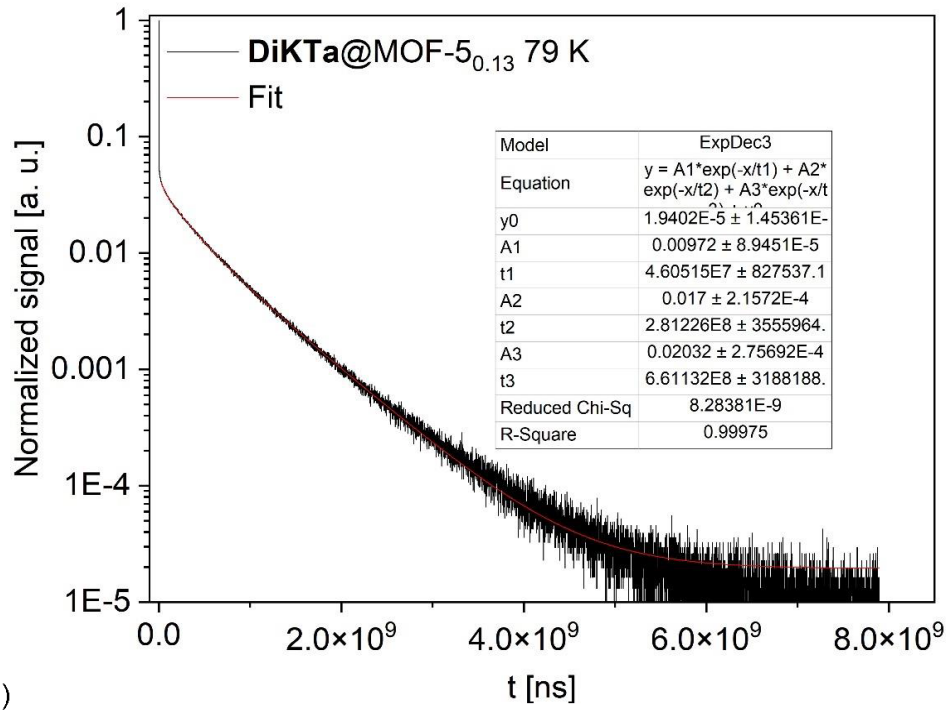

b)

Figure S27. a) prompt and b) delayed time-resolved photoluminescence decay (black) of **DiKTa**@MOF-5$_{0.13}$ at 79 K with the respective exponential fitting parameters including pre-exponential factors A_i, lifetimes t_i, and confidence limits.

References

[1] J. E. Field and D. Venkataraman, *Chemistry of Materials* **2002**, *14*, 962-+.
[2] D. Hall, S. M. Suresh, P. L. dos Santos, E. Duda, S. Bagnich, A. Pershin, P. Rajamalli, D. B. Cordes, A. M. Z. Slawin, D. Beljonne, A. Köhler, I. D. W. Samuel, Y. Olivier and E. Zysman-Colman, *Advanced Optical Materials* **2020**, *8*.
[3] S. B. Han, Y. H. Wei, C. Valente, I. Lagzi, J. J. Gassensmith, A. Coskun, J. F. Stoddart and B. A. Grzybowski, *Journal of the American Chemical Society* **2010**, *132*, 16358-16361.
[4] M. Eddaoudi, H. L. Li, T. Reineke, M. Fehr, D. Kelley, T. L. Groy and O. M. Yaghi, *Topics in Catalysis* **1999**, *9*, 105-111.

5.2 Photoconductive pyrenephosphonate thin films

Marcus N. A. Fetzer, Ayşenur Limon, Christoph Janiak*, Jan Christoph Goldschmidt, Lukas Wagner*, Gündoğ Yücesan*

Kurzzusammenfassung

Hier berichten wir über zwei organische photoleitende Verbindungen auf Pyrenbasis, nämlich Pyren-1,3,6,8-tetrayltetrakis([1,1'-biphenyl]-4',4-diyl))tetrakis(phosphonsäure) (H_8-PyTPPA) und dessen Esterform Octaethyl(pyren-1,3,6,8-tetrayltetrakis(([1,1'-biphenyl]-4',4-diyl)))tetrakis(phosphonat) (Et_8-PyTPPE). Beide Verbindungen weisen Photolumineszenzpeaks im sichtbaren Bereich von 1,9 eV bzw. 2,1 eV auf und die Dünnschichten von H_8-PyTPPA zeigen eine lichtempfindliche elektrische Leitfähigkeit. Die P-C-Bindungen in H_8-PyTPPA sind unter UV-Licht stabil und weisen chemische Stabilität in 37 %iger HCl sowie eine gute thermische Stabilität und eine vernachlässigbare Abnahme der Photolumineszenzintensität bei hohen Temperaturen auf, was für photovoltaische Anwendungen von entscheidender Bedeutung ist. Darüber hinaus berichten wir über eine neue Strategie zur Synthese längerer, verknüpfter Arylphosphonsäuren mit einem Pyrenkern. Dünne Schichten solcher Verbindungen können potenziell in der nächsten Generation von Photovoltaikanwendungen eingesetzt werden und bieten im Vergleich zu schwermetallhaltigen Materialien umweltfreundlichere Optionen.

Photoconductive pyrenephosphonate thin films

Marcus N. A. Fetzer[1], Ayşenur Limon[1], Christoph Janiak*[1], Jan Christoph Goldschmidt[2], Lukas Wagner[2]*, Gündoğ Yücesan[1]*

1. Institute for Inorganic Chemistry and Structural Chemistry, Heinrich Heine University Düsseldorf, Universitätsstr. 1, D-40225 Düsseldorf, Germany.
2.

E-mail: janiak@hhu.de, guendog.yuecesan@hhu.de and lukas.wagner@physik.uni-marburg.de

Keywords: Stable organic semiconductors, photovoltaics, photoconductive materials

Herein, we report two pyrene based organic photoconducting compounds, namely pyrene-1,3,6,8-tetrayltetrakis([1,1'-biphenyl]-4',4-diyl))tetrakis(phosphonic acid) (H_8-PyTPPA) and its ester form octaethyl(pyrene-1,3,6,8-tetrayltetrakis(([1,1'-biphenyl]-4',4-diyl)))tetrakis(phosphonate) (Et_8-PyTPPE). Both compounds exhibit photoluminescence peaks in the visible range of 1.9 eV and 2.1 eV, respectively, and the thin films of H_8-PyTPPA exhibit photo-responsive electrical conductivity. The P-C bonds in H_8-PyTPPA are stable in the presence of UV light and exhibit chemical stability in 37% HCl, and good thermal stability and negligible decrease in photoluminescence intensity at high temperatures, which are crucial for photovoltaic applications. In addition, we report a new strategy to synthesize longer tethered aryl phosphonic acids with a pyrene core. Thin films of such compounds can be potentially used in the next generation of photovoltaics and provide environmentally friendlier options compared to heavy metal containing materials.

1. Introduction

Pyrene is a fundamental photoluminescent compound due to its exceptional light-emitting properties. [1-4] Its functionalization with organic functional groups has enabled the development of novel materials for organic electronics, which could provide more sustainable alternatives to inorganic semiconductors. Furthermore, a carboxylic acid functionalized pyrene core has been used to create microporous metal-organic frameworks (MOFs) and covalent organic frameworks (COFs) for applications such as sensing and CO_2 capture.[5,6] However, many reported pyrene-based photoresponsive materials, including MOFs and COFs, conductive polymers, and quantum dots, suffer from stability challenges depending on the choice of attached organic functional groups such amines, imines, carboxylates, etc. These types of organic functional groups can act as Lewis acids and bases, and undergo variety of decomposition reactions.[7-13] They also have questionable long term stability especially under UV-light, which is a prerequisite for applications such as photovoltaics.[14] Due to the recent growing interest in the sustainable organic semiconductor field, there is an urgent need for novel organic semiconductors and constructing the thin films of supramolecular organic semiconductors to produce the next-generation of sustainable photovoltaic devices. Functionalizing pyrene with robust hydrogen-bonding, covalent bonding and metal-binding functional groups presents a promising pathway to create sustainable materials. Hypothetically, such materials can provide high surface areas creating optimized optoelectronic properties. Arylphosphonic acids are versatile compounds capable of forming multiple families of stable microporous compounds, and their thin films haven't been studied in the literature targeting optoelectronic applications.[15-22] In this work, we investigate the thin film formation of extended tetraphosphonic acids with the pyrene core.

In more detail, one of the important advantages of phosphonic acids is the stability of P–C and P–O bonds, which provide high resistance to hydrolysis in the presence of strong acids, UV exposure, and high temperatures, which makes them promising candidates for the next generation of supramolecular photovoltaic materials, particularly when integrated with luminescent linker cores such as pyrene.[20] To the best of our knowledge, the synthesis of pyrene-1,3,6,8-tetrayltetrakis([1,1'-biphenyl]-4',4-diyl))tetrakis(phosphonic acid) (H_8-PyTPPA) and its ester form, octaethyl(pyrene-1,3,6,8-tetrayltetrakis(([1,1'-biphenyl]-4',4-diyl)))tetrakis(phosphonate) (Et_8-PyTPPE), have not been reported in the literature. To date, only one pyrenetetraphosphonic acid linker and two corresponding MOF structures have been

reported by Shimizu and Horcajada where they demonstrated proton conductivity and photocatalytic properties respectively; however, no further applications have been explored.[23,24] In addition to the MOF synthesis, pyrenephosphonates have the potential to anchor fluorescent cores onto metal surfaces. This property makes arylphosphonic acids excellent candidates for optoelectronic applications and solar panels, where stability under chemically harsh conditions is essential. The pyrene core itself exhibits high fluorescence quantum yields and features a planar structure that could facilitate π–π stacking interactions, which are beneficial for charge transport.

From the synthetic perspective, the synthesis of arylphosphonic acids is a difficult task to achieve due to the high energy requirement for the formation of P-C bonds.[20] There are two major pathways to synthesize arylphosphonic acid which require a Ni catalyst or a Pd catalyst.[25,26] Recently, we reported Pd-catalyzed Suzuki Cross Coupling reaction to produce longer tethered arylphosphonic acids.[27] Our previous method required a difficult synthesis of p-methylphosphonatophenylboronic acid. In this new work, we adapted more sustainable approach eliminating the use of organotin compounds in the preparation of *p*-$(MeO)_2(O)P$-$(C_6H_4)_2$-$B(OH)_2$,[27] and we prepared H_8-PyTPPA in a relatively more sustainable four step organic synthesis as seen in the synthesis section. To the best of our knowledge, H_8-PyTPPA and its ester form Et_8-PyTPPE have never been synthesized, and the optoelectronic properties of pyrene phosphonates remain unexplored (see synthesis section below for further synthetic details).

2. Synthesis

Scheme 1. Synthesis of Et_8-PyTPPE and H_8-PyTPPA

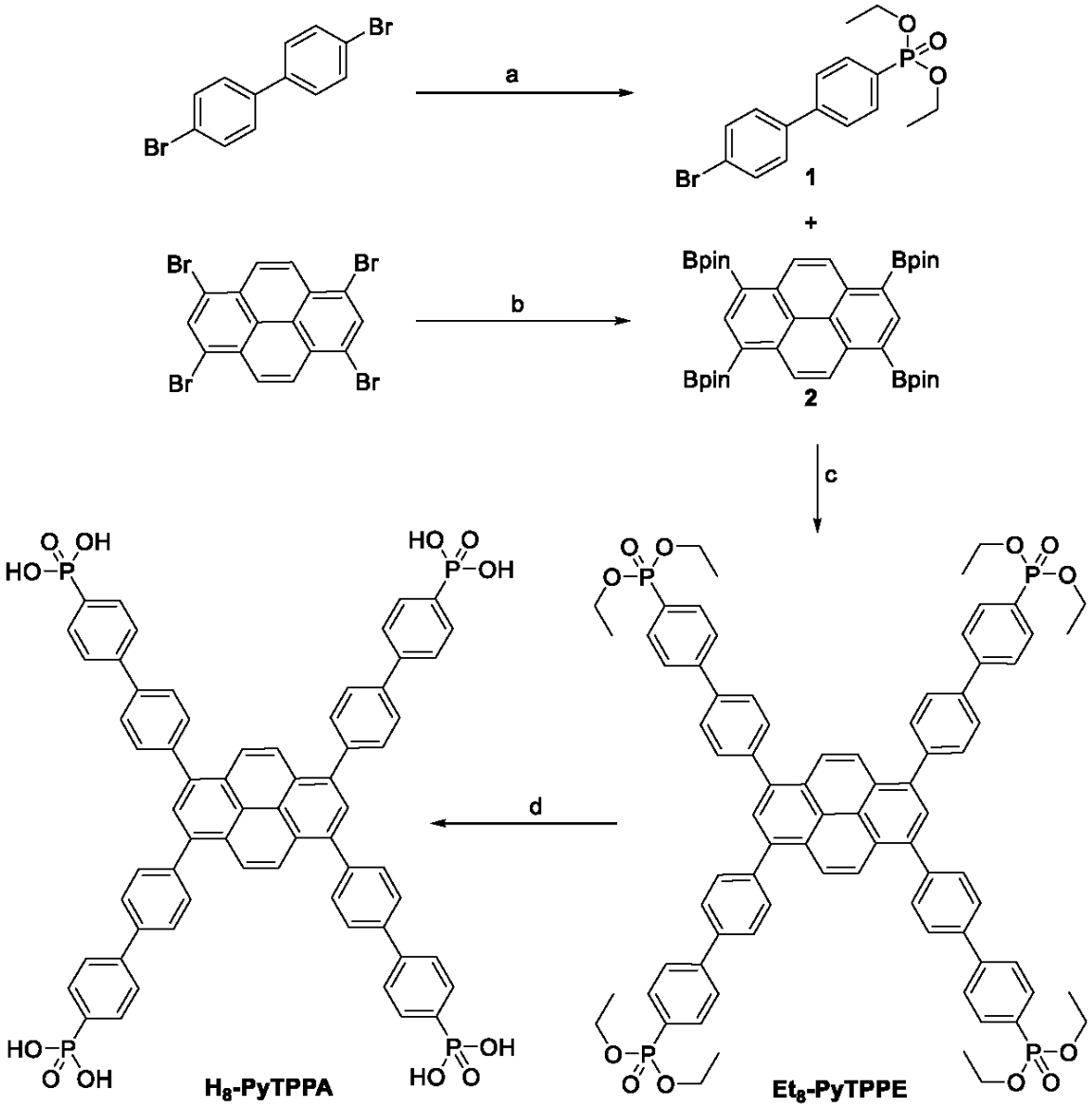

a) $P(OEt)_3$, $NiBr_2$, 170 °C, 3 h; b) B_2pin_2, $Pd(dppf)Cl_2$, KOAc, 104 °C, 24 h; c) K_2CO_3, $Pd(dppf)Cl_2$, 104 °C, 48 h; d) HCl (37%), 100 °C, 2d.

Diethyl(4'-bromo-[1,1'-biphenyl]-4-yl)phosphonate (1)

In a two neck round bottom flask, 4,4'-dibromo-1,1'-biphenyl (4.0 g, 12.8 mmol) and $NiBr_2$ (600 mg, 2.75 mmol) were suspended in 20 mL of 1,3 diisopropylbenzene under a nitrogen atmosphere. The suspension was heated under stirring to 170 °C. Triethyl phosphite (2.5 mL, 14.6 mmol) was added over a period of 2 hours. The reaction mixture was stirred for a further hour at 170 °C, then cooled to room temperature and excess of triethyl phosphite and solvent

were removed under reduced pressure. The crude product was purified by column chromatography using ethyl acetate as eluent. The product obtained was a colorless oil, which turned into a colorless solid after one day (2.1 g, 5.68 mmol, 44 %).

^{1}H-NMR (300 MHz, $CDCl_3$) δ 7.87 (ddt, *J* = 12.9, 8.2, 1.7 Hz, 2H), 7.67 – 7.60 (m, 2H), 7.60 – 7.55 (m, 2H), 7.48 – 7.43 (m, 2H).4.25-4.04 (m, 4H), 1.34 (t, *J* = 7.1 Hz, 6H) ppm (Figures S2).

1,3,6,8-tetrakis(4,4,5,5-tetramethyl-1,3,2-dioxaborolan-2-yl)pyrene (2)

Under a nitrogen atmosphere, 1,3,6,8-tetrabromopyrene (1.0 g, 1.93 mmol, 1 eq.) and B_2pin_2 (3.5 g, 13.7 mmol, 7 eq.) were placed in a 100 ml two-neck flask. KOAc (2.0 g, 20.3 mmol, 10 eq.), $PddppfCl_2$ (70 mg, 0.09 mmol, 0.05 eq.) and 50 mL of degassed 1,4-dioxane were added to the flask. The reaction mixture was heated to 104 °C for 24 h. After 24 h the reaction was cooled to room temperature. To the crude product 50 mL of ethyl acetate was added and the organic phase was washed with 50 mL water and 50 mL of brine. The organic phase was dried of magnesium sulphate, concentrated and purified by column chromatography using dichloromethane and cyclohexane (5:1) as eluent. The resulting product was a pale-yellow powder (980 mg, 72 %). ^{1}H-NMR (300 MHz, $CDCl_3$) δ 9.16 (s, 4H), 8.99 (s, 2H), 1.50 (s, 48H) ppm (Figure S3).

Octaethyl(pyrene-1,3,6,8-tetrayltetrakis(([1,1'-biphenyl]-4',4-diyl)))tetrakis(phosphonate) (Et_8-PyTPPE)

Under a nitrogen atmosphere, 1,3,6,8-tetrakis(4,4,5,5-tetramethyl-1,3,2-dioxaborolan-2-yl)pyrene (400 mg, 0.57 mmol), diethyl(4'-bromo-[1,1'-biphenyl]-4-yl)phosphonate (1.25 g, 3.39 mmol), potassium carbonate (630 mg, 4.56 mmol), and $PddppfCl_2$ (40 mg, 0.05 mmol) were dissolved in 50 mL of degassed 1,4-dioxane. The reaction mixture was heated to 104 °C for 48 h. The reaction mixture was then cooled to room temperature, mixed with 50 mL of ethyl acetate and washed twice with 50 mL water. The organic phase was dried over magnesium sulphate and concentrated under reduced pressure. The crude product was purified by column chromatography using a mixture of ethyl acetate and methanol (10:1 v:v) as eluent. The resulting product was a yellow to orange powder (364 mg, 0.27 mmol, 47 %).

^{1}H-NMR (300 MHz, $CDCl_3$) δ 8.29 (s, 4H), 8.12 (s, 3H), 7.98-7.91 (m, 8H), 7.83-7.79 (m, 24H), 4.25-4.10 (m, 16H), 1.37 (t, *J* = 7.1 Hz, 24H) ppm (Figure S4). ^{13}C-NMR (75 MHz, $CDCl_3$) δ 144.7 (d, *J*=3.1 Hz), 140.9, 139.1, 136.9, 132.5 (d, *J*=10.3 Hz), 129.5, 129.2 (d,

J=315.7 Hz), 128.5, 128.4, 127.4 (d, *J*=4.3 Hz), 127.1, 126.1, 126.0, 125.6, 62.3 (d, *J*=5.4 Hz), 16.5 (d, *J*=6.5 Hz) ppm (Figure S5). ^{31}P-NMR (121 MHz, $CDCl_3$) δ 18.8 (s) ppm (Figure S6). MALDI-TOF MS: $[M]^+$ = 1354.68 m/z, calc ($C_{80}H_{78}O_{12}P_4$) = 1354.44 m/z (Figure S9). HR-ESI-MS: obs. 678.2307 m/z, calc. 678.2295 m/z $[M+2H]^{2+}$ (Figure S10).

Et_8-PyTPPE could be crystallized from chloroform and *n*-hexane and the single-crystal X-ray structure determination verifies the molecular constitution (Figure 1).

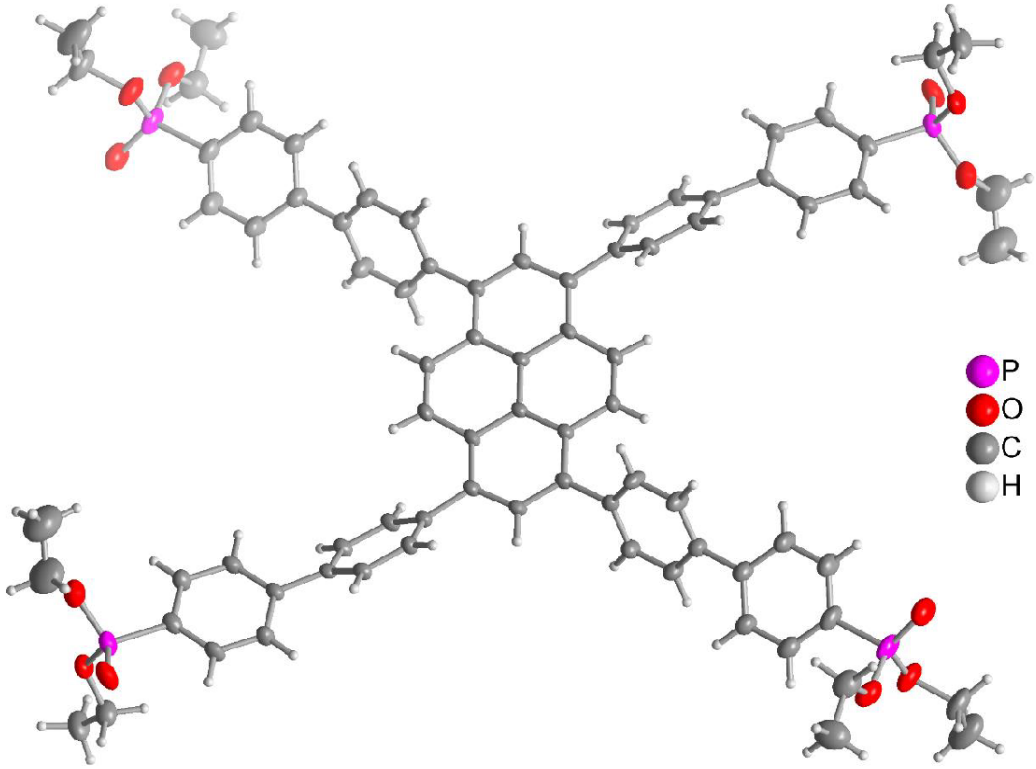

Figure 1. Molecular structure of Et_8-PyTPPE in the crystal (50% thermal ellipsoids; H atoms with arbitrary radii; a slight disorder in one of the ethyl groups is not shown; for a figure with atom labelling see Section S3, Supp. Info.).

There are no π-π stacking and only weak C–H···π interactions between the Et_8-PyTPPE molecules. Relevant π-π stacking interactions require centroid-centroid contacts of less than 3.8 Å, near parallel ring planes, small slip angles and small vertical displacements (slippage <1.5 Å) which would translate into a sizable overlap of the aryl-plane areas [1]. In the packing of Et_8-PyTPPE the shortest centroid-centroid contact is 3.97 Å (ring C21-C26 to C21-C26 with symmetry relation 1-x, 1-y, 1-z) with parallel ring planes but large slip angles and a large

slippage of 1.95 Å. Significant intermolecular C-H··· π contacts are below 2.7 Å for the (C-)H···ring centroid distances with H-perp also below 2.6-2.7 Å and C-H·· centroid > 145° [2,3]. In the structure of Et_8-PyTPPE the shortest (C-)H···ring centroid distance is 2.79 Å with H-perp 2.71 Å and C-H·· centroid 146° (Figure S1).

1. Janiak, C. A critical account on π–π stacking in metal complexes with aromatic nitrogen-containing ligands. *J. Chem. Soc., Dalton Trans.* **2000**, 3885–3896. https://doi.org/10.1039/B003010O

2. Nishio, M. The CH/π Hydrogen Bond in Chemistry. Conformation, Supramolecules, Optical Resolution and Interactions Involving Carbohydrates. *Phys. Chem. Chem. Phys.* **2011**, *13*, 13873. https://doi.org/10.1039/c1cp20404a

3. Nishio, M.; Umezawa, Y.; Honda, K.; Tsuboyama, S.; Suezawa, H. CH/π Hydrogen Bonds in Organic and Organometallic Chemistry. *CrystEngComm* **2009**, *11*, 1757. https://doi.org/10.1039/b902318f

(Pyrene-1,3,6,8-tetrayltetrakis([1,1'-biphenyl]-4',4-diyl))tetrakis(phosphonic acid) (H_8-PyTPPA)

In a 100 mL round bottom flask, a suspension of octaethyl(pyrene-1,3,6,8-tetrayltetrakis(([1,1'-biphenyl]-4',4-diyl)))tetrakis(phosphonate) (150 mg, 0.11 mmol) in a 37 % solution of HCl in water (50 mL) was heated to reflux for 2 d. The product precipitated as a green solid and was filtered off. The product was dried in a vacuum oven at 60 °C for 24 h (98 mg, 0.09 mmol, 78 %). ^{1}H-NMR (300 MHz, D_2O+NaOD) δ 8.37 (s, 4H), 8.24 (s, 2H), 8.01-7.98 (m, 8H), 7.88-7.85 (m, 24H) ppm (Figure S7). ^{31}P-NMR (121 MHz, D_2O+NaOD) δ 11.1 ppm (Figures S8).

3. Thin film formation:

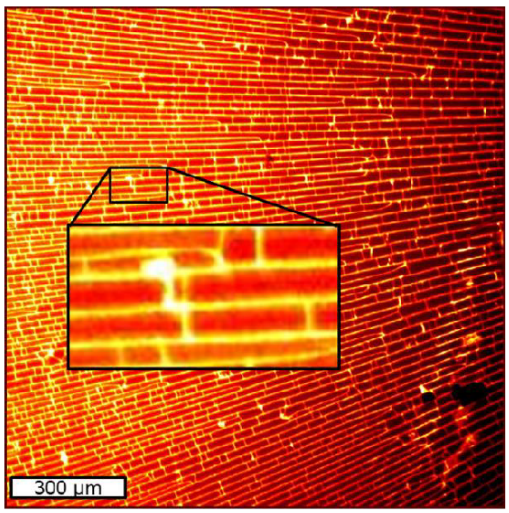

Figure 2. Photoluminescence microscopy image of the H_8-PyTPPA film for PL signals at wavelengths at 520 nm. The sample was excited with a 365 nm LED. The white scale bar corresponds to 300 µm

H_8-PyTPPA was dissolved in NaOH and this solution were applied on a glass surface and allowed to dry slowly to form the crystalline thin films of H_8-PyTPPA. Figure 1 shows the hyperspectral photoluminescence (PL) microscope image of the film. The sample was optically excited with an LED of 365 nm peak wavelength. The image shows the PL intensity at an emission wavelength of 520 nm. We interpret the features of highest PL emission as cracks that have formed during the crystallization or drying, propagating from or to the center of the film. The film pattern as seen in Figure 1 represents a polycrystalline layer with rod shaped grains with a width of approximately 20 µm and lengths up to several hundred micrometers. The higher PL intensity could then be the results of better light out-coupling at the edges of the grains.

4. Photoluminescence spectra

As seen in Figure 3, PL spectra of the H_8-PyTPPA film and the powder of its ester Et_8-PyTPPE are illuminated with a 405 nm laser diode at an intensity of approximately 100 mW/cm^2. Both samples display three distinct PL peaks at approximately 490 nm (peak 1), 510 nm (peak 2) and 560 nm (peak 3). Moreover, a long tail at higher wavelengths is visible. To gain a better understanding on the structure of the spectrum, we fit to the measured data a superposition (dashed blue line) of four Gaussian curves (solid blue lines).

For the Et_8-PyTPPE powder, the Gaussian peaks were observed at 481.5, 500.5, 544.0, and 609.0 nm, with relative peak intensities of 1.00, 0.97, 0.81, and 0.10, respectively, and full width at half maximum (FWHM) values of 31.9, 45.9, 97.1, and 164.9 nm. Similarly, for the H_8-PyTPPA film, the fitted Gaussian peaks appeared at 479.3, 502.8, 554.7, and 633.0 nm, with relative peak intensities of 0.16, 0.70, 1.00, and 0.21, respectively, and FWHM values of 19.8, 19.8, 19.8, and 184.51 nm. The alignment of peak positions and FWHM values across both samples suggests the presence of the same photoactive species, though their relative photoluminescence (PL) activity varies. Consequently, the emission profile of Et_8-PyTPPE

powder can be described either as two dominant Gaussian PL peaks at approximately 480 and 500 nm or as a single peak centered around 490 nm. Additionally, the peak at approximately 550 nm exhibits roughly half the intensity of the peak at 590 nm, while the tail at longer wavelengths remains less pronounced.

The H_8-PyTPPA film also displays two peaks at 480 and 500 nm or likewise one single peak at 490 nm, and another peak at approximately 550 nm. However, the peak intensity at 550 nm is almost as high as the intensity of the peak at 490 nm. In comparison to the other peaks, the long wavelength tail is also much more pronounced for this sample. This could be due to a higher density of shallow, photoactive defect states. We note that spectra were measured until a wavelength of 1100 nm but data is only displayed until 800 nm as beyond this point, the signal intensity was negligible.

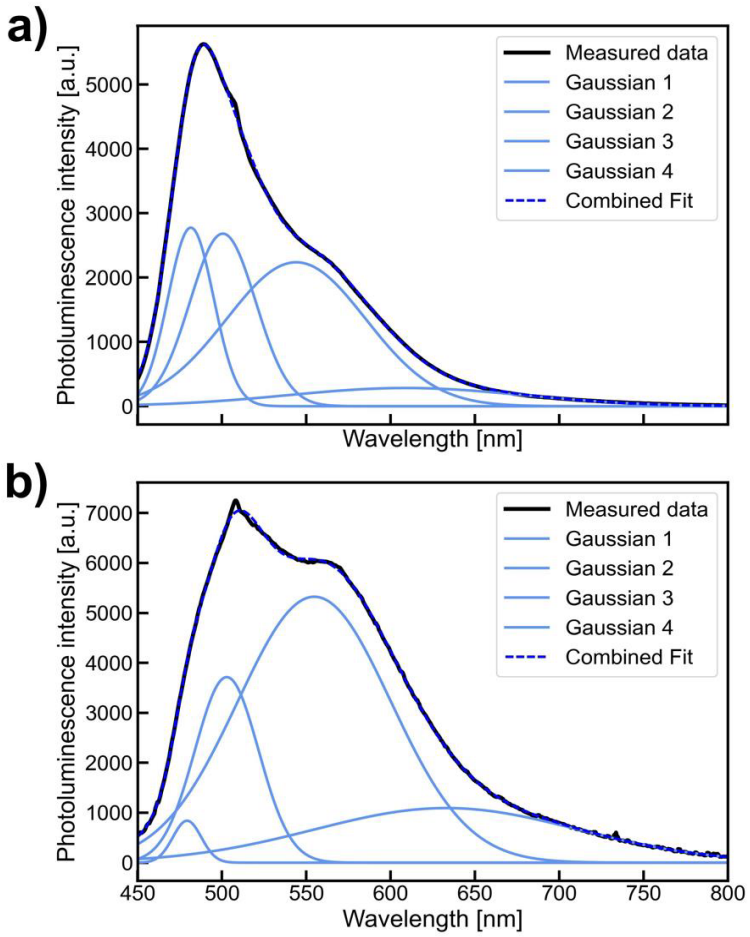

Figure 3. Photoluminescence spectra (black line) of Et_8-PyTPPE (a) and H_8-PyTPPA film (b), illuminated with a 405 nm laser diode. The blue solid lines represent three Gaussian curves fit to the data to yield optimal accordance with the measured data in the combined fit adding the three curves (dashed blue line).

5. Temperature variable PL spectra

To study the temperature dependence of the PL spectra, the Et_8-PyTPPE powder was encapsulated with UV curable glue between two glass plates and was placed on a temperature controllable stage and illuminated with a 405 nm laser at an intensity of approximately 100 mW/cm². As shown in Figure 4, the PL peak intensity at 490 nm reduced to approximately 78% when the sample was heated to 80 °C in comparison to the highest PL intensity recorded at 25 °C. Normalizing the curves to the main peak shows a relative change of the intensity at the shoulder between 550 and 650 nm.

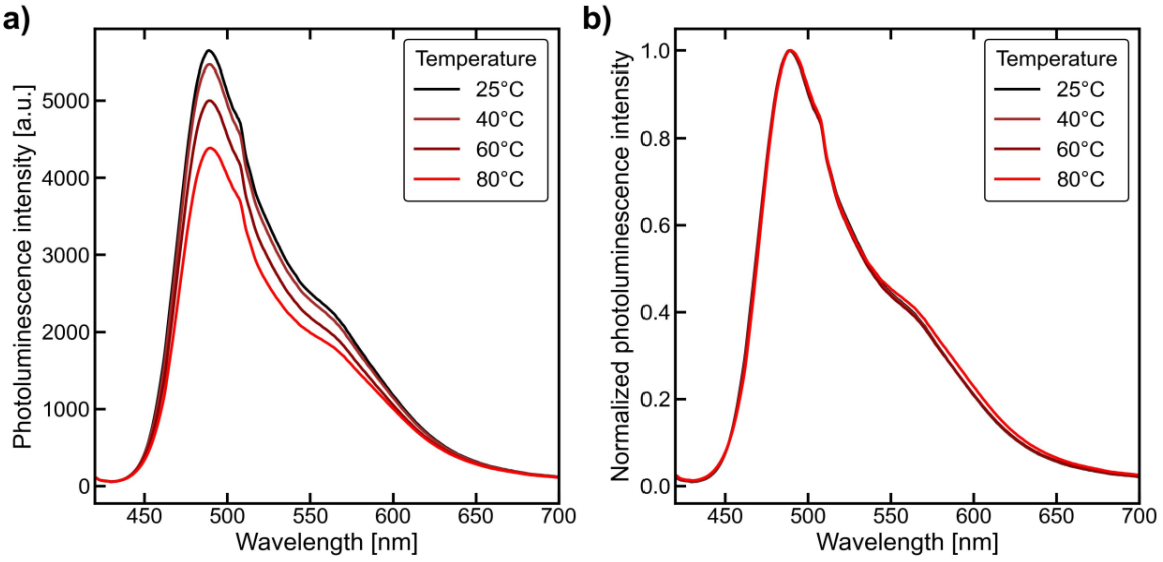

Figure 4. Photoluminescence spectra of H_8-PyTPPA film at different temperatures. The sample was illuminated with a 405 nm laser diode.

6. Electrical response to illumination

The film of H_8-PyTPPA was placed on a 4-point-probe station, whereby the film is contacted with four gold-plated pogo-pin contact arranged in a straight line with a distance of 1.27 mm between each pin. A constant current of 10 nA was applied through the outer pins and the voltage along the inner two pins was measured. As depicted in Figure 5, the induced voltage showed a clear photoresponse to the change of the illumination intensity of a white LED, whereas "1" corresponds to approximately 100 mW/cm². When the light is switched off, the voltage first increases and then falls below the initial value. The inverse behavior can be observed when the light is again switched on. This is an indication of photoconductivity, which needs to be assessed in detail in further studies.

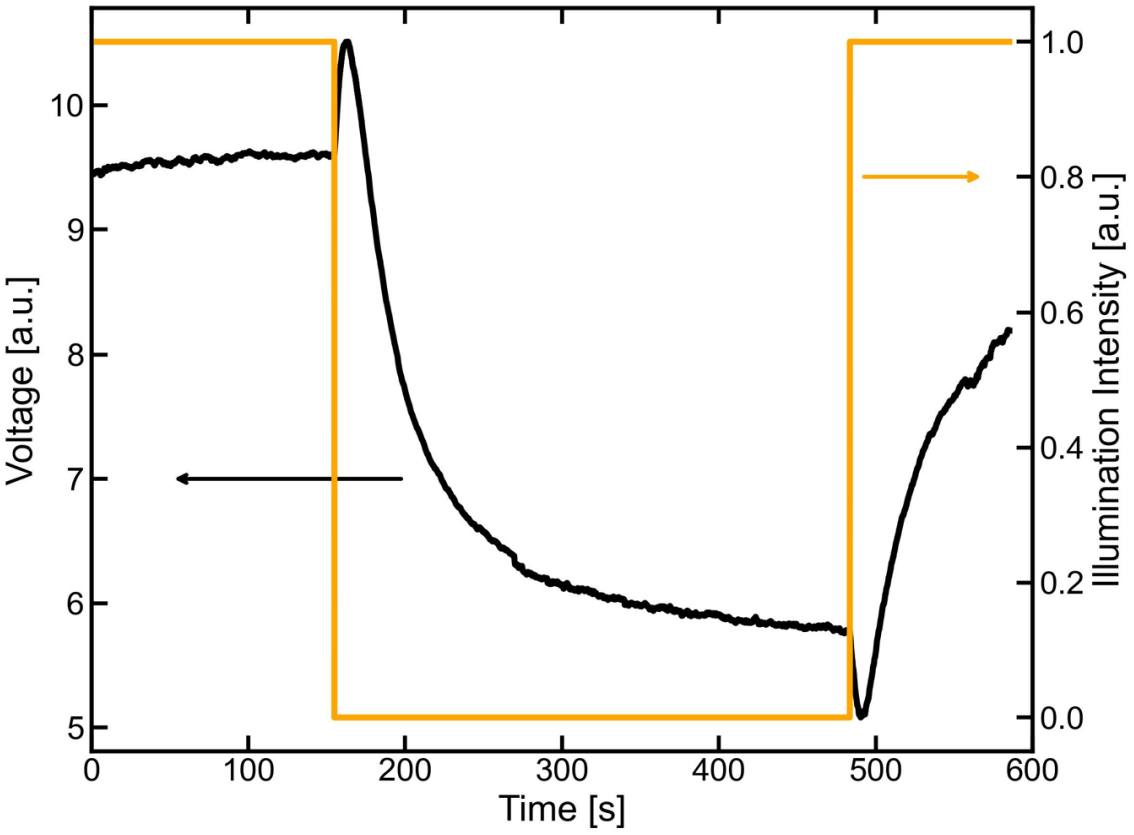

Figure 5. Photoresponse of the H_8-PyTPPA film voltage in a 4-point-probe measurement setup.

7. Thermogravimeteric analysis

As seen in **Figure 6,** the weight loss until 400 °C indicates the loss of solvent molecules of H_8-PyTPPA, the additional lostafter 200 °C is associated with the water lost after the condensation of phosphonic acids forming polyphosphonate COFs and polymers, and the pyrolysis of the pyrene core begins after 500 °C. On the other hand, the loss of organic components of the ester form begins after 200 °C and ends at ca. 300 °C. Similarly, the pyrene core in the ester form also decomposes after 500 °C.

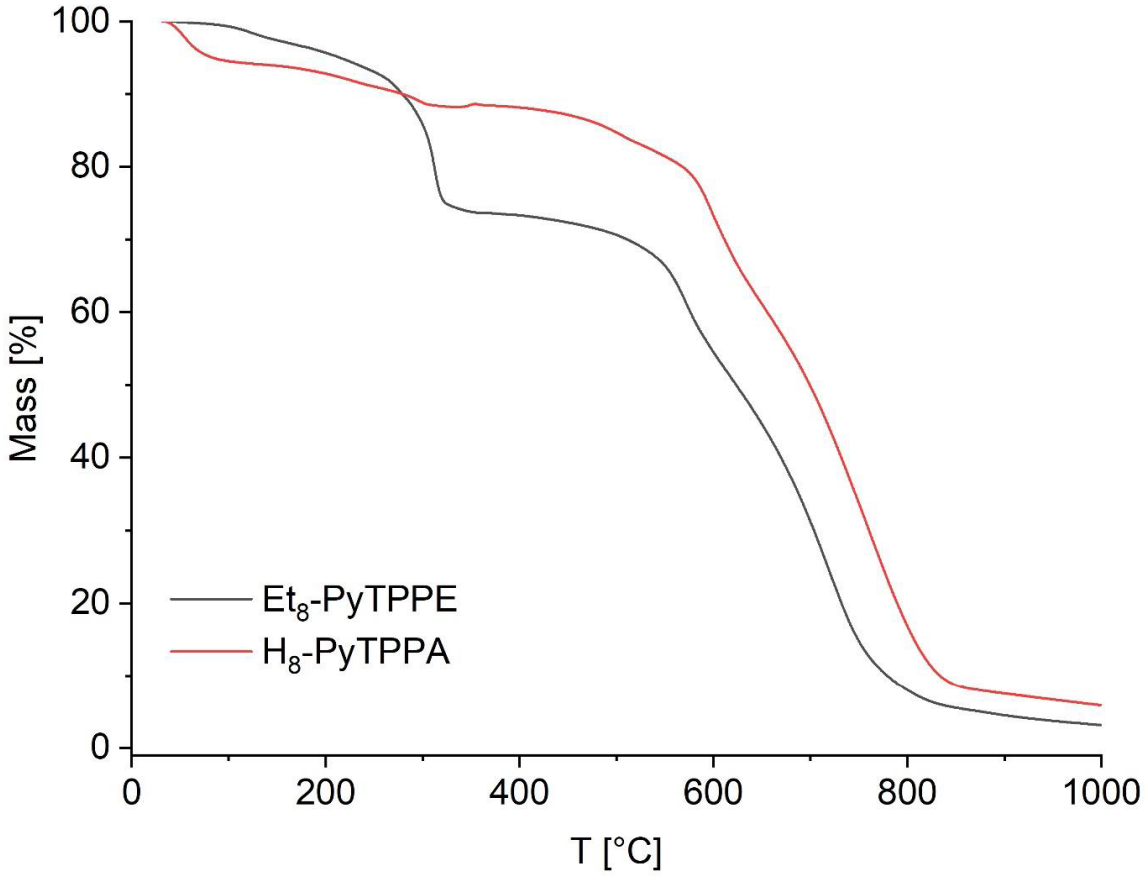

Figure 6. Thermogravimetric analysis of H_8-PyTPPA (red curve) and its ester form Et_8-PyTPPE (black curve).

Conclusion

We present the synthesis and characterization of two new organic semiconductors H_8-PyTPPA, a pyrene tetraphosphonic acid and its ester form Et_8-PyTPPE with a distinctive X-shaped planar structure. Both compounds generated band gaps below 1.9 and 2,1 eV respectively, which is

within the semiconducting regime. Our optoelectronic studies reveal that the thin films of H_8-PyTPPA exhibits light-responsive electrical conductivity, positioning it as a strong candidate for next-generation optoelectronic devices. Notably, it demonstrates exceptional stability in harsh conditions, withstanding 37% HCl and temperatures exceeding 500 °C before pyrolysis of the pyrene core begins. The negligible decrease in photoluminescence intensity at higher temperatures indicates the efficiency of H_8-PyTPPA as a photovoltaic material at high temperatures. The observed voltage increase highlights its potential in photovoltaic applications, offering a sustainable alternative to heavy metal-based materials. With resilience against UV light, acidity, and high temperatures, H_8-PyTPPA paves the way for more durable and environmentally sustainable energy solutions.

Supporting Information

Supporting Information for the details of synthesis, mass spectrometry, crystal structure refinement, NMR, IR and optical spectroscopy is available.

Data Availability Statement: The CCDC number XXXXXX for compound Et_8-PyTPPE contains the supplementary crystallographic data reported in this paper. These data can be obtained free of charge from the Cambridge Crystallographic Data Centre via www.ccdc.cam.ac.uk/data_request/cif

Acknowledgements

G. Y. would like to thank DFG for fundings DFG YU 267/2-1 and DFG YU 267/9-1.

Author Contributions

References

1 Yu, Y. *et al.* Pyrene-Based Emitters with Ultrafast Upper-Level Triplet–Singlet Intersystem Crossing for High-Efficiency, Low Roll-Off Blue Organic Light-Emitting Diode. *Adv. Opt. Mater.* **11**, 2202217 (2023).

2 Zeng, J. *et al.* Y-Shaped Pyrene-Based Aggregation-Induced Emission Blue Emitters for High-Performance OLED Devices. *Adv. Opt. Mater.* **10**, 2200917 (2022).

3 Liu, Y. *et al.* Highly Efficient Blue Organic Light-Emitting Diode Based on a Pyrene[4,5-d]Imidazole-Pyrene Molecule. *CCS Chem.* **4**, 214 (2022).

4 Liu, Y. *et al.* Pyrene[4,5-d]imidazole-Based Derivatives with Hybridized Local and Charge-Transfer State for Highly Efficient Blue and White Organic Light-Emitting Diodes with Low Efficiency Roll-Off. *ACS Appl. Mater. Interfaces* **12**, 16715 (2020).
5 Boyd, P. G. *et al.* Data-driven design of metal–organic frameworks for wet flue gas CO2 capture. *Nature* **576**, 253-256 (2019). https://doi.org:10.1038/s41586-019-1798-7
6 Kinik, F. P., Ortega-Guerrero, A., Ongari, D., Ireland, C. P. & Smit, B. Pyrene-based metal organic frameworks: from synthesis to applications. *Chemical Society Reviews* **50**, 3143-3177 (2021). https://doi.org:10.1039/D0CS00424C
7 Chen, Z., Kirlikovali, K. O., Shi, L. & Farha, O. K. Rational design of stable functional metal–organic frameworks. *Materials Horizons* **10**, 3257-3268 (2023). https://doi.org:10.1039/D3MH00541K
8 Chueh, C.-C. *et al.* Harnessing MOF materials in photovoltaic devices: recent advances, challenges, and perspectives. *Journal of Materials Chemistry A* **7**, 17079-17095 (2019). https://doi.org:10.1039/C9TA03595H
9 Ding, M., Cai, X. & Jiang, H.-L. Improving MOF stability: approaches and applications. *Chemical Science* **10**, 10209-10230 (2019). https://doi.org:10.1039/C9SC03916C
10 Biswal, B. P., Chaudhari, H. D., Banerjee, R. & Kharul, U. K. Chemically Stable Covalent Organic Framework (COF)-Polybenzimidazole Hybrid Membranes: Enhanced Gas Separation through Pore Modulation. *Chem. - Eur. J.* **22**, 4695 (2016).
11 Ding, S. Y. & Wang, W. Covalent organic frameworks (COFs): from design to applications. *Chem. Soc. Rev.* **42**, 548 (2013).
12 Jia, C. *et al.* Boosting Hydrostability and Carbon Dioxide Capture of Boroxine-Linked Covalent Organic Frameworks by One-Pot Oligoamine Modification. *Chemistry – A European Journal* **29**, e202300186 (2023). https://doi.org:https://doi.org/10.1002/chem.202300186
13 Xu, K. *et al.* Polyphosphonate covalent organic frameworks. *Nature Communications* **15**, 7862 (2024). https://doi.org:10.1038/s41467-024-51950-1
14 Bůžek, D., Adamec, S., Lang, K. & Demel, J. Metal-Organic Frameworks vs. Buffers: Case Study of UiO-66 Stability. *Inorg. Chem. Front.* **8**, 720 (2021).
15 Adelani, P. O., Jouffret, L. J., Szymanowski, J. E. S. & Burns, P. C. Correlations and Differences between Uranium(VI) Arsonates and Phosphonates. *Inorganic Chemistry* **51**, 12032-12040 (2012). https://doi.org:10.1021/ic301942t
16 Bao, S.-S., Shimizu, G. K. H. & Zheng, L.-M. Proton conductive metal phosphonate frameworks. *Coordination Chemistry Reviews* **378**, 577-594 (2019). https://doi.org:https://doi.org/10.1016/j.ccr.2017.11.029
17 Clearfield, A. & Demadis, K. *Metal Phosphonate Chemistry: From Synthesis to Applications*. (2012).
18 Gagnon, K. J., Perry, H. P. & Clearfield, A. Conventional and unconventional metal-organic frameworks based on phosphonate ligands: MOFs and UMOFs. *Chem Rev* **112**, 1034-1054 (2012). https://doi.org:10.1021/cr2002257
19 Goura, J. & Chandrasekhar, V. Molecular Metal Phosphonates. *Chemical Reviews* **115**, 6854-6965 (2015). https://doi.org:10.1021/acs.chemrev.5b00107
20 Sevrain, C. M., Berchel, M., Couthon, H. & Jaffrès, P.-A. Phosphonic acid: preparation and applications. *Beilstein Journal of Organic Chemistry* **13**, 2186-2213 (2017). https://doi.org:10.3762/bjoc.13.219
21 Shearan, S. J. I. *et al.* New Directions in Metal Phosphonate and Phosphinate Chemistry. *Crystals* **9** (2019). https://doi.org:10.3390/cryst9050270

22 Yücesan, G., Zorlu, Y., Stricker, M. & Beckmann, J. Metal-organic solids derived from arylphosphonic acids. *Coordination Chemistry Reviews* **369**, 105-122 (2018). https://doi.org:https://doi.org/10.1016/j.ccr.2018.05.002

23 Taylor, J. M., Vaidhyanathan, R., Iremonger, S. S. & Shimizu, G. K. Enhancing water stability of metal-organic frameworks via phosphonate monoester linkers. *J Am Chem Soc* **134**, 14338-14340 (2012). https://doi.org:10.1021/ja306812r

24 Salcedo-Abraira, P. *et al.* High Proton Conductivity of a Bismuth Phosphonate Metal–Organic Framework with Unusual Topology. *Chem. Mater.* **35**, 4329 (2023).

25 Schütrumpf, A. *et al.* Tetrahedral Tetraphosphonic Acids. New Building Blocks in Supramolecular Chemistry. *Crystal Growth & Design* **15**, 4925-4931 (2015). https://doi.org:10.1021/acs.cgd.5b00811

26 Rhauderwiek, T. *et al.* Crystalline and permanently porous porphyrin-based metal tetraphosphonates. *Chem. Commun.* **54**, 389 (2018).

27 Schütrumpf, A., Duthie, A., Lork, E., Yücesan, G. & Beckmann, J. Synthesis of Some Di- and Tetraphosphonic Acids by Suzuki Cross-Coupling. *Zeitschrift für anorganische und allgemeine Chemie* **644**, 1134-1142 (2018). https://doi.org:https://doi.org/10.1002/zaac.201800197

28 Guo, L.-R., Bao, S.-S., Li, Y.-Z. & Zheng, L.-M. Ag(i)-mediated formation of pyrophosphonate coupled with C–C bond cleavage of acetonitrile. *Chemical Communications*, 2893-2895 (2009). https://doi.org:10.1039/B902162K

Supporting Information

Photoconductive pyrenephosphonate thin films

Marcus N. A. Fetzer[1], Ayşenur Limon[1], Christoph Janiak*[1], Jan Christoph Goldschmidt[2], Lukas Wagner[2]*, Gündoğ Yücesan[1]*

[1] Institut für Anorganische Chemie und Strukturchemie, Heinrich-Heine-Universität Düsseldorf, 40204 Düsseldorf, Germany

E-Mail: Christoph Janiak* - janiak@uni-duesseldorf.de * Corresponding author

Fax: +49-211-81-12287; Tel: +49-211-81-12286

Emails: Marcus N. A. Fetzer – fetzer@uni-düsseldorf.de; Aysenur Limon – aysenur.limon@uni-düsseldorf.de,

S1. General information

Unless otherwise noted, all commercially available compounds were used as provided without further purification. Solvents for analytical thin-layer chromatography (TLC) and ambient pressure column chromatography for the preparative purification of synthesis products were technical grade and distilled prior to use. TLC was performed on Macherey-Nagel silica gel aluminium plates with F-254 indicator, visualized by irradiation with UV light (λ_{exc} = 254 and 360 nm). Column chromatography was performed using silica gel Merck 60 (particle size 0.063 – 0.2 mm). Solvent mixtures are understood as volume/volume. ^{1}H-NMR, ^{13}C-NMR and ^{31}P-NMR spectra were obtained on a Bruker Avance III 300 MHz-NMR in $CDCl_3$ or D_2O + NaOD. The spectra were referenced on the residual solvent peak (^{1}H-NMR δ = 7.26 ppm for $CDCl_3$ or 4.79 ppm for D_2O, ^{13}C-NMR δ = 77.1 ppm for $CDCl_3$). Data are reported in the following order: chemical shift (δ) in ppm; multiplicities are indicated s (singlet), d (doublet), t (triplet), q (quartet), m (multiplet). ESI-MS was measured on a Bruker Daltonics UHR-QTOF maXis 4G. MALDI-MS was measured on a Bruker Daltonics MALDI-TOF/TOF UltrafleXtreme. Fourier transform infrared spectroscopy (FT-IR) measurements were conducted by a Bruker TENSOR 37 IR spectrometer in the range of 4000–400 cm^{-1}. Single-crystal X-ray diffraction (SCXRD) data were collected using a Rigaku XtaLAB Synergy S diffractometer (Rigaku, Tokyo, Japan) equipped with a hybrid pixel array detector and a PhotonJet copper X-ray source (λ = 1.54184 Å). Suitable crystals were selected under a Leica M80 polarized-light micro-scope (Leica, Wetzlar, Germany) and mounted on a cryo-loop in oil. The data were processed using CrysAlisPro, which includes cell refinement, reduction, and absorption correction. The structure was solved and refined with Olex2, using SHELXT for structure solution and SHELXL for refinement [1-3]. The molecular graphics were created using the Diamond 5 software [4].

S2. Sources of chemicals

Reagent	Manufacturer
4,4'-dibromo-1,1'-biphenyl	BLDpharm
1,3 diisopropylbenzene	TCI Chemicals
Nickel(II)bromide	Thermos scientific
Triethyl phosphite	Thermos scientific
1,3,6,8-Tetrabromopyrene	BLDpharm
B_2pin_2	BLDpharm
Potassium acetate	AppliChem
$Pd(dppf)Cl_2$	Carbolution
1,4-Dioxane	Fisher Chemical
magnesium sulphate	VWR Chemicals
Potassium carbonate	Fisher Chemical
HCl (37%)	Sigmal-Aldrich

S3. X-ray structure of compound Et_8-PyTPPE

CCDC reference number is XXXXX.

Table S1a. Crystal data and structure refinement details for **Et_8-PyTPPE**.

Crystal data

$C_{80}H_{78}O_{12}P_4$	Z = 1
M_r = 1355.30	F(000) = 714
Triclinic, $P\bar{1}$	D_x = 1.261 Mg m^{-3}
a = 8.0003 (1) Å	Cu $K\alpha$ radiation, λ = 1.54184 Å
b = 9.3223 (1) Å	Cell parameters from 34962 reflections
c = 24.1656 (3) Å	θ = 3.7–79.1°
α = 95.150 (1)°	μ = 1.48 mm^{-1}
β = 94.929 (1)°	T = 150 K
γ = 93.172 (1)°	Plate, translucent light yellow
V = 1784.77 (4) Å^3	0.46 × 0.21 × 0.16 × 0.12 (radius) mm

Data collection

XtaLAB Synergy, Dualflex, HyPix diffractometer	6499 independent reflections
Radiation source: micro-focus sealed X-ray tube, PhotonJet (Cu) X-ray Source	6199 reflections with $I > 2\sigma(I)$
Mirror monochromator	R_{int} = 0.066
Detector resolution: 10.0000 pixels mm^{-1}	θ_{max} = 68.0°, θ_{min} = 3.7°
ω scans	h = -9→9
Absorption correction: for a sphere *CrysAlis PRO* 1.171.41.90a (Rigaku Oxford Diffraction, 2020) Spherical absorption correction using equivalent radius and absorption coefficient. Empirical absorption correction using spherical harmonics, implemented in SCALE3 ABSPACK scaling algorithm.	k = -11→11
T_{min} = 0.761, T_{max} = 0.773	l = -29→29
49761 measured reflections	

Refinement

Refinement on F^2	Primary atom site location: dual
Least-squares matrix: full	Hydrogen site location: inferred from neighbouring sites

$R[F^2 > 2\sigma(F^2)] = 0.095$	H-atom parameters constrained
$wR(F^2) = 0.200$	$w = 1/[\sigma^2(F_o^2) + (0.0173P)^2 + 8.5821P]$ where $P = (F_o^2 + 2F_c^2)/3$
$S = 1.18$	$(\Delta/\sigma)_{max} = 0.001$
6499 reflections	$\Delta\rangle_{max} = 0.80$ e Å^{-3}
447 parameters	$\Delta\rangle_{min} = -0.73$ e Å^{-3}
35 restraints	

Table S1b. Selected bond distances (Å) and bond angles (°) for **Et$_8$-PyTPPE** referring to the atom numbering in the image below:

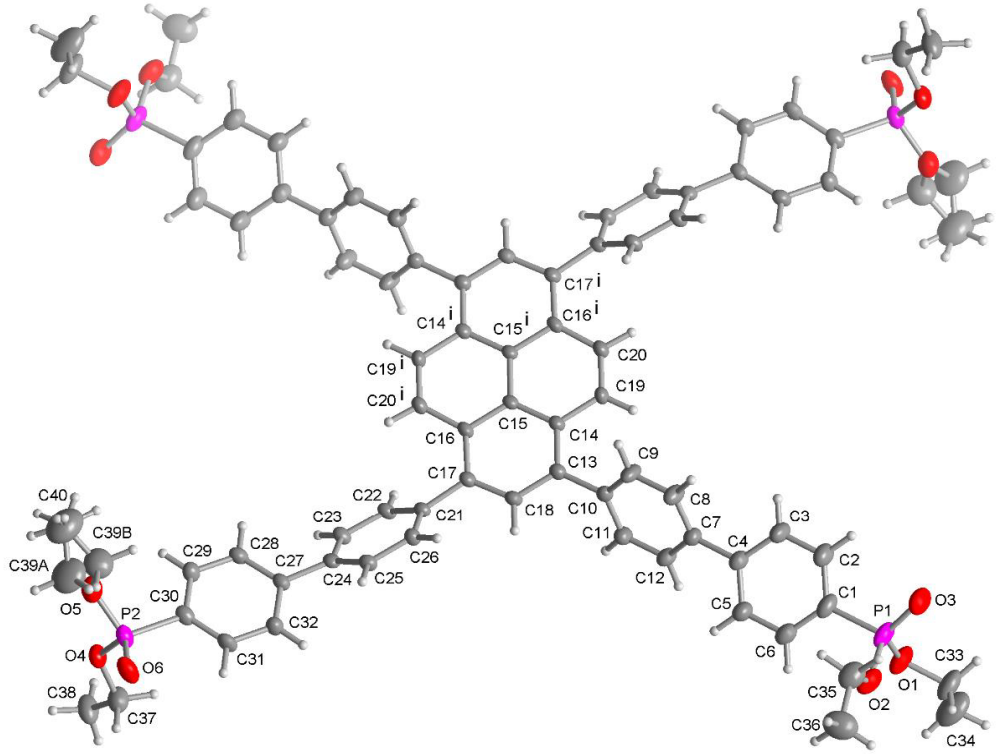

The CH_2 group (C39) of one of the ethoxy groups at P2 is slightly disordered with the major contributing atom denoted with the suffix A having a site occupation factor (SOF) of 0.54. The minor contribution of the disordered atom has a SOF of 0.46 and is denoted with the suffix B (50% thermal ellipsoids, H atoms with arbitrary radii). Symmetry code: (i) -*x*+2, -*y*+2, -*z*+1.

P1—O2	1.585 (4)	P2—O4	1.577 (3)
P1—O1	1.570 (4)	P2—O6	1.463 (3)
P1—O3	1.465 (4)	P2—O5	1.571 (4)
P1—C1	1.789 (5)	P2—C30	1.791 (4)

O2—P1—C1	106.5 (2)	O4—P2—C30	106.79 (19)
O1—P1—O2	100.4 (2)	O6—P2—O4	116.4 (2)
O1—P1—C1	102.4 (2)	O6—P2—O5	115.8 (2)
O3—P1—O2	115.8 (2)	O6—P2—C30	111.9 (2)
O3—P1—O1	116.6 (2)	O5—P2—O4	98.04 (19)
O3—P1—C1	113.4 (2)	O5—P2—C30	106.5 (2)

Table S2. Analysis of *inter*molecular C-H...Cg(Pi-Ring) Interactions (H..Cg < 3.0 Ang. - Gamma < 30.0 Deg) in **Et_8-PyTPPE**.

- Cg(J) = Center of gravity of ring J (Plane number above)

- H-Perp = Perpendicular distance of H to ring plane J

- Gamma = Angle between Cg-H vector and ring J normal

- C-H..Cg = C-H-Cg angle (degrees)

- C..Cg = Distance of X to Cg (Angstrom)

- C-H, Pi = Angle of the X-H bond with the Pi-plane (i.e.' Perpendicular = 90 degrees, Parallel = 0 degrees)

X--H(I)	Res(I)	Cg(J) [ARU(J)]	H..Cg	H-Perp	Gamma	X-H..Cg	X..Cg	X-H,Pi
C25 -H25	[1] ->	Cg4 [2676.01]	2.82	2.81	2.32	130	3.500(4)	37
C25 -H25	[1] ->	Cg5 [1455.01]	2.82	2.81	2.32	130	3.500(4)	37
C34 -H34C	[1] ->	Cg1 [2777.01]	2.86	2.83	7.85	136	3.627(8)	40
C37 -H37A	[1] ->	Cg2 [2566.01]	2.79	2.71	13.73	146	3.659(6)	58
C40 -H40C	[1] ->	Cg1 [2576.01]	2.96	2.95	4.84	165	3.911(10)	76

[2676] = 1-X,2-Y,1-Z

[1455] = -1+X,Y,Z

[2777] = 2-X,2-Y,2-Z

[2566] = -X,1-Y,1-Z

[2576] = -X,2-Y,1-Z

Cg1 = centroid of ring C1-C2-C3-C4-C5-C6

Cg2 = centroid of ring C7-C8-C9-C10-C11-C12

Cg4 = centroid of ring C14-C15-C19-C20-C15i-C16i

Cg5 = centroid of ring C15-C16-C14i-C15i-C19i-C20i

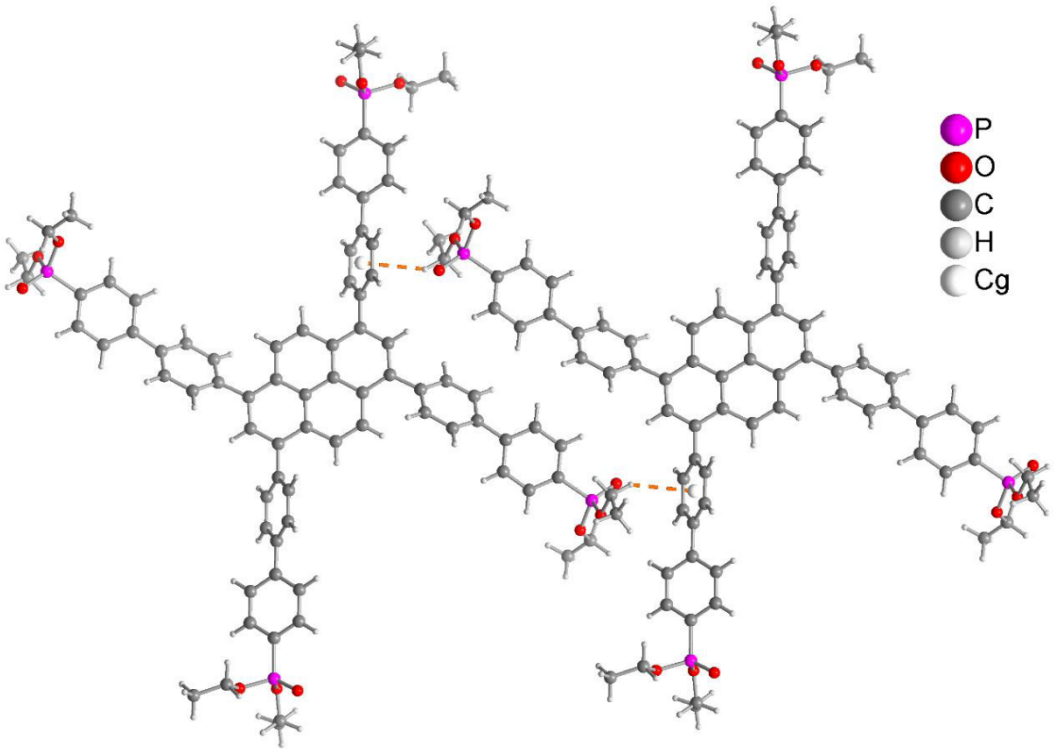

Figure S1. The shortest C-H···π interaction (C37-H37···Cg2) in the packing of **Et_8-PyTPPE** in the crystal, indicated as dashed orange lines. Further details of these C-H···π interactions, including the symmetry transformations are listed in the above Table SXX (Cg = ring centroid).

S4. NMR and MS

Diethyl(4'-bromo-[1,1'-biphenyl]-4-yl)phosphonate (**1**)

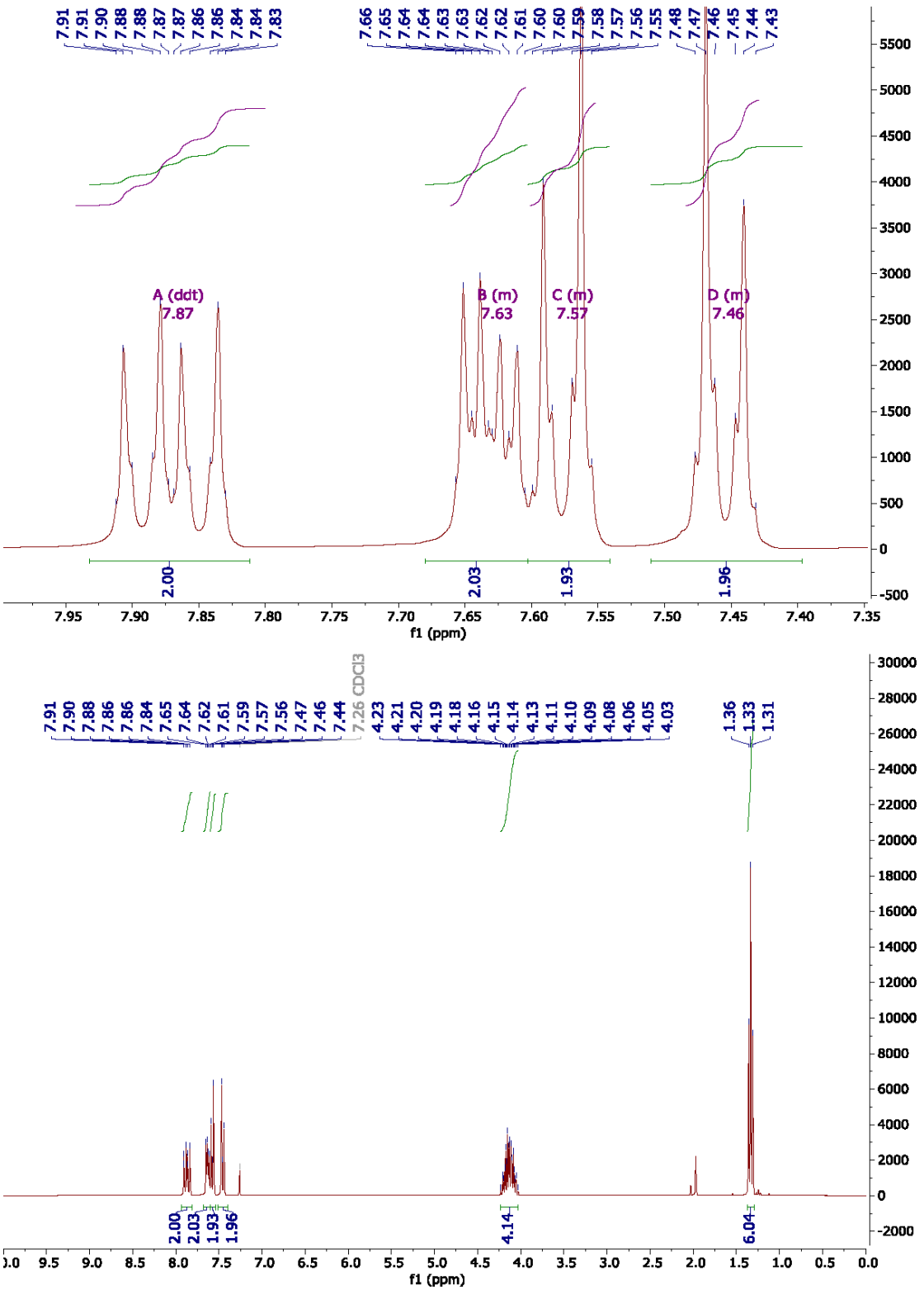

Figure S2. ^{1}H-NMR spectrum (300 MHz) of **1** in $CDCl_3$.

1,3,6,8-tetrakis(4,4,5,5-tetramethyl-1,3,2-dioxaborolan-2-yl)pyrene (**2**)

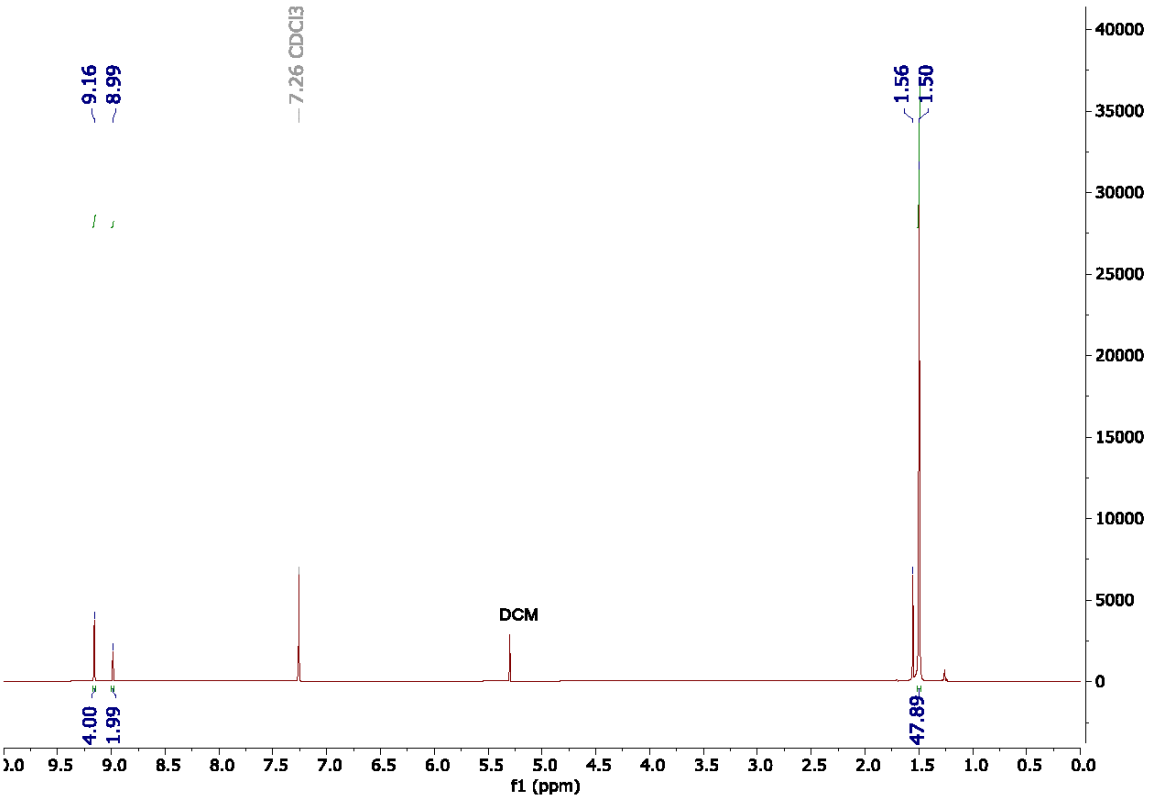

Figure S3. ^{1}H-NMR spectrum (300 MHz) of **2** in $CDCl_3$.

Et_8-PyTPPE

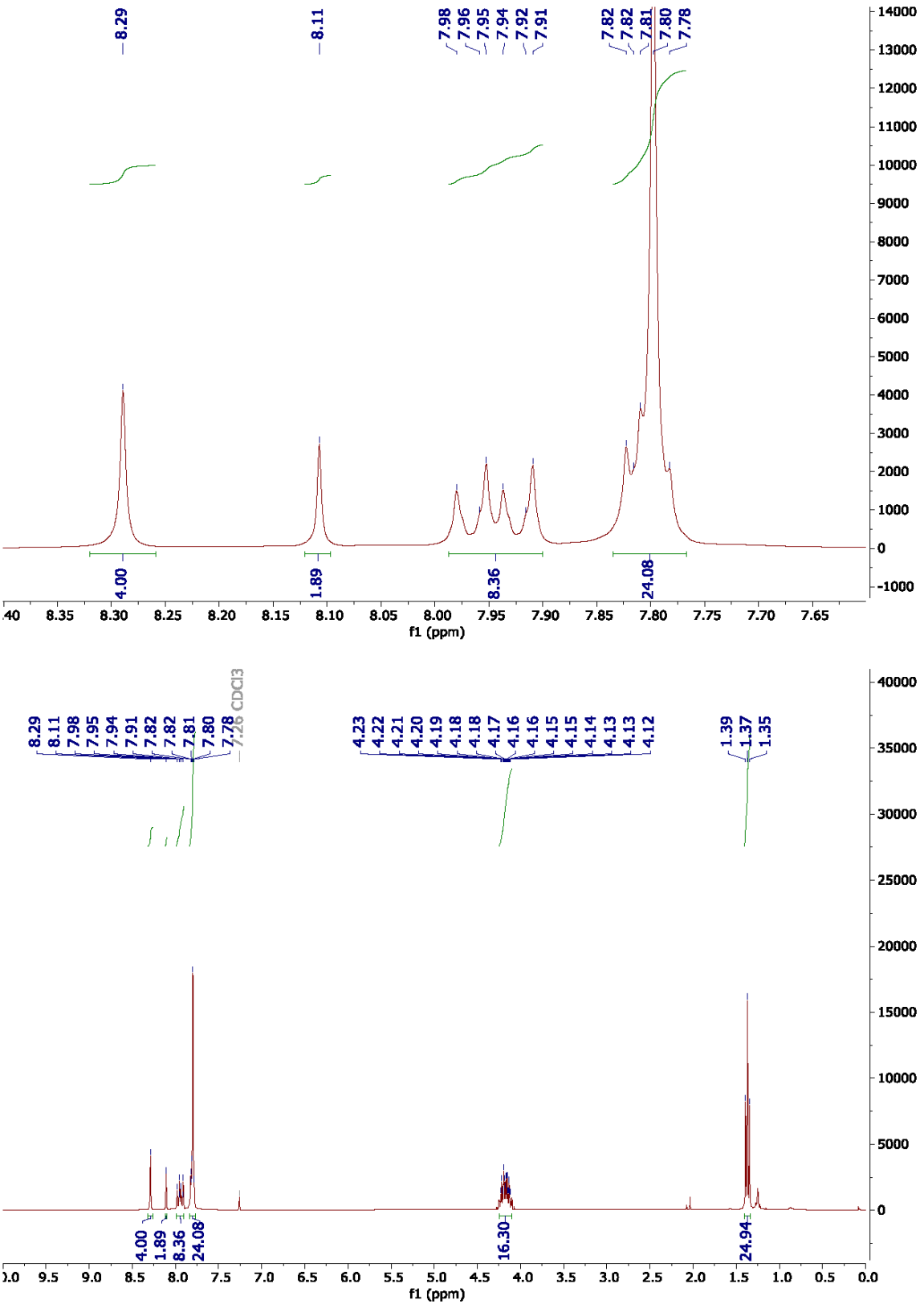

Figure S4. ^{1}H-NMR spectrum (300 MHz) of **Et_8-PyTPPE** in $CDCl_3$.

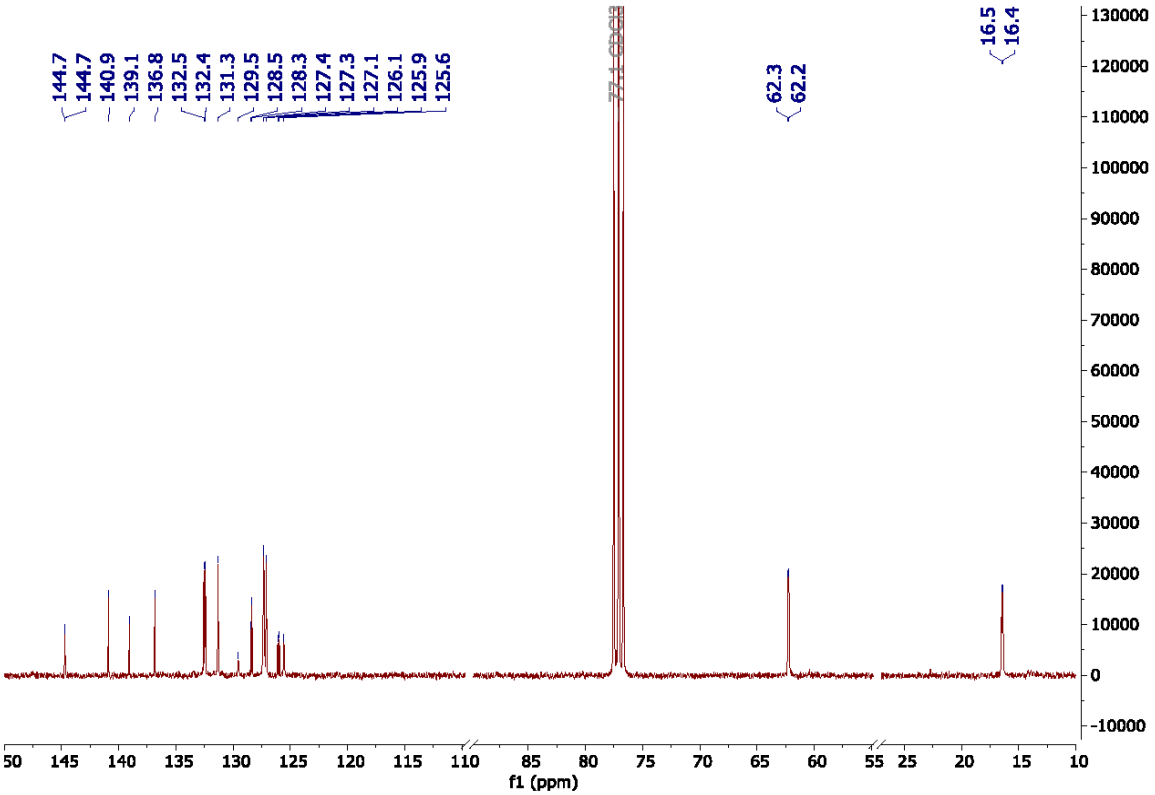

Figure S5. ^{13}C-NMR spectrum (75 MHz) of **Et$_8$-PyTPPE** in $CDCl_3$.

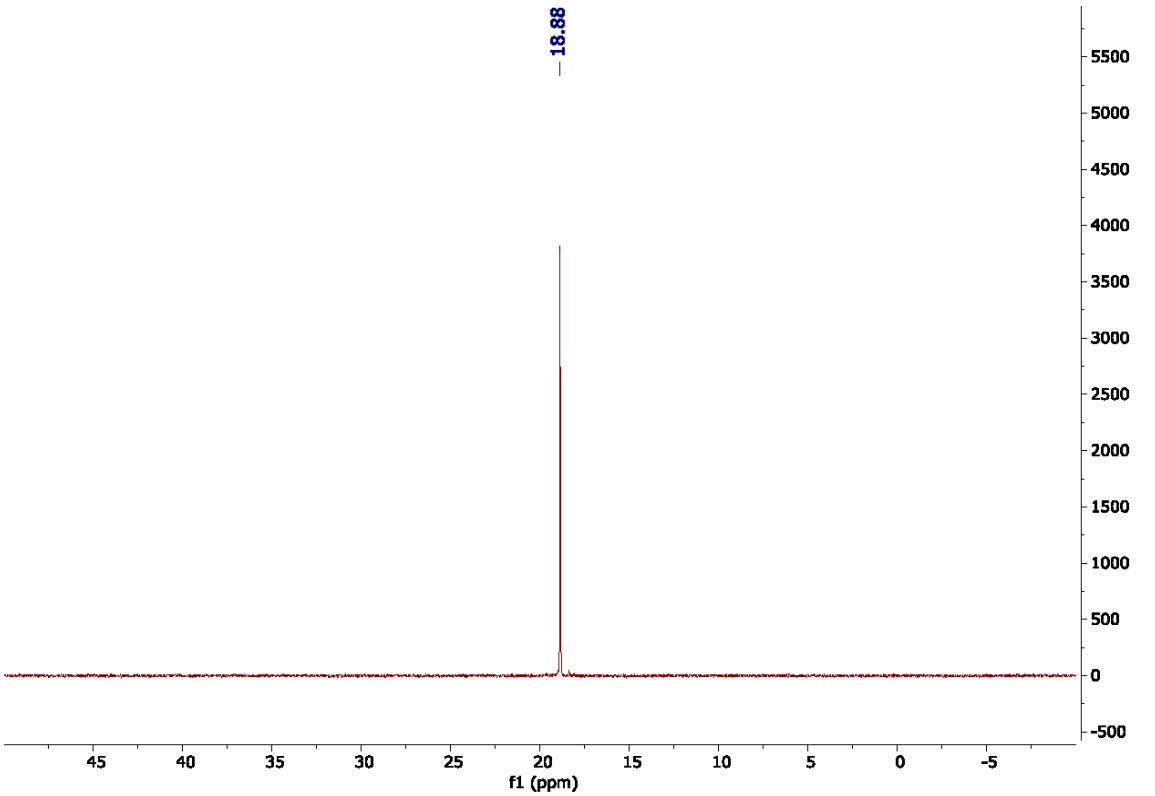

Figure S6. ^{31}P-NMR spectrum (121 MHz) of **Et$_8$-PyTPPE** in $CDCl_3$.

H_8-PyTPPA

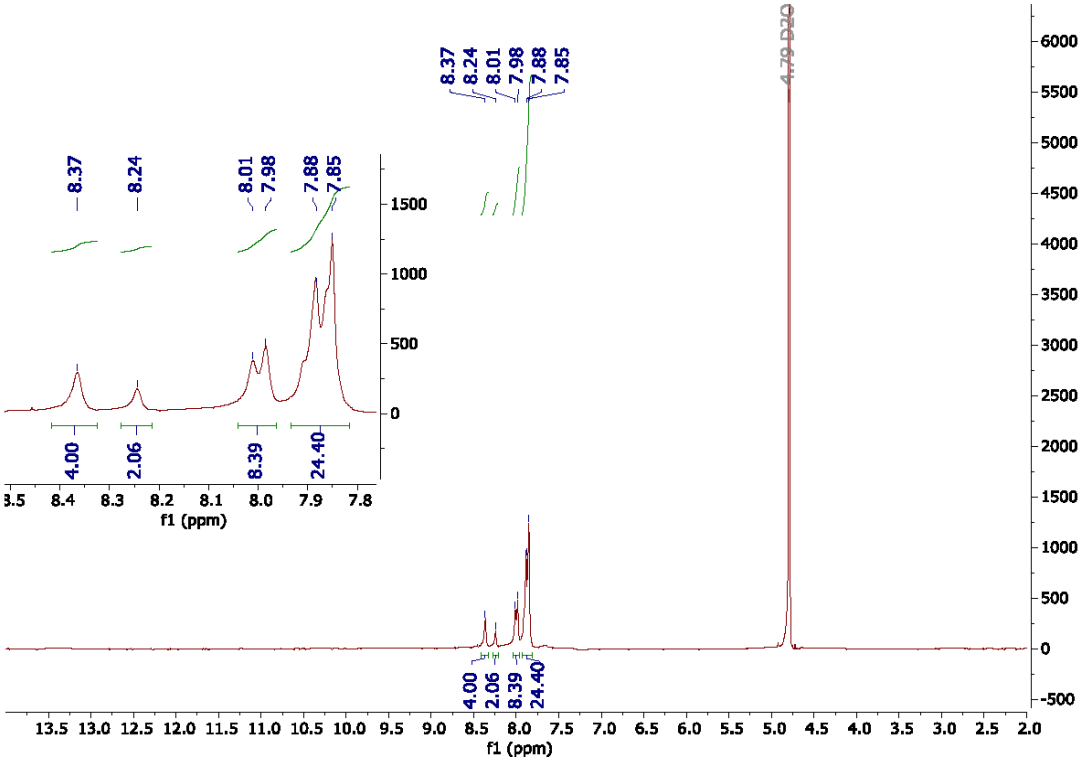

Figure S7. ^{1}H-NMR spectrum (300 MHz) of **H_8-PyTPPA** in D_2O+NaOD.

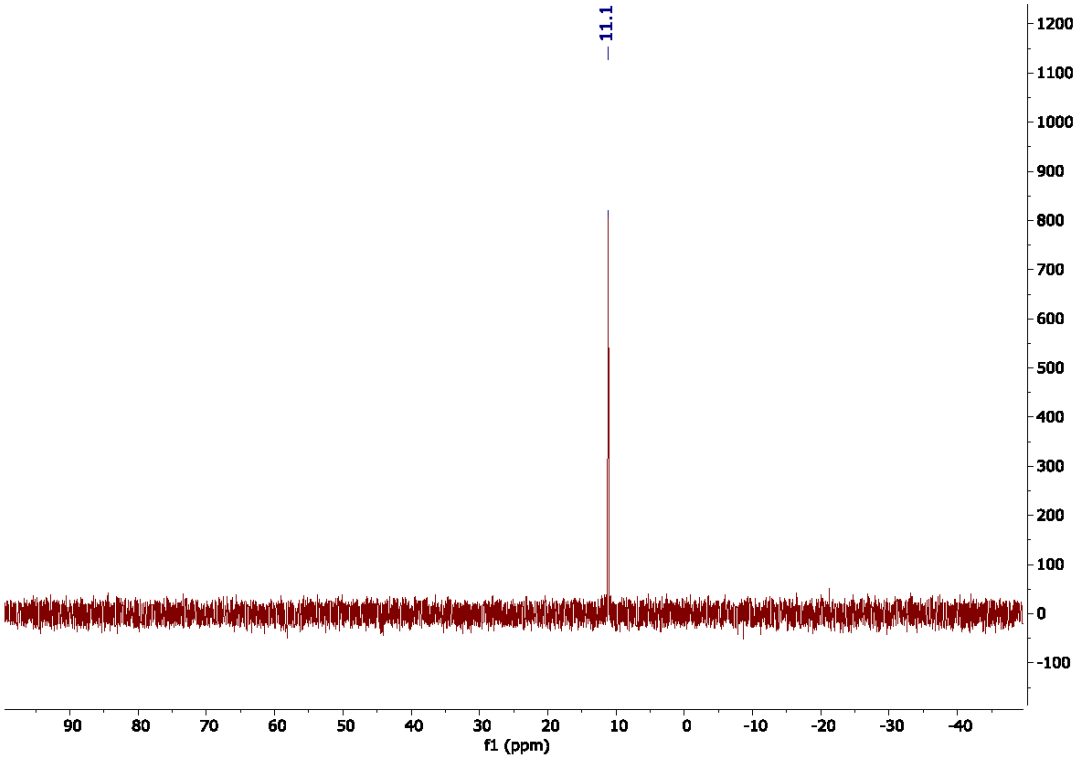

Figure S8. ^{31}P-NMR spectrum (121 MHz) of **H_8-PyTPPA** in D_2O+NaOD.

S5. MS spectra

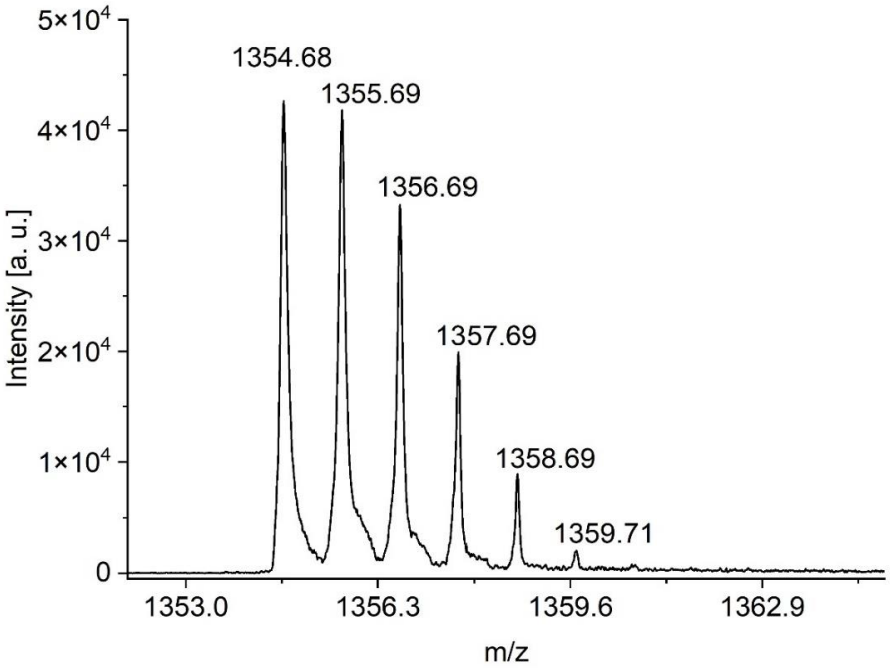

Figure S9. MALDI-TOF-MS of **Et$_8$-PyTPPE** (1354.44 g/mol) with *trans*-2-[3-(4-*tert*-Butylphenyl)-2-methyl-2-propenyliden]malononitril as matrix.

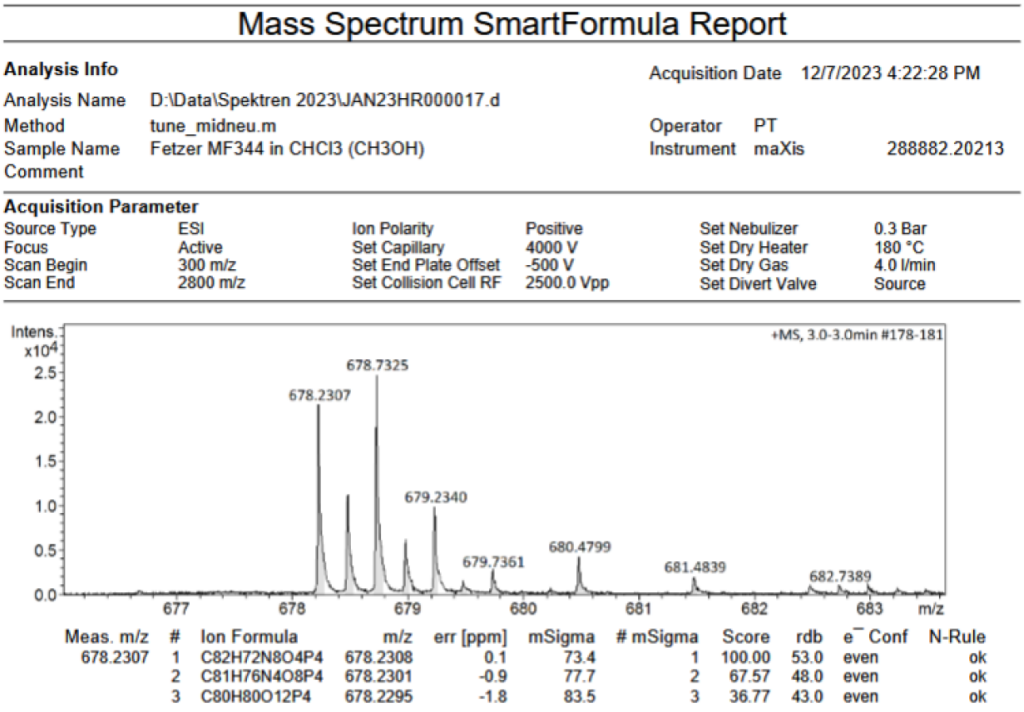

Figure S10. HR-ESI-MS of **Et$_8$-PyTPPE** Calc. for $[M+2H]^{2+}$: 678.2295 m/z – found: 678.2307 m/z.

S6. FT-IR spectra

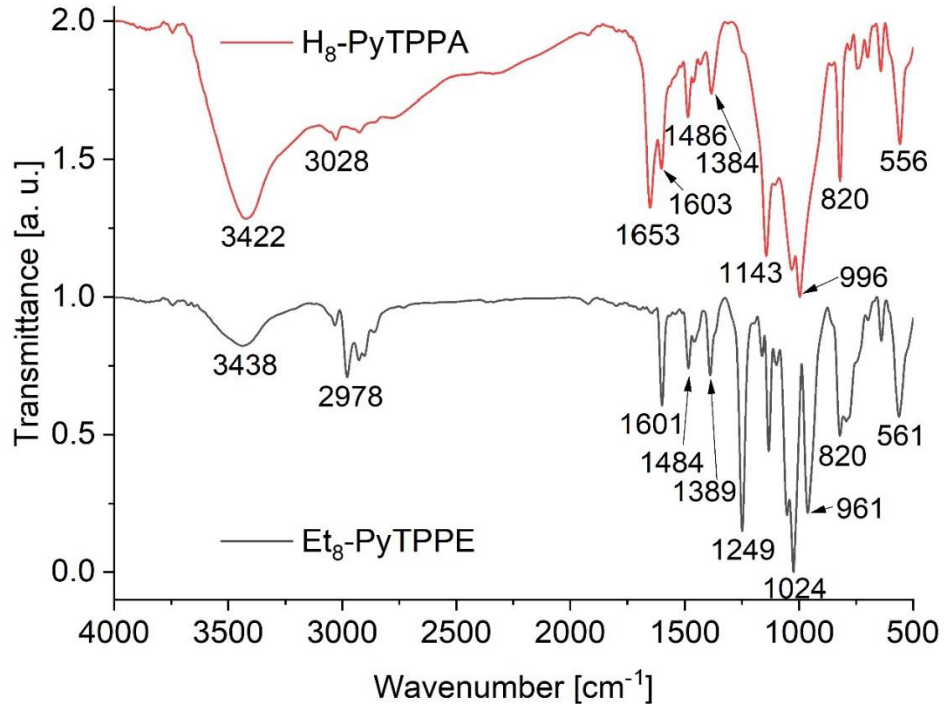

Figure S11. FT-IR of **Et_8-PyTPPE** and **H_8-PyTPPA.**

S7. Photoluminescence quantum yield

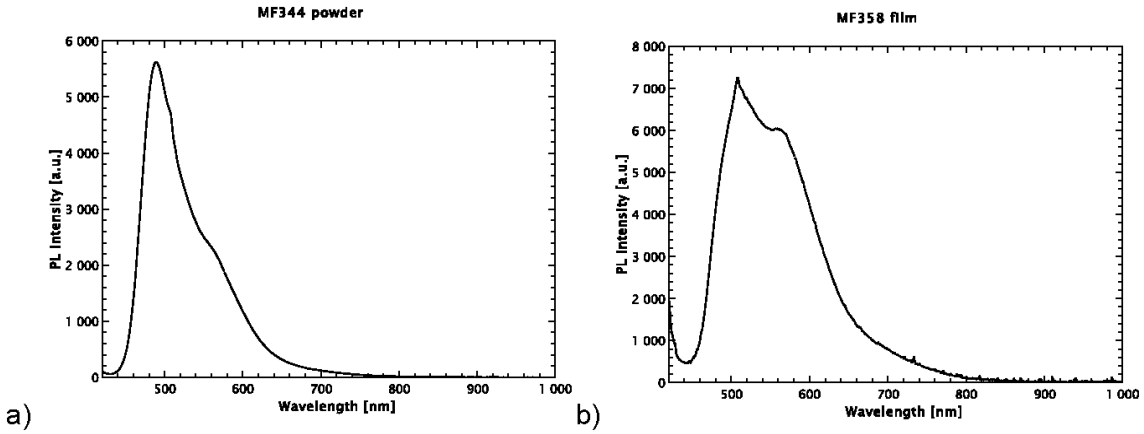

a) b)

Figure S12. Photoluminescence spectra used to determine the PL quantum yield of a) **Et_8-PyTPPE** as powder and b) **H_8-PyTPPA** as film.

S8. References

1. Dolomanov, O.V.; Bourhis, L.J.; Gildea, R.J.; Howard, J.A.K.; Puschmann, H. OLEX2: A complete structure solution, refinement and analysis program. *J. Appl. Crystallogr.* **2009**, *42*, 339–341. https://doi.org/10.1107/S0021889808042726.
2. Sheldrick, G.M. SHELXT—Integrated space-group and crystal-structure determination. *Acta Crystallogr. A* **2015**, *71*, 3–8 https://doi.org/10.1107/S2053273314026370.
3. Sheldrick, G.M. Crystal structure refinement with SHELXL. *Acta Crystallogr. C* **2015**, *71*, 3–8. https://doi.org/10.1107/S2053229614024218.
4. Brandenburg, K. Diamond, Version 5.0.0; Crystal and Molecular Structure Visualization, Crystal Impact; K. Brandenburg & H. Putz Gbr: Bonn, Germany, 1997-2023.

6. Unveröffentlichte Ergebnisse

Im folgenden Kapitel werden weitere, unveröffentlichte Ergebnisse zusammengefasst. Die Nummerierung der Abbildungen, Tabellen und Schemata folgt dem Haupttext.

6.1 Einlagerung des MR-TADF Emitter DiKTa in ZIF-8

Aufgrund der erfolgreichen Einlagerung des Emitters DiKTa in MOF-5, wurde in diesem Abschnitt die Einlagerung desselben Emitters in ZIF-8 durchgeführt. Die Einlagerung erfolgte als *in situ* Einlagerung in Anlehnung an Beldon *et al.* mittels einer Kugelmühlen-Synthese.[99] Hierbei wurden unterschiedliche Mengen (50-500 µL) einer DiKTa-Stammlösung (20 mg/ml in Dichlormethan (DCM)) zur Reaktion gegeben. Neben den Kompositen wurde auch reines ZIF-8 auf die gleiche Art hergestellt. PXRD-Analysen ergaben, dass sich phasenreines ZIF-8 in allen Ansätzen gebildet hat. Es konnten keine Reflexe der verwendeten Edukte oder des eingelagerten DiKTas gefunden werden. Die BET-Analysen ergaben, dass alle hergestellten Komposite eine vergleichbare Oberfläche zu reinem ZIF-8 aufweisen. Ihre Werte liegen im Bereich von 1187-1376 m^2/g. Die Oberfläche des reinen ZIF-8 lag dabei bei 1390 m^2/g. Abbildung 17 zeigt sowohl die gemessenen PXRDs als auch die N_2-Isothermen bei 77 K.

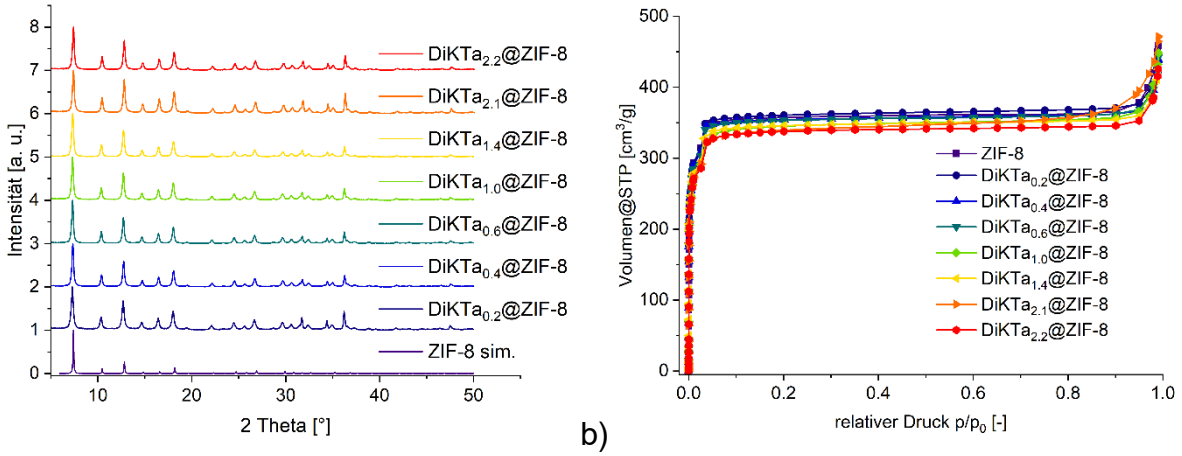

a) b)

Abbildung 17: *a) PXRDs Übersicht aller Komposite zusammen mit der ZIF-8 Simulation (CCDC: 1429243 (ZIF-8)[28]). b) Stickstoffadsorptionsisothermen aller hergestellten Komposite zusammen mit reinem ZIF-8 bei 77 K.*

Unter UV-Licht zeigen alle Komposite die für DiKTa charakteristische Lumineszenz, wodurch davon ausgegangen werden kann, dass die Einlagerung in allen Kompositen erfolgreich war. Zur genauen Bestimmung der eingelagerten Menge an DiKTa in den jeweiligen Kompositen wurden Zersetzungs-UV-Vis-Messungen in Anlehnung an die

in Abschnitt 5.1 beschriebene Methode durchgeführt. Dadurch konnten die Beladungen auf einen Bereich zwischen 0.2 und 2,2 Gewichtsprozent (Gew. %) bestimmt werden (siehe Tabelle 1).

Tabelle 1: *Bestimmung der DiKTa-Beladung aller hergestellten ZIF-8-Komposite.*

Zersetzung [mg]	Intensität bei 437 nm	Beladung [Gew. %]	Name
6,3	1,09	0,2	DiKTa$_{0.2}$@ZIF-8
4,2	1,46	0,4	DiKTa$_{0.4}$@ZIF-8
3,7	1,93	0,6	DiKTa$_{0.6}$@ZIF-8
4,6	3,99	1,0	DiKTa$_{1.0}$@ZIF-8
3,2	3,88	1,4	DiKTa$_{1.4}$@ZIF-8
3,6	6,56	2,1	DiKTa$_{2.1}$@ZIF-8
3,0	5,73	2,2	DiKTa$_{2.2}$@ZIF-8

Alle Beladungen werden in den jeweiligen Namen als Indizes angegeben. Zur Sicherstellung der erfolgreichen Einlagerung von DiKTa in ZIF-8 wurde zusätzlich zu den *in situ* hergestellten Kompositen auch ein post-synthetischer Ansatz ausprobiert. Dabei wird davon ausgegangen, dass aufgrund der Größe der Porenfenster in ZIF-8 eine erfolgreiche Einlagerung nicht stattfinden kann. Der Farbstoff sollte sich also ausschließlich an der Oberfläche des MOFs befinden. Hierfür wurde für eine bessere Vergleichbarkeit die gleiche Menge an DiKTa auf die gleiche Menge an ZIF-8 aufgetragen, wie es in der zu vergleichenden *in situ* Probe vermessen wurde. Die so hergestellte Probe wurde als DiKTa$_{post}$@ZIF-8 bezeichnet. Die Emissionsmessungen der zu vergleichenden Proben DiKTa$_{1.0}$@ZIF-8 und DiKTa$_{post}$@ZIF-8 zeigen, dass sich sowohl das Emissionsmaximum als auch die Halbwertsbreite der Emissionsbande von DiKTa$_{post}$@ZIF-8 deutlich von der in DiKTa$_{1.0}$@ZIF-8 unterscheidet. Sowohl die Emissionsmessungen als auch Bilder unter UV-Licht der beiden Proben sind in Abbildung 18 gezeigt.

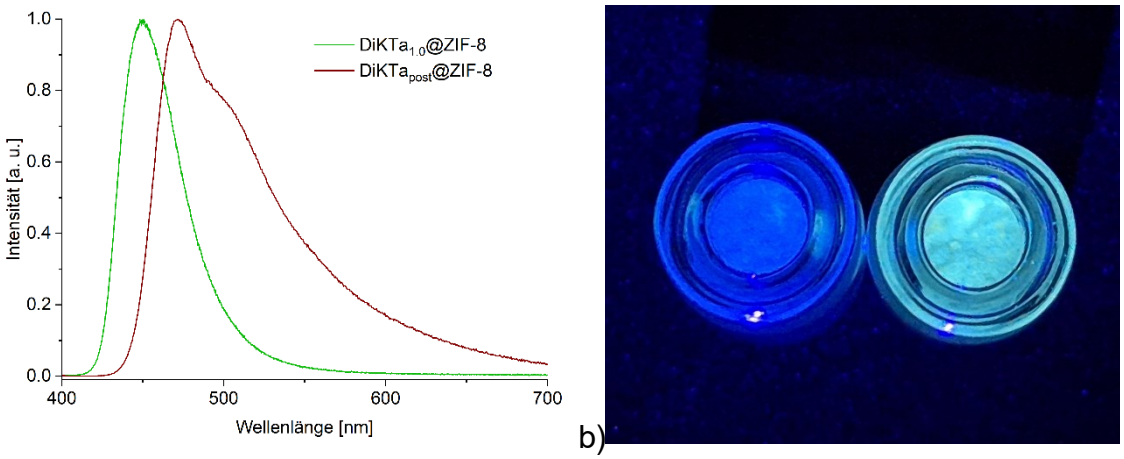

Abbildung 18: *a) Emissionsmessungen der beiden DiKTa@ZIF-8 Proben. Beide Proben wurden mit einer Wellenlänge von 330 nm angeregt. b) Foto der beiden Proben unter UV-Licht mit einer Wellenlänge von 365 nm. Links: DiKTa1.0@ZIF-8, rechts: DiKTapost@ZIF-8.*

Durch diese Messung kann davon ausgegangen werden, dass sich der Farbstoff in die ZIF-8 Poren eingebettet hat und sich nicht an der Oberfläche des MOFs befindet. Emissionsmessungen aller Komposite zeigen, dass es, ähnlich wie in Lösung, mit zunehmender Beladung zu einer bathochromen Verschiebung kommt. Dieses Verhalten ist in Abbildung 19 a) gezeigt. Vergleichend dazu wird in Abbildung 19 b) auch DiKTa in DCM-Lösung mit unterschiedlichen Konzentrationen gezeigt.

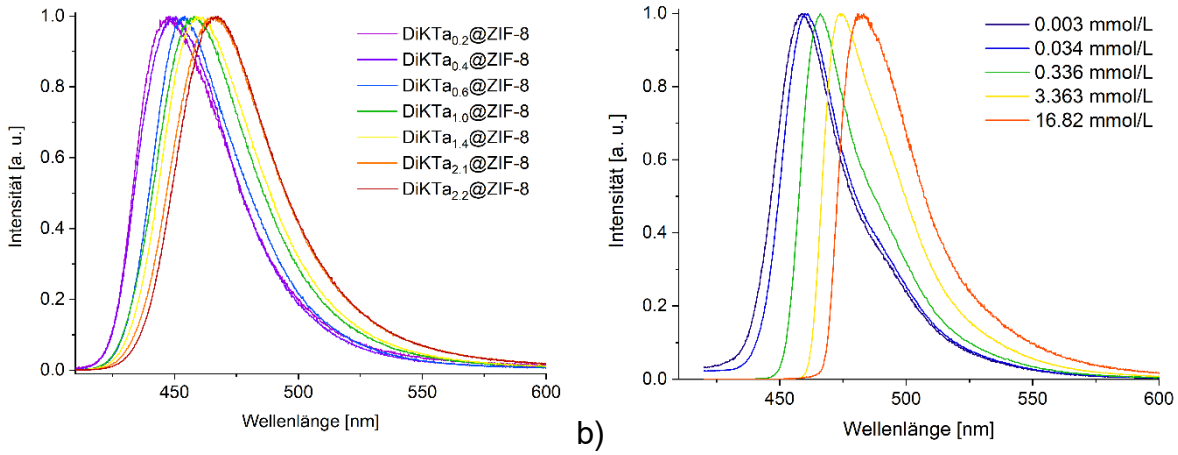

Abbildung 19: *a) Konzentrationsabhängige bathochrome Verschiebung der hergestellten DiKTa@ZIF-8 Komposite. b) Konzentrationsabhängige bathochrome Verschiebung von DiKTa in DCM-Lösung. Alle Proben wurden mit einer Wellenlänge von 330 nm angeregt.*

Lebenszeiten-Messungen zeigen eine prompte Komponente mit einer Zerfallszeit von 3.9 ns. Eine genaue Bestimmung der gesamten Lebenszeit stellt sich jedoch als schwierig heraus, da von einem Energietransfer zwischen ZIF-8 und DiKTa ausgegangen werden muss. Diese Annahme beruht auf Emissionsmessungen bei 79 K. Abbildung 20 zeigt sowohl die Emissionsmessungen der ZIF-8 Komposite als auch die Messungen der DiKTa-Lösungen sowohl bei Raumtemperatur (RT) als auch bei 79 K. Sowohl in Lösung als auch in MOF-5 wird bei dieser Temperatur eine deutliche Verschiebung der Emissionsbande beobachtet, die mit einer Verlängerung der Lebensdauer auf mehrere Millisekunden einhergeht. Diese Veränderungen sind auf die Unterdrückung des *reversed intersystem crossing* (rISC) zurückzuführen. Durch die Unterdrückung erfolgt die Emission aus dem Triplettzustand, was auch die verlängerte Lebenszeit erklärt.

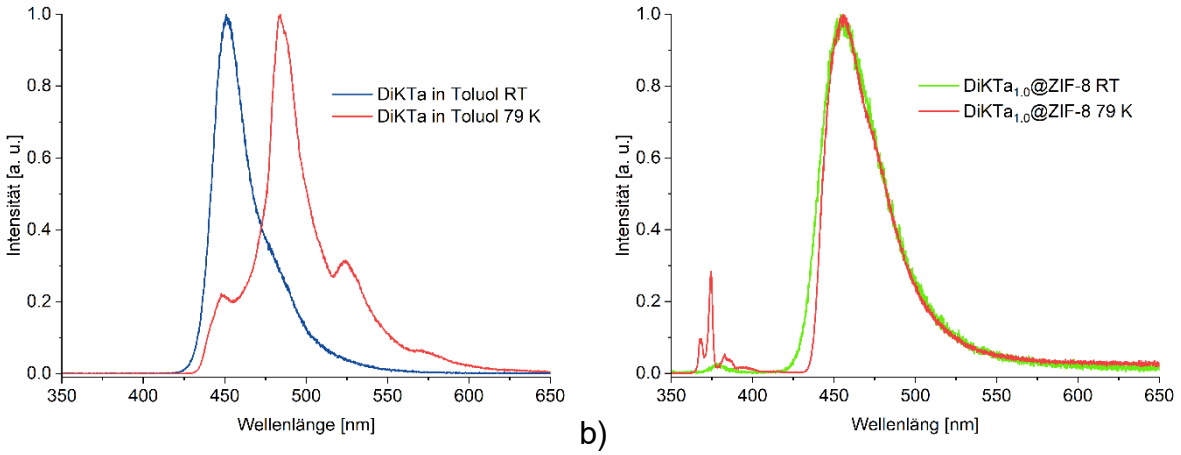

Abbildung 20: *Emissionsbande von a) DiKTa in Toluol und b) DiKTa im ZIF-8 Komposit sowohl bei RT als auch bei 79 K. Für alle Messungen wurde eine Anregungswellenlänge von 330 nm verwendet.*

Da die untersuchten Proben dieses Verhalten nicht zeigen, ist eine präzise Bestimmung der Lebenszeit schwierig. Um die gefundenen photophysikalischen Prozesse genauer verstehen zu können, ist eine umfangreiche Untersuchung unabdingbar. Diese sollte sowohl den Mechanismus des Energietransfers als auch die genaue Lebenszeit des DiKTas in der ZIF-8-Matrix aufklären.

6.2 Synthese eines auf DiKTa-basierenden Linkers und die Verwendung in der MOF-Synthese.

Nach der erfolgreichen Einlagerung des MR-TADF-Emitters DiKTa in MOF-5 (siehe Abschnitt 5.1) wurde im Rahmen dieses Projektes das DiKTa-Molekül zu einem geeigneten Carboxylat-basierten Linker umgesetzt. Dieser neue Linker könnte dann in der Synthese neuer lumineszenter MOFs verwendet werden. Dort sollte dann das Hauptaugenmerk auf den bereits zuvor beschriebenen MR-TADF-Eigenschaften liegen. Nachfolgend wird auf die einzelnen Synthesestufen eingegangen (Schemata 1 und 2).

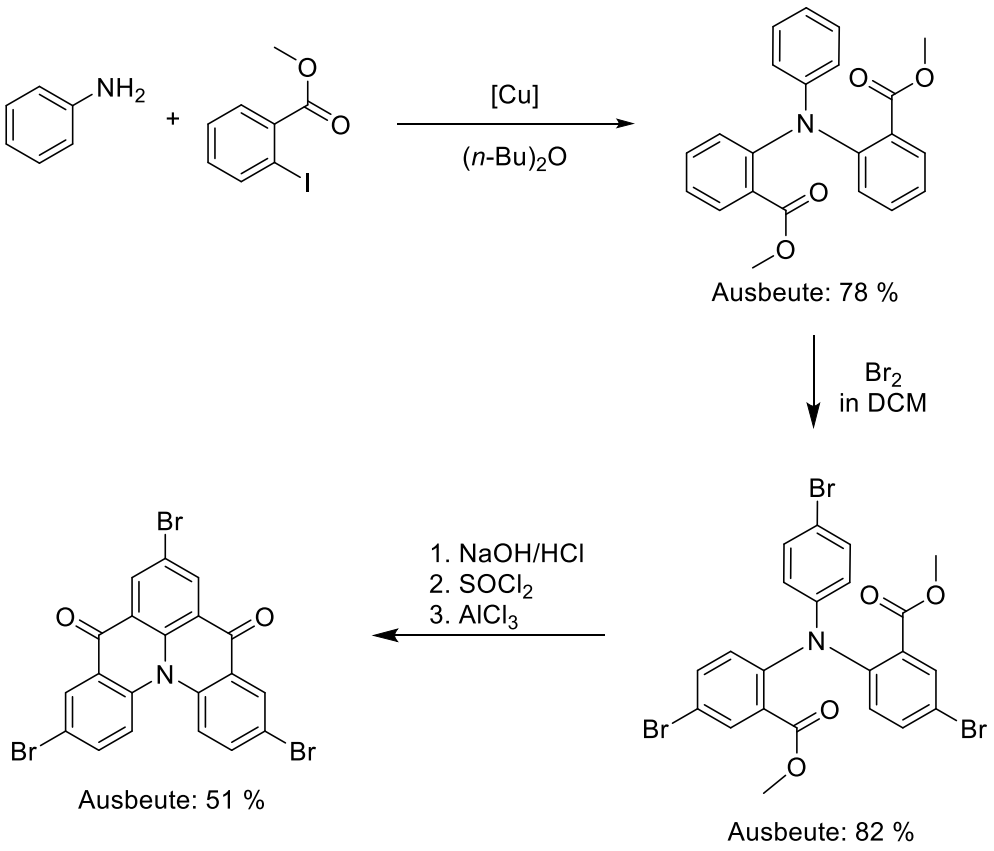

Schema 1: *Reaktionsschema zur Synthese des benötigten Br_3DiKTa.*

Die Synthese des Triarylamins erfolgte in Anlehnung an Field *et al.*[100] Der erste Schritt wird in der Literatur als Jourdan-Ullmann-Kupplung beschrieben. Bei dieser Kupplung handelt es sich um eine artverwandte Reaktion zur Ullmann-Kupplung. Beide Reaktionen verwenden Kupfer als Katalysator. Im Gegensatz zur „klassischen" Ullmann-Kupplung, welche Arylhalogenide zu Diarylen umsetzt, wird bei der Jourdan-Ullmann-Kupplung Anilin als Nukleophil eingesetzt, wodurch Di- bzw. Triarylamine

gebildet werden. Auf diese Weise konnten in der ersten Synthesestufe unter Verwendung von Anilin und einem Überschuss von 2-Iodbenzoesäure-methylester das gewünschte Triarylamin mit einer Ausbeute von 78 % erhalten werden. Sowohl die nachfolgende Bromierung als auch die Ringschlusssynthese wurden in Anlehnung an Hall *et al.* durchgeführt.[101] Für die Synthese des Dimethyl-6,6'-((4-bromphenyl)azandiyl)bis(3-brombenzoat) wurde elementares Brom in einem dreifachen Überschuss verwendet. Hierfür wurde das zuvor hergestellte Triarylamin in DCM gelöst. Das Produkt, welches ein blassgelber Feststoff ist, konnte mit einer Ausbeute von 82 % isoliert werden. Der anschließende Ringschluss erfolgte identisch zur Synthese von DiKTa in drei Schritten (Abschnitt 5.1). Der erste Schritt umfasste dabei die quantitative Entschützung der Carbonsäure. Im zweiten Schritt wurde die hergestellte Säure mit Thionylchlorid in trockenem DCM zu dem entsprechenden Säurechlorid umgesetzt. Der dritte Schritt entspricht einer Friedel-Crafts-Acylierung. Hierbei wurde wasserfreies Aluminiumchlorid als Katalysator in der Reaktion verwendet. Das dabei gewonnene Rohprodukt entspricht einem gelben Feststoff, der durch mehrfache Extraktion mit DCM und anschließendem aufeinanderfolgendem Refluxieren in Cyclohexan, Methanol und Ethylacetat aufgereinigt werden konnte. Die Gesamtausbeute der Ringschlussreaktion belief sich auf 51 %. Das so hergestellte bromierte DiKTa (Br_3DiKTa) konnte in einer Suzuki-Kupplung mit 4-Methoxycarbonylphenylborsäure zur gewünschten Linkervorstufe (Me_3L) umgesetzt werden (siehe Schema 2).

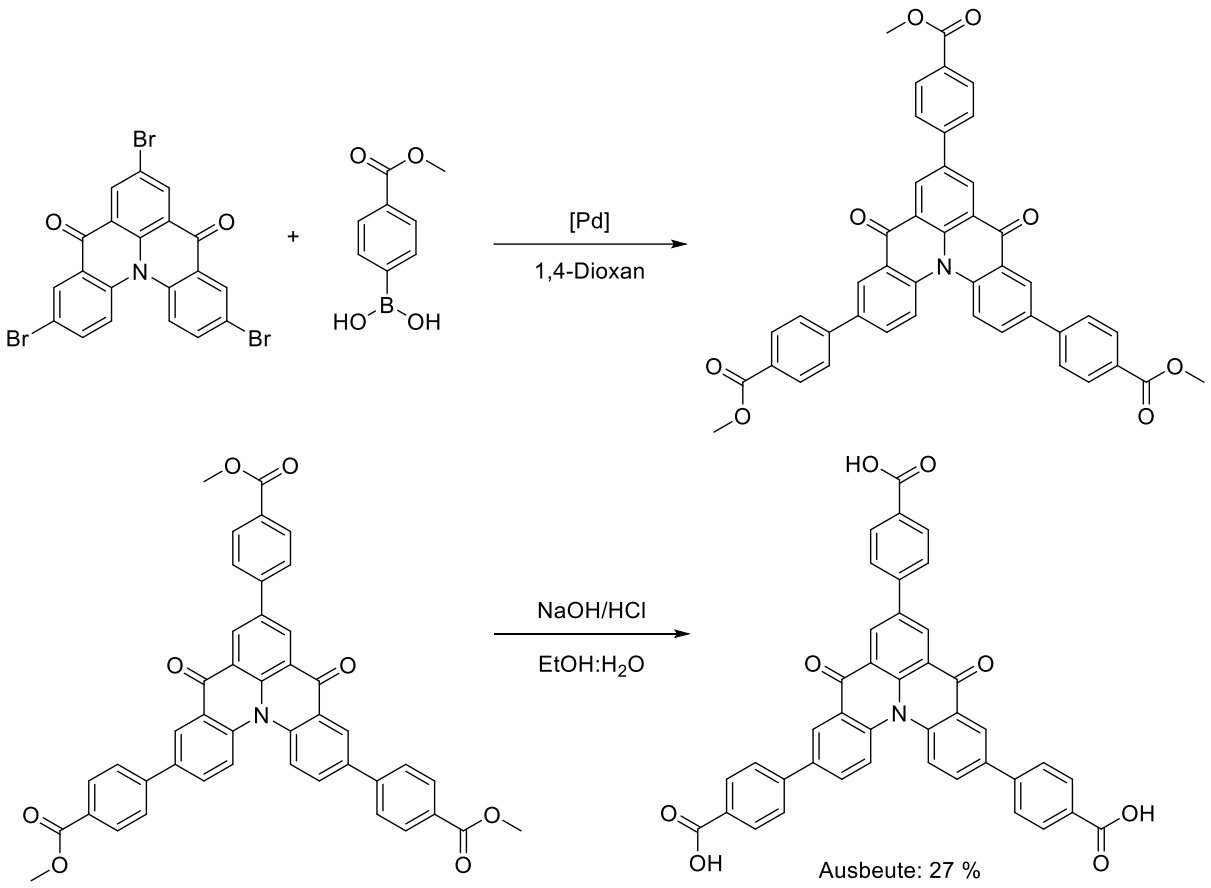

Schema 2: *Reaktionsschema zur Synthese eines auf DiKTa basierenden Linkers.*

Der nach der Kupplung erhaltene Ester wurde hierbei mittels Säulenchromatographie an Silica aufgereinigt. Das erhaltene Produkt ist ein gelber Feststoff, der in Lösung unter UV-Licht eine türkis-grüne Lumineszenz zeigt. Der Erfolg der Synthese konnte anhand von einer NMR-Messung bestätigt werden (siehe Abbildung 26). Durch das Eindampfen von *n*-Hexan in eine konzentrierte Chloroform-Lösung konnten Kristalle für eine Kristallstrukturanalyse gewonnen werden (siehe Tabelle 4). Die in Abbildung 21 gezeigte Struktur bestätigt den Erfolg der vorangegangenen Synthese.

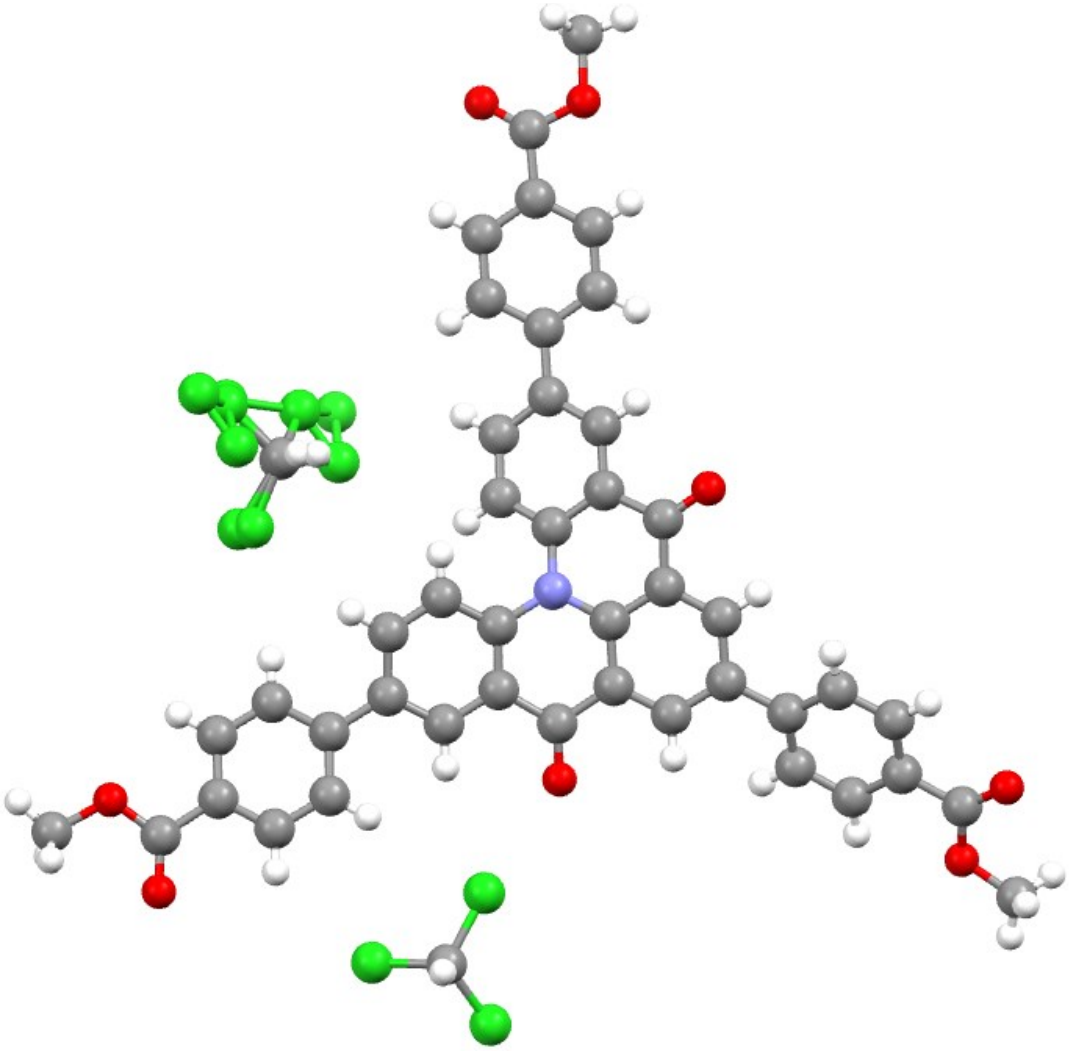

Abbildung 21: *Kristallstrukturanalyse des Trimethylesters des DiKTa-Linkers, (Me_3L) der als Solvat mit Chloroform vorliegt.*

Die anschließende Entschützung zum gewünschten Linker ergab einen hellbraunen Feststoff, welcher in einer DMF-Lösung eine grüne Lumineszenz zeigt. Hierbei konnte eine Gesamtausbeute der Kupplung und Entschützung von 27 % erreicht werden. Dies entspricht einer Gesamtausbeute über alle Syntheseschritte von 8,8 %.

Erste Ansätze im Bereich der MOF-Synthese wurden mit Kupferacetat in einer 1:1-Mischung aus DMF und Methanol bei 80 °C durchgeführt. Dabei konnte nach 24 Stunden ein mikrokristalliner Feststoff gewonnen werden. Die erhaltenen Kristalle zeigen in Lösung eine deutliche grüne Farbe. Abbildung 22 zeigt die gewonnenen Kristalle sowohl im Falcon-Tube als auch unter dem Mikroskop.

a) 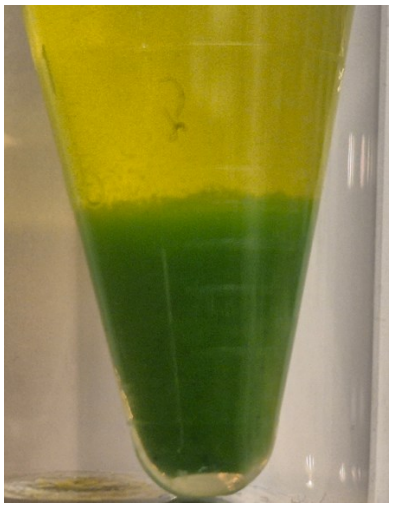 b) 

Abbildung 22: *Mit Kupferacetat und dem neu synthetisierten DiKTa-Linker hergestellte Kristalle a) im Falcon-Tube als grüner Feststoff und b) unter einem Mikroskop als kleine Nadeln.*

Dabei handelt es sich um sehr feine gelbgrüne Nadeln, die aufgrund ihrer geringen Größe nicht in einer Kristallstrukturanalyse vermessen werden konnten. PXRD-Messungen zeigten, dass die Kristalle an Luft nicht beständig sind und sich innerhalb weniger Minuten ein amorpher brauner Feststoff bildet. Aus diesen Gründen konnten sowohl die Struktur als auch deren photophysikalische Eigenschaften noch nicht genauer untersucht werden.

7. Experimentalteil

In diesem Abschnitt werden die verwendeten Chemikalien, Geräte und die Synthesevorschriften für die Ergebnisse im unveröffentlichten Teil (Abschnitt 5) aufgelistet.

7.1 Geräte und Materialien

7.1.1 Verwendete Chemikalien

Folgende Chemikalien wurden in den unterschiedlichen Synthesen verwendet.

Tabelle 2: *Chemikalienliste samt Hersteller.*

Chemikalie	Hersteller
Zinkoxid	Sigma-Aldrich
2-Methylimidazol	ThermoFisher Scientific
Ethanol	Fisher scientific
[1,1′-Bis(diphenylphosphino)ferrocen] dichlorpalladium(II)	Carbolution
Kaliumcarbonat	Fisher Chemical
1,4-Dioxan	Fisher scientific
4-Methoxycarbonylphenylborsäure	BLDpharm

7.1.2 Pulverröntgendiffraktometrie (PXRD)

Alle Pulverröntgendiffraktogramme wurden an einem Miniflex 300 der Firma Rigaku (600 W, 40 kV, 15 mA) vermessen. Hierfür wurden die Proben auf flache Si-Probenhalter aufgetragen und in einem Bereich von 2-50 °2Theta vermessen. Für die Messungen wurde monochromatische Cu-Kα-Strahlung (λ = 1,54182 Å) bei RT verwendet.

7.1.3 Sorptionsmessungen

Die Gassorptionsmessungen wurden an einem Belsorb Max II der Firma Microtrac durchgeführt. Der für die Sorptionsmessung verwendete Stickstoff besaß eine Reinheit von 99,999%. Alle Proben wurden vor der Messung bei 120 °C für 16 Stunden im Vakuum aktiviert. Die Sorptionsmessungen wurden bei 77 K (Flüssigstickstoff) durchgeführt.

7.1.4 Lumineszenzmessungen

Die Anregungs- und Emissions-Spektren wurden mit einer 150 W Xe-Bogenlampe an einem FS5 Spektrofluorometer der Firma Edinburgh Instruments in einem reflektiven Setup im Wellenlängenbereich von 350 bis 750 nm bei Temperaturen zwischen 79 K und RT aufgenommen.

7.1.5 NMR-Spektroskopie

Alle NMR-Messungen wurden an einem Bruker Avance III 300 MHz NMR Spektrometer durchgeführt. Zum Lösen der Proben wurden entsprechende deuterierte Lösungsmittel verwendet. Die Messungen wurden bei RT durchgeführt. Die chemischen Verschiebungen sind in ppm angegeben.

7.1.6 Kugelmühle

Die Kugelmühlensynthesen wurden mit einer MM 400 Kugelmühle der Firma Retsch bei Raumtemperatur unter Verwendung von 2 Stahlkugeln mit einem Durchmesser von 7 mm durchgeführt.

7.2 Synthesevorschriften

7.2.1 Synthese der DiKTa@ZIF-8 Komposite

Die *liquid-assisted-grindig* (LAG) Synthese von ZIF-8- und allen ZIF-8-Kompositen wurde im 1 mmol Maßstab durchgeführt. 80 mg Zinkoxid und 164 mg 2-Methylimidazol wurden zusammen mit zwei Stahlkugeln (7 mm Durchmesser) in einen 10 ml Edelstahlbehälter gegeben. Als Flüssigkeit wurden 50 µL Ethanol hinzugegeben. Das Reaktionsgemisch wurde im geschlossenen Behälter bei RT für 30 Minuten bei 29,5 Hz gemahlen. Das erhaltene Produkt wurde mit Methanol (3 × 15 ml) gewaschen, anschließend getrocknet und mittels PXRD charakterisiert.

Die Komposite wurden durch die Zugabe einer DiKTa-Stammlösung (20 mg/ml in DCM) zu den Edukten und anschließendem Verdampfen des DCMs vorbereitet. Anschließendes Mahlen und Waschen der Proben führte zu den verwendeten Kompositen.

Tabelle 3: *Auflistung der verwendeten Stammlösung und der sich ergebenden Komposite.*

Stammlösung [µl]	Menge an DiKTa [mg]	Komposite
50	1	$DiKTa_{0.2}$@ZIF-8
100	2	$DiKTa_{0.4}$@ZIF-8
150	3	$DiKTa_{0.6}$@ZIF-8
250	5	$DiKTa_{1.0}$@ZIF-8
350	7	$DiKTa_{1.4}$@ZIF-8
450	9	$DiKTa_{2.1}$@ZIF-8
500	10	$DiKTa_{2.2}$@ZIF-8

7.2.2 Synthese von Dimethyl-6,6'-((4-bromphenyl)azandiyl)bis(3-brombenzoat)

Zu dem zuvor hergestellten Triarylamin (4 g, 11,10 mmol, 1 Äquivalent) in 100 ml DCM wurde unter Rühren Brom (1,7 ml, 33,3 mmol, 3 Äquivalente) tropfenweise zugegeben. Nach 1 Stunde Rühren bei RT wurde weiteres Brom (0,1 ml) tropfenweise zugegeben und für weitere 30 Minuten gerührt. Die Reaktion wurde durch Zugabe einer 10%igen Natriumhydroxidlösung (50 ml) gestoppt. Die organische Schicht wurde abgetrennt, mit Wasser (3 × 50 ml) gewaschen, mit wasserfreiem Natriumsulfat getrocknet und unter vermindertem Druck konzentriert. Das Rohprodukt wurde mittels Säulenchromatographie an Silicagel gereinigt. Als Eluent wurde eine Mischung aus Ethylacetat und Cyclohexan (1 : 9, V : V) verwendet. Das gewünschte Produkt konnte als hellgelber Feststoff erhalten werden.

^{1}H-NMR (300 MHz, $CDCl_3$) δ 7.81 (d, *J* = 2.4 Hz, 2H), 7.53 (dd, *J* = 8.6, 2.5 Hz, 2H), 7.24 (d, *J* = 9.0 Hz, 2H), 7.05 (d, *J* = 8.7 Hz, 2H), 6.60 (d, *J* = 8.9 Hz, 2H), 3,46 (s, 6H).

7.2.3 Synthese von Br_3DiKTa

Dimethyl-6,6'-((4-bromphenyl)azandiyl)bis(3-brombenzoat) (4 g, 6,7 mmol, 1 Äquivalent) wurde mit Natriumhydroxid (1,5 g, 37,5 mmol, 5,6 Äquivalente) in 40 ml einer 1 zu 1 Mischung aus Ethanol und Wasser für 12 Stunden unter Rückfluss erhitzt. Anschließend wurde der pH-Wert durch Zugabe von verdünnter Salzsäure sauer gestellt. Die ausfallende Disäure wurde abfiltriert, gründlich mit Wasser gewaschen,

und unter Vakuum getrocknet (3,78, 99 % Ausbeute). Das Produkt wurde ohne weitere Aufreinigung oder Charakterisierung verwendet. Die Disäure (3,5 g, 6,1 mmol, 1 Äquivalent) wurde unter Stickstoffatmosphäre zu 60 ml Dichlormethan gegeben. Zu der Reaktionsmischung wurden nacheinander Thionylchlorid (1,0 ml, 13,6 mmol, 2,2 Äquivalente) und 7 Tropfen DMF zugegeben. Anschließend wurde das Reaktionsgemisch für 3 Stunden bis zum Rückfluss erhitzt. Nach 3 Stunden wurde im Stickstoffgegenstrom Aluminiumchlorid (8,2 g, 61,5 mmol, 10 Äquivalente) langsam zugegeben. Nach weiteren 12 Stunden unter Rückfluss wurde das Reaktionsgemisch auf Raumtemperatur abgekühlt und die Reaktion durch tropfenweise Zugabe von Wasser unter kräftigem Rühren gestoppt. Das Reaktionsgemisch wurde mit DCM (3 × 200 ml) extrahiert. Das Lösungsmittel wurde unter vermindertem Druck entfernt. Das Rohprodukt wurde anschließend nacheinander mit jeweils 50 ml Cyclohexan, Methanol und Ethylacetat für jeweils 1 Stunde refluxiert. Das Produkt wurde als gelben Feststoff erhalten.

^{1}H-NMR (300 MHz, $CDCl_3$) δ 8.81 (s, 1H), 8.59 (d, *J* = 2.4 Hz, 1H), 7.95 (d, *J* = 9.0 Hz, 1H), 7.80 (dd, *J* = 9.0, 2.4 Hz, 1H).

7.2.4 Suzuki-Kupplung

Zu dem zuvor hergestellten Br_3DiKTa (750 mg, 1,4 mmol) wurden unter Schutzgasatmosphäre 4-Methoxycarbonylphenylborsäure (1,47 g, 8,2 mmol), K_2CO_3 (1,5 g, 10,8 mmol) und Pd(dppf)Cl_2 (50 mg, 0,07 mmol) zugegeben. Anschließend wurde das Reaktionsgemisch mit 50 ml entgastem 1,4-Dioxan versetzt und für 2 Tage auf 105 °C erhitzt. Nach zwei Tagen wurde 30 ml Wasser zur Reaktion zugegeben und das Reaktionsgemisch mit DCM extrahiert (3 × 150 ml). Durch Entfernen des Lösungsmittels konnte das Rohprodukt gewonnen werden. Anschließen konnte es mittels Säulenchromatographie aufgereinigt werden. Als Eluent wurde hier eine 1 zu 1 Mischung von Ethylacetat und Cyclohexan verwendet. Der erhaltene Trimethylester (Me_3L) ist ein gelber Feststoff.

1H-NMR (300 MHz, $CDCl_3$) δ 8.99 (s, 2H), 8.73 (d, J = 2.3 Hz, 2H), 8.24 (d, J = 8.9 Hz, 2H), 8.17 (d, J = 8.5 Hz, 6H), 7.99 (dd, J = 8.9, 2.4 Hz, 2H), 7.87 (d, J = 8.5 Hz, 2H), 7.80 (d, J = 8.6 Hz, 4H), 3.98 (s, 9H).

7.2.5 Entschützung des Trimethylesters

In einem 100 ml-Rundkolben werden 200 mg (0,29 mmol) des hergestellten Trimethylesters (Me_3L) in einer 1 zu 1 Mischung aus Wasser und 1,4-Dioxan (je 20 ml) zusammen mit einem 10-fachen Überschuss an Natriumhydroxid (120 mg, 3,0 mmol) für einen Tag bis zum Reflux erhitzt. Anschließend wird das Reaktionsgemisch mit verdünnter Salzsäure sauer gestellt. Das dabei ausfallende Produkt wird abfiltriert und getrocknet. Es handelt sich hierbei um einen braunen Feststoff. Die Ausbeute der Kupplung mit anschließender Entschützung lag bei 27 %. Die Gesamtausbeute aller Syntheseschritte beträgt 8,8 %

^{1}H-NMR (300 MHz, DMSO) δ 13.02 (s (breit), 3H), 8.43 (s, 2H), 8.19 (d, *J* = 1.8 Hz, 2H), 8.05 – 7.89 (m, 10H), 7.69 (dd, *J* = 8.4, 2.0 Hz, 6H).

7.2.6 Kristallstrukturanalyse

Durch das Eindampfen von *n*-Hexan in eine Chloroformlösung des Trimethylesters (Me_3L) entstanden einzelne klare, hellgelbe, nadelförmige Kristalle von $Me_3L{\cdot}1{,}5(CHCl_3)$. Ein geeigneter Kristall mit den Abmessungen $0{,}58 \times 0{,}04 \times 0{,}04$ mm^3 wurde ausgewählt und auf einem geeigneten Träger auf einem XtaLAB Synergy, Dualflex, HyPix-Diffraktometer befestigt. Der Kristall wurde während der Datenerfassung bei einer konstanten Temperatur von T = 150,1(2) K gehalten. Die Struktur wurde mit dem Strukturlösungsprogramm ShelXT unter Verwendung der Intrinsic-Phasing-Lösungsmethode und unter Verwendung von Olex2 als grafische Schnittstelle gelöst.[102] Das Modell wurde mit der Version 2019/3 von ShelXL 2019/3 unter Verwendung der Methode der kleinsten Quadrate verfeinert.

Kristalldaten: $C_{45.5}H_{30.5}Cl_{4.5}NO_8$, M_r = 878.73, monoklin, $P2_1/c$ (No. 14), a = 22.7253(4) Å, b = 7.24717(16) Å, c = 25.8317(4) Å, b = 109.5798(19)°, $a = g$ = 90°, V = 4008.33(14) Å^3, T = 150.1(2) K, Z = 4, Z' = 1, m(Cu K$_a$) = 3.472, 36690 gemessene Reflexionen, 8538 einzigartige (R_{int} = 0,0464), die in allen Berechnungen verwendet wurden. Das endgültige wR_2 betrug 0,2164 (alle Daten) und R_1 betrug 0,0701 (I > 2(I)).

8. Anhang

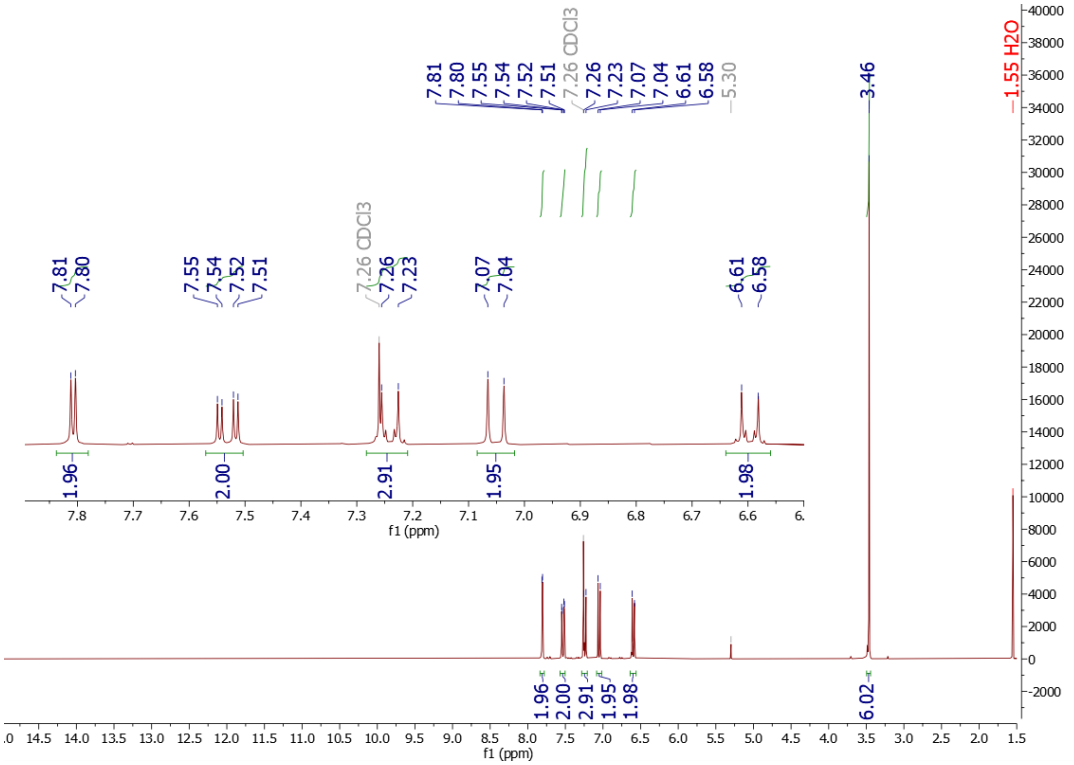

Abbildung 24: *^{1}H-NMR Spektrum (300 MHz) von Dimethyl-6,6'-((4-bromphenyl)azandiyl)bis(3-brombenzoat) in $CDCl_3$ (zu Abschnitt 7.2.2).*

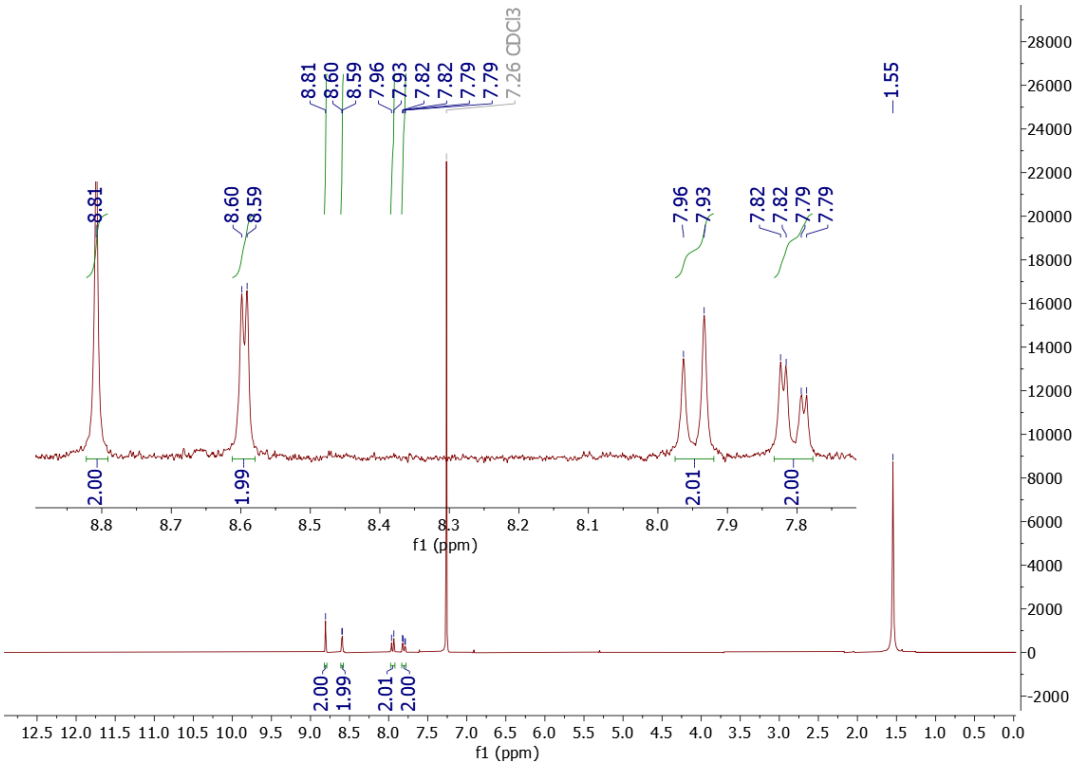

Abbildung 25: *^{1}H-NMR Spektrum (300 MHz) von Br_3DiKTa in $CDCl_3$ (zu Abschnitt 7.2.3).*

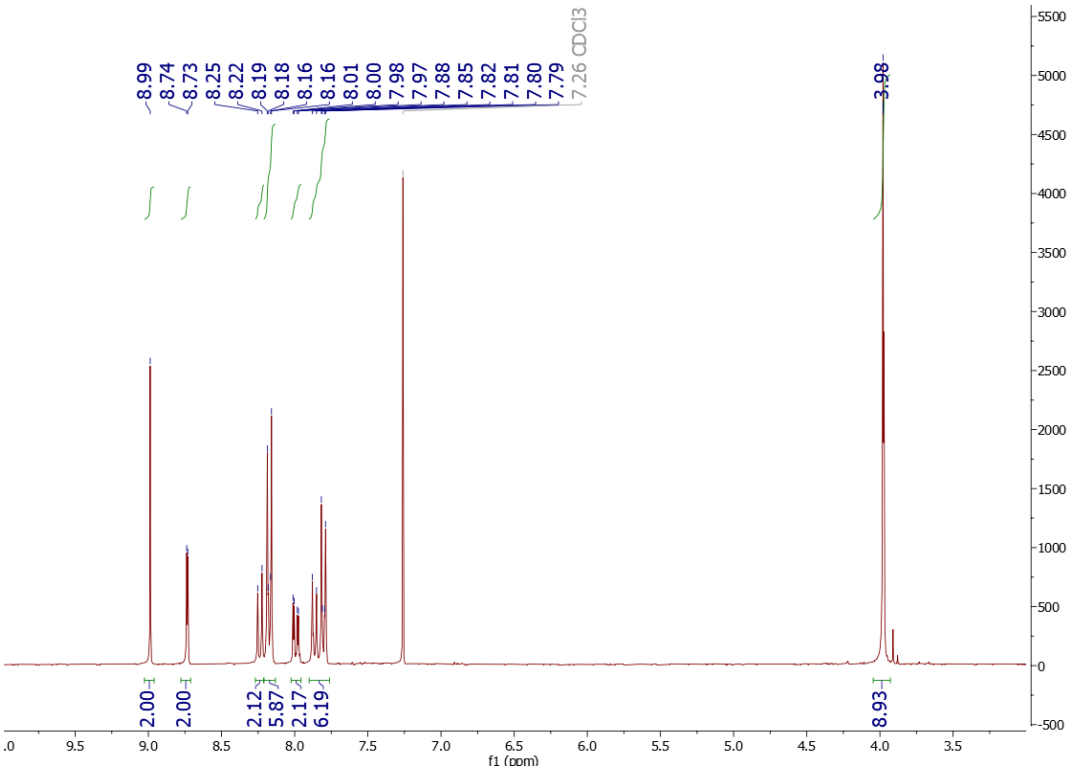

Abbildung 26: *^{1}H-NMR Spektrum (300 MHz) des Trimethylesters (Me_3L) in $CDCl_3$ (zu Abschnitt 7.2.4).*

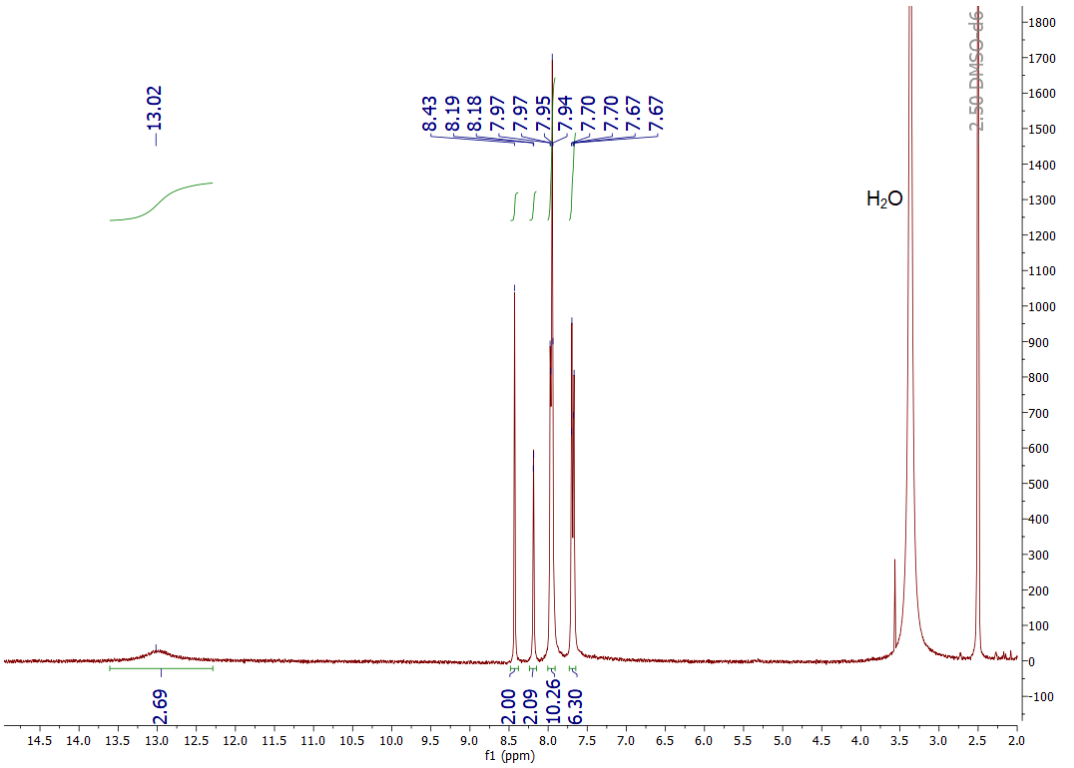

Abbildung 27: *^{1}H-NMR Spektrum (300 MHz) des entschützten DiKTa-Linkers in DMSO-d_6 (zu Abschnitt 7.2.5).*

Tabelle 4: *Kristalldaten und Strukturverfeinerung für $Me_3L \cdot 1{,}5(CHCl_3)$.*

Compound	**$Me_3L \cdot 1.5(CHCl_3)$**
Formula	$C_{45.5}H_{30.5}Cl_{4.5}NO_8$
$D_{calc.}$/ g cm^{-3}	1.456
m/mm^{-1}	3.472
Formula Weight	878.73
Colour	clear light yellow
Shape	needle
Size/mm^3	0.58×0.04×0.04
T/K	150.1(2)
Crystal System	monoclinic
Space Group	$P2_1/c$
a/Å	22.7253(4)
b/Å	7.24717(16)
c/Å	25.8317(4)
a/°	90
b/°	109.5798(19)
g/°	90
V/Å^3	4008.33(14)
Z	4
Z'	1
Wavelength/Å	1.54184
Radiation type	Cu K_a
Q_{min}/°	4.129
Q_{max}/°	79.615
Measured Refl.	36690
Independent Refl.	8538
Reflections with I > 2(I)	6910
R_{int}	0.0464
Parameters	590
Restraints	109
Largest Peak	1.116
Deepest Hole	-0.599
GooF	1.062
wR_2 (all data)	0.2164
wR_2	0.2019
R_1 (all data)	0.0820
R_1	0.0701

9. Literaturverzeichnis

[1] S. R. Batten, N. R. Champness, X. M. Chen, J. Garcia-Martinez, S. Kitagawa, L. Öhrström, M. O'Keeffe, M. P. Suh and J. Reedijk, *Pure and Applied Chemistry* **2013**, *85*, 1715-1724.

[2] C. Janiak and J. K. Vieth, *New Journal of Chemistry* **2010**, *34*, 2366-2388.

[3] a) F. Herren, P. Fischer, A. Ludi and W. Halg, *Inorganic Chemistry* **1980**, *19*, 956-959; b) H. J. Buser and A. Ludi, *Journal of the Chemical Society-Chemical Communications* **1972**, 1299.

[4] R. A. Love, T. F. Koetzle, G. J. B. Williams, L. C. Andrews and R. Bau, *Inorganic Chemistry* **1975**, *14*, 2653-2657.

[5] a) L. L. Böhm, *Angewandte Chemie-International Edition* **2003**, *42*, 5010-5030; b) L. E. Heim, N. E. Schlörer, J. H. Choi and M. H. G. Prechtl, *Nature Communications* **2014**, *5*, 3621; c) A. F. Henwood and E. Zysman-Colman, *Topics in Current Chemistry* **2016**, *374*, 36.

[6] a) B. F. Hoskins and R. Robson, *Journal of the American Chemical Society* **1989**, *111*, 5962-5964; b) B. F. Hoskins and R. Robson, *Journal of the American Chemical Society* **1990**, *112*, 1546-1554.

[7] a) J. P. Zhang, Y. B. Zhang, J. B. Lin and X. M. Chen, *Chemical Reviews* **2012**, *112*, 1001-1033; b) C. S. Diercks and O. M. Yaghi, *Science* **2017**, *355*, eaal1585.

[8] a) O. M. Yaghi and H. L. Li, *Journal of the American Chemical Society* **1995**, *117*, 10401-10402; b) O. M. Yaghi, G. M. Li and H. L. Li, *Nature* **1995**, *378*, 703-706.

[9] *https://www.nobelprize.org/prizes/chemistry/2025/press-release/ Seite wurde abgerufen am 09.11.2025.*

[10] H. Li, M. Eddaoudi, M. O'Keeffe and O. M. Yaghi, *Nature* **1999**, *402*, 276-279.

[11] a) S. S. Y. Chui, S. M. F. Lo, J. P. H. Charmant, A. G. Orpen and I. D. Williams, *Science* **1999**, *283*, 1148-1150; b) G. Férey, C. Mellot-Draznieks, C. Serre, F. Millange, J. Dutour, S. Surblé and I. Margiolaki, *Science* **2005**, *309*, 2040-2042; c) J. H. Cavka, S. Jakobsen, U. Olsbye, N. Guillou, C. Lamberti, S. Bordiga and K. P. Lillerud, *Journal of the American Chemical Society* **2008**, *130*, 13850-13851.

[12] *Suchergebnisse bei SciFinder® des Chemical Abstracts Service (CAS):https://scifinder-n.cas.org/search/reference/68a34b307d1de0580340e3cd/1 Seite wurde aufgerufen am 18.08.2025*.

[13] K. K. Gangu, S. Maddila, S. B. Mukkamala and S. B. Jonnalagadda, *Inorganica Chimica Acta* **2016**, *446*, 61-74.

[14] a) J. F. Lyu, X. Zhang, K. Otake, X. J. Wang, P. Li, Z. Y. Li, Z. J. Chen, Y. Y. Zhang, M. C. Wasson, Y. Yang, P. Bai, X. H. Guo, T. Islamoglu and O. K. Farha, *Chemical Science* **2019**, *10*, 1186-1192; b) X. Q. Li, L. Zhang, Z. Q. Yang, P. Wang, Y. F. Yan and J. Y. Ran, *Separation and Purification Technology* **2020**, *235*, 116213.

[15] a) R. R. F. Fonseca, R. D. Ferreira and P. P. Luz, *Journal of Solid State Electrochemistry* **2025**, *29*, 837-854; b) H. Furukawa, F. Gándara, Y. B. Zhang, J. C. Jiang, W. L. Queen, M. R. Hudson and O. M. Yaghi, *Journal of the American Chemical Society* **2014**, *136*, 4369-4381; c) S. Biswas, T. Ahnfeldt and N. Stock, *Inorganic Chemistry* **2011**, *50*, 9518-9526.

[16] W. Mori, F. Inoue, K. Yoshida, H. Nakayama, S. Takamizawa and M. Kishita, *Chemistry Letters* **1997**, 1219-1220.

[17] J. Hungerford, S. Bhattacharyya, U. Tumuluri, S. Nair, Z. L. Wu and K. S. Walton, *Journal of Physical Chemistry C* **2018**, *122*, 23493-23500.

[18] H. Li, M. Eddaoudi, T. L. Groy and O. M. Yaghi, *Journal of the American Chemical Society* **1998**, *120*, 8571-8572.

[19] a) T. Zhao, F. Jeremias, I. Boldog, B. Nguyen, S. K. Henninger and C. Janiak, *Dalton Transactions* **2015**, *44*, 16791-16801; b) P. Horcajada, S. Surblé, C. Serre, D. Y. Hong, Y. K. Seo, J. S. Chang, J. M. Grenèche, I. Margiolaki and G. Férey, *Chemical Communications* **2007**, 2820-2822.

[20] Y. Li, Y. Q. Fu, B. L. Ni, K. N. Ding, W. K. Chen, K. C. Wu, X. Huang and Y. F. Zhang, *Aip Advances* **2018**, *8*, 035012.

[21] a) H. Q. Zheng, C. Y. Liu, X. Y. Zeng, J. Chen, J. Lu, R. G. Lin, R. Cao, Z. J. Lin and J. W. Su, *Inorganic Chemistry* **2018**, *57*, 9096-9104; b) J. E. Mondloch, W. Bury, D. Fairen-Jimenez, S. Kwon, E. J. DeMarco, M. H. Weston, A. A. Sarjeant, S. T. Nguyen, P. C. Stair, R. Q. Snurr, O. K. Farha and J. T. Hupp, *Journal of the American Chemical Society* **2013**, *135*, 10294-10297; c) M. Dan-Hardi, C. Serre, T. Frot, L. Rozes, G. Maurin, C. Sanchez and G. Férey, *Journal of the American Chemical Society* **2009**, *131*, 10857-10859.

[22] V. Guillerm, S. Gross, C. Serre, T. Devic, M. Bauer and G. Férey, *Chemical Communications* **2010**, *46*, 767-769.

[23] O. I. Lebedev, F. Millange, C. Serre, G. Van Tendeloo and G. Férey, *Chemistry of Materials* **2005**, *17*, 6525-6527.
[24] N. Tannert, C. Jansen, S. Niessing and C. Janiak, *Dalton Transactions* **2019**, *48*, 2967-2976.
[25] T. Loiseau, C. Serre, C. Huguenard, G. Fink, F. Taulelle, M. Henry, T. Bataille and G. Férey, *Chemistry-a European Journal* **2004**, *10*, 1373-1382.
[26] a) X. C. Huang, Y. Y. Lin, J. P. Zhang and X. M. Chen, *Angewandte Chemie-International Edition* **2006**, *45*, 1557-1559; b) D. N. Dybtsev, H. Chun and K. Kim, *Angewandte Chemie-International Edition* **2004**, *43*, 5033-5036.
[27] K. S. Park, Z. Ni, A. P. Cote, J. Y. Choi, R. D. Huang, F. J. Uribe-Romo, H. K. Chae, M. O'Keeffe and O. M. Yaghi, *Proceedings of the National Academy of Sciences of the United States of America* **2006**, *103*, 10186-10191.
[28] H. T. Kwon, H. K. Jeong, A. S. Lee, H. S. An and J. S. Lee, *Journal of the American Chemical Society* **2015**, *137*, 12304-12311.
[29] M. Cognet, T. Gutel, R. Gautier, X. F. Le Goff, A. Mesbah, N. Dacheux, M. Carboni and D. Meyer, *Materials Letters* **2019**, *236*, 73-76.
[30] S. Wöhlbrandt, C. Meier, H. Reinsch, E. S. Grape, A. K. Inge and N. Stock, *Inorganic Chemistry* **2020**, *59*, 13343-13352.
[31] D. Woschko, S. Yilmaz, C. Jansen, A. Spiess, R. Oestreich, T. J. M. M. Ntep and C. Janiak, *Dalton Transactions* **2023**, *52*, 977-989.
[32] Z. G. Hu, T. Kundu, Y. X. Wang, Y. Sun, K. Y. Zeng and D. Zhao, *Acs Sustainable Chemistry & Engineering* **2020**, *8*, 17042-17053.
[33] C. Volkringer, T. Loiseau, M. Haouas, F. Taulelle, D. Popov, M. Burghammer, C. Riekel, C. Zlotea, F. Cuevas, M. Latroche, D. Phanon, C. Knöfelv, P. L. Llewellyn and G. Férey, *Chemistry of Materials* **2009**, *21*, 5783-5791.
[34] M. Eddaoudi, J. Kim, N. Rosi, D. Vodak, J. Wachter, M. O'Keeffe and O. M. Yaghi, *Science* **2002**, *295*, 469-472.
[35] a) B. Van de Voorde, I. Stassen, B. Bueken, F. Vermoortele, D. De Vos, R. Ameloot, J. C. Tan and T. D. Bennett, *Journal of Materials Chemistry A* **2015**, *3*, 1737-1742; b) M. R. Ryder, B. Civalleri and J. C. Tan, *Physical Chemistry Chemical Physics* **2016**, *18*, 9079-9087.
[36] a) J. Lippke, B. Brosent, T. von Zons, E. Virmani, S. Lilienthal, T. Preusse, M. Hülsmann, A. M. Schneider, S. Wuttke, P. Behrens and A. Godt, *Inorganic Chemistry*

2017, *56*, 748-761; b) W. Y. Gao, C. Y. Tsai, L. Wojtas, T. Thiounn, C. C. Lin and S. Q. Ma, *Inorganic Chemistry* **2016**, *55*, 7291-7294.

[37] Z. H. Mai and D. X. Liu, *Crystal Growth & Design* **2019**, *19*, 7439-7462.

[38] a) M. J. Katz, Z. J. Brown, Y. J. Colón, P. W. Siu, K. A. Scheidt, R. Q. Snurr, J. T. Hupp and O. K. Farha, *Chemical Communications* **2013**, *49*, 9449-9451; b) H. Furukawa, Y. B. Go, N. Ko, Y. K. Park, F. J. Uribe-Romo, J. Kim, M. O'Keeffe and O. M. Yaghi, *Inorganic Chemistry* **2011**, *50*, 9147-9152.

[39] G. Nickerl, M. Leistner, S. Helten, V. Bon, I. Senkovska and S. Kaskel, *Inorganic Chemistry Frontiers* **2014**, *1*, 325-330.

[40] a) J. A. Greathouse and M. D. Allendorf, *Journal of the American Chemical Society* **2006**, *128*, 10678-10679; b) Y. Ming, J. Purewal, J. Yang, C. C. Xu, R. Soltis, J. Warner, M. Veenstra, M. Gaab, U. Müller and D. J. Siegel, *Langmuir* **2015**, *31*, 4988-4995; c) J. R. Alvarez, E. Sánchez-González, E. Pérez, E. Schneider-Revueltas, A. Martínez, A. Tejeda-Cruz, A. Islas-Jácome, E. González-Zamora and I. A. Ibarra, *Dalton Transactions* **2017**, *46*, 9192-9200.

[41] a) Z. H. Wang, A. Bilegsaikhan, R. T. Jerozal, T. A. Pitt and P. J. Milner, *Acs Applied Materials & Interfaces* **2021**, *13*, 17517-17531; b) M. Kandiah, M. H. Nilsen, S. Usseglio, S. Jakobsen, U. Olsbye, M. Tilset, C. Larabi, E. A. Quadrelli, F. Bonino and K. P. Lillerud, *Chemistry of Materials* **2010**, *22*, 6632-6640; c) F. Ahmadijokani, R. Mohammadkhani, S. Ahmadipouya, A. Shokrgozar, M. Rezakazemi, H. Molavi, T. M. Aminabhavi and M. Arjmand, *Chemical Engineering Journal* **2020**, *399*, 125346; d) M. Y. Zorainy, M. G. Alalm, S. Kaliaguine and D. C. Boffito, *Journal of Materials Chemistry A* **2021**, *9*, 22159-22217.

[42] T. Pal, T. Kambe, T. Kusamoto, M. L. Foo, R. Matsuoka, R. Sakamoto and H. Nishihara, *Chempluschem* **2015**, *80*, 1255-1258.

[43] N. Stock and S. Biswas, *Chemical Reviews* **2012**, *112*, 933-969.

[44] H. Kaur, N. Devi, S. S. Siwal, W. F. Alsanie, M. K. Thakur and V. K. Thakur, *Acs Omega* **2023**, *8*, 9004-9030.

[45] I. Walton, C. Chen, J. M. Rimsza, T. M. Nenoff and K. S. Walton, *Crystal Growth & Design* **2020**, *20*, 6139-6146.

[46] G. R. Cai and H. L. Jiang, *Angewandte Chemie-International Edition* **2017**, *56*, 563-567.

[47] a) H. Wu, Y. S. Chua, V. Krungleviciute, M. Tyagi, P. Chen, T. Yildirim and W. Zhou, *Journal of the American Chemical Society* **2013**, *135*, 10525-10532; b) J. J. Wang, L. M. Liu, C. L. Chen, X. L. Dong, Q. Wang, L. Alfilfil, M. R. AlAlouni, K. X. Yao, J. F. Huang, D. L. Zhang and Y. Han, *Journal of Materials Chemistry A* **2020**, *8*, 4464-4472.

[48] Y. W. Liu, S. M. Liu, D. F. He, N. Li, Y. J. Ji, Z. P. Zheng, F. Luo, S. X. Liu, Z. Shi and C. W. Hu, *Journal of the American Chemical Society* **2015**, *137*, 12697-12703.

[49] D. Sahoo, R. Suriyanarayanan and V. Chandrasekhar, *Dalton Transactions* **2014**, *43*, 10898-10909.

[50] a) K. J. Gagnon, H. P. Perry and A. Clearfield, *Chemical Reviews* **2012**, *112*, 1034-1054; b) G. K. H. Shimizu, R. Vaidhyanathan and J. M. Taylor, *Chemical Society Reviews* **2009**, *38*, 1430-1449.

[51] J. M. Taylor, A. H. Mahmoudkhani and G. K. H. Shimizu, *Angewandte Chemie-International Edition* **2007**, *46*, 795-798.

[52] S. R. Miller, G. M. Pearce, P. A. Wright, F. Bonino, S. Chavan, S. Bordiga, I. Margiolaki, N. Guillou, G. Féerey, S. Bourrelly and P. L. Llewellyn, *Journal of the American Chemical Society* **2008**, *130*, 15967-15981.

[53] H. M. Xie, K. O. Kirlikovali, Z. J. Chen, K. B. Idrees, T. Islamoglu and O. K. Farha, *Journal of Materials Chemistry A* **2024**, *12*, 6399-6404.

[54] T. Araki, A. Kondo and K. Maeda, *Chemical Communications* **2013**, *49*, 552-554.

[55] F. Steinke, T. Otto, S. Ito, S. Woehlbrandt and N. Stock, *European Journal of Inorganic Chemistry* **2022**, *2022*, e202200562.

[56] R. Vaidhyanathan, A. H. Mahmoudkhani and G. K. H. Shimizu, *Canadian Journal of Chemistry* **2009**, *87*, 247-253.

[57] K. Maeda, J. Akimoto, Y. Kiyozumi and F. Mizukami, *Journal of the Chemical Society-Chemical Communications* **1995**, 1033-1034.

[58] a) F. P. Zhai, Q. S. Zheng, Z. X. Chen, Y. Ling, X. F. Liu, L. H. Weng and Y. M. Zhou, *Crystengcomm* **2013**, *15*, 2040-2043; b) C. T. P. da Silva, A. J. Howarth, M. Rimoldi, T. Islamoglu, A. W. Rinaldi and J. T. Hupp, *Israel Journal of Chemistry* **2018**, *58*, 1164-1170.

[59] Y. P. Zhu, J. Yin, E. Abou-Hamad, X. K. Liu, W. Chen, T. Yao, O. F. Mohammed and H. N. Alshareef, *Advanced Materials* **2020**, *32*, 1906368.

[60] T. Zheng, W. Z. Tan and L. M. Zheng, *Accounts of Chemical Research* **2024**, *57*, 2973-2984.
[61] F. Steinke, S. Bette, N. Ruser, T. Otto, H. Terraschke, R. Dinnebier, N. Stock and M. Suta, *Advanced Functional Materials* **2024**, *34*, 2403631.
[62] Y. Zhang, J. D. Wang, P. Apostol, D. Rambabu, A. E. Lakraychi, X. L. Guo, X. Z. Zhang, X. D. Lin, S. Pal, V. R. Bakuru, X. H. Chen and A. Vlad, *Angewandte Chemie-International Edition* **2023**, *62*, e202310033.
[63] X. D. Huang, B. K. Hong, G. H. Wen, S. H. Li and L. M. Zheng, *Chemical Science* **2023**, *14*, 1852-1860.
[64] a) M. T. Kapelewski, T. Runcevski, J. D. Tarver, H. Z. H. Jiang, K. E. Hurst, P. A. Parilla, A. Ayala, T. Gennett, S. A. FitzGerald, C. M. Brown and J. R. Long, *Chemistry of Materials* **2018**, *30*, 8179-8189; b) Z. J. Zhang, Y. G. Zhao, Q. H. Gong, Z. Li and J. Li, *Chemical Communications* **2013**, *49*, 653-661; c) T. Yoskamtorn, P. Zhao, X. P. Wu, K. Purchase, F. Orlandi, P. Manuel, J. Taylor, Y. Y. Li, S. Day, L. Ye, C. C. Tang, Y. F. Zhao and S. C. E. Tsang, *Journal of the American Chemical Society* **2021**, *143*, 3205-3218; d) J. Perego, C. X. Bezuidenhout, A. Pedrini, S. Bracco, M. Negroni, A. Comotti and P. Sozzani, *Journal of Materials Chemistry A* **2020**, *8*, 11406-11413; e) J. Dechnik, A. Nuhnen and C. Janiak, *Crystal Growth & Design* **2017**, *17*, 4090-4099; f) P. Brandt, S. H. Xing, J. Liang, G. Kurt, A. Nuhnen, O. Weingart and C. Janiak, *Acs Applied Materials & Interfaces* **2021**, *13*, 29137-29149.
[65] H. B. T. Jeazet, C. Staudt and C. Janiak, *Dalton Transactions* **2012**, *41*, 14003-14027.
[66] S. Soltani and K. Akhbari, *Crystengcomm* **2022**, *24*, 1934-1941.
[67] H. Zhang, Y. Shang, Y. H. Li, S. K. Sun and X. B. Yin, *Acs Applied Materials & Interfaces* **2019**, *11*, 1886-1895.
[68] Y. F. Chen, S. H. Zhang, F. Chen, S. J. Cao, Y. Cai, S. Q. Li, H. W. Ma, X. J. Ma, P. F. Li, X. Q. Huang and B. Wang, *Journal of Materials Chemistry A* **2018**, *6*, 342-348.
[69] A. Spiess, J. Wiebe, E. Iwaschko, D. Woschko and C. Janiak, *Molecular Systems Design & Engineering* **2022**, *7*, 1682-1696.
[70] Y. M. Li, L. M. Cao, H. Ren, C. Y. Ji, W. J. Li and L. Cheng, *Catalysis Letters* **2023**, *153*, 1193-1204.
[71] a) M. H. D. Dang, T. T. T. Nguyen, B. Q. G. Le, L. H. T. Nguyen, N. X. D. Mai, M. V. Nguyen, P. H. Tran and T. L. Doan, *Journal of Industrial and Engineering Chemistry*

2022, *111*, 111-120; b) S. A. A. Rahman, C. N. Patra, G. K. Kole, S. Peters, T. Sadhukhan and B. Baskar, *New Journal of Chemistry* **2024**, *48*, 3513-3524.

[72] J. Jin, S. P. Wan, S. Lee, C. Oh, G. Y. Jang, K. Zhang, Z. Y. Lu and J. H. Park, *Small* **2023**, *19*, 2302776.

[73] Alamgir, K. Talha, Y. J. Wang, R. Ullah, B. Wang, L. Wang, W. Wu, S. Chen, L. H. Xie and J. R. Li, *Rsc Advances* **2021**, *11*, 23838-23845.

[74] A. Sarkar, A. Adhikary, A. Mandal, T. Chakraborty and D. Das, *Crystal Growth & Design* **2020**, *20*, 7833-7839.

[75] W. R. Zheng and L. Y. S. Lee, *Acs Energy Letters* **2021**, *6*, 2838-2843.

[76] a) H. B. Aiyappa, J. Thote, D. B. Shinde, R. Banerjee and S. Kurungot, *Chemistry of Materials* **2016**, *28*, 4375-4379; b) D. N. Xing, Y. Y. Wang, P. Zhou, Y. Y. Liu, Z. Y. Wang, P. Wang, Z. K. Zheng, H. F. Cheng, Y. Dai and B. B. Huang, *Applied Catalysis B-Environment and Energy* **2020**, *278*, 119295; c) L. Tao, C. Y. Lin, S. Dou, S. Feng, D. W. Chen, D. D. Liu, J. Huo, Z. H. Xia and S. Y. Wang, *Nano Energy* **2017**, *41*, 417-425; d) S. Dou, C. L. Dong, Z. Hu, Y. C. Huang, J. L. Chen, L. Tao, D. F. Yan, D. W. Chen, S. H. Shen, S. L. Chou and S. Y. Wang, *Advanced Functional Materials* **2017**, *27*, 1702546.

[77] a) M. Liu, L. J. Kong, X. M. Wang, J. He, J. J. Zhang, J. Zhu and X. H. Bu, *Nano Research* **2021**, *14*, 4680-4688; b) A. I. Khan and D. O'Hare, *Journal of Materials Chemistry* **2002**, *12*, 3191-3198.

[78] W. R. Zheng, M. J. Liu and L. Y. S. Lee, *Acs Catalysis* **2020**, *10*, 81-92.

[79] a) T. H. Y. Beglau, L. Rademacher, R. Oestreich and C. Janiak, *Molecules* **2023**, *28*, 4464; b) L. Sondermann, W. Jiang, M. Shviro, A. Spiess, D. Woschko, L. Rademacher and C. Janiak, *Molecules* **2022**, *27*, 1241; c) M. Jahan, Z. L. Liu and K. P. Loh, *Advanced Functional Materials* **2013**, *23*, 5363-5372; d) S. Yu, Y. Wu, Q. Xue, J. J. Zhu and Y. Z. Zhou, *Journal of Materials Chemistry A* **2022**, *10*, 4936-4943.

[80] S. Pramanik, C. Zheng, X. Zhang, T. J. Emge and J. Li, *Journal of the American Chemical Society* **2011**, *133*, 4153-4155.

[81] O. Pajuelo-Corral, E. Alkain, R. F. Mendes, F. A. A. Paz, A. Rodriguez-Diéguez, J. A. García, J. M. Seco and J. Cepeda, *Journal of Materials Chemistry C* **2025**, *13*, 11299-11309.

[82] X. Y. Liu, K. Xing, Y. Li, C. K. Tsung and J. Li, *Journal of the American Chemical Society* **2019**, *141*, 14807-14813.

[83] U. Ryu, H. S. Lee, K. S. Park and K. M. Choi, *Polyhedron* **2018**, *154*, 275-294.
[84] a) Y. Cui, F. Chen and X. B. Yin, *Biosensors & Bioelectronics* **2019**, *135*, 208-215; b) X. S. Yang, W. Liu, X. G. Liu, Y. L. Sun, X. Y. Wang, Y. L. Shao and W. S. Liu, *Inorganic Chemistry* **2024**, *63*, 3921-3930; c) T. F. Xia, F. L. Zhu, K. Jiang, Y. J. Cui, Y. Yang and G. D. Qian, *Dalton Transactions* **2017**, *46*, 7549-7555; d) Y. M. Wang, X. T. Tian, H. Zhang, Z. R. Yang and X. B. Yin, *Acs Applied Materials & Interfaces* **2018**, *10*, 22445-22452; e) F. Q. Wang, K. H. Xu, Z. Jiang, T. Yan, C. M. Wang, Y. Y. Pu and Y. N. Zhao, *Journal of Luminescence* **2018**, *194*, 22-28; f) P. Rouschmeyer, N. Guillou, C. Serre, G. Clavier, C. Martineau, P. Audebert, E. Elkaïm, C. Allain and T. Devic, *Inorganic Chemistry* **2017**, *56*, 8423-8429; g) W. Cho, H. J. Lee, G. Choi, S. Choi and M. Oh, *Journal of the American Chemical Society* **2014**, *136*, 12201-12204; h) P. I. Scheurle, A. Mähringer, A. C. Jakowetz, P. Hosseini, A. F. Richter, G. Wittstock, D. D. Medina and T. Bein, *Nanoscale* **2019**, *11*, 20949-20955; i) H. Z. Li, Q. M. Chen, Z. X. Zhang, Z. L. Wang, Z. J. Gong and M. K. Fan, *Dyes and Pigments* **2023**, *210*, 111035; j) S. M. Zhang, X. F. Ma, Y. T. Yang, H. J. Ren, W. K. Li, Y. Y. Liu, C. Y. Xi, L. C. Zheng and Z. Miao, *Journal of Solid State Chemistry* **2025**, *351*, 125525; k) Z. W. Wei, Z. Y. Gu, R. K. Arvapally, Y. P. Chen, R. N. McDougald, J. F. Ivy, A. A. Yakovenko, D. W. Feng, M. A. Omary and H. C. Zhou, *Journal of the American Chemical Society* **2014**, *136*, 8269-8276.
[85] a) C. Y. Sun, X. L. Wang, X. Zhang, C. Qin, P. Li, Z. M. Su, D. X. Zhu, G. G. Shan, K. Z. Shao, H. Wu and J. Li, *Nature Communications* **2013**, *4*, 2717; b) W. W. Chen, Y. X. Zhuang, L. Wang, Y. Lv, J. B. Liu, T. L. Zhou and R. J. Xie, *Acs Applied Materials & Interfaces* **2018**, *10*, 18910-18917.
[86] Y. F. Chen, B. Yu, Y. D. Cui, S. J. Xu and J. B. Gong, *Chemistry of Materials* **2019**, *31*, 1289-1295.
[87] T. Xiong, Y. Zhang, N. Amin and J. C. Tan, *Molecules* **2021**, *26*, 7583.
[88] D. Püschel, S. Hédé, I. Maisuls, S. P. Höfert, D. Woschko, R. Kühnemuth, S. Felekyan, C. A. M. Seidel, C. Czekelius, O. Weingart, C. A. Strassert and C. Janiak, *Molecules* **2023**, *28*, 2877.
[89] a) S. Let, P. Samanta, S. Dutta and S. K. Ghosh, *Inorganica Chimica Acta* **2020**, *500*, 119205; b) D. M. Chen, N. N. Zhang, C. S. Liu and M. Du, *Acs Applied Materials & Interfaces* **2017**, *9*, 24671-24677.

[90] N. Z. Zhang, D. W. Zhang, J. Zhao and Z. G. Xia, *Dalton Transactions* **2019**, *48*, 6794-6799.
[91] J. Xiong, Y. F. Xiao, J. M. Liang, J. Sun, L. X. Gao, Q. J. Zhou, D. Hong and K. J. Tan, *Spectrochimica Acta Part a-Molecular and Biomolecular Spectroscopy* **2023**, *285*, 121863.
[92] C. Wang, L. Tian, W. Zhu, S. Q. Wang, P. Wang, Y. Liang, W. L. Zhang, H. W. Zhao and G. T. Li, *Acs Applied Materials & Interfaces* **2017**, *9*, 20076-20085.
[93] Y. K. Li, Z. H. Wei, Y. Zhang, Z. F. Guo, D. S. Chen, P. Y. Jia, P. Chen and H. Z. Xing, *Acs Sustainable Chemistry & Engineering* **2019**, *7*, 6196-6203.
[94] T. H. Y. Beglau, M. N. A. Fetzer, I. Boldog, T. Heinen, M. Suta, C. Janiak and G. Yücesan, *Chemistry-a European Journal* **2024**, *30*, e202302765.
[95] F. Bigdeli, M. N. A. Fetzer, B. Nis, A. Morsali and C. Janiak, *Journal of Materials Chemistry A* **2023**, *11*, 22105-22131.
[96] C. Empel, M. N. A. Fetzer, S. Sasmal, T. Strothmann, C. Janiak and R. M. Koenigs, *Chemical Communications* **2024**, *60*, 7327-7330.
[97] R. Oestreich, M. N. A. Fetzer, Y. F. Zhang, A. Schreiber, A. Knebel, M. Suta, C. Janiak, G. Hanna and G. Yücesan, *Angewandte Chemie-International Edition* **2025**, *64*, e202513788.
[98] M. N. A. Fetzer, M. Vieten, L. A. and C. Janiak, *Molecules* **2025**, *30*, 4151.
[99] P. J. Beldon, L. Fábián, R. S. Stein, A. Thirumurugan, A. K. Cheetham and T. Friscic, *Angewandte Chemie-International Edition* **2010**, *49*, 9640-9643.
[100] J. E. Field and D. Venkataraman, *Chemistry of Materials* **2002**, *14*, 962-964.
[101] D. Hall, S. M. Suresh, P. L. dos Santos, E. Duda, S. Bagnich, A. Pershin, P. Rajamalli, D. B. Cordes, A. M. Z. Slawin, D. Beljonne, A. Köhler, I. D. W. Samuel, Y. Olivier and E. Zysman-Colman, *Advanced Optical Materials* **2020**, *8*, 1901627.
[102] O. V. Dolomanov, L. J. Bourhis, R. J. Gildea, J. A. K. Howard and H. Puschmann, *Journal of Applied Crystallography* **2009**, *42*, 339-341.